ORNL/TM-11859

ornl

OAK RIDGE NATIONAL LABORATORY

MARTIN MARIETTA

Ceramic Technology for Advanced Heat Engines Project Semiannual Progress Report for October 1990 Through March 1991

CERAMIC TECHNOLOGY FOR ADVANCED HEAT ENGINES

MANAGED BY
MARTIN MARIETTA ENERGY SYSTEMS, INC.
FOR THE UNITED STATES
DEPARTMENT OF ENERGY

ORNL/TM-11859

Metals and Ceramics Division

CERAMIC TECHNOLOGY FOR ADVANCED HEAT ENGINES PROJECT SEMIANNUAL PROGRESS REPORT FOR OCTOBER 1990 THROUGH MARCH 1991

D. R. Johnson
Project Manager

Date Published: July 1991

Prepared for
U.S. Department of Energy
Assistant Secretary for Conservation and Renewable Energy
Office of Transportation Technologies
Advanced Materials Development Program
EE 04 00 00 0

Prepared by the
OAK RIDGE NATIONAL LABORATORY
Oak Ridge, Tennessee 37831-6285
managed by
MARTIN MARIETTA ENERGY SYSTEMS, INC.
for the
U.S. DEPARTMENT OF ENERGY
under Contract DE-AC05-840R21400

REPORTS PREVIOUSLY ISSUED

ORNL/TM-9325	Period March 1983-September 1983
ORNL/TM-9466	Period October 1983-March 1984
ORNL/TM-9497	Period April 1984-September 1984
ORNL/TM-9673	Period October 1984-March 1985
ORNL/TM-9947	Period April 1985-September 1985
ORNL/TM-10079	Period October 1985-March 1986
ORNL/TM-10308	Period April 1986-September 1986
ORNL/TM-10469	Period October 1986-March 1987
ORNL/TM-10705	Period April 1987-September 1987
ORNL/TM-10838	Period October 1987-March 1988
ORNL/TM-11116	Period April 1988-September 1988
ORNL/TM-11239	Period October 1988-March 1989
ORNL/TM-11489	Period April 1989-September 1989
ORNL/TM-11586	Period October 1989-March 1990
ORNL/TM-11719	Period April 1990-September 1990

Research sponsored by the U.S. Department of Energy, Assistant Secretary for Conservation and Renewable Energy, Office of Transportation Technologies, as part of the Ceramic Technology for Advanced Heat Engines Project of the Advanced Materials Development Program, under contract DE-AC05-84OR21400 with Martin Marietta Energy Systems, Inc.

CONTENTS

SUMMARY 1

0.0 PROJECT MANAGEMENT AND COORDINATION 3

1.0 MATERIALS AND PROCESSING 5

INTRODUCTION 5

1.1 MONOLITHICS 7

1.1.1 Silicon Carbide 7

Improved Processing of Ceramic Composites (Southern Illinois University) 7

1.1.2 Silicon Nitride 16

Sintered Silicon Nitride (AMTL) 16

Microwave Sintering of Silicon Nitride (ORNL) . . . 23

Characterization of Attrition Milled Silicon Nitride Powder (NIST) 32

Novel Si_3N_4 Process (Sullivan) 38

1.1.4 Processing of Monolithics 42

Improved Processing (Norton) 42

Improved Processing (ORNL) 79

Improved Processing (GTE) 84

Processing Science for Si_3N_4 Ceramics (University of California) 155

1.2 CERAMIC COMPOSITES 160

1.2.2 Silicon Nitride Matrix 160

SiC-Whisker-Toughened Silicon Nitride (CCD) 160

In-Situ Toughened Silicon Nitride (CCD) 171

Fabrication of SiC-AlN Composites (University of Michigan) 179

Optimization of Silicon Nitride Ceramics (University of Michigan) 186

1.2.3 Oxide Matrix 191

Dispersion Toughened Ceramic Composite (ORNL) . . . 191

1.2.4 Silicate Matrix 199

Low Expansion Ceramics for Diesel Engine Applications (VPI) 199

1.3 THERMAL AND WEAR COATINGS 211

Fabrication and Testing of Corrosion Resistant Coatings (ORNL) 211

Development of Adherent Ceramics Coatings to Reduce Contact Stress Damage of Ceramics (GTE) 214

Wear-Resistant Coatings (Caterpillar) 220

1.4 JOINING 232

1.4.1 Ceramic-Metal Joints 232

Joining of Ceramics for Heat Engine Applications (ORNL) 232

Analytical and Experimental Evaluation of Joining Silicon Nitride to Metal and Silicon Carbide to Metal for Advanced Heat Engine Applications (GTE) 237

2.0 MATERIALS DESIGN METHODOLOGY 253

INTRODUCTION 253

2.1 MODELING 254

2.1.1 Modeling 254

Microstructural Modeling of Cracks (University of Tennessee) 254

2.2 CONTACT INTERFACES 256

2.2.1 Static Interfaces 256

Elastic Properties and Adherence of Thin Films and Coatings (University of Tennessee) 256

2.2.2 Dynamic Interfaces 261

Studies of Dynamic Contact of Ceramics and Alloys for Advanced Heat Engines (Battelle) 261

2.3 NEW CONCEPTS 268

Advanced Statistical Concepts of Fracture in Brittle Materials (GE) 268

3.0 DATA BASE AND LIFE PREDICTION 283

INTRODUCTION 283

3.1 STRUCTURAL QUALIFICATION 284

Microstructural Analysis of Structural Ceramics (NIST) 284

Microstructural Characterization (ORNL) 295

Project Data Base (ORNL) 306

3.2 TIME-DEPENDENT BEHAVIOR 310

Characterization of Toughened Ceramics (AMTL) . . . 310

Fracture Behavior of Toughened Ceramics (ORNL) . . 313

Cyclic Fatigue of Toughened Ceramics (ORNL) 319

Rotor Data Base Generation (ORNL) 340

Toughened Ceramics Life Prediction (NASA Lewis Research Center) 362

Life Prediction Methodology (Allison) 375

Life Prediction Methodology (GAPD) 385

3.3 ENVIRONMENTAL EFFECTS 398

Environmental Effects in Toughened Ceramics (University of Dayton Research Institute) 398

3.4 FRACTURE MECHANICS 424

Testing and Evaluation of Advanced Ceramics at High Temperature in Uniaxial Tension (North Carolina A&T State University) 424

Standard Tensile Test Development (NIST) 428

Development of a Fracture Toughness Microprobe (Rice University) 440

3.5 NONDESTRUCTIVE EVALUATION DEVELOPMENT 444

Nondestructive Characterization (ORNL) 444

NDE Standards for Advanced Ceramics (ORNL) 449

X-ray Computed Tomographic Imaging (ANL) 450

Nuclear Magnetic Resonance Imaging (ANL) 458

Physicochemical Characterization and Surface Modification of Silicon Nitride Ceramic Powders (University of Wisconsin-Madison) 461

Surface Adsorption (University of Florida) 467

Physicochemical Characterization and Surface Modification of Silicon Nitride Ceramic Powders (Rutgers University) 470

4.0 TECHNOLOGY TRANSFER 491

4.1 TECHNOLOGY TRANSFER 491

4.1.1 Technology Transfer 491

Technology Transfer (ORNL) 491

IEA Annex II Management (ORNL) 492

Characterization of Ceramic Powders (NIST) 499

Ceramic Mechanical Property Test Method Development (NIST) 502

CERAMIC TECHNOLOGY FOR ADVANCED HEAT ENGINES PROJECT SEMIANNUAL PROGRESS REPORT FOR OCTOBER 1990 THROUGH MARCH 1991

SUMMARY

The Ceramic Technology For Advanced Heat Engines Project was developed by the Department of Energy's Office of Transportation Systems (OTS) in Conservation and Renewable Energy. This project, part of the OTS's Advanced Materials Development Program, was developed to meet the ceramic technology requirements of the OTS's automotive technology programs.

Significant accomplishments in fabricating ceramic components for the Department of Energy (DOE), National Aeronautics and Space Administration (NASA), and Department of Defense (DoD) advanced heat engine programs have provided evidence that the operation of ceramic parts in high-temperature engine environments is feasible. However, these programs have also demonstrated that additional research is needed in materials and processing development, design methodology, and data base and life prediction before industry will have a sufficient technology base from which to produce reliable cost-effective ceramic engine components commercially.

An assessment of needs was completed, and a five year project plan was developed with extensive input from private industry. In July 1990 the original plan was updated through the estimated completion of development in 1993. The objective of the project is to develop the industrial technology base required for reliable ceramics for application in advanced automotive heat engines. The project approach includes determining the mechanisms controlling reliability, improving processes for fabricating existing ceramics, developing new materials with increased reliability, and testing these materials in simulated engine environments to confirm reliability. Although this is a generic materials project, the focus is on the structural ceramics for advanced gas turbine and diesel engines, ceramic bearings and attachments, and ceramic coatings for thermal barrier and wear applications in these engines. This advanced materials technology is being developed in parallel and close coordination with the ongoing DOE and industry proof of concept engine development programs. To facilitate the rapid transfer of this technology to U.S. industry, the major portion of the work is being done in the ceramic industry, with technological support from government laboratories, other industrial laboratories, and universities.

This project is managed by ORNL for the Office of Transportation Technologies, Office of Transportation Materials, and is closely coordinated with complementary ceramics tasks funded by other DOE offices, NASA, DoD, and industry. A joint DOE and NASA technical plan has been established, with DOE focus on automotive applications and NASA focus on aerospace applications. A common work breakdown structure (WBS) was developed to facilitate coordination. The work described in this report is organized according to the following WBS project elements:

0.0 Management and Coordination

1.0 Materials and Processing

- 1.1 Monolithics
- 1.2 Ceramic Composites
- 1.3 Thermal and Wear Coatings
- 1.4 Joining

2.0 Materials Design Methodology

- 2.1 Modeling
- 2.2 Contact Interfaces
- 2.3 New Concepts

3.0 Data Base and Life Prediction

- 3.1 Structural Qualification
- 3.2 Time-Dependent Behavior
- 3.3 Environmental Effects
- 3.4 Fracture Mechanics
- 3.5 Nondestructive Evaluation Development

4.0 Technology Transfer

- 4.1 Technology Transfer

This report includes contributions from all currently active project participants. The contributions are arranged according to the work breakdown structure outline.

0.0 PROJECT MANAGEMENT AND COORDINATION

D. R. Johnson
Oak Ridge National Laboratory

Objective/scope

This task includes the technical management of the project in accordance with the project plans and management plan approved by the Department of Energy (DOE) Field Office, Oak Ridge, and the Office of Transportation Technologies. This task includes preparation of annual field task proposals, initiation and management of subcontracts and interagency agreements, and management of ORNL technical tasks. Monthly management reports and bimonthly reports are provided to DOE; highlights and semiannual technical reports are provided to DOE and program participants. In addition. the program is coordinated with interfacing programs sponsored by other DOE offices and federal agencies, including the National Aeronautics and Space Administration (NASA) and the Department of Defense (DoD). This coordination is accomplished by participation in bimonthly DOE and NASA joint management meetings, annual interagency heat engine ceramics coordination meetings, DOE contractor coordination meetings, and DOE Energy Materials Coordinating Committee (EMaCC) meetings, as well as special coordination meetings.

1.0 MATERIALS AND PROCESSING

INTRODUCTION

This portion of the project is identified as project element 1.0 within the work breakdown structure (WBS). It contains four subelements: (1) Monolithics, (2) Ceramic Composites, (3) Thermal and Wear Coatings, and (4) Joining. Ceramic research conducted within the Monolithics subelement currently includes work activities on green state ceramic fabrication, characterization, and densification and on structural, mechanical, and physical properties of these ceramics. Research conducted within the Ceramic Composites subelement currently includes silicon carbide, silicon nitride, and oxide-based composites. Research conducted in the Thermal and Wear Coatings subelement is currently limited to oxide-base coatings and involves coating synthesis, characterization, and determination of the mechanical and physical properties of the coatings. Research conducted in the Joining subelement currently includes studies of processes to produce strong stable joints between zirconia ceramics and iron-base alloys.

A major objective of the research in the Materials and Processing project element is to systematically advance the understanding of the relationships between ceramic raw materials such as powders and reactant gases, the processing variables involved in producing the ceramic materials, and the resultant microstructures and physical and mechanical properties of the ceramic materials. Success in meeting this objective will provide U.S. companies with new or improved ways for producing economical, highly reliable ceramic components for advanced heat engines.

1.1 MONOLITHICS

1.1.1 Silicon Carbide

Improved Processing of Ceramic Composites
D. E. Wittmer (Southern Illinois University)

Objective/scope

The purpose of this work is to continue the investigation of the turbomilling process as a means of improved processing for SiC whisker-ceramic matrix composites and dispersion of matrix powders prior to composite processing.

Technical progress

Phase II is divided into 4 major tasks:

Task 1. Beneficiation of SiC whiskers.
Task 2. Development of aspect ratio reduction parameters.
Task 3. Dispersion Trials and ß-Si_3N_4 Seed Development
Task 4. Final Report

Task 1. Beneficiation of SiC whiskers

Task 1 was completed ahead of schedule as reported in the previous semi-annual report.

Task 2. Development of aspect ratio reduction parameters.

Task 2 was completed ahead of schedule with respect to the new target date. The pyrex vertical flow chamber, designed for measuring whisker lengths on the Lasentec-150 fiber analyzer, was constructed and passed the preliminary test under static conditions. Dynamic measurements of Si_3N_4 slurry particle size were completed on standard solutions and dilute Si_3N_4 suspensions.

Task 3. Dispersion Trials and β-Si_3N_4 Seed Development

Dispersion Trials

During this reporting period, microstructural evaluation and fractography were completed for the following hot-pressed compositions, that were processed by turbomilling and pressure casting:

- Ball milled A2Y6 matrix
- Turbomilled A2Y6 matrix
- 25 vol.% SiCw-Si_3N_4 composite containing as-received SiCw[1]
- 25 vol.% SiCw-Si_3N_4 composite containing beneficiated coarse SiCw fraction
- 25 vol.% SiCw-Si_3N_4 composite containing beneficiated fine SiCw fraction
- 25 vol.% SiCw-Si_3N_4 composite containing beneficiated, heat-treated, coarse SiCw fraction
- 25 vol.% SiCw-Si_3N_4 composite containing beneficiated, heat-treated, fine SiCw fraction

4-Pt. Flexural strength

Fig. 1 represents the summary of 4-pt. flexural strength results and for the Si_3N_4 matrices and the SiCw-Si_3N_4 composite formulations evaluated.

A2Y6-Si_3N_4 Matrix

It is clear from these results that the flexural strength of the Si_3N_4 matrix prepared by turbomilling (TMM σ_{ave}=1021 MPa) was significantly improved, compared with the same composition processing by ball milling (BMM σ_{ave}=449 MPa). The low strength for the ball milled samples is due to the high porosity and presence of sintered agglomerates, associated with poor dispersion and deagglomeration of the matrix powders in the ball mill. The flexural strength of the turbomilled matrix was also much higher than reported previously for the baseline Si_3N_4 from prior work (σ_{ave}=660 MPa), likely due to longer turbomilling time (increased from 30 to 60 min).

Si_3N_4 Composites Containing As-Received SiCw

Similar behavior was observed in comparing the ball milled composite (BMC) with the turbomilled composite (TMC), both containing as-received SiCw. The low strength values for the ball milled composite samples (σ_{ave}=449 MPa) can be attributed to the high porosity (≈10-12 %), associated with agglomerated SiCw and matrix materials. These flaws were easily observed by optical microscopy and SEM. The high

[1] For this work Grade 1 silicon carbide whiskers from the former American Matrix Inc. (AMI) were used. The AMI whisker technology and equipment has recently been purchased by Advanced Refractories Technologies, Buffalo, NY.

strength of the turbomilled composite samples (σ_{ave} = 1093 MPa) is most likely due to the improved dispersion and deagglomeration of the SiCw and matrix materials, resulting in near theoretical hot-pressed density. This strength is similar to 925 MPa reported in prior work for the same composition processed by turbomilling.

Si_3N_4 Composites Containing Beneficiated SiCw

The beneficiation routine used for separating the fine and coarse SiCw fractions produced about 40 wt.% fine and 60 wt.% coarse SiCw. Material losses to the screens and from material handling were less than 5% of the initial batch weight. The flexural strengths was somewhat reduced for composites containing beneficiated, fine SiCw (FF) (σ_{ave} = 945 MPa), and significantly reduced for composites containing beneficiated, coarse SiCw (CF) (σ_{ave} = 759 MPa), compared to composites containing as-received SiCw (TMC). Results from preliminary SEM and optical microscopy indicate that the fine fraction is comprised largely of fine and ultra-fine particulate and fine, small diameter SiCw. The effect of this large amount of fine particulate would be a decrease in the volume of SiCw per unit weight present in the composite for the given formulation. It is reasonable for composites containing the coarse SiCw fraction to suffer a significant reduction in strength, since the coarse fraction contains most of the large whiskers, particulate, and agglomerates from the as-received SiCw, which could be acting as critical flaws. SEM and optical analyses of the coarse SiCw fraction revealed an increased number of large particulate, compared to the fine SiCw fraction. The high volume of large particulate effectively decreases the number and volume of SiCw per unit weight of the composite. It is not surprising that such a reduction in strength was observed for composites containing the coarse SiCw fraction, since the sedimentation process used for beneficiation would tend to concentrate the known large sintered agglomerates and unreacted raw materials (primarily silica) from the whisker making process in the coarse fraction.

Si_3N_4 Composites Containing Beneficiated, Heat-Treated SiCw

Heat-treating the beneficiated, fine SiCw fraction (FHT) was observed to further reduce the composite flexural strength (σ_{ave} = 760 MPa). These results were somewhat expected, since the thermal treatment was expected to improve debonding of the whiskers by removal of the silica layer from the whisker surfaces. Increasing the debonding would result in less load transfer to the SiCw, and should allow for greater whisker pull-out; hence lower strength but higher fracture toughness. Reduction in flexural strength may be due to partial digestion of the fine

SiCw, during thermal treatment process (observed optically), which would tend to weaken the whiskers.

The flexural strength for composites containing beneficiated, coarse, heat-treated SiCw (CHT) appear to be unaffected by the thermal treatment. There is no clear explanation for these results, since the heat treatment was expected to reduced the whisker-matrix bond strength, which should have resulted in less load transfer and lower strength. However, these results could be related to the composition of the coarse fraction. Also, the coarse SiCw had significantly larger diameters than the fine fraction, which might be relatively unaffected by any slight surface decomposition during heat-treatment.

Fracture toughness

Fig. 2 represents a summary of the fracture toughness results obtained for Si_3N_4 matrices and the SiCw-Si_3N_4 composite formulations evaluated.

A2Y6-Si_3N_4 Matrix

As with the flexural strength, the fracture toughness for the turbomilled Si_3N_4 matrix (K_{IC}=5.7 MPa-$m^{½}$) was nearly double the fracture toughness for the ball milled Si_3N_4 matrix (K_{IC}=3.0 MPa-$m^{½}$). These results are not surprising, since the ball milled matrix was observed to contain a greater number of flaws, related to porosity and sintered agglomerates, associated with poor dispersion and deagglomeration of the matrix powders in the ball mill.

Si_3N_4 Composites Containing As-Received SiCw

Similar to the matrix results, the turbomilled composite, containing as-received SiCw (TMC), had greater than twice the fracture toughness of the ball milled composite (BMC). (TMC K_{IC}=10.2 MPa-$m^{½}$ compared to BMC K_{IC}=4.8 MPa-$m^{½}$.) Again, this would be expected since the ball milled composite was observed, optically and by SEM, to contain high porosity and agglomerated SiCw and matrix materials, which would reduce both strength and fracture toughness.

Si_3N_4 Composites Containing Beneficiated SiCw

There is only a slight decrease in the fracture toughness when comparing the results for turbomilled composites, containing beneficiated, fine SiCw (FF) with composites containing as-received SiCw. (FF K_{IC}=9.3 MPa-$m^{½}$ compared to TMC K_{IC}=10.2 MPa-$m^{½}$.) Preliminary results from

optical microscopy examination indicate that the fine fraction contains primarily whiskers with L<12 μm and a large volume of fine and ultra-fine particulate. Since mainly the coarse particulate and larger diameter whiskers with L>12 μm were removed during the beneficiation process, the toughness should remain essentially unchanged.

Further decrease in fracture toughness was observed for composites containing beneficiated, coarse SiCw. (CF K_{IC}=6.9 MPa-$m^{1/2}$) This may be due to the much lower volume of SiCw per unit weight of the composite for the coarse fraction and the composition of the coarse particulate.

Si_3N_4 Composites Containing Beneficiated, Heat-Treated SiCw

Heat-treating the beneficiated, fine SiCw caused a slight decrease in fracture toughness (FHT K_{IC}=8.6 MPa-$m^{1/2}$), instead of the expected increase that one might expect from decreasing the whisker-matrix bond strength. This decrease could be associated with the thermal degradation and weakening of the fine whiskers.

Fracture toughness was somewhat increased by heat-treating the beneficiated, coarse SiCw (CHT K_{IC}=8.1 MPa-$m^{1/2}$), but was still below that observed for either the fine or fine, heat-treated, fractions, and significantly less than for composites containing the as-received SiCw. This increase in toughness for the heat-treated coarse SiCw would be expected if the whisker-matrix bond strength was reduced, since it would allow for more whisker pull-out.

General comments

From these results it would appear that there is no need to beneficiate or heat-treat AMI SiCw, since neither appeared to improve strength or fracture toughness. However, it should be noted that these results were for room temperature properties only. It is clear from these results that the beneficiation and heat-treating processes used in this research were detrimental to room temperature strength and fracture toughness. This is not all that surprising, since the room temperature properties of the composite depend to a large extent on the volume and composition of the glass phase of the Si_3N_4 matrix and the whisker-matrix interface. The surface composition of the whiskers can also have a significant effect on the near-surface composition of the whisker-matrix interface. Therefore, it is possible that the high-temperature properties could be improved by using beneficiated or beneficiated, heat-treated whiskers. Improvement in high-temperature properties for composites containing heat-treated SiCw has be reported in previous bimonthly and semiannual reports by T. Tiegs, ORNL.

ß-Si_3N_4 Seed Development

In preliminary work four commercial Si_3N_4 powders without any additives were investigated (UBE, E-10 and E-5 and H. C. Starck, LC-12SX and LC-10N). Based on previous work, each powder was heated to 1875°C for 4h in a closed BN crucible in order to effect conversion of α to ß-Si_3N_4. The idea was to use the ß-Si_3N_4 as a source of seed material for enhanced microstructural control in sintered Si_3N_4 compositions. However, for the thermal conditions employed the powders did not completely convert to the ß phase and therefore were not suitable as seed materials. As a result, small additions of rare earth oxides and other oxides were investigated as nucleating agents for the UBE Si_3N_4 powders.

Initially Y_2O_3 was added to the Si_3N_4 powders by turbomilling for 1 h. Several heat treatment schedules were used to explore the effect on nucleation and growth of the ß-Si_3N_4. E-10 doped with Y_2O_3 converted completely to ß-Si_3N_4, but the morphology of the resulting ß crystals was dependent on the heating schedule. Uniform seeds approximately 1-1.5 μm in diameter by 4-5 μm long were obtained by heating to 1800°C for 4 h. E-5 doped with Y_2O_3 also converted completely to ß-Si_3N_4 but the ß crystals produced had both elongated and equiaxed morphology. There was also a large variation in diameter and length of the elongated fraction.

La_2O_3 additions to E-10 Si_3N_4 were also investigated. All of the compositions investigated were found to be completely converted to ß-Si_3N_4, however the diameter of the crystals formed were much smaller than obtained for the same doping with Y_2O_3.

An addition of 2% Al_2O_3 with 0.5% MgO was also made to the E-10 Si_3N_4 and the materials was heat treated under the same conditions which produced complete ß-Si_3N_4 conversion for Y_2O_3 doping. This resulted in only a 24% conversion to ß-Si_3N_4 and no elongated grains were observed.

A selected Si_3N_4 composition (A2Y6), containing 5 and 10 wt.% additions of ß seed, has been made by turbomilling and pressure casting. Pressure cast discs of the baseline Si_3N_4 (composition without seeds) and the seeded Si_3N_4 have been sintered to 99-100% of theoretical density at 1880°C for 4 h at 300 psig N_2. Machined test bars (MIL Std.-Type B) have been received for the base line Si_3N_4 and 5 wt.% seed addition. Based on a very limited number of test bars 4-pt flexural strength was found to be 925-1025 MPa for the baseline Si_3N_4 and 750-950 MPa for the seeded Si_3N_4. Fracture toughness, using the Lawn and Cook modified indentation method was found to be 8-10 MPa-$m^{1/2}$ for the baseline Si_3N_4 and 10-13 MPa-$m^{1/2}$ for the seeded Si_3N_4. These results would suggest that the seeded Si_3N_4 developed a more mature ß-Si_3N_4 grain structure than the baseline composition. The microstructures are presently being examined to determine if the difference in microstructure is observable. Additional materials are being prepared to produce more statistically significant data.

Based on these results a 6 months extension of this project has was requested and approved.

Status of milestones

1. Run Beneficiation Trials and Report in Bimonthly	Completed
2. Run Aspect Ratio Reduction Trials and Report in Bimonthly	Completed
3. Run Matrix Dispersion Trials and Report in Bimonthly	On Schedule New Target
4. Rough Draft of Final Report to Contract Monitor	On Schedule New Target

Publications

D. E. Wittmer and T. E. Paulson, "Evaluation of SiCw-Si_3N_4 Composites Containing Beneficiated/Heat-Treated SiCw," Ceramic Engineering and Science Proceedings, in review.

Presentations

D. E. Wittmer* and T. E. Paulson, "Evaluation of SiCw-Si_3N_4 Composites Containing Beneficiated/Heat-Treated SiCw," 15th Annual Conference on Composites, Materials and Structures, Jan. 16-18, 1991.

Fig. 1 Summary of 4-Pt. Flexural Strengths

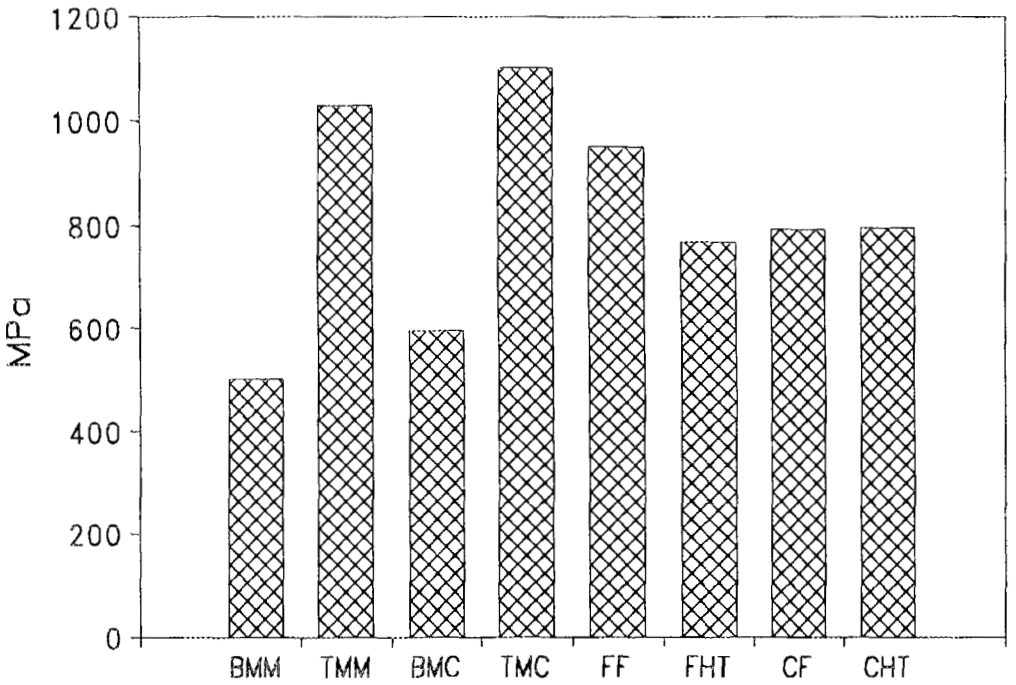

BMM: Ball Milled Matrix
TMM: Turbomilled Matrix
BMC: Ball Milled Composite; As-Received SiCw
TMC: Turbomilled Composite; As-Received SiCw
FF: Turbomilled Composite; Beneficiated, Fine SiCw
FHT: Turbomilled Composite; Beneficiated, Fine, Heat-Treated SiCw
CF: Turbomilled Composite; Beneficiated, Coarse SiCw
CHT: Turbomilled Composite; Beneficiated, Coarse, Heat-Treated SiCw

Fig. 2 Summary of Fracture Toughness Results

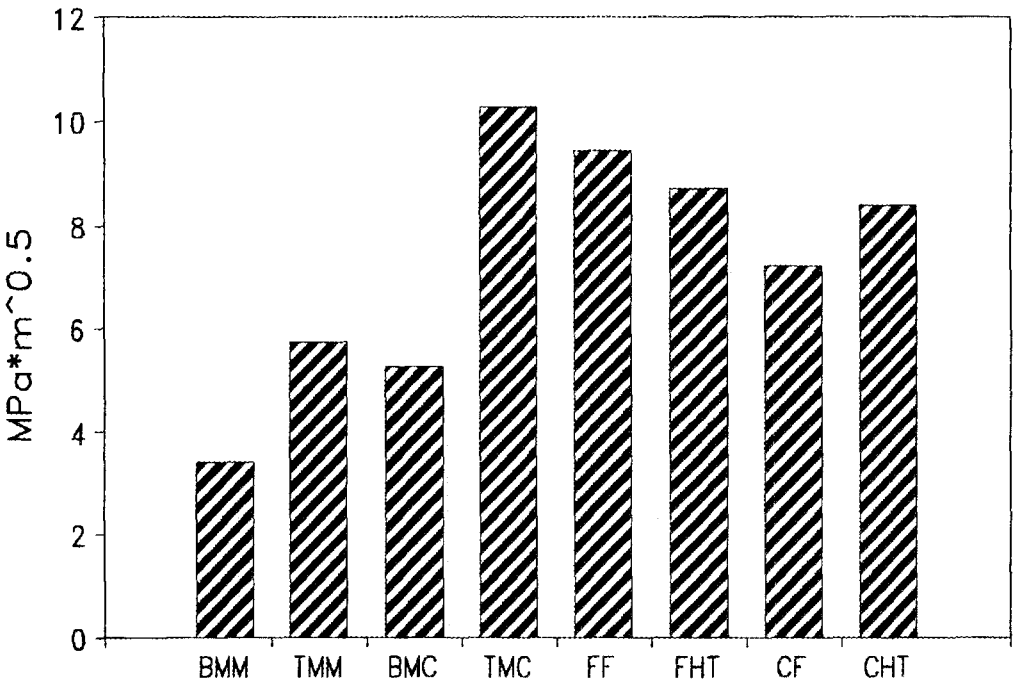

BMM: Ball Milled Matrix
TMM: Turbomilled Matrix
BMC: Ball Milled Composite; As-Received SiCw
TMC: Turbomilled Composite; As-Received SiCw
FF: Turbomilled Composite; Beneficiated, Fine SiCw
FHT: Turbomilled Composite; Beneficiated, Fine, Heat-Treated SiCw
CF: Turbomilled Composite; Beneficiated, Coarse SiCw
CHT: Turbomilled Composite; Beneficiated, Coarse, Heat-Treated SiCw

1.1.2 Silicon Nitride

Sintered Silicon Nitride

G. E. Gazza (Army Materials Technology Laboratory)

Objective/scope

The program is currently conducted on contract to Ceradyne Inc. with support from AMTL. The contract has the overall objective of developing scale-up processing conditions for a silicon nitride material having the general composition 85.8m/o Si3N4-4.73m/o Y2O3-9.47m/o SiO2-1.0m/o Mo2C and characterizing the properties of this composition with the goal of producing complex components for testing in related heat engine programs. The first task of the program will concentrate on processing studies and data base generation while the second task will focus on producing and characterizing engine components.

Technical progress

Mixing Experiments: The silica powder (Cab-O-sil) is highly agglomerated due to its high surface area (180 m^2/g). Dilute suspensions of this powder in water were used to determine the most efficient method of dispersing the powder. The degree of dispersion was measured by determining the silica agglomerate size using a centrifugal particle size analyzer (Horiba CAPA 300). Suspensions were mixed mechanically, ultrasonically, and using both methods simultaneously. The combination of ultrasonic with mechanical mixing was shown to reduce the silica-water agglomerates in the 10-50 um range by a factor of 10 over the mechanically mixing alone. The silica suspension obtained by the combined mixing contained > 90v/o of agglomerates below 1 um in size whereas the mechanically mixed suspensions contained 95% greater than 1 um. This technique was incorporated in the batch preparation process for Mix 4 and 5 which were used for Matrix 3.

Raw Materials: A new source of of Mo_2C was used for Matrix 3 (Hermann C. Starck grade 1.5-2.5). This powder had an average particle size of 3.2 um. The use of this powder eliminates the extensive powder preparation step required with the original Mo_2C powder.

Batch Preparation: A dilute suspension of the silica was prepared by ultrasonic plus mechanical mixing according to the previously described procedure. The other sintering additives, Y_2O_3 and Mo_2C, were added to the suspension and dispersed in the same way. This suspension was added to the attritor mill. The Si_3N_4 was then added to the attritor mill and the entire mixture was processed for 1 hour. The slurry was then spray dried. Spray dried powder and "green" body characterization is summarized in Table I. The solids content of the batched slurry was significantly increased from 38% to 55% with a decrease in viscosity from 300 cps to 150 cps. This improvement is attributed to the improved mixing.

Sintering: The sintering variables investigated were:

(1) Temperature (1900C, 1950C)
(2) Time (3, 5 hours)
(3) Packing powder composition (0, 2% silica)
(4) Amount of Packing powder (Buried, Covered)
(5) Amount of Mo_2C (0, 1m/o)

The experiments were performed in four sintering runs (MTL 11-14) using an L32 array. The results were analyzed using the QUEST software program.

Density: The experiment showed that densities of 100 T.D. were achieved. The analysis showed that the density was affected by two processing variables; time and packing powder composition.

Weight Loss: The weight losses in Matrix 3 were reduced to 1-5%. Typically, the Mo_2C parts exhibited higher weight losses than the 0% Mo_2C material for the same processing conditions.

Phase Composition and Microstructure: The phase composition of the Matrix 3 samples consisted of β-Si_3N_4, and mainly H-phase. In some cases, $Y_2Si_2O_7$, Y_2SiO_5, or $Y_2Si_3N_4O_3$ was observed. It appears that the phase composition is a function of both the sintering temperature and sintering environment.

Matrix 3 Confirmation Runs:

A total of five runs (MTL 15-19) were made with Matrix 3 samples (mixes 4 and 5). MTL run 15 was performed to determine the lower limit for the sintering temperature for the compositions. The remaining runs investigated the sinterability of large samples (over 1/2" thick).

Densities:

MTL 15: Run at 1850C for 5 hours with small pellets produced dense samples in 2% SiO2 packing powder. Samples sintered in 0% packing powder were only 90-95% dense.

MTL 16-17: Performed at 1850C and 1900C on larger samples (2"x 1"x 1/2") packed in 2% SiO2 powder (based on MTL 15). Samples form Mix 4 (no Mo2C) were dense but samples from Mix 5 (1m/o Mo2C) were bloated. The bloated samples had dense edges and porous interiors with large cracks produced by gas buildup.

MTL 18-19: Performed at 1900C for 3.5 hours at 0.66 MPa nitrogen pressure (MTl 18) and 5 hours with a regular high pressure schedule (MTL 19) using both packing powders and various sample sizes. These experiments were designed to find the cause of bloating. Out of all samples in the runs, only large rods containing Mo2C and placed in 2% SiO2 powder exhibited bloating. Other samples has densities from 90 to 99% of theoretical. Generally, densities of Mo2C containing samples or samples from 2% SiO2 packing powder had higher densities if not bloated.

Phase Composition:

The interiors of bloated samples has 3-5 times more Mo2C than in regular samples. The edges of the same samples contained regular amounts of Mo2C in addition to H phase or yttrium silicate. The data indicates that the 2% SiO2 packing powder accelerated the sintering near the sample edges well beyond the closed porosity stage. The interior of the sample meanwhile was still porous and did not have a chance to finalize its gas evolving reactions with Mo2C, therefore causing bloating. Mix 4 samples did not have a bloating problem because no Mo2C was present. Small samples with Mo2C (pellets) also did not bloat because their cross section thickness was roughly twice the thickness of the dense surface layer on the bloated samples. Samples placed in 0% SiO2 packing powder did not bloat because the reactions with Mo2C had a chance to be completed before the sample edges densified, followed by uniform densification of the sample as a whole.

Matrix 4:

Matrix 4 objectives were (1) to eliminate the 40-100 um porosity observed in previously sintered samples by improving the dispersion of the Si3N4 powder and (2) to adjust the powder composition by adding more

silica to the mix in order insure the presence of the Y2Si2O7 phase after sintering.

Composition:

Powder compositions were adjusted by following the general formula given in the introduction. However, in this case, there was no compensation for any SiO2 which may be present in the Si3N4 powder. Earlier components assumed a contribution of SiO2 from the Si3N4 powder. The actual weight percents of the powders used are given in Table II.

The composition adjustment was done for two reasons; (1) to ensure the final phase composition of the material contains the yttrium disilicate phase, and (2) to prevent bloating of Mo2C containing samples sintered in packing powders containing silica.

HCST Mo2C powder (grade 1.5-2.5) was again used in Matrix 4. The average particle size of the powder was measured to be 3.2 um which is in good agreement with SEM observations.

Powder Preparation:

Matrix 4 (mixes 6 and 7) powder batches were prepared using an ultrasonic chamber placed in line with the recirculating attritor mill. The flow rate through the ultrasonic chamber was approximately 100 ml/s of slurry.

Powder dispersion was started by adding SiO2, Y2O3, (and Mo2C) to the required amount of water (including dissolved binders) and mechanically dispersing the mixture in the attritor. After 2 min. in the attritor, the ultrasonic was turned on for 20 minutes. Finally, the required amount of Si3N4 powder was added. The attritor and the ultrasonic ran simultaneously for 1 hour. The pH of the slurry was adjusted to 9 with NH4OH. Viscosity of the slurry was adjusted to 150 cps by adding up to 5 ml of dispersant and wetting agent. The slurry was pumped out of the attritor, screened through a 325 mesh screen, and then spray dried.The powder was isopressed into 4" long, 1/2" diameter rods at 15,000 and 25,000 psi. Each rod was sliced into four pieces of approximately equal lengths which were used as sintering samples. The samples were burned out in air. Examination of the binderless sample surface showed that the dispersion of powders were uniform.

Sintering:

Three sintering runs were performed at 1900C, 1850C, and 1800C with a five hour hold at temperature (MTL 20-22). Packing powder with 0% and 2% SiO2 were used in each run with two samples of each composition packed in each powder. The sintering data from these runs are summarized in Tables III-V.

Densities:

In all three sintering runs (1800-1900C) theoretical densities were achieved in all samples irrespective of packing powder, isopressing pressure or material composition. Bloating was not observed in any of the samples. Lower sintering temperature and absence of bloating are a result of the composition adjustment in the samples.

Linear Shrinkage:

Linear shrinkages were measured for samples in run MTL 20 for samples isopressed at 15000 and 25000 psi (Table III). Shrinkages range from 20 to 25% and are higher for samples pressed at 15000 psi.

Weight Losses:

Weight losses remained in the 2-5% range despite the increase in the SiO2 content. The presence of SiO2 in the packing powder significantly reduced the weight losses in both material compositions.

The weight losses also decreased with the decrease in the sintering temperature as seen in Figure 1.

Phase Composition:

Phase composition of all Matrix 4 samples consisted of ▌-Si3N4 and Y2Si2O7 in two distinctly different forms as found on JCPDS card nos. 22-1103 (Y2Si2O7) and 38-223 (a-Y2Si2O7). It appears that the a-Y2Si2O7 is preferred in samples sintered in 0% SiO2 packing powder and the Y2Si2O7 in 2% packing powder (Tables III-V).

Microstructure:

Microstructure of samples from all Matrix 4 sintering runs was greatly improved over previous Matrices with respect to porosity. Pores over 20-30 um in size have been eliminated. Presently, samples with Mo2C tended to be more porous than without Mo2C. Grain size of the samples sintered at the three different temperatures did not appear to change substantially. Samples that did not contain Mo2C had a distinct macrostructure in the cross-section consisting of concentric rings of different shades of gray. This macrostructure had a certain dependence on the composition of the packing powder. Conversely, Mo2C containing samples were uniformly dark gray/black.

Hardness and Fracture Toughness:

Hardness (Vickers at 5 kg load) and fracture toughness values were measured. Hardness values were between 1400 and 1450 kg/sq.mm and apparently not dependent on sintering conditions. The toughness values were between 6.9 and 7.5 MPa/mm1/2 also independent of sintering temperature.

Established milestones

(A) Establish powder processing approach for preparing selected composition. Determine preferred sintering conditions. Generate data base for room temperature and high temperature properties.

July 1991

(B) Fabricate, inspect, and make components available for engine testing in a gas turbine ceramic component development/evaluation program.

July 1992

TABLE I

Batch Powder/Green Compact Characterization

Batch	Comp. I	Comp.II
Mix No.	4	5
Vol.% Solids	45	55
pH	8.5	8.5
Viscosity (cps)	20	150
Spray dried Powder		
Bulk Density (g/cc)	0.61	0.67
Tap Density (g/cc)	0.74	0.75
Green Compact		
Green Density (g/cc)	1.64	1.66
Compaction Ratio	2.66	2.48

TABLE II

Powder Compositions

	Powder	Weight %
Mix 6	Si_3N_4	88.03
	Y_2O_3	7.81
	SiO_2	4.16
Mix 7	Si_3N_4	86.60
	Y_2O_3	7.78
	SiO_2	4.14
	Mo_2C	1.48

TABLE III

MTL 20- 1900C-5 hours

packing powders: (1) 0% SiO_2 (2) 2% SiO_2
parts: rods: mix 6 (0 Mo_2C) mix 7 (1m/o Mo_2C)
crucible - graphite

parts	mix 6		mix 7	
pack.powder	1	2	1	2
wt. loss (%)				
15000 psi	3.400	2.400	5.000	3.000
25000	3.100	1.700	6.500	2.800
25000	3.200	2.800	2.500	3.000
density				
15000 psi	3.272	3.267	3.292	3.288
25000	3.270	3.250	3.300	3.273
25000	3.274	3.257	3.280	3.282
% theoret.				
15000 psi	1.004	1.002	1.001	0.999
25000	1.003	0.997	1.003	0.995
25000	1.004	0.999	0.999	0.998
Shrinkage %				
15000 psi (diam)	22.500	22.500	22.500	22.500
(length)	26.500	25.600	24.200	22.800
25000 (diam)	20.900	21.900	20.000	21.000
(length)	20.800	21.100	21.000	21.500
Hardness (kg/sq.mm)	1416		1434	
Tough.(MPam1/2)	7.5		6.8	
Phase Comp.	a-Y2Si2O7		a-Y2Si2O7 Mo2C (?)	a-Y2Si2O7 MoSi2

TABLE IV

MTL 21-1850C-5 hours

packing powders: (1) 0% SiO2 and (2) 2% SiO2
parts/rods: mix 6 (0 Mo2C) mix 7 (1m/o Mo2C)
crucible -graphite

parts	mix 6		mix 7	
pack. powder	1	2	1	2
weight loss (%)				
15000 psi	3.100	1.000	4.700	2.700
25000	2.900	2.200	4.500	2.200
density 15000	3.270	3.256	3.299	3.292
25000	3.274	3.267	3.297	3.288
% theor.15000	1.003	0.999	1.003	1.001
25000	1.004	1.002	1.002	0.999
Hardness (kg/sq.mm)	1401	1430	1436	1401
Tough.(MPam1/2)	3.4	6.6	7.2	6.6
Phase Comp. + β-Si3N4	a-Y2Si2O7	a-Y2Si2O7	a-Y2Si2O7 (Mo2C (?) MoSi2 (?)	Y2Si2O7 MoSi2

TABLE V

MTL 22-1800C-5 hours

pack. powder: (1) 0% SiO2 (2) 2% SiO2
parts/rods: mix 6 (0 Mo2C) mix 7 (1m/o Mo2C)
crucible -graphite

Parts	mix 6		mix 7	
pack. powder	1	2	1	2
weight loss (%)				
	2.900	1.500	4.200	3.000
	2.800	1.200	4.300	1.800
density	3.263	3.255	3.286	3.279
	3.273	3.256	3.290	3.258
% theor.	1.001	0.998	0.999	0.997
	1.004	0.999	1.000	0.990
Hardness (kg/sq.mm)	1436	1420		1347
Tough.(MPam1/2)	7.2	6.9		7.4

Phase Comp.	a-Y2Si2O7	Y2Si2O7	a-Y2Si2O7	Y2Si2O7
+ β-Si3N4				

a-Y2Si2O7 (38-223)
Y2Si2O7 (22-1103)

Microwave Sintering of Silicon Nitride

T. N. Tiegs, J. O. Kiggans, M. K. Ferber, K. L. More, C. M. Hubbard, H. D. Kimrey, and D. W. Coffey (Oak Ridge National Laboratory)

Objective/scope

The objective of this research element is to identify those aspects of microwave processing of silicon nitride that might (1) accelerate densification, (2) permit sintering to high density with much lower levels of sintering aids, (3) lower the sintering temperature, or (4) produce unique microstructures. The investigation of microstructure development is being done on dense silicon nitride materials annealed in the microwave furnace. The sintering of silicon nitride involves two approaches. The first approach comprises heating of silicon nitride and sialon powder compositions in the 2.45- or 28-GHz units. The second approach deals with using reaction-bonded silicon nitride as the starting material and is done entirely in the 2.45-GHz microwave furnace.

Technical highlights

Sintering of silicon nitride

A series of samples have been fabricated to investigate the effects of alternative coupling methods to improve sintering of the Si_3N_4 materials in the microwave. Densification behavior for the samples with various additive contents is summarized in Fig. 1. As expected, increasing the additive content improved

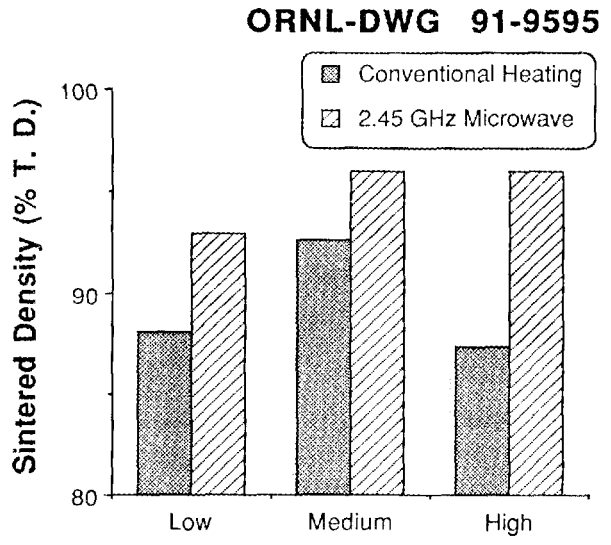

Fig. 1. Increasing the sintering additive content improves the heating efficiency and densification of Si_3N_4 materials. Low contained 6 % Y_2O_3 and 2 % Al_2O_3, medium contained 9 % Y_2O_3 and 3 % Al_2O_3, and high contained 12 % Y_2O_3 and 4 % Al_2O_3. The low and medium specimens were turbomilled and slip-cast, while the high samples were ball milled and iso-pressed. Sintering was done at 1750°C for 1 h. The lower densification for the high additive contents is a result of the powder compact fabrication techniques and not the sintering conditions.

densification. Comparison of the two heating methods showed that, in every case, higher densities were obtained for the microwave-sintered samples as compared to conventional heating at comparable conditions. The effect of using La_2O_3 in place of Y_2O_3 as a sintering aid is shown in Fig. 2. Because of the lower melting point for the eutectic in the La_2O_3-Al_2O_3 system, good densification was observed for both the conventional and microwave-sintered materials. Elongated grain growth was observed for both densification methods (Fig. 3).

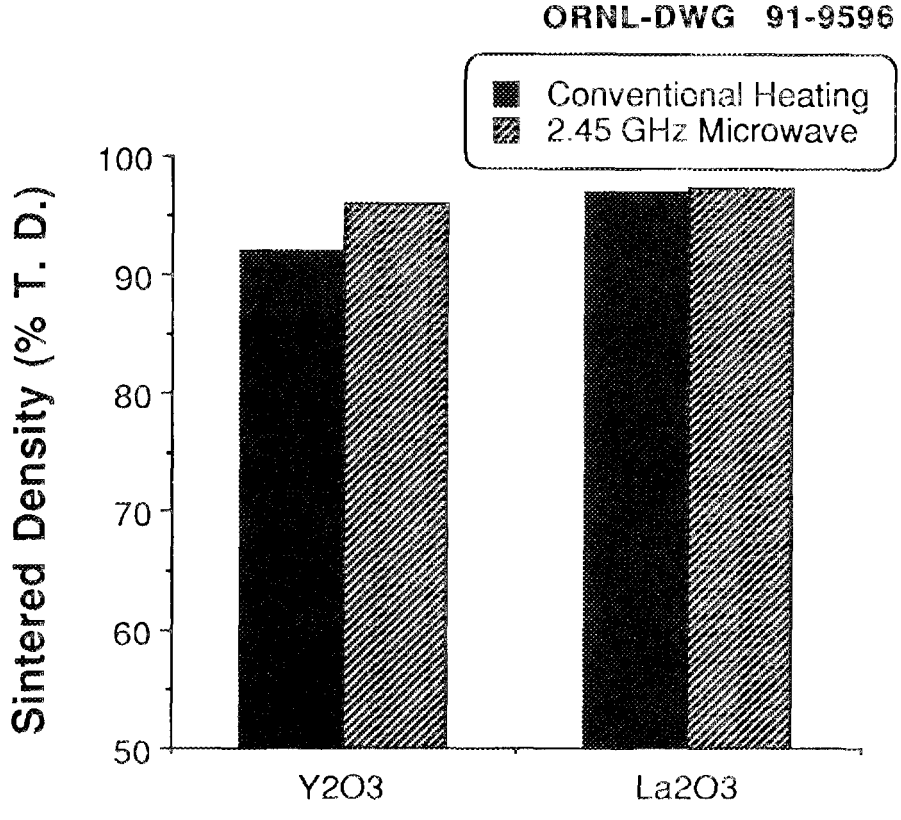

Fig. 2. Effect of Y_2O_3 and La_2O_3 sintering additives on densification of Si_3N_4 materials. Y_2O_3 contained 9 % Y_2O_3 and 3 % Al_2O_3; La_2O_3 contained 9 % La_2O_3 and 3 % Al_2O_3. The specimens were turbomilled and slip-cast. Sintering was done at 1750°C for 1 h.

Additional coupling additives to the silicon nitride compacts are also being examined for improving the heating uniformity. Samples containing aluminum metal particles have been fabricated and heated in the microwave. The samples required low power and had excellent heating efficiencies. However, densification of the compacts was inhibited in comparison to compacts containing AlN additives. Further samples are being fabricated that will incorporate other coupling additives, such as sialon powders.

ORNL-PHOTO 17829

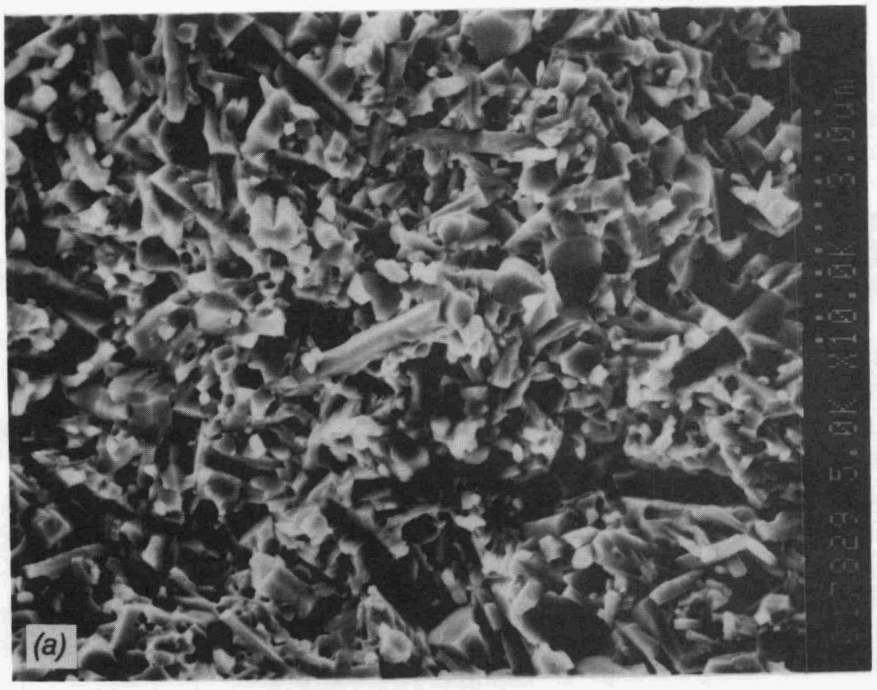

ORNL-PHOTO 17872

Fig. 3. Fracture surface of Si_3N_4- 9 % La_2O_3-3 % Al_2O_3 sintered at 1750°C for 1h in: (*a*) a conventional furnace and (*b*) a 2.45-GHz microwave furnace. The additive content was sufficient for grain growth in both cases, but some enhancement occured for the microwave case. Samples were turbomilled and slip-cast. Density for the conventional material was ~97% T. D. and ~98% T. D. for the microwave material.

Microstructure development

As reported previously, an annealing study was performed to investigate microstructural development of silicon nitride during heat treatment in a microwave furnace. Samples of Si_3N_4-4% Y_2O_3 and Si_3N_4-6% Y_2O_3-2% Al_2O_3 were hot pressed to full density and annealed both by microwave and conventional heating at 1200, 1400, and 1500°C for 10 and 20 h. Initial results showed increased, enhanced grain growth for the microwave-sintered samples at temperatures significantly lower than observed with conventional heating (>300°C) and improvements in the high-temperature creep rate.

Further analyses on the annealed samples by X-ray diffraction have been performed. X-ray diffraction on the as-fabricated materials showed significant amounts of aå-Si_3N_4 in both the Si_3N_4-4% Y_2O_3 and Si_3N_4-6% Y_2O_3-2% Al_2O_3. During microwave heat treatment for 20 h at 1400°C and 1200°C, respectively for the two compositions, complete transformation to ß-Si_3N_4 occurred. Literature on the aå-to-ß transformation indicates that it only occurs by vapor or liquid transport mechanisms. Interestingly, in the microwave-annealed samples, the bulk temperatures are 100 to 150°C below the solidus temperatures for the compostions investigated. The conventional heat-treated samples showed significant amounts of retained aå-Si_3N_4. In addition, no amorphous phases were observed in either the conventional or microwave-annealed samples.

Indent fracture toughness measurements on the Si_3N_4-4% Y_2O_3 and Si_3N_4-6% Y_2O_3-2% Al_2O_3 samples are shown in Figs. 4 and 5, respectively. As

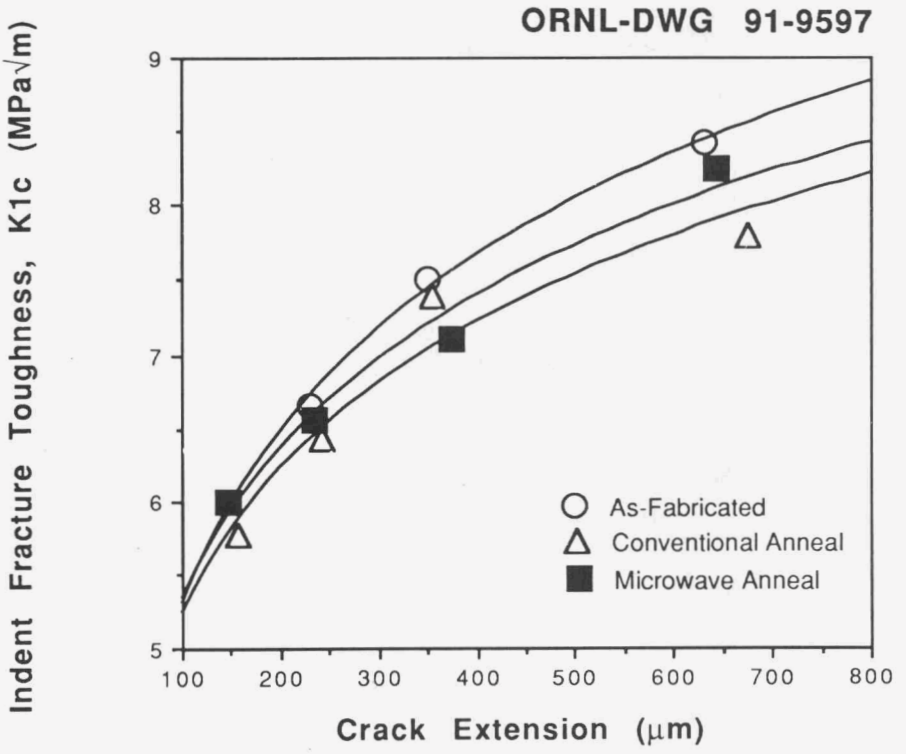

Fig. 4. Indent fracture toughness for Si_3N_4-4% Y_2O_3. Specimens were conventionally and microwave annealed at 1400°C for 20 h. Microwave annealing was done in the 2.45-GHz furnace.

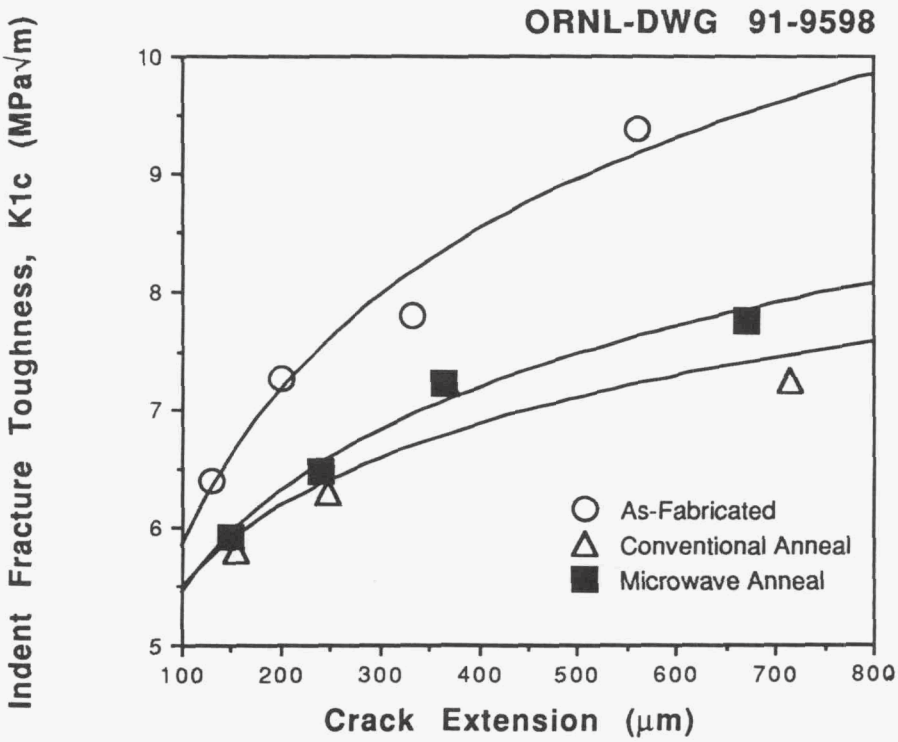

Fig. 5. Indent fracture toughness for Si_3N_4-6% Y_2O_3-2% Al_2O_3. Specimens were conventionally and microwave annealed at 1200°C for 20 h. Microwave annealing was done in the 2.45-GHz furnace.

shown, both sets of materials exhibit R-curve behavior, with increasing K_{IC} with increasing crack extension. The decrease in toughness for the annealed samples is indicative of crystallization of the grain-boundary phases that takes place for both the conventional and microwave heat treatments. The increased toughness for the microwave-annealed materials, as compared to the conventionally heated samples, is believed due to the coarsening of the grains that takes place in the microwave. This enhanced grain growth has been reported previously.

Initial fatigue testing has given encouraging results for the microwave-annealed materials. Additional tests on Si_3N_4-6% Y_2O_3-2% Al_2O_3 have been made. In a stepped-stress test, the microwave-annealed sample also had improved fatigue resistance (Fig. 6). As shown, the microwave samples exhibited excellent fatigue resistance. The improvement in fatigue resistance is most likely due to microstructural changes in the microwaved materials.

Additional annealing experiments have been performed on hot-pressed Si_3N_4-4% Y_2O_3 and Si_3N_4-6% Y_2O_3-2% Al_2O_3 to provide more specimens for mechanical testing. The packing powders were modified to aid in decreasing weight losses that occur during the high-temperature anneals. As shown in Table 1, weight losses were observed for the Si_3N_4-6% Y_2O_3-2% Al_2O_3 specimens only. Weight losses were significantly lower than for the previous compositions annealed. In those tests, corresponding weight losses for Si_3N_4-6% Y_2O_3-2% Al_2O_3 at 1400°C for 10 h were 2.5% as compared to 1.1% in the present test. In every case, the bars showed only a slight change in color.

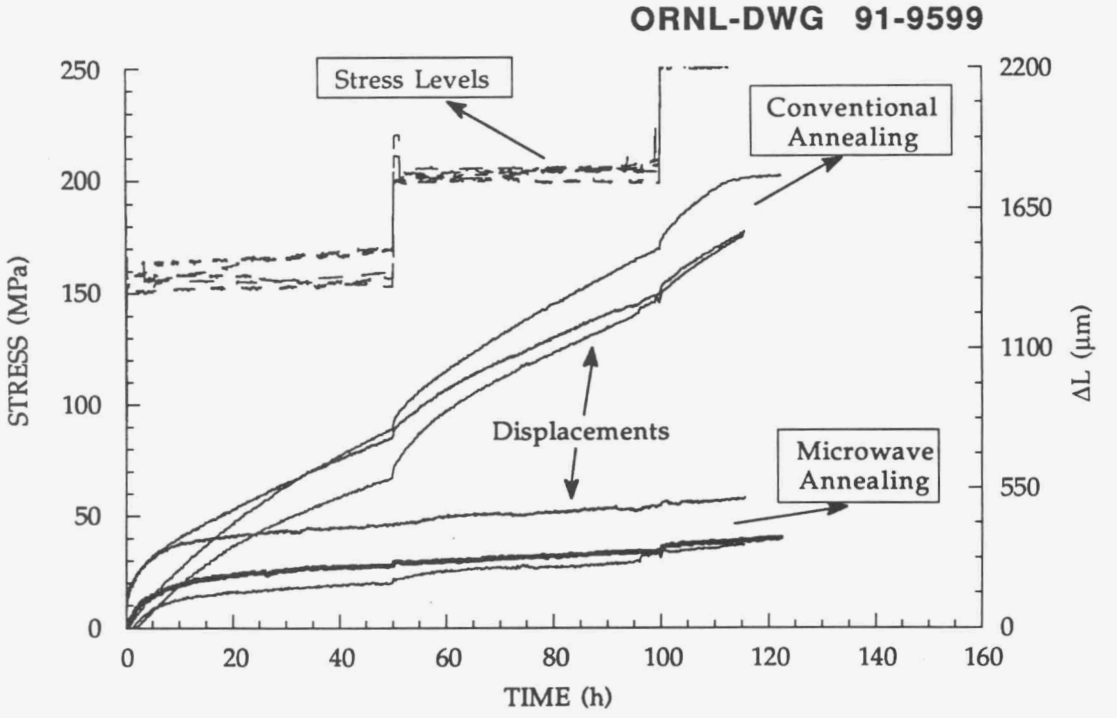

Fig. 6. Stepped-stress fatigue testing on Si_3N_4-6% Y_2O_3-2% Al_2O_3. Test temperature was 1600°C. Specimens were microwave annealed in the 2.45-GHz furnace.

Table 1. Summary of weight losses (%) during microwave annealing of silicon nitride

Composition	Annealing conditions			
	1400°C/20 h	1400°C/10 h 1200°C/10 h	1500°C/2 h	1500°C/2 h 1400°C/10 h 1200°C/10 h
Si3N4-4% Y2O3	< 0.0	< 0.0	< 0.0	< 0.0
	1000°C/10 h	1200°C/10 h	1400°C/10 h	1400°C/10 h 1200°C/10 h 1000°C/10 h
Si3N4-6% Y2O3-2% Al2O3	< 0.0	0.1	1.1	1.3

Transmission electron microscopy (TEM) was used to examine the nature of the grain-boundary phases in selected annealed samples. Minor differences of the intergranular phases were observed between the conventional and microwave-annealed samples (1400°C for 20 h) containing 4 % Y_2O_3. The as-fabricated samples and those conventionally heated contained two crystalline grain-boundary phases: $Y_2Si_2O_7$ and a yttrium-silicon-oxynitride phase. The microwave-annealed sample contained only the yttrium-silicon-oxynitride as a grain-boundary phase (Fig. 7).

YP12132

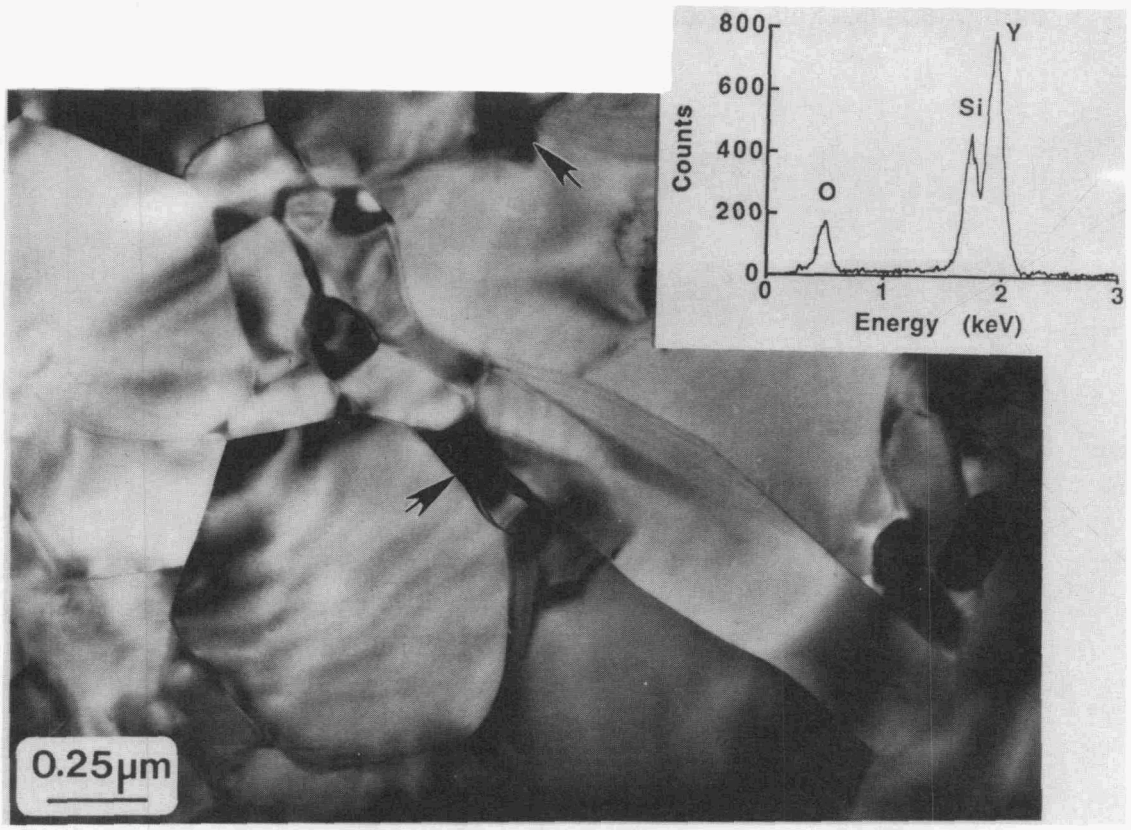

Fig. 7. TEM micrograph showing crystalline yttrium-silicon-oxynitride grain-boundary pockets in microwave-annealed Si_3N_4-4% Y_2O_3. Microwave annealing conditions were 1400°C for 20 h.

Examination of the Si_3N_4-6% Y_2O_3-2% Al_2O_3 materials by TEM showed the intergranular phases in the as-fabricated samples to be amorphous, as expected. During conventional annealing at 1400°C for 10 h, large grain-boundary pockets of $Y_2Si_2O_7$ crystallized with the aluminum existing predominantly in small amorphous pockets, which is also typical for this material composition. When the material was microwave annealed for 10 h at 1400°C, there was a significant improvement in

crystallization and, in fact, no amorphous phases were found in this sample. As noted in the sample conventionally heated under the same conditions, when there are some residual amorphous phases present, it is due to the aluminum segregating into discrete areas as the $Y_2Si_2O_7$ or other Y-Si-O-N phases crystallize. In this case, however, the aluminum was found in solid solution within the crystalline grain-boundary pockets in a high Y-containing silicate (but not $Y_2Si_2O_7$), as shown in Fig. 8.

TEM was also performed on samples microwave annealed at 1200°C for 20 h. These conditions resulted in an inhomogeneous distribution of phases: in some areas, the majority of the grain-boundary pockets had fully crystallized as a high Y-containing phase with no aluminum, whereas in other relatively large regions adjacent to these areas, there were no crystalline pockets, only residual amorphous pockets. These regions ranged in size from 1 to 10 μm.

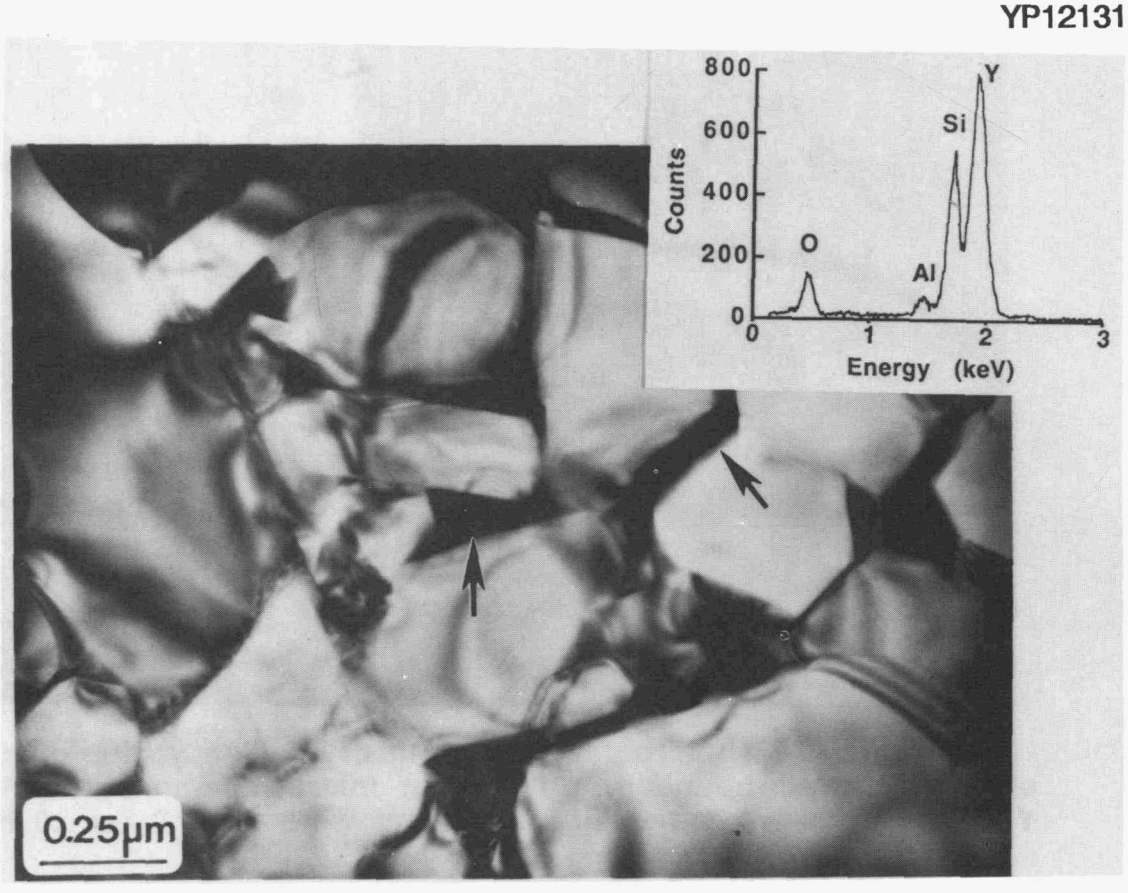

Fig. 8. TEM micrograph showing high Y-containing silicate containing aluminum phases in microwave-annealed Si_3N_4-6% Y_2O_3-2% Al_2O_3. Microwave annealing conditions were 1400°C for 10 h.

New microwave furnace construction

The new microwave furnace has been moved from the Y-12 facility in Oak Ridge, Tennessee, and has been installed in the Metals and Ceramics Division. The furnace is currently in operation.

Status of milestones

All milestones are on schedule.

Publications

"Microwave Sintered Silicon Nitride," by T. N. Tiegs, J. O. Kiggans, and H. D. Kimrey, to be published in Ceramic Engineering Science Proceedings, Vol. 12, No. 9-10

"Microstructure Development During Microwave Annealing of Dense Silicon Nitride," by T. N. Tiegs, M. K. Ferber, J. O. Kiggans, K. L. More, C. M. Hubbard, and D. W. Coffey, to be published in Ceramic Transactions, Am. Ceram. Soc.

"Characterization of Silicon Nitride Synthesized By Microwave Heating," by J. O. Kiggans, C. R. Hubbard, R. R. Steele, H. D. Kimrey, C. E. Holcombe, and T. N. Tiegs, to be published in Ceramic Transactions, Am. Ceram. Soc.

Characterization of Attrition Milled Silicon Nitride Powder

S. G. Malghan, L.-S. H. Lum and D. B. Minor
(National Institute of Standards and Technology)

Objective/scope

Currently, the starting materials in the manufacture of silicon nitride ceramic components are fine powders. These fine sized powders tend to form agglomerates due to van der Waals attractive forces. For improved reliability in the manufacture of ceramic components, the agglomerates in the powders should be eliminated since they form defects. In addition, the powders should have an appropriate range of size distribution and specific surface area for achieving a near-theoretical density of the ceramic after densification. These factors necessitate the use of powder milling as one of the major powder processing unit operations. Therefore, milling of powders is an integral unit operation in the manufacture of silicon nitride components for advanced energy applications. The production and use of these powders require the use of efficient milling techniques and understanding of characteristics of the milled powders in a given environment. High energy attrition milling appears to offer significant advantages over conventional tumbling and attrition mills.

The objectives of this project are to: (1) develop fundamental understanding of surface chemical changes taking place when silicon nitride powder is attrition milled in aqueous environment, and (2) demonstrate the use of high energy attrition milling for silicon nitride powder processing, by developing measurement techniques and data on the effect of milling variables on the resulting powder. This study will provide data and models for effective application of high energy attrition milling to industrial processing of silicon nitride powder. It also will provide recommended procedures for physical and surface chemical characterization of powders and slurries involved in the milling process.

Technical progress

During this period, the primary effort was towards data analysis, experiments on the effect of media size, and simulation of milling behavior of silicon nitride powder in a high energy attrition mill.

Data Analysis. The results of milling experiments with 2 mm diameter media of a 2^3 factorial design were evaluated. These experiments examined the influence of rotor speed, feed rate and % solids in the feed slurry. The response variables were particle size distribution, specific surface area, surface chemistry, morphology and power consumption. The data evaluation showed that milling was accompanied by not only physical changes (particle size distribution, specific surface area, and particle morphology) but also surface chemical modification of the powder. In general, the following observations were derived from these data:

- Initially, there was a rapid reduction of the mean size indicating that deagglomeration of the powder was a dominant mechanism, where loosely held particles were separated from each other due to shearing action in the mill.

- The rate of particle size reduction was highest when the rotor speed and slurry flow rate were high. The percent solids in the slurry had a minor effect on the rate of milling. When the mill speed and slurry flow rate were 2800 rpm and 480 cc/min, respectively, the mean feed size decreased from 1.05 μm to 0.77 μm by milling for 160 min. This type of fast milling kinetics is considered to be 8-10 times faster than that in a tumbling ball mill.

- Comparison of specific surface area measurement with particle size distribution yields information relating to the degree of dominance of size reduction mechanisms. A large surface area change with a relatively little change in the mean particle size is an evidence of production of too many extremely fine particles, which contribute to increase of specific surface area. Such conditions were observed by milling at 2800 rpm rotor speed, 240 cc/min slurry flow rate and 44 % solids in the slurry.

- Morphology of the milled particles showed a marked difference by changing the rotor speed and slurry flow rate. The blocky morphology of the SNE-3 powder could be altered either to rounded particles without significantly modifying size distribution or to rounded particles of significantly finer size distribution. The former type of particles were produced by shear dominated attrition milling; whereas, the latter type of particles were produced by compression dominated impact.

- Surface chemistry of milled particles varied as a function of milling time and milling parameters. As particles undergo fracture, freshly formed surfaces undergo oxidation and readsorption of ammonia, amine and impurities from the bulk solution. These reactions lead to a complex surface on the silicon nitride powder surface. The pH_{iep} (pH at which the particle surface carries a net zero charge) was found to decrease indicating progressive surface oxidation as a function of milling time and milling intensity.

Effect of Media Size. The media size was changed to 3.00 mm diameter balls. Using the 3.00 mm media, eight experiments (2^3 factorial design) were carried out. Effect of three variables (slurry flow rate, rotor speed and % solids in the slurry) was studied. Experimental conditions were maintained the same as in the case of 2.0 mm diameter media.

Milling rate is slower than that with the 2.0 mm media. This is expected based on reduced number of contacts between media and

particles, which leads to breakage of a fewer number of particles per unit time. However, the major purpose was to see if 3.00 mm media were more effective than the 2.0 mm media in the fracture of coarser particles. As shown in Fig. 1-4, under all sets of parameters (high rotor speed/high % solids or low rotor speed/low % solids at low and high slurry flow rates) the kinetics of 3.00 mm media were slower than those with the 2.0 mm media. This is an indication that irrespective of which mechanism of size reduction (shear dominated attrition and compression dominated impact) is prevalent in the mill, the larger size media yielded lower rate of milling. Typically, under compression dominated impact (low % solids and high rotor speed), there is an optimum ratio of particle to media diameter that promotes higher milling rate. Under the milling parameters examined in this study, the 3.0 mm media may not have produced sufficiently large number of impacts on the particles. From these data it can be concluded that 3.0 mm media tend to decrease milling rate by decreasing the number of collisions between the media and particles.

Observation of data in Figures 1 and 2 on the decrease of mean spherical diameter as a function of milling time, shows that the particle size distribution continues to become finer by using either size of the media. However, the rate of decrease is smaller for the 3.0 mm diameter media, especially in the case of 34% volume of solids and 2000 rpm. With the use of 3.0 mm media, there is a rapid decrease of mean size in the initial milling period. After about 60 min. milling, the rate of milling decreases. This effect is probably due to deagglomeration of loosely held particles in the initial milling period. Relatively speaking, the milling rate is much slower with the 3.0 mm media at 44 % V solids loading than at 34 % V solids. The increased number of particles per unit volume at 44 % V solids leads to decrease in the ratio of number of 3.0 mm media to the number of particles to be milled.

The specific surface area data are presented in Figure 3 and 4 for the same tests as in Figures 1 and 2, respectively. These data demonstrate an interesting feature of milling with 3.0 mm media. At lower solids loading (34 % V), in Figure 4, the increase in the specific surface area with milling time is beginning to plateau after about 100 min. milling. However, in the case of high solids loading (44 % V) the specific surface area continues to increase gradually. As the milling time is increased, the gap between the two specific surface areas is continuing to enlarge due to interference of fine particles in the size reduction of large particles. The fine particles are expected to produce a cushioning action during impact between the particles and milling media. This cushioning effect is ore detrimental during impact dominated size reduction than compression dominated size reduction.

Simulation of Milling Behavior. A linear, size-discretized model for breakage kinetics is used in the simulation studies. The primary purpose of this task is to develop a model for simulation applications, including off-line optimization, on-line optimization and scale-up of milling systems. Our studies have focussed on the

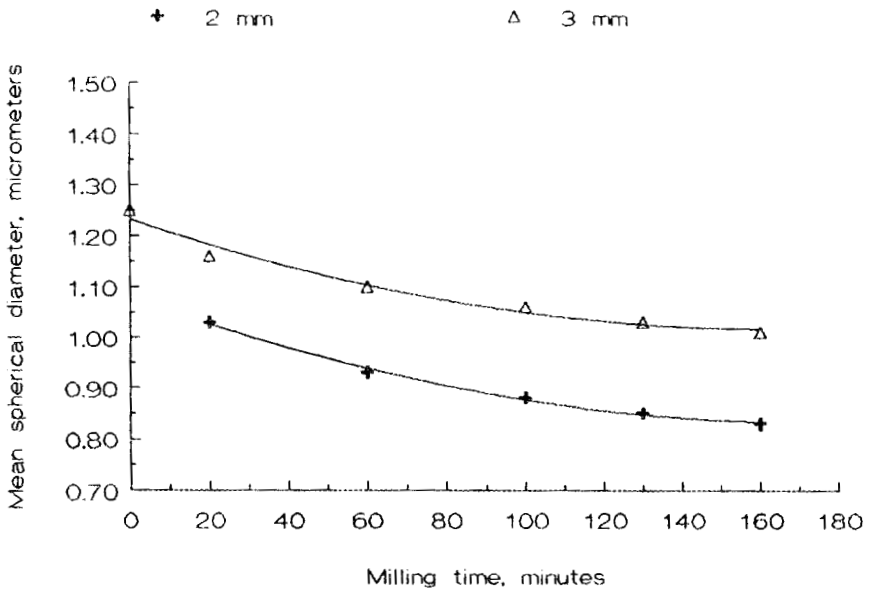

Figure 1. Comparison of milling kinetics of 2.0 and 3.00 mm diameter media. The d_{50}, mean diameter of particles, is compared at 44% volume of solids, 2800 rpm rotor speed, and 480 cc/min. feed rate.

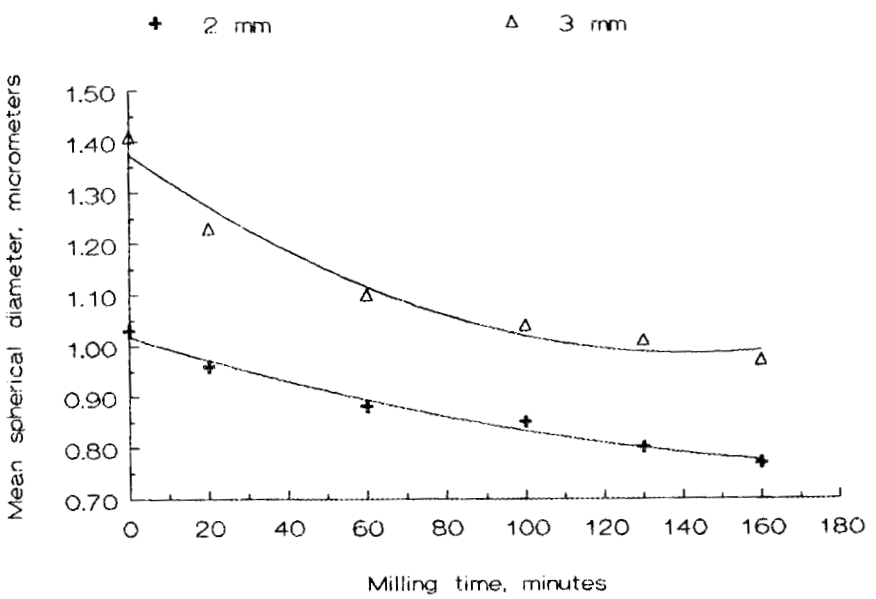

Figure 2. Comparison of milling kinetics of 2.0 and 3.00 mm diameter media. The d_{50}, mean diameter of particles, is compared at 34% volume of solids, 2000 rpm rotor speed, and 480 cc/min. feed rate.

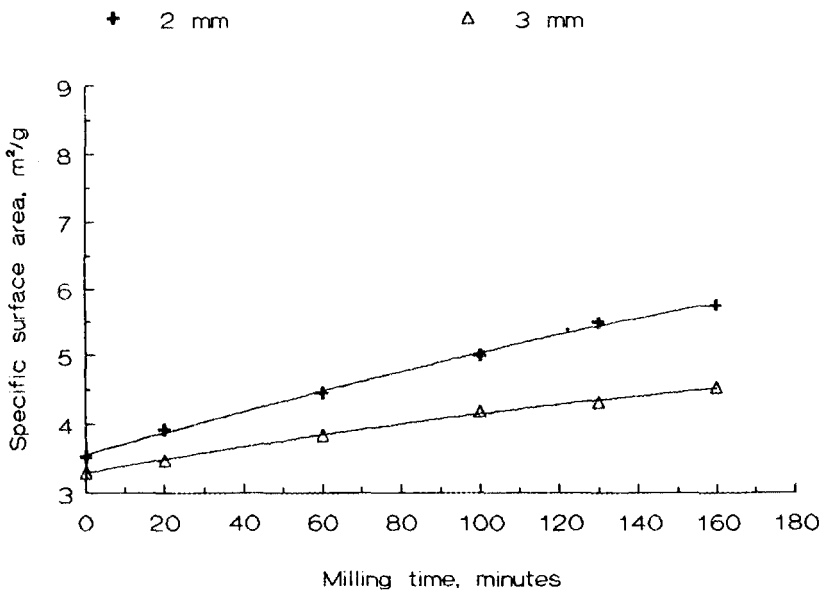

Figure 3. Increase of specific surface area by milling with 2.0 and 3.0 mm diameter media at 44% volume solids, 2800 rpm rotor speed and 480 cc/min. feed rate.

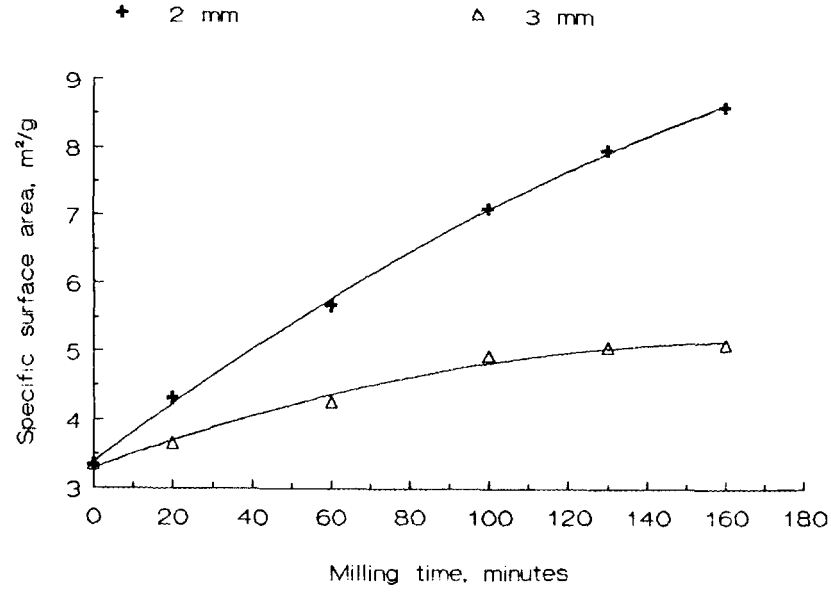

Figure 4. Increase of specific surface area by milling with 2.0 and 3.0 mm diameter media at 34% volume solids, 2800 rpm rotor speed and 480 cc/min. feed rate.

parameter estimation schemes. The selection function, which represents rate of breakage of particles from a given size, is found to be abnormally small, compared to those of milling particles in the 100 μm range. This type of behavior of the 1.0 μm range particles breakage is being included in the size reduction model.

Status of Milestones

Slightly behind due to expanded experimental design.

Publication

A Chapter on "Comminution of Powders" was prepared for inclusion in the ASM Handbook.

S. G. Malghan, D. B. Minor and L.-S. H. Lum, "Physical and Surface Chemical Changes in High Energy Agitation Milling of Si_3N_4 Powder". Submitted for publication in Powder Processing Science III, Eds. S. Hirano and G. Messing.

Novel Si_3N_4 Process

T. M. Sullivan (Sullivan Mining Corporation)

Objective/scope

This work involves scale-up of the Sullivan™ Process for silicon nitride with the delivery of over 864 net shape flexural bars and other test samples for evaluation by the High Temperature Materials Laboratory at Oak Ridge National Laboratory. Both a low temperature and a high temperature silicon nitride shall be produced and characterized. Data on process optimization and system economics will be obtained to establish the operating parameters for a larger Sullivan™ Process system.

Technical progress

Four-Inch System

The design, procurement and assembly of a 4" system has been completed. Components of the system have been tested and are reliable under operating conditions up to 2000 psi which demonstrates overall system integrity. The operating system which is capable of producing 1-2 tons of net shape and/or near net shape Si_3N_4 products per year. This process system is operated using computer control and data acquisition to monitor process variables in order to identify cause and effects relationships between process operating conditions and the physical, chemical, mechanical and thermal properties of produced product. A schematic of the Sullivan™ Process is shown in Figure 1.

Polymerization

Key to development of a low-cost high volume production Si_3N_4 ceramic process is the necessity for utilizing a cost-effective polymeric precursor made from a silane such as R_ASiX_{4-A}. Dependence on a single commercial source might result in a high-priced starting material. As such, demonstration of large scale polymer making has been initiated at test laboratories of vendor equipment suppliers. The other reactant is NH_3, a low-cost commercial product available in ton quantities which contributes to the favorable economics of the Sullivan™ Process.

Net Shaping

In addition to the utilization of low-cost precursors or starting materials, the Sullivan™ Process has the additional advantage of producing net shape and/or near net shape products. This has been accomplished by reacting the precursors in molds under the proper temperature and pressure conditions to form

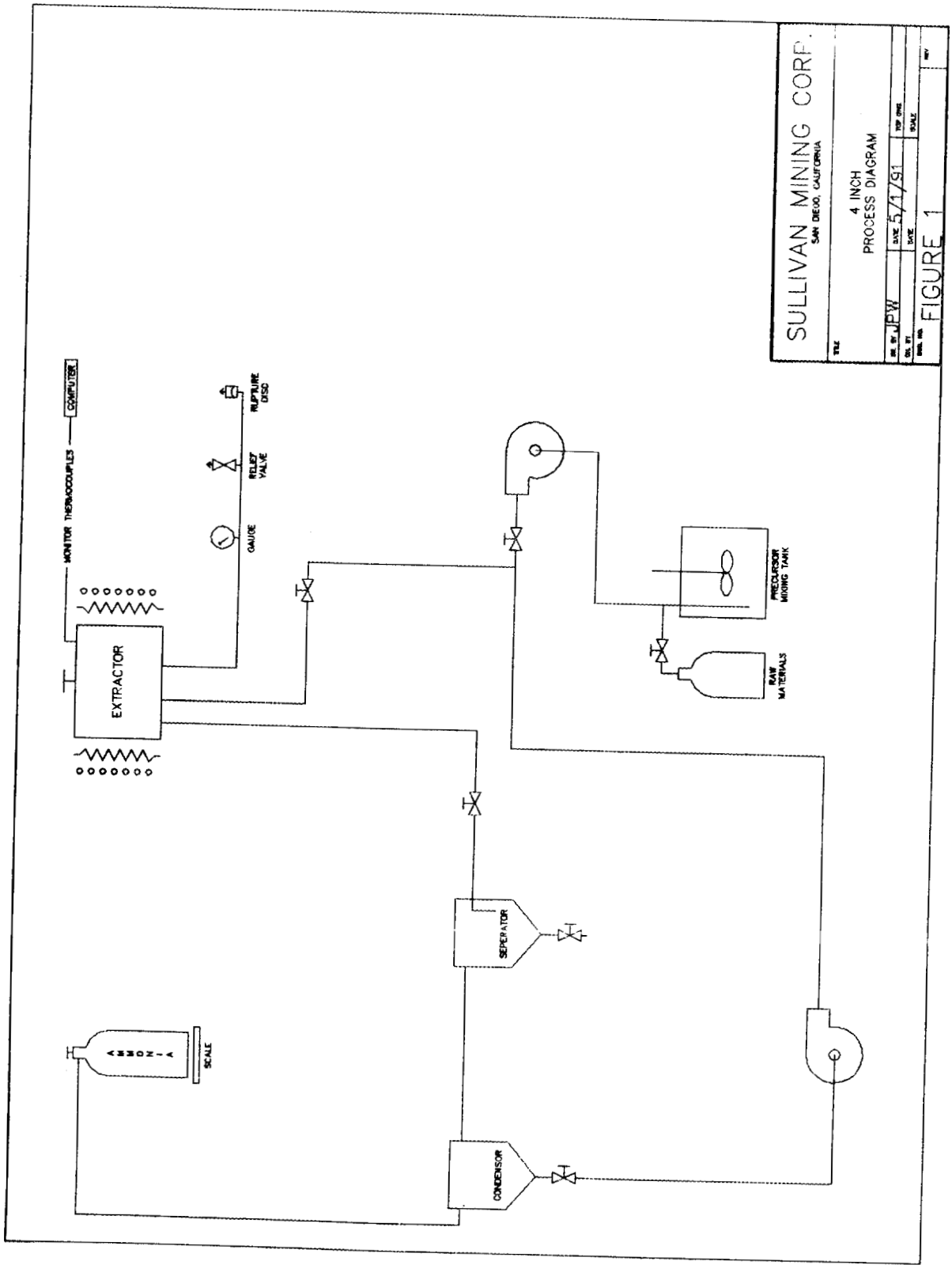
SULLIVAN MINING CORP.
SAN DIEGO, CALIFORNIA
4 INCH
PROCESS DIAGRAM
FIGURE 1
JPW
5/1/91
COMPUTER
MONITOR THERMOCOUPLES
RUPTURE DISC
RELIEF VALVE
GAUGE
EXTRACTOR
PRECURSOR MIXING TANK
RAW MATERIALS
SEPERATOR
CONDENSOR
AMMONIA
SCALE

flexural bars of silicon nitride. Key to this activity are both design of the mold and process operating conditions to assure the product is easily released from the mold. Depending on the required dimensional tolerance of the product mold release agents may be employed to provide more process flexibility.

The silicon nitride component produced in the mold is slowly heated at low temperatures in-situ prior to high temperature "flash" heating for a brief interval for conversion to the ß Si_3N_4 under a controlled atmosphere. Figure 2 is a comparison of the overall Sullivan™ Process with the traditional ceramic manufacturing processes which illustrates the former's cost advantages by eliminating the many additional processing steps required for conventional ceramic components.

MOR Bar Casting

MOR bars have been individually cast. A multiple cavity mold is under construction with an anticipated mid-April delivery.

Modify Composition

MOR bars were successfully cast without additives. These bars are being heat treated to obtain ß Si_3N_4. Final microstructure will then be determined.

Status of milestones

The milestones are on schedule.

Publications

None.

PROCESS COMPARISON

Current Ceramic Processing Versus The SULLIVAN™ Process

	Powder Material	Compounds	Granulation	Molding	Primary Processing	Sintering	Secondary Processing	Assembly	Product
Current Ceramic Industry Process	Synthesis	Mixing Pulverizing	Drying	Injection Cold Isostatic Injection Extrusion Slip Casting	Green Machining	Reaction Normal Press Hot Press HIP	Grinding Finishing		

	Raw Materials	Primary Process		Secondary Process	Product
SULLIVAN™ Ceramic Process	Liquid A Liquid B	Formation of Net Shape & Near-Net Shape Products	Flash Heat Treating	Polishing (If Required)	

* SMC part production is accomplished in two steps with only two process equipment units used.

Figure 2

1.1.4 Processing of Monolithics

IMPROVED PROCESSING

V. K. Pujari, D. M. Tracey, N. D. Corbin, M. R. Foley, A. K. Garg, N. I. Paille, P. J. Pelletier, L. C. Sales, R. H. van de Merwe, C. A. Willkens, R. L. Yeckley (Norton Company)

OBJECTIVE/SCOPE

The goals of the program are to develop and demonstrate significant improvements in processing methods, process controls, and nondestructive evaluation (NDE) which can be commercially implemented to produce high-reliability silicon nitride components for advanced heat engine applications at temperatures to 1370°C. Achievement of this goal shall be sought by:

- The use of silicon nitride - 4% yttria composition which is consolidated by glass encapsulated HIP'ing.
- The generation of baseline data from an initial process route involving injection molding.
- Fabrication of tensile test bars by colloidal techniques - injection molding and colloidal consolidation.
- Identification of (critical) flaw populations through NDE and fractographic analysis.
- Correlation of measured tensile strength with flaw populations and process parameters.
- Minimization of these flaws through innovative improvements in process methods and controls.

The quantitative program goals are: 1) mean RT tensile strength of 900 MPa and Weibull modulus of 20, 2) mean 1370°C fast fracture tensile strength of 500 MPa, and 3) mean 1230°C tensile stress rupture life of 100 hours at 350 MPa.

TECHNICAL PROGRESS

The technical progress against the major tasks described in the statement of work is summarized. The major tasks are: 1) Material Selection and Characterization; 2) Material Processing and Process Control; 3) Development and Application of NDE; 4) Property Testing and Microstructural Evaluation; 5) Reporting; 6) Quality Assurance.

During this period major effort was directed towards: i) raw material handling and powder processing control and monitoring, ii) screening and evaluation of pressure casting process variables, e.g. slip chemistry, mold design and effect of HIP to HIP variation, iii) analysis and fractography of baseline pressure cast tensile test data, iv) comparison of tensile strength database from pressure casting (PC) and

injection molding (IM) processes, v) establishment of detection sensitivities of ultrasonics (UT), computed tomography (CT) and nuclear magnetic imaging (NMRI)/spectroscopy (NMRS), vi) development of experimental plans and schedules for stage II process optimization utilizing key process variables identified during stage I experimentation.

Raw powder handling and milling process control procedures were demonstrated, respectively, by harpoon sampling procedure and p.s.d. and surface area reproducibility from batch to batch.

Screening tests, to evaluate key pressure casting variables, showed minimal effect of mold design on the tensile strength. However, slip chemistry and HIP conditions showed statistically significant effects on tensile strength and Weibull modulus. Co-milled (C-series) powder suspension produced bars with mean tensile strength and Weibull of 862 MPa and 10.1 respectively. Fractography of cast tensile bar showed only one type of flaw (agglomerate) which should pave the way for higher Weibull moduli in subsequent iterations. In comparison, injection molding NSF bars showed higher frequency of metallic inclusions at the fracture origins with resultant tensile strength and Weibull modulus of 454 MPa and 4.5 respectively. Based upon this comparison PC process was selected as the forming method for the remainder of the program.

Technique development phase of the NDE effort was completed and the detection sensitivities of UT, CT and NMRI/NMRS were established. Using novel toric ultrasonic transducer, cylindrical silicon nitride specimens were successfully examined and 50 μm seeded Fe inclusions and cracks up to 100μm dimensions were detected. CT was used to delineate green density gradients as low as 3% and seeded defects in the range 50-100μm. NMRS was employed to determine the mode of attachment of surfactant on powder surface.

Finally, experimental plans (factorial design experiments) for the Stage II total process optimization have been laid out. These experiments will help delineate the cause-effect relationship involving key process variables and in turn pave the way for achieving the final program objectives.

TASK 1 MATERIAL SELECTION AND CHARACTERIZATION

All materials at various stages of processing are being analyzed as per established S.O.P. Statistical Process Control (SPC) charts have also been established for all key process parameters which will be used in Stage II of the program for overall process monitoring purposes.

TASK 2 MATERIALS PROCESSING AND PROCESS CONTROL

i) Powder Processing

Lot C (previously lots A and B were used to develop various unit operations) of Ube silicon nitride powder (300 kg) was received. Samples were analyzed from the top, middle and bottom of the 50 kg drums of each grade of the powder. Samples were removed using a stainless steel "harpoon". No significant variation in either oxygen, surface area or particle size distribution as a function of position in the 50kg drum (Figures 1 and 2) was noticed.

Although very little variation in the powder properties has been observed within a 300 kg lot, significant variation in properties was measured from Lot B to Lot C. The change in starting particle size was accommodated by modifying the milling parameters, yielding an acceptable final particle size distribution (Figure 3).

The water comilled process (C-series) has been used to produce twelve 30kg batches (C003-C014). The conditions used are considered to be our baseline process, and a standard operating procedure (SOP) has been written. The slurry produced has been used directly for casting studies or dried and used for injection molding. Process control charts for the baseline aqueous co-milling process are shown in Figures 4 and 5. Even though all measured variables seem to fall within 3σ limits, oxygen content and surface area (Figure 5) measurements show greater scatter. Possible cause for the observed scatter may include poor resolution of the fine fraction by Sedigraph and/or sampling errors caused by segregation during drying. Various studies are underway to determine the cause.

The W-series process involves adding the sintering aid via a chemical precipitation route. This process is now considered developmental due to scaleup difficulties. The C-series process is currently the "standard" process. A modified Y(OH)3 precipitation method was developed which eliminated the yttrium rich (agglomerate) regions in full 30kg batches. However, with the modified approach some difficulty was encountered in concentrating the W-series slurry to higher solids content. The cause appears to be either the modified precipitation route or the variability in the starting yttrium salt. An additional quantity of the baseline yttrium salt has been obtained to identify the causes for this anomaly.

ii) Colloidal Consolidation

a) Slip Formulation

A study to determine the effects of pressure casting parameters on cast body uniformity is underway. Casting experiments have been performed using different pressures, casting rates, mold materials, slip solids content, and mold geometries. Evaluation of cast body microstructural uniformity is underway.

Kinetic measurements suggest that the casting rate continues to decrease with (casting) time for a given casting pressure. The initial casting rate can be an order of magnitude greater than the casting rate at extended times. By determining the casting behavior at a given constant pressure we were able to predict the appropriate time/pressure parameters for achieving a constant casting rate. Figure 6 is a plot of cast thickness versus time for different constant pressures, demonstrating the nonlinear behavior. Figure 7 is a plot of thickness versus time using a modified pressure cycle which results in linear casting behavior. Specimens cast under constant pressure and constant casting rate conditions are currently being examined by computed tomography technique (see Task 3) to establish density uniformity and overall green microstructural features.

A comparison was made between casting kinetics on flat and curved surfaces. When casting on a flat surface the casting behavior follows that described by Adcock and McDowall (1) which is linear when wall thickness squared is plotted versus time. Casting on a curved surface exhibits a nonlinear casting behavior. It is anticipated that an understanding of casting behavior on curved surface will result in uniform green microstructures. Based upon the above study pressure profiles were developed to cast NSF bars as described in the following section.

b) Tensile Bar Casting

As described in the previous section, various process parameters which influence the cast body uniformity (green microstructure) and hence its behavior during drying (cracking or no cracking) were evaluated. Based upon these results three key parameters were identified and evaluated by casting NSF (net shape formed) tensile bars and by

establishing base line tensile strength data.

All milled suspensions described in section (i) were sonicated, de-aired and adjusted for pH as per established SOP. Viscosity and solids-loading measurements were also made on all the slips. No binder addition was made to these slips prior to casting. All NSF bar castings were performed using two piece plaster molds.

Pressure casting results from the baseline iteration were analyzed with respect to the above mentioned (three) key variables, namely: 1) slip chemistry, ii) mold design and iii) HIP to HIP variation. Cause-effect relationships involving these variables will be established during the process optimization stage of the program.

Effect of slip chemistry was examined by casting NSF bars from both precipitated (W-series) and comilled (C-series) slurries. Both slurries were concentrated to the highest level possible prior to the casting experiments. Powder loadings in C and W series powders were approximately 73W% and 66W% respectively. As reported in Task 4, NSF bars cast from C-series slip displayed much higher tensile strength and Weibull modulus.

The mold design modification effort was directed towards simultaneously minimizing the green density gradients (radial in the cross-section of the bars) as well as drying related cracking along the length of the NSF bars. This factor was evaluated by altering the filtration surface and its location inside the mold cavity. Two mold designs incorporating these features (designated as full and half mold) were also evaluated for their effects on the green microstructure uniformity and resulting HIP properties. Both full and half mold designs produced statistically equivalent tensile strength results. Finally all tensile strength data from NSF bars were also plotted as a function of HIP runs. Tensile strength and Weibull modulii were found to be substantially effected by HIP variations as shown in Figure 8. The specific reasons for this variation are explained in Task 4. From the above mentioned experiments a sufficient number of NSF bars were cast and densified to establish tensile strength database (as described in TASK 4). SPC chart from 144 cast bars showed less than $\pm 4\%$ variation in weight. A few MLP bars with maximum cross-sectional diameter of 50mm were also cast and dried crack-free as shown in Figure 9. MLP bars were cast from one end only to

minimize radial density gradients.

iii) Injection Molding

a. Mold Design

The mold modification of the MLP mold was completed. This eliminated the sharp transition which caused problems in earlier molding of this shape (Figure 9).

b. Molding

Two additional changes, in addition to the mold modification noted above, were made for the second molding of MLP specimens. The first change involved a change in the binder system in order to improve the binder removal characteristics for this large shape. The second change was to improve binder filtration methods to remove impurities from this source.

A total of 11 MLP specimens were molded from batch C004 material. Initial microfocus X-ray results indicated fewer inclusions and voids when compared to earlier specimens.

In addition to the MLP specimens, a set of NSF bars (batch L) were molded using the improved filtration system with binder "D" to compare with the IM baseline data (Iteration - 1). Use of microfocus X-ray on the filtered binder indicated that the inclusions from this source were reduced by a factor of ten. Microfocus X-ray of the green molded NSF bars indicated a significant reduction in voids when compared to Iteration 2 specimens, see Figure 10, and a slight reduction in the size of inclusions when compared to batch I, see Figure 11. A limited number of these bars were HIP'ed, machined and tested for fast fracture strength as described in Task 4.

c. Dewaxing

Dewaxing of the molded MLP specimens resulted in a few surface cracks. This indicated that the binder removal schedule, the same as that used for NSF bars, was not suitable for these larger shapes.

d. Summary of Injection Molding

Fast fracture results (Task 4) from batches I and L indicate a slight but not a statistically

significant improvement when compared to the baseline data. The improvements in the injection molding process accomplished as a result of work done under the contract include:

1. The optimization of mold design using FEM.
2. The significant reduction in the number of voids due to mold design and process optimization using experimental designs.
3. The reduction in size of inclusions resulting from process improvements.
4. Increase in MOR mean flexure strength values from 600 to 760 MPa.

Relative to pressure casting, injection molding was found to be a production process which gives a relatively high yield with reproducible results. The disadvantages are that the process as it now stands requires long cycle times and is hampered by more deleterious strength limiting flaws (inclusions).

iv) Hot Isostatic Pressing

NSF bars fabricated by injection molding and pressure casting techniques were HIP'ed using the established fixturing method and HIP parameters. The HIP pressure and temperature were the same as those used to compare mechanical properties of alcohol and water milled powders, described in the semi-annual October 1989-March 1990 report.

Dimensional measurement of as HIP'ed IM and PC bars showed an interesting trend. IM bars, in general, showed less bending (<1.5mm TIR) than that measured on PC bars (>2.0mm TIR). This was traced to higher radial green density gradients in PC bars. As described before, further modifications in the pressure casting and mold design parameters have resulted in reduced density gradients and hence less HIP distortion.

Data from various HIP runs were also analyzed to study HIP process reproducibility. Figure 8 shows room temperature tensile strengths of cast bars as a function of HIP run. The numbers next to the data point indicate the specific batch numbers of the milling process from which the tensile rods have been fabricated (4, 6 and 9 indicate C-series mill batches, and 17-18 indicate W-series mill batches). Some of these rods did not achieve the minimum cut-off density required in the testing process and were, therefore, not included in the calculation of baseline room temperature average strength/Weibull modulus reported under TASK 4. The discrepancies in the average strength and standard deviation from HIP run to the next could indicate a HIP

variation and/or batch variation or a combination of the two. This issue will be examined in detail in Stage II of the program.

One MLP bar from each of the IM and PC processes were HIP'ed. Full densification was not achieved for either specimen. The reasons for this anomaly is under investigation at the present time.

During the performance period, detailed technical meetings were held at ABB Cerama, licensor of the ASEA HIP technology, for the purpose of an ASEA license technology update. A number of critical HIP issues were reviewed such as recent changes in HIP processing cycles, component packing techniques for various shapes, HIP glass modifications, heat transfer issues, HIP economics and scale-up problems.

TASK 3: DEVELOPMENT AND APPLICATION OF NDE

i) Microfocus Radiography

a) Colloidal Suspensions

Samples from batches CO11, CO12 and CO13 were radiographed to establish agglomerates and inclusion content. The suspensions were found free of these defects based upon evaluation of 33 cm^3 samples prepared immediately after milling of the suspensions. However, agglomeration was determined to occur with age of the slip. Samples were radiographed two weeks after slip preparation and agglomerates in the 100-500μm size range were detected. These findings prompted a change in the casting SOP which now demands fresh slip for the casting process.

b) As-received powder

Samples (30g) from the six 50kg drums of as-received Lot C UBE Si_3N_4 powder were radiographed to assess the presence of metallic inclusions. Two samples were found to contain single 50 μm size inclusions, consistent with the purity specifications of the powder. The magnetic separation stage of the milling process is designed to extract the impurities found in this x-ray evaluation.

ii) Computed Tomography (Argonne National Laboratory)

Density gradient, metallic inclusion and void defects were considered in detection sensitivity

experiments conducted using the ANL 3-D x-ray CT system. The system has a 10μm focal spot size, 0.223 mm detector pixel size and an 8-bit (256 gray level) frame grabber board. The object of the study was to establish detection sensitivity for defects in 10 mm diameter green (presintered) tensile bars.

a) Green density gradient

A calibration phantom was fabricated to conduct density measurements. The phantom has a hollow cylindrical shape (44 mm O.D./11 mm I.D.) with 4 mm holes for inserts of known density, Figure 12. The NSF bar being evaluated is placed in the interior 11 mm hole. The gray level calibration plot established from the insert density values is also shown in Figure 12. The standard deviation of the image intensities of the pixels covering the inserts can be used as a measure of detection sensitivity. The result is that a 3% detection sensitivity was found from the calibration data, scaled to the 10 mm specimen of interest and a 1 mm spatial resolution. This can be compared to an 8-bit theoretical value of 1.95%.

b) Metallic Inclusions

Green NSF bars with Fe inclusion seeds were supplied to ANL for this study. Samples were fabricated with inclusions of a fixed size, either 50, 100 or 200μm. The 100μm and 200μm inclusions were readily detected and displayed in tomographic images (0.13 mm slices). The randomness of the seed location made tomography unduly laborious in case of the 50μm inclusions, involving excessive data sets over the 35 mm gage length. In lieu of scanning the gage length for seeds fabricated into the specimen, a 50μm inclusion was physically pasted upon the outside surface of the bar. Radiographic projections were obtained over 360°, with the result that the pasted inclusion was detectable at all orientations on a sinogram image. The 8-bit theoretical value for minimum detectable iron inclusion in the 10 mm bar is 5.35μm. No work on seeds smaller than 50μm was pursued so that the 50μm value is taken as the experimentally established detection limit.

c) Voids

Green NSF bars seeded with 100μm and 200μm

PMMA spheres were supplied to ANL for this study. The NSF bars were presintered at a temperature above the PMMA dissociation temperature, thus burnout locations were designed to simulate forming voids. However, there is a degree of uncertainty as to the resulting size and composition of these burnout voids. While a 200μm feature was detected in the reference sample in two separate experiments, no reliable detection capability was established using the PMMA seeded reference samples.

iii) NMR Spectroscopy (Argonne National Laboratory)

Detection sensitivity experiments on Si_3N_4 powder - surfactant adsorption were concluded during the reporting period. An organometallic surfactant was used in the study and proton (^1H) spectra were obtained to derive adsorption and structural information about the surfactant. The experiments were performed on the ANL Bruker AM-300 spectrometer.

Three concentrations (2.00%, 0.666% and 0.0666%) of the surfactant by weight of water were used. Two types of slurries containing 40% Si_3N_4 powder were prepared, one milled in the surfactant solution and the other stirred in the solution. The slurries were centrifuged to recover supernatant surfactant solution for the NMRS analysis.

The NMR spectra revealed (Figure 13) that the inorganic part of the surfactant is complexed with the hydroxyl groups of propylene glycol. The signal arising from the methyl groups in the surfactant chain was integrated to determine surfactant concentration in the various solutions.

The 2.00% solution without Si_3N_4 powder was evaluated to establish detection sensitivity. A value of 0.25% for the standard deviation in three repeated NMRS measurements of concentration level of this analytically prepared solution was used to establish an error magnitude of 12.7% in the remaining evaluations.

The individual evaluations suggest minimal or no adsorption of the organic part of the surfactant. The proton analysis is not capable of assessing the adsorption of the inorganic part of the surfactant on the silicon nitride surface. This determination will be left for future work.

iv) NMR Imaging (Argonne National Laboratory)

NMRI was directed to injection molded Si_3N_4 specimens with the goal of demonstrating capability to

map binder distribution in the as-molded state. During the reporting period, the NMR probe hardware was modified and appropriate RF coils were developed to accommodate the full scale NSF tensile bar geometry. Imaging of the NSF bar was successfully demonstrated. Extruded 4 mm diameter concentration phantoms (14-20 w/o binder) have also been imaged along with the reference NSF bar for calibration of the binder distribution. The spatial resolution attainable in the 9 mm NSF bar is 500μm. Resolution is proportional to sample size and thus can be lowered by using sub-scale specimens.

Conclusions on sensitivity limitations using the concentration phantoms will be reported in an ANL report in preparation. Due to the choice of colloidal consolidation (pressure casting) for future forming development in the Norton program, this NMRI effort which has been supporting injection molding development will be curtailed with completion of the report.

v) Ultrasonics (Precision Acoustics Devices)

Work during the reporting period was directed to imaging the interior of HIP'ed cylindrical tensile bar reference samples using toric transducers and contact shear wedge transducers, and quantifying the detection limits of these and the previously developed techniques.

100 MHz PVDF copolymer toric transducers were fabricated in order to improve resolution. Seeded defects of 200, 100 and 50μm were successfully detected in the reference specimens. Images of seeded 50μm iron inclusions (Figure 14) were found to have a signal to noise ratio of -6 to 10 dB, which suggests a detection limit somewhere between 30-40μm for metallic inclusions.

Reference samples with surface cracks were produced by Norton using Vickers indentation with subsequent machining of the indent impression. Sharply focused transducers were used in the surface wave imaging for detection of the remaining indentation cracks. 50 MHz was found too low a transducer frequency for crack detection. Cracks of 100μm length were detected using 300 MHz imaging.

Conformal PVDF copolymer film transducers were found to be impractical due to the fragility of the film material.

Wedge coupled shear wave transducers were completed and mounted during the reporting period. Images obtained using these in evaluation of the samples with 100μm Fe inclusions showed no evidence of the seeded inclusions. The limiting factor in this transducer appears to be the large spot size necessitated by the lack of focussing.

TASK 4: PROPERTY TESTING AND MICROSTRUCTURAL EVALUATION

i) Injection Molded NSF Specimen Update

The tensile strength data base for injection molded specimens is shown in Figure 15 as a funcion of testing temperature.

In Figure 15 the open circles represent the original (reported in June-July 1990 report) average tensile fast fracture baseline data along with the standard deviation. The full circles represent the heat treated specimens from the same batch tested during the current reporting period. The room temperature strength of the heat treated specimens falls right in line with the original data.

Specimens from new Batch I (five tests) and new Batch L (three tests) were also tested. Batch I and L tensile specimens were molded using binders which were filtered twice through finer mesh screen to remove foreign contaminants. As shown in Figure 15, the strengths are still equivalent to the baseline data. Eleven out of the total of 13 specimens tested during this reporting period, failed from a volume metallic inclusion. Even with the "improvements" made in Batches I and L, the strengths were limited due to the same type of large inclusions found in the specimens used to develop the original database.

As reported in the original database, the stress rupture lives were very short (<20 minutes) at 1230°C/350 MPa. Fast fracture tests were performed on five specimens at 1230°C. The average strength was 393 MPa. Therefore, it is very reasonable to expect low stress rupture lives when the applied stress is approximately 90% of the fast fracture strength. Additional specimens are available for stress rupture testing at 1230°C at stresses below 350 MPa.

Ten green and six presintered injection molded specimens were also tensile tested at room temperature. The average strengths and standard deviations were 2.73 $\pm$ .26 MPa and 7.07 $\pm$ 1.39 MPa for the green and presintered specimens, respectively. The fracture surface did show some evidence of agglomerates, dewaxing cracks and metallic inclusions from the molding process.

ii) Pressure Cast NSF Specimens - Iteration II

a) Room Temperature Fast Fracture

Fast fracture tensile testing was performed on 28 HIP'ed specimens at room temperature. However, as shown in Figure 16, strength is dependent on

density up to ≈ 99% T.D. Therefore for statistical analyses, only those specimens which measured densities ≥ 99% T.D. were used.

Table 1 summarizes the strength data, for the 20 specimens which met the density criteria (≥ 99% T.D.), resulting in 9 volume, 6 surface, 4 buttonhead and one unknown failure origins. The overall average tensile strength and Weibull modulus are 709 MPa and 4.7, respectively. These baseline results compare very well with the latest published data on NT154, (ATD CCM Oct.1990, Dearborn, MI).

The Weibull Modulus of all the strength data was found to be 4.7 which is not surprising considering the range of strength values (397-1010 MPa). A factor in this variability is likely the different mold designs which were used in the course of the iteration while attempting to resolve the radial density gradient-HIP warpage problem. Another factor is the HIP-to-HIP variability discussed under TASK 2. If data from 3 HIP runs are considered separately, the Weibull modulus ranges from 4 to 24. The Weibull plot for the overall iteration as well as the three HIP runs is shown in Figure 17. Considering the data pooling that was undertaken, the baseline Weibull modulus of 4.7 reported here is considered artificially low for pressure casting.

As mentioned in TASK 2, in order to evaluate the effect of slip chemistry, the tensile specimens were cast from two different slips (C-series and W-series) as part of a larger matrix of experiments.

Table 2 summarizes the strength data according to slip type. The bars cast from C series slip show a much higher tensile strength (862 MPa) and Weibull modulus (10.1) than that measured from W series slip. Based upon these results, it is anticipated that in Stage II of the program, C-series slip will go through further extensive evaluation.

After tensile testing all fracture surfaces were analyzed for flaw types and their size. Extensive fractography has shown that the major flaw origins are agglomerates. The agglomerates were found both in the volume and at the surface. It should be noted that the specimens that failed from machining damage also had an agglomerate in the vicinity at the surface as shown in Figure 18. The agglomerate shown in Figure 18 also represents a typical agglomerate seen in all fracture surfaces of the tensile bars tested. The size range of the

flaws (agglomerates) at the fracture origin for the NSF bars made from C and W series slip were measured to be 10-25μm and 25-100μm respectively.

Another interesting finding was the difference in grain morphology between the agglomerate and the surrounding matrix. There are more fines in the agglomerates than in the matrix. This could have occurred during the slip preparation. Improved sonication procedure and control during aging are expected to further minimize the size of the agglomerates. It should also be noted that no foreign inclusions were found in any specimen. A silicon inclusion was observed inside an agglomerate in only one specimen. In all other instances the chemistry of the failure origin was identical to the matrix as determined by EDS in the SEM (Figure 18).

b) Fracture Toughness

Fracture toughness was measured by the indentation strength technique on MOR bars machined from NSF tensile rods. The values ranged from 4.5 to 6.2 MPa*$m^{1/2}$. Powder XRD was performed on the specimens with the lowest and highest toughness values to determine the amount of retained α crystal structure. The specimen with the toughness of 4.5 MPa*$m^{1/2}$ had 64% α phase as compared to only 18% α phase for those specimens which measured K_{IC} of 6.2 MPa*$m^{1/2}$.

The toughness value measured by the indentation fracture technique is plotted in Figure 19 as a function of % α phase silicon nitride for each of the iteration tensile specimens. As expected, a definite trend of decreasing fracture toughness with increasing retained α phase is apparent from the plot.

Thus it may be concluded that the overall Weibull modulus value is affected by the K_{IC} variation as well as the variation in actual flaw size. This issue will be addressed during Stage II HIP experiments as described in TASK 2. These HIP experiments will be utilized to develop the optimum time-temperature profiles to achieve full $\alpha \rightarrow \beta$ conversion and in turn higher K_{IC}.

c) Elevated Temperature Fast Fracture

Fast fracture tensile tests were performed on four specimens at 1370°C in air. The average strength and standard deviation is 361 $\pm$ 3.5 MPa.

Optical fractography showed two volume and two surface flaw origins consisting of agglomerates (same composition as surrounding matrix). High temperature fast fracture testing was also performed on 20 flexure specimens machined from tensile rods, with a resulting average strength of 575 ± 52 MPa.

d) Stress Rupture Testing

Stress rupture tests were performed on three flexure specimens machined from tensile rods at 1230°C in air at an applied stress of 350 MPa. All three specimens survived in excess of 200 hours prior to termination of the testing.

e) Tensile Tests on Presintered Pressure Cast Specimens

Strength data from "green" specimens can provide valuable insight and feedback to the processing and forming unit operations without the high costs of densification (HIPPING in our case) and machining. One of the major objectives of TASK 4 is to obtain tensile strength data from specific batches of material on both presintered and densified specimens. The dual sets of data can be correlated using Weibull statistics and fractography and establish the effects of processing steps on the strength limiting flaw origins. To that end, room temperature tensile tests were performed on 25 presintered pressure cast rods from Batch C-006. The average strength and standard deviation were 6.0 ± 1.6 MPa. These data include six buttonhead, nine surface, five near surface, two volume and three unknown failures. Optical fractography did show evidence of agglomerates, pores, and drying hoop cracks.

SELECTION OF STAGE II-III FORMING METHOD

A requirement for conclusion of Stage I (1/31/91) was a comparison of databases generated in the Injection Molding (IM) and Colloidal Consolidation (CC) baseline iterations. On the basis of this comparison, it was required (TASK 1-2, Milestone #7) to select one of the two forming techniques for the remainder of the program with the approval of the ORNL technical monitor.

Data obtained from the forming and testing of NSF (Net Shape Formed) specimens and the forming of MLP (Machined from Large Piece) specimens were used in the comparison of the IM

and CC processes. Specific data used in this comparison includes: 1) yield at each major processing sub-step, 2) total process yield, 3) total process cycle time, 4) green density uniformity, 5) room temperature average tensile strength and Weibull modulus from tensile testing iteration NSF specimens, 6) fracture toughness from MOR flexure bars machined from NSF specimens, 8) stress rupture data from MOR flexure bars machined from NSF specimens, 9) formability of MLP specimens.

The data which favors IM relative to CC are the total process yield and the uniformity of green density. CC on the other hand was found to offer a considerably shorter total process cycle time, significantly greater mean room and elevated temperature tensile strength and large section (MLP) formability in the sense of demonstrated capability to process specimens free of macroscopic drying/dewaxing cracks. The average yield of the pressure casting process has been improved considerably since the completion of this comparative study and is now comparable to IM process yield.

The overriding goal of the program is a processing methodology which delivers NSF specimens with an average tensile strength of 900 MPa and high reliability. The methodology should also be extendible to large cross-sections, such as that of the MLP specimens. The CC forming technique has the advantage in both respects, on the basis of these iteration data. The CC room temperature average tensile strength (692 MPa) is 52% higher than that of the IM route (454 MPa). Furthermore, several CC specimens had strengths in excess of the 900 MPa goal, with one being in excess of 1000 MPa. In comparison, the maximum strength recorded in the IM iteration was 663 MPa. In fact, if the pressure cast tensile strength data are separated based upon the slip type used, tensile strength and Weibull modulus as high as 862 MPa and 10.1 respectively have been recorded for the co-milled powder batch. Formability was found to be a serious problem for larger cross-sections using the IM process. As discussed under TASK 2, optimal conditions of the dewax unit operation for MLP specimens were not achieved and cracking during dewaxing remains as a technical barrier in need of resolution for large cross-sections.

On the basis of demonstrated attainable strength and MLP formability, the colloidal consolidation process route was selected and approved as the forming technique for the remainder of the program.

References

1. Adcock, D.S., and McDowall, I.C., "The Mechanism of Filter/Pressing and Slip Casting", J. Am. Ceram. Soc., 40 [10] 355 (1957)

Status of Milestones

All Milestones are on schedule. Milestone #114114 (Determine the detection capability of ultrasonics, computed tomography and nuclear magnetic imaging/spectroscopy) completed as scheduled on 3/31/91.

Publications

Fraser, J.D., Amin, K.E. and Khuri-Yakub, B.T., "High Frequency Ultrasonic Inspection of Green and HIP'ed Silicon Nitride Cylindrical Samples", presented at the Annual ASNT meeting, Oakland, CA., March 19, 1991.

Table 1

BASELINE PROPERTY DATA FOR
PRESSURE CAST SILICON NITRIDE
(ITERATION #2)

RT FAST FRACTURE

FAILURE LOCATION	MEAN (MPa)	STD. DEV. (MPa)	RANGE (MPa)	NUMBER OF SPECIMENS
GAGE/VOLUME	636	193	397-1010	9
GAGE/SURFACE	845	118	701-961	6
BUTTONHEAD	628	121	532-810	4
ALL	709	174	397-1010	20*
FLEXURE	857	126	527-1177	60

*INCLUDES ONE UNKNOWN FLAW ORIGIN

Table 2

SLIP COMPARISON
C-SERIES vs. W-SERIES

SLIP	MEAN STRENGTH (MPa)	STD. DEV. (MPa)	CHARACTERISTIC STRENGTH (MPa)	m	n
CO-MILLED (C-SERIES)	862	136	911	10.1	5
PRECIPITATED (W-SERIES)	658	158	719	4.6	15
BOTH	709	174	776	4.7	20

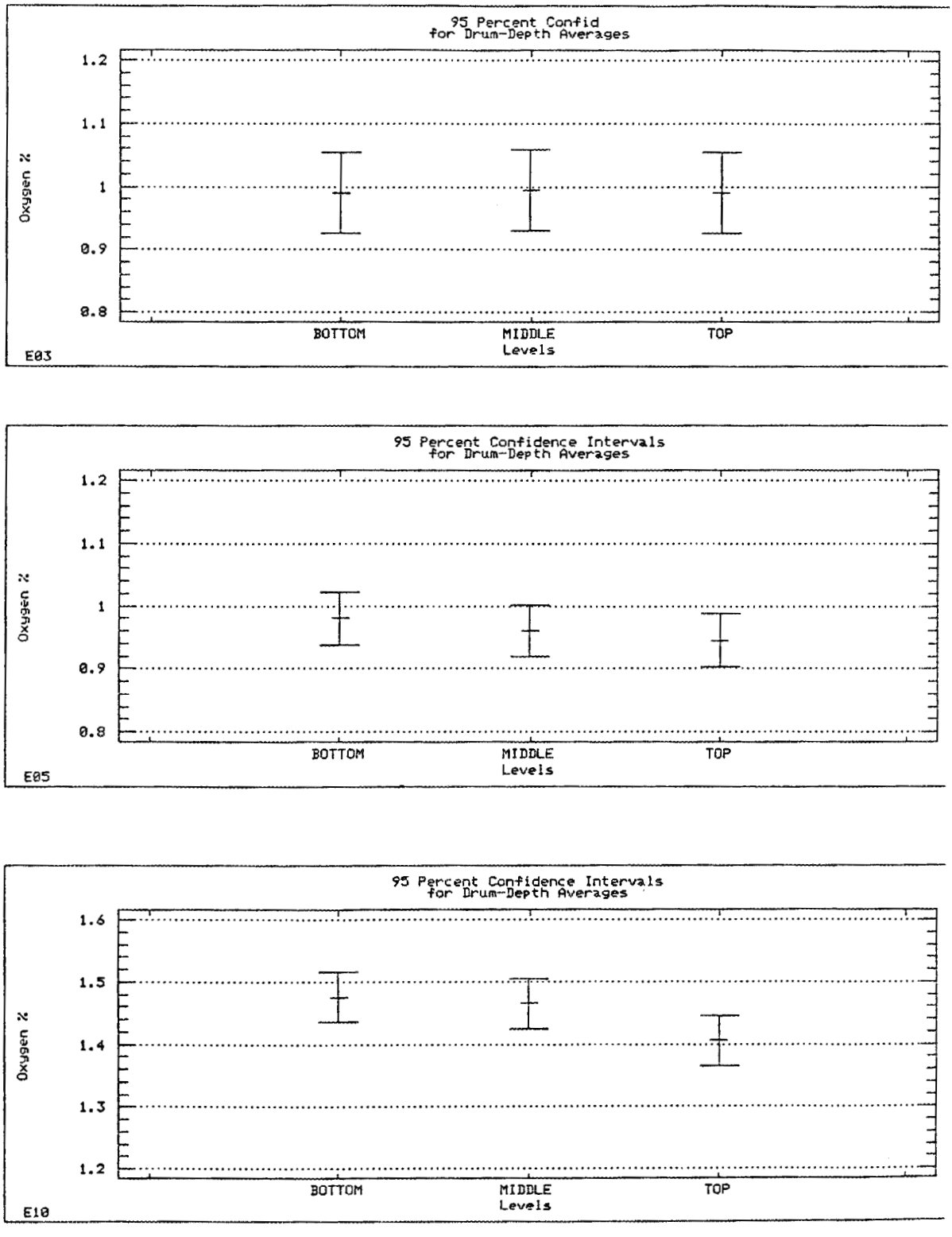

Figure 1: Oxygen level in as received Ube Powder grades E03, E05 and E010

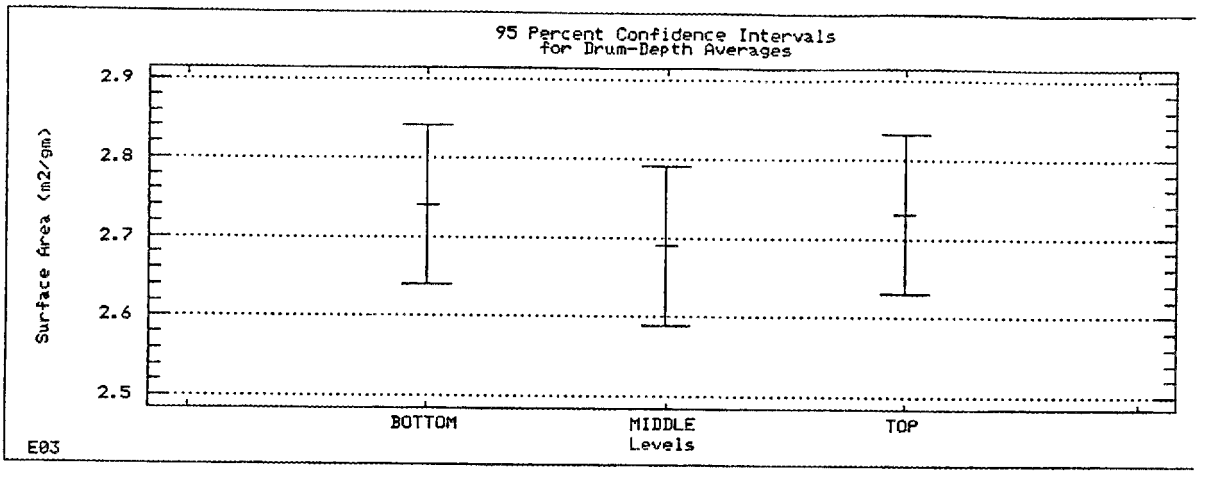

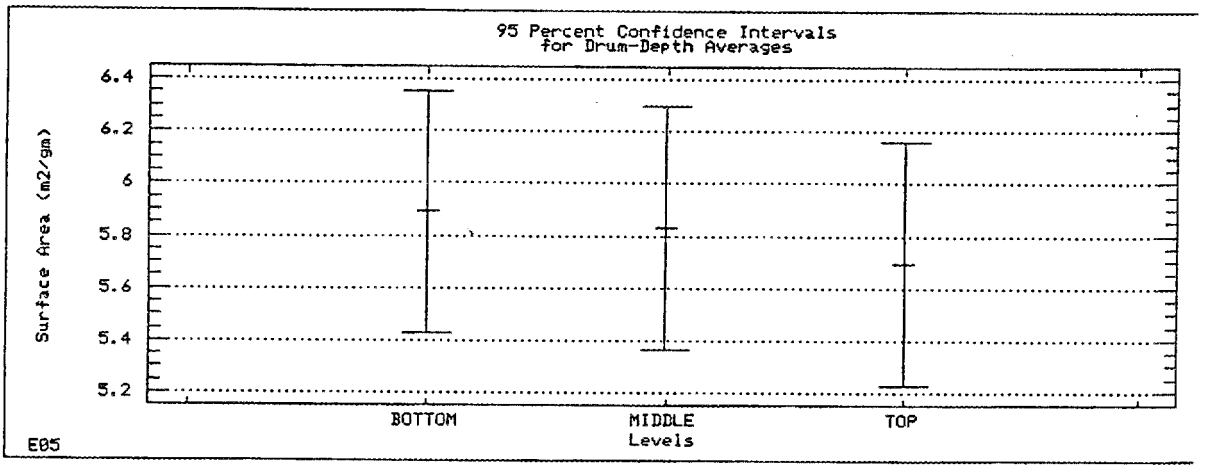

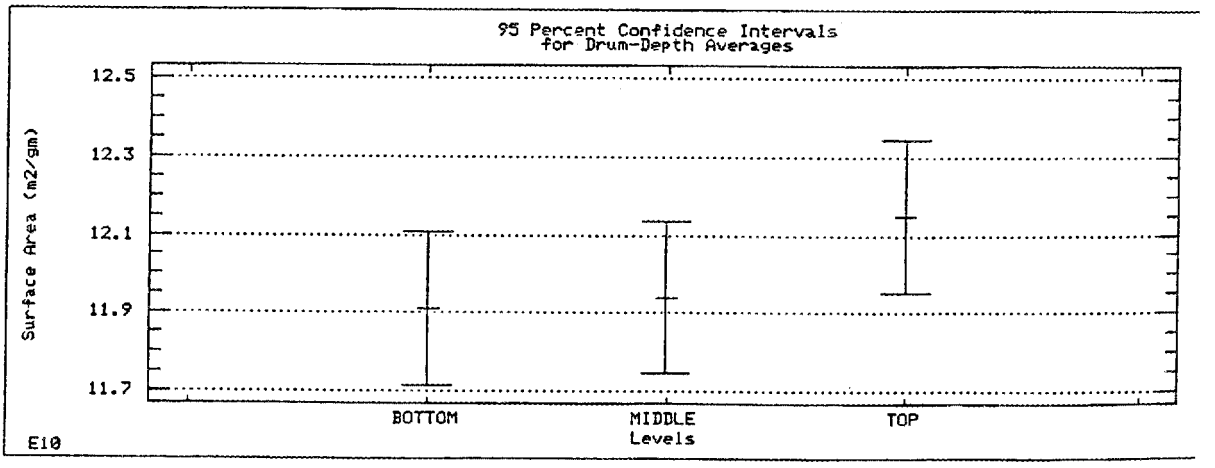

Figure 2: Surface area of as received Ube powder grades E03, E05 and E010

Figure 3:

PARTICLE SIZE - D50 FOR C-SERIES MILL BATCHES

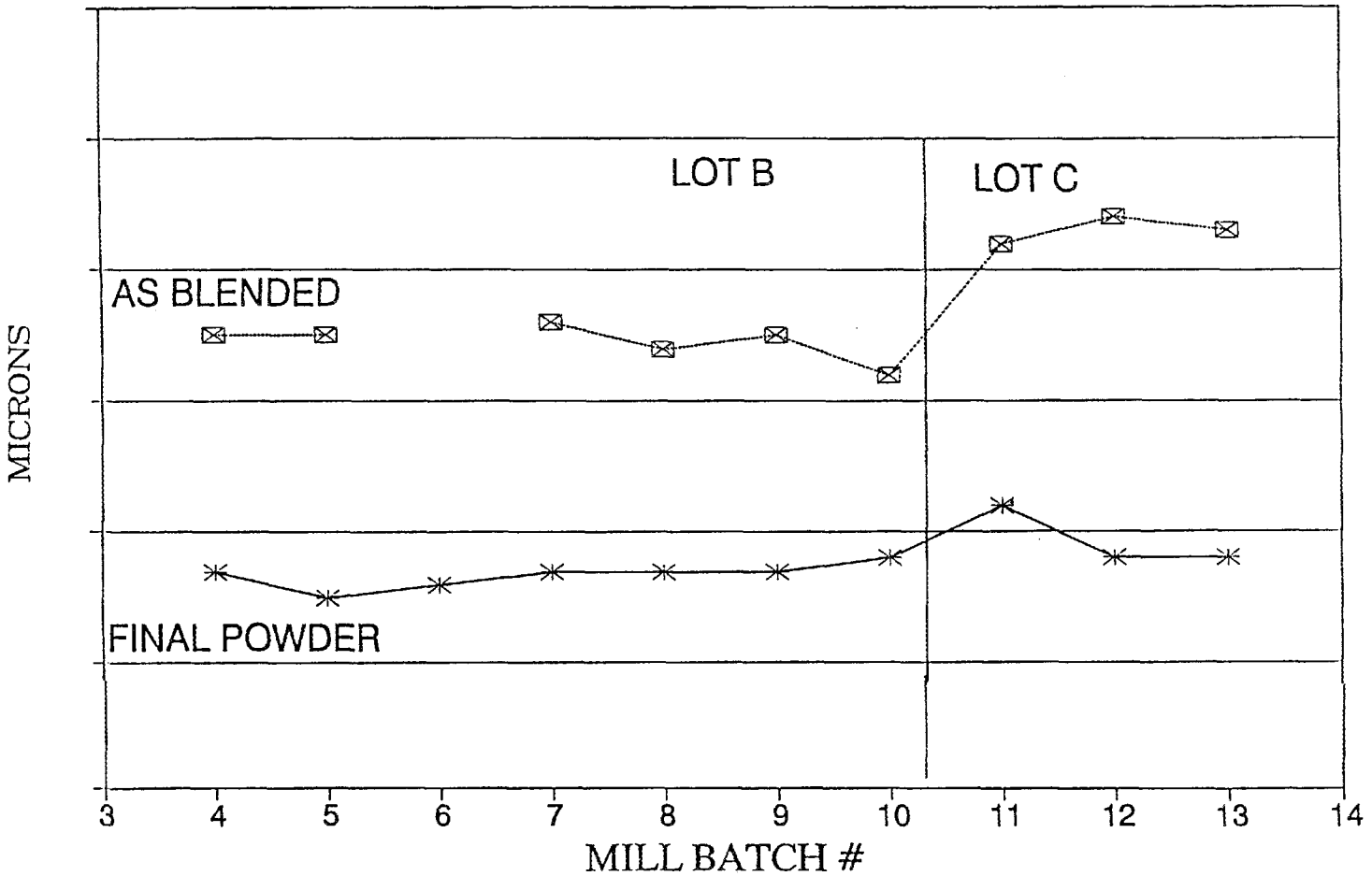

Figure 4:

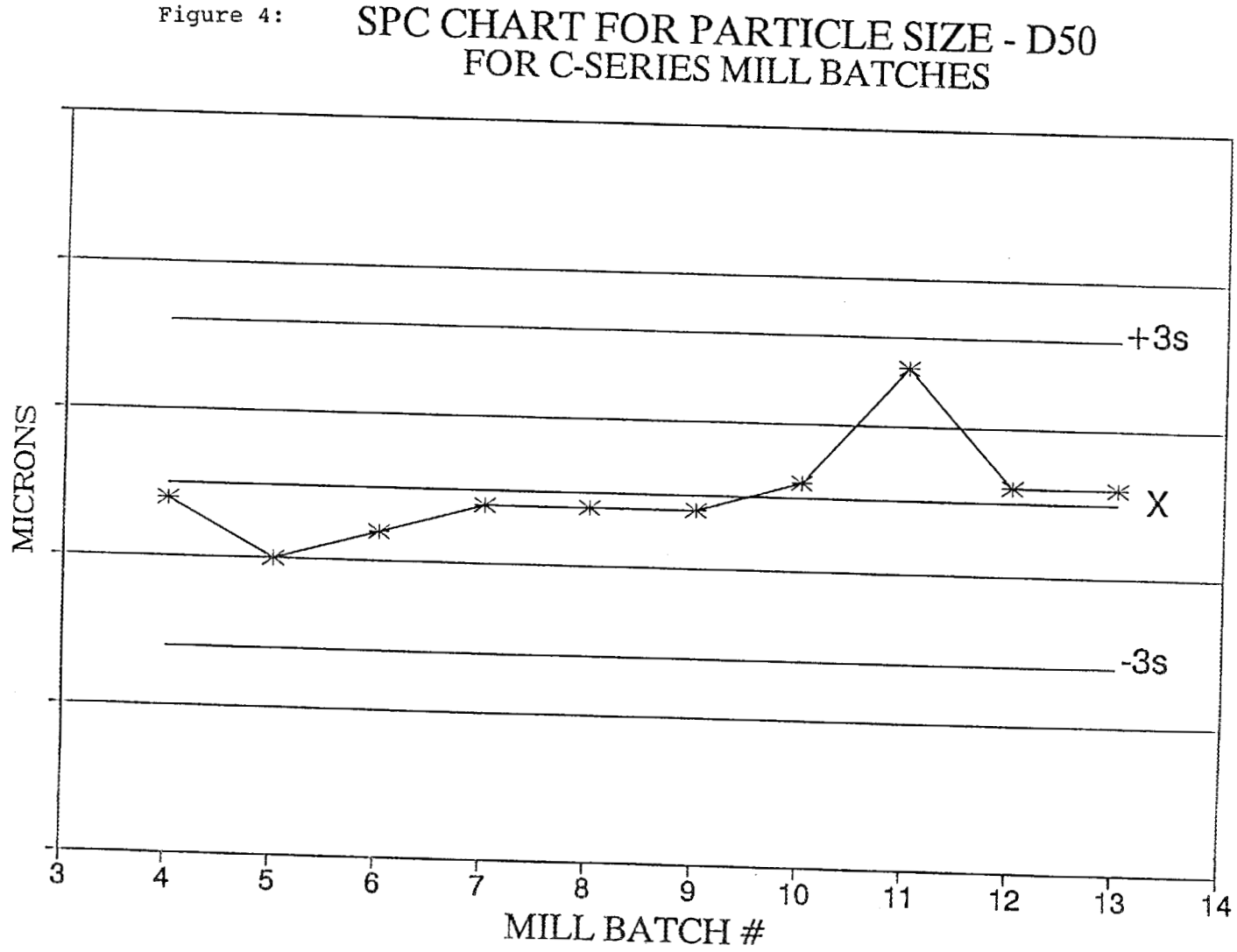
SPC CHART FOR PARTICLE SIZE - D50
FOR C-SERIES MILL BATCHES
MICRONS
+3s
X
-3s
3
4
5
6
7
8
9
10
11
12
13
14
MILL BATCH #

Figure 5:

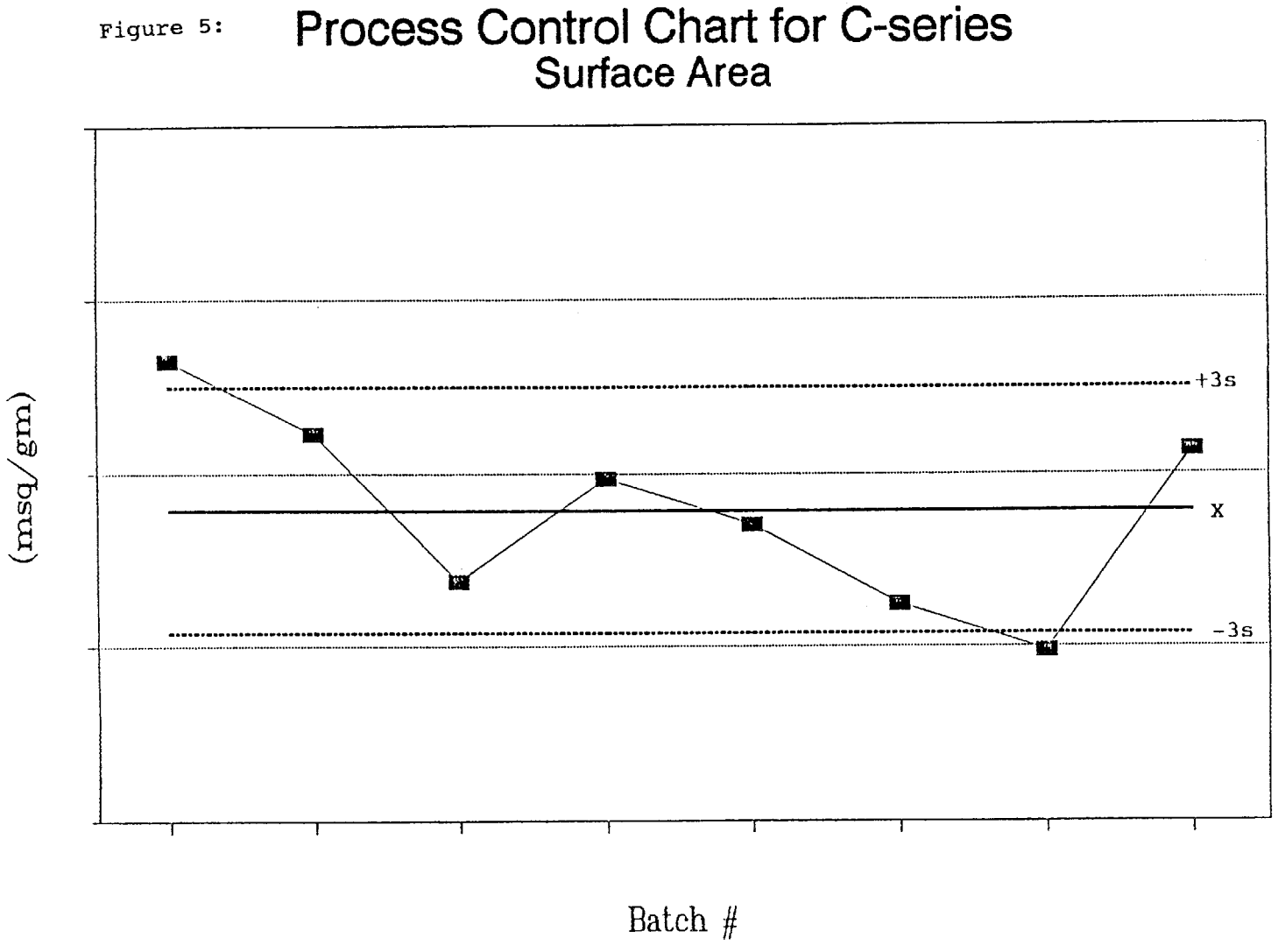
Process Control Chart for C-series
Surface Area
(msq/gm)
+3s
X
-3s
Batch #

Figure 6:

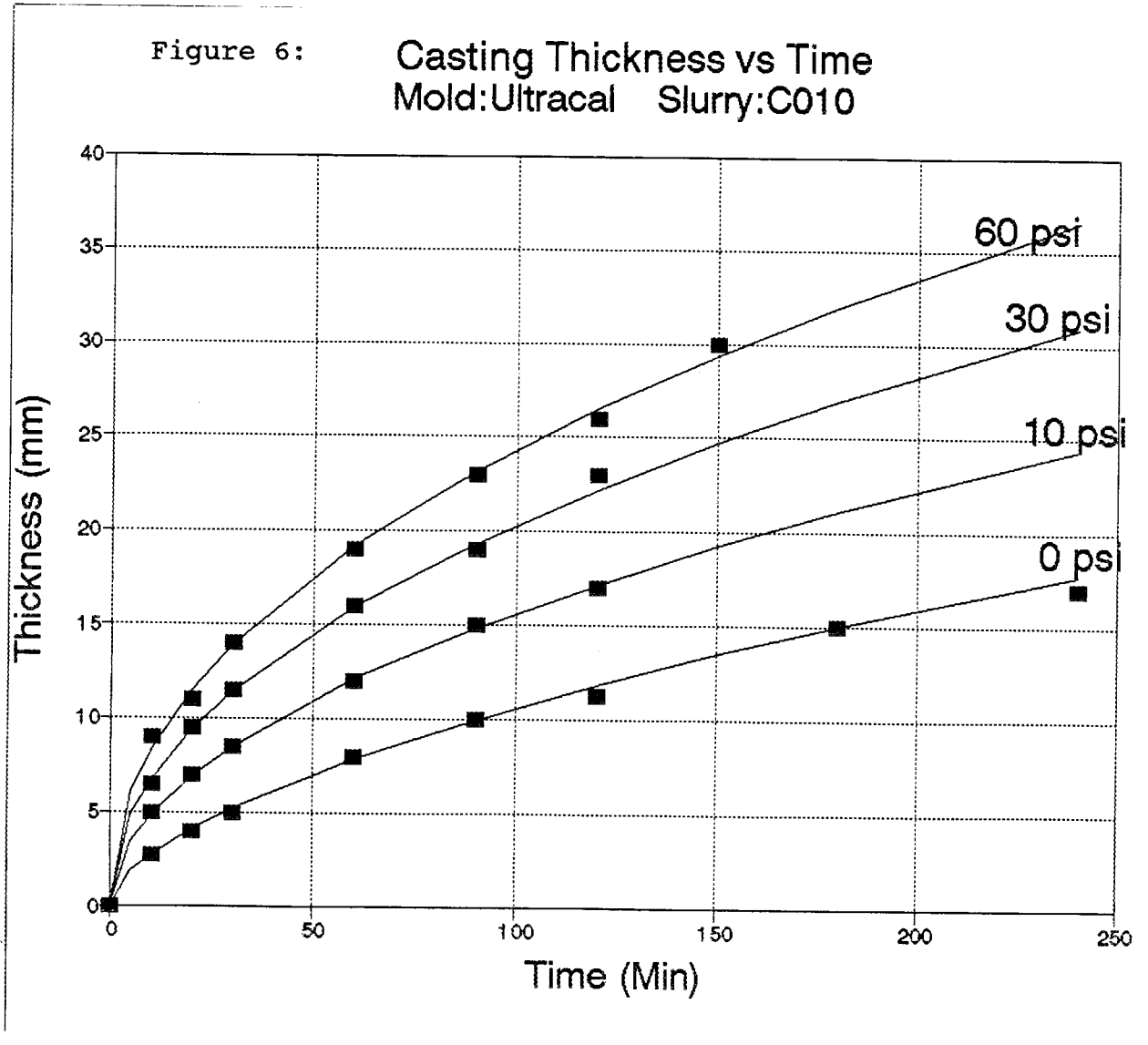
Casting Thickness vs Time
Mold:Ultracal Slurry:C010
Thickness (mm)
Time (Min)
60 psi
30 psi
10 psi
0 psi
0
5
10
15
20
25
30
35
40
0
50
100
150
200
250

Figure 7: CASTING THICKNESS vs TIME FOR C010 SLIP

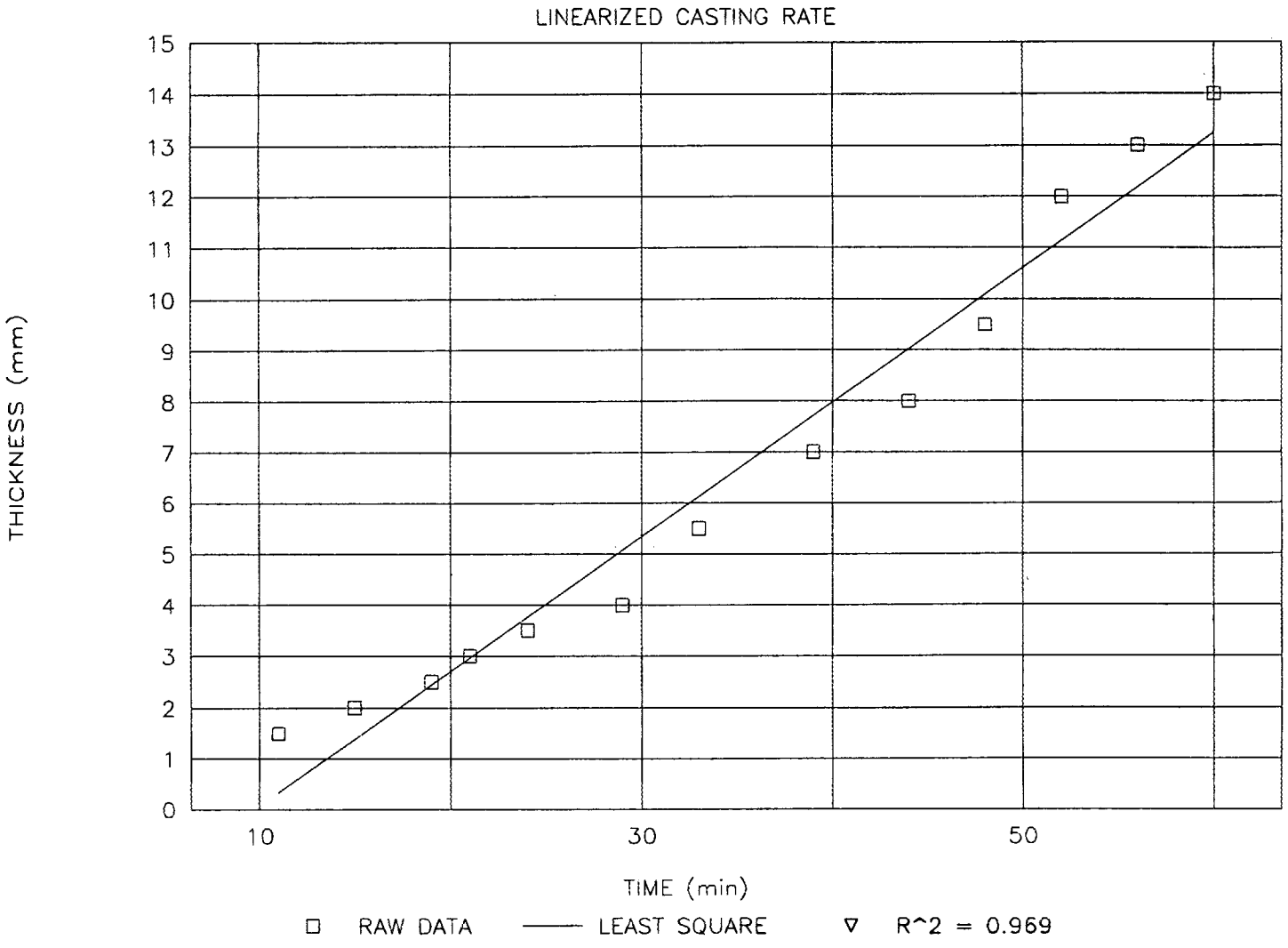

Figure 8:

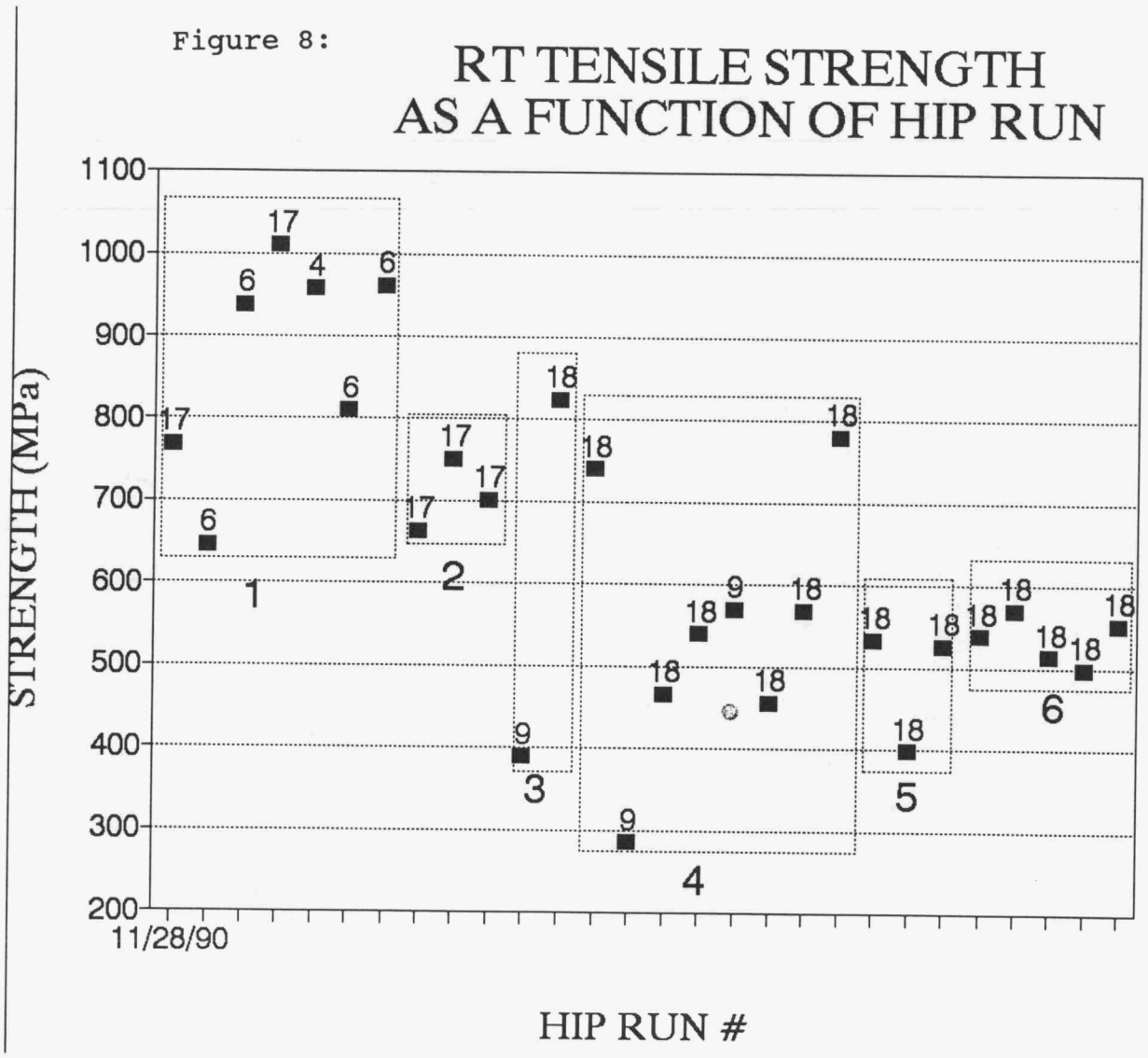
RT TENSILE STRENGTH
AS A FUNCTION OF HIP RUN
STRENGTH (MPa)
1100
1000
900
800
700
600
500
400
300
200
11/28/90
HIP RUN #
1
2
3
4
5
6

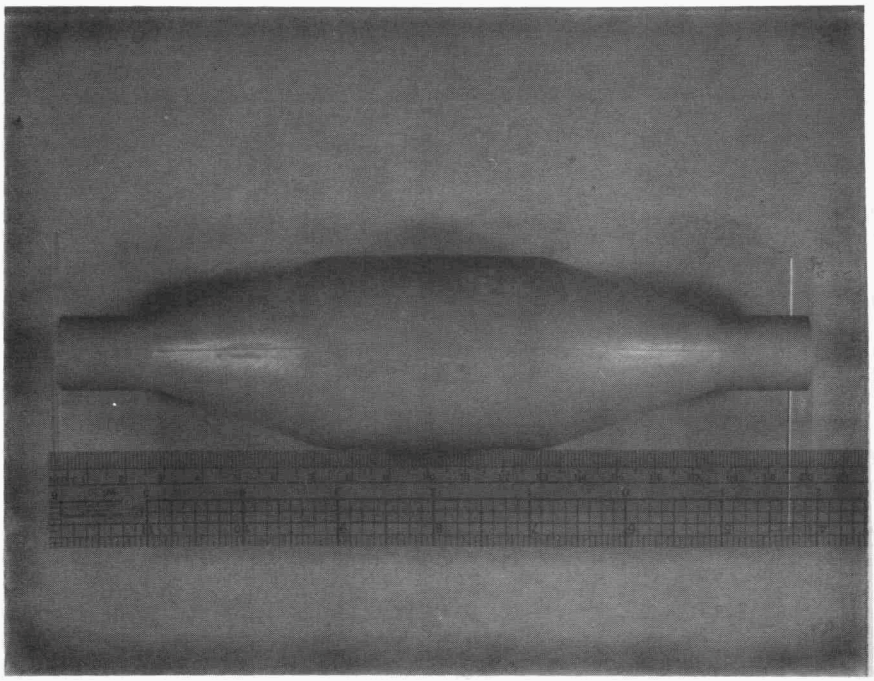

(A)

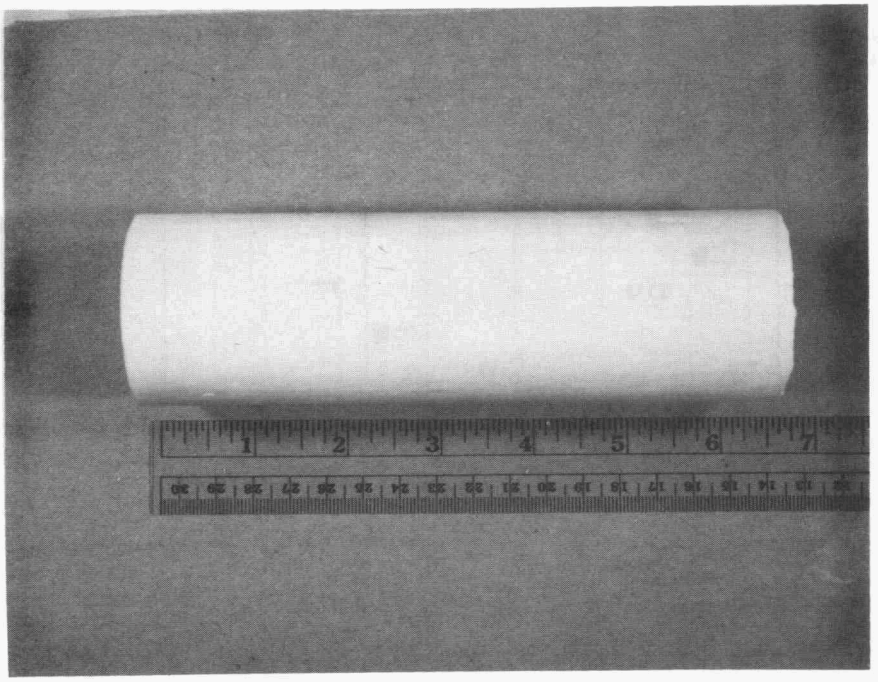

(B)

Figure 9: As formed machined from large piece (MLP) specimens:
(A) injection molded and (B) pressure cast

Figure 10:

Distribution of Voids in Green Si3N4 Rods of Iteration 1 and Batch L

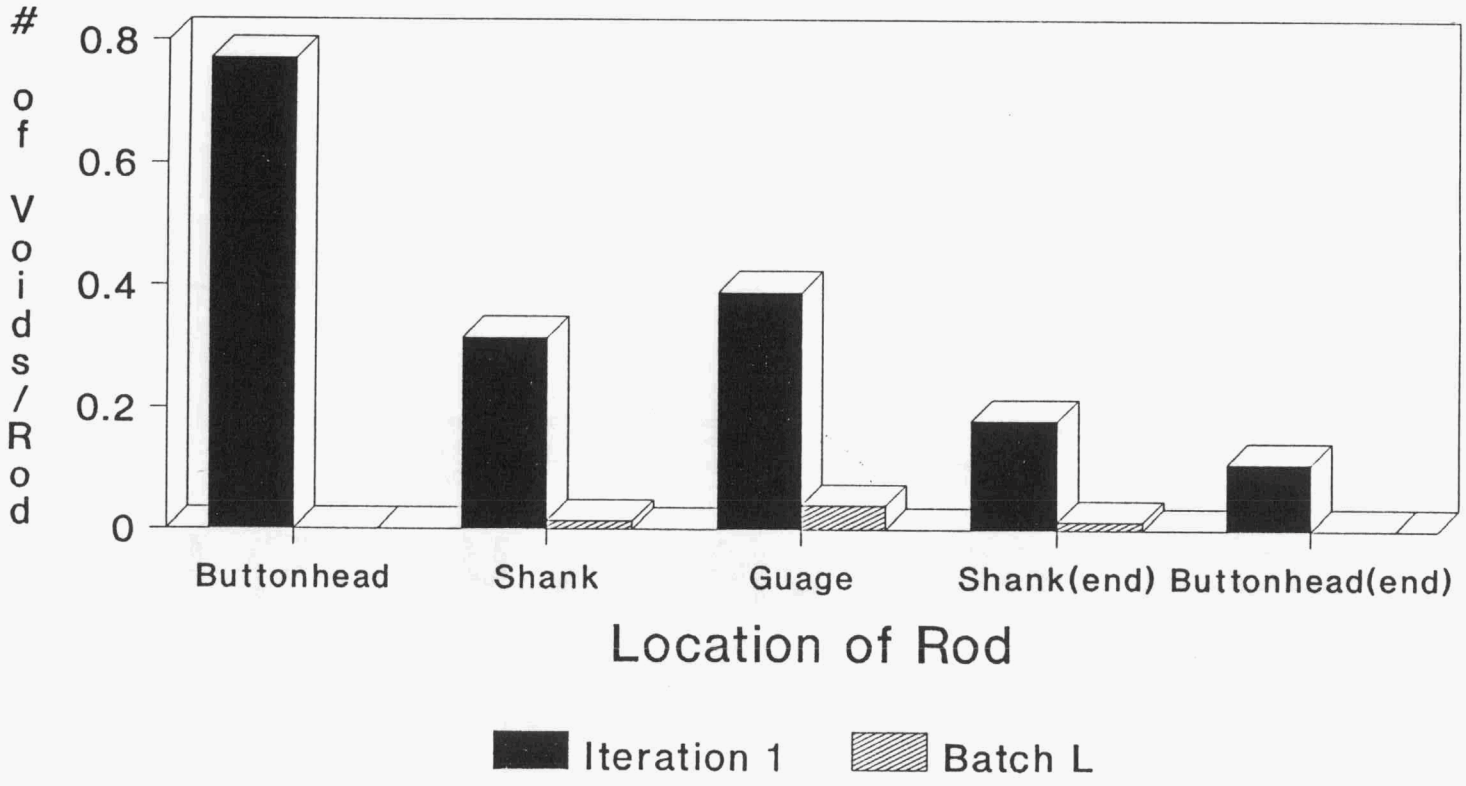

Size Distribution of Inclusions in Green SI3N4 Rods From Batchs I and L

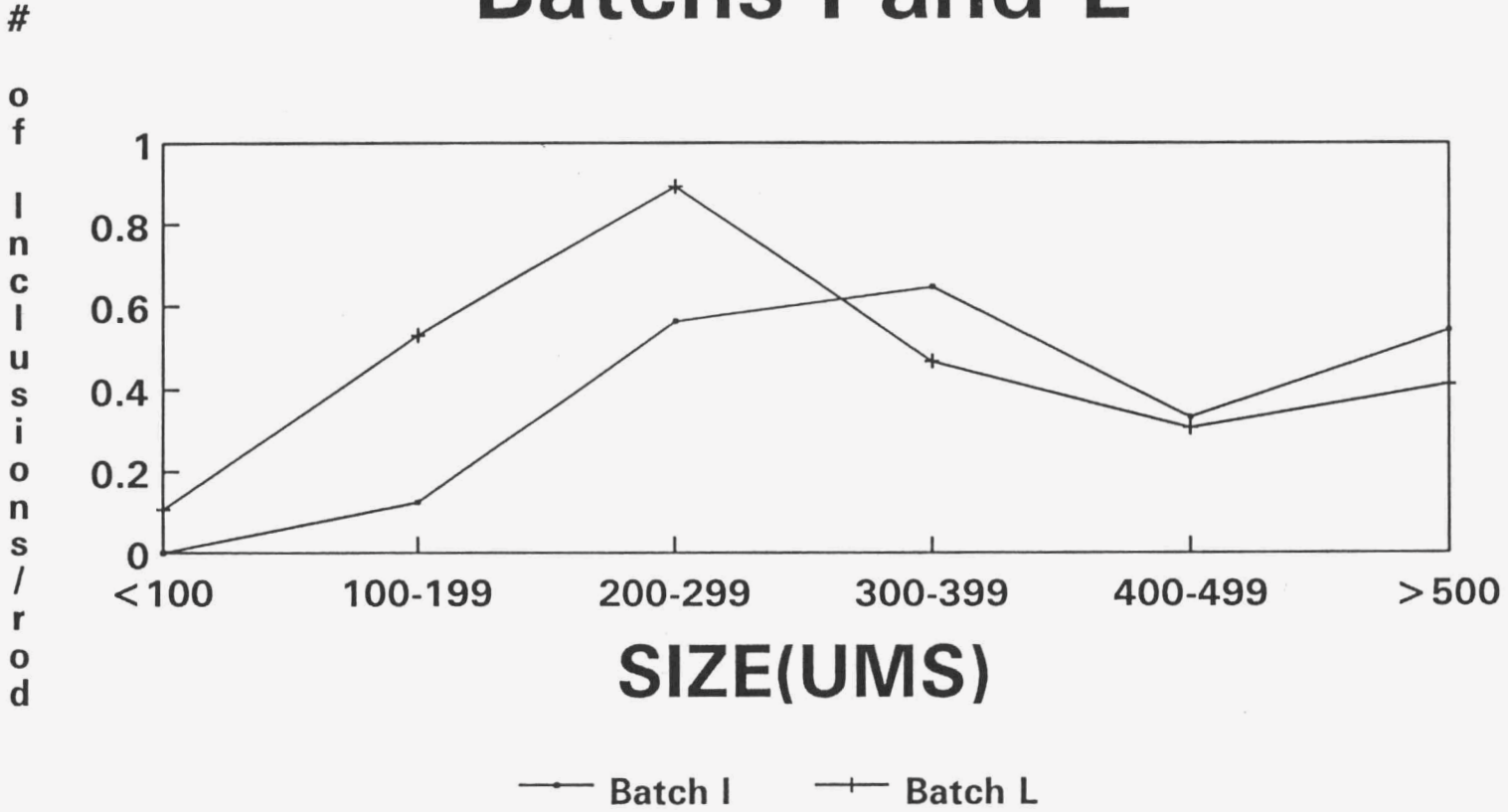

Figure 11

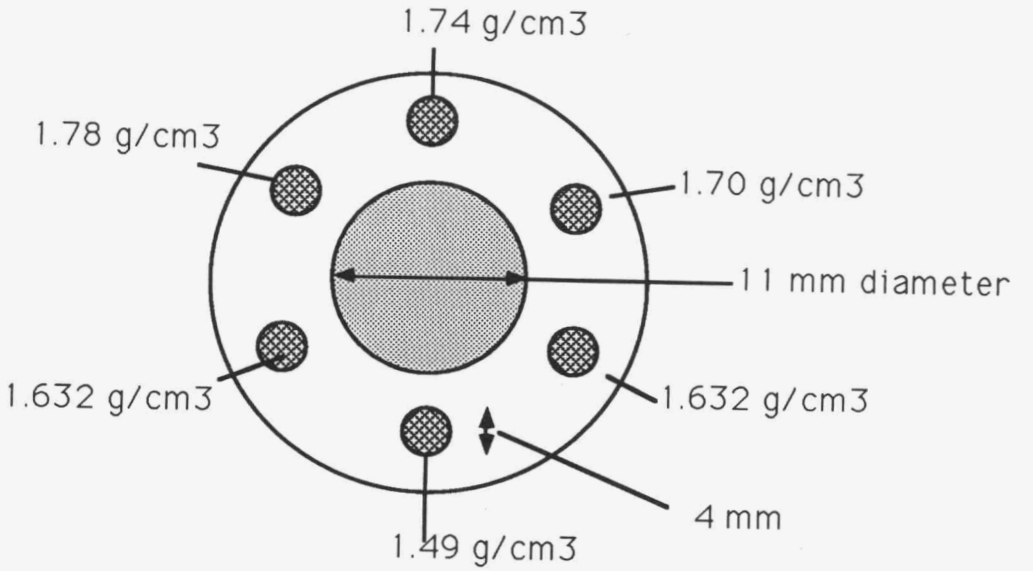

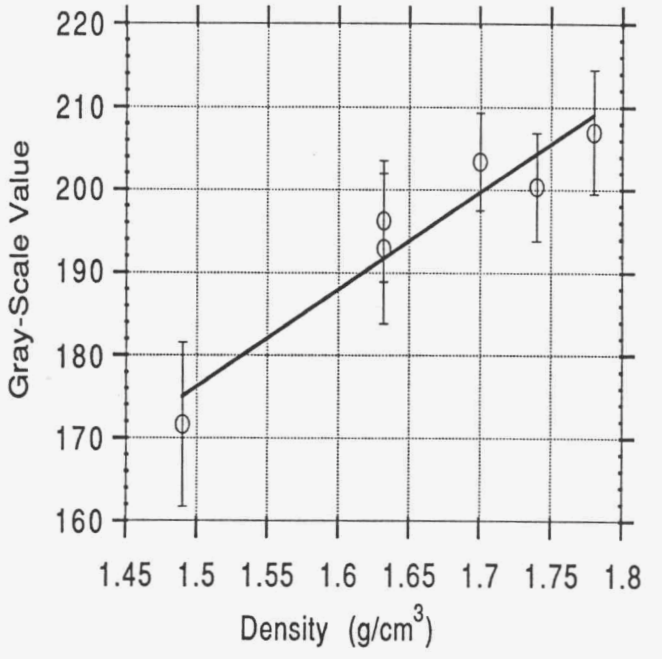

Figure 12: CT calibration phantom and density calibration plot

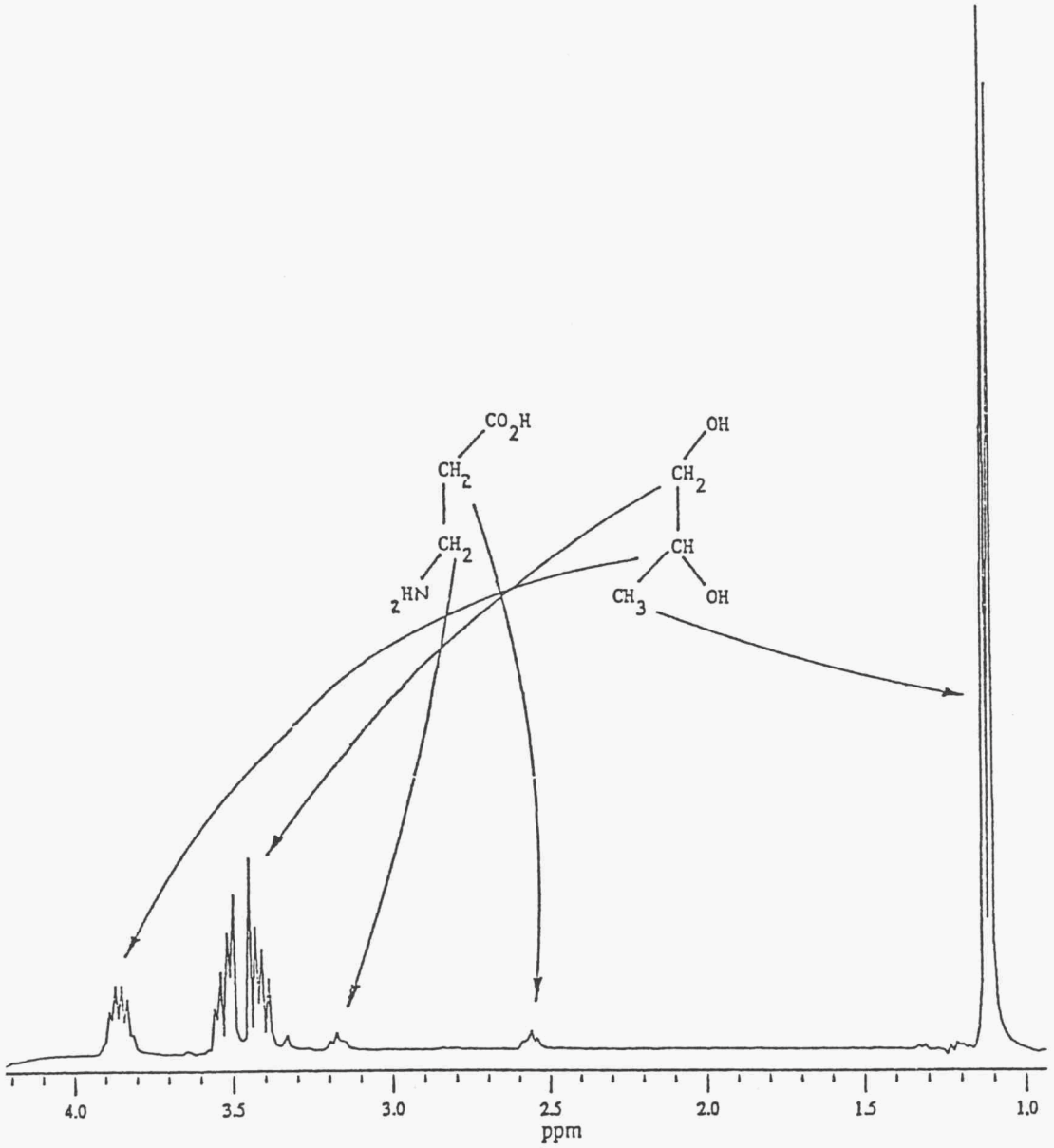

Figure 13: Proton NMR spectrum of a 1% aqueous solution of deflocculent agent with presaturation of water resonance.

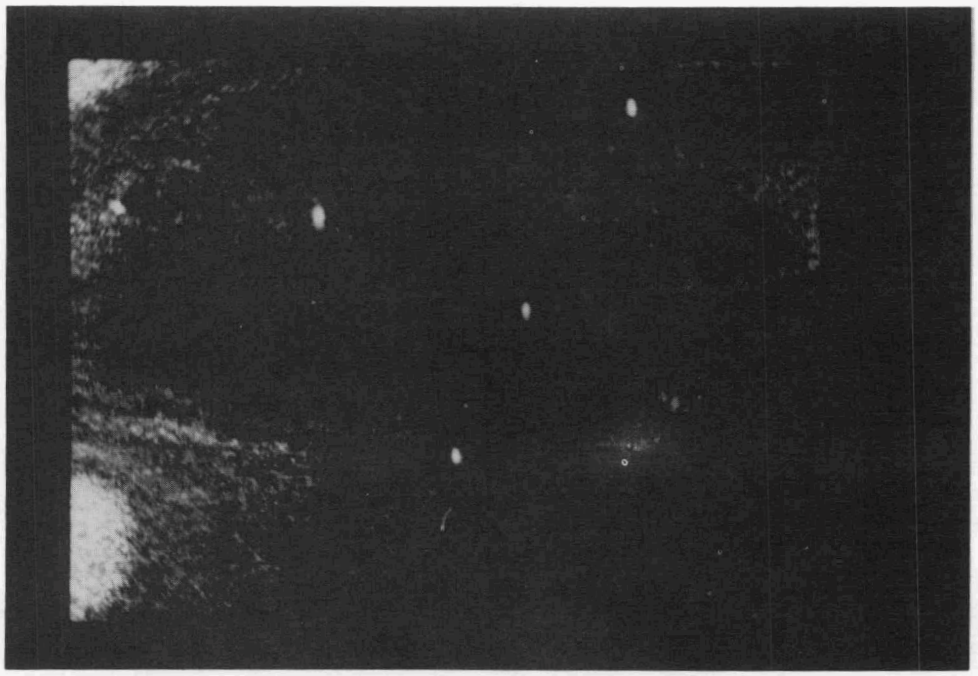

Figure 14: C-scan image of silicon nitride 8.87 mm diameter rod with 50μm seeded Fe defect (650 x 480 pixels - 40μm/pixel)

FIGURE 15. Tensile strength of injection molded bars as a function of temperature.

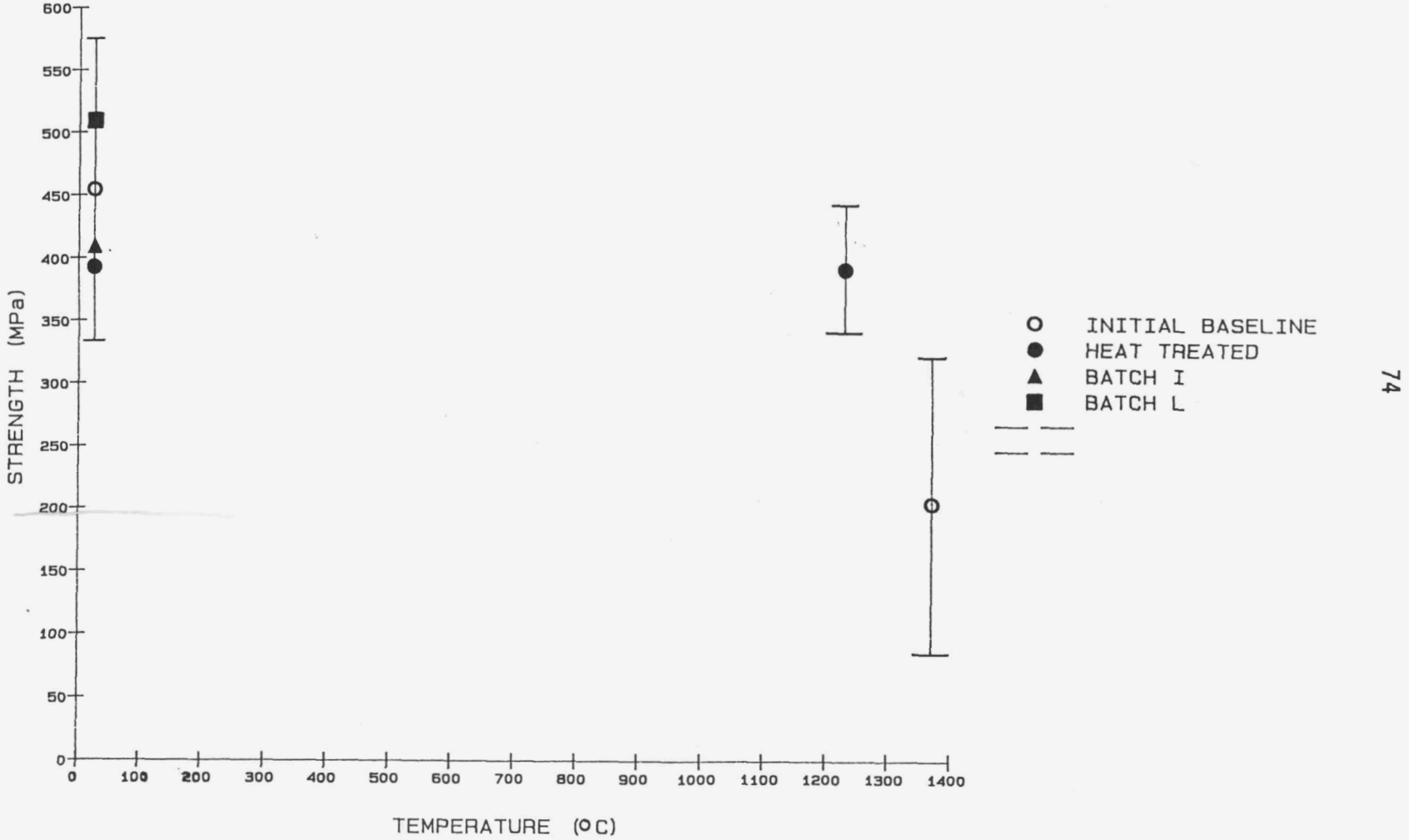

Figure 16:

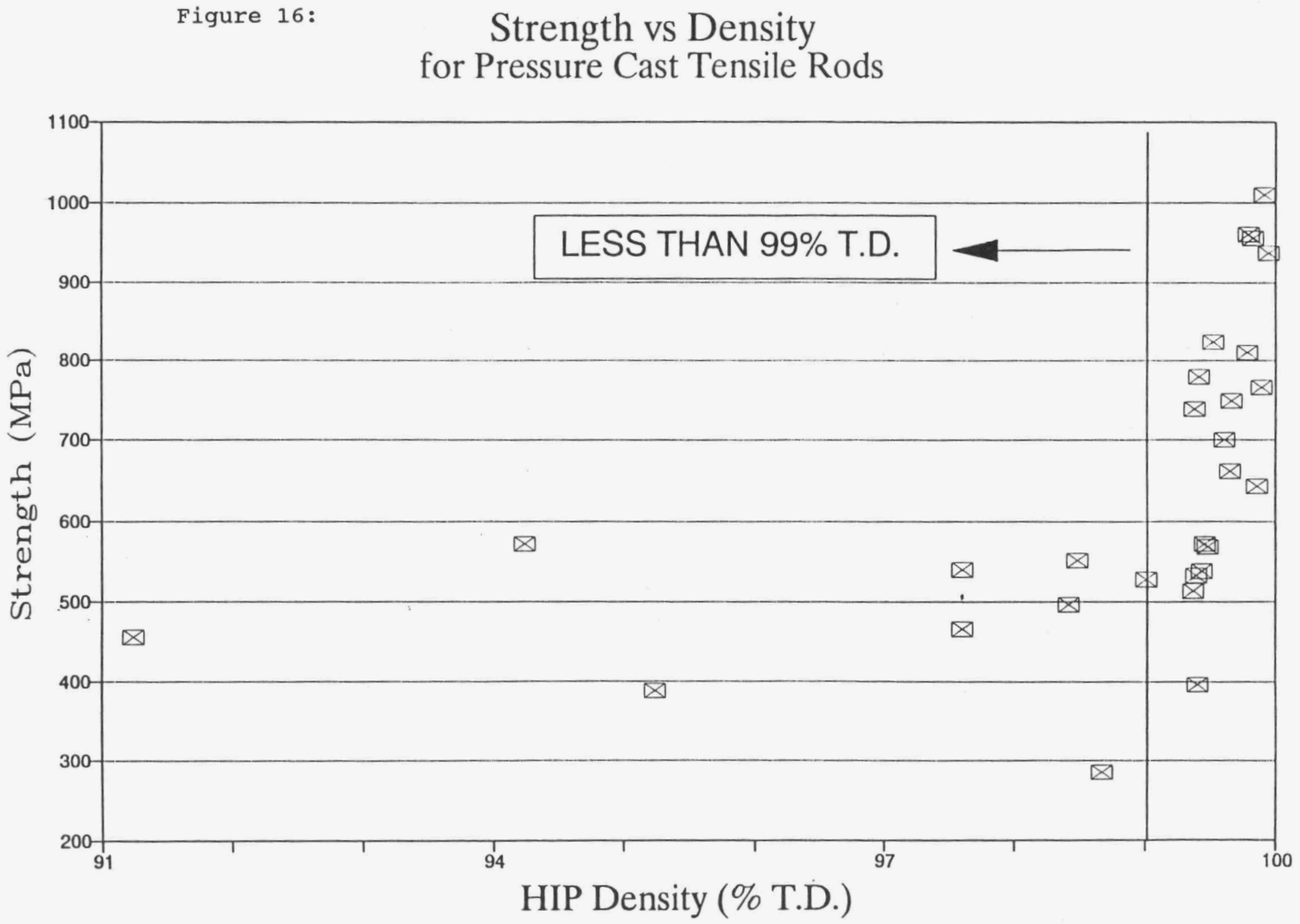
Strength vs Density
for Pressure Cast Tensile Rods
LESS THAN 99% T.D.
Strength (MPa)
1100
1000
900
800
700
600
500
400
300
200
91
94
97
100
HIP Density (% T.D.)

Figure 17 WEIBULL ANALYSIS FOR ITERATION #2

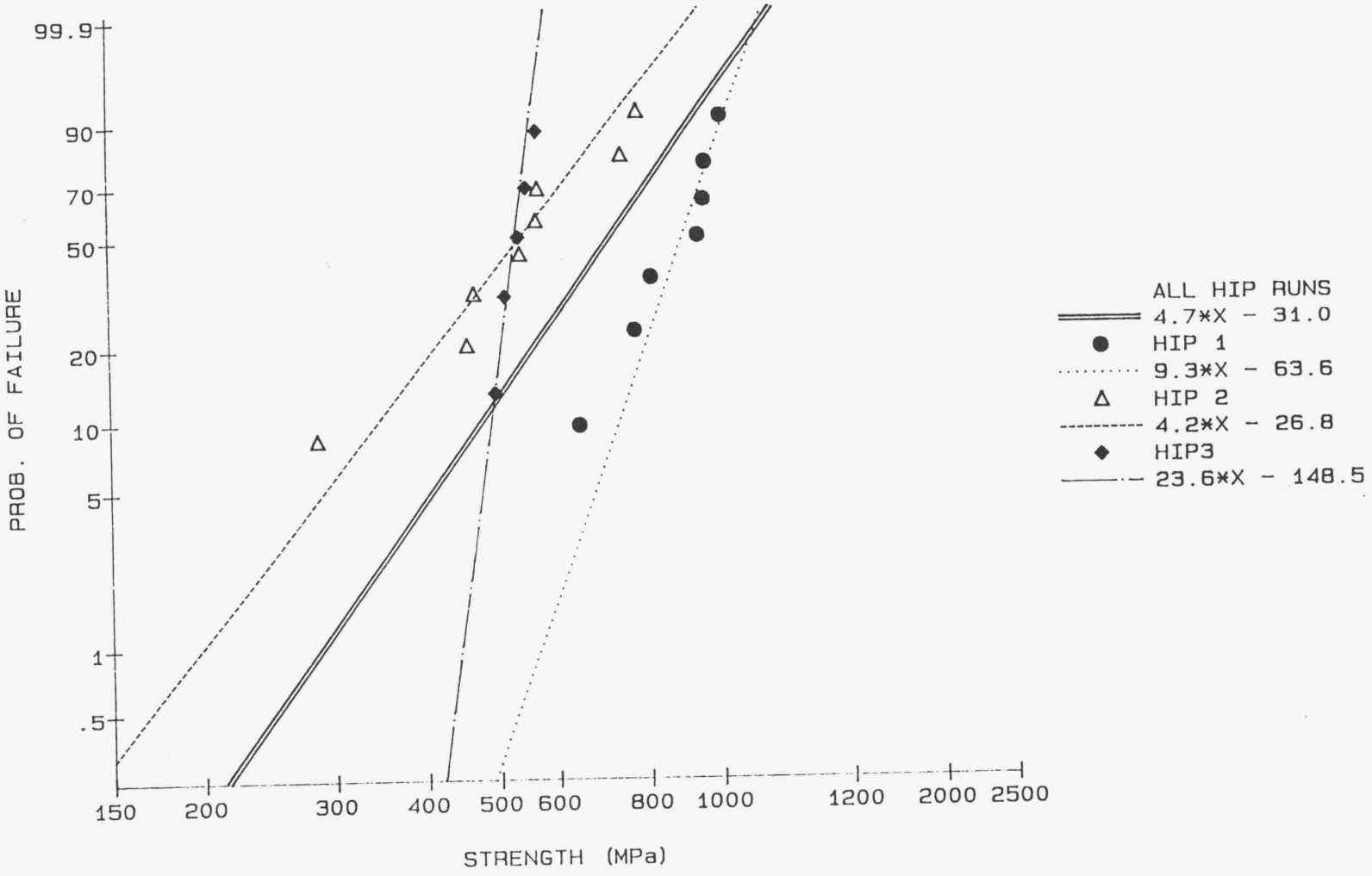

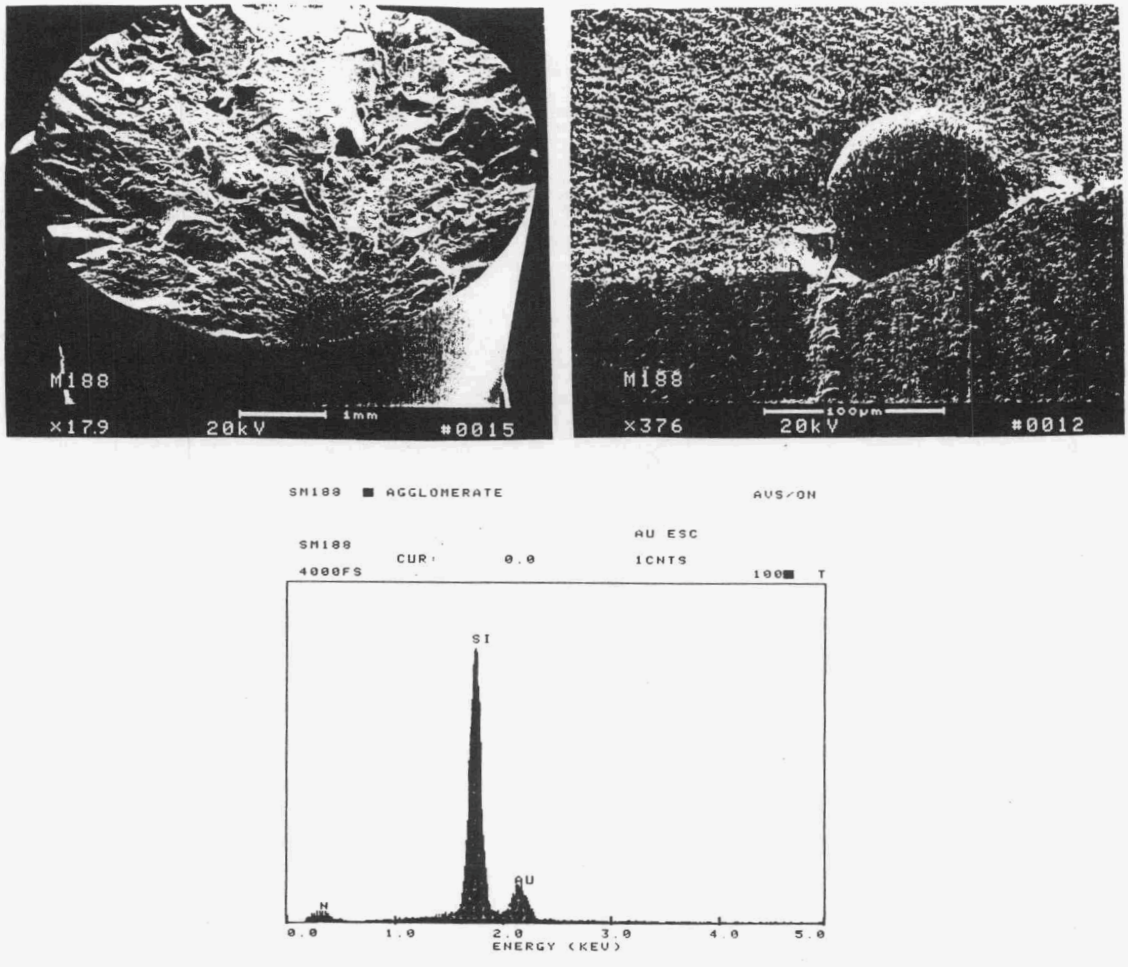

Figure 18: Fracture surface of silicon nitride tested at room temperature showing an agglomerate surface flaw associated with some machining damage.

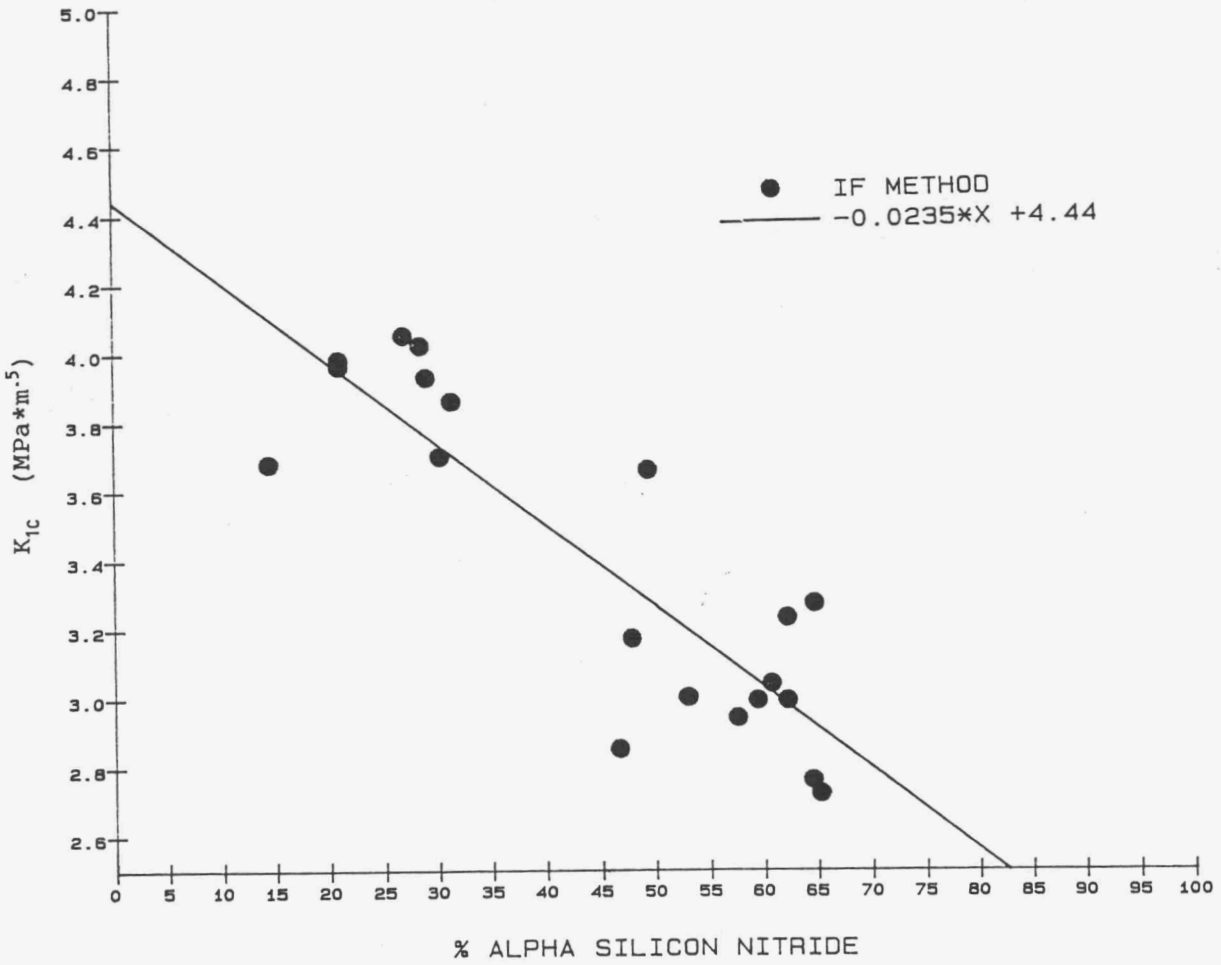

Figure 19: Fracture Toughness versus % Alpha Silicon Nitride

Improved Processing

R. L. Beatty, R. A. Strehlow, and O. O. Omatete (Oak Ridge National Laboratory)

Objective/scope

The objective of this research is to determine and develop the reliability of selected advanced ceramic processing methods. This program is to be conducted on a scale that will permit the potential for manufacturing use of candidate processes to be evaluated. The emphasis of this program is on silicon nitride. Issues of practicality; safety, hygiene, and environmental issues; and in-process testing methods are to be addressed in addition to technical feasibility. The methodology includes selection of candidate processes and evaluation of their range of applicability to various kinds of commercially available ceramic powders.

Technical progress

I. Silicon nitride gelcasting and sintering

A cooperative research and development agreement was signed with Garrett Ceramic Components Division of Allied Signal Aerospace Company. This work is described in Section III.

A series of apparently successful plate castings have been made with an 8% yttria, 4% alumina-silicon nitride formulation. A model piston cap mold, successfully tested earlier with alumina, appeared to be successful with this silicon nitride formulation. The specimens prepared in this period include:

6	Plates for subsequent tensile testing
2	Pistons
2	3-cm-diam rods
3	"Doughnut" specimens - to test for flaw introduction due to shrinkage on gelation

Three of the plates have been sintered and are being prepared for tensile testing.

II. Drying studies

Drying is a unit operation that has been thoroughly studied and is a well known part of ceramic processing. A study has been completed on the drying of gelcast parts to minimize the time needed to produce stress-free, dried bodies while maintaining part-to-part size uniformity. The powders used in this study were: alumina RCHP-DBM[a] (d_{mean} = 0.6 μm), sialon AA[b] (S_{mean} = 9 m^2/g), and silicon nitride, Denka 9S[c] (d_{mean} = 1.25 μm). The gelcasting reagents were the monomer,

[a]Malakoff Industries, Inc., Malakoff, Tex.

[b]Denka, New York.

[c]Vesuvius Research, Pittsburgh.

acrylamide [CH_2=$CHCONH_2$]; the crosslinking agent, N,N'-methylene bisacrylamide [$(CH_2$=$CHCONH)_2CH_2$]; and the free radical initiator, ammonium persulfate [$(NH_4)_2S_2O_8$]. The detailed process has been described previously. Two drying chambers were built. In one the relative humidity was controlled at room temperature and the shrinkage was measured as the sample dried; in the other, the relative humidity and the temperature were controlled independently. In both chambers, the variation of the mass of the drying part with time was recorded, and high-velocity fans circulated the air in the chamber.

Slurries containing 51.3-54.2 vol % solids of three powders were cast in the form of a plate (8.9 x 90.2 x 228.6 mm). After gelation, the plate was removed from the mold and put immediately into the drying chamber with preset relative humidity (RH) and temperature. The plate was placed in an oven at 65°C for 2 h, and its final mass was measured as the bone-dry mass. At room temperature (21 to 23°C), sialon plates were dried at RHs of 75, 85, 92, and 96%; RHs for silicon nitride and alumina plates were 75 and 92%. An alumina plate was also dried at 50°C and 75% RH to determine the effect of temperature.

The results of the drying studies are shown in Figs. 1 through 3. The moisture content, X, is defined:

$$X = [M_{wb} - M_{bd}]/M_{bd} \quad (1)$$

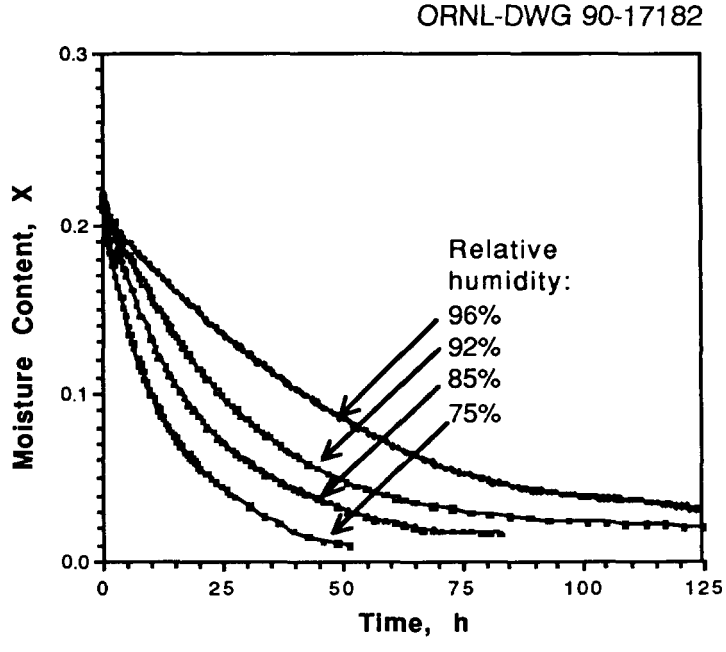

Fig. 1. Moisture content vs time at various RHs for sialon at 54.7 vol % and temp = 21 to 23°C.

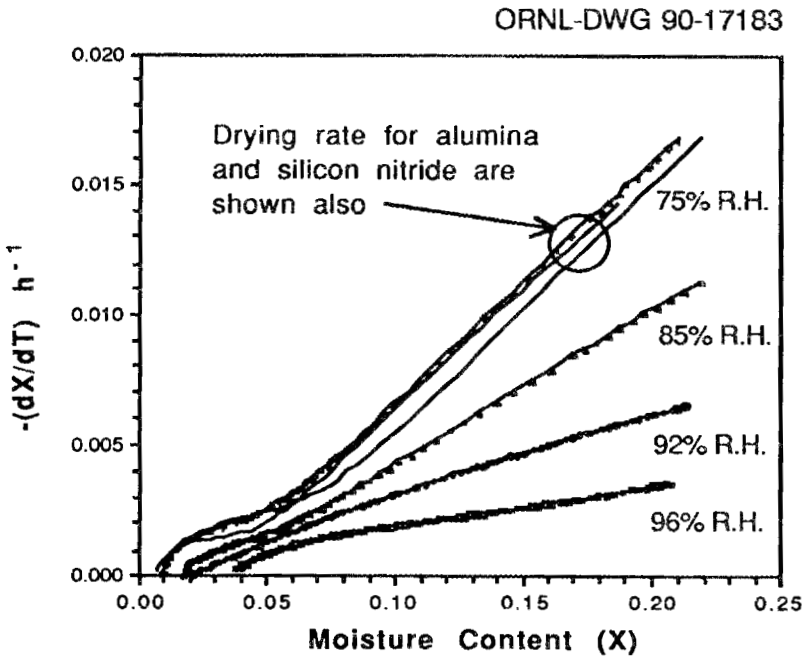

Fig. 2. Drying rate curves for sialon at temp = 21 to 23°C show no constant rate period.

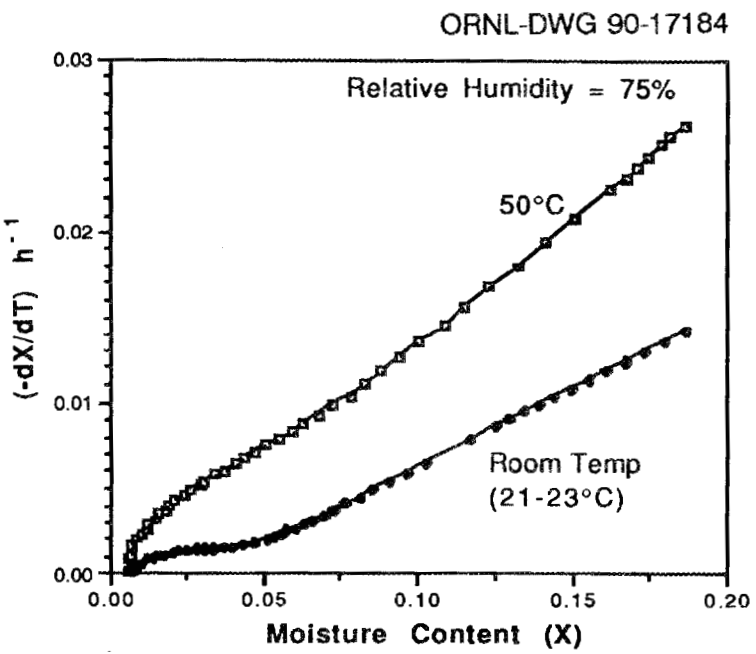

Fig. 3. Drying rate curves for alumina at two temperatures.

where M_{wb} is the mass of the wet body and M_{bd} is the bone-dry mass. The rate of drying, -dX/dt, does not include the area of the drying plate.

Figure 1 shows the drying of sialon at several RHs. The total time for drying depends on the RH; the lower the RH, the shorter the time of drying. Earlier, we established that shrinkage does not change after about 20 h although moisture content continues to change for up to 100 h. This is interpreted as follows. As the body loses moisture, the gel shrinks and the particles move closer until there is particle-to-particle contact. Shrinkage of the body then ceases. The gel shrinks and tears as drying continues. Because the particles are bonded by the dried gel, gelcast parts have relatively high strength when dried and are readily machinable.

Figure 2 shows there was no constant-rate period for any of the gelcastings studied at any humidity. Also shown in Fig. 2 is the drying rate for some other powders used in this work. Both the solids content and the particle size of the powders were approximately the same. It is not surprising that the drying behavior is similar. The absence of a constant-rate period is independent of temperature as seen in Fig. 3, which shows the rate of drying curve for alumina at 75% RH at 21 to23° and 50°C, respectively.

The absence of a constant-rate period means that evaporation is not surface controlled and that the drying is controlled from the beginning by some internal moisture movement. The nature of this internal moisture movement, whether diffusion or capillary controlled, will be investigated in the continuing study of gelcast ceramic parts.

Figure 3 shows that the drying rate increased at a higher drying temperature even at the same RH. This offers a second way to reduce the total drying time. The gelcast part is first dried slowly at high RH and room temperature until shrinking stops and then the temperature may be raised and/or the humidity may be lowered to complete the drying.

The implications and explanations of some of these findings, especially the absence of a constant-rate period, will be the focus of future work. In addition, the effect of the variation of sample shapes and sizes will also be examined.

The drying data obtained are summarized as follows:

1. Humidity is the dominant variable and room-temperature drying may be adequate for thin parts.
2. There is no constant-rate drying period.
3. The length of drying can be significantly reduced by varying the humidity and/or the temperature.

III. Cooperative research agreement with Garrett Ceramic Components

The objective of this work is for Garrett Ceramic Components (GCC) and the Oak Ridge National Laboratory (ORNL) to perform a collaborative research program to examine the gelcasting process for fabrication of ceramic components

using GCC's GN-10 silicon nitride material. This program will investigate whether the process exhibits advantages over slip casting, pressure slip casting, or injection molding in terms of the resultant material properties, parts quality, and shape-forming ability. The applicability of the process to GN-10 complex-shaped parts, such as turbocharger rotors and advanced gas-turbine rotors, will be examined.

All parts scheduled to be gelcast have been. Parts cast using the Garrett formulation and awaiting final processing and shipping to Garrett include:

11	Flat plates for subsequent tensile testing
11	T-25 Turbocharger rotors
4	3-cm-diam rods
2	"Doughnut" specimens - to test for flaw introduction due to shrinkage on gelation

During the course of the work, some inadequately deaired molds were used; therefore, a request was made and agreed to by Garrett to supply six additional molds and materials. These are planned as a supplement to the work scheduled earlier for the purpose of determining run-to-run dimensional variations.

Improved Processing

A. E. Pasto and S. Natansohn (GTE Laboratories Incorporated)

Objective/scope

The overall project objective is to develop and demonstrate a process for reproducibly fabricating a series of tensile specimens of silicon nitride with the following properties:

Average tensile strength of 900 MPa at 25°C
Average tensile strength of 500 MPa at 1370°C
Weibull modulus of 20 in both instances.

This is being accomplished by determining the source(s) of failure-causing defects, and modifying and controlling the manufacturing process to minimize their occurrence. All potential sources of defects are evaluated, from raw materials through individual powder processing and densification steps and finally through machining and surface finishing of the test specimen.

The material selected by GTE Laboratories for this program is a commercial silicon nitride powder of high purity with 6 w/o of yttria as sintering aid (GTEL's PY6 composition). Injection molding is being used to form the components which are densified by hot isostatic pressing. The composition and fabrication process were selected because they have been shown to yield ceramics capable of meeting the challenging goals of this program.

Iterative changes are being applied to the GTEL baseline material preparation process so as to eliminate failure-causing flaws, especially those generated during processing and machining.

The realization of the goals of this program is predicated heavily on understanding the factors affecting the quality of finished ceramic components. To this end, all the starting materials are being completely characterized to assure their quality. Statistical control techniques are applied throughout the process to monitor its performance and to establish operating parameters. Samples are being evaluated at all stages by both destructive and non-destructive techniques to assess the effect of process variations or modifications on part quality; primary emphasis is on identifying cause-effect relationships. Appropriate modifications of the fabrication process arrived at and implemented by statistical process control techniques are resulting in a substantial reduction of the failure-causing flaw population and thus increasing both the strength and the reliability of the structural ceramics.

Major efforts in this, the second year, involve development of process improvements aimed at reducing all sources of flaws, especially particulate contamination, but also voids, cracks, and machining defects. Process equipment and procedures are designed to yield low contamination levels. Voids and cracks are being minimized by improvements to the powders, binders, compounding and molding equipment, and burnout and HIPing procedures. Post-HIP processing (machining and annealing) is being developed to prevent compromising the material's mechanical behavior. Designed experimentation with statistical analysis is heavily utilized.

Technical progress

Task 1 - Material Selection and Characterization(S. Natansohn and W. Rourke)

POWDER MODIFICATION

The statistically-designed study to define the optimum conditions for thermal modification of the baseline powder is nearly complete. The interim results confirm the previously reported initial findings concerning the advantages of the treatment and are consistent with the underlying assumptions about the system; no surprises have been encountered to date.

In the meantime a 4.5 kg lot of powder, sufficient for the fabrication of tensile strength test rods, was prepared under the previously established modification conditions. The treated powder was then milled with the sintering additive, i.e. 6 w/o yttria. This powder lot was fully characterized and a billet was hot-pressed for the determination of the mechanical properties. Table 1 summarizes its properties in comparison to the baseline material as well as to a previously evaluated small lot of modified powder.

These results demonstrate the reproducibility of the enhanced properties of the modified powder. The powder data were obtained on fully processed material, thus including the sintering aid, and prior to densification. The smaller surface area and changes in surface composition are a consequence of the modification treatment. These characteristics manifest themselves in higher density and flexural strength, both at room and elevated temperatures. Powder modification also improves the oxidation resistance of the ceramic. Fabrication of tensile test specimens from this powder is in progress.

An electron microscopic examination of ceramic specimens made from the baseline powder, from a treated powder and from one containing an admixed amount of silica equivalent to the oxygen content increase realized during the modification treatment was completed. Bright-field transmission images taken by STEM show comparable grain size ranges for all three materials (from less than 0.5 to over 3 μm); many grains have aspect ratios of 3-5. The intergranular phase is visible as dark contrast regions around the silicon nitride grains and is present in triple point junctions as well as a thin boundary layer

between grains. Electron diffraction patterns show that the intergranular phases in all three samples are amorphous except for one small region of the modified material where a crystalline phase was detected. Quantitative microanalysis of the intergranular region yielded the results shown on Table 2. (See also the following section of this report).

These data indicate that the additional silica present in the system, as a result of either the treatment or the silica addition, enters the intergranular phase, an anticipated result. And while this compositional change may cause the observed improvement in the strength at room temperature, it appears to have no effect on the strength at high temperature as evidenced by the fact that the silica-admixed ceramic has the same flexural strength at 1370°C as the baseline material whereas the treated material is stronger by about 40% (Table 3).

The atomic ratios of Y/Si found in the intergranular phase by AEM (Analytical Electron Microscopy) differ from those found in the leaching solution resulting from treating the ceramics in a closed vial with 1 M HCl at 90°C for 24 hours (see the section entitled Chemical Characterization of Ceramics, below). The probable reason is that under these conditions the HCl treatment results in the dissolution of only a fraction of the intergranular phase as indicated by the amount of the samples leached out, the nominal value for these samples being 6 w/o. The AEM examines the intergranular phase in situ and thus provides a direct measurement of the composition. However, the amount and the composition of the soluble fraction correlates directly with the flexural strength at room temperature as shown in Figure 1. This relationship was observed in a previous experiment and reported in the previous Bimonthly Report and has been confirmed on this sample set. The room temperature modulus of rupture values are plotted as a function of the amount of material dissolved in Fig. 1. The relationship is linear with a correlation coefficient exceeding 0.9. Studies are continuing to further define and clarify these interactions.

POWDER PARTICLE MORPHOLOGY AND EFFECTS ON STRENGTH:
Silicon nitride powders which were either modified(see above) or treated with HF were milled with 6 w/o Y_2O_3, hot-pressed to full density, and the strengths compared to the baseline material. The modified material had the highest strength while the HF-treated had the lowest strength.

The powders were examined by SEM both before and after hot-pressing to determine whether there were any microstructural differences. No visible differences in the particle surfaces or size distributions were apparent in the treated powders prior to densification. After hot-pressing, however, substantial differences in the Si_3N_4 grain development were revealed in polished and etched sections of each densified billet.

The HF-treated powder displayed a substantial increase in grain size(Fig. 3) relative to the baseline powder after hot-pressing(Fig. 2). X-ray diffraction analyses indicated that, similar to the baseline, the alpha-to-beta Si_3N_4 transformation was complete for the HF-treated material. Conversely, the billet produced from the modified powder(Fig. 4) had significantly smaller grains than the baseline material, with many in the submicron range. These were probably alpha-Si_3N_4 grains since X-ray diffraction analyses indicated the presence of 18% residual alpha-Si3N4. That is, increasing the oxygen content of alpha silicon nitride powder in PY6 results in a reduced amount of transformation and growth of beta grains during densification, while the strength at both 25°C and 1370°C is improved relative to the baseline material.

AGEING BEHAVIOR

The ageing study described previously was continued for another 66 days. The results of measurements of the soluble silicon and ammonia on the powder surface are given in Table 4 and compared with data obtained at earlier time intervals. The data indicate that, within the accuracy of these determinations, the solubility of silicon and ammonia in powders stored under these four conditions is comparable, confirming the long term stability of the powder surface and therefore its shelf life.

CHEMICAL INCORPORATION OF SINTERING ADDITIVES:

The study of the effects of chemical incorporation of the yttrium oxide sintering aid on the properties of silicon nitride ceramics has been expanded to inlude the use of a methanolic solution of yttrium nitrate and of yttrium isopropoxide as the metal source. In the former case, the requisite amount of yttrium nitrate was dissolved in methyl alcohol, mixed with silicon nitride powder to form a homogenous slurry, slowly evaporated to dryness and then thermally converted to the oxide. The yttrium isopropoxide was in a toluene solution which contained 19.8 w/o of the reagent. The appropriate amount of this solution was added dropwise to a vigorously stirred slurry of silicon nitride powder in isopropanol. Upon completion of this addition, a solution of 5 ml of water in 25 ml of isopropanol was added dropwise to the slurry to hydrolyze the isopropoxide to the hydroxide. The solids were filtered, dried overnight and then converted to yttrium oxide by calcination. The presence of the required amount of yttria was confirmed in both powder formulations by chemical analysis.

The resulting powders were sieved and used to hot-press billets, without any additional processing. The ceramics appeared fairly inhomogeneous. The data obtained in the evaluation of their flexure strength at room temperature and at 1370°C are given in Table 5 and compared to a standard preparation (which includes a powder processing step) and to

one made directly from powder into which the sintering aid was added by means of an aqueous yttrium nitrate solution.

The results listed in Table 5 show that neither of these addition routes has a beneficial effect on strength of the ceramics. The incorporation of the yttria from an alcoholic solution provides ceramics which are, at best, comparable to those made from a powder treated with an aqueous solution and the latter technique is easier and less expensive. The isopropoxide method leads to clearly poorer materials; it is also very costly as the current reagent price is $ 1000/lb of contained Y-isopropoxide.

CHEMICAL CHARACTERIZATION OF CERAMICS:

An effort has been initiated to study the acid solubility of densified PY6 ceramics so as to assess the relation of the chemical behavior with mechanical properties such as strength. A particular goal of this investigation is the determination of the intergranular phase composition. The reagents used are 1M HF and 1M HCl; there is little reaction upon treating the ceramics with these acids at room temperature but at 90°C both dissolve substantial amounts of material. However, results of initial time studies indicate that the two acids react quite differently with the PY6 ceramics.

An experiment was performed in which weighed ceramic bars were placed in plastic vials (one per vial), a fixed volume of 1M HF was added, the vials were tightly sealed and a whole sample set was heated at 90°C. A vial was withdrawn at time intervals over a span of 186 hours, the liquid analyzed and the dried bar weighed to determine its weight loss. It was found that the dissolved fraction of the bar increased with increasing reaction time, reaching16 w/o after 186 hours. Furthermore, the molar ratio of Si:N found in the solution after a reaction time of only 48 hours was comparable to that of silicon nitride (0.75). Both of these facts indicate that the ceramic matrix rather than the intergranular phase is being dissolved. An additional disadvantage of this technique is that Y is not soluble in HF and was not found in the solution.

The results are quite different when the ceramics are reacted with 1M HCl in the same manner; the experiment was carried out at 90°C over a time span of 357 hours. The total amount of dissolved matter is below 5 w/o. Most of the dissolution occurs in the initial 2-3 days; a slower reaction period follows during which there is a gradual increase in the amount of dissolved yttrium and silicon but not ammonia. A similar behavior was observed[1] in a study of the dissolution of Y and Al from silicon nitride ceramics and ascribed to a shrinking core mechanism during the rapid initial reaction and to a diffusion controlled mechanism during the slower portion. The HCl treatment is useful for the purpose of characterization of silicon nitride ceramics in that it dissolves primarily the

grain boundary as evidenced by the presence of Y, Si and N in varying amounts in the solution, whereas HF dissolves the silicon nitride as indicated above. Thus, it is selective and affords a facile distinction between the intergranular phase and the matrix. The extent of the dissolution reaches a reasonable level after only 24 hours and it is this condition, i.e., digestion for 24 hours at 90°C in 1M HCl, that has been adopted as a new analytical technique for the characterization of silicon nitride ceramics.

The results of such a characterization performed on a set of PY6 ceramics hot-pressed from modified silicon nitride powders prepared previously are summarized in Table 6. The table lists the weight fraction of the various bars dissolved in the HCl treatment as well as the amounts of Y, Si and NH_3 found in the acid solution per gram of the original sample weight. The penultimate column gives the molar ratios of the constituents while the last one lists the four-point room temperature bending strength measured on these bars.

The data show significant variations in the amount of dissolved material as well as in the relative concentrations of soluble constituents present in the leachates from these ceramics which were made from differently treated powder. The largest variation is in the amount of yttrium found which indicates a different solubility and therefore a different composition of the phase in which it is present in the various ceramics. The amount of Y present in a material containing 6 w/o yttria (PY6 formulation) is 47 mg/g; the Y found in this experiment is 16-63% of this total. The weight of dissolved ceramic corresponds well to the amount of dissolved yttrium; this is to be expected because yttrium is a primary constituent of the boundary phase which is attacked by the HCl.

But the most striking correlation is that between the room temperature flexural strength and the molar ratio of Y to Si found in the leaching solutions which is plotted in Figure 5. The relationship is linear with a high correlation coefficient. It lends support to the postulate that the composition, as manifested by the solubility, of the intergranular phases in these ceramics made from differently treated powders is different. The Y:Si ratio in the ceramics with the highest strength is 1.0, implying the presence of yttrium silicate, $Y_2Si_2O_7$. This compound was not detected by x-ray diffraction but its concentration may have been too low for the detectability of this technique, or it may not have been well crystallized. Its presence may be inferred from the chemical data and from the high material strength. This material also had the lowest soluble nitrogen content. As the ratio of Y:Si increases, the strength of the ceramic decreases, implying the formation of other, more soluble Y-compound and glass phases, with higher nitrogen content and with inferior mechanical properties. It is to be emphasized that all these variations were observed on ceramics made from the same powder which has undergone various, rather mild, treatments to modify its surface composition. These results demonstrate the all-important impact that powder

surface stoichiometry has on ceramic properties, the underlying premise of this experimental approach.

Task 2 - Material Processing and Process Control(F. Avella, G. Dodds, A. Hecker, J. Neil, A. Pasto, F. Sivo,D. Sordelet, C. Tarry, J. Vickery)

This task has two major thrusts: the first is to develop and apply appropriate techniques for controlling the injection molding/HIPing processes for the chosen silicon nitride composition and shapes through statistical process control (SPC) so as to minimize the occurrence of defects. The second thrust is to improve each individual process step and incorporate these improvements into the overall process.

BASELINE MATERIAL PREPARATION:

The first set of deliverable tensile rods was shipped to ORNL in October. The second set, representing a second iteration of the baseline processing sequence, was sent in November. The third iteration, cut from MLP specimens, was shipped in March, 1991.

A set of 63 tensile specimens was shipped to the University of Dayton Research Institute (UDRI), for ambient and 1370°C fast fracture, as well as stepped-temperature stress rupture and static stress rupture testing, to assist in establishing the baseline mechanical properties of our material(see UDRI report in Task 4). Ambient fast fracture data on baseline material will thus be available from GTEL, UDRI, and ORNL for comparison purposes. Results of the testing at GTEL and UDRI, and other characterization tests, are discussed in Task 4.

The NSF die has been received and has been utilized to prepare test specimens. It will be used for all other deliverables with the exception of a final set of rods to be prepared from the MLP die.

Over fifty MLP rods were molded, dewaxed, HIPed, and finished into test specimens. The object of preparing 6 mm diameter tensile specimens from a green blank with a 45 mm diameter(MLP) cross-section was to demonstrate that the dewaxing process did not result in cracking of the blank. Cracking of thick cross-section components during dewaxing has long been considered a weak link in the injection molding process for high performance materials. The current baseline process is free of this problem, as demonstrated by the fact that none of the HIPed blanks showed dewax-type cracking patterns. Some surface cracking was noticed on a few of the blanks at the gate-to-blank joint, but these were shallow and were readily removed during grinding. Tensile specimens were prepared, with some being sent to ORNL and others tested at GTEL.

Test results on the GTEL specimens are described in Task 4.

LIQUID PROCESSING:

Equipment for liquid processing has been received and a dedicated facility to perform a thorough and meaningful assessment of the benefits of such a process completed. The facility permits a variety of processing procedures to be evaluated on a scale adequate to provide kilogram batches of powder-binder mixtures for injection molding. Each piece of equipment is also scaleable, with larger units of increased throughput available, such that any desirable processes may be adopted in a production capacity. The layout of the liquid processing lab is detailed in Figure 6.

The dispersion of powders in a variety of solvents is now possible by means of milling, high shear mixing or ultrasonication, also the dissolution of injection molding binders in the same or different solvents. The high shear mixing together of powder suspensions with binder solutions or molten binder, or powder with molten binder, will now be investigated. Milling, mixing and reaction vessels have full temperature control by means of one of two different water recirculator heater/chiller systems. Those mill and mixer parts subject to wear have already been either plastic coated or hardfaced to reduce or prevent metallic contamination. Powder suspensions can be screened through a variety of mesh sizes using a vibratory screen with the assistance of vacuum if required. Where the attritor mill is used to generate the powder suspensions, the liquid ring vacuum pump can be used to transport these suspensions from the milling container through the vibratory screen and into the mixing tank ready for further processing. This should reduce handling losses and contamination. Two types of high shear mixer were purchased in order to investigate the effectiveness of both rotor stator and saw tooth impeller types in mixing different combinations of powders, binders and solvents. The former mixer type is better suited to low viscosities; less than 10,000 centipoise, while the latter is better suited to higher viscosities; 500 to 3,000,000 centipoise. Processing solvents will be removed using either an explosion proof forced air dryer or a rotary evaporator. For future manufacturing, if these processing routes are successful, it is intended to remove such solvents in the final mixing/compounding operation from a closed container by evaporation under vacuum, recovering the solvents using a condenser and cold traps for small volumes or absorbant media such as activated carbon for larger volumes.

While awaiting completion of the liquid processing lab, an investigation of liquid processing procedures was begun using equipment in operation at the GTE-Chemical and Metallurgical Division in Towanda, PA to compare the following:

*Type of milling:
Attritor vs Sweco

*Screening:
No screening vs screening after milling vs screening before and after milling

*Milling medium:
Dry vs water vs 2-propanol vs xylene vs octamethylcyclotetrasiloxane (OMTS)

*Surface area of Y_2O_3:
7 m2/gm vs 20 m2/gm vs 40 m2/gm

Powders were prepared where possible with stearic acid addition to act as a wetting agent for the waxes used for injection molding. Attritor-milled powders were also prepared without stearic acid for initial densification studies by hot pressing and HIPing. Powders were isostatically pressed at 310 MPa to give 25 x 25 x 50 mm billets for HIPing. Sweco-milled powders were all prepared with stearic acid addition, and were subjected to an air burn out treatment at 550°C/5hrs prior to densification.

Hot pressing at 1750°C/5ksi/3hrs gave high densities for most attritor-milled powders; densities of 3.258 ± 0.003 were typically achieved. Under these same conditions, Sweco-milled powders did not yield good densities. Further attempts to densify these powders by hot pressing at 1775°C/5ksi/3hrs did not show any improvement. Previous hot pressing at 1750°C of PY6 compositions made from Ube SN-ESP powder by Sweco milling has achieved high densities. It should also be noted that of the previously investigated ESP powders, the particular lot used for these milling investigations is the only one which did not give consistently high densities in repeat hot pressing runs.

Hot isostatic pressing at 1825°C/24ksi/1.5hrs gave high densities of 3.252 ± 0.003 for all powders.

Densified materials were machined into MIL STD 1942 "A" geometry MOR bars. For each material 10 bars were broken at room temperature and 3 bars at 1370°C. Weibull modulus (m) was calculated for the room temperature bars from the mean strength (x) and standard deviation (s) of the data using the expression;

$$m = 1.21 (x/s) - 0.47$$

Tables 7 to 10 summarize the densities and MOR data resulting for the different materials.

Several conclusions can be drawn from these data about factors affecting modulus of rupture; however, different conclusions may be found concerning factors affecting tensile

strength when this has been measured for these same materials. Adequate quantities of each of the different materials were prepared to manufacture tensile rods. These are awaiting the development of a non-contaminating compounding and molding process to allow observation of the influence of the various powder treatment variations. Without such a process any powder treatment effects will be masked by the presence of high density inclusions.

For carefully processed powders there is no benefit to screening of the powders after milling, as mean strength and Weibull modulus are unchanged by this procedure. The volume of material tested in MOR is very small, and this procedure may very well yield improvements in tensile strength, particularly in the Weibull modulus. A small strength improvement was observed in both hot pressing and HIPing for screening of powders prior to attritor milling, which warrants further investigation.

There is a small effect of the liquid vehicle used for milling; the polar liquids, water and 2-propanol, give slightly higher strengths than the low dielectric constant liquids, xylene and OMTS. This may relate to the dispersion of the powders in these liquids, good dispersion being easily obtained in the polar liquids but considerably more difficult to achieve in the others.

Attritor-milled materials yielded superior strength to Sweco-milled materials; however this observation is somewhat complicated by the incorporation of stearic acid lubricant into the Sweco milled powder necessitating a burn out treatment which is not yet optimised.

The major factor affecting the ambient temperature modulus of rupture was the conditions of densification. Hot pressed material data gave an indication of the potential strength of the ESP PY6 material, yielding room temperature MOR values in excess of 1000 MPa for powders attritor-milled in polar liquids. For all materials, densification by HIPing resulted in ~20% lower strength values, indicating the need for development and optimisation of the HIPing procedure. Weibull modulus was typically of the order of 20 irrespective of the method of densification, with the hot pressed materials being more consistent than those HIPed.

High temperature MOR followed essentially the same trends as the room temperature MOR. Again the major factor affecting strength was the conditions of densification. The hot pressing procedure typically gave 1370°C MOR values in excess of 500 MPa, with values in excess of 650 MPa for powders screened before attritor milling in 2-propanol. For all materials, densification by HIPing resulted in ~40% lower strength values at 1370°C, an even more significant difference than that found for room temperature MOR.

This study was expanded to include another silicon nitride powder and two other compositions. The goal was to determine whether the poor mechanical properties attained with Ube-ESP powder when Sweco-milled and HIPed are due to an inherent problem with the powder, or to the PY6 composition in conjunction with the ESP powder, or whether they are the result of a less than optimal HIP cycle for the ESP powder.

Previously, RT MOR values of ~1450 MPa have been obtained for PY6 and A2Y6 compositions hot pressed from attritor milled Ube E10, while lower RT MOR values of ~1050 MPa have been obtained for hot pressed PY6 from similarly milled Ube ESP. RT MOR values of only ~750 MPa have been obtained for HIPed PY6 from attritor milled Ube ESP, similar to the baseline Sweco milled materials. Hence the current study was initiated to investigate the properties of several compositions made from both ESP and E10, densified by hot pressing, HIPing, and possibly sintering. The compositions chosen for investigation were PY6, S2Y6, and A2Y6, where Y denotes Y_2O_3, A denotes Al_2O_3, and S denotes SiO_2.

Powder lots used for this investigation were as follows:

Si_3N_4	Ube grade: ESP	Lot #S910342
Si_3N_4	Ube grade: E10	Lot #A710462
SiO_2	Degussa grade: Aerosil OX50	Lot #not given
Al_2O_3	GTE grade: S25	Lot #BL783
Y_2O_3	Molycorp grade: 5600	Lot #1867

The compositions were attrition milled using milling media manufactured from high purity SN502 silicon nitride. Each composition was milled using 2-propanol as the milling liquid, and the resultant slurry was screened through a 635 mesh stainless steel screen. The milled slurries were dried in pyrex glass trays with aluminum covers using a forced air explosion proof dryer. Dried cakes were granulated by manually screening through an 80 mesh nylon screen, and several 25mm x 25mm x 50mm billets were isopressed at 310 MPa from each composition.

The milled PY6, S2Y6, and A2Y6 compositions were densified by hot pressing and HIPing after different thermal treatments, including; no burn out; air burn out incorporating a 5 hour hold at 550 °C; high pressure nitrogen burn out incorporating a slow ramp to 550 °C followed by an air burn out incorporating a 7 hour hold at 700 °C. For hot pressing, the milled powders were burned out in covered alumina crucibles, while for HIPing the billets isopressed from the milled powders were burned out according to the regular practice used for injection molded parts.

Hot pressing was performed using the standard cycles developed for each composition: PY6 and S2Y6 at 1750 °C / 35 MPa / 180 mins, and A2Y6 at 1725 °C / 35 MPa / 180 mins. HIPing was performed using the same standard cycle for all compositions: 1825 °C / 165 MPa / 90 mins

Resultant densities from these hot pressing and HIPing procedures are given in Table 11. Considerable difficulty was experienced in densifying parts by HIPing: several sets of parts were destroyed at some point in the cycle. Various procedures were tried to overcome this problem including use of a double protective barrier layer. These met with limited success, and a reliable procedure for HIPing requires further development.

The data of Table 11 show a small general trend of decreasing density with increasing temperature and time of thermal treatment in air for hot pressed materials, but a constant density for HIPed materials. There is a prominent effect of air only burn out at 550 °C for ESP PY6 and S2Y6 compositions. These compositions show a significantly reduced density following this treatment in both hot pressing and HIPing. It is unclear at present whether the alternate burn out procedure which yields good densities derives its benefit from the use of a nitrogen burn out followed by an air burn out, or whether it is due to the higher 700 °C temperature of the air treatment. This observation is somewhat consistent with previous attempts to densify Sweco milled ESP PY6 materials. Powders burnt out using this same air treatment at 550 °C could not be hot pressed to high density under the usual cycle; 1750 °C / 35 MPa / 180 mins. Density was also not improved using a higher temperature cycle; 1775 °C / 35 MPa / 180 mins. The same materials in isopressed billet form subjected to the same burn out cycle were, however, successfully densified by HIPing using the standard cycle; 1825 °C / 165 MPa / 90 mins.

Materials densified from powders having no burn out, and materials densified from powders subjected to the high pressure nitrogen burn out followed by an air burn out, were machined to give MIL STD 1942 "A" geometry MOR bars for room temperature and high temperature strength determination. To date 10 bars have been broken at room temperature, and high temperature testing is in process.

RT MOR and Weibull modulus are plotted versus composition in Figures 7 to 14. MOR of materials made using ESP can be seen to be essentially identical irrespective of whether or not the powders were burned out. There is a small difference in MOR of compositions made using E10, strengths are slightly lower after burn out for hot pressing and a little higher after burn out for HIPing. Two batches of E10 PY6 were processed and properties were determined for each in order to assess material reproducibility. The resultant data was very similar for each batch and is plotted as open symbols in Figures 11 to 14, while

the combined data is plotted as full symbols for comparison to the other compositions. Figure 15 illustrates the effects of powder type and densification process on the three compositions PY6, S2Y6, and A2Y6 without a burn out treatment. The data clearly show the superiority of hot pressing over the currently used HIP cycle. The hot pressed materials illustrate the strengths which are possible and indicate the need for further development of the HIPing process. There is also a clear compositional influence upon the strength. For the A2Y6 composition E10 yields higher strengths than does ESP, however the difference is not great, being of the order of 100 to 200 MPa; 1450 vs 1350 MPa for hot pressed materials and 1270 vs 1060 MPa for HIPed materials. For the PY6 composition however, the strengths for E10 are considerably greater than those for ESP; 1500 vs 1000 MPa for hot pressed materials and 930 vs 690 MPa for HIPed materials. For the S2Y6 composition the status is reversed, here the strengths for E10 are similar to or less than those for ESP; 1310 vs 1260 MPa for hot pressed materials and 750 vs 900 MPa for HIPed materials. In the absence of an additional oxide sintering aid to Y_2O_3, the oxygen content of the Si_3N_4 powder and/or SiO_2 addition is a critical factor in controlling the material strength. There would appear to be some optimal SiO_2 content dependent upon the Si_3N_4 powder type and the amount of Y_2O_3 addition. Weibull modulus of these materials as calculated is somewhat variable which is to be expected from the sample size, but for PY6 and A2Y6 compositions is typically in the range of 15 to 30. The S2Y6 compositions generally have the lowest Weibull modulus, typically in the range of 10 to 15. This is likely due to poor dispersion of the extremely fine particle size fumed SiO_2 addition.

PROCESS IMPROVEMENT - COMPOUNDING:

In an attempt to overcome the metallic contamination associated with the currently used sigma blade mixers, experiments have been carried out to develop a noncontaminating compounding system.

Initial experiments were made using a small orbital mixer with an oval chamber constructed of Nylon. A single silicon nitride mixing ball was used for dispersion. This small mixer was found to be capable of compounding 20 gram batches of PY6 using a preheated mixing chamber and ball. Melt index measurements indicated that a 10 minute orbital mixing time resulted in a melt index value comparable to that observed from sigma blade compounded PY6 batches.

A larger scale mixing system (capable of compounding 600 grams of PY6 per batch) was then constructed . The mixing chamber was again constructed of Nylon with an oval internal configuration. The system utilizes a 3-way orbital mixing approach and a single mixing ball. Several large diameter mixing balls have been evaluated;

- Isopressed and HIPed PY6 (density = 3.2 g/cc)
- Isopressed and sintered zirconia (density = 6 g/cc)
- Nylon capped steel ball (composite density = 3.5 g/cc)
- Nylon capped WC ball (composite density = 6 g/cc)

To perform the compounding, the powder, binder and mixing ball are loaded into the Nylon mixing container and preheated to the compounding temperature. The sealed mixing chamber is then loaded into the orbital mixer and compounded for the desired period (typically 10 minutes). The compounded mix is then removed, cooled and granulated.

Since no metallic component contacts the silicon nitride mix during compounding with this approach, such contamination can be eliminated. This was confirmed by warm pressing compounded mix from the plastic mixer and examining the disks using microfocus x-radiography (See Task 3 for details).

The quality of compounded mix prepared by this technique has been evaluated further by melt index viscosity measurements for four processing conditions:

- PY6 mixing ball and warm mixer
- PY6 mixing ball and warm mixer, then twin screw compounding
- Nylon capped WC ball and warm mixer
- Nylon capped WC ball and cooler mixer

The resulting viscosity curves are shown in Figure 16. The material mixed with the lower density PY6 ball possesses a high viscosity, but it is still within the range suitable for injection molding. Use of twin screw compounding after this mixing results in a substantial decrease in viscosity. It was also observed that the use of a higher density mixing ball showed a major improvement in compounding, and that a higher temperature preheat is desirable for best mixing quality.

The conditions of a high density mixing ball along with a warmer mixer resulted in a mix viscosity comparable to that processed through the high shear twin screw compounder. Through all of the mixing to date using this system, there has been no observable wear of the Nylon mixing container or the capped balls.

Based on these experimental findings, the larger mixer was utilized to produce sufficient compounded mix for tensile specimen injection molding trials. Half of the prepared mix was used direct from the plastic compounder; the remaining material was passed through

the twin screw compounder prior to granulation. Other batches were prepared with the standard large Abbe sigma-blade compounder to serve as a baseline, and with a smaller, much less-used Abbe machine which was shown to produce less contamination. Material from these batches has been molded into tensile specimens, dewaxed, and HIPed. They are being machined into tensile test specimens. Green-state NDE proved that less metallic contamination was incurred utilizing the non-contaminating mixer, as expected(Table 12).

As as followup to this work, an Abbe sigma-blade compounder similar to the standard equipment used at GTEL was located, which had been carefully outfitted with seals to minimize metallic contamination. It had also been used for preparation of silicon nitride materials, and a procedure developed for it which was shown to produce low contamination levels. Two batches of PY6 were prepared with this compounder, and samples examined by the x-ray microfocus technique described previuosly. Results of the number of high-density inclusions (HDIs) per unit volume in these materials are compared to the previous results in Table 12. They show that with appropriate care, the standard Abbe compounder can produce materials with excellent HDI characteristics. These batches will similarly be prepared as tensile specimens.

Another effort in contamination reduction is now underway. This work is aimed at evaluating potential plastics for use in silicon nitride processing equipment. The goal of the activity is to replace with plastic those metallic equipment components which are prone to wear, thus decreasing or eliminating metallic inclusion defects in injection molded silicon nitride.

The current study is designed to evaluate a range of plastic materials for room temperature erosion and abrasion resistance. Plastics investigated have ranged in capability from low use temperature to high temperature and low cost to high cost. Generally, higher temperature capable plastics are substantially higher in cost.

Abrasion resistance is measured by calculating the sample volume loss when it is abraded against a 30 μm metal-bonded diamond polishing wheel under a 1 Kg load. The weight losses on 0.5 x 0.5 x 0.25 inch samples are measured at 1-minute intervals (5 minute total test time) and converted to volume loss using the sample density. The linear slope of the volume loss versus abrasion time is calculated to determine abrasion rate.

Erosion resistance is measured by grit blasting the samples at 80 psi using 50 μm Al_2O_3 powder. The sample is placed 13 mm from the blaster nozzle and sample volume loss calculated after 1 minute of blasting.

Tests such as these are useful in a general way in ranking the performance of different

materials, but neither test accurately duplicates the actual wear mechanism. It is expected that the flow of a submicron Si_3N_4 powder in a heated fluid binder over a surface will produce wear mostly by abrasion, but with some erosive contribution as well.

Table 13 shows the results of the study to date, including information on maximum use temperature (temperature where deflection occurs under a 264 psi load) and bulk raw material cost where available. Also included in the study was a hardened tool steel sample (Crucible 95) for comparison with the plastics. The materials are listed in Table 14.

Measured wear rates for both tests span two orders of magnitude, showing the wide performance range of available plastics. While many of the plastics tested exhibit poor wear resistance relative to tool steel, several plastics show comparable or superior wear rates. For room temperature applications, ultra-high molecular weight polyethylene (UHMW PE) would be desirable. This material shows minimal wear in both tests, but it is only usable at low temperatures. At intermediate temperatures (50-90°C) nylon would be a good choice. Its wear is comparable to tool steel and it is readily available at low cost and large sizes. For high temperature use, or moderate temperature/high stress application polyetheretherketone (PEEK) appears to be the first choice. This material is, however, expensive and somewhat limited in sizes of stock available. A second choice in this temperature range is possibly polyetherimide (PEI). PEI had a medium wear rate, but is readily available in large sizes at 20% of the cost of PEEK. It was also noted in the study that materials with good abrasion resistance were also generally good in erosion resistance.

To evaluate the performance of an actual plastic component, an injection screw for a 15-ton Boy injection molding machine was fabricated from PEEK (Figure 17). This screw was used to injection mold about 5 Kg of PY6 silicon nitride turbocharger test samples. Inspection of the screw after this test revealed some polishing of the screw, but no significant wear. Based on this result, four screw segments for the Betol BTS-40 twin screw compounder were fabricated of PEEK. The segments produced were for the feed end of the compounder, where conditions are believed to be most abrasive. Forty Kg of precompounded PY6/binder was passed through the Betol compounder. The barrel was removed after the test and no noticeable wear of the PEEK segments was observed. It is now planned to construct a complete pair-set of PEEK screws for this compounder. In addition, a PEEK injection screw has been designed for the 200 ton injection molding machine. This screw is in the final stages of fabrication at this time.

The program baseline compounder (ABBE) has been completely rebuilt with new components, resulting in more precise tolerances between the moving parts. Some

materials modifications were incorporated, via subsititution of higher quality materials, in the expectation of reducing metallic contamination.

PROCESS IMPROVEMENT-MOLDING (Brunel University):
The stripped, cleaned, and reassembled Mk. 1 compounder/molder was used to produce three sets of 50 ASCERA tensile specimens. Its operation continued to be trouble-free during this period. The three sets represent Mk. 1 molding of baseline material, Mk. 1 molding with variable packing pressure, and Mk. 1 molding with cavity evacuation. The material used was precompounded PY6 baseline material.

Some difficulty was encountered with ASCERA tensile specimens molded with an evacuated cavity. The problems were associated with determination of the proper size of the O-rings and establishment of a workable cavity evacuation procedure. Once these problems were overcome, molding proceeded without further incident. To ensure a fully evacuated cavity, the injection nozzle was also modified to contain an O-ring. It worked well in preventing vacuum leaks at the nozzle/sprue bushing interface.

These 150 samples were delivered to GTEL during the program review and progress report conducted on November 12 and 13, 1990. A report detailing the molding conditions accompanied the ASCERA parts. The ASCERA rods will be subjected to NDE evaluation, dewaxed, HIPed, machined, and tested.

A delay was encountered in construction of the Mk. 2 machine, in the return to Dassett of some injection stage parts from borofuse processing at Materials Development Corporation (MDC). However, the construction of the Mk. 2 compounder/molder is complete. Operational testing of the Mk. 2 has been performed at Dassett Processing Engineering, and at Brunel University.

The injection stage assembly, which is comprised of the Betol twin-screw extruder, injection barrel, and connecting manifold was the last major assembly to be installed on the Mk. 2. The greater size and complexity of the injection stage, as compared to a normal reciprocating screw injection stage, necessitated some special design features. Ease of disassembly and cleaning was a major consideration in the design of the injection stage.

Programming of the Manual, Semi-Automatic, and Automatic modes of operation were completed. Some modifications were required subsequent to operation with GTE feedstock at Brunel, but, in general, the unit performed as described in the Design Review Meeting of April 1990. Some corrective changes were necessary to the hydraulic systems to satisfy the unique requirement of the continuously operating extruder. These were

accomplished without difficulty. All other aspects of the trials were completely satisfactory.

An experiment in the compounding of PY6 from powder was conducted using the Mk. 1 compounder/molder. Difficulty had been encountered at GTEL in compounding from powder and binder without some form of precompounding procedure. The problem encountered is jamming of the screws prior to fusion or plasticizing of the powder/binder mixtures. It was postulated that the Mk. 1 extruder, which has received considerable wear during its lifetime, might have greater clearances between screw flights and the barrel walls. If compounding proceeded without jamming in the Mk. 1, this would be strong evidence that these clearances need to be increased. This apparently does have some effect, as compounding of the PY6 (without epoxy) was achieved without any squealing or jamming. The Mk. 1 was set up with a screw section profile which could be easily utilized on the Betol machine at GTEL. The extruder had been operating with and contained precompounded PY6 material at the start of the experiment. A mixture of PY6 was mixed by hand in a beaker. Although the wear-related loose tolerances of the screw sections in the Mk. 1 are believed to be a significant factor in this result, other factors may have played some role. The fact that the extruder contained fully compounded material may ease the start of fusion. The configuration of the screw section dimensions certainly effects the tendency to jam prior to fusion. However, the experiment does indicate that extruder configurations do exist which allow compounding from simple powder/binder mixtures. The screw section profile information was provided to GTEL.

The Mk. 2 compounder/molder was shipped to and installed in the Wolfson Centre at Brunel University, and has been operated extensively with GTE injection molding feedstock. This effort has been concerned with addressing start-up issues and achieving reliable operation of the GTE injection molding process.

The majority of these issues have been routine in nature. They involve repair of some minor shipping damage, wiring modifications for cosmetic and safety considerations, and a faulty bearing in the hydraulic motor for screw rotation. Two issues which effect operation required attention. The first involved the ball and seat check valve in the connecting manifold. Although the design is essentially the same as that used successfully in Mk. 1, leakage through the valve prevented the holding of a cushion under injection pressure. It has been determined that the ball diameter in the Mk. 2 valve was smaller than in Mk. 1. A larger ball has been installed and the valve operation is now satisfactory.

The second involves injection piston pushback by the extrudate from the twin screw extruder. Serious problems, which prevented consistent operation, were encountered in the Mk. 1 design with respect to this phase of operation. Thus far in the evaluation, Mk. 2

has exhibited consistent piston pushback under all conditions except when the extruder is "starve fed". A modification to the hydraulic system which minimizes the steady state back pressure on the injection piston during filling has been carried out. Preliminary trials indicate satisfactory operation. Hydraulically assisted piston pushback has been considered as an option but does not now appear to be necessary.

Temperature control is excellent throughout the system. A single water circulating unit is used to heat both the connecting manifold and the injection barrel.

All zones of the extruder, the connecting manifold, and the injection piston have been set to control at 70°C. Some difficulty has been encountered with injection piston retraction under these temperature conditions. The extrudate easily forced the piston to retract, filling the injection chamber, when the extruder was flooded with material. However, when the extruder was "starve-fed", insufficient pressure was generated to move the piston back. The controlling thermocouples for each component are embedded in the steel as close to the melt path as practical. Measurement of the actual melt temperature in each component revealed that melt temperatures in the extruder were slightly above the controlling thermocouple readings. Actual melt temperatures in the connecting manifold and injection piston were slightly lower than the controlling thermocouple readings. Under these conditions, hot (low viscosity) material in the extruder was attempting to move cooler (high viscosity) material through the remainder of the system. Attempts are now underway to determine the effect of a proper temperature profile on piston retraction. In any event, the equipment has the ability to retract the piston hydraulically. This can be done at a controlled rate during the filling cycle should it be necessary.

In order to obtain the melt temperature readings, the connecting manifold and injection unit were removed and dismantled. The combination metal-on-metal, O-ring seals in the connecting manifold worked well with no bleeding observed. No difficulty was encountered in removing the slide-in components of the manifold. The units were cleaned and reassembled. The total time required was approximately one day.

The large cross section tensile specimen(MLP) tool was mounted in the Mk. 2 and some test moldings were made. As a final test of the machine, GTEL-derived PY6 was molded into MLP specimens, delivered to GTE, and will be dewaxed and densified there. These will be machined into tensile specimens and tested. These parts represent the final efforts at Brunel University. These moldings as well as the remainder of finishing work for the Mk. 2 are expected to be complete on April 12th. At that time the 50 cycle motors will be replaced by 60 cycle motors and the machine packed and shipped to GTEL by Dassett.

MICROSTRUCTURE CONTROL: HIPing

The study which utilizes Taguchi Methods to identify the steps in the HIP cycle impacting PY6 strength is continuing on schedule. The control factors and noise factors which are being investigated in the L12 X L4 orthogonal array include ramp rates of temperature and pressure, hold times and temperatures, environmental storage and crucible conditions. All of the HIP experiments have been performed. Ten of the twelve experiments ran according to plan; however, two of the experiments (#10 and #11) were aborted due to electrical difficulties in the hot isostatic press. Using orthogonal array data analysis techniques, the missing data were estimated so that the most influential control factors involved in HIPing could be determined within a reasonable degree of certainty.

The density and the surface appearance of each as-HIPed test sample were assessed. Additionally, MOR strength measurements of machined specimens at both room temperature and 1370°C were performed. Results to date are discussed below.

One of the control factors is the temperature at which the test samples are air flashed to fully remove any residual carbon after binder burnout. It was anticipated that, by raising the air flash temperature, this processing step could also be utilized to increase the green strength of the part. Thus the likelihood of damaging the part during handling prior to HIP would be reduced. Indeed, the green strength of the test samples flashed at the higher temperature was significantly improved. However, results obtained to date indicate that the temperature of air flash has a very significant effect on densification during HIP. The majority of bars which were air flashed at the standard temperature (600°C) reached >98% theoretical density (TD). Those which were flashed at the higher temperature (900°C) did not densify fully, all falling between 95-98% TD. Parts which are less than 98% TD are expected to be lower in strength than is useful for this program. Therefore, in order to save machining costs, the majority of bars which were HIPed to less than 98% TD were not tested for MOR strength. Materials from these experiments will still be useful in analyzing the remaining quality characteristics, i.e. density and surface appearance.

Another control factor which is being examined is whether or not a barrier layer is used as a liner in the HIP crucible. While the layer eases removal of the encapsulated components from the crucible after HIP, previous experiments have indicated that the same purpose could be achieved through a slight modification to the HIP cycle. The barrier layer is an expensive item which must be replaced after each HIP run. Also, it can cause discoloration of the Si_3N_4 part surface when contact is made during HIP. Therefore elimination of the layer would be desirable. In order to determine whether removal of the layer affects Si_3N_4 properties, it was included as a control factor.

Three of the nine experiments conducted to date eliminated the layer from the HIP process.

While many samples densified, excessive foaming of the encapsulation glass occurred causing difficult removal of the crucibles from the HIP furnace. Alternatives to the barrier have subsequently been attempted, but a suitable replacement has yet to be identified.

Preliminary data indicate improvements in strength at both 20°C and 1370°C for PY6 HIPed at the conditions of Experiment #3. As shown in Figure 18, the 20°C MOR strength increased 10% relative to the baseline, and the 1370°C strength increased 38%. The experimental HIP cycle was repeated using three different injection-molded lots of tensile rod materials. The average MOR strengths were 894 MPa at 20°C (14 % increase over the baseline) and 436 MPa at 1370°C (28% increase), confirming the results of the initial trial.

These strength improvements can be related to the microstructure of the modified material. Qualitative and quantitative microscopic analyses have revealed significant differences between PY6 from the baseline and modified (Experiment #3) HIP cycles. Tensile rod cross-sections were polished, etched, and examined microscopically to reveal the Si_3N_4 grains. Qualitatively, the modified HIP cycle appeared to produce a microstructure of whisker-like grains interspersed in a very fine-grained matrix. This was confirmed by quantitative image analysis of digitized scanning electron micrographs of the etched cross-sections. The data obtained regarding the grain size and shape are listed in Table 15 as compared to the previously reported baseline data. Based on this information it appears that a desirable microstructure has been achieved in HIPed PY6. That is, the structure of somewhat equiaxed submicron grains closely packed between whisker-like grains results in a well dispersed intergranular phase and high strength, especially improved at elevated temperatures.

X-ray diffraction analysis of the modified material was also performed, showing 88% beta-Si_3N_4 and 12% alpha-Si_3N_4. This agrees with the microscopic analyses in that the equiaxed submicron grains are probably residual alpha-Si_3N_4. The presence of the equiaxed alpha grains results in a lower average aspect ratio, although many very acicular grains actually formed. Other material characteristics (e.g. elastic properties, fracture toughness, and hardness) were also measured for the PY6 produced using the modified HIP cycle. As shown in Table 16, no significant changes occurred relative to the baseline material properties. Young's Modulus was measured via ultrasonic means, yielding a value of 317-322 GPa. When measured via mechanical means (strain gauging, Task 4), the same material exhibits a Young's Modulus of 295 GPa. This value correlates well with modulus measurements performed in tension on PY6 at the HTML^2, which yielded 305±3.5 GPa.

A summary of the results is shown in Table 17. The preferred setting (Level 1 or Level 2) for each control factor is listed along with the quality characteristics which it strongly affects. It is anticipated that in addition to improving the material properties the revised HIP cycle will also result in less HIP equipment deterioration and lower cost. The confirmation run will be performed and evaluated during the next reporting period.

FINISHING AND ANNEALING:

The annealing study designed to determine optimum annealing conditions for machined PY6 has been completed. Utilizing Taguchi methods of experimental design, an L18 x L8 orthogonal array was implemented. Control factors included: temperature, time, atmosphere, powder characteristics, heating and cooling rates, and gas flow rate. Noise factors included a variety of surface characteristics designed to evaluate the "robustness" of the annealing schedule. Room temperature MOR was the quality characteristic used to determine the effectiveness of the various treatments.

Due to the statistical nature of the strength of structural ceramics, it was decided that more than one data point for each response would be required to avoid erroneous conclusions formed by an aberrant data point. Consequently, four MOR bars were tested for each response to increase confidence in the analysis.

All strength measurements were made with MIL STD 1942 "A" size MOR bars. The thermal treatments were performed in an alumina tube furnace.

Results obtained were analyzed via Taguchi Signal/Noise (S/N) ratio techniques. Since strength is a characteristic which is treated as a "Larger-the-Better" attribute, higher S/N ratios indicate higher strengths. Analysis is performed for each variable individually to identify its effect on the overall result in a response graph.

A response graph for the control variable "temperature" is illustrated in Figure 19. The data indicate that changes in temperature (which ranged from 1100° to 1350° C) created the largest changes in strength. As shown in the temperature response plot, strength values increased with decreasing annealing temperature. In the 1100° - 1150°C temperature range, strength values leveled off.

Three different atmospheres were tested; air, Nitrogen, and Argon, with all three yielding similar results. Signal/Noise graphs of the other experimental variables, including time, also showed flat responses, indicating that these variables had little effect on strength.

Variables which yielded the best results for each control variable were combined and tested

in a confirmation run against untreated MOR bars of the same material. In addition, since the original experiments were performed in a small capacity tube furnace, a larger box furnace was used to evaluate process scale-up potential. Each group consisted of 8-10 bars. The results are shown in Figure 20. As illustrated, thermally treated bars from both furnaces show higher strengths and higher Weibull modulus than the untreated bars. These results indicate an overall 6-9% mean strength improvement was realized.

As a follow-up to this Taguchi study, a study which evaluates the effect of lower temperatures (<1100° C) will be performed. Finally, the optimized thermal treatment process will be used on tensile test specimens in the near future.

Task 3 - Development and Application of NDE Methods(D. Cotter and W. Koenigsberg)
IN-PROCESS NDE: MONITORING FOR PROCESS CONTROL
Compositional determination of the constituent elements found at the failure origins of tensile specimens has shown that the ceramic processing machinery (compounder, granulator, and injection molder) is the major contributor to metallic contamination. In the last batch of 20 tensile specimens, 16 failed at stainless steel inclusions, implicating the compounder. A capital equipment expenditure to replace all the wearing components in the primary compounder being used for this program had previously been initiated, and the decision is clearly supported by these recent failure analysis data. Additionally, in-process nondestructive evaluation results from specimens prepared during the intermediate processing steps have corroborated compositional analysis findings. In-process nondestructive evaluation is also providing the feedback necessary to evaluate alternative mixing methods.

A warm-pressing technique was developed to prepare green ceramic specimens from compounded, granulated, and as-molded materials for microfocus X-ray imaging. The specimens are hydraulically pressed in a 25.4-mm diameter die with heated rams. The warm rams soften the coarse material, which flows under pressure into a uniform compact. The pressed specimens provide a homogeneous matrix for X-ray imaging. In the past, conventionally pressed samples exhibited a nonhomogeneous structure which made detection of high density inclusions ambiguous. Warming the rams rather than the large thermal mass die allows for rapid pressing of multiple samples. A group of 6 specimens (a total volume of approximately 18 cubic centimeters) can be pressed in 20 minutes. This corresponds to the aggregate gage volume of 18 tensile specimens. The sleeve on the internal diameter of the die and the ram faces were made from tungsten carbide to minimize contamination.

Nondestructive evaluation was used to compare the metallic contamination levels of

several compounding process routings. The large ABBE compounder, which is the standard compounder for the program, was compared to a small ABBE compounder that has experienced less wear. Also, a novel orbital mixer (See Task 2-Compounding, above)was investigated, utilizing a nylon mixing chamber and non-metallic ball. Some material from the noncontaminating mixer was passed through a high shear Betol twin screw compounder which has tool steel components. A group of 6 warm-pressed specimens from each batch of material was inspected with microfocus X-ray imaging. Imaging was done at 10X magnification on high contrast film. A summary of the number of high density inclusions (HDIs) detected was previosly given in Table 12.

The HDI count was normalized to 1 cubic centimeter, which is the gage volume of the tensile specimens used in the program. The severity of metallic contamination contributed by compounding is apparent when the data are presented in this way: it is expected that the majority of tensile specimens will fail at HDIs until the frequency of occurrence is reduced to less than 1 HDI per cubic centimeter. All of the HDIs detected by x-ray were larger than 50 micrometers in size and would be critical defects. No high density inclusions were detected in the material from the noncontaminating compounder. Scaling up of this orbital mixer and evaluation of the molding properties of the material it produces are in progress. The NDE technique has been incorporated into the process routing to monitor all future batches for HDI count and experiments to minimize metallic contamination are continuing.

IN-PROCESS NDE: LASER-SURFACE PROFILOMETRY

Laser-surface profilometry is being employed to investigate the relationship between the surface roughness characteristics and mechanical behavior of machined ceramics. Data relating surface defects to the strength of tensile test specimens have not been obtained to date because virtually all the samples have failed from internal flaws, primarily metallic contamination. Nonetheless, in the present study, silicon nitride MOR (modulus of rupture) test bars prepared for the annealing experiment were examined. All of the bars inspected were tested to failure in four-point bending and failed from surface defects.

The Rodenstock profilometry system utilizes a solid state laser focussed to an 800-nanometer diameter spot size to allow non-contact determination of surface topography on a microscopic scale. As a precise linear slide traverses the laser across the specimen, the feedback signal which adjusts the optics to maintain the spot size is monitored. This signal is directly related to the peaks and valleys of the surface profile. The system will respond to surfaces with a reflectivity between 2 and 98 percent.

Numerous roughness values have been developed for characterization of machined

metals[3]; however, they have limited applicability to assessment of ceramics. The mechanical behavior of ceramics is likely dependent on the one deepest valley present, which would be a Griffith flaw (the most critical flaw under the applied stress). The roughness characteristics shown below are believed to be the most pertinent to ceramics that are readily determined from algorithms intended for metallic surface inspection.

Ra is the arithmetic average of deviations from the calculated mean line of the profile.

Rq is the RMS (root mean square) value of the roughness profile.

Sk is the skewness, a measure of the asymmetry about the mean line of the profile (the third moment of the roughness data).

Rv is the deepest valley in the scan. This value was not available from the software which is primarily concerned with assessment of surface peaks, but was calculated given the maximum peak to valley excursion and the largest peak present in the scan.

Roughness characteristics were determined for three samples of as-machined and annealed MOR bars (1.27x2.54x25.4 mm). The bars were longitudinally ground to a 320 grit specification. Five longitudinal scans 5 mm long were obtained at random locations on the tensile surface of each bar. The average of the roughness characteristics for the 5 scans is shown in Table 18 along with the average strength for both sample sets.

In view of the limited database, care should be taken in assessing the significance of the results. It appears that the average roughness did not change appreciably with annealing. The average maximum valley depth was greater for the as-machined specimens, as expected. More importantly, the average negative skewness was consistently more negative for all as-machined specimens indicative of a higher density of deeper valleys. Sparse peaks which could also cause the skew were not observed in the individual profiles. Profiles shown in Figure 21 are representative of those recorded for as-machined and annealed MOR bars. Asymmetry of the as-machined roughness profile was visually apparent on most scans. Annealing the material appears to effectively redistribute material about the mean line.

The roughness profiles were acquired by sampling 8000 points in the 5-mm scan length. Average roughness (Ra displayed is 3.56 micrometers for as-machined versus 2.44 micrometers for annealed) was significantly different for the two conditions of the MOR bars when examined on the finer scale. The skewness, average maximum valley, and similar characteristics related to surface profiling will be monitored at various scales as the

occurrence of failure from surface related defects increases for tensile specimens tested in the program.

NDE OF SPECIMENS FOR MACHINING CHARACTERISTICS:
In the annealing study, inspection revealed that the baseline as-molded bars were mistakenly machined to a different finish specification (400 grit versus 320 grit) than the samples designated for annealing, potentially confounding the results of the experiment.

Roughness and waviness profiles of an as-machined MOR bar are shown in Figure 22. The roughness profile exhibits clusters of deep valleys. These valley clusters were not observed on profiles of similarly machined surfaces. The roughness also appears to modulate a background waviness profile. Machined metallic materials typically exhibit high frequency roughness on a lower frequency wave pattern, the former being caused by the tool and the latter dependent on the tooling or machine employed. The Fourier spectrum of a portion of the roughness scan is shown in Figure 23. The Fourier spectrum simply shows how the magnitude of the roughness (magnitude squared is actually displayed) is distributed as a function of frequency. Periodicities in the roughness profile may be related to the machining technique. Discussions with the machine shop subcontractor are in progress to investigate the cause of valley clusters.

ULTRASONIC INSPECTION SYSTEM DEVELOPMENT:
The ultrasonic inspection system was received at GTEL on November 29, following favorable testing results at Panametrics Inc., Systems Division, in Ithaca, NY. A remote pulser/preamplifier and modified pulser receiver were added to the system configuration to improve performance and allow for through transmission inspection of green ceramics. A group of 4 GTEL staff attended a 40 hour ultrasonics training session at Panametrics in Waltham, MA the week of December 3, 1990. Joint experimentation with the staff from the Panametrics Waltham facility was conducted. The major capabilities of the ultrasonic inspection system were successfully demonstrated on representative ceramic samples. Dr. Ron Roberts , the consultant on Ultrasonics from the Center of NDE at Ames Laboratory, has delivered a report on modelling and green density mapping of ceramics which is being reviewed. A number of image quality indicators with simulated flaws are being designed to verify modelling results.

ULTRASONIC INSPECTION OF GREEN-STATE SILICON NITRIDE:
Nondestructive evaluation of selected as-molded specimens was conducted by Dr. Roberts to investigate the efficacy of green-state inspection, and to support selection of transducers for the ultrasonic testing system at GTEL. As-molded specimens were examined in a through-transmission mode using a pair of 10 MHz 1.0 in. focal length 0.75 in. diameter Panameterics V310 transducers. Due to the severe attenuation in the green material, the

transducers were driven by a gated continuous wave signal generated by a combination of a LeCroy 9100 programmable waveform generator and a 200 watt power amplifier. The amplitude and transit time of the transmitted pulses were digitally recorded.

Results were obtained on a 6-mm thick by 1.7-cm diameter green disk at frequencies of 5 and 10 MHz. Amplitude and transit time images are shown in Figure 24. Interesting features of these images are the large-scale non-uniformities in amplitude and transit time. This indicates that non-uniform compaction occurred during the injection molding process. The mold gate (injection port) was located in the upper left hand corner of the images. The patterns seen in the images are similar in appearance to those observed in disks molded from powder contaminated with iron, in which flow lines were optically visible due to discoloration from the contamination. The 10 MHz image displays slightly more detail than the 5 MHz image, due to the shorter wavelength. However, the 10 MHz image exhibits considerably more noise, due to significantly increased ultrasonic attenuation.

Scans were also performed of a green tensile specimen in the 1.3-cm diameter gauge section. Due to the greater specimen thickness, the driving frequency was limited to under 5 MHz. Transmitted amplitude images are shown in Figure 25. The images represent transmitted amplitude as a function of axial position and specimen rotation angle. The top image was obtained at 4 MHz. The bottom image was obtained using a broadband excitation, which after transmission, was centered around 1.5 to 2 MHz. These images demonstrate that it is possible to penetrate the cylindrical green specimens. However, obtaining focussed images as shown in Figure 24 for the planar disk is not easily done due to the greater thickness of the specimen, and the focussing aberrations caused by the curved specimen interface. It is conceivable that such scans may have use in determining overall material uniformity, or perhaps the detection of gross internal delaminations. Note that the scan did detect the parting line (mold seam) running the length on either side of the specimen (imaged as a dark shaded region).

The capability of ultrasonically inspecting as-molded specimens will be a valuable tool for investigating the injection molding process and assessing the effects of modifications, such as gating design and molding parameter changes. Previously conducted experiments on ultrasonic inspection of burned-out specimens, which were encapsulated (sealed in plastic wrap), yielded similar promising results. A quotation on a matched transducer set and an arbor with a yoke assembly designed specifically for the GTEL ultrasonic system has been received, and a capital expense request has been initiated. Plans have been made to prepare core samples from the NSF and MLP molded specimens for future testing.

Task 4 - Property Testing and Microstructural Evaluation(A. Hecker and F. Sivo)

MECHANICAL TEST DEVELOPMENT: STRAIN GAUGING

Since even the best tensile grip configurations are known to impart bending as well as axial loads, a system was recently installed to monitor the magnitude of bending loads. The system is similar to the one used at HTML by M. Jenkins and M. Ferber. It consists of a data acquisition system (System 10 by Daytronics Corporation) which monitors strain (1/4 bridge completion circuits) on four channels. Four strain gauges are mounted in the gage section. They are placed at 90° intervals around the periphery at the midpoint of the rod. The bending loads are expressed by the equation shown below:

$$\% \text{ Bending} = \frac{[(\Delta g_{1,3})^2 + (\Delta g_{2,4})^2)]^{1/2}}{g_0} \text{ X } 100$$

where:

$$\Delta g_{1,3} = [(g_1 - g_o) - (g_3 - g_o)]/2 = (g_1 - g_3)/2$$

$$\Delta g_{2,4} = [(g_2 - g_o) - (g_4 - g_o)]/2 = (g_2 - g_4)/2$$

$$g_0 = (g_1 + g_2 + g_3 + g_4)/4$$

The gauges are located in a co-planar fashion at 90-degree intervals around the circumference. M. Jenkins (HTML) uses an allowable bending magnitude of 5% at 6500 Newtons (1,461 lbf). If the bending value exceeds 5% at 6500 N, the test is terminated, grips are adjusted, and the procedure repeated. GTEL has adopted the same methods and practice. Figure 26 illustrates a typical response generated with this system. Notice the % bending value is within the allowable range (<5%, @ 1461 lbf).

Since strain gauging is now utilized on a regular basis, very accurate data may be obtained on other physical measurements (i.e. Young's Modulus, shown in Figure 27).

PHYSICAL PROPERTIES OF BASELINE MATERIAL:

The oxidation resistance of the baseline tensile rod material has been measured. Machined test samples were heated in air at either 1200°C or 1370°C for a total of 500 hours. The change in sample weight per unit surface area was measured after 50 hours and at 100 hour intervals thereafter. The results are shown in Figure 28 in comparison to the hot pressed baseline powder.

The weight gain per unit area for both the 1200°C and the 1370°C oxidation tests of the injection molded/HIPed baseline material is similar to that which was hot pressed. However, the specimen surface appearances are quite different. After exposure to air at 1200°C, the HIPed samples changed from their initial gray color to tan, while the hot pressed samples remained gray. Microscopically, the surfaces of both sample types remained relatively unchanged.

After being oxidized at 1370°C, the differences between HIPed and hot pressed materials became more apparent. The color of the HIPed samples was nearly white, while the hot pressed specimens were gray. Also, the HIPed bar formed tiny hollow beads of crystallized glassy material covering its surface. The hot pressed sample appears to have formed a small amount of a crystalline phase on its surface.

During the next reporting period, the oxidation tests will be repeated as a confirmation. Analyses of the oxidized samples will follow, to identify possible crystalline phases and/or impurities which may contribute to the apparent differences between the HIPed and hot pressed materials.

Measurement of the MOR strength of the baseline injection-molded and HIPed tensile rod material is complete. Tensile rod ends were machined into military standard size "A" MOR bars and tested at both 25°C (10 samples) and 1370°C (5 samples). The room temperature strength of HIPed baseline material is 780.5±68.3 MPa (Weibull modulus = 11) and the 1370°C strength is 339.5±18.4 MPa (Weibull modulus = 15).

Room temperature tensile testing of the first two sets of baseline material has been completed by GTE Laboratories. Also, ambient temperature testing has been performed by the University of Dayton Research Institute(UDRI) on specimens fabricated intermediate in time between the above two sets. The data are presented on Table 19, shown as a function of specimen number on Figure 29, and displayed on a Weibull format in Figure 30. The average strength of the rods increases from 545 MPa to 716 MPa as specimen number increases (Figure 29). The specimen number reflects the specimen's place in the fabrication sequence. The increased strength (and also Weibull modulus) may be a result of several minor changes made during the sequence, such as initiating the use of screened injection-molding binder wax between the first and second sets, and the switch to a second lot of silicon nitride powder between the second and third sets. On the other hand, as Figure 29 shows, the scatter of the data is large, and the apparent increase in strength may merely be a manifestation of this variation.

Tensile rod blanks(MLPs) made with large cross-sectional area (dia. = 1.5") were machined into tensile specimens. Fifteen of these tensile specimens were tested at GTE

Laboratories and the remaining specimens delivered to ORNL. A summary of the results obtained is listed in Table 20.

The average strength obtained (412 ± 71 MPa) was less than that previously obtained (average baseline strength = 624 ± 126 MPa). Optical inspection at 40X indicated that all samples had broken from volume inclusions; none appeared to be a result of cracks formed during the burn-out or firing processes. The densities of all parts were measured to be greater than 99.5% theoretical density. X-ray diffraction was performed on samples #31, #34, and #49. In each case the analysis showed 100% conversion to ß-Si_3N_4. Indentation fracture toughness was also performed on samples #31, #34, and #49. The results indicated a lower fracture toughness than previously tested baseline material; K_{Ic} = 4.1 MPa•$m^{1/2}$ compared to 4.2 MPa•$m^{1/2}$ for the baseline material. While there is a reduction in the fracture toughness of these specimens, it does not appear that this factor alone accounts for the lower fracture strengths observed. Further investigation is currently underway to accurately assess the size and composition of each fracture origin.

ELEVATED TEMPERATURE PROPERTIES OF BASELINE MATERIAL:
(D. McCullum and N. Hecht; University of Dayton Research Institute)

Fast fracture testing of NNS-derived baseline tensile specimens at 1370°C has been completed and the results are contained in Table 21 and displayed on the Weibull plot on Figure 30. The mean tensile strength calculated based on a 14 specimen population was 216 MPa (31 ksi) with a standard deviation of 22 MPa (3 ksi), and a Weibull modulus of about 10. Specimen 176, which was the first specimen tested in this group, failed early during the high temperature soak period. During subsequent tests the collet deformation preload was removed before the high temperature soak. Initial fracture origin analysis indicated that most initiation sites originated at the surface in the specimens' gage sections.

Tensile stress rupture tests of similar baseline material at 1230°C have been completed. The data obtained are contained in Table 22. All of the specimens subjected to a static stress of 350 MPa failed on loading or immediately after the test began. Similarly, specimens subjected to static stresses of 250 MPa and 200 MPa failed after short exposure times. At a static stress of 150 MPa specimens survived from 65 to 88 hours, however, even at this reduced stress the desired 100 hour exposure was not observed. With the exception of one specimen all fracture origins occurred at the surface.

Stepped temperature tensile stress rupture (STSR) testing has been initiated on these baseline materials. Eight of the 13 specimens provided for STSR have been tested. As shown in Table 23, none of the specimens tested at stress levels of 350 MPa or 250 MPa

have survived 24 hours at each of the four specified test temperatures. Specimen 305 failed on loading. The failure stress was 292 MPa at 800°C. Specimens 292, 289, 283, and 291 failed before the test furnace temperature had stabilized at 1230°C. Temperature overshoot was 11, 6, 9, and 15°C, respectively, when going from a test temperature of 1000 to 1230°C. With the exception of specimen 284 all failure initiation sites were observed to occur at the surface. Specimen 284 failed after 3.2 hours exposure to 250 MPa stress at 800°C. Failure originated from an inclusion at the surface of the specimen.

Future efforts will focus on the completion of the stepped temperature tensile stress rupture testing at a stress level of 150 MPa. In addition, fractographic analysis for all of these specimens will be completed.

Status of milestones

Number	*Milestone*	*Scheduled*	*Completed*
1.0	**MATERIAL SELECTION AND CHARACTERIZATION**		
114301	Select silicon nitride and yttria for purchase	6/30/90	4/30/90
114302	Complete baseline process powder deliverables	6/30/90	4/30/90
114303	Select procedures for preparation of modified silicon nitride powders	5/31/91	
114304	Select materials for final process demonstration	12/31/91	
2.0	**MATERIAL PROCESSING AND PROCESS CONTROL**		
114305	Develop design and fabrication technique for NNS specimens	8/31/90	8/31/90
114306	Select NDE techniques for process control in final process demonstration	6/30/92	
114307	Determine effectiveness of SPC in controlling baseline process	12/31/91	
114308	Decision on control methodology for final process demonstration	6/30/92	
114309	Assess potential of "wet process" approach	10/31/90	
114310	NNS specimens fabricated with new molding equipment	3/31/91	2/28/91
114311	Evaluate improved compounding effect on green body	10/31/90	11/30/90
114312	Machining process decision for baseline specimens	6/30/90	6/30/90
114313	Complete microstructure/properties parametric study evaluating Task 1 powder variables	6/30/91	
114314	Initiate final process demonstration	6/30/92	
114315	Complete final process specimen deliverables	10/31/92	
3.0	**DEVELOPMENT AND APPLICATION OF NDE METHODS**		
114316	Establish x-ray microfocus detectability limits for all test specimen shapes	5/31/90	6/30/90
114317	Select surface measurement parameters relating to strength and reliability	9/30/90	1/31/91
114318	Determine feasibility of pulse-echo ultrasonic NDE for both green and burned-out ceramics	2/28/91	2/28/91
4.0	**PROPERTY TESTING AND MICROSTRUCTURAL EVALUATION**		
114319	Finalize tensile specimen geometry and procedure	2/28/90	2/28/90
114320	Institute preliminary tensile test technique	6/30/90	4/30/90

Milestone #114309 (Assess the potential of the wet processing approach) was delayed until the end of 6/91 while major processing laboratory facility modifications are being completed. Milestone #114311 (Evaluate improved compounding effect on green body)

was completed with the evaluation results discussed in this report under Task 2.2. The effect of the improved compounding will now also be followed through to the final dense specimens, and confirmed by tensile and MOR testing. Milestone 114317, "Select surface measurement parameters relating to strength" was completed, as described in Task 3 above. The program remains largely on schedule, with the milestone schedule shown below. Milestone 114310, due this period, has been altered slightly to utilize MLP specimens instead of NSF specimens, as this molding die could be sent to England for use at Brunel without compromising the program's deliverables schedule. The specimens are expected to arrive in April. Efforts on the remaining milestones are on schedule.

Publications and presentations

A. Pasto and S. Natansohn presented a paper entitled "Improved Processing Methods for High Reliability Silicon Nitride" at the ATD-CCM meeting.

References

1. T. Sato et al., J. Am. Ceram. Soc., 71, 1074 (1988).

2. M. Jenkins, M. Ferber, and R. Martin, "Rotor Data Base Generation", Pp.40-44 in CTAHE Project Bimonthly Technical Progress Report for Oct. - Nov. 1990, ORNL/CF-90/385, 12/31/90.

3. Surface Texture (Surface Roughness, Waviness, and Lay), ANSI/ASME B46.1-1985.

Table 1. Properties of Modified Silicon Nitride Materials

		Modified Powder	
	Baseline	Small Lot	Large Lot
Properties of Processed Powders:			
Surface Area (m^2/g)	11.2	9.6	9.4
Oxygen (w/o)	3.25	3.73	3.29
Oxygen (mg/m^2)	2.90	3.87	3.50
Soluble Si (mg/m^2)	0.75	1.17	1.04
Mechanical Properties:			
Density (g/m^3)	3.219	3.251	3.259
Density (% of 3.26)	98.8	99.7	100
RT MOR (MPa)	910	1110	1140
1370°C MOR (MPa)	570	775	700
Oxidation Resistance:			
ΔW after 500 hrs			
at 1200°C (g/m^2)	1.4	0.77	0.77
at 1370°C (g/m^2)	2.8	1.5	1.6

TABLE 2. Composition of Intergranular Phase in PY6 Ceramics

	Si (a/o)	Y (a/o)	Si:Y (at. ratio)
Baseline	53	47	1.13
Modified	56	44	1.27
Added Silica	56.5	43.5	1.30

Table 3. Intergranular Phase Composition Data from AEM and Leaching Experiments

Powder	Baseline	Modified	Added Silica
Atomic Ratio Y/Si (AEM)	0.89	0.79	0.77
Atomic Ratio Y/Si (Leachate)	2.26	1.0	0.90
Amount Leached (w/o)	3.60	2.84	0.90
RT MOR (MPa)	944	993	1151
1370°C MOR (MPa)	549	758	532

Table 4. Characteristics of Aged Silicon Nitride Powders

Conditions		Soluble Si (mg/g)	Soluble NH3 (mg/g)	Si:N (molar ratio)
Initial		4.6±0.13	0.65±0.10	4.3
Dry Air-	139 Days	4.7±0.19	0.62±0.07	4.6
	257 Days	4.9±0.06	1.2 ±0.2	2.5
	323 Days	4.4±0.08	0.92±0.04	2.9
Wet Air-	139 Days	5.0±0.01	0.27±0.07	11
	257 Days	4.9±0.2	0.6 ±0.2	4.9
	323 Days	4.4±0.04	0.66±0.03	4.2
Dry Argon -	139 Days	4.6±0.1	0.49±0.04	5.6
	257 Days	5.0±0.2	0.85±0.13	3.6
	323 Days	4.4±0.09	0.85±0.08	3.1
Wet Argon -	139 Days	4.4±0.3	0.35±0.04	7.6
	257 Days	4.6±0.1	0.7 ±0.2	4.0
	323 Days	3.8±0.07	0.80±0.03	2.9

Table 5. Properties of PY6 Ceramics Hot-Pressed from Powders With Chemically Incorporated Sintering Aids

		Addition Route		
	Standard	Nitrate (aq)	(alc)	Isopropoxide
Density				
(g/cm3)	3.19	3.22	3.21	3.18
(% of 3.26):	97.8	98.7	98.6	97.6
MOR (MPa)				
RT	960±50	930±120	840±160	745±45
1370°C	540±55	545±18	550±30	385±20

Table 6. Solubility Behavior of Hot-Pressed PY6 Ceramics in Hot HCl

Powder Treatment	Amount (w/o)	DISSOLVED Yttrium (mg/g)	Silicon (mg/g)	Ammonia (mg/g)	Molar Ratio Y : Si : N	Flexure Strength (Mpa)
None	2.9	18.6	3.0	1.1	2.0: 1.0: 0.60	960
Modification	1.6	7.6	2.4	0.4	1.0: 1.0: 0.28	1080
Nitric Acid	3.9	26.5	3.4	1.1	2.5: 1.0: 0.53	900
Hydrogen Peroxide	4.2	29.6	4.0	1.5	2.3: 1.0: 0.62	910
Hydrofluoric Acid	2.2	17.2	1.9	1.0	2.9: 1.0: 0.87	840
Hydrolysis	3.6	23.4	3.7	1.2	2.0: 1.0: 0.52	970

Table 7. Density and RT MOR of hot-pressed ESP PY6

MILL TYPE	MILLING LIQUID	PRE SCREEN	POST SCREEN	Y10		Y20		Y40	
				DENSITY (gm/cm^3) / % 3.260	MOR (MPa) / WEIBULL	DENSITY (gm/cm^3) / % 3.260	MOR (MPa) / WEIBULL	DENSITY (gm/cm^3) / % 3.260	MOR (MPa) / WEIBULL
ATTRITOR	2-PROPANOL	-500 -625 -850	-500 -625	3.257 99.9%	1037 25	3.257 99.9%	1119 32	-	-
	2-PROPANOL	-	-500 -625	3.259 100.0%	1025 20	3.259 100.0%	976 21	3.244 99.5%	1018 17
	2-PROPANOL	-	-	3.257 99.9%	1023 21	-	-	-	-
	WATER	-	-500 -625	3.222 98.9%	1003 15	-	-	-	-
	XYLENE	-	-500 -625	3.261 100.0%	950 22	-	-	-	-
	OMTS	-	-500 -625	3.258 99.9%	956 47	-	-	-	-
SWECO	DRY ST AC	-	-	ABO 3.172 97.3%	LOW DENSITY -	ABO 3.198 98.1%	LOW DENSITY -	-	-
	DRY ST AC	-500 -625 -850	-	ABO 3.238 99.3%	LOW DENSITY -	ABO 3.205 98.3%	LOW DENSITY -	-	-

Table 8. Density and 1370°C MOR of hot-pressed ESP PY6

MILL TYPE	MILLING LIQUID	PRE SCREEN	POST SCREEN	Y10		Y20		Y40	
				DENSITY (gm/cm^3) / % 3.260	MOR (MPa)	DENSITY (gm/cm^3) / % 3.260	MOR (MPa)	DENSITY (gm/cm^3) / % 3.260	MOR (MPa)
ATTRITOR	2-PROPANOL	-500 -625 -850	-500 -625	3.257 99.9%	654	3.257 99.9%	694	-	-
	2-PROPANOL	-	-500 -625	3.259 100.0%	588	3.259 100.0%	547	3.244 99.5%	565
	2-PROPANOL	-	-	3.257 99.9%	550	-	-	-	-
	WATER	-	-500 -625	3.222 98.8%	544	-	-	-	-
	XYLENE	-	-500 -625	3.261 100.0%	481	-	-	-	-
	OMTS	-	-500 -625	3.258 99.9%	627	-	-	-	-
SWECO	DRY ST AC	-	-	ABD 3.172 97.3%	LOW DENSITY -	ABD 3.198 98.1%	LOW DENSITY -	-	-
	DRY ST AC	-500 -625 -850	-	ABD 3.238 99.3%	LOW DENSITY -	ABD 3.205 98.3%	LOW DENSITY -	-	-

Table 9. Density and RT MOR of HIPed ESP PY6

MILL TYPE	MILLING LIQUID	PRE SCREEN	POST SCREEN	Y10		Y20		Y40	
				DENSITY (gm/cm^3) % 3.260	MOR (MPa) WEIBULL	DENSITY (gm/cm^3) % 3.260	MOR (MPa) WEIBULL	DENSITY (gm/cm^3) % 3.260	MOR (MPa) WEIBULL
ATTRITOR	2-PROPANOL	-500 -625 -850	-500 -625	3.252 99.8%	804 26	3.251 99.7%	842 17	-	-
	2-PROPANOL	-	-500 -625	3.253 99.8%	743 20	3.252 99.8%	794 24	3.249 99.7%	824 17
	2-PROPANOL	-	-	3.252 99.8%	778 23	-	-	-	-
	WATER	-	-500 -625	3.254 99.8%	736 30	-	-	-	-
	XYLENE	-	-500 -625	3.252 99.8%	675 9	-	-	-	-
	OMTS	-	-500 -625	3.252 99.8%	754 23	-	-	-	-
SWECO	DRY ST AC	-	-	ABO 3.255 99.8%	634 20	ABO 3.251 99.7%	684 29	-	-
	DRY ST AC	-500 -625 -850	-	ABO 3.254 99.8%	685 9	ABO 3.256 99.9%	645 20	-	-

Table 10. Density and 1370°C MOR of HIPed ESP PY6

MILL TYPE	MILLING LIQUID	PRE SCREEN	POST SCREEN	Y10		Y20		Y40	
				DENSITY (gm/cm^3) / % 3.260	MOR (MPa)	DENSITY (gm/cm^3) / % 3.260	MOR (MPa)	DENSITY (gm/cm^3) / % 3.260	MOR (MPa)
ATTRITOR	2-PROPANOL	-500 -625 -850	-500 -625	3.252 99.8%	355	3.251 99.7%	365	-	-
	2-PROPANOL	-	-500 -625	3.253 99.8%	335	3.252 99.8%	314	3.249 99.7%	334
	2-PROPANOL	-	-	3.252 99.8%	310	-	-	-	-
	WATER	-	-500 -625	3.254 99.8%	324	-	-	-	-
	XYLENE	-	-500 -625	3.252 99.8%	312	-	-	-	-
	OMTS	-	-500 -625	3.252 99.8%	327	-	-	-	-
SWECO	DRY ST AC	-	-	ABO 3.255 99.9%	279	ABO 3.251 99.7%	285	-	-
	DRY ST AC	-500 -625 -850	-	ABO 3.254 99.9%	296	ABO 3.256 99.9%	303	-	-

Table 11. Densification of UBE SN-ESP and SN-E10 Containing Compositions

COMPN	Si3N4	HOT ISOSTATIC PRESSED			HOT PRESSED		
		No B.O.	Air:550/5	Air:700/7	No B.O.	Air:550/5	Air:700/7
Y6	E10	3.248	floater	3.250	3.266	3.265	3.263
Y6	E10	3.245	3.250	3.246	3.266	3.264	3.264
Y6	ESP	3.254	3.195	3.252	3.263	3.223	3.261
S2Y6	E10	3.233	3.233	3.233	3.253	3.249	3.245
S2Y6	ESP	3.239	3.214	3.236	3.251	3.246	3.243
A2Y6	E10	3.241	3.242	3.247	3.258	3.257	3.254
A2Y6	ESP	3.247	3.247	3.247	3.255	3.254	3.251

Table 12. NDE characterization of the occurrence of high density inclusions (HDIs) in samples of compounded PY6 as a function of their preparation route.

Number of HDIs / cm^3

	Mean	Std.	Max.	Min.
Large ABBE	2.93	0.96	4.69	1.97
Small ABBE	1.66	0.32	2.12	1.32
Noncontaminating Mixer	0.00	0.00	0.00	0.00
Noncontaminating Mixer with Twin-Screw Compounder	0.98	0.52	1.72	0.49
IMPROVED ABBE Batch #1	0.04	0.10	0.23	0.0
Batch #2	0.00	0.00	0.00	0.00

Table 13. Results of wear study.

Material	Heat Deflection Temp (°C)	Bulk Cost ¢/cu in.	$x10^{-3}$ Erosive Wear Rate (cc/min)	$x10^{-3}$ Abrasive Wear Rate (cc/min)
UHMW PE	48	3.3	0.3	0.5
Nylon 6/6	88	6.4	3.9	2.0
Tool Steel	—	—	8.1	2.0
PEEK	160	109.3	4.4	2.4
Teflon (PTFE)	56	48	19.2	3.7
Low Pressure PE	38	1.6	6.4	4.1
PP	54	1.5	2.1	4.8
PI (Unfilled)	349	95	30.9	5.0
PEI	200	21.5	13.8	8.8
PI (Filled)	360	97	56.1	13.0
PAI	282	96	49.2	23.6
LCP (Filled)	204	100	44.4	24.2

Table 14. Abbreviations used to designate plastics.

Abbreviation	Name
UHMW PE	Ultra-high molecular weight polyethylene
Nylon 6/6	Polyamide
PEEK	Polyetheretherketone (Victrex 450G)
PE	Polyethylene
PP	Polypropylene
PI	Polyimide (unfilled: Vespel SP-1, filled: VespelSP-21)
PEI	Polyether imide (Ultem 1000)
PAI	Polyamide imide (Torlon 4301)
PTFE	Polytetrafluoroethylene
LCP	Liquid Crystal Polymer

Table 15: Quantitative microstructural characteristics of PY6 produced using the modified HIP cycle as compared to the baseline material.

SI3N4 GRAIN FEATURE	BASELINE HIP CYCLE	MODIFIED HIP CYCLE
Average Area (sq. μm)	0.5	0.3
Minimum Area (sq. μm)	0.01	<0.01
Maximum Area (sq. μm)	9.5	6.8
Average Aspect Ratio (*L/D*)	2.1	2.0
Maximum Aspect Ratio	12	7
Number of Data	415	641

Table 16: Properties of PY6 produced with the standard and modified HIP cycles.

MATERIAL PROPERTY	BASELINE HIP CYCLE	MODIFIED HIP CYCLE
DENSITY (g/cm3)	3.257	3.252
ELASTIC MODULUS (GPa)	317	322
POISSON'S RATIO	0.3	0.3
K_{IC} (MPa•√m)	4.2 ± 0.2	4.3 ± 0.1
KNOOP HARDNESS (GPa)	13.3 ± 0.3	12.8 ± 0.2
PHASE COMPOSITION	100% Beta Si3N4	88% Beta Si3N4

Table 17. Results of Taguchi Methods experiments on the HIPing process.

QUALITY CHARACTERISTICS - Preferred Factor Levels

CONTROL FACTORS		25°C MOR	1370°C MOR	DENSITY	SURFACE	CONFIRM. RUN
A	BURNOUT TYPE	2		2	1 *	INT.
B	CRUCIBLE TYPE			1	1	B1
C	HEATING RATE R1				1	C1
D	TEMPERATURE T1			1	1	D1
E	PRESSURE P1				1	E1
F	HEATING RATE R2	1	1			F1
G	TEMPERATURE T2					G1
H	PRESSURE P2					H1
I	HOLD TIME		1	1		I1
J	COOLING RATE R3					INT.

NOISE FACTORS		25°C MOR	1370°C MOR	DENSITY	SURFACE
M	PART LOCATION	1			
N	STORAGE TIME		1	2	1

WEAK / NO EFFECT

* VERY STRONG EFFECT

INT. INTERMEDIATE LEVEL CHOSEN

Table 18. Surface characteristics of machined and annealed PY6 MOR bars.

	Ra (μm)	Rq(μm)	Sk	Rv(μm	MOR(MPa)
As-Machined					
Bar 1	2.02	2.70	-0.99	13.6	
Bar 2	2.07	2.70	-0.85	12.2	
Bar 3	2.13	2.80	-0.90	12.0	
Average	**2.07**	**2.73**	**-0.91**	**12.6**	**711**
Annealed					
Bar 1	2.05	2.58	-0.47	8.10	
Bar 2	1.98	2.50	-0.53	10.98	
Bar 3	2.11	2.66	-0.43	11.5	
Average	**2.05**	**2.58**	**-0.48**	**10.2**	**814**

Table 19. Results of Tensile Testing of Baseline Material

Spec. #	Strength (MPa)	Tester/Set#	Spec. #	Strength (MPa)	Tester/Set#	Spec. #	Strength (MPa)	Tester/Set#
69	424.4	GTEL-#1	158	534.65	UDRI-#2	357	659.36	GTEL-#3
70	418.4	GTEL-#1	159	459.42	UDRI-#2	361	742.13	GTEL-#3
74	516.3	GTEL-#1	161	709.99	UDRI-#2	362	802.07	GTEL-#3
81	442.3	GTEL-#1	165	762.72	UDRI-#2	364	736.18	GTEL-#3
84	428.6	GTEL-#1	173	669.58	UDRI-#2	365	725.01	GTEL-#3
88	476.3	GTEL-#1	179	602.50	UDRI-#2	367	674.13	GTEL-#3
98	507.7	GTEL-#1	182	657.83	UDRI-#2	370	740.96	GTEL-#3
103	562.1	GTEL-#1	187	431.06	UDRI-#2	371	775.95	GTEL-#3
110	435.6	GTEL-#1	189	481.63	UDRI-#2	375	492.96	GTEL-#3
113	519.1	GTEL-#1	190	546.85	UDRI-#2	376	686.63	GTEL-#3
117	533.1	GTEL-#1	191	736.74	UDRI-#2	378	622.16	GTEL-#3
122	737.7	GTEL-#1	192	754.59	UDRI-#2	379	730.31	GTEL-#3
131	659.9	GTEL-#1	194	915.75	UDRI-#2	382	744.35	GTEL-#3
138	632.8	GTEL-#1	195	505.18	UDRI-#2	383	737.33	GTEL-#3
141	682	GTEL-#1	198	593.43	UDRI-#2	384	799.12	GTEL-#3
145	614.5	GTEL-#1	243	568.80	UDRI-#2	387	766.14	GTEL-#3
146	436.3	GTEL-#1	244	664.39	UDRI-#2	388	674.13	GTEL-#3
147	596.7	GTEL-#1	247	765.08	UDRI-#2	395	544.92	GTEL-#3
149	737.7	GTEL-#1	248	607.54	UDRI-#2	399	810.36	GTEL-#3
153	530.7	GTEL-#1	250	450.41	UDRI-#2	400	657.28	GTEL-#3
			252	561.77	UDRI-#2	402	688.17	GTEL-#3
			254	351.14	UDRI-#2			
			255	724.44	UDRI-#2			
			261	619.35	UDRI-#2			

Dataset#	Strength (MPa)	Weibull Modulus
1	545	6.1
2	611	5.5
3	716	12.8

Table 20. Tensile strength test results for MLP specimens.

Sample #	Strength(MPa)	Fracture Origin
21	421.5	inclusion
13	407.5	inclusion
14	375.4	inclusion
7	365.3	inclusion
31	5459	inclusion
4	566.6	inclusion
29	347.3	inclusion
8	417.3	inclusion
36	421.3	inclusion
23	339.9	inclusion
26	381.0	inclusion
9	467.4	inclusion
48	372.6	inclusion
34	342.8	inclusion

Ave. Strength 412.3±70.9
Weibull modulus 6

Table 21. Tensile fast fracture results at 1370°C for baseline PY6.

SPECIMEN NUMBER	DIAMETER (in)	LOAD (lbs)	TENSILE STRENGTH (ksi)	(MPa)	FRACTURE ORIGIN
156	0.2500	1950	40	274	S.
181	0.2497	1300	27	183	S.
267	0.2500	1540	31	216	V.
271	0.2499	1400	29	197	S.
277	0.2501	1400	28	196	S.
278	0.2500	1550	32	218	S.
276	0.2502	1510	31	212	S.
266	0.2500	1610	33	226	S.
263	0.2500	1470	30	206	S.
275	0.2505	1590	32	222	S.
265	0.2504	1540	31	216	V.I.
273	0.2504	1520	31	213	S.
269	0.2500	1730	35	243	S.
274	0.2500	1440	29	202	S.
176	0.2501	1000	~		S.
		Average	31	216	
		St. Dev.	3	22	
		Weibull	10		

Fracture Origin- V. (volume failure), S. (surface failure), and I. (failed at inclusion)

NOTES 1: Specimens were preloaded to 1000 lbs at 20 C, held for 5 min. The preload was then reduced to 100 lbs and the specimens were put in the furnace where they soaked at temperature for 15 min. before testing.

2: Fracture surfaces were difficult to read. There were no completely smooth mirror regions and mirrors were very large.

3: Specimen 176 did not have the preload removed before it was put in the furnace. It failed at 1000 lbs after 50 s at 1370 C. The fracture origin was at the surface and showed evidence of slow crack growth.

Table 22. Tensile stress rupture results for baseline PY6.

Specimen Number	Test Stress (MPa)	Diam. (in)	Failure Load (lbs)	Failure Strength (MPa)	Time To Failure	Collets	Fracture Origin
299	350	0.2500	2300	323	-	17(2)	Surface
295	350	0.2515	2492	346	ls	17(3)	Surface
288	350	0.2500	2492	350	5s	17(4)	Volume
296	250	0.2511	1779	248	103s	17(5)	Surface
297	250	0.2535	1779	243	265s	17(6)	Surface
286	225	0.2571	1601	213	741s	17(7)	Surface
298	150	0.2501	1068	150	88.7hr	18(1)	Surface
304	150	0.2504	1068	150	65.4hr	18(2)	Surface
293	150	0.2502	1068	150	81.6hr	18(3)	Surface
306	150	0.2503	1068	150	84.7hr	18(4)	Surface

Test Procedure: 0.001 in/min to 1000#; 5 min; reduce load rapidly to 100#; furnace at temperature for 15 min: 0.1 in/min to test stress.

Table 23. Tensile stepped temperature stress rupture results on baseline PY6.

SPECIMEN NUMBER	TEST STRESS (MPA)	TIME AT 800 C (hrs)	TIME AT 1000 C (hrs)	TIME AT 1230 C	TIME AT 1370 C
305	350	0	-	-	-
285	350	24	4.6	-	-
281	350	24	15.6	-	-
292	350	24	24	5 s	-
289	350	24	24	10 s	-
283	250	24	24	22 s	-
291	250	24	24	29 s	-
284	250	3.2	-	-	-

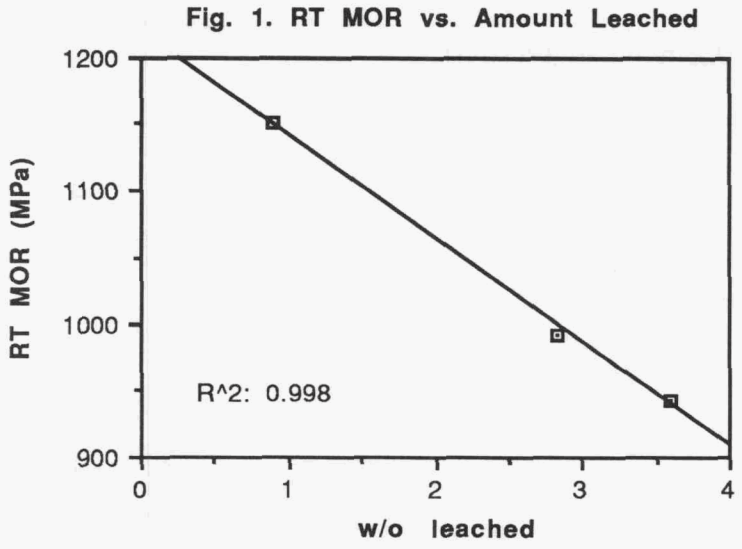

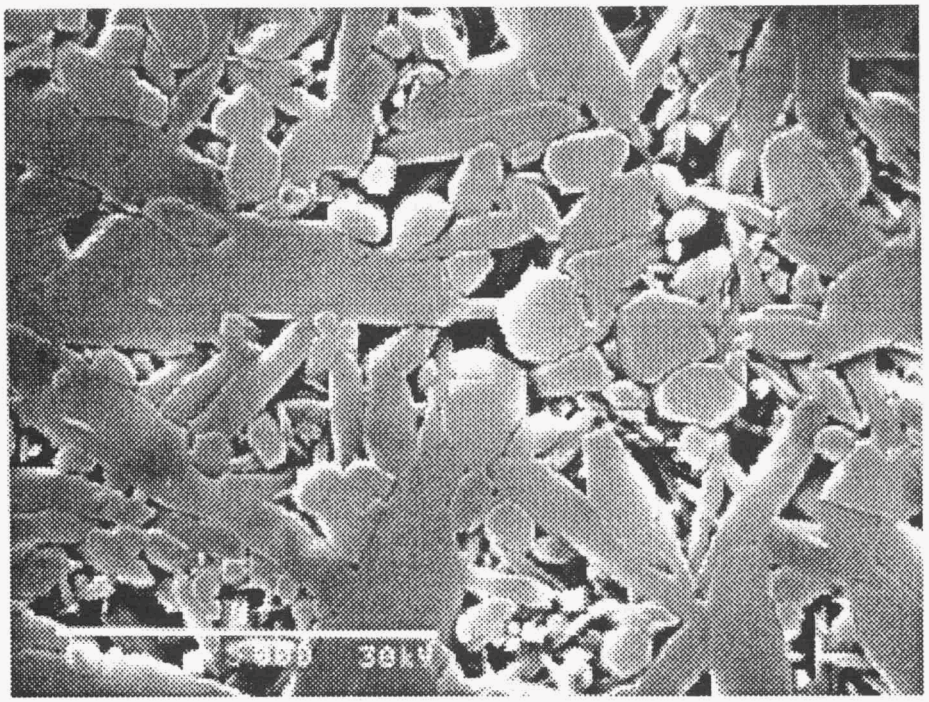

Figure 2. Baseline material microstructure.

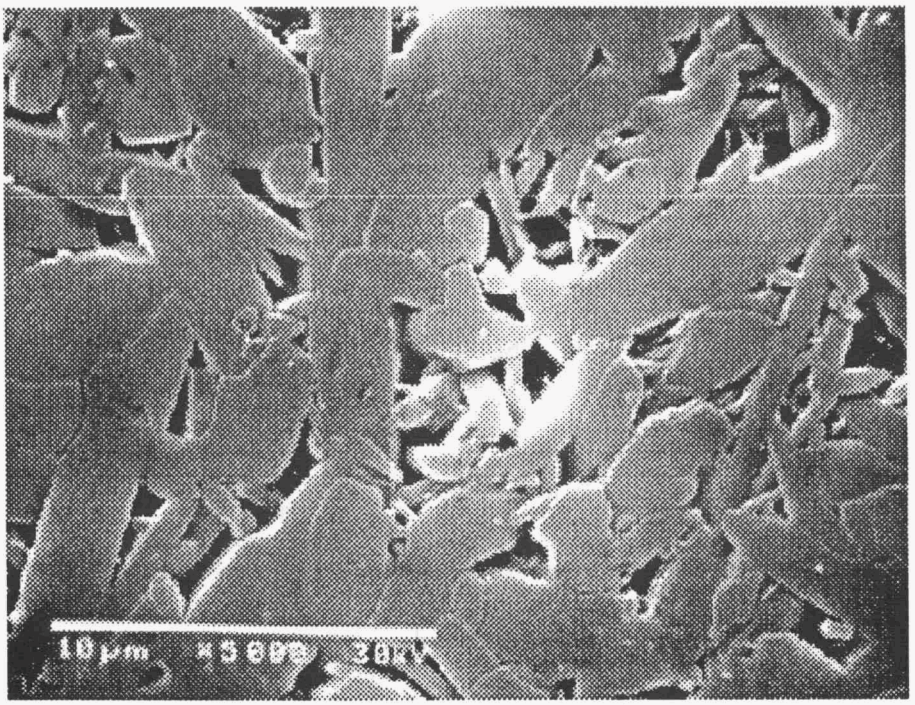

Figure 3. HF-treated material microstructure.

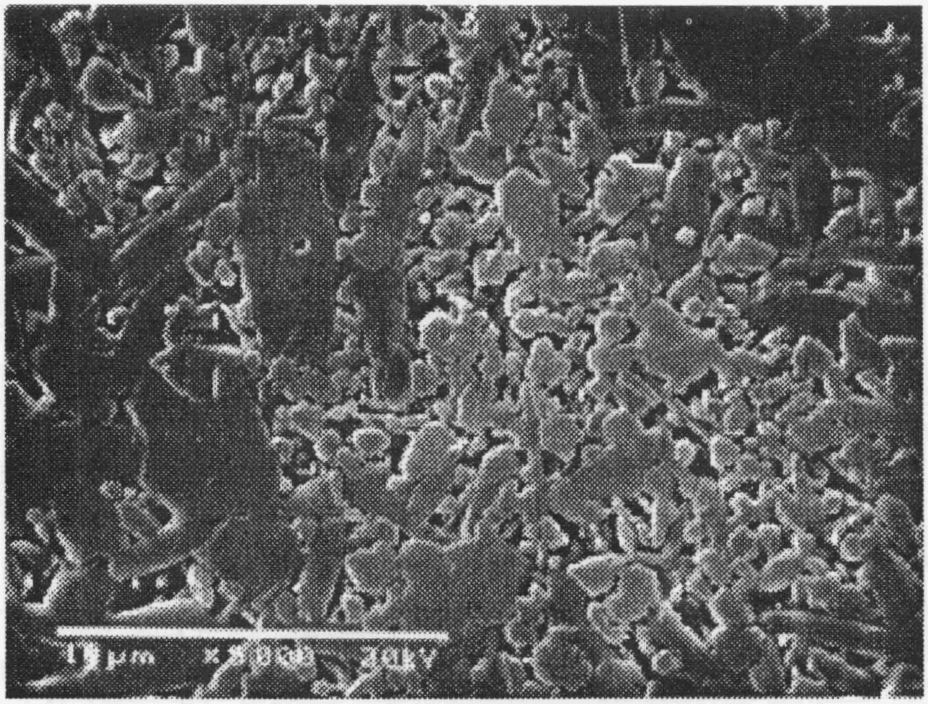

Figure 4. Modified material microstructure.

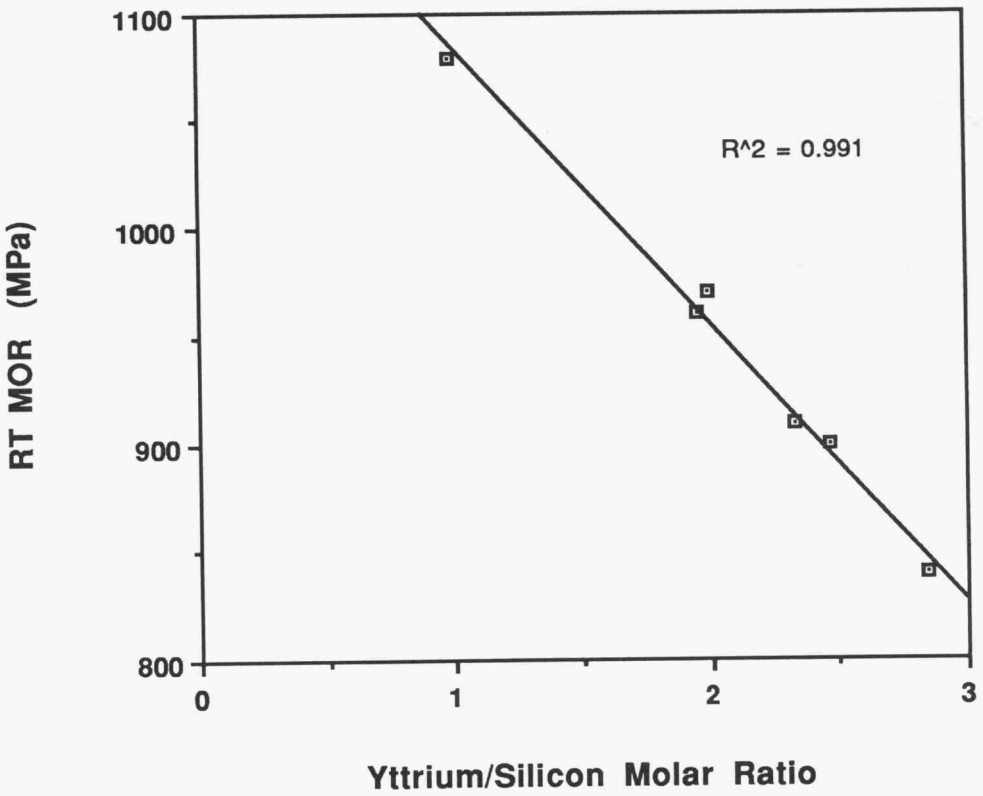

Figure 5. Flexural strength of hot-pressed PY6 as a function of the yttrium/silicon ratio of material leached from the test bars with HCl.

Figure 6. Schematic layout for the liquid processing laboratory.

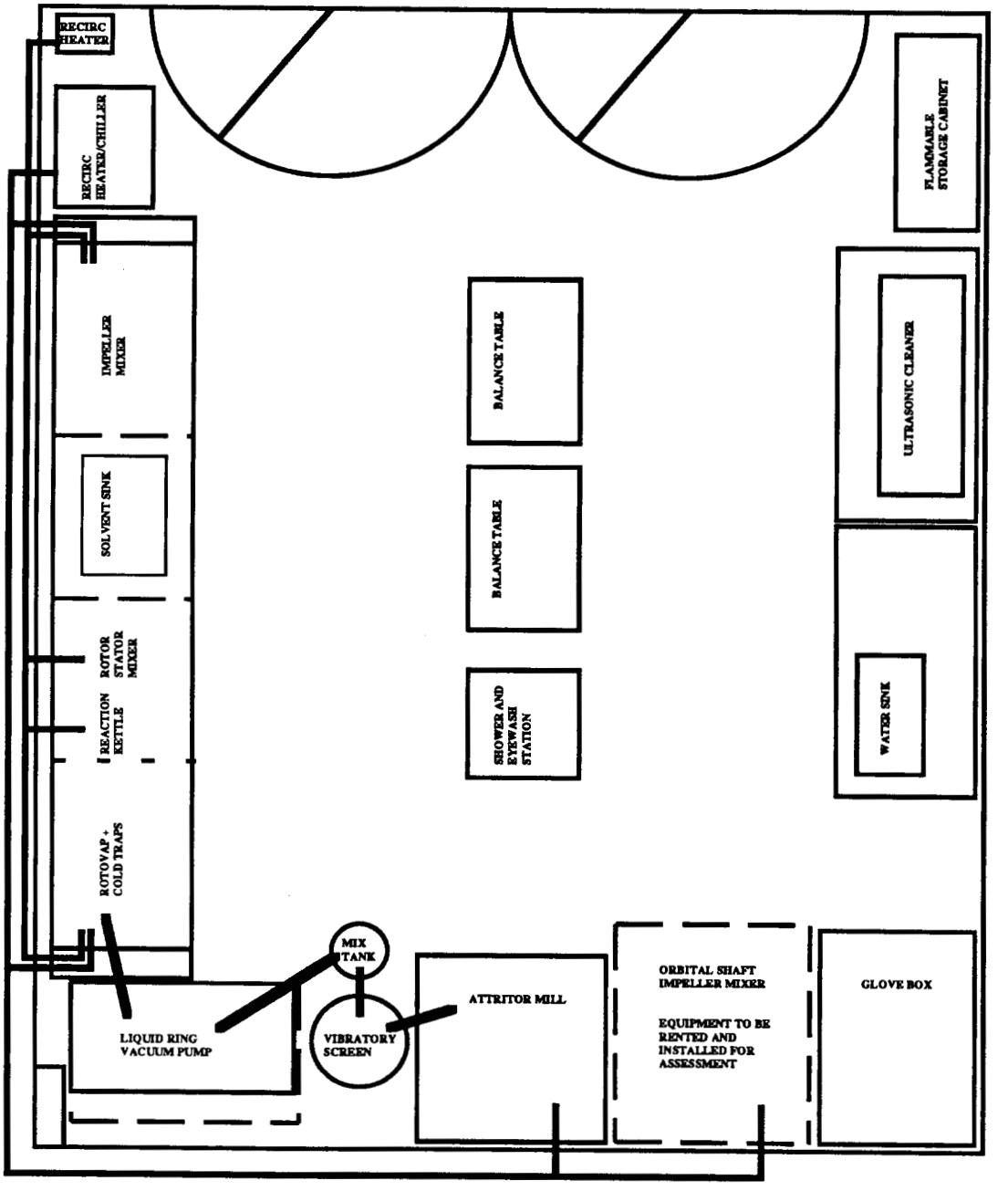

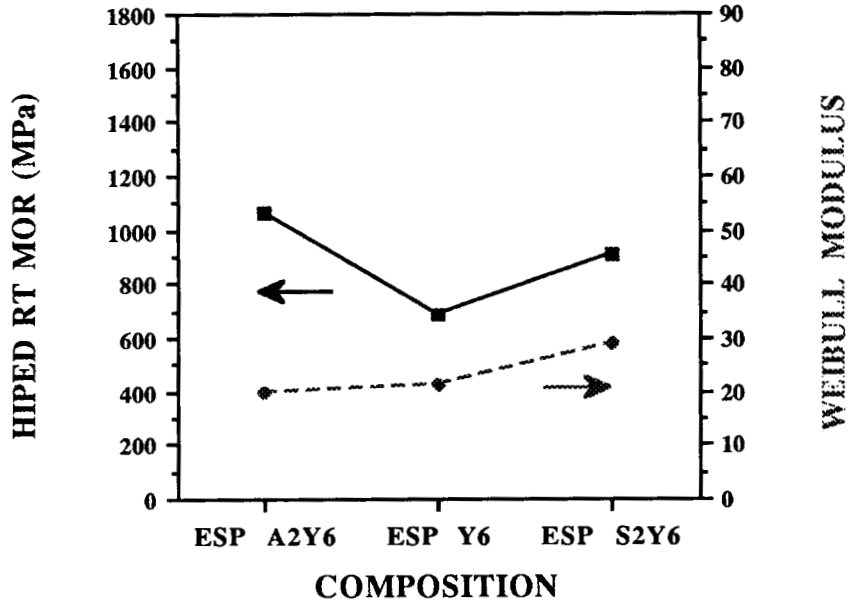

Figure 7. RT MOR and Weibull modulus of HIPed ESP compositions.

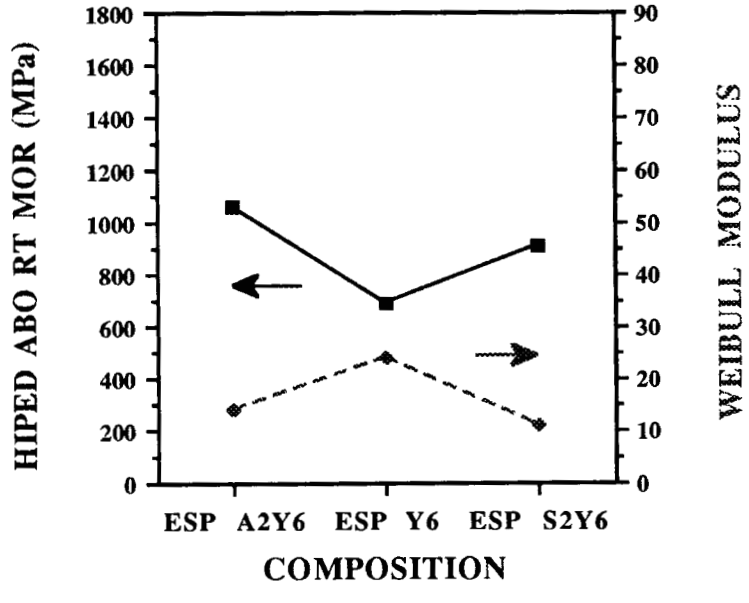

Figure 8. RT MOR and Weibull modulus of HIPed air-burned-out(ABO) ESP compositions.

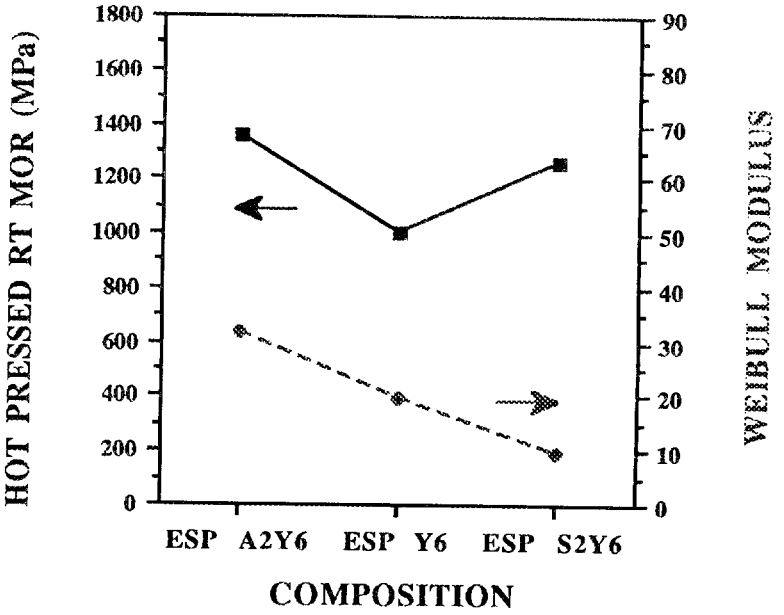

Figure 9. RT MOR and Weibull modulus of hot-pressed ESP compositions.

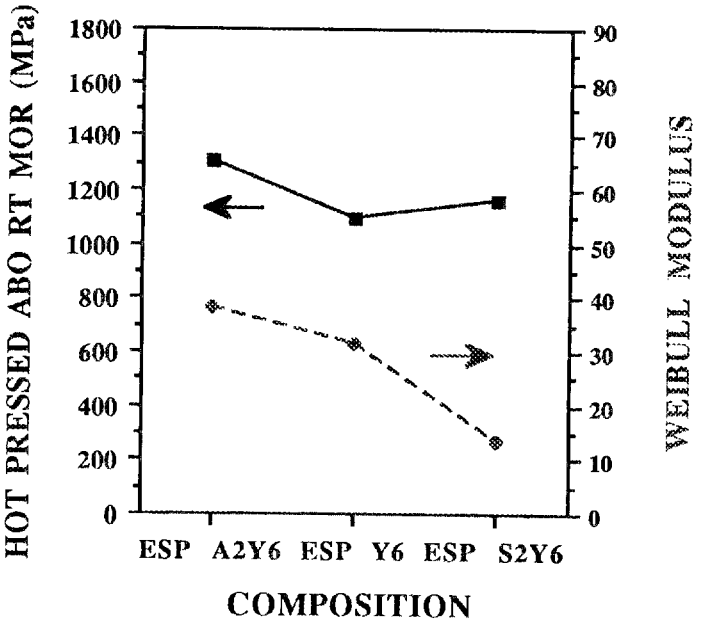

Figure 10. RT MOR and Weibull modulus of hot-pressed ABO ESP compositions.

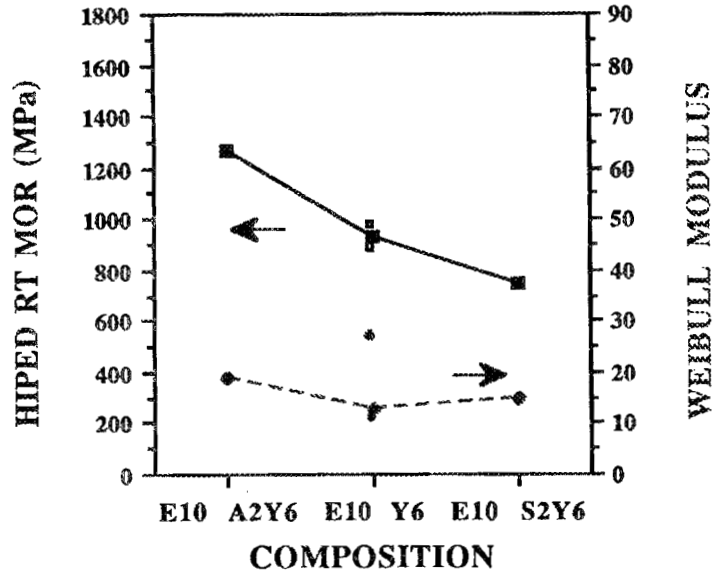

Figure 11. RT MOR and Weibull modulus of HIPed E10 compositions.

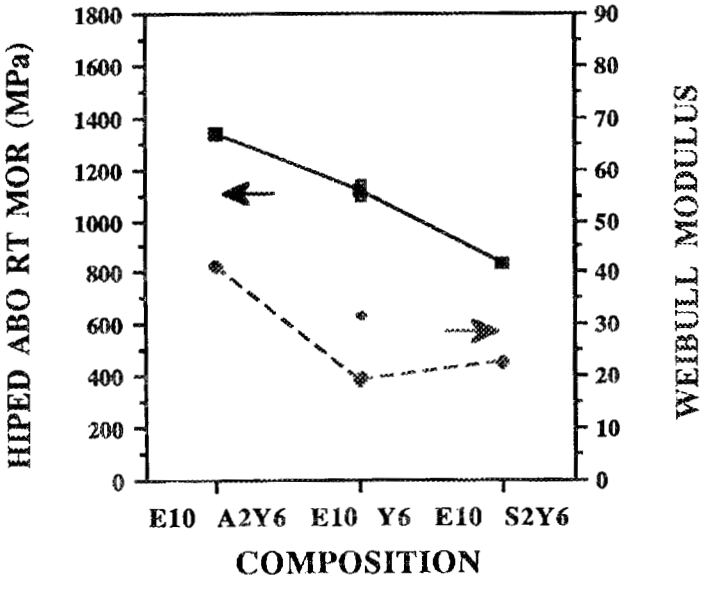

Figure 12. RT MOR and Weibull modulus of HIPed ABO E10 compositions.

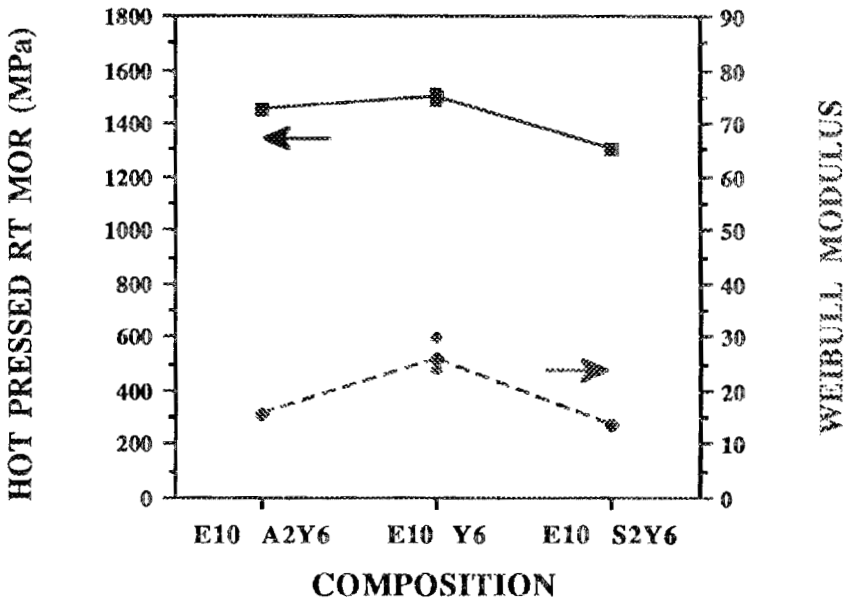

Figure 13. RT MOR and Weibull modulus of hot-pressed E10 compositions.

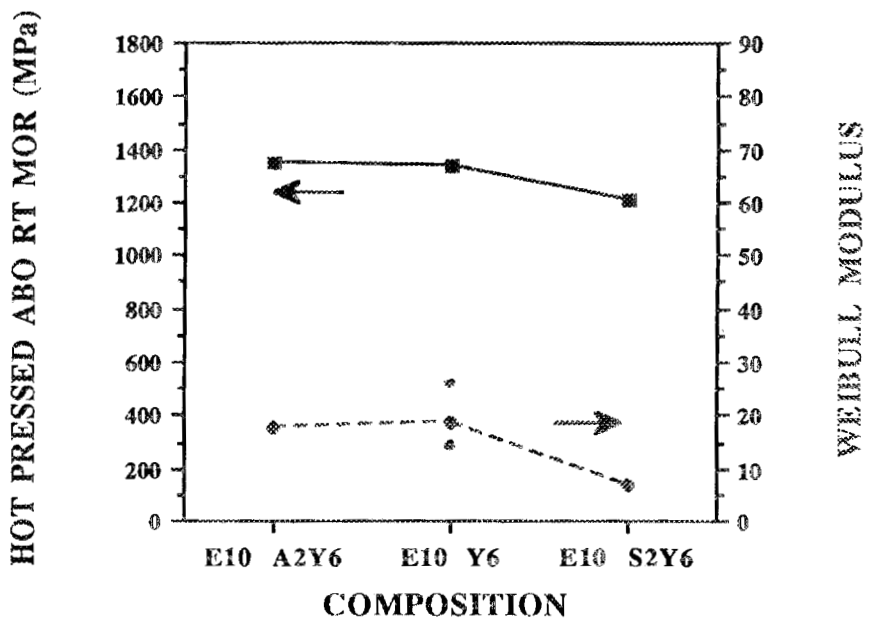

Figure 14. RT MOR and Weibull modulus of hot-pressed ABO E10 compositions.

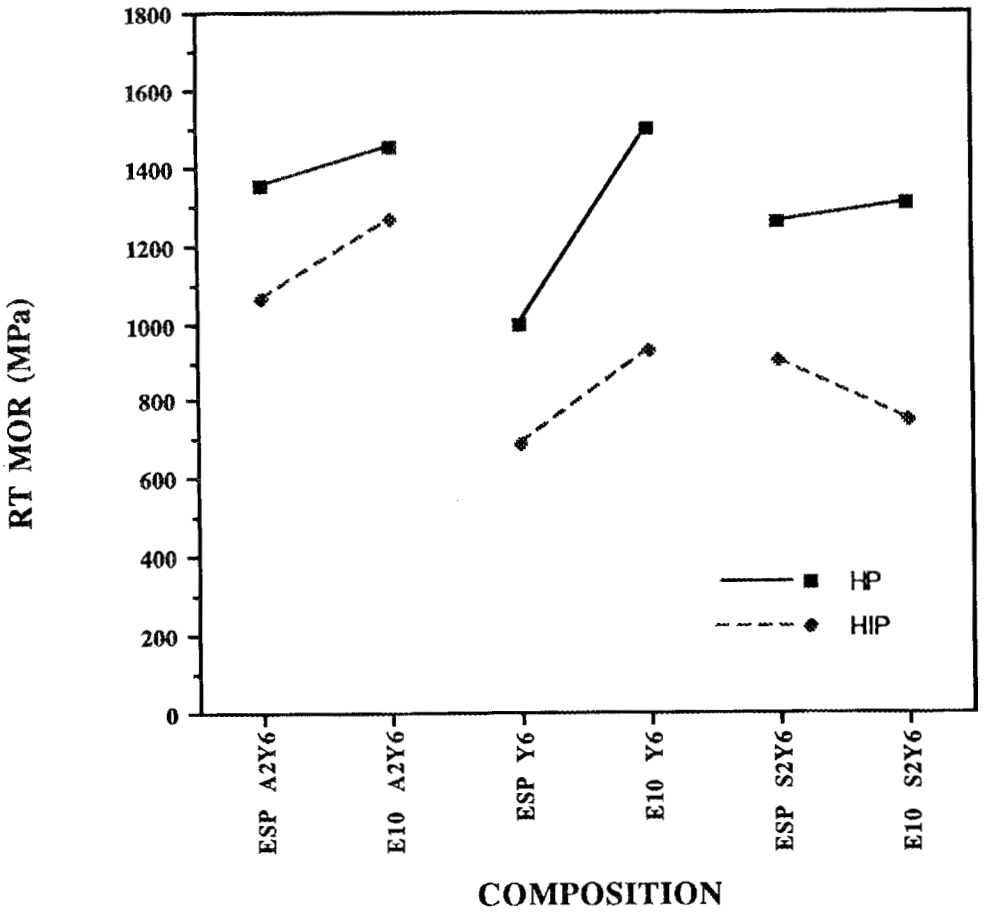

Figure 15. RT MOR of hot-pressed and HIPed ESP and E10 powder compositions.

Figure 16. Viscosity for several batches compounded using the noncontaminating compounder.

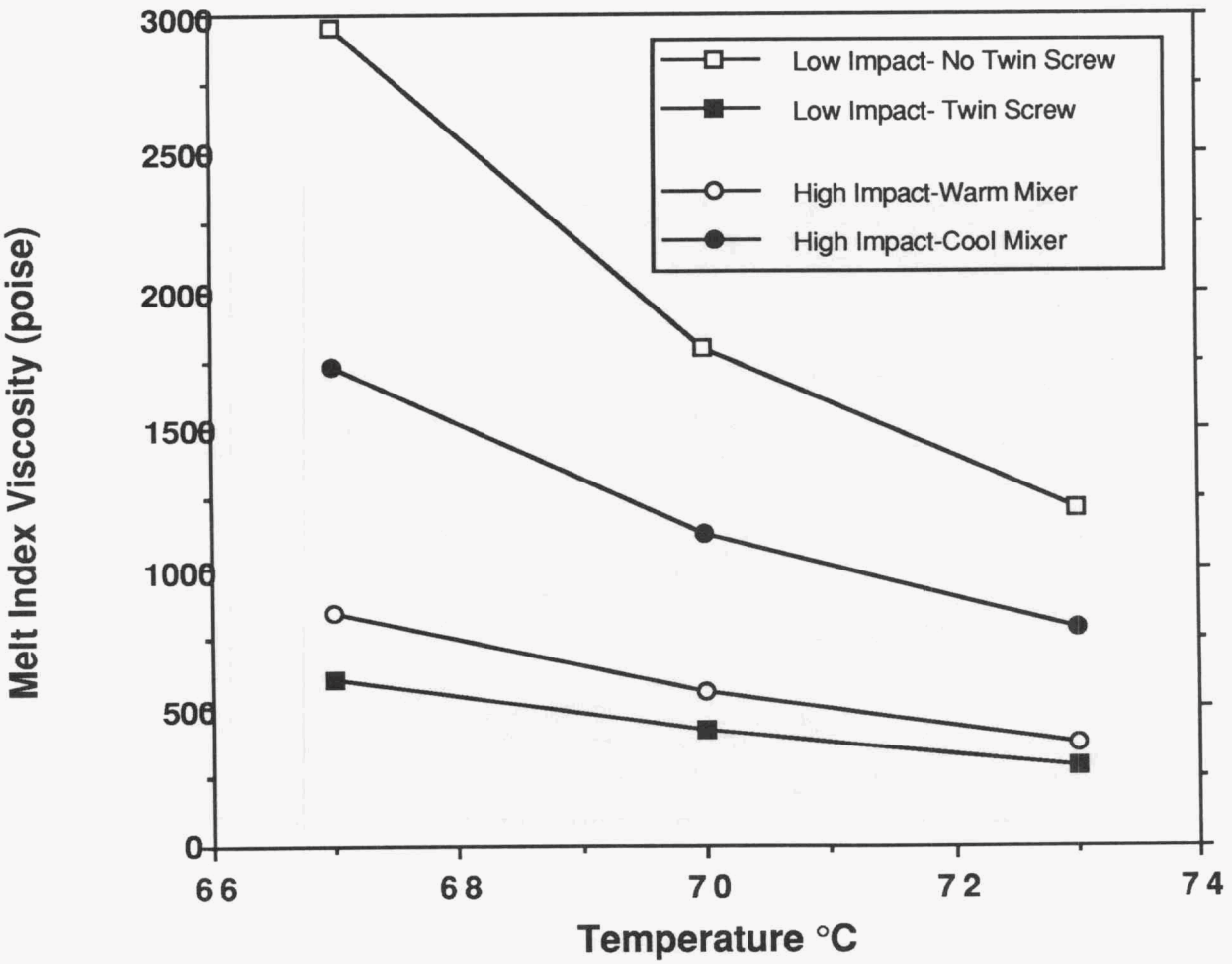

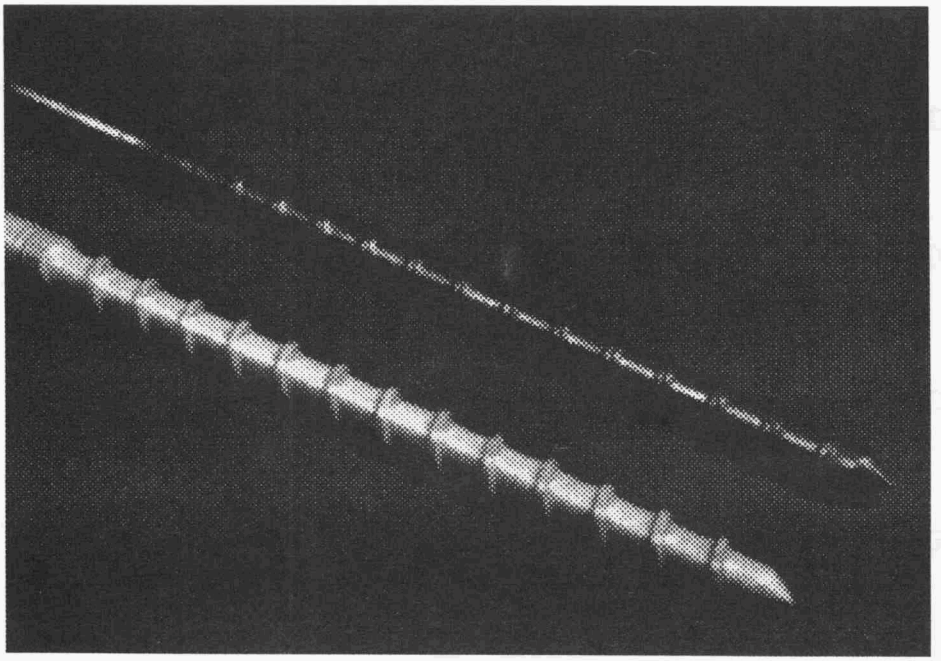

Figure 17. Injection molding screw fabricated from metal (top) and PEEK plastic (bottom)

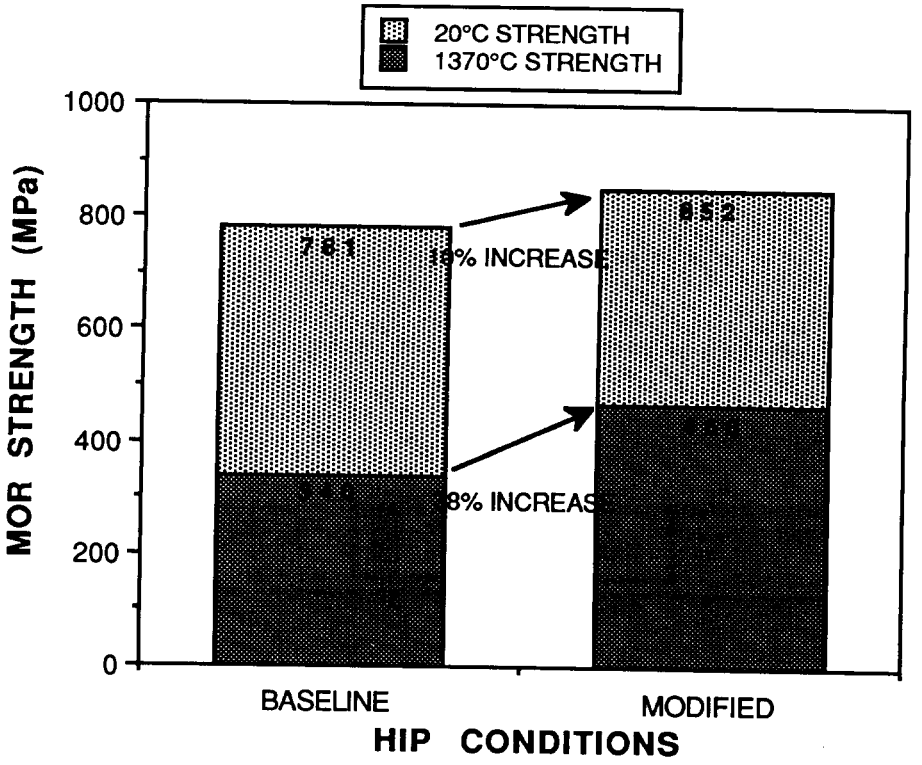

Figure 18: MOR strength of PY6 HIPed at the conditions of Experiment #3 as compared to the baseline material.

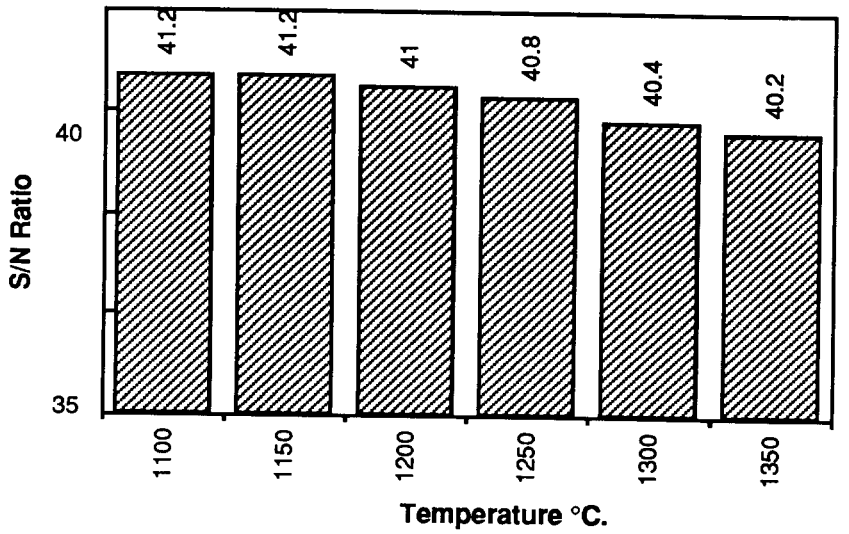

Figure 19: Results of Taguchi Methods experiment to optimize the post-machining annealing cycle. Best annealing temperature is attained at temperatures of 1100-1150°C.

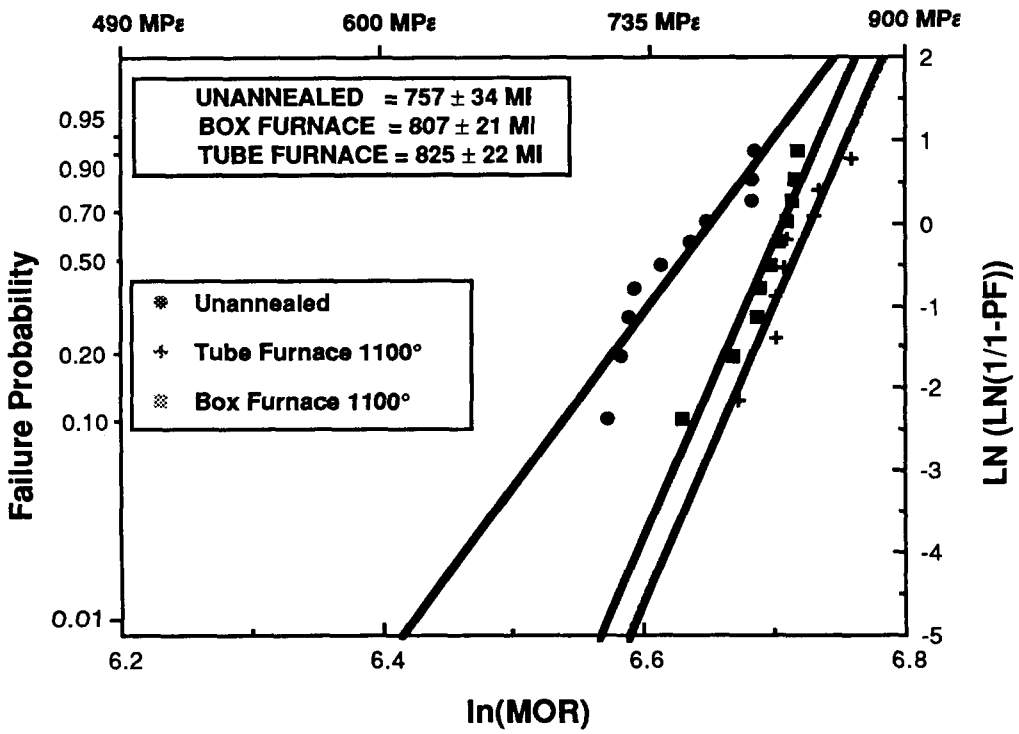

Figure 20: Results of Taguchi Methods experiment to optimize the annealing cycle. Confirmation experiments show improvement in strength is gained by annealing

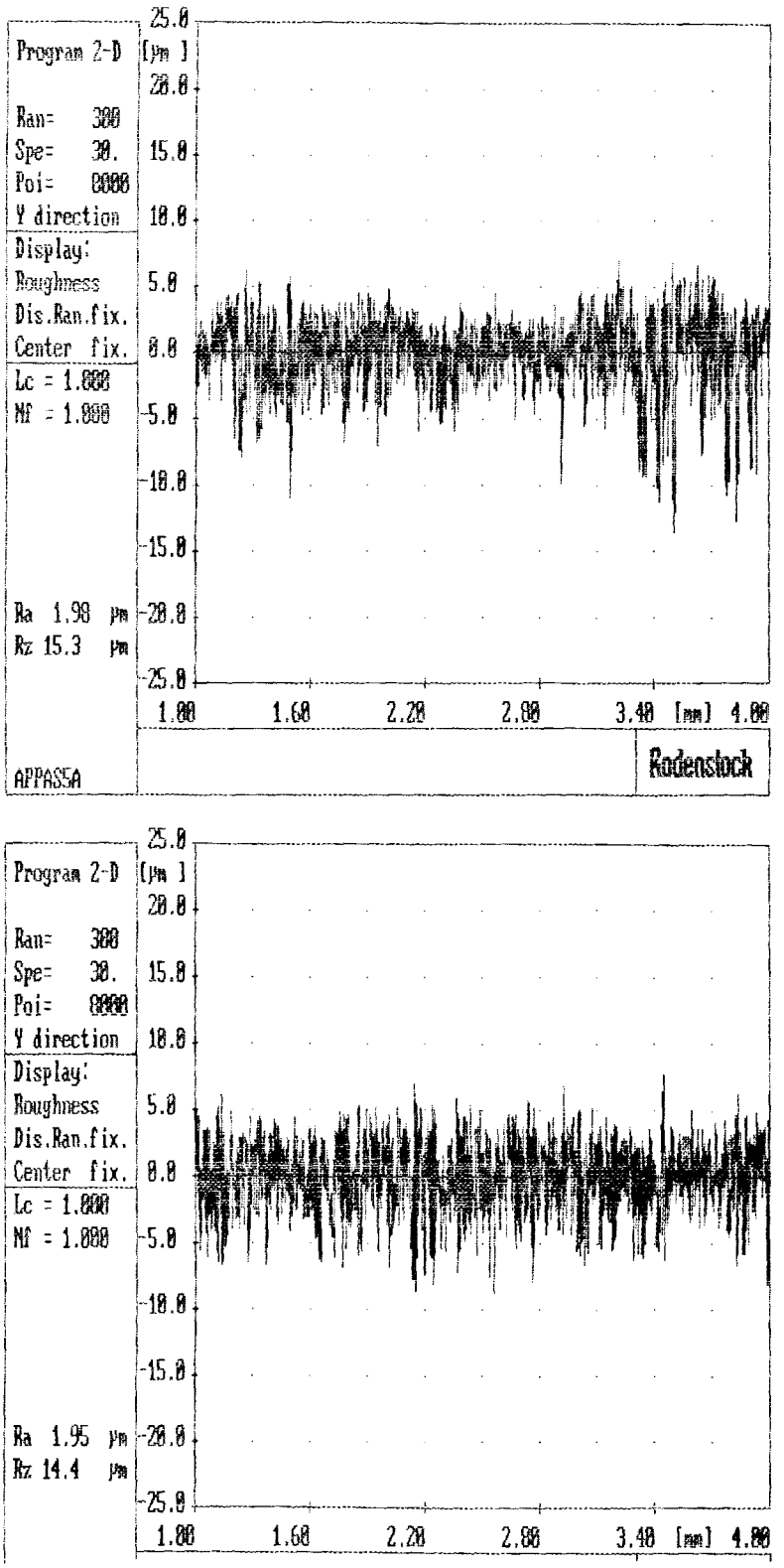

Figure 21. Roughness profiles shown are representative of those recorded for as-machined(top) and annealed (bottom) MOR bars. Asymmetry of the as-machined roughness profile was visually apparent on most scans.

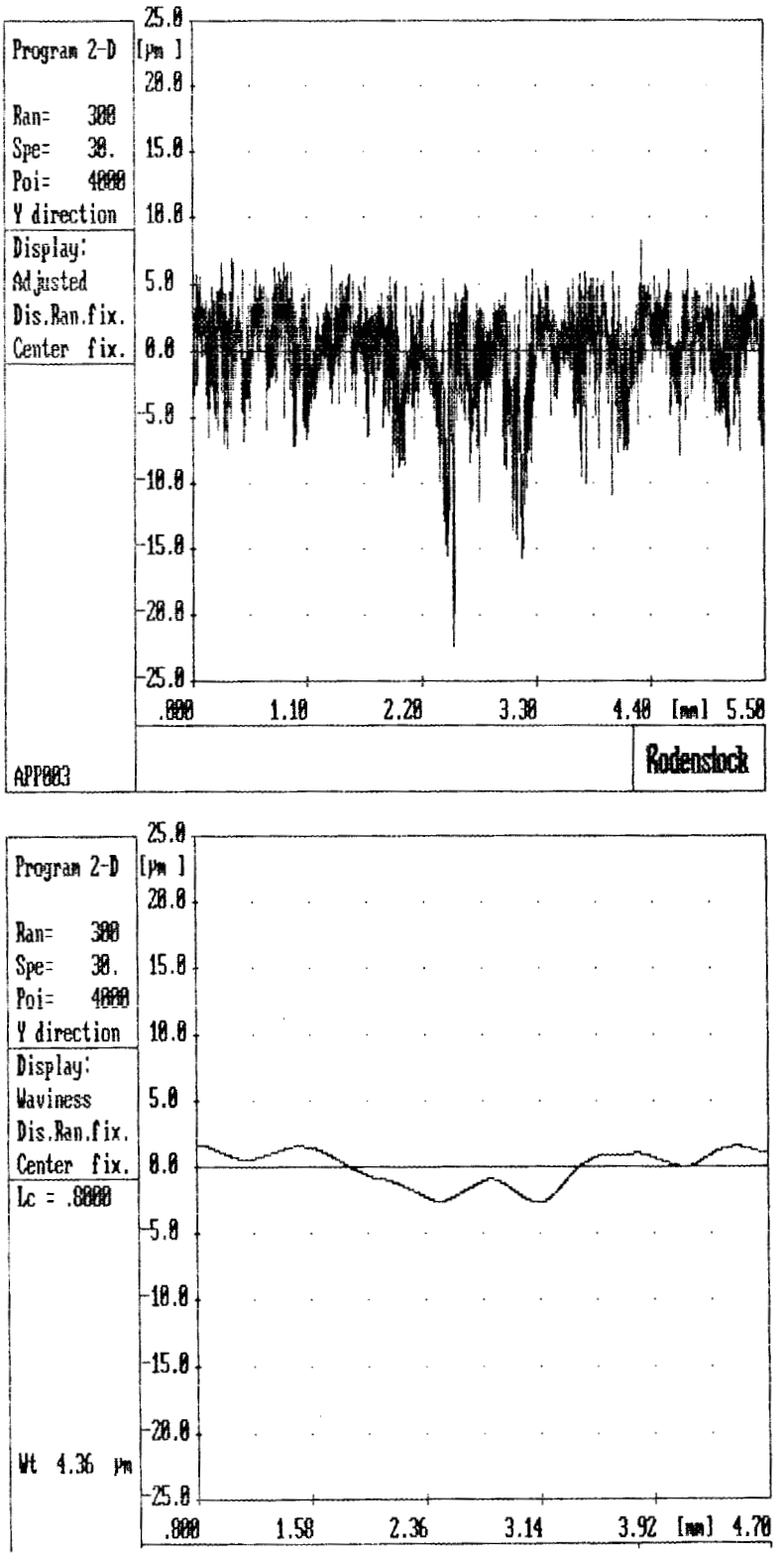

Figure 22. An as-machined MOR bar roughness profile is shown (top) which reveals clusters of deep valleys. The profile is filtered, revealing the background waviness pattern (bottom).

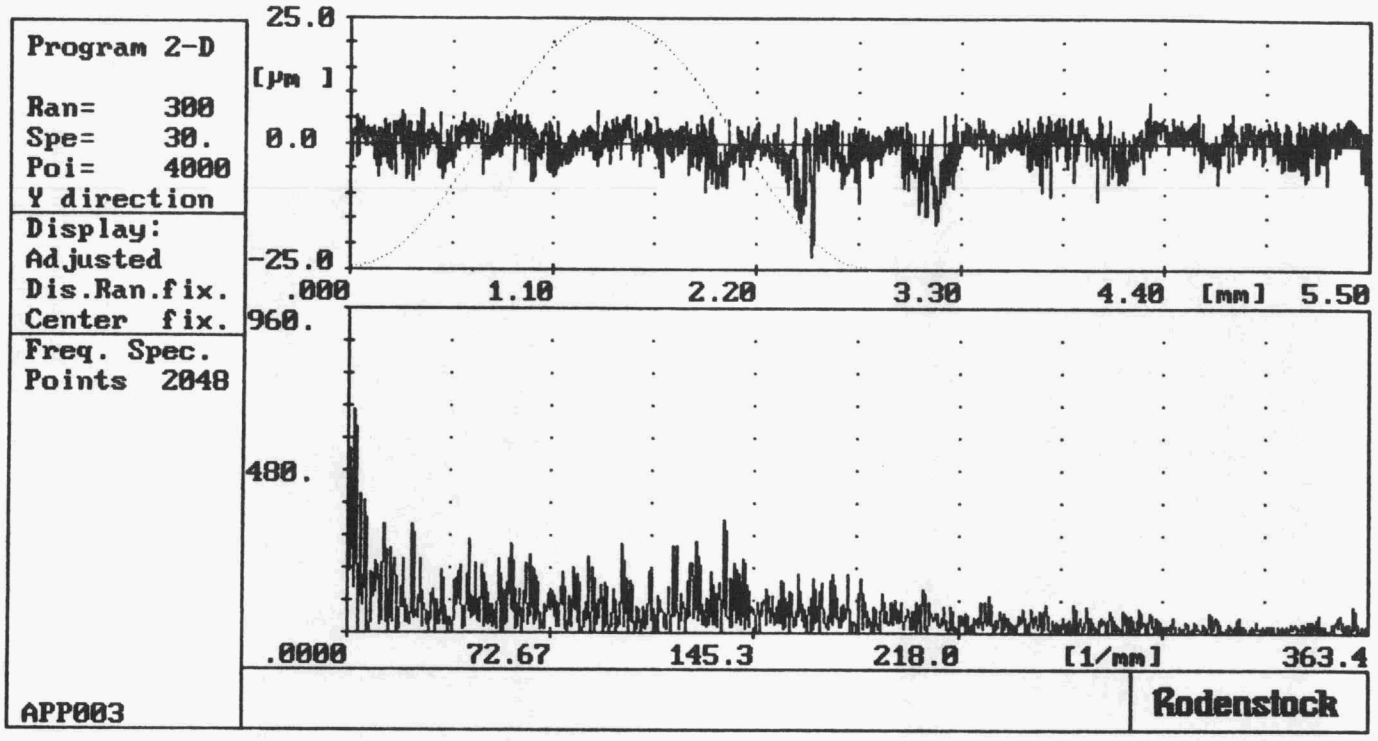

Figure 23. The Fourier spectrum of a portion of the roughness scan is shown which reveals how the magnitude of the roughness (magnitude squarted is actually displayed) is distributed as a function of frequency.

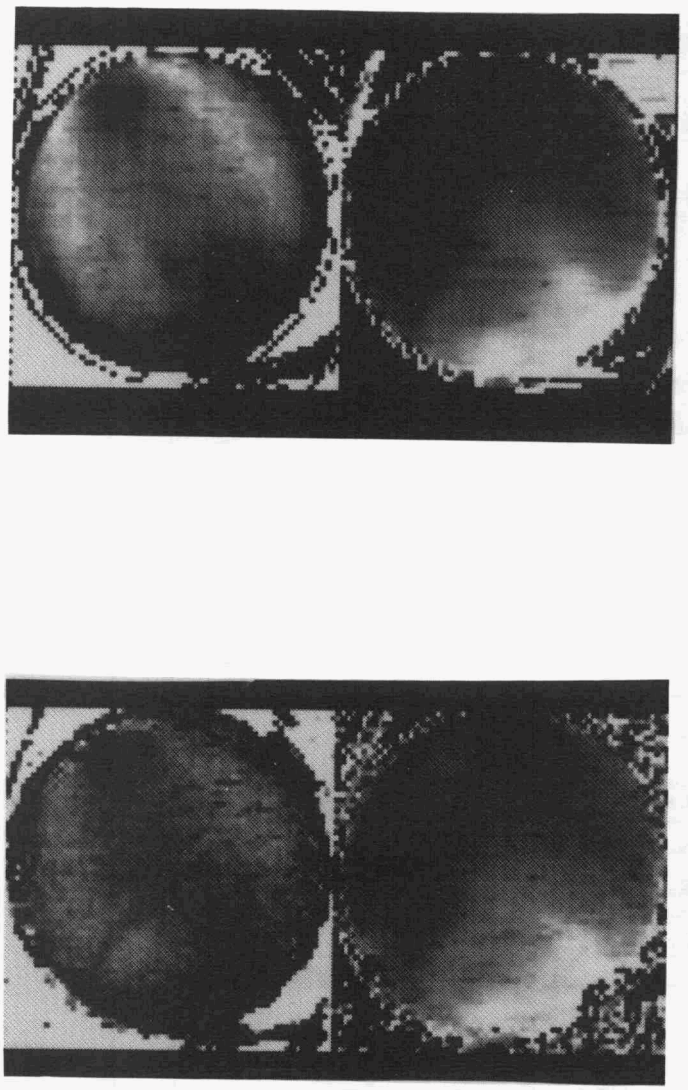

Figure 24. Ultrasonic images of as-molded disks of silicon nitride, taken at two frequencies (5MHz, top; 10 MHz, bottom). Left-hand image is an amplitude plot, right-side image is transit time plot. Inhomogeneities imaged indicate that non-uniform compaction occurred during the injection molding process.

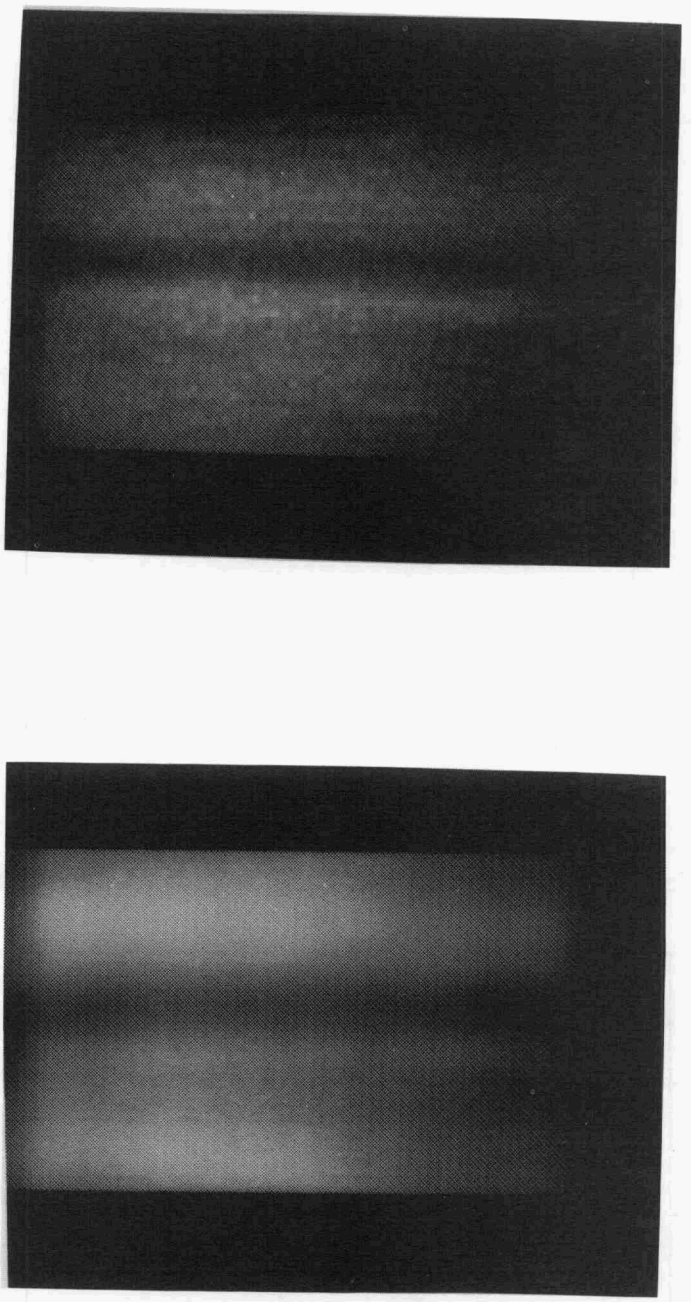

Figure 25. Transmitted amplitude images of green cylindrical tensile specimens, taken at 4 MHz single frequency (top) and with broadband frequency(bottom) ultrasonic scanning. The images were taken as the specimen was rotated. The dark shaded linear indication is an image of the parting line along the as-molded specimen.

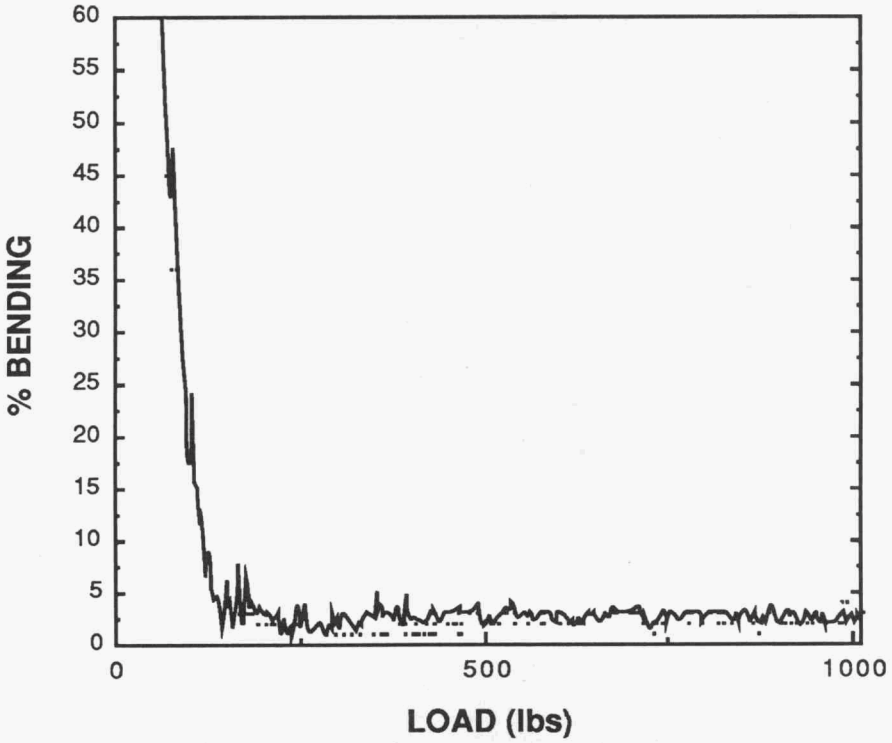

Figure 26: Tensile test strain data, showing < 5% bending moment at high loads.

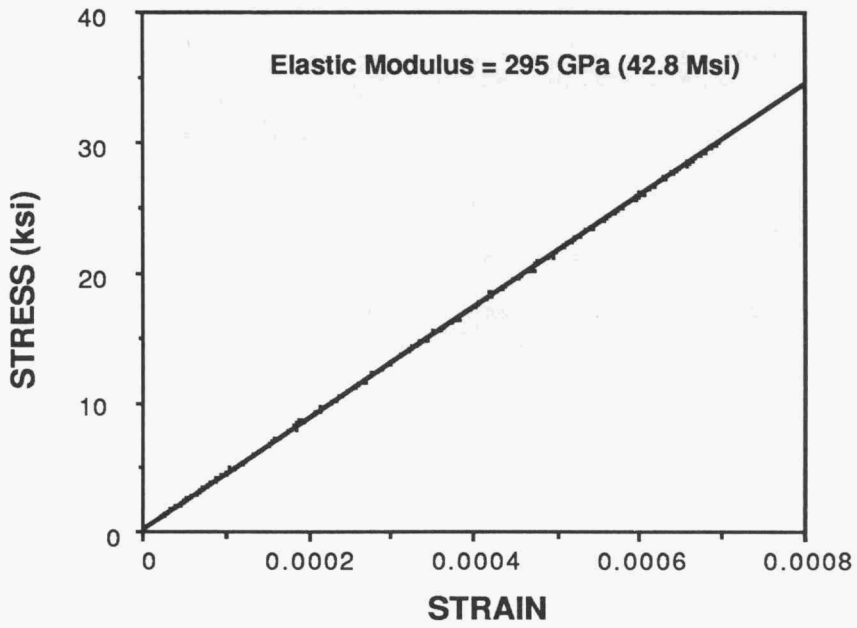

Figure 27. Strain gauge data taken on a PY6 tensile rod yields a Young's Modulus of 295 GPa.

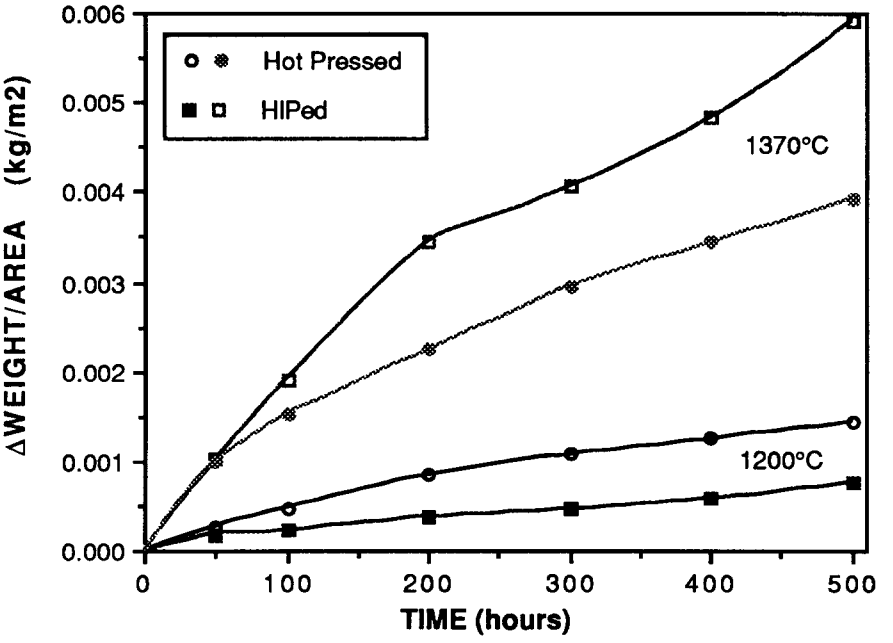

Figure 28. Oxidation behavior of injection molded/HIPed baseline material.

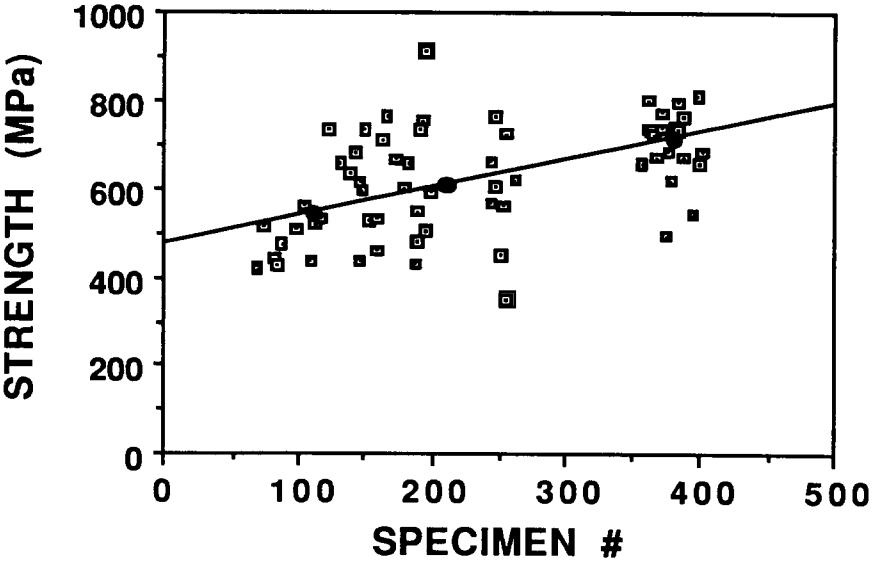

Figure 29. Baseline PY6 tensile strength data show an apparent increase as experience has been gained working with the material.

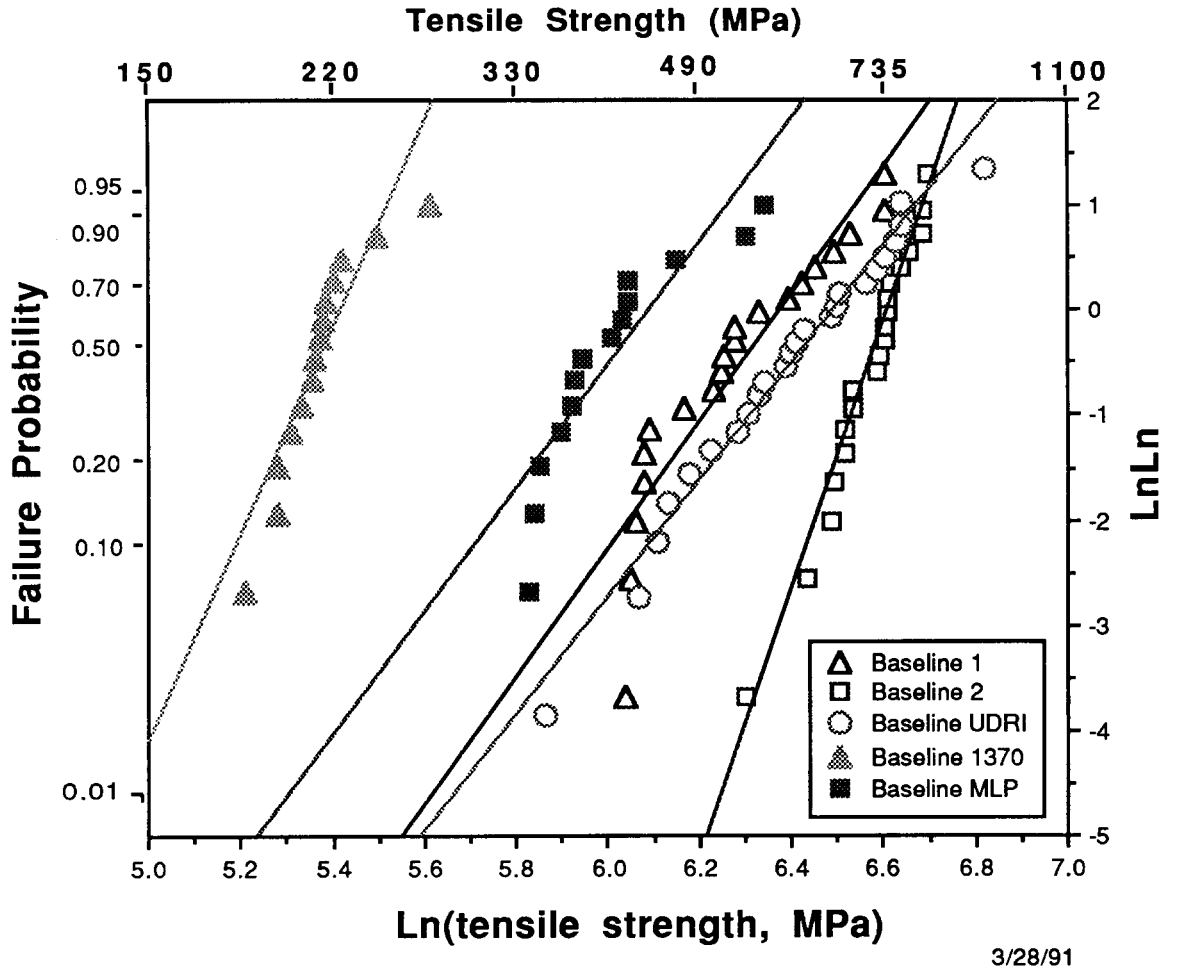

Figure 30. Weibull plot of tensile strength data for baseline HIPed PY6, as measured at GTEL and UDRI in fast fracture at ambient temperature, for near-net-shape(NNS) fabricated specimens(open symbols) and for large cross-section fabricated materials (MLP) as filled squares. Tensile strength at 1370°C was measured at UDRI for NNS specimens, and the results are shown as filled triangles.

Processing Science for Si_3N_4 Ceramics

F. F. Lange, D. S. Pearson (University of California, Santa Barbara)

Objective/scope

We are trying to increase the understanding of the role of interparticle forces in the processing of ceramics. The effects of electrolyte addition and pH changes on the rheological properties of dispersions, the kinetics of pressure filtration, and the mechanical properties and microstructure of the resulting bodies will be compared to each other and to existing models of interparticle forces (*i.e.* DLVO theory).

Technical progress

We are formulating a new processing paradigm. The current paradigm is based on producing slurries with long-range repulsive forces. We propose that strong, short-range repulsive forces produce better slurries and green bodies. Unlike long-range repulsive forces which permit particle segregation, short-range repulsive forces prevent particle segregation by permitting particles to weakly agglomerate without surface/surface contact. We are examining two silicon nitride systems with short-range repulsive forces: one aqueous and the other non-aqueous.

This short-range repulsive force can be tailored to create a shear-thinning slurry where particles can be separated and mixed at high shear rates and the mixing frozen in place when no shear is applied. The green bodies formed from these weakly agglomerated slurries are plastic when saturated and dry without cracking.

Aqueous systems

Alumina slurries have shown improved processing when salt is added[1] and we have attempted to determine if this effect occurs in silicon nitride. In alumina, the viscosity of the slurry is increased by the addition of salt while the green body remains plastic with little effect on the green-density.

Salt addition increases the viscosity of silicon nitride slurries but never as high as that of a flocced slurry (one formed by uncharged powders). We consolidated powders of the three types: dispersed (pH2), 'coagulated' (pH2, 0.5M NH_4Cl), and flocced (pH6.5) by pressure filtration or centrifugation. The resulting

densities are shown in Figure 1. Note that the dispersed and 'coagulated' slurry were pressure independent while the flocced slurry was pressure dependent. Unfortunately the density of the 'coagulated' slurry was much lower than that of the dispersed. The coagulated slurry did flow plastically, but only after a very large yield-stress had been exceded.

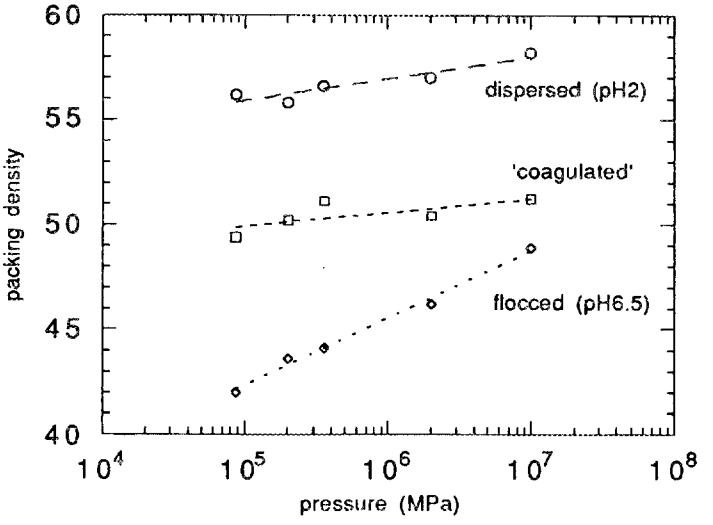

Figure 1. Packing density increases less with increasing pressure for dispersed and 'coagulated' slurries than for flocced slurries.

Nonaqueous systems

Using a process developed by Iler[2] for making organophilic silica, two silicon nitride powders have been reacted (UBE E10 and UBE E3) with octadecyl alcohol. The reaction was carried out at 200C for 2h under a nitrogen atmosphere. This alkylated-E10 powder was washed with toluene to remove unreacted alcohol. The resulting powder was analyzed by TGA (1% weight loss = 0.5nm^2/molecule) and IR spectroscopy (absorption bands at 2850 and 2920 cm^{-1}, indicative of hydrocarbons). Water did not wet this powder.

As a control, UBE E10 powder was mixed with octadecyl alcohol at room temperature and then with toluene. The silicon nitride in this mixture appeared dispersed. It was then washed and examined as described above. It lost <0.1% in the TGA and did not

display the IR bands. Water did wet this powder. After washing this exposed-E10 flocced rapidly in toluene.

UBE E3 was used to make a larger batch of alkylated silicon nitride. The same time and temperature were used but a larger batch size (50g). This material was analyzed by TGA (0.3% weight loss, 0.43nm^2/molecule).

Several other chain-lengths were reacted. Slurries of thes powders were formed by mixing powder and solvent in a mortar and pestle. The rheology of these slurries was examined using cone and plate geometry (40mm diameter, 0.04 radians) in a constant stress rheometer. Both slurries were shear-thinning (Figure 2) but the S-8 did not exhibit a measurable yield stress, while the S-2 did.

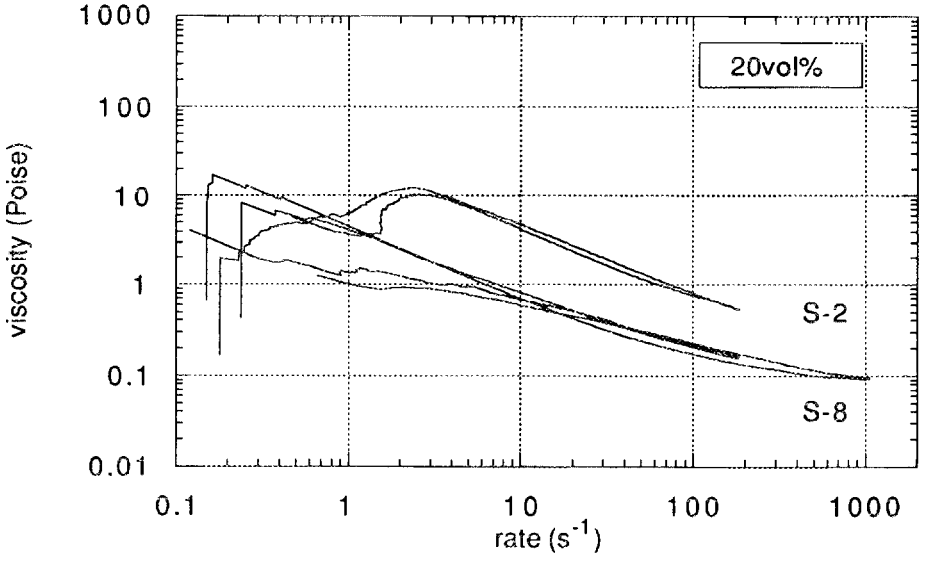

Figure 2. Shear thinning behavior for samples with different short-range repulsive forces.

Contrary to expectations, a higher viscosity does not produce a lower density, Table 1 shows the densities of pellets formed by colloidal-pressing pellets from slurries with different surface reactants. The best density of the alkylated powders is better than the best aqueous-dispersed density and higher than the 'coagulated' aqueous slurries.

Table 1. Density Results

SAMPLE	density (volume %)*	coverage (weight %)+
S-2	60	0.21
S-2x	55	0.07
S-8	56	0.20
S-8b	57	0.20

* measured by weight (wt) loss on drying compact:
V(powder) = dry wt/density powder
V(solvent) = (wet wt - dry wt)/density solvent
density = V(powder)/(V(powder) + V(solvent))

\+ measured by TGA:
coverage = (wt (200C) - wt (500C))/wt(200C)

Status of milestones

114401	Survey rheological characteristics of slurries produced under a variety of pH/electrolyte conditions. Develop methodologies for characterization of slurry rheological properties and green body mechanical properties.	1 Oct 90
114402	Status report on testing procedures and preliminary results.	1 Nov 90
114403	Determine effect of pH/electrolyte conditions on green body properties including processing rates, mechanical properties, and density.	1 Oct 91
114404	Status report on green body properties and processing relationships.	1 Nov 91
114405	Explore other means to modify interparticle interactions (polymers such as PVA).	1 Apr 92
114406	Status report on polymer effects.	1 May 92
114407	Examine flaw populations in sintered bodies.	1 Oct 92
114408	Final report on colloidal processing.	1 Nov 92

Publications

None.

References

(1) B.V. Velamakanni, J.C. Chang, F.F. Lange, D.S. Pearson, "New Method for Efficient Colloidal Particle Packing via Modulation of Repulsive Lubricating Hydration Forces", Langmuir **6**, p.1323 (1990).

(2) R.K. Iler, US Patent 2,657,149 (1953) referenced p.573
R.K. Iler, The Chemistry of Silica, Wiley-Interscience, New York, (1979)

1.2 CERAMIC COMPOSITES

1.2.2 Silicon Nitride Matrix

SiC-Whisker-Toughened Silicon Nitride

H. Yeh, E. Solidum (Garrett Ceramic Components),
K. Karasek, G. Stranford and D. Yuhas (Allied-Signal Research Technology),
S. Bradley (UOP Research Center), and
J. Schienle (Garrett Auxiliary Power Division)

Objective/scope

The objective of this program (Phase II) is to maximize the toughness in a high strength, high temperature SiC whisker/Si_3N_4 matrix material system that can be formed to shape by slip casting and densified by a method amenable to complex shape mass production. The ASEA glass encapsulation hot isostatic pressing (HIP) technique shall be used for densification throughout the program.

The program is divided into seven technical tasks with multiple iterations of process development and evaluation. Parametric studies shall be conducted to optimize processing steps developed in the Phase I effort, guided by established analytical and NDE techniques. The seven technical tasks are: Task 1 - Selection of SiC whiskers, Task 2 -Baseline Casting Process, Task 3 - Parametric Densification Study, Task 4 - Effect of Specimen Size and Shape, Task 5 - On-Going Evaluation of Alternate Whisker, Task 6 - Nanometer Deposition of Sintering Aids, and Task 7 - In Process Characterization and Process Control During Drying of Cast Ceramic Parts.

The technical effort was initiated in June 1988. Task 1 was completed in January 1989. Based on the results, HF-etched American Matrix Inc. SiC whisker was selected for use for Tasks 2-4. Task 2 was initiated in February 1989 and was completed in June 1989. Task 3 effort was initiated in July 1989, and was completed in December 1990-January 1991 Bi-monthly reporting period. Based on contract modification No. 14, dated 12/12/90, the last part of Task 3 (Subtask 3.C) and the entire Task 4 efforts were deleted.

Research sponsored by the U.S. Department of Energy, Assistant Secretary for Conservation and Renewable Energy, Office of Transportation Technologies, as part of the Ceramic Technology for Advanced Heat Engines Project of the Advanced Materials Development Program under contract DE-AC05-84OR2140 with martin Marietta Energy Systems, Inc., Work Breakdown Structure Subelement 1.2.2.1.

Tasks 5, 6 and 7 tasks were added onto this contract and work began in August 1989 to supplement the mainline activities. Task 5 was completed in the August-September 1990 reporting period; Task 7 was completed in the October-November 1990 reporting period; and Task 6 was completed in this reporting period. This completes all the technical efforts for this program (Phase II).

Technical progress

TASK 1 - Selection of Whisker

All technical efforts had been completed and the results were reported in Semi-Annual Report October 1988 - March 1989.

In summary, Tateho, as received American Matrix, HF-etched American Matrix, and Advanced Composite Material Corporation (ACMC, formerly ARCO) were evaluated by fabricating 20 wt% SiCw/GN-10 Si_3N_4 composites with the baseline process established under Phase I. Based on the mechanical properties and availability, HF-etched American Matrix SiCw was selected for use under Tasks 2 and 3.

TASK 2- Baseline Casting Process

All technical efforts had been completed and the results were summarized in the April-September 1989 Semi-Annual Report.

In summary, four iterations were conducted to optimize the green forming process for composites containing 10, 20, 30 and 40 wt% SiC whiskers, respectively. In these, the Si_3N_4 powder, prior to blending with SiC whiskers, contained the standard GN-10 sintering aids concentration. The optimized process, was used to fabricate another set of four composites (10, 20, 30 and 40 wt% SiC whiskers), in which the sintering aids concentrations in the Si_3N_4 powder were increased with SiC whisker loading to maintain a constant ratio between sintering aids and the sum of Si_3N_4 and SiC whisker. These series of composites are referred as 10%SiCw/GN-10A, 20%SiCw/GN-10A, 30%SiCw/GN-10A, and 40%SiCw/GN-10A. The purpose of these was to determine the effect of sintering aids concentration on the structure/properties of densified composites. The green composites, a total of eight varieties, plus a monolithic GN-10 were to be densified under Task 3.A -statistical matrix to determine the effect of HIP parameters.

TASK 3 - Parametric Densification Study

Two subtasks (A and B) were to be conducted to evaluate the effects of key densification parameters on microstructures/properties of Si_3N_4/SiCw composites. Samples containing 10 to 40 wt% whiskers and two levels of sintering aids fabricated under Task 2 were densified by a HIP matrix (six runs), resulting in forty-eight (48)

different composites. A baseline monolithic GN-10 green sample was also included in each HIP run as a reference. Based on the results, the more promising composites (20 and 30 wt% SiCw) were selected and refabricated at the selected optimun HIP cycle (T_2°C/$t_2$hr) for a more detailed mechanical property characterization.

Table I summarizes the strength results. No improvement over GN-10 monolith in strength was observed by SiCw reinforcement, in either GN-10 or GN-10A series. Rather, the strength decreased as the whisker content increased. The sintering aids adjustment (GN-10A) was beneficial for both room and 1375°C strengths but not significantly. Fractography results indicated that GN-10A composites exhibited more inclusion failure origins. All composites exhibited slow crack growth in 1375°C tests.

TABLE I

Four-Point Flexural Strength
(MPa/ksi)

Material	RT		1375°C	
	Avg	Std	Avg	Std
GN-10	890/129	124/18	514/74.6	22/3.2
GN-10 + 20 wt% SiCw	708/102	83/12	381/55.3	20/2.9
GN-10 + 30 wt% SiCw	626/91	49/7	362/52.5	34/4.9
GN-10A + 20 wt% SiCw	756/110	77/11	393/57.0	26/3.7
GN-10A + 30 wt% SiCw	648/94	110/16	419/60.8	57/8.3

Note: 1. Ten bars per material were tested at room temperature, five at 1375°C.
2. GN-10 denotes matrix without adjustment in the starting powder, GN-10A denotes matrix with adjustment in the starting powder.
3. Test bar size: 3mm x 4mm x 50mm.

The Chevron notch toughness measurements for the same series of materials at room temperature and 1200°C were also conducted. These tests were conducted at NASA-Lewis Research Center by Jon Salem. Table II summarizes the results. The 1200°C toughness was lower than the room temperature toughness for all materials. Overall the composites did exhibit higher toughnesses than the GN-10 monolith, at both temperatures, with those of GN-10 + 30 wt% SiCw being the highest, 6.4 MPa·$m^{1/2}$ at room temperature, 5 MPa·$m^{1/2}$ at 1200°C. However, the improvement over the monolith GN-10 is only 12.8% at room temperature and 8.6% at 1200°C.

This completed all technical efforts for Task 3. In summary, the results indicated that SiC whisker reinforcement is not an

effective approach to improving the mechanical properties of GN-10 Si_3N_4.

TABLE II

Chevron Notch Toughness

($MPa \cdot m^{1/2}$)

Material	RT		1200°C	
	Avg	Std	Avg	Std
GN-10	5.67	0.13	5.48	0.11
GN-10 + 20 wt% SiCw	5.99	0.45	5.74	0.23
GN-10 + 30 wt% SiCw	6.40	0.40	5.95	0.42
GN-10A + 20 wt% SiCw	6.11	0.20	5.48	0.18
GN-10A + 30 wt% SiCw	6.02	0.46	5.42	0.30

Note: 1. Six bars of each material were tested at room temperature, five at 1200°C.
2. GN-10 denotes matrix without adjustment in the starting powder, GN-10A denotes matrix with adjustment in the starting powder.
3. Test bar size: 3mm x 6mm x 50mm.

TASK 4 - Effect of Size and Shape

Deleted.

TASK 5 - On-Going Evaluation of Alternate Whiskers

This task was completed in August-September 1990 bi-monthly reporting period.

In summary, the whiskers examined were obtained from Kobe Steel (AT received 3/89) and A'T received 4/89), Tokai Carbon (TWS-400 received 2/89 and TWS-100 received 5/89), Advanced Ceramic Technologies of Somerset, NJ (Grade L7V5 received 11/11/89), and Keramont Corporation of Tucson, AZ (grade 91#49-51 received 9/89). Although two of the whisker versions were more attractive than the others (Tokai TWS-400 and Kobe Steel A'T), there is no reason to expect these whiskers to offer significantly better properties than the American Matrix whiskers (selected under Task 1) when incorporated into a silicon nitride matrix.

Task 6 - Nanometer Deposition of Sintering Aids

The objective of this task was to evaluate the the potential benefits of nanometer deposition of sintering aids for preparing GN-10 Si_3N_4. This effort was conducted in three stages.

In stage 1, a screening study was conducted to investigate eight different nanometer deposition methods using small batch size (300g) materials. Based on the uniformity of sintering aids distribution achieved in the green state and the sinterability of the green samples, two methods (spray drying and polymer precipitation) were selected for stage 2 evalution. Stage 1 results were summarized in the last Semi-Annual report.

In stage 2, intermediate batch size (600g) materials were prepared using spray drying, polymer precipitation, and conventional method (wett ball milling), and were slip-cast into plates (2"x3"x1/2"). These green plates were then densified by glass encapsulation HIP and machined into test bars for strength comparisons. The effects of sintering aids level and HIP cycle were included in the study.

Table III lists the flexural strengths of the stage 2 materials at 23, 1100, and 1370^{o}C. Due to the limited strength data (5 tests per room temperatue and 3 per elevated temperature condition) and the large number of variables involved, no clear trend was observed as to which sintering aids deposition method is better. However, within each deposition method, materials densified at $T_2{}^{o}C/t_2$hr and containing higher level of sintering aids have higher strengths. Since the polmer precipitation prepared green cast plates were more fragile and had a high tendency to cracking, reported in the last semi-annual report, only spray drying method was retained for comparison with the conventionally prepared material in stage 3 study.

X-ray diffraction phase analysis was conducted on some of the materials listed in Table III, which included spray dried samples with 10 and 6 wt% sintering aids and the conventionally ball milled sample with 6 wt% sintering aids that were glass encapsulation HIP'ed at $T_2{}^{o}C/t_2$h. The spray dried sample with 10 wt% sintering aids that was densified at $T_4{}^{o}C/t_2$h was also analyzed. Only beta-Si_3N_4 was detected in the two samples containing 10% sintering aids. However, the spray dried and conventionally prepared samples with 6 wt% sintering aids densified at $T_2{}^{o}C/t_2$h contained around 7% and 14% alpha-Si_3N_4, respectively, the balance being beta-Si_3N_4. The presence of alpha phase in these samples is probably a result of the lower liquid phase content. The higher degree of alpha to beta phase conversion in the spray dried than in the conventional samples would suggest a better sintering aids distribution in the spray dried material.

Table III
Four Point Flexure Strengths of Si_3N_4.

% Sintering Aids/ Deposition Route	HIP Conditions	Average Strength MPa/ksi Test Temperature 23°C	1100°C	1370°C
10%/Spray Dried	T_2^oC/t_1h	814.3/118.1	428.2/62.1	350.3/50.8
8%/Spray Dried	T_2^oC/t_1h	577.1/ 83.7	321.3/46.6	184.4/26.8
6%/Spray Dried	T_2^oC/t_1h	749.5/108.7	315.1/45.7	
10%/Polym. Precip.	T_2^oC/t_1h	499.2/ 72.4		
8%/Polym. Precip.	T_2^oC/t_1h	787.4/114.2		
6%/Polym. precip.	T_2^oC/t_1h	748.1/108.5		
10%/Conventional	T_2^oC/t_1h	706.7/102.5	459.9/66.7	302.7/43.9
10%/Spray Dried	T_2^oC/t_2h	841.9/122.1	516.4/74.9	273.0/39.6
6%/Spray Dried	T_2^oC/t_2h	851.5/123.5	563.3/81.7	314.4/45.6
8%/Polym. Precip.	T_2^oC/t_2h	817.7/118.6	430.9/62.5	363.4/52.7
6%/Polym. Precip.	T_2^oC/t_2h	793.6/115.1	312.3/45.3	
6%/Conventional	T_2^oC/t_2h	876.4/127.1	559.9/81.2	382.0/55.4
8%/Conventional	T_3^oC/t_2h	737.8/107.0	578.5/83.9	376.5/54.6
6%/Conventional	T_3^oC/t_2h	679.8/ 98.6	469.5/68.1	467.5/67.8
10%/Spray Dried	T_4^oC/t_2h	589.5/ 85.5	173.1/25.1	
8%/Spray Dried	T_4^oC/t_2h	646.8/ 93.8	153.1/22.2	
8%/Conventional	T_4^oC/t_2h	659.9/ 95.7	437.8/63.5	208.9/30.3
6%/Conventional	T_4^oC/t_2h	728.1/105.6	460.6/66.8	231.7/33.6

In stage 3, the batch size was increased to 3000g. This was to allow the evaluation of scale-up potential, and provide sufficient materials for an in-depth characterization. Three batches of materials were prepared with 10% sintering aids using conventional milling method, small bench-top spray drier, and large pilot size spray drier. The small spray drier was the one used for stages 1 and 2, but the material fed into the drier was blended as a single 3000g batch rather than the smaller batches previously. The reason for using two different driers was to determine the effect of spray drier on the properties of spray dried powders and the subsequent material property/structure. All three materials were cast into large size plates (5"x5"x3/4"), glass encapsulation HIP'ed, and machined into test bars for various characterizations. Based on stage 2 results, T_2^oC/t_2hr was selected as the HIP densification cycle.

The four-point flexural strengths and Chevron notch toughnesses of the three stage 3 materials are listed in Tables IV and V,

respectively. The results show that the experimental material with sintering aids deposited by a small spray drier (SMSD) exhibited higher room temperature and 1200°C (2200°F) strength and toughness than the other two materials. Stress rupture tests were also conducted under four-point flexural condition at 1200°C, and the results are plotted in Figure 1. The data show that at 1200°C the conventional material is the best, the SMSD the second, and the LRGSD the worst.

X-ray diffraction phase analysis of the three materials shows that SMSD sample has the highest degree of alpha-Si_3N_4 to beta-Si_3N_4 conversion during densification, while LRGSD the lowest. SMSD sample contains 90% beta-Si_3N_4, conventional 70%, and LRGSD 50%. The more complete phase conversion in SMSD could be one of the reasons for the better mechanical properties.

TABLE IV

Average Four-Point Flexural Strengths
(MPa/ksi)

Deposition Method	R^{T1}	1200°C[2] (2200°F)	1370°C[2] (2500°F)
Conventional	821.2/119.1	618.5/89.7	450.2/65.3
SMSD	909.5/131.9	660.5/95.8	408.9/59.3
LGRSD	792.2/114.9	408.9/59.3	275.1/39.9

SMSD = Small spray drier prepared; SRGSD = Large spray drier prepared

1. Average of ten tests
2. Average of three tests

TABLE V

Average Chevron Notch Toughness [1]
($MPa.m^{1/2}$)

Deposition Method	RT	1200°C (2200°F)
Conventional	4.80 +/- 0.18	4.02 +/-0.04
SMSD	5.94 +/- 0.19	5.06 +/-0.04
LGRSD	4.24 +/- 0.05	3.94 +/-0.58

(SMSD = Small spray drier prepared; LRGSD = Large spray drier prepared

1. Average of three tests.

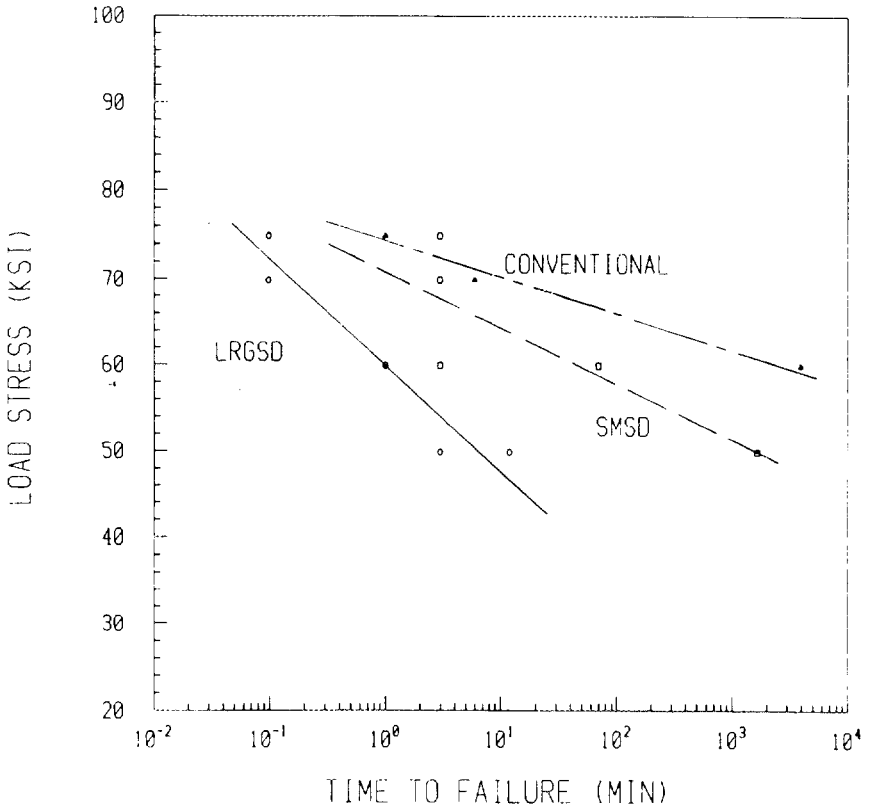

Figure 1. 1200°C Four-Point Flexural Stress Rupture Test Results. Conventional=prepared by ball milling; SMSD=prepared by a

small spray drier; LRGSD=prepared by a large spray drier.

To compare the distribution of sintering aids in the three materials, scanning electron microscopy (SEM) was conducted on the polished sections cut from the test bars. Back scattered images (Figure 2) show that the sintering aids are much more uniformly distributed in the two spray dried materials than the conventional. This is in agreement with the results of the green samples prior to densification. However, there is no detectible difference between the two spray dried materials in sintering aids distribution.

Scanning transmission electron microscopy (STEM) was conducted to examine the microstructure of the materials. There are several apparent differences in microstructure between the SMSD and conventional materials. First, for the conventional material there are two different crystalline grain-boundary-pocket phases and a small number of non-crystalline grain-boundary pockets. Grain-boundaries were non-crystalline. The two crystalline grain-boundary-pocket phases are the H-like or apatite-type and the N-melilite-like phases. The SMSD sample only exhibited a single crystalline grain-boundary-pocket phase. This phase has a structure similar to that of the H-like phase. No non-crystalline grain-boundary pockets could be found. Grain boundaries are noncrystalline, however. In addition, the results of a detailed grain-boundary and grain-boundary-pocket phase composition analysis suggest that the distribution of sintering aids in SMSD sample is more uniform. As for LRGSD sample, the major difference between this sample and the other two is the presence of a large number of Fe-based (possibly silicide) submicron particles. This Fe is the likely cause of the low beta-Si_3N_4 content and poor mechanical properties.

Task 7 - In Process Characterization/Control During Drying of Cast Ceramic Parts

This task was completed and the results were presented in October-November 1990 Bi-Monthly Report. In summary, experimental results showed that attenuation monitored from the freshly cast ceramic parts did not correlate with the moisture contents of the parts, and sonic velocity as a function of moisture content was double-valued. The couplant non-uniformity was identified as one of the major reasons for the experimental difficulties. The methodology for modeling drying was established using ANSYN code. However, it was found that this code is not cost effective to perform the intended modeling.

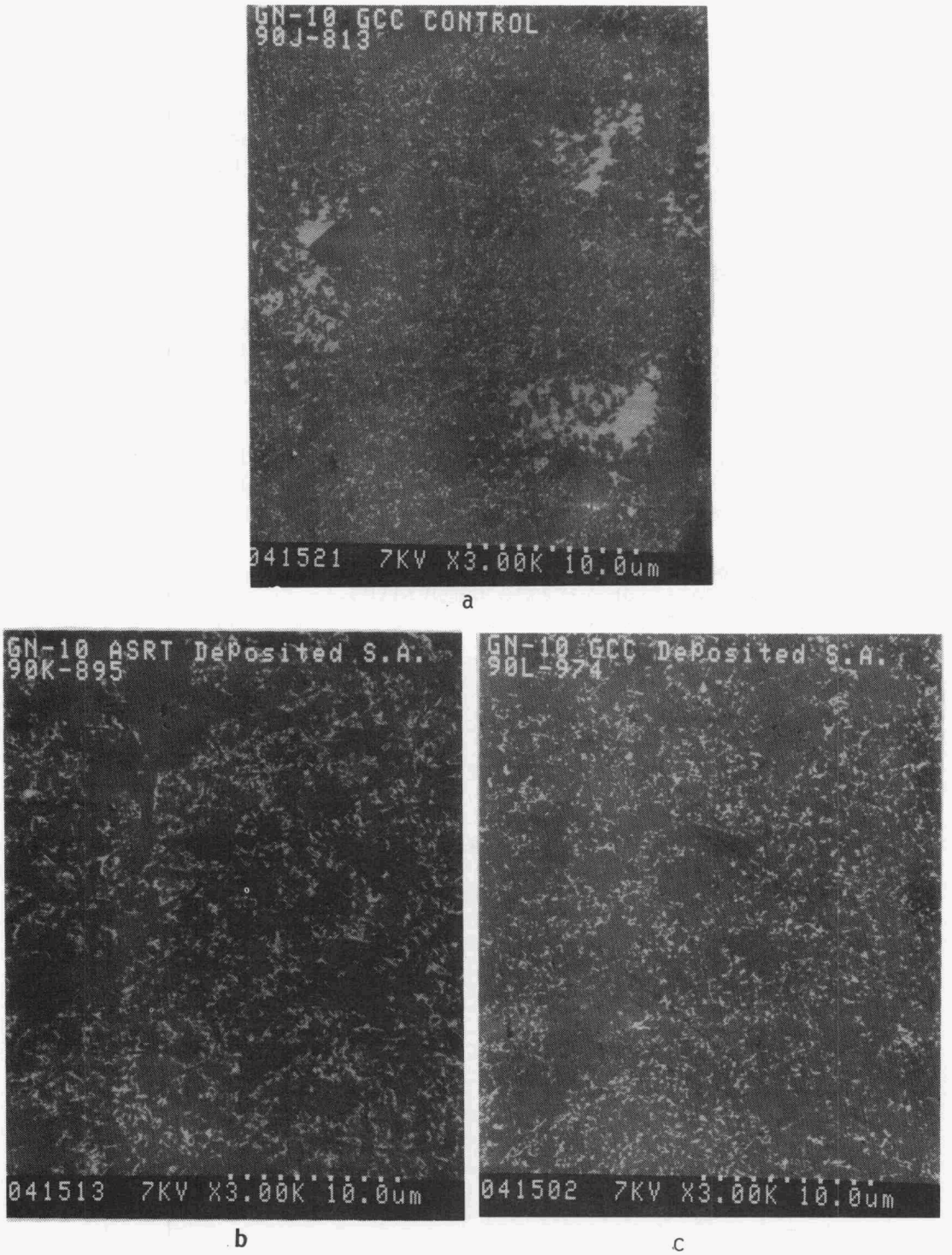

Figure 2. SEM back scattered images of polished sections of samples prepared by conventional ball milling (a), a small spray drier (b), and a large spray drier (c).

Status of milestones

Milestone 122116 (Task 6) "complete the in-depth characterization of the optimized Si_3N_4 material prepared using a nanometer deposition method" was completed during this reporting period. This completes all technical milestones. Milestone 122112 "Final Report" is to be submitted (draft version) May End 1991.

Publications

H. Yeh, E. Solidum, J. Schienle, K. Karasek, and J. Salem, "Processing and Mechanical Behavior of Whisker-Toughness Silicon Nitride", presented at the 28th ATD/CCM, Oct. 24, 1990, Dearborn, MI.

K. R. Karasek, S. A. Bradley, J. T. Donner, J. L. Schienle, H. C. Yeh, "SiC Whisker Characterization: An Update," Bulletin of the American Ceramic Society, Vol. 70, No. 2, February 1991.

K. R. Karasek, S. A. Bradley, and H. C. Yeh, "Whisker and Fiber Reinforcements for Ceramic Composites," Proceedings of the 37th agamore Army Materials Research Conference, Plymouth, MA, October 2, 1990.

In-Situ Toughened Silicon Nitride

H. Yeh, J. Pollinger (Garrett Ceramic Components)
J. Yamanis (Allied-Signal Research and Technology)

Objective/scope

The objective of this program is to improve the properties of a newly developed in-situ reinforced high temperature Si_3N_4 material (AS700), and to develop net-shape component fabrication processes. This effort is targeted for heat engine applications, and the goals for the key properties are listed below:

Flexural Strength at 1370°C	490 MPa
Stress Rupture 490 MPa @1200°C	>100 hr
Fracture Toughness	> 10 $MPa \cdot m^{1/2}$
Weibull Modulus	> 18

This effort consists of five (5) technical tasks: Task 1 - Slip Casting Development; Task 2 - Improvements of Densification and Grain Growth Processes; Task 3 - Alternate Raw Materials; Task 4 - Fabrication of Test Specimens and Task 5 - Material Characterization.

The technical efforts were initiated January 2, 1991; Tasks 1, 2, and 3 were conducted in this reporting period.

Technical progress

TASK 1 - SLIP CASTING DEVELOPMENT

The objective of this task is to develop a process to pressure slip cast the baseline AS700 Si_3N_4 material in thin cross-section test plates and thick parts with varying cross-sections. Material shall be densified and heat-treated using established baseline procedures. Mechanical properties and microstructures will be characterized and compared with current baseline cold isostatic pressed AS700.

Research sponsored by the U.S. Department of Energy, Assistant Secretary for Conservation and Renewable Energy, Office of Transportation Technologies, as part of the Ceramic Technology for Advanced Heat Engines Project of the Advanced Materials Development Program under contract DE-AC05-840R2140 with Martin Marietta Energy Systems, Inc., Work Breakdown Structure Subelement 1.2.2.1.

1.1 Slip Development

The goal of this subtask is to develop an AS700 Si_3N_4 slip with desirable properties for slip casting both thin and thick cross-section components.

Initial efforts focussed on extensive characterization of AS700 raw materials. Properties measured included as-received powder surface area and particle size. Colloidal aqueous suspension properties measured included zeta potential as a function of pH and determination of iso-electric point (zeta potential = 0 mV), and the effect of electrostatic/ steric dispersants on individual powder dispersion properties. The most suitable combination of pH and dispersant composition and concentration was selected (based on generation of same-sign large magnitude zeta potentials for each powder).

The selected pH and dispersant conditions were then utilized to prepare baseline AS700 slips for evaluation. Two solids contents were examined and small plates (2" by 3" by 0.625") were cast. Table I presents the resulting slip and cast plate properties. The baseline solids content (S_1) resulted in a slip with acceptable viscosity and no indications of agglomerates during slip screening. The higher solids content (S_2) slip exhibited a much higher viscosity and exhibited agglomerates during slip screening after milling, indicative of too high a solids content for the baseline slip preparation process. Both solids content slips were able to be cast into visibly defect-free plates with good green densities. The plates were successfully dried using the baseline drying procedure, no drying defects were generated. Solids content S_1 was chosen as the baseline for future slip development.

TABLE I

Baseline AS700 Slip and Cast Part Properties as a Function of Solids Content

	SOLIDS CONTENT	
	S_1	S_2
Viscosity (cps)	54	329
Green Density (% Theoretical)	57.9	57.6

Improvements to the baseline AS700 slip process were then explored, as shown in Table II. Two milling times were explored to evaluate the effect of:

1) Milling time on oxygen pickup by the Si_3N_4 powder (due to hydroxylation) and subsequent mechanical properties and grain boundary phases.
2) Homogeneity of the as-cast green microstructure.
3) AS700 powder particle size distribution.
4) Slip stability and rheology.

The degree of Si_3N_4 powder oxygen pickup due to milling time is currently being measured. Green microstructure homogeneity was evaluated using scanning electron microscopy (SEM) with backscatter (BSE) and energy dispersive X-ray (EDX) analysis. The baseline milling time (M_1) microstructure was very uniform with a few sintering aid agglomerates approximately 5 to 10 times their average particle size. The longer milling time (M_2) microstructure exhibited extensively reduced amounts and sizes of agglomerates, but it is felt that further improvements can be made. Evaluation of slip particle size distributions revealed no detectable effect of the different milling times. The longer milling time (M_2) resulted in reduced viscosities for all slips that have been fabricated. The effect on slip stability can only be evaluated by casting for long times and is currently being evaluated by slip casting of the large billets in Subtask 1.2, described below.

For each milling time, the optimization of slip solids content and dispersant concentration were investigated. Increasing solids content from level S_1 to level S_3 resulted in increased slip viscosity, with no change in presintered density for milling time M_1 and a slight increase for milling time M_2. Higher slip solids contents are desirable because they increase casting rates and green packing density, but powder dispersion must be maintained or coagulation/flocculation will result in higher viscosities and lower cast packing densities and agglomerated microstructures.

Three alternative dispersant concentrations to the baseline (D_1) were evaluated to further reduce slip viscosity and increase slip stability, thus allowing further increases in slip solids content, as well as potential increases in green packing density. Table III shows the results. Concentration D_2 resulted in decreased viscosities, while levels D_3 and D_4 resulted in higher viscosities. The actual dispersant concentration changes between D_1, D_2, D_3, and D_4 are very small, so that D_2 looks to be the dispersant concentration that produces a minimum in the slip viscosity.

TABLE II

AS700 Slip and Cast Part Properties as a Function of Process Development Using Milling Times M_1 and M_2.

MILLING TIME M_1

	SLIP REVISIONS		
	Baseline	Rev. 2	Rev. 3
Dispersant Conc.	D_1	D_1	D_2
Solids Content	S_1	S_3	S_3
Viscosity (cps)	54	141	126
Presinter Density (% Theoretical)	59.9	59.8	59.9

MILLING TIME M_2

	SLIP REVISIONS		
	Rev. 1	Rev. 4	Rev. 5
Dispersant Conc.	D_1	D_1	D_2
Solids Content	S_1	S_3	S_3
Viscosity (cps)	41	90	78
Presinter Density (% Theoretical)	62.3	62.6	63.1

CONDITIONS: SOLIDS CONTENT $S_2 > S_3 > S_1$
DISPERSANT CONCENTRATION $D_2 > D_1$
MILLING TIME $M_2 > M_1$

TABLE III

Evaluation of Dispersant Levels for AS700 Slip.

	DISPERSANT CONCENTRATION			
	D_1	D_2	D_3	D_4
Viscosity (cps)	141	126	143	192
Presinter Density (% Theoretical)	59.8	59.9	59.8	60.0

CONDITIONS: SOLIDS CONTENT S_3
MILLING TIME M_1
DISPERSANT CONCENTRATION $D_4>D_3>D_2>D_1$

Over the next reporting period, Subtask 1.1 work will investigate further improvements in AS700 slip including higher solids contents, lower viscosities, slip stability, green microstructure homogeneity, further casting and green density improvements, as well as continue characterization of slip process and resultant part properties.

1.2 Forming Development

The goal of this subtask is to take the AS700 slip developed in Subtask 1.1 and develop pressure slip casting process parameters for generation of uniform high green density, warpage and crack-free green parts, both thin and thick varying-cross-section. Improvements in the baseline drying cycle will also be investigated, the goal being to dry parts in the shortest cycle that yields a 100% defect-free part reproducibly.

Initially, all slipcast AS700 has been in the form of 2" by 3" or 5" by 5" plates, approximately 0.5 to 0.625" thick. No cracking has been detected during drying or presintering. The green densities that have been achieved are acceptable although further improvements are being explored by increasing slip solids contents and optimizing slip dispersion/stability under Subtask 1.1.

With the excellent properties of the current AS700 slips (revisions 3 and 5), forming development is now focussing on large cross-section billet fabrication. AS700 billets (3.25" dia. by 2" tall) are being fabricated for evaluation of the ability of the AS700 densification/heat treatment process to produce a uniform in-situ reinforced Si_3N_4 microstructure throughout such a large cross-section

part. The larger component also allows a better evaluation of slip stability since it takes much longer to cast these parts compared to relatively thin plates.

Two pressure slipcasting approaches are being evaluated: unidirectional dewatering through the billet bottom, and side and bottom dewatering. Billets have been cast using both slip revisions 3 and 5. The parts are currently being dried. After presintering the billets will be sliced into small subsections and the presintered density will be determined as a function of position (both radially and vertically). Defect-free billets of uniform green density will be used for densification/heat treatment and subsequent microstructure and mechanical property evaluation in Task 2.

TASK 2 - Improvement of Densification and Grain Growth Processes

The objective of this task is to establish improved densification and heat treatment process conditions for AS700 Si_3N_4. The evaluation criteria shall be density, microstructure, mechanical properties, as-processed surface quality, and shape retention. Density and mechanical properties shall be the primary screening criteria. Large AS700 samples (approximately 3" diameter by 2" high) will be used as the primary samples for densification and grain growth process development.

Isostatically pressed cylindrical AS700 billets are being used for densification/heat treat development until slipcasting of cylindrical billets is developed. Four large cylindrical billets of AS700 were fabricated by isostatic pressing during this reporting period. Three of the billets have been presintered and subsequently densified and heat treated using a range of processing conditions, as described in Table IV. Although significant density was achieved, the billets cracked extensively during densification. The cracks are similar to those seen in some samples which have cracked during presintering. Potential causes of the cracking include:

1) Fast heating rate during densification.
2) Presintering cycle conditions.
3) Large green density gradient in the isostatically pressed billets.

The baseline AS700 material, which is isopressed and processed using the baseline presintering cycle P_1 and sinter/heat treat cycle F_1, does not have cracking problems. Further adjustments of the presintering and densification cycles are being examined to solve the large billet cracking problem. Large slipcast billets with more homogeneous green densities are being fabricated under Subtask 1.2 and will be utilized during the next reporting period for AS700 densification and heat treatment development.

TABLE IV

Densification Results of Large Isostatically Pressed Billets

	Isopressed Samples		
	LIP-1	LIP-2	LIP-3
Presinter Cycle	P_2	P_1	P_3
Firing Cycle	F_2	F_3	F_2
Green Density (% Theoretical)	48.0	48.0	48.0
Fired Density (% Theoretical)	93.1	87.1	96.1

Initial densification/heat treatment processing of baseline slip plates using presintering cycle P_4 and sinter/heat treat cycle F_1 has resulted in some cracking of the plates, also believed to occur during heatup. The potential causes are postulated to be a too fast heating rate or potential stresses/defects introduced during drying that are undetectable at that stage. The cracking during heatup is being explored by sintering/heat treating plates that have been processed with various presintering cycles. The variation of presintering conditions can change presintered plate mechanical properties and affect critical factors such as thermal shock resistance.

The slipcast plates did achieve >99% of theoretical density and crack-free test bars were able to be machined from the plates. Room temperature average strength of three bars was 714 MPa (103.5 ksi), which is similar to strengths obtained from small isostatically pressed plates. Strength at 1375^{o}C was 408 MPa (59.2 ksi), which again is similar to isopressed AS700 properties.

TASK 3 - ALTERNATE RAW MATERIALS

The objective of this task is to evaluate the influence of the chemistry and physical characteristics of the starting Si_3N_4 powders on in-situ reinforcement processing and resultant properties.

Work was initiated under this task during this reporting period. Critical Si_3N_4 powder characteristics to be evaluated were selected:

1) Surface area/particle size distribution.
2) Oxygen content.
3) Trace element impurity levels.

Alternate Si_3N_4 powders were then selected. Selection criterion was to keep all other powder properties similar to the baseline powder, while having a lower or higher value of one of the three critical Si_3N_4 powder characteristics to be evaluated. Six commercially available powders meeting this requirements were selected and efforts are now underway to evaluate them in the AS700 system.

The evaluation procedure being used is to develop AS700 slip properties of the alternate powders so that equivalent green density and green microstructure to the baseline AS700 process are achieved. This will eliminate any convolution of results due to different packing densities or green microstructure. The alternate powders will be processed into AS700 slipcast plates, sintered/heat-treated and properties and microstructure compared with the baseline AS700 system.

Status of milestones

Milestones are on schedule.

Publications

None

FABRICATION OF SiC-AlN COMPOSITES

G. E. Hilmas and T. Y. Tien
(The University of Michigan)

Objective/scope

The goal of this project is to obtain dense SiC-AlN composites containing AlN-polytypoid phases(s) as a dispersed second phase. AlN-polytypoids (8H, 15R, 12H, 21R and 27R) form as elongated rod-like or platelet-like grains and are stable at high temperatures potentially producing an in-situ reinforcement phase in advanced composites. Hot-pressing was selected for this study to optimize densification at high temperatures.

Technical progress

1.0 INTRODUCTION

The formation of AlN-polytypoids and subsequent SiC matrix:AlN-polytypoid composites have been described in the last semi-annual report [1], including some preliminary microstructural and mechanical property data. It is the intent of this report to enhance the understanding of the mechanical properties of these materials by obtaining room and elevated temperature flexural strength measurements on a series of SiC:AlN-polytypoid samples containing a decreasing percentage of AlN-polytypoid second phase.

The starting powders are β-SiC and AlN - Al_2O_3 in the ratio 3AlN : 1Al_2O_3 designed in this case to form 12H(II) polytypoid as a second phase (see previous semi-annual report for explanation of designation type "I" or type "II" polytypoids [1]). The materials for this series are referred to by their respective starting powders in terms of volume percent of material: i.e. 90 vol.% β-SiC + 10 vol.% 12H(II)-polytypoid = BS90:12H(II).

2.0 EXPERIMENTAL

2.1 Specimen Preparation

The starting powders were placed in a graphite die and cold-pressed isostatically under a 15 MPa load. The samples were then hot-pressed in a graphite resistance furnace under a "static" nitrogen atmosphere at 2100 °C for 1 hour. A 24 MPa load was applied during the heating cycle above 1000 °C and released upon cooling below 1000 °C.

Hot-pressed billets of all five compositions (BS90:12H(II), BS80:12H(II), BS70:12H(II), BS60:12H(II) and BS50:12H(II)) were prepared. Twelve test bars were then diamond machined from each billet to a final size of 20 x 3 x 2.25 mm in preparation for four-point bending. In order to alleviate any strength or toughness anisotropies, all test specimens were machined such that the tensile face was perpendicular to the hot-pressing direction. The tensile surfaces were polished to a 0.1 μm diamond finish, and the edges of the bars were chamfered. All tests were performed using a specially designed self-aligning four-point bend test fixture made from hot-pressed SiC. The fixture also contained cylindrical Hexalloy SA (α-SiC) supports and had an outer span of 16 mm and inner span of 8 mm. A universal Instron testing machine was utilized to fracture the test bars using computer control. The crosshead speed was 5 x 10^{-3} in/min, corresponding to a strain rate of 1 x 10^{-4} /sec, and the room temperature was ~27 °C.

2.2 Mechanical Properties

All flexural strength measurements were made in four-point bending utilizing the following equation:

$$\sigma = 3P(L_1 - L_2) / 2bd^2$$

where P = load at failure (N), L_1 = outer fixture span (m), L_2 = inner fixture span (m), b = width of the test bar (m) and d = thickness of the test bar (m). Flexural strength measurements were obtained from three bars at each of four different temperatures (room temperature - 27 °C, 900 °C, 1200 °C and 1400 °C).

The controlled surface flaw method was utilized for the fracture toughness measurements. This method was used only on sample BS90:12H(II) to corroborate the high K_{IC} values obtained with the direct crack method of Anstis et al.[2]. A Vicker's diamond point indentation was made at the center of the test bars on the tensile surface while making sure to keep the indent oriented orthogonally to the longitudinal axis of the test bar. An indentation load of 15 kg was used for all test bars, and following fracture the critical stress intensity factor, K_{IC}, was calculated using the equation from Chantikul et al. [3]:

$$K_{IC} = 0.59(E/H)^{1/8}(\sigma P_i^{1/3})^{3/4}$$

where E = Young's modulus (GPa), H = hardness (GPa), P_i =Vicker's indent load (N) and σ = indented flexure strength (MPa). Young's modulus was measured for each hot-pressed billet using a non-destructive acoustic pulse-echo method.

3.0 RESULTS AND DISCUSSION

The fracture toughness results obtained on three BS90:12H(II) samples using the controlled surface flaw method are summarized in Table 1. These can be compared to the average value obtained by direct crack measurements, also shown in Table 1. This value was determined from ten Vickers indents using a load of 20 kg. The data shows that the controlled surface flaw values were quite uniform and comparable to the direct crack measurements.

The results of the room temperature and elevated temperature flexural strength measurements are shown graphically in figures 1-5. The flexural strength values were generally quite consistent, indicating a fairly narrow flaw size distribution. The only data point that was out of character with the rest of the results was the room temperature data for BS60:12H(II) (see figure 2). A review of these bend-test bars revealed that all three fractured outside the limit of the fixtures inner span. The required set-up in the Instron testing machine is different for room temperature versus elevated temperature measurements, and it is likely that the room temperature set-up was not aligned properly during these tests. To date all microstructural and mechanical property results have shown little difference between samples BS50:Polytypoids and BS60:Polytypoids, thus the room temperature flexure strength for composition BS60:12H(II) is probably in the range of 800 - 850 MPa.

The gradual change in the slope of each curve in the range of 1000 - 1400 °C can be likely attributed to grain boundary creep due to a silicate-based glassy phase remaining at the grain boundary. As yet though, no compositions in this study have been tailored to obtain a crystallizable grain boundary phase.

The most remarkable results are still for the composition BS90:12H(II) having a fracture toughness of 8.5 - 9.0 MPa-$\sqrt{m}$, an elongated microstructure with a grain size in the range of 10 - 15 μm [1], and a room temperature strength of ~550 MPa. Examination of the fracture surfaces for all the compositions is still incomplete and so will not be discussed further at this point. Additional analysis is also currently underway to accurately measure the grain size of all compositions in this series for a complete comparison between their grain size, fracture toughness and flexural strengths.

Status of milestones

On Schedule.

Publications

None.

References

[1] G. E. Hilmas and T. Y. Tien, "Fabrication of SiC-AlN Composites," Semi-annual report submitted to ORNL under Contract No. SC-19X-SA125C, October, 1990.

[2] G. R. Anstis, P. Chantikul, B. R. Lawn and D. B. Marshall, "A Critical Evaluation of Indentation Techniques for Measuring Fracture Toughness: I. Direct Crack Measurements," *J. Am. Ceram. Soc.*, **64** [9] 533-543 (1981).

[3] P. Chantikul, G. R. Anstis, B. R. Lawn and D. B. Marshall, "A Critical Evaluation of Indentation Techniques for Measuring Fracture Toughness: II, Strength Method," *J. Am. Ceram. Soc.*, **64** [9] 539-543 (1981).

Table 1. Mechanical Property Data for BS90:12H-II Composites

Sample Code	Width (mm)	Thickness (mm)	E (GPa)	H (GPa)	K_{IC} (C.F.)† (MPa-√m)	K_{IC} (D.C.)†† (MPa-√m)
BS90:12H(II)-4	3.04	2.25	428	14.7	8.44	----
BS90:12H(II)-5	3.04	2.25	428	14.7	9.25	----
BS90:12H(II)-9	3.04	2.25	428	14.7	8.97	----
BS90:12H(II)	----	----	428	14.7	----	8.50 ±0.6

† C.F. = Controlled surface flaw measurement

†† D.C. = Direct radial/median crack measurement

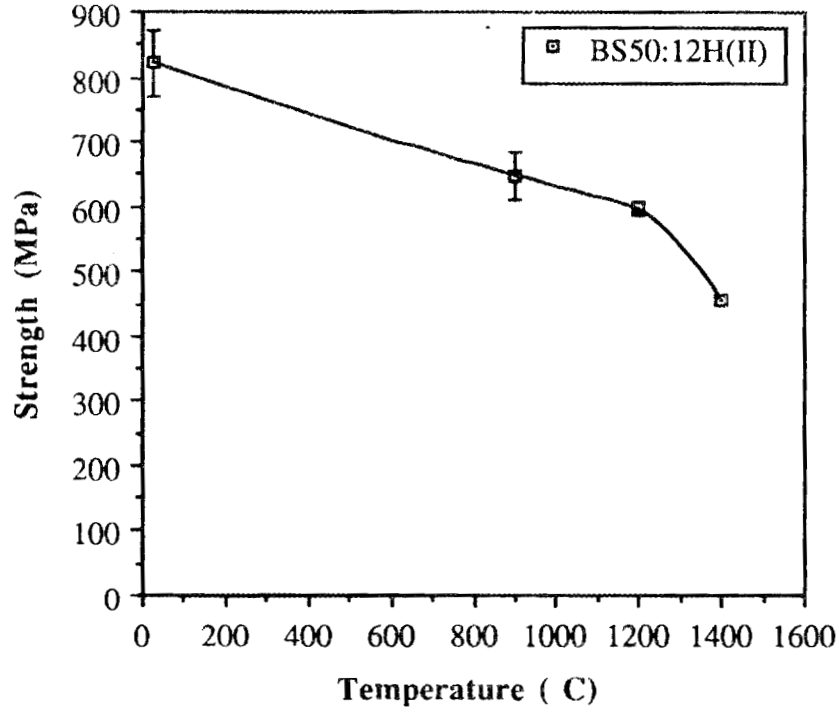

Figure 1. Plot of flexural strength versus temperature for sample BS50:12H(II).

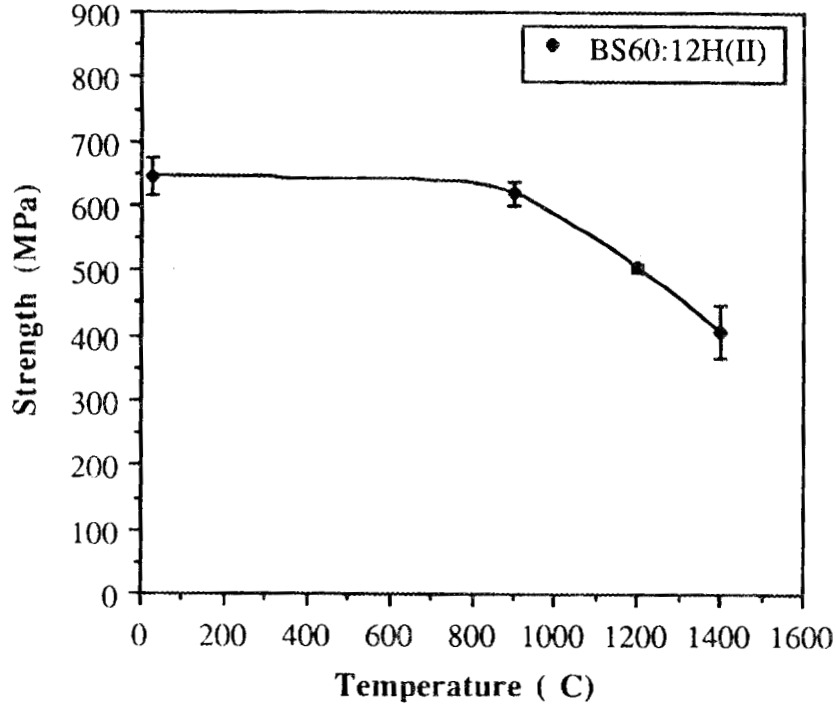

Figure 2. Plot of flexural strength versus temperature for sample BS60:12H(II).

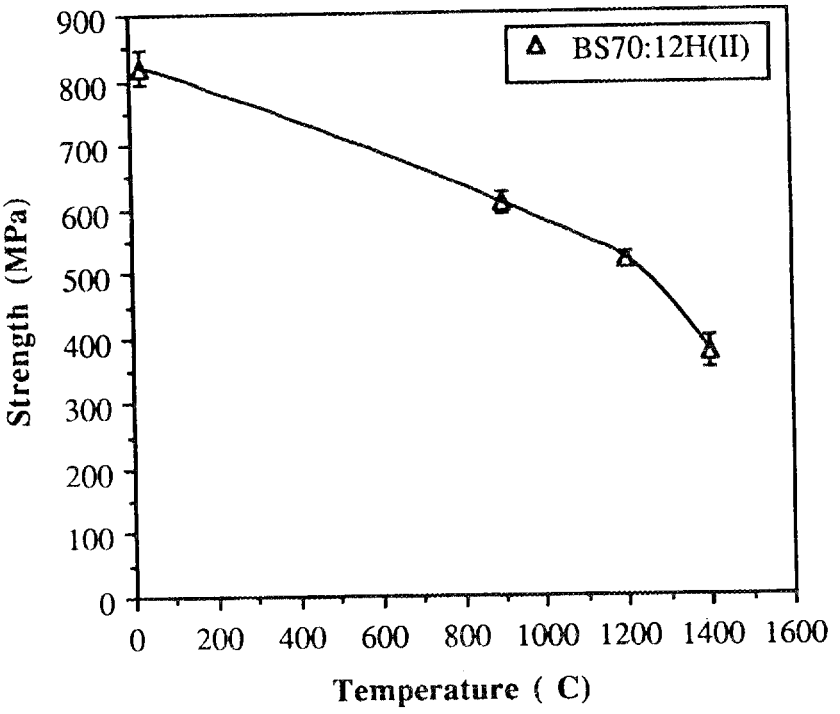

Figure 3. Plot of flexural strength versus temperature for sample BS70:12H(II).

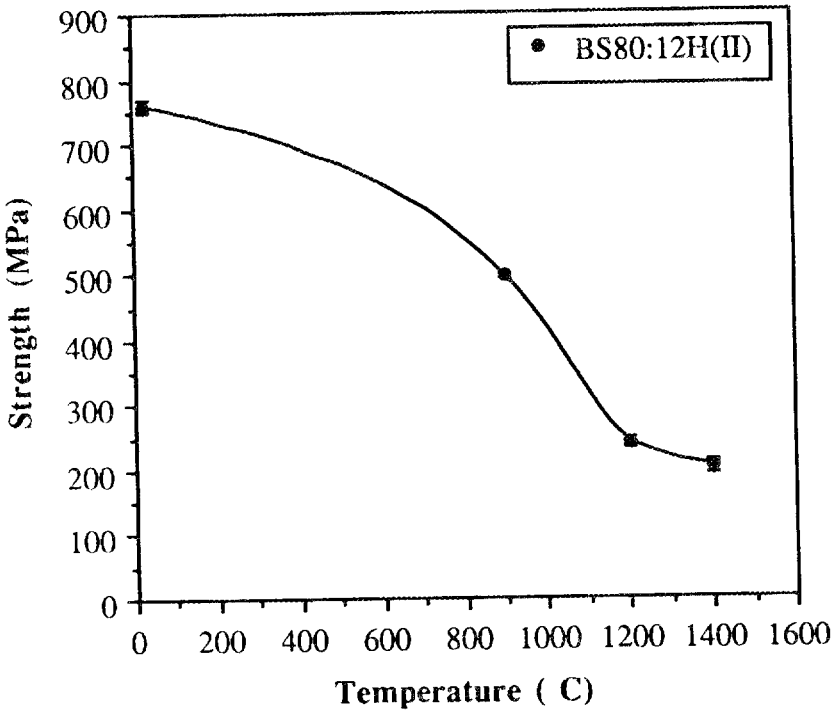

Figure 4. Plot of flexural strength versus temperature for sample BS80:12H(II).

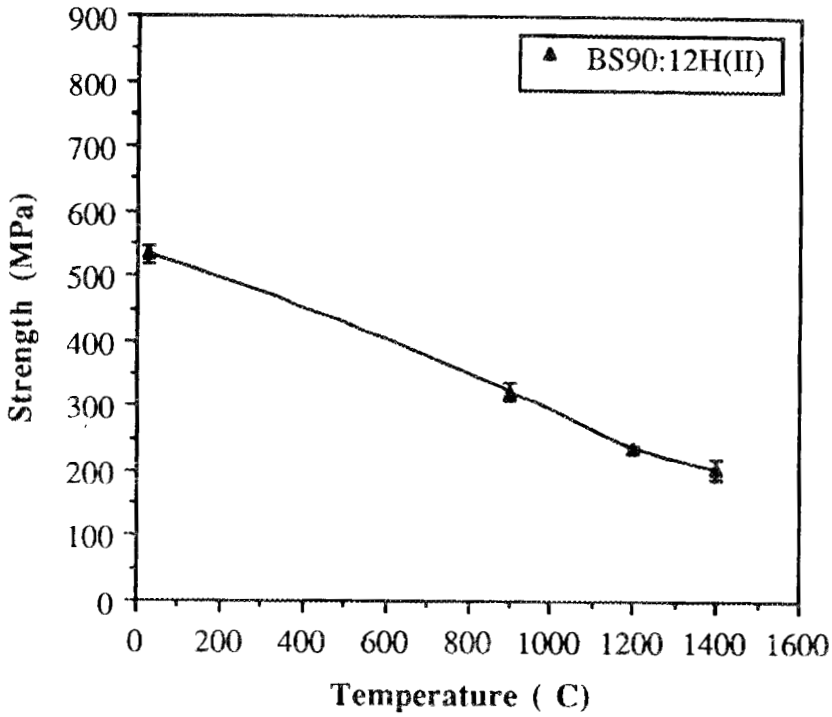

Figure 5. Plot of flexural strength versus temperature for sample BS90:12H(II).

Optimization of Silicon Nitride Ceramics

K. R. Lai and T. Y. Tien
(The University of Michigan)

Objective/scope

To develop processing methods to obtain silicon nitride ceramics with a fibre-like grain morphology. Silicon nitride ceramics containing β-Si_3N_4 grains with fibre-like morphology have high fracture strength, high fracture toughness and superior creep resistance. The fibre-like structure of the β-Si_3N_4 grains can be obtained by sintering the silicon nitride ceramics at higher temperatures under a higher nitrogen pressure. The composition of the sintering additives will also affect the microstructure development. The mechanical properties can further be improved by controlling the composition and structure of the grain boundary phase. The major goal of this project is to develop monolithic silicon nitride ceramics with optimum mechanical properties and to understand their microstructure - property relationships.

Technical progress

Silicon nitride compositions containing 10 weight % of YAG as densification additives were prepared. Samples were sintered in a high nitrogen pressure furnace at temperatures up to 1900°C under a nitrogen pressure up to 20 atmospheres. Samples with densities greater than 98% of theoretical were obtained when sintered at temperature higher than 1800°C for one hour or longer. Ceramics with fibre-like structure were obtained for all of the samples. Kinetics of microstructure development of samples sintered at different temperature under 10 atmosphere of nitrogen pressure with holding time up to 10 hours were studied. The results are given in Figs. 1 through 3.

These results showed that the growth rates in both the length and width directions of the β-Si_3N_4 grains followed the empirical equation:

$$L^n - L_0^n = K_L t \quad \text{and} \quad W^n - W_0^n = K_W t$$

where L and W are the grain sizes and K_L and K_W are the rate constants in the length and width directions of the β-Si_3N_4 grains respectively. L_0 and W_0, the initial grain sizes. L_0 and W_0 are negligible when α-Si_3N_4 were used as the starting materials.

The best fits of these curves gives the exponents of 3 and 5 for the length and the width directions of the β-Si_3N_4 grains respectively.

The Aspect Ratio (AR) is defined as the length to width ratio of the of the β-Si_3N_4 grain. Then:

$$A\ R = L/W = (K_L/K_W)\ t^{(2/15)}$$

The line of AR vs time plot should have a slop of 2/15 which agrees with the experimental results as shown in Fig. 3.

Status of milestones

On schedule.

Publications

None

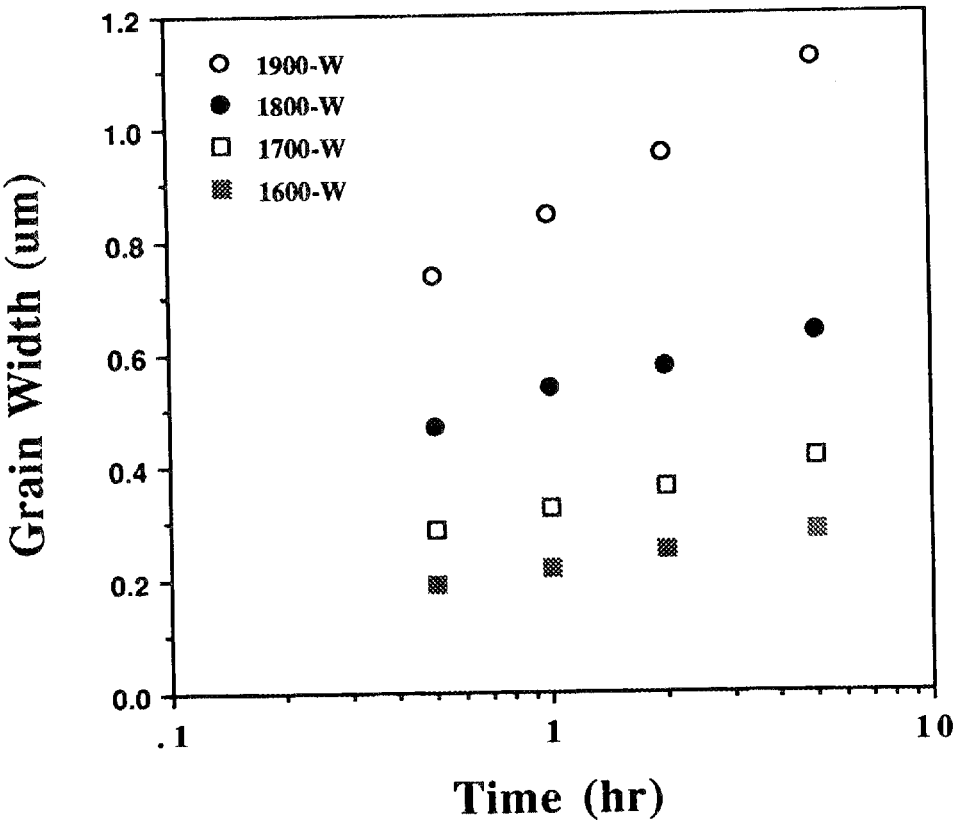

Fig. 1. Widths of the β-Si_3N_4 Grains in Specimens sintered at different temperatures under 10 atmosphere of nitrogen pressure. Samples composition: 10 wt.% of YAG.

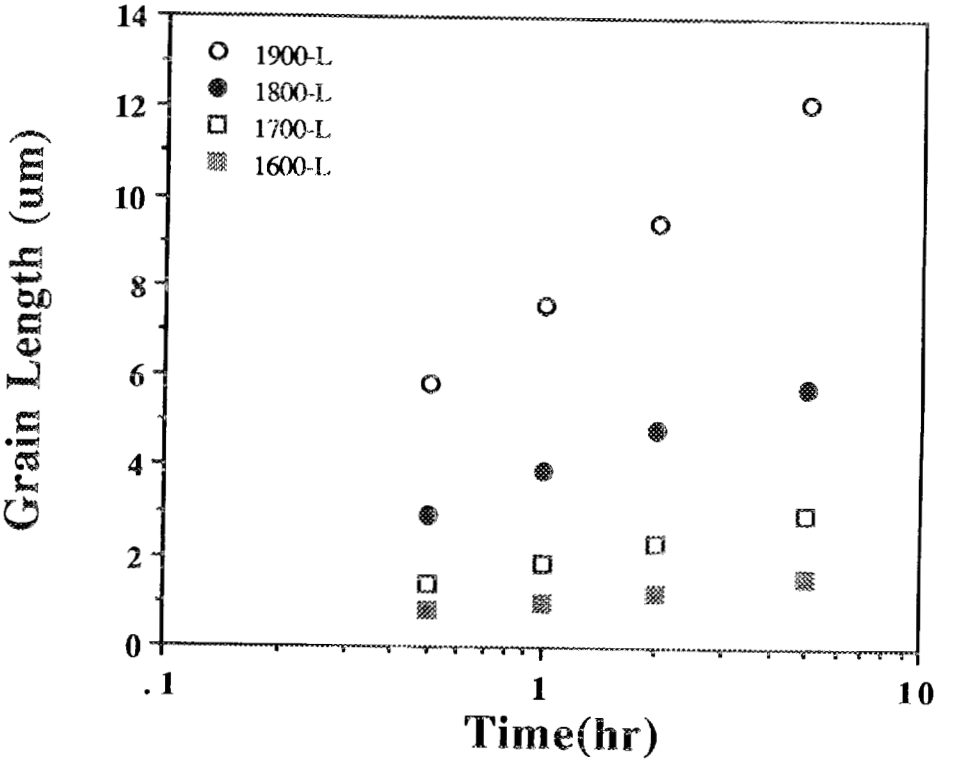

Fig. 2. Lengths of the β-Si_3N_4 Grains in Specimens sintered at different temperatures under 10 atmosphere of nitrogen pressure. Samples composition: 10 wt.% of YAG.

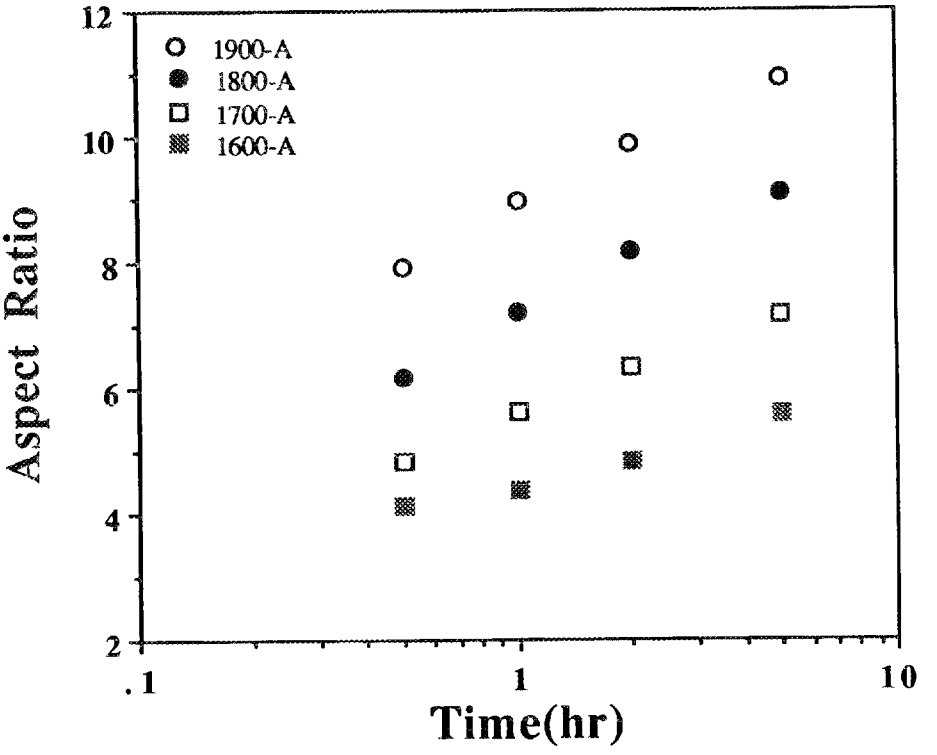

Fig. 3. Aspect Ratios of the β-Si_3N_4 Grains in Specimens sintered at different temperatures under 10 atmosphere of nitrogen pressure. Samples composition: 10 wt.% of YAG.

1.2.3 Oxide Matrix

Dispersion-Toughened Ceramic Composite

T. N. Tiegs, P. F. Becher, P. A. Menchhofer, W. H. Elliott, D. J. Kim, and D. W. Coffey (Oak Ridge National Laboratory)

Objective/scope

This work involves development and characterization of SiC whisker-reinforced ceramic composites for improved mechanical performance. To date, most of the work has dealt with alumina as the matrix because it was deemed a promising material for initial study. However, an effort in SiC whisker-reinforced silicon nitride and sialon is in progress. In addition, studies of whisker growth processes were initiated to improve the mechanical properties of SiC whiskers by reducing their flaw sizes. In-situ acicular grain growth is also being investigated to improve fracture toughness of silicon nitride materials.

Technical progress

Hot-pressed silicon nitride and sialon-SiC whisker composites

As reported previously, samples of various compositions, where the intergranular-glass phases were modified, have been fabricated and machined into test specimens. At the present time they are being flexural-strength tested at room and elevated temperature.

Evaluation of experimental SiC whiskers from Materials and Electrochemical Research (MER) Corp. is in progress. These whiskers were produced under an Small Business Innovative Research (SBIR) contract from the Department of Energy. Scanning electron microscopy characterization showed the whisker diameters to vary from 0.2 to 1.5 μm (Fig. 1). Alumina and silicon nitride matrix composites containing 20 vol % whiskers have been hot pressed and are being machined into test bars for fracture toughness, hardness, and flexural-strength measurements.

Microstructure development

The series of silicon nitride materials to assess the role of elongated-grain microstructure on fracture toughness has been fabricated and is being machined into test specimens. The compositions and hot-pressing conditions are given in Table 1. In addition, supplemental samples have been fabricated where the hot pressing has been stopped at intermediate densities. From these specimens we will determine the microstructure development by X-ray diffraction and electron microscopy.

Summaries of the initial mechanical properties and phase compositions are given in Tables 1 and 2. As shown, a wide range of compositions and processing has resulted in a wide range of mechanical properties and phase contents. Further testing of the materials is in progress. Selected compositions were tested at elevated temperatures and the results are summarized in Table 3.

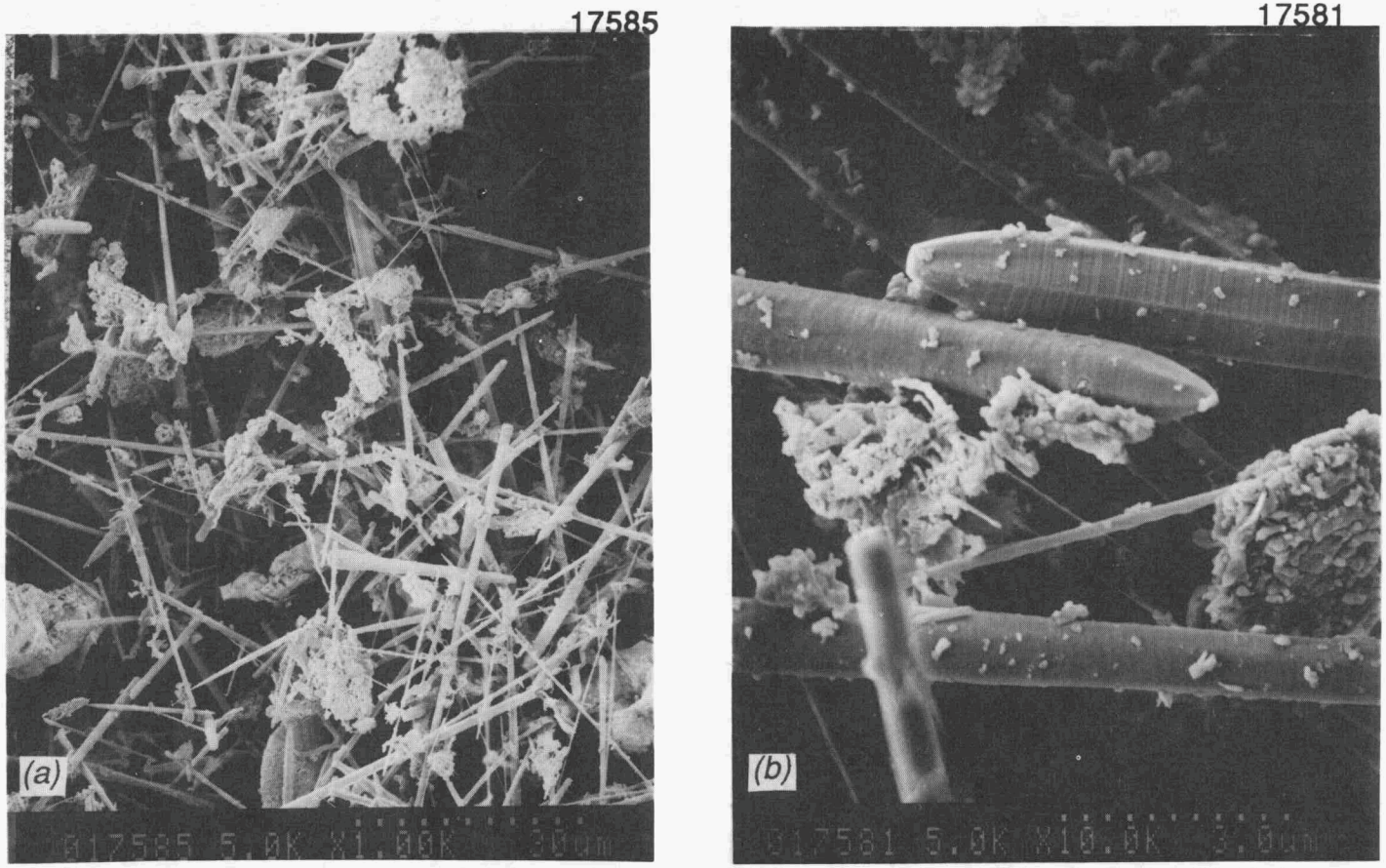

Fig. 1. SiC whiskers fabricated by MER Corp.: (*a*) low magnification and (*b*) high magnification.

Table 1. Summary of initial results to date on silicon nitride materials for microstructure development-property relationships

Composition 1900/90	Hot-pressing conditions (°C/min)				
	1725/60	1800/90	1800/180	1800/90	1650/60
6% Y_2O_3-2% Al_2O_3					
Density (% T.D.)	100.0	100.0	100.0		99.6
ß-Si_3N_4 Content (%)	75.0	100.0	100.0		100.0
Flexural strength (MPa)	916±48	1142±125	942±185	849±101	1234±107
Fracture toughness (MPa√m)	6.6±0.7				
6% Y_2O_3-2% Al_2O_3[a]					
Density (% T.D.)	98.0				99.2
ß-Si_3N_4 Content (%)	82.0				100.0
Flexural strength (MPa)	777±123				809±70
Fracture toughness (MPa√m)	7.6±1.1				
GN-10-Additives					
Density (% T.D.)	98.0	100.0	100.0		
ß-Si_3N_4 Content (%)	75.0	97.0			
Flexural strength (MPa)	943±32	1042±232	1044±121		
Fracture toughness (MPa√m)	6.2±0.6				
8% La_2O_3-2% Al_2O_3					
Density (% T.D.)	98.2	100.0			99.7
ß-Si_3N_4 Content (%)	100.0	100.0			100.0
Flexural strength (MPa)	1088±30	1043±111	1075±64		1065±129
Fracture toughness (MPa√m)	5.9±0.6				
3% Y_2O_3-4% La_2O_3-2% Al_2O_3					
Density (% T.D.)	98.6	99.5	100.0		
ß-Si_3N_4 Content (%)	96.0	100.0	100.0		
Flexural strength (MPa)	883±108	1052±137	1010±122		
Fracture toughness (MPa√m)	6.7±1.3				

[a]Contained 40% ß-Si_3N_4.

Table 2. Summary of initial results to date on sialon materials for microstructure development-property relationships

Composition 1850/90	Hot-pressing conditions (°C/min)				
	1725/60	1800/90	1800/180	1800/90	1650/60
2% Y_2O_3-4% AlN					
Density (% T.D.)	98.2	99.4	98.7		99.8
ß-Si_3N_4 Content (%)	79.0	87.0			91.0
Flexural strength (MPa)	707±19	727±88			741±85
Fracture toughness (MPa√m)	6.1±0.2				
4% Y_2O_3-6% AlN	s				
Density (% T.D.)	99.3	99.5	97.6		98.7
ß-Si_3N_4 Content (%)	45.0	50.0			50.0
Flexural strength (MPa)	555±96	723±115			694±33
Fracture toughness (MPa√m)	5.1±0.3				
6% Y_2O_3-10% AlN					
Density (% T.D.)	99.9		97.1		97.9
ß-Si_3N_4 Content (%)	15.0			15.0	
Flexural strength (MPa)	489±41				632±31
Fracture toughness (MPa√m)	4.0±0.2				

Table 3. Summary of results of high-temperature fast-fracture flexural strength

Composition	Flexural strength (MPa)				
	22°C	1000°C	1200°C	1300°C	1400°C
6% Y_2O_3-2% Al_2O_3	1142±125		937±28		660±4
8% La_2O_3-2% Al_2O_3	1043±111	842±75	726±14		
3% Y_2O_3-4% La_2O_3-2% Al_2O_3	1052±137	834±101	715±41		
6% Y_2O_3-2% BaO	1072±107	957±89	720±41		
6% Y_2O_3-2% SrO	1041±121		963±8	688±106	780±33
4 % Y_2O_3	1090±121		917±54		
8 % Y_2O_3	800±137				
11.5 % La_2O_3	788±103		697±90		751±101

Initial compositions of Si_3N_4-6% Y_2O_3-2% Al_2O_3 containing ß-Si_3N_4 seeds densified poorly during hot pressing. Evidently, during formation of the ß-Si_3N_4 seeds, the SiO_2 content was sufficiently reduced so that the liquid content during fabrication was too low for adequate densification. To increase the SiO_2 content, the ß-seed material was oxidized at 700°C for 1 h. Samples containing 5 and 20 wt % of the oxidized ß-seed have been fabricated. In addition, samples containing ß'-sialon powder as a seed material have also been fabricated. Initial microstructural examination of Si_3N_4-6% Y_2O_3-2% Al_2O_3 containing 20 wt % ß'-sialon powder showed extensive grain growth (Fig. 2). Fracture toughness measurements on this composition are in progress.

Previous results from other researchers have shown that gas-pressure sintering of silicon nitride materials at temperatures ≥ 1900°C can develop large grains and high fracture toughness.[1-3] In our hot-pressing studies, certain materials densified at temperatures ≥1850°C had some of the highest fracture toughness values and microstructurally had extensive grain growth. However, these samples also experienced excessive weight losses due to silicon nitride

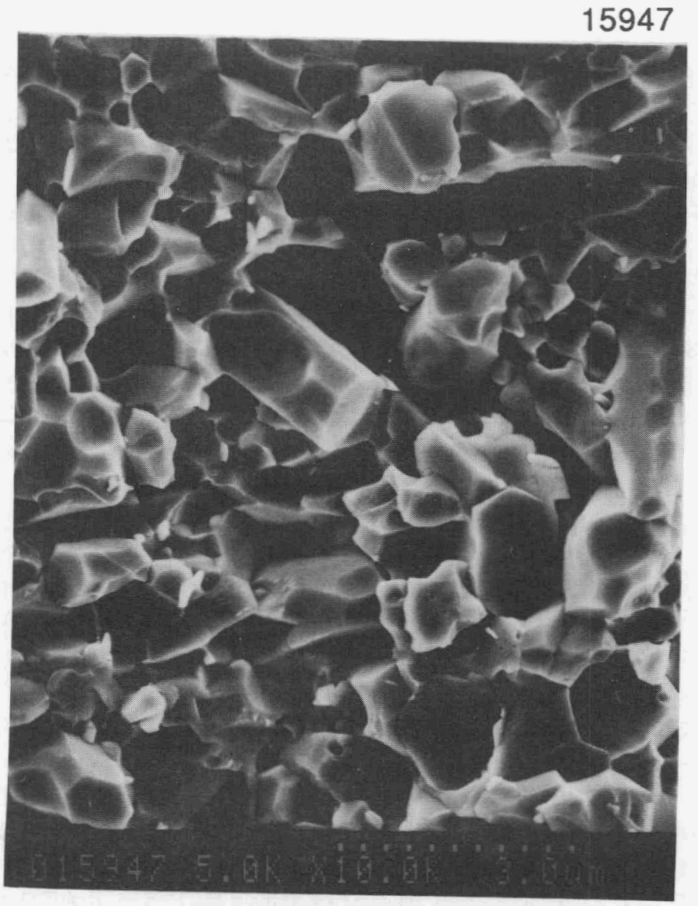

Fig. 2. Fracture surface of Si_3N_4-6% Y_2O_3-2% Al_2O_3 containing 20 wt % ß'-sialon powder showing extensive grain growth during hot pressing.

decomposition. To examine the effect of high-temperature sintering at high nitrogen gas over pressures on microstructural development, a series of samples have been fabricated. Compositions include: Si_3N_4-6% Y_2O_3-2% Al_2O_3, 8% La_2O_3-2% Al_2O_3, and Si_3N_4 with GN-10 additives. All of the samples were processed by turbomilling of the powders and slip casting into plaster molds. Microstructures and mechanical properties will be compared to those from the initial hot-pressing study.

As shown in Table 3, the additive chemistry greatly affects the high-temperature mechanical properties. Generally, the rare-earth additions without other oxides, such as Al_2O_3 and BaO, exhibit better high-temperature properties. This behavior has been observed previously and reported in the literature.[4-9] Additional samples are currently being fabricated with 1 to 12% rare-earth oxide (Y_2O_3, La_2O_3, or Nd_2O_3) and 1 to 8% SiO_2 additives to take advantage of some of the good high-temperature properties. With a sufficient volume of liquid phase present during fabrication, elongated ß-Si_3N_4 growth will occur for increased fracture toughness, but the intergranular phases will be refractory enough for good high-temperature properties The SiO_2 additions will be used to control the intergranular phases and maintain the composition in an appropriate phase compatibility area so oxidation problems are not encountered. If the rare-earth contents are too high without the SiO_2 additions, phases, such as melilite, can be obtained that undergo dramatic volume expansions during oxidation.[10,11] Lewis and co-workers have demonstrated good mechanical properties for these types of compositions.[6,7] Mechanical property reductions, due to volume decreases associated with the crystallization of the glass phase in these systems, have been observed. Crystallization under pressure will be used to try to minimize the strength and toughness decreases.

Because the rare-earth SiO_2 compositions are highly refractory, they are more difficult to sinter to high density. Recent literature has shown that combinations of rare-earth oxides can be used to aid in promoting densification.[9,12] Samples with different Y_2O_3-La_2O_3 ratios have been fabricated and are currently being examined for densification behavior by hot pressing, pressureless sintering, and gas-pressure sintering.

Alternate grain-boundary phases are also being examined that will aid in densification but be of a transient nature and crystallize into a refractory grain-boundary phase. Some possible grain-boundary phases include the rare-earth oxide and nitride apatites as discussed by Thompson.[13] These include a wide range of stable apatites of composition $A_2B_8(SiO_4)_6O_2$ where A is a divalent cation (typically Mg, Mn, Pb, Ca, Sr, Ba) and B is a trivalent cation (typically Y, La, Ce, Nd). An advantage of the nitrogen apatite is that it can oxidize without a large volume expansion. Samples using various combinations of Y_2O_3, La_2O_3, Nd_2O_3, Yb_2O_3, BaO, and SrO to develop these grain-boundary phases are being fabricated. Densification and microstructure development during hot pressing, pressureless sintering, and gas-pressure sintering will be assessed. Formation of ß-Si_3N_4 by the nitridation of Si additions to the compositions will also be done.

References

1. E. Tani, S. Umebayashi, K. Kishi, K. Kobayashi, and M. Nishijima, "Gas-Pressure Sintering of Si_3N_4 With Concurrent Addition of Al_2O_3 and 5 wt % Rare Earth Oxide: High Fracture Toughness with Fiber-Like Structure," *Am. Ceram. Soc. Bull.* **65**[9], 1311–15 (1986).

2. C. Li and J. Yamanis, "Super-Tough Silicon Nitride With R-Curve Behavior," *Ceram. Eng. Sci. Proc.* **10**[7-8], 632–45 (1989).

3. K. Matsuhiro and T. Takahashi, "The Effect of Grain Size on the Toughness of Sintered Si_3N_4," *Ceram. Eng. Sci. Proc.* **10**[7-8], 807–16 (1989).

4. G. E. Gazza, "Hot Pressed Si_3N_4," *J. Am. Ceram. Soc.* **56**[12], 662–69 (1973).

5. G. E. Gazza, "Effect of Yttria Additions on Hot-Pressed Si_3N_4," *Am. Ceram. Soc. Bull.* **54**[9], 778–81 (1975).

6. I. P Tuersley, G. Leng-Ward, and M. H. Lewis, "High-Temperature Si_3N_4-Based Ceramics," *Brit. Ceram. Proc.* **46**, 231–46 (1990).

7. I. P Tuersley, G. Leng-Ward, and M. H. Lewis, "Silicon Nitride-Based Ceramics For Gas Turbine Applications," pp. 856–70 in *Proc. 3rd Internat. Symp. on Ceramic Materials and Components for Engines,* ed V. J. Tennery, Amer. Ceram. Soc., Westerville, Ohio (1989).

8. C. L. Quackenbush, J. T. Smith, J. T. Niel, and K. W. French, "Sintering, Properties, and Fabrication of Si_3N_4 + Y_2O_3 Based Ceramics," pp. 669-82 in *Progress in Nitrogen Ceramics,* ed. F. L. Riley, Martinus Nijhoff Pub., The Netherlands (1983).

9. Y. R. Xu, T. S. Yen, and X. R. Fu, "Grain Boundary Tailoring of High Performance Nitride Ceramics and Their Creep Property Studies," pp. 739–50 in *Proc. 3rd Internat. Symp. on Ceramic Materials and Components for Engines,* ed V. J. Tennery, Amer. Ceram. Soc., Westerville, OH (1989).

10. F. F. Lange, S. C. Singhal, and R. C. Kuznicki, "Phase Relationships and Stability Studies in the Si_3N_4-SiO_2-Y_2O_3 Pseudoternary," *J. Amer. Ceram. Soc.* **60**(5-6), 249–52 (1977).

11. K. H. Jack, "The Crystal Chemistry of the Sialons and Related Nitrogen Ceramics,"pp. 109–28 in *Nitrogen Ceramics*, ed. F. L. Riley, Noordhoff Pub., Netherlands (1977).

12. N. Hirosaki, A. Okada, and K. Matoba, "Sintering of Si_3N_4 With the Addition of Rare-Earth Oxides," *J. Am. Ceram. Soc.* **71**[3], C-144–47 (1988).

13. D. P. Thompson, "Alternative Grain-Boundary Phases for Heat-Treated Si_3N_4 and ß'-Sialon Ceramics," *Brit. Ceram. Proc.* **45**, 1–13 (1990).

Status of milestones

Milestone 123110, "Determine effects of process parameters on flaw generation in SiC whiskers," was not completed.

Publications

None.

1.2.4 Silicate Matrix

Low Expansion Ceramics for Diesel Engine Applications
D. A. Hirschfeld and J. J. Brown (VPI)

Objective/scope

Optimize the chemistry, properties, and processing of selected low thermal expansion compositions based on the zircon (NZP) and the β-eucryptite-$AlPO_4$ systems. The major long-term goal is to develop an economical, isotropic, ultra-low thermal expansion ceramic material capable of having stable properties above 1200°C.

Technical progress

Zircon (NZP) System

The fabrication of large pieces of $(Ca,Mg)Zr_4(PO_4)_6$ is required to demonstrate that this material is ready for testing in advanced heat engines. These large samples will demonstrate the ability to manufacture this ceramic on an industrial scale and allow a more complete characterization of the thermo-mechanical properties. During this reporting period, 5 kg of $(Ca_{0.6},Mg_{0.4})Zr_4(PO_4)_6$ (CMZP) powder were prepared by sol-gel synthesis techniques described in previous reports. The CMZP produced was pure with no secondary phases detected by X-ray diffraction analysis. The majority of this powder will be hot pressed and/or hot isostatically pressed into large plates for characterization. The remainder will be used as a matrix reinforced with SiC whiskers to evaluate the composite material properties.

The effects of sintering temperature and time on the thermal expansion and microstructure of CMZP prepared using a solid-state reaction method were investigated. Bars containing 1 wt% ZnO (sintering aid) were pressed, and then sintered at temperatures of 1150°C to 1300°C. Densities greater than 95% of theoretical were achieved when the sintering temperature was higher than 1150°C. As shown in Figure 1, with an increase in sintering temperature from 1150°C to 1300°C (sintering time = 24 h), the bulk thermal expansion of CMZP decreased from 9.0 x 10^{-7}/°C to -9.0 x 10^{-7}/°C while the grain size increased from 2 μm to 8 μm. Similarly, an increase in grain size from 5 to 8 μm was observed with longer sintering times (sintering temperature = 1200°C) while the bulk thermal expansion coefficient decreased to -14.4 x 10^{-7}/°C as illustrated in Figure 2. Scanning electron micrographs of the microstructure revealed the presence of a glassy phase within the grain boundaries and microcracks as

shown in Figure 3. The decrease in thermal expansion with increased sintering time and temperature may be attributed to microcracking and the glassy phase which appears to be a zinc phosphate.

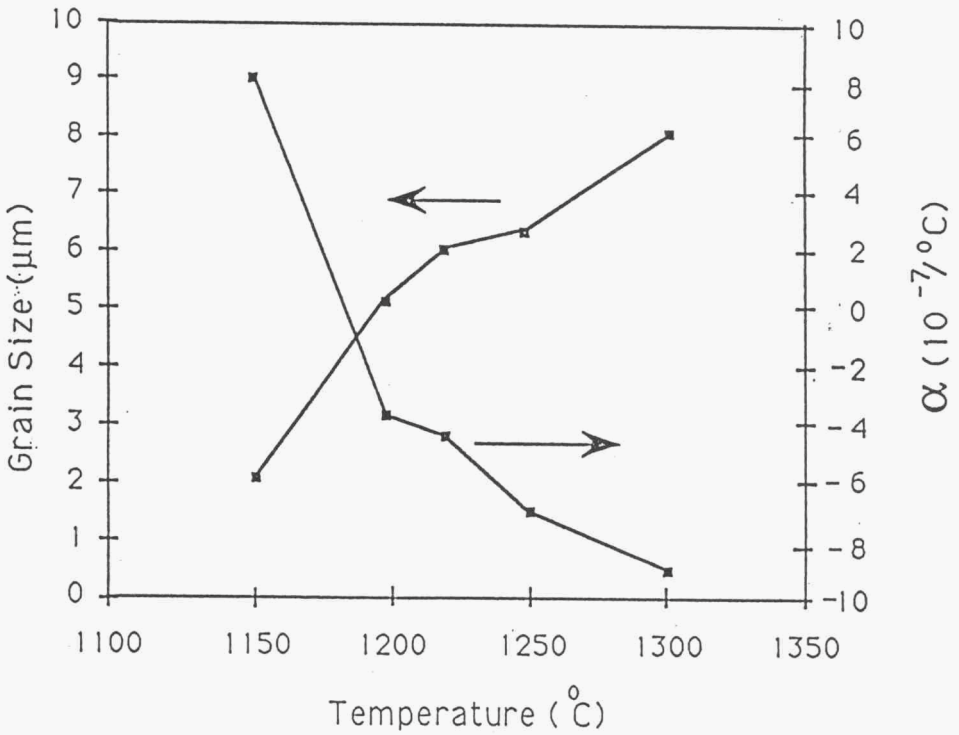

Figure 1. Grain size and thermal expansion of CMZP as a function of sintering temperature

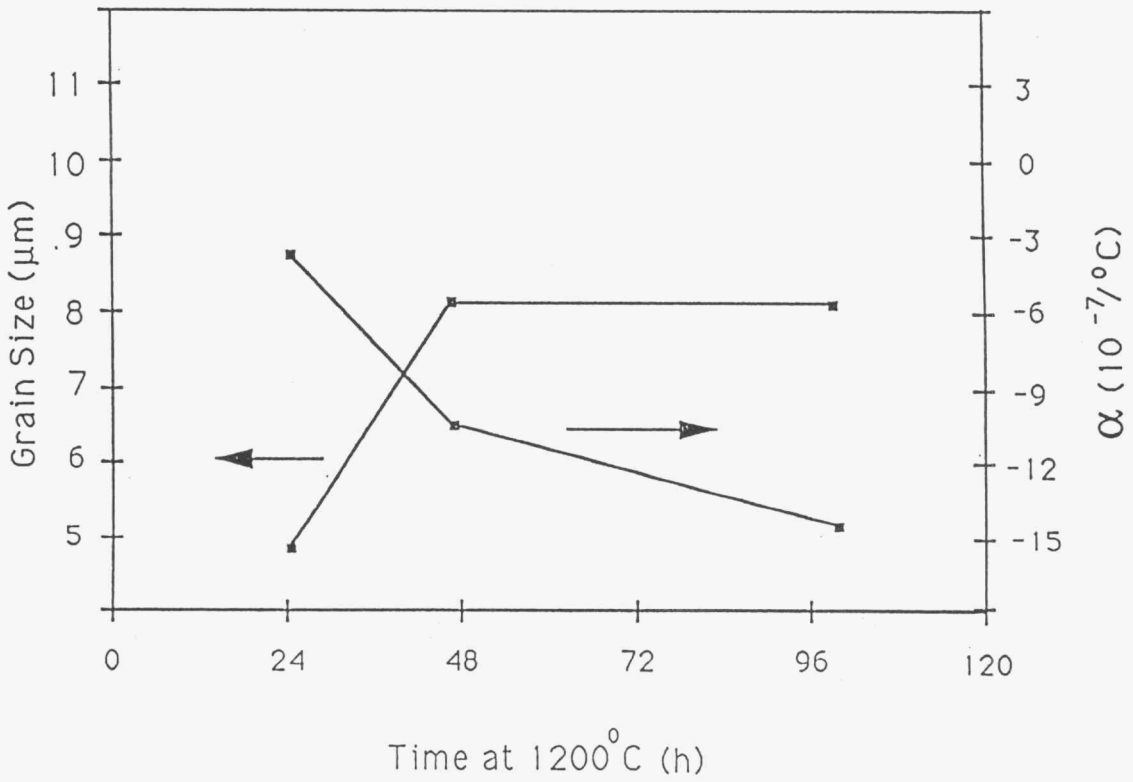

Figure 2. Grain size and thermal expansion of CMZP as a function of sintering time

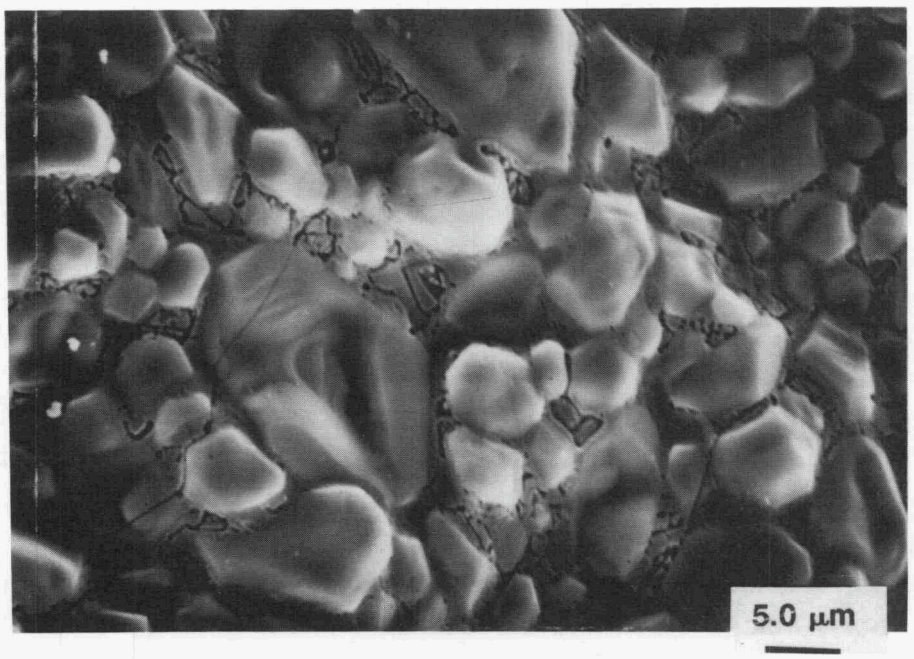

Figure 3. Microstructure of CMZP sintered at 1300°C for 24 h

Ceramic Composites

The effects of aging heat treatments and fiber volume fraction on the bulk thermal expansion of chopped Nicalon-SiC fiber-reinforced $(Ca_{0.6},Mg_{0.4})Zr_4(PO_4)_6$ (CMZP) were investigated.

A composite containing 5 vol% chopped fibers was hot pressed in air at 1220°C at 14 MPa pressure for 6 h, then aged in air at 1200°C for 4 h without pressure. The average bulk coefficient of thermal expansion (CTE) of the composite was $-2.0 \times 10^{-7}/°C$. Another composite containing 5 vol% fibers was hot pressed in N_2 under similar conditions, then aged in N_2 at 1220°C for 20 h. This sample had a bulk CTE of $-8.0 \times 10^{-7}/°C$. Preliminary results indicate that the hot pressing atmosphere has no significant effect on CTE and, similar to previous observations for monolithic CMZP, the CTE becomes more negative with aging. It is noted that both these composites had densities greater than 96% of theoretical.

Composites containing 20 vol% chopped fibers were prepared by hot-pressing in air or Ar at 1230°C and 30 MPa pressure for 3 h. Densities of these samples, 90 - 92% of theoretical, were lower than those of composites containing lower fiber volume fractions. The bulk CTE of the high fiber volume fraction composites was $14 \times 10^{-7}/°C$, independent of hot pressing atmosphere.

The nature of the fiber-matrix interface is known to have a significant effect on the toughness-related properties of ceramic composites. The chemistry of the interface between Nicalon-SiC fibers and a $(Ca_{0.6},Mg_{0.4})Zr_4(PO_4)_6$ (CMZP) matrix was characterized thermodynamically using SOLGASMIX-PV, a computer program for calculating equilibrium relationships in complex chemical systems.[1] Since the CMZP composites are currently produced in the laboratory by hot pressing at approximately 1230°C in either air or Ar atmospheres, these conditions were used in the thermodynamic calculations.

The results of the SOLGASMIX analysis for these conditions indicate that CMZP reacts with SiC in either air or Ar to form $Ca_{3-x}MgSi_2O_{8-x}$ (x may be 0, 1, or 2) and possibly MgO, ZrP_2O_7, $Zr_2P_2O_9$, $ZrSiO_4$, or SiO_2, depending on system conditions. Even when SiO_2 is assumed present with SiC and CMZP, it is noted that the SiC is oxidized even in an Ar atmosphere suggesting that oxygen may be provided to the interface by the CMZP.

Energy Dispersive X-ray Analysis (EDX) was used to examine the hot pressed CMZP composites to determine the Si, Ca, Mg, Zr, and P contents in both the fiber surfaces and the interfacial area of the matrix exposed by fiber removal (matrix trough). The EDX results indicate that the Si content in the matrix trough of the sample pressed in air is significantly higher than that of the sample pressed in Ar. Since Si is not likely to exist in the form of SiC in the matrix, the

high Si content in the trough indicates the possible oxidation of SiC fibers when the composite is pressed in air.

The fiber-matrix interface of CMZP composites that were hot pressed in air and argon are shown in Figures 4 and 5, respectively. The composite pressed in air exhibited some bonding between the fiber and matrix and the fiber surfaces appeared to be rough, probably due to SiO_2 formation. The composites pressed in argon exhibited fiber/matrix debonding and smooth fiber surfaces.

A new technique for processing a self-reinforced CMZP composite has been developed. Information on this technique is being withheld pending patentability determination.

Lightweight Ceramics

The flexural strength of lightweight $(Ca_{1-x},Mg_x)Zr_4(PO_4)_6$ ceramics where $x = 0.0$-0.3 are shown in Figure 6 as a function of relative density. Included in the figure is the strength of open cell ZrO_2. As shown in the figure, the strength determined by 3-point bending compares favorably with that of open cell ZrO_2. The strengths were independent of composition.

The room temperature compressive strength of lightweight $(Ca_{1-x},Mg_x)Zr_4(PO_4)_6$ ceramics was measured. Figure 7 shows the strength of lightweight $(Ca,Mg)Zr_4(PO_4)_6$ as compared to lightweight ZrO_2-4%MgO, a conventional thermal barrier material. Both materials have relative densities varying between 0.2 and 0.7. The compressive strength of $(Ca,Mg)Zr_4(PO_4)_6$ is strongly related to the density. Furthermore, it appears to be independent of the composition as noted previously for MOR and tensile strengths. The compressive strength compares favorably with that of partially-stabilized zirconia.

The thermal shock resistance of lightweight $(Ca_{0.9}, Mg_{0.1})Zr_4(PO_4)_6$ was investigated during this reporting period. The lightweight ceramics were made by the polymer powder method (NZP and a polymer powder were mixed, pressed, and sintered). As shown in Figure 8, lightweight ceramics with relative densities of 0.87 and 0.54 exhibit no significant strength losses following air quenching from any temperature up to 1550°C. The addition of ZnO, a sintering aid, increased the modulus of rupture and did not appear to affect the thermal shock resistance.

β-Eucryptite System

It was previously reported that the processing of $AlPO_4$-modified β-eucryptite utilizing conventional glass-ceramic techniques resulted in severe micro-cracking due to the thermal expansion mismatch between the parent glass and

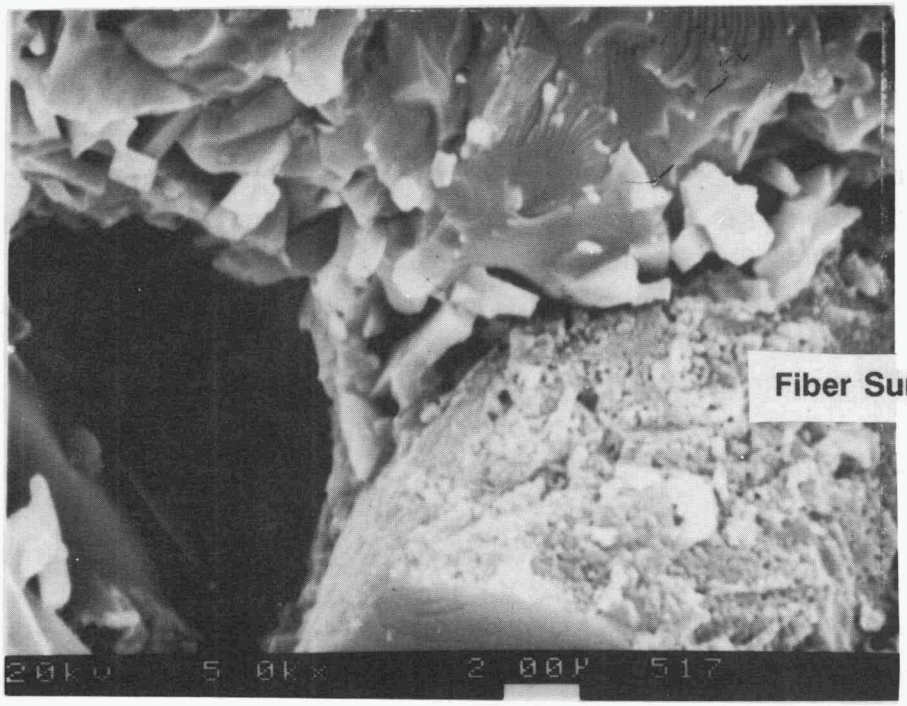

Figure 4. Nicalon-SiC/CMZP composite hot pressed in air

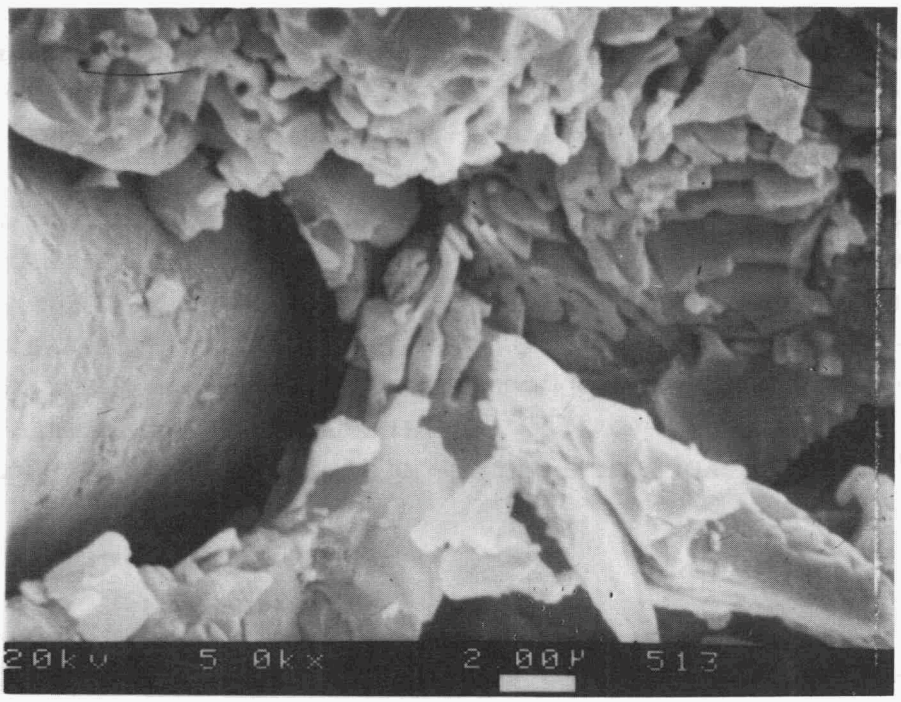

Figure 5. Nicalon/SiC CMZP composite hot pressed in Ar

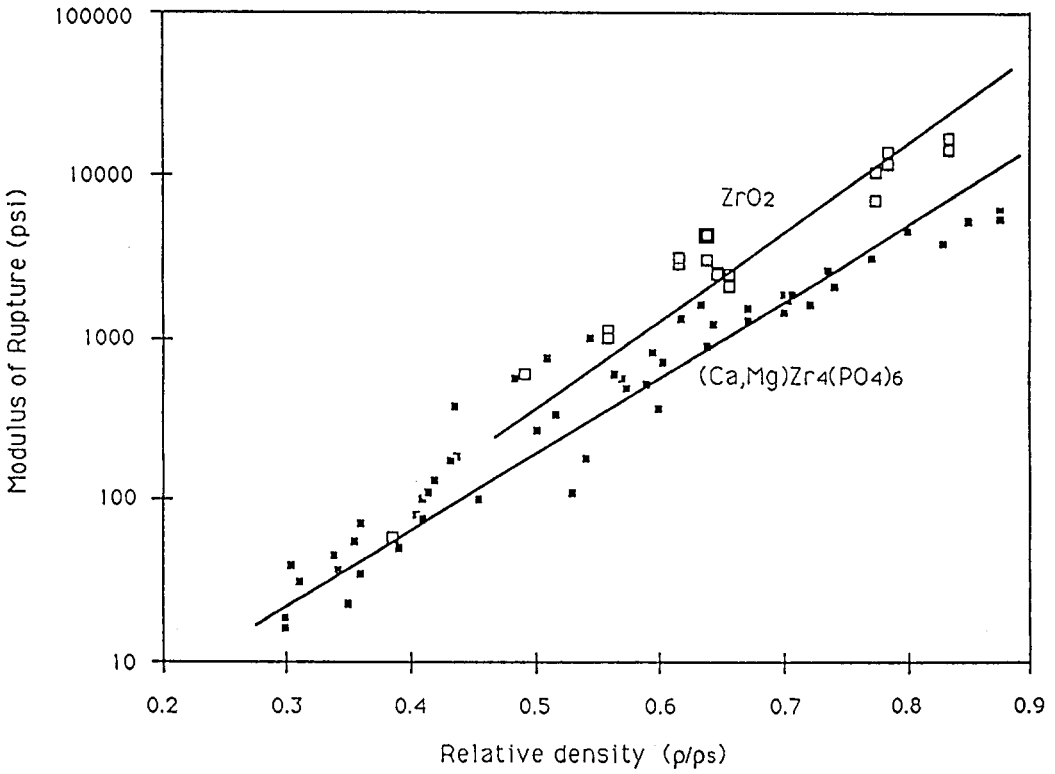

Figure 6. Flexural strength of lightweight $(Ca,Mg)Zr_4(PO_4)_6$ as a function of relative density

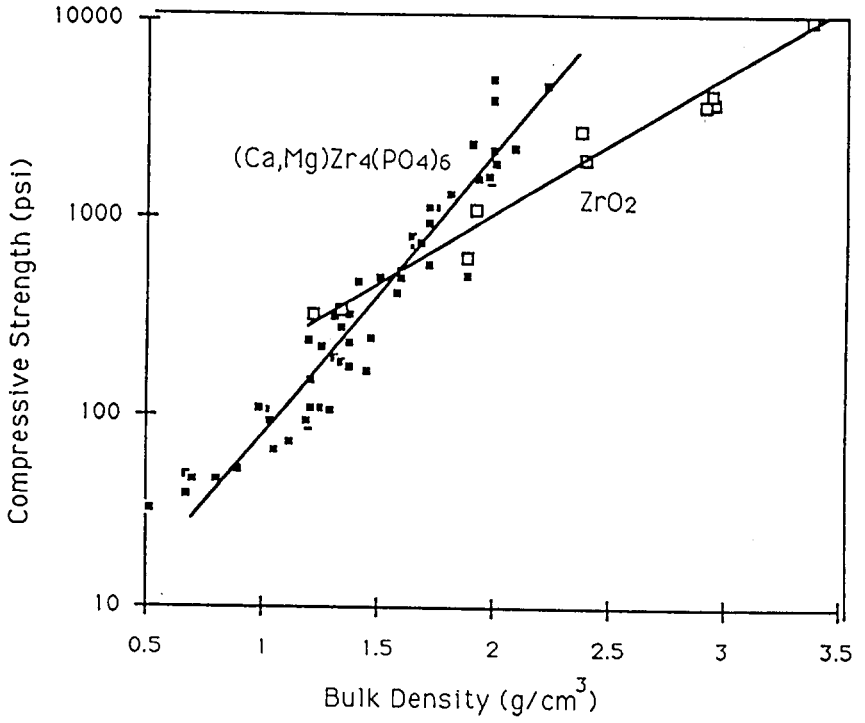

Figure 7. Compressive strength as a function of bulk density of lightweight $(Ca,Mg)Zr_4(PO_4)_6$ and stabilized zirconia

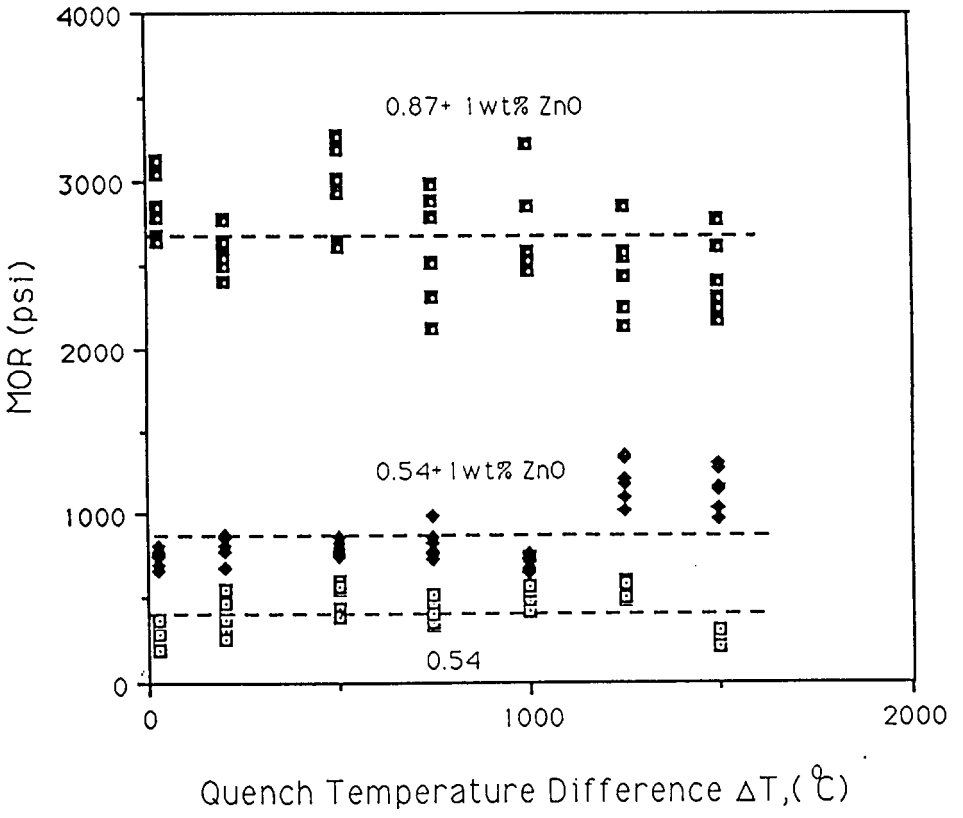

Figure 8. Thermal shock resistance of lightweight CMZP.

the recrystallized phase. To overcome this problem, two approaches have been taken. One is the development of an alternate method to produce near-zero thermal expansion β-eucryptite. A patent disclosure on this process has been filed and characterization of the thermal and mechanical properties has been initiated. The second approach is to reduce the viscosity of the glass during recrystallization and thus relieve the internal stresses induced by the volume change. The viscosity of the glass was reduced by adding 2 wt% CaO to the modified β-eucryptite. After heat treatment, the resulting material had no microcracks; however, the melting temperature was reduced to 1000°C making this material unacceptable for high temperature applications.

The corrosion resistance of modified β-eucryptite processed by conventional glass-ceramic techniques and by the newly developed method has been compared to a commercial lithium alumino-silicate glass-ceramic (LAS) provided by Garrett Auxiliary Power Div., Allied Signal Corp., Phoenix, AZ. Samples were exposed to either aqueous HCl solutions at 25°C and 100°C or molten Na_2SO_4 at 1000°C and their weight change was monitored as a function of exposure time. When exposed to HCl, greater weight loss was recorded for the modified β-eucryptite than for the commercial LAS. With exposure to molten Na_2SO_4, both materials gained weight due to the formation of an alkali melt. The β-eucryptite material gained more weight than the commercial LAS. Scanning electron microscopy with EDX analysis of the exposed specimens revealed that the corrosion of the β-eucryptite produced by the conventional technique resulted from acid or molten salt penetrating the sample through the microcracks and removing $AlPO_4$ from the lattice. The β-eucryptite produced by the new method was corroded to a lesser extent because the $AlPO_4$ was removed from the sample surface only.

Status of milestones

Table 1 contains the key to major milestones and Figure 9 contains the milestone status chart.

Table 1. KEY TO MAJOR MILESTONES (WBS ELEMENTS)

		Completion Date
VPI 2.4.1	Property Optimization by Hot Isostatic Pressing	July 31, 1992
VPI 2.4.2	Optimization of Compositions	Mar. 31, 1991
VPI 2.4.3	Mechanical Properties of NZP Ceramics	
	a. Characterization at Room Temperature	Dec. 31, 1991
	b. Characterization at High Temperature	July 31, 1992
VPI 2.4.4	Fiber Reinforced Composites	
	a. Synthesis of SiC/NZP Composites	July 31, 1991
	b. Characterization of Mechanical Properties	July 31, 1992
VPI 2.4.5	Lightweight Insulation	Sept. 30, 1991
VPI 2.4.6	Characterization of In-Situ Toughened Composites	
	a. Modified β-eucryptite Composites	July 31, 1992
	b. NZP Whisker Reinforced Composites	July 31, 1992
VPI 2.4.7	Submit Technical Paper on Research Results for Publication	July 31, 1991
VPI 2.4.8	Final Report	Sept. 30,1992

Figure 9 Status of milestones

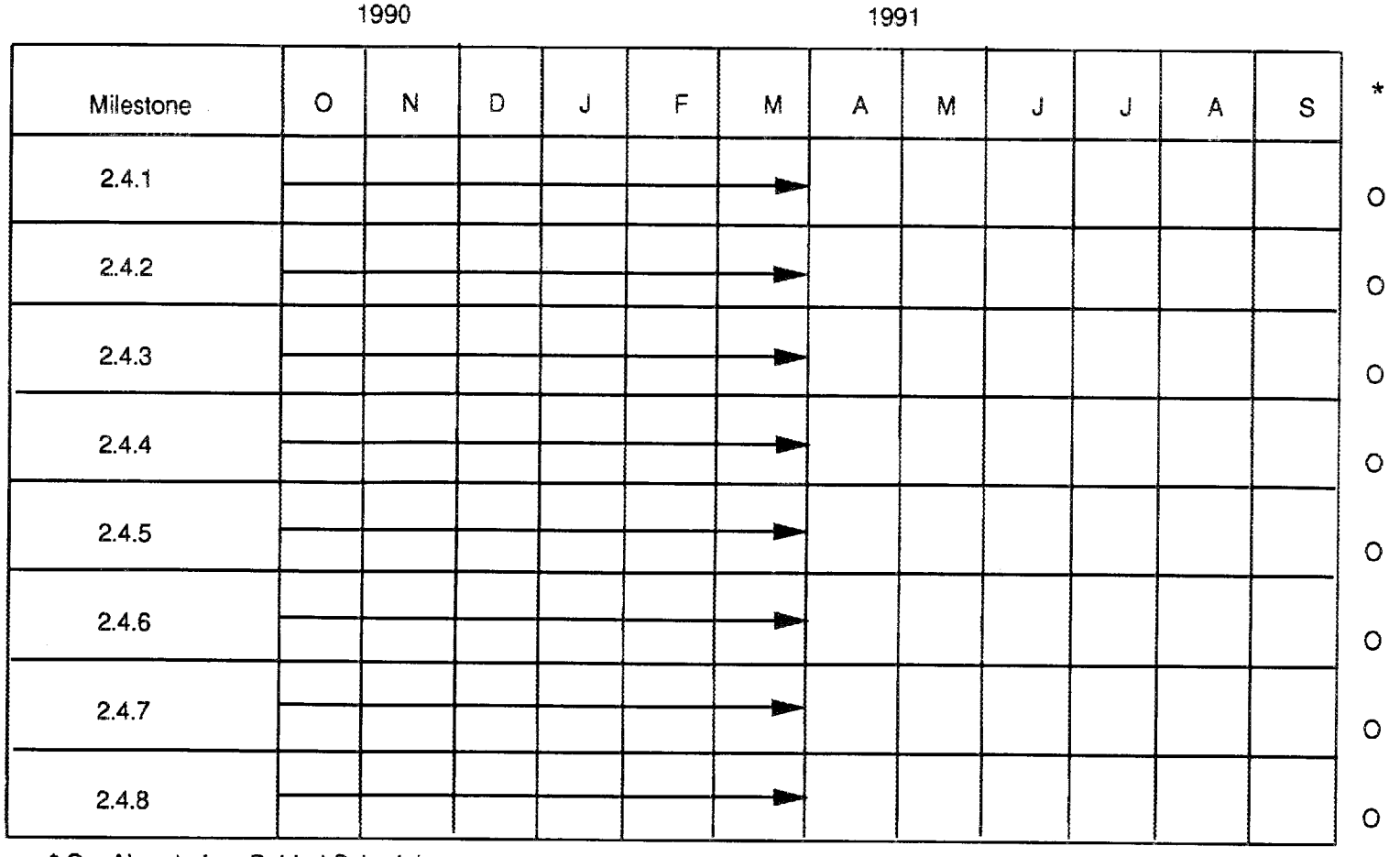

* On, Ahead of, or Behind Schedule

Publications

1. D. Hirschfeld and J. Brown attended the 28th Automotive Technology Development Contractor's Coordination Meeting on Oct. 22-24, 1990. Dr. Brown gave a presentation entitled "Development of Ultra-Low Expansion Ceramics."

2. Y. Yang and T. Li attended the Materials Research Society meeting in Boston, MA on November 28-29, 1990 where Y. Yang presented a paper entitled "Effect of Grain Size and Microcracking on the Thermal Expansion of $(Ca_{0.6},Mg_{0.4})Zr_4(PO_4)_6$."

3. Two patent disclosures have been submitted to Virginia Tech Intellectual Properties for evaluation:

1. NZP Whisker Ceramics

2. An In-Situ Whisker Reinforced Glass-Ceramic Based on β-Eucryptite

4. The following presentations were made at the Second Annual Program Review of the Center for Advanced Ceramic Materials at Virginia Tech, Blacksburg, VA, on February 7 and 8, 1991:

1. Synthesis and Thermal Properties of $(Ca_{1-x},Mg_x)Zr_4(PO_4)_6$, S. Van Aken
2. Effect of Grain Size and Microstructure on the Thermal Expansion of $(Ca_{1-x},Mg_x)Zr_4(PO_4)_6$, Y. Yang and T. K. Li
3. Lightweight $(Ca_{1-x},Mg_x)Zr_4(PO_4)_6$ Ceramics, D. M. Liu
4. Synthesis and Thermal Properties of $(Rb,Cs)Zr_2(PO_4)_3$, D. Raqué
5. Corrosion Resistance of Modified β-Eucryptite, L. Battu

Posters were presented on Fiber-Reinforced CMZP Ceramics, Corrosion Resistance of Modified β-Eucryptite, Processing of Modified β-Eucryptite, and Development of Lightweight CMZP Materials.

References

1. T.M.Besmann, "SOLGASMIX-PV - A Computer Program to Calculate Equilibrium Relationships in Complex Chemical Systems," ORNL/TM-5775, Oak Ridge National Laboratory, Oak Ridge, TN, April, 1977.

1.3 THERMAL AND WEAR COATINGS

Fabrication and Testing of Corrosion-Resistant Coatings

D. P. Stinton, J. C. McLaughlin, and L. Riester (Oak Ridge National Laboratory)

Objective/scope

Sodium corrosion of silicon carbide and silicon nitride components in gas turbine engines is a potentially serious problem. The outer surfaces of SiC and Si_3N_4 parts oxidize at high temperatures to form an SiO_2 layer that inhibits further oxidation. However, sodium (which is present in high-temperature combustion atmospheres) reacts with the SiO_2 layer, such that it is no longer protective. The objective of this program is to develop a coating that will protect the underlying SiC or Si_3N_4 from sodium corrosion and provide simultaneous oxidation protection. To evaluate the behavior of potential materials in sodium-containing atmospheres, the corrosion resistance of hot-pressed samples will first be evaluated. A chemical vapor deposition (CVD) process will be developed for application of the appropriate coatings. The effect of the combustion environment upon coating characteristics such as microstructure, strength, adherence, and other properties will then be evaluated.

Technical progress

Development of coatings to protect SiC or Si_3N_4 turbine engine components from sodium and steam corrosion continued this period. In order to protect engine components from corrosive atmospheres, the coatings must adhere to the substrates and remain impermeable and crack free throughout the life of the engine. Considering the large number and severity of the thermal cycles, adherence is a serious problem that can only be addressed by carefully designed coatings. Zirconia-toughened alumina coatings for SiC and Si_3N_4 engine components have been under development at GTE Laboratories for several years. They addressed the adherence issue by applying an AlN interlayer to the substrate prior to deposition of the coating. The purpose of the AlN interlayer was to improve the adherence of the coating to the substrate by forming a thin reaction layer and to allow a gradual increase in the coefficient of thermal expansion (CTE) of the coatings from that of the substrate (5×10^{-6}/°C) to that of the coating ($> 8 \times 10^{-6}$/°C). Despite this, Al_2O_3 coatings could never be applied to SiC or Si_3N_4 without cracking or spalling. Coatings that were applied at 1000°C could not be utilized at turbine temperatures above 1200°C because the coatings would still crack when heated due to the mismatch in thermal expansion. Coatings that were applied at higher temperatures to avoid cracking on heating would spall when cooled to room temperature, again because of the large thermal expansion mismatch.

To avoid cracking or spalling, the coefficient of thermal expansion of protective coatings must still more closely match that of the substrate. Experience at GTE Laboratories indicates that the best adherence (for coated cutting tools) is achieved when the CTE of the coating is slightly less than the CTE of the substrate. Under these conditions the coating will be placed in compression at temperatures less than the deposition

temperature. The coatings are, of course, much stronger (more resistant to cracks) in compression than in tension.

Utilizing the above concept, the list of potential materials for corrosion protection becomes very limited. The material must be an oxide (for oxidation resistance) with a CTE less than or equal to SiC. Protective coatings for carbon/carbon composites are of interest because these materials must also have very low CTEs and be stable to very high temperatures. Therefore, a search of the literature dealing with the oxidation protection of carbon/carbon composites has identified several coatings with the potential for improved corrosion resistance. Table 1 is a partial listing of several materials that appear promising.

Table 1. Refractory oxides with potential for corrosion protection

Compound	Density (g/cm^3)	Thermal expansion coefficient ($\times 10^{-6}\ °C^{-1}$)
Ta_2O_5	8.02	3.6
$3Al_2O_3 \cdot 2SiO_2$	3.20	5.7
Al_2TiO_5	3.68	2.2
$ZrTiO_4$		*
$HfTiO_4$		*
$Ta_2O_5 \cdot 6ZrO_2$		*
$Ta_2O_5 \cdot 6HfO_2$		*
SiC	3.21	5.5
Si_3N_4	3.19	3.0

*CTEs of these materials have been reported to be very low.

In order to more easily evaluate the corrosion resistance of potential materials, dense pellets of the materials listed in Table 1 are being purchased or prepared by hot pressing. Commercial suppliers were identified that could provide dense pellets of $ZrTiO_4$, $HfTiO_4$, and Al_2TiO_5. These materials have been ordered and will be corrosion tested upon arrival. A specimen of $3Al_2O_3 \cdot 2SiO_2$ was hot pressed at Oak Ridge National Laboratory. The sample appeared to be dense when examined at 400X with the optical microscope. X-ray diffraction of this pellet showed that it was mullite with no unreacted Al_2O_3 or SiO_2. Specimens of $Ta_2O_5 \cdot 6ZrO_2$ and $Ta_2O_5 \cdot 6HfO_2$ have been prepared both by hot and cold pressing and sintering. Unfortunately, X-ray diffraction patterns showed that the desired phases have not yet been produced. Specimens of Al_2TiO_5 and $ZrTiO_4$ prepared by hot pressing were corrosion tested for 100 h at 1000°C in a combustion atmosphere. Examination of the samples after corrosion testing was very encouraging as they appeared to be unaffected by the corrosive atmosphere. A control sample of SiC in the corrosion test had a thick layer of SiO_2 glass.

One additional material of particular interest is Ta_2O_5 because of its reported corrosion resistance, low thermal expansion (3.6×10^{-6}/°C), and ease of CVD. Therefore, development of a process for the deposition of Ta_2O_5 coatings was initiated this period. A search of the technical literature revealed several references that identified suitable conditions for the deposition of dense Ta_2O_5 films onto single-crystal silicon substrates. After a limited amount of experimentation, adherent coatings were deposited onto silicon substrates at a temperature of 1200°C and pressures varying from 5 to 760 torr. Characterization of the coatings by X-ray diffraction revealed crystalline Ta_2O_5. The process has been modified to deposit the coatings onto SiC-coated graphite disks that simulate SiC and Si_3N_4 engine components.

Protective coatings for SiC and Si_3N_4 engine components are being corrosion tested in a simulated engine atmosphere at 1000°C. Initially, natural gas and building air were mixed in a 1:10 ratio to simulate the engine environment (Table 2). Sodium was introduced by pumping a mixture of NaOH and water (1g NaOH/1 H_2O) into the furnace. Unfortunately, the atmosphere contained nearly 20% water vapor instead of the desired 7.3%. In addition, the burning of natural gas created a hot spot that occasionally cracked the alumina tube. Therefore, it was decided to purchase a premixed bottle of gas that, when mixed with the NaOH solution and heated to 1000°C, would produce the engine environment. Thermodynamic calculations were performed to determine the appropriate gas composition – a mixture of 5.2% O_2, 80.2% N_2, and 14.6% CO_2 plus the NaOH solution (Table 2). Gas bottles of this composition have been ordered to use in future corrosion tests.

Table 2. Combustion atmospheres

Gas	Typical combustion environment (%)	Equilibrium composition (bottled gas + H_2O-NaOH solution)
CO_2	13.6	13.4
O_2	3.5	4.9
N_2	75.3	73.8
H_2O	7.3	7.9
Alkali	20 ppm	20 ppm

Development of Adherent Ceramics Coatings to Reduce Contact Stress Damage of Ceramics
- H. E. Rebenne and J.H. Selverian (GTE Laboratories Incorporated)

Objective/Scope

The objective of this program is to develop oxidation-resistant, high toughness, adherent coatings for silicon-based ceramics for use in an advanced gas turbine engine. These coatings will be deposited by chemical vapor deposition (CVD) onto reaction bonded Si_3N_4 (RBSN), sintered SiC (SSC), and HIP'ed Si_3N_4 (HSN). The coating will be designed to provide the best mix of mechanical, thermal and chemical properties for the application.

Technical Progress

Contact Stress/Friction Coefficient Tests

Room-temperature pin-on-disk tests on coated samples are underway. The test procedure being used was described in the April 1990 Bimonthly Progress Report. Sets of pins and disks of RBSN, SSC, and HPSN were coated with AlN and Al_2O_3+ZrO_2 coatings. The friction results to date are shown in Table I. In previous reports, the velocity of the pin relative to the disk was incorrectly reported as 0.1 m/s; the actual velocity used in these tests was 0.01 m/s.

Table I. Results from pin-on-disk friction tests of uncoated and coated RBSN, HPSN, and SSC. All tests were done on self-mated samples. Reported values, unless otherwise indicated, are an average of three tests on the same pair of samples.

Material	Test Temperature (°C)	Breakaway Friction Coefficient	Kinetic Friction Coefficient	
			initial	after 1km
RBSN				
uncoated	25	0.1	0.5	0.8
coated	25	0.2	0.2	0.8*
HPSN				
uncoated	25	0.3	—	0.8
uncoated	1000	0.15	0.5	0.9*
SSC				
uncoated	25	0.1	—	0.3
uncoated	1000	0.25	0.5	0.7

*only 1 sample has been tested at this condition to date.

The remaining pin-on-disk tests are currently being carried out. It is anticipated that they will be completed in time for presentation in the June 1991 Bimonthly Progress Report.

Oxidation Testing

Oxidation tests of the current coating configuration were suspended until a meeting could be held with the ORNL Technical Monitor, D.P. Stinton, to review recent findings. Results obtained to date have shown that the current coating configuration is not oxidation-resistant for 500 hours at temperatures above 1000°C. The poor protection given by the coating is due to cracks in the Al_2O_3+ZrO_2 layer, which allow oxygen to penetrate this layer and react with AlN (see "Residual Stress" section below). The kinetics of oxidation of AlN are sufficiently slow at 1000°C for the coating to protect the substrate for 500 hours [1]. However, above 1000°C, the oxidation rate of AlN is rapid enough to cause the AlN to fully oxidize to Al_2O_3 before 500 hours. This oxidation is accompanied by cracking, which in turn worsens the problem.

In an effort to produce a crack free coating for oxidation testing, Al_2O_3 was deposited onto AlN-coated Si_3N_4 by electron beam evaporation at 200°C. The AlN was deposited by the standard CVD technique. The Al_2O_3 deposition occurred at low temperatures and was used to produce a crack-free coating. However, in some areas the AlN was exposed where the Al_2O_3 appeared to have spalled off during handling. The spalling of the Al_2O_3 coating was attributed to the poor adhesion typical of this type of deposition technique. Oxidation testing of this sample resulted in similar behavior to that of the coated substrate.

Based on the apparent inability to produce a crack-free oxide coating in this system, it is suggested that no further oxidation tests be done with the current coating configuration. Instead, an alternative coating configuration that is better able to accommodate stress is being searched for. This was discussed with D.P. Stinton on April 2 and will be discussed further before doing any new work.

In an effort to reduce the residual stresses in the coating a ductile material will be deposited on the substrate before Al_2O_3+ZrO_2 deposition. The presence of a 'thick' ductile interlayer (~50 μm) should act to reduce the stresses in the coating layer by plastically deforming. This approach has proven successful in the project "Analytical and Experimental Evaluation of Joining Silicon Nitride to Metal and Silicon Carbide to Metal for Advanced Heat Engine Applications" [2].

Residual Stress

The cause of cracking in the Al_2O_3+ZrO_2 layer was determined to be large residual stresses in the coating due to thermal expansion mismatch between Al_2O_3 or ZrO_2 and Si_3N_4 or SiC. Figure 1 shows the coefficients of thermal expansion (CTE) for the materials in this system. Using this data along with the Young's modulus (E_c) and Poisson's ratio for the coating (v_c), the residual stress in the coating (σ_f) was calculated at 20°C as a function of deposition temperature (T_d) from Eq. 1:

$$\sigma_f = \frac{1}{1-v_c}\int_{20°C}^{T_d} E_c(T)\,\Delta CTE\,dT \qquad \text{Eq. 1}$$

Calculated room-temperature stress values for Al_2O_3 on Si_3N_4, Al_2O_3 on SiC, AlN on Si_3N_4, and AlN on SiC are shown in Fig. 2. It should be noted that the stress in the outer layer of the coating is nearly independent of the presence of an interlayer provided that the interlayer is sufficiently thin [3]. For this system, an AlN interlayer 10 μm thick is sufficiently thin [3]. Hence, it is only necessary to calculate the stress due to the total difference in CTE between the outer coating layer and the substrate. Notice that, in all cases, the coating has a large tensile residual stress at room temperature due to the fact that the coating has a larger CTE than the substrate.

This suggests that the coating and interlayer should both be cracked in the as-coated state, which has been confirmed by scanning electron microscope examination for coatings on Si_3N_4.

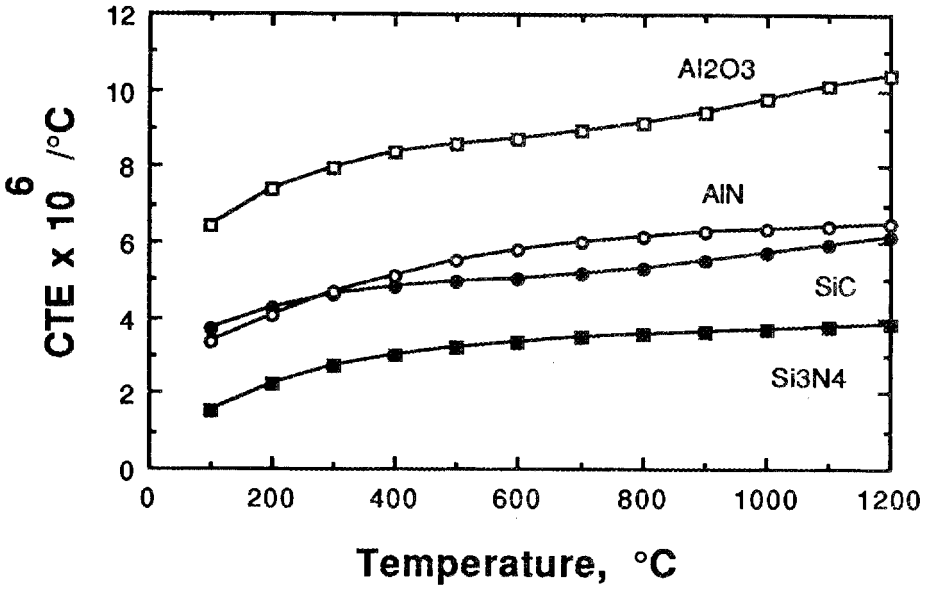

Figure 1. Thermal expansion coefficients of the various materials present in this system over the temperature range 20°C to 1400°C.

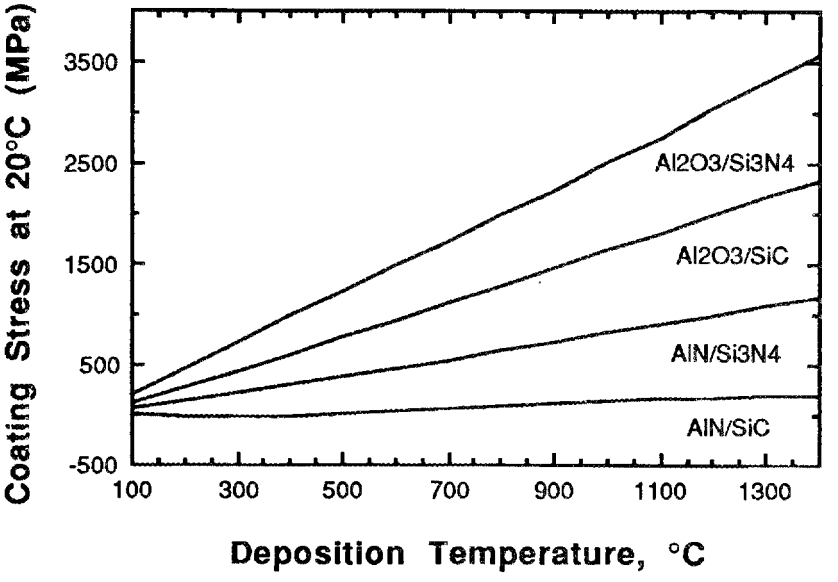

Figure 2. Calculated room-temperature stress in Al_2O_3 and AlN coatings on Si_3N_4 and SiC.

In order to confirm the calculations described above, residual stress measurements were done using the radius of curvature method. Samples of HSN, measuring 25.4 mm x 6.35 mm x 0.292 mm were stress-relieved at 1200°C in vacuum for 1 hour. These samples were then coated on one side with AlN at 1000°C. The weight gain was converted into a coating thickness, assuming a uniform coating along the entire sample. The radius of curvature was measured over a length of 20 mm with an optical profilometer and the stress in the AlN film was calculated according to Equation 2 [4].

$$\sigma_c = \frac{E_s t_s^2}{6t_f(1-\upsilon_c)} \left(\frac{1}{R_c} - \frac{1}{R_{uc}}\right) \qquad \text{Eq. 2}$$

where E_s is the Young's modulus of the substrate, 300 GPa, t_s is the thickness of the substrate, 0.292 mm, t_c is the thickness of the AlN coating, υ_c is Poisson's ratio of the AlN coating, 0.24, R_c is the radius of curvature of the coated substrate, and R_{uc} is the radius of curvature of the uncoated substrate. The results of the residual stress measurements are listed in Table II.

Table II. Results from residual stress measurements of AlN coatings on HSN.

Sample	Weight Gain (mg)	Coating Thickness (μm)	R_{uc} (m)	R_c (m)	Stress in AlN Coating (MPa)
A	3.5	11.0	0.9213	0.4404	673
B	2.81	8.84	0.8474	0.3925	709
C	4.45	14.0	0.9027	0.3120	708

Samples A and B from Table II were examined in an SEM for cracks. Cracks were seen in sample B but not in sample A. The cracks in sample B were approximately 40 nm wide and were spaced 125 μm apart. The crack size and spacing were used to estimate the amount of stress relief that took place by the cracking (see February Bimonthly Progress Report). The result was 98 MPa. Adding this stress to the measured stress in the AlN coating on sample B (709) gives 807 MPa. This result can be compared to predicted residual stresses shown in Figure 2. For AlN deposited on Si_3N_4 at 1000°C the predicted stress was 811 MPa. The measured and predicted results are in good agreement. This confirms that large stresses are present in the CVD coatings upon cooling after deposition, and these stresses are relieved by cracking.

Future Plans for 1991

In order to address the cracking problem more thoroughly, the modeling part of this project will be restarted. The effects of cracks in the coating on the behavior of a coated part subjected to contact stress will be examined. Finite element analysis and fracture interface mechanics will be used to study the propagation of cracks under the stress field that is generated during contact stress. The results of these investigations will be compared to the behavior of actual coated samples subjected to a scratch test. This information can be used to optimize the coating layer thicknesses and materials to obtain improved performance.

Status of Milestones

Milestone	Due	Status
Microstructural evaluation of the Al_2O_3+ZrO_2 composite layer.	12/89	Completed
Studies of first generation coating configuration to determine cause of failure during oxidation tests at 1200°C and 1375°C.	03/90	Completed
Modification of coating configuration to improve oxidation resistance at ≥1200°C. Develop CVD process and coat samples for testing the following modifications: a) add Al_2O_3 layer between AlN and the Al_2O_3+ZrO_2 composite layer.	09/90	Delayed to 3/91 due to necessary equipment modifications.
Feasibility study of measuring friction coefficient and contact stress damage using conventional pin-on-disk or ball-on-disk wear tests.	12/90	In progress.
Performance tests of modified coating configuration including: i) 500 hour oxidation, ii) thermal shock, and iii) flexure strength. Each test will be done on coated and uncoated samples. All tests will be conducted at room-temperature,1000°C, 1200°C, and 1375°C.	03/91	Will be delayed due to delays in above milestones.
Test feasibility of coating a commercial part or equivalent.	06/91	On schedule.
Submit draft of final report covering Phase II results.	09/91	On schedule.

Publications and Meetings

D.R. Johnson (ORNL), D.P. Stinton (ORNL), E. Long (ORNL), S. Winslow (ORNL), and T. Besmann (ORNL), met with H.J. Kim (GTE Laboratories), H.E. Rebenne (GTE Laboratories), and S.F. Wayne (GTE Laboratories) on April 2 at Oak Ridge National Laboratory. The current status of the project was discussed. It was decided that E. Long and staff from GTE Laboratories would travel to Garrett Turbine Engine Company to learn more about specific use conditions and requirements of coatings in the gas turbine engine. This meeting is scheduled for April 19. After this meeting, the remaining milestones for Phase II may be modified to direct the program toward achieving workable coatings for specific parts and conditions.

References

1. T. Sato, K. Haryu, T. Endo, and M. Shimada, "High temperature oxidation of hot-pressed aluminum nitride by water vapour," J. Materials Science, Vol. 22, 2277-2280 (1987).

2. S. Kang, J. Selverian, H. Kim, and D. O'Neil, "Analytical and Experimental Evaluation of Joining Silicon Nitride to Metal and Silicon Carbide to Metal for Advanced Heat Engine Applications," subcontract #DE-AC05-840R21400, GTE Laboratories Incorporated, (1990).

3. T.-L. Sham and V.K. Sarin, "Residual Stress Calculations in Coating Configurations using Finite Element Analysis," Ceramics Eng. and Sci. Proc., Vol. 9 (9,10), 1189-98 (1988).

4. P.A. Flinn, D.S. Gardner, and W.D. Nix, "Measurement and Interpretation of Stress in Aluminum-Based Metallization as a Function of Thermal History," IEEE Transactions on Electron Devices, vol. ED-34, no. 3, p. 689-698, March 1987.

Wear-Resistant Coatings

M. H. Haselkorn (Caterpillar, Inc.)

Objective/scope

The goal of this technical program is to develop wear-resistant coatings for piston ring and cylinder liner components for low heat-loss diesel engines.

Wear resistant coatings will be applied to metallic substrates using plasma spraying, vapor deposition (CVD/PVD), and enameling coating processes. First, the adherence of each coating for each coating process to the metallic substrate will be optimized. Methods which can be used for improving the adherence of these coatings include development of unique substrate preparation methods before application of the coating, grading coating compositions to match thermal expansion; compositional changes; laser or electron beam fusing and/or optimizing coating thickness. Once the adherence of each coating system is optimized, each coating will be screened for friction and wear at 350°C under lubricated conditions. Coatings which show promise after this initial screening will be further optimized to meet the friction and wear requirements. Then, the optimized coating systems will be fully characterized for oxidation resistance, adherence, uniformity, and thermal shock resistance, as well as friction and wear.

Selection of the most promising coatings and coating processes will be made after the characterization task. Criteria for selection will include not only performance (i.e., wear, adhesion, friction coefficient, thermal shock resistance and thermal stability) but also manufacturability and economic factors, as well. Using both criteria a coating system having acceptable cost/benefit relationships will be selected.

Technical progress

Candidate wear resistant piston ring coatings identified from the pin-on-disk friction and wear screening included:

1. Plasma sprayed chromia-silica composite,
2. Plasma sprayed high carbon iron-molybdenum blend,
3. Plasma sprayed, self-lubricating, PS212, and,
4. Mid-temperature chemical vapor deposited Ti(C,N).

Candidate wear resistant cylinder liner coatings also identified from this friction and wear screening included:

1. Low temperature arc vapor deposited (LTAVD) chrome nitride,
2. Plasma sprayed chromia-silica composite, and,
3. Plasma sprayed high carbon iron-molybdenum blend.

Each candidate piston ring/cylinder liner pair was then further optimized for friction and wear using the Hohman A-6 Double Rub Shoe Friction and Wear Test Machine. All tests were run at 350 C, under lubricated conditions. The results of this testing are contained in Tables 1-3. (Note: one of the overall goals of this program is to obtain an average wear coefficient of at least 1.0x10-8 $mm^3/N-m$ for each coating pair.)

Running plasma sprayed high carbon iron-molybdenum coated rub shoes against a plasma sprayed chromia-silica coated disk (Table 1) produced coefficient of friction values below 0.15 and average wear coefficients ranging from 2.3 to 0.4x10-8 $mm^3/N-m$ for the shoes and from 2.43 to 14.2x10-8 $mm^3/N-m$ for the disks. The Hohman test results obtained from this coating pair showed that this piston ring/cylinder liner coating pair would meet the program goals for both friction and wear.

Coefficient of friction values of above 0.2 were obtained running plasma sprayed PS212 rub shoes against a plasma sprayed chromia-silica disk. These high coefficient of friction values, in turn, caused high PS212 wear coefficients and, for this reason, this coating pair ran only 480 hours before the chromia-silica coating completely wore through the PS212. Table 1 lists average wear coefficients of 9.11x10-9 for the chromia-silica and 1.70x10-7 $mm^3/N-m$ for the PS212 coatings.

Running plasma sprayed chromia-silica or mid-temperature chemical vapor deposited titanium carbo-nitride coated rub shoes against the plasma sprayed chromia-silica coated disks produced friction coefficients above 0.2 and average disk wear coefficients ranging from 10-5 to 10-6 $mm^3/N-m$, respectively. Very little wear was apparent on either set of rub shoes. The friction and average disk wear coefficients for these coating pairs were above the program goals.

Another coating pair which met the program's friction and wear goals is plasma sprayed high carbon iron-molybdenum rub shoes running against a low temperature arc vapor deposited (LTAVD) chrome nitride coated disk (Table 2). This coating pair had coefficient of friction values below 0.15 and, in three tests, had average wear coefficients which ranged from 1.23x10-9 to 7.16x10-8 $mm^3/N-m$ for the high carbon iron-molybdenum coated shoes and from 3.13x10-7 to 1.48x10-8 $mm^3/N-m$ for the chrome nitride coated disk.

Running plasma sprayed chromia-silica or mid-temperature chemical vapor deposited titanium carbo-nitride coated rub shoes against the plasma sprayed chromia-silica coated disks produced friction coefficients above 0.2 and average disk wear coefficients ranging from 10-5 to 10-6 $mm^3/N-m$, respectively. Very little wear was apparent on either set of rub shoes. The friction and average disk wear coefficients for these coating pairs were above the program goals.

Running either plasma sprayed chromia-silica or mid-temperature titanium carbo-nitride CVD rub shoes against the LTAVD chrome nitride coated disk resulted in coefficient of friction values above 0.20 and very high chrome nitride average wear coefficients (10-6 mm^3/N-m). For this reason, these tests had to be terminated after only 5-30 minutes of testing since none of the chrome nitride coating remained on the surface of the disk.

Average disk wear coefficients of 1.04x10-4 mm^3/N-m were obtained running plasma sprayed PS212 coated rub shoes against a chrome nitride coated disk. This wear coefficient was well above the desired 10-8 mm^3/N-m wear coefficient of this program. High friction coefficients were the probable reason for the poor average wear coefficient for the PS212.

The Hohman friction and wear results for the mid-temperature titanium carbo-nitride, LTAVD chrome nitride and chromia-silica coated rub shoes running against plasma sprayed high carbon iron-molybdenum coated disks are contained in Table 2. Running the mid-temperature titanium carbo-nitride rub shoes against the high carbon iron-molybdenum disk resulted in friction coefficients of below 0.15 and average wear coefficients of 1.42x10-9 to 9.55x10-8 mm^3/N-m for the titanium carbo-nitride coated shoes and 1.56x10-8 to 1.86x10-8 mm^3/N-m for the high carbon iron-molybdenum shoes. These results indicate that this coating pair will meet the friction and wear goals of this program.

Wear testing of the 5 micron thick chrome nitride coated rub shoes against the high carbon iron-molybdenum coated disks could not be completed due to the chrome nitride coating spallation. The first instance of spallation occurred during a heat-up cycle after the test was stopped to obtain an initial set of wear measurements. Prior to the castrophic coating failure the rub shoe and disk had average wear coefficients of 10-9 mm^3/N-m. The second instance of coating spallation occurred prior to testing when the rub shoes were heated to the 350 C test temperature.

Friction coefficients below 0.15 and average wear coefficients of less than 10-9 mm^3/N-m were obtained for the rub shoes and the disk running plasma sprayed chromia-silica rub shoes against a high carbon iron-molybdenum disk. The friction and wear coefficients obtained from this coating pair were similar to those obtained running high carbon iron-molybdenum shoes against a chromia-silica disk (Table 3). These results indicate that this material pair can be interchanged, and either coating can be used for a cylinder liner or piston ring coating.

Wear curves were obtained for the high carbon iron-molybdenum blend running against the chromia-silica composite and the high carbon iron-molybdenum blend running against the LTAVD chrome nitride.

These wear curves were obtained by running the specimens on the Hohman A-6 Double Rub-Shoe machine, at 350 C, with a normal load of 89 N, and a surface velocity of 3.4 m/sec. During the testing, an experimental synthetic lubricant from Lubrizol was used. The lubricant was delivered to each shoe surface using a peristatic pump at a rate of 3mm/min. After every 120 minutes the test was interrupted to measure the wear on the shoe and disk surfaces. Wear curves for each coating pair were then developed from these wear

measurements. The wear curves for the high carbon iron-molybdenum running against the chromia-silica are contained in Figures 1A and 1B. Figures 2A and 2B contain the wear curves for the high carbon iron-molybdenum running against the chrome nitride.

The wear scar volumes measured on the high carbon iron-molybdenum coated rub shoes after 980 hours of friction and wear testing against the chromia-silica coated disks were 0.55, 0.27 and 0.05 mm^3, for Tests 56, 70, and 72, respectively (Figure 1B). The wear scars measured on two of the corresponding chromia-silica coated disks from Tests 56 and 70 were 0.05 and 2.0 mm^3. The third chromia-silica coated disk (Test 72) had a wear scar volume greater than 8.0 mm^3. However, over 50 percent of the volume of this wear scar occurred after 380 minutes of testing when one of the rub shoes "slipped" off the disk. Eliminating the wear which occurred when the rub shoe "slipped," the volume of the wear scar would have been less than 4.0 mm^3. The volumes of the wear scars measured on both the shoes and disks after 980 hours of testing indicated that this coating pair, a high carbon iron-molybdenum coated piston ring and a chromia-silica coated cylinder liner, will have wear rates which would meet the commercial durability requirements.

The wear curves obtained from running the high carbon iron-molybdenum coated rub shoes against a low temperature arc vapor deposited chrome nitride coated disk showed that very little wear occurred on either the rub shoes or the disk. One set of high carbon iron-molybdenum shoes exhibited essentially no wear after 680 hours of testing, Test 43, while the second set had a 0.2 mm^3 wear scar after 380 hours of testing, Test 54. However, the majority of the wear occurred during the initial 100 hours of testing and after this break-in period very little wear was seen on these shoes. The wear scars measured on the corresponding chrome nitride coated disks were 0.1 mm^3 or less. Although the wear scars on the chrome nitride disks were very small, the tests had to be terminated after 650 hours and 380 hours because the high carbon iron-molybdenum coated shoes had worn completely through the three micron thick chrome nitride coating. These wear curves show that a three micron thick chrome nitride coating, although meeting the program goals with respect to both friction and wear, will not meet the commercial durability goals. Using these wear curves as a guide, it was calculated that a 15 to 20 micron thick chrome nitride coating is required to meet these commercial durability goals.

The oxidation resistance of the plasma sprayed high carbon iron-Molybdenum and plasma spray chromia-silica coatings was evaluated by exposing these coatings to a simulated diesel exhaust atmosphere, for 500 hours at 400 C, in a tube furnace. The simulated diesel atmosphere was obtained from the mixing of various gases. The composition of this simulated diesel exhaust atmosphere was:

Oxygen (O2) 9.6%
Carbon Dioxide (CO2) 8.3%
Carbon Monoxide (CO) 1439 ppm
Nitric Oxide (NO) 1439 ppm
Hydrocarbons 264 ppm
Water Vapor (H20) 7.3%
Nitrogen (N2) Balance

The plasma sprayed chromia-silica coating was not affected by the simulated diesel exhaust atmosphere. No coating spallation or discoloration was observed on any of the five specimens exposed. In fact, the physical appearance of these specimens was identical to the physical appearance of plasma sprayed chromia-silica specimens which had not been exposed to the simulated diesel exhaust atmosphere.

The high carbon iron-molybdenum plasma sprayed coated discolored during the 500 hour exposure to the simulated diesel exhaust atmosphere. This discoloration was caused by oxidation of the iron on the surface of the specimens which was in direct contact with the atmosphere. The oxidation was limited to the very top surface of the coating and for this reason no significant increase in coating thickness or spallation occurred.

The thermal shock resistance of the plasma sprayed high carbon iron-molybdenum and plasma spayed chromia-silica coatings was determined by quenching plasma sprayed cast iron Falex specimens fifty (50) times from 650 C into boiling water. Each specimen was thermocoupled to assure that it attained a 650 C temperature prior to each quench. The thermocouple also illustrated that it took approximately seven (7) seconds for the Falex disks to be quenched from 650 to 100 C.

Cracks were noticed in both coatings after three thermal shock cycles. Although additional crack propagation occurred during the subsequent thermal shock cycles, no coating disbonding or coating spallation occurred. In addition, no excess oxidation was observed on any of the plasma sprayed coated specimens after completion of the thermal shock testing.

The cracking observed within these plasma spray coatings after the thermal shock testing is not considered a problem since plasma sprayed piston ring coatings used in current production diesel engines exhibit similar crack patterns and these cracks are not detrimental to the friction and wear properties of these coatings.

Wear resistant enamel coating development

To reduce the coefficient of friction of the enamel and improve its wear properties, one method evaluated was the addition of solid lubricants to the enamel. The solid lubricants evaluated included boron nitride, calcium flouride, barium fluoride, silver flake, and cesium oxythiomolybdate.

Silverflake additions above 5 weight percent were required to reduce the coefficient of friction of the enamel. Additions of 10 weight percent silver flake to the enamel reduced the coefficient of friction for the enamel from 0.036 (no additions) to 0.26. However, even with this coefficient of friction, the enamel had unacceptable wear rates during the initial pin-on-disk screening.

A 5 weight percent barium fluoride addition to the enamel reduced the coefficient of friction of the composition to 0.26. Further barium fluoride additions to the enamel increased the coefficient of friction to above 0.30. For this reason, the barium fluoride did not improve the wear resistance of the enamel.

Up to 10 weight percent additions of boron nitride, calcium fluoride, and cesium oxythimolybdate solid lubricants did not reduce the coefficient of friction and/or reduce the wear properties of the enamel.

The following combinations of solid lubricant additions to the enamel were evaluated:

1. 2.5 weight percent barium fluoride plus 5 or 10 weight percent silver flake, and,
2. 5 weight percent barium fluoride plus 5 or 10 weight percent silver flake.

These combinations of solid lubricants reduced the coefficient of friction of the enamel to 0.26. Again with this coefficient of friction the enamel compositions had unacceptable wear rates.

Examination of the wear surfaces of the enamel compositions after pin-on-disk friction and wear screening showed that the reason for the poor wear characteristics of the enamel was the presence of bubbles in its microstructure which significantly reduced the compressive strength of the enamel.

A program was initiated to determine if the number and size of the bubbles in the enamel could be reduced by changing the firing cycle of the enamel. Fast heating rates (less than one minute to attain temperature), slow heating rates (less than 2 C/minute), as well as long and short soak times at temperature were evaluated.

The fast heating rate resulted in the formation of very large bubbles in the enamel. Reducing the heating rate resulted in the formation of numerous small bubbles evenly dispersed within the enamel's microstructure. Time at temperature or increasing the soak temperature had little affect on the bubbles which developed within the enamel's microstructure. In summary, none of the firing cycle changes were able to produce a bubble free enamel microstructure.

Table 1
Hohman A-6 Friction and Wear Results
Candidate Piston Ring Coatings Run Against a Chromia-Silica Coated Disk

Candidate Piston Ring Coating	Time (Min.)	Average Wear Coefficient (mm3/N-m) Shoe Coating	Chromia-Silica
Chromia-Silica Composite	120	1.7x10-9	3.36x10-6
PS 212	480	7.61x10-7	9.11x10-9
Mid-Temperature Ti(C,N)	55	3.50x10-9	1.52x10-5
High Carbon Iron-Molybdenum	370	2.30x10-8	2.43x10-8
	975	7.56x10-8	1.66x10-8
	960	4.14x10-8	5.91x10-8
	899	4.48x10-9	1.42x10-7

Table 2
Hohman A-6 Friction and Wear Results
Candidate Piston Ring Coatings Run
Against a LTAVD Chrome Nitride Coated Disk

Candidate Piston Ring Coating	Time (Min.)	Average Wear Coefficient (mm3/N-m) Shoe Coating	Chrome Nitride
Chromia-Silica Composite	8	2.17x10-8	8.36x10-7
	5	2.17x10-7	6.95x10-6
Mid-Temperature Ti(C,N)	6	1.72x10-7	1.05x10-6
	5	2.95x10-7	6.35x10-6
	30	4.03x10-9	7.72x10-6
PS 212	120	7.86x10-9	1.04x10-4
High Carbon Iron-Molybdenum	120	1.23x10-9	3.13x10-7
	650	2.85x10-8	1.92x10-8
	375	7.16x10-8	1.48x10-8

Table 3
Hohman A-6 Friction and Wear Results
Candidate Piston Ring Coatings Run Against a
High Carbon Iron-Molybdenum Coated Disk

Candidate Piston Ring Coating	Time (Min.)	Average Wear Coefficient (mm3/N-m) Shoe Coating	High Carbon Iron-Mo
Mid-Temperature Ti(C,N)	34	9.55x10-8	1.68x10-8
	241	1.42x10-9	1.56x10-8

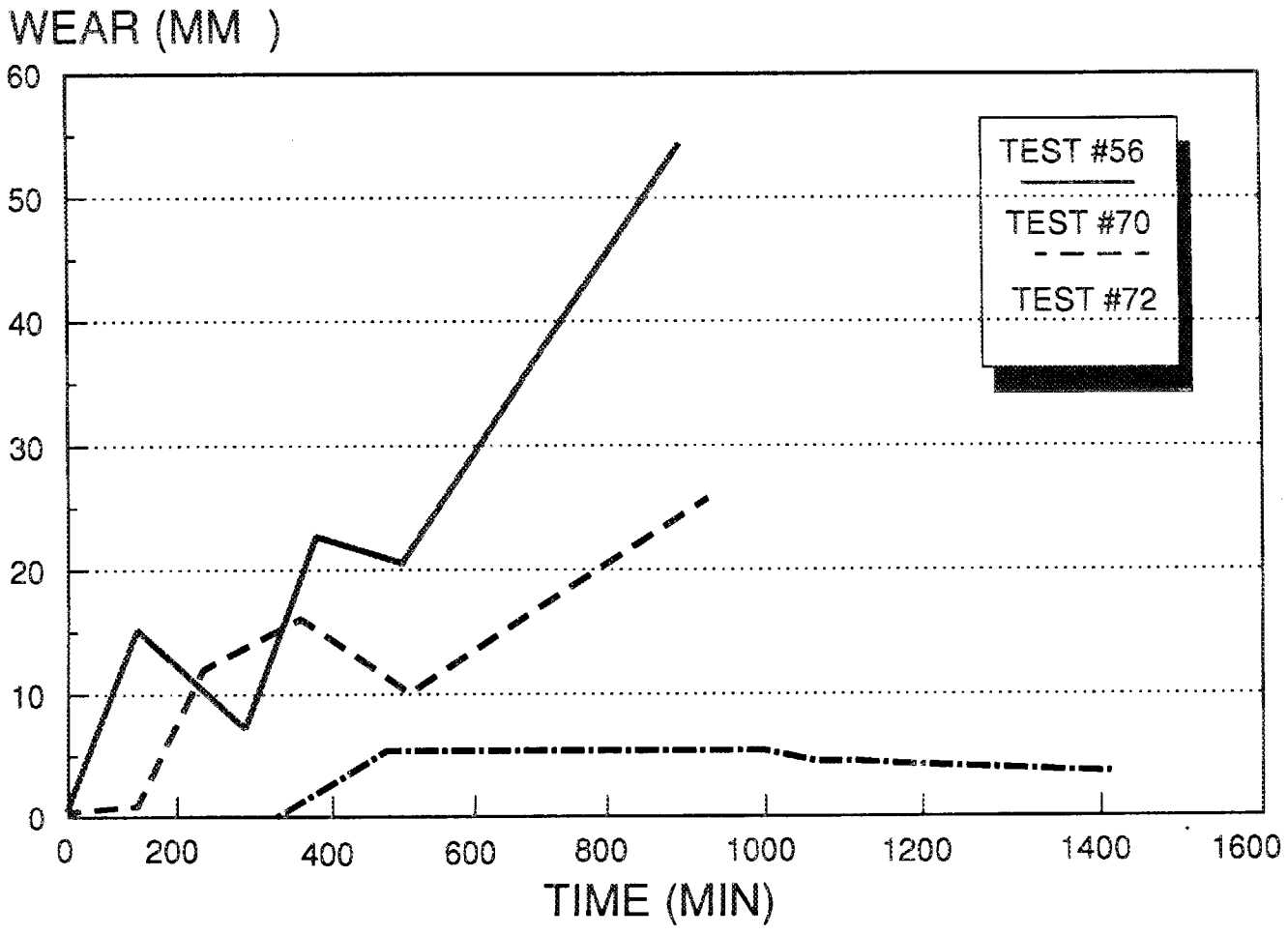

Figure 1A: Wear Curve For High Carbon Iron Molybdenum Shoes Running Against a Chromia-Silica Disk

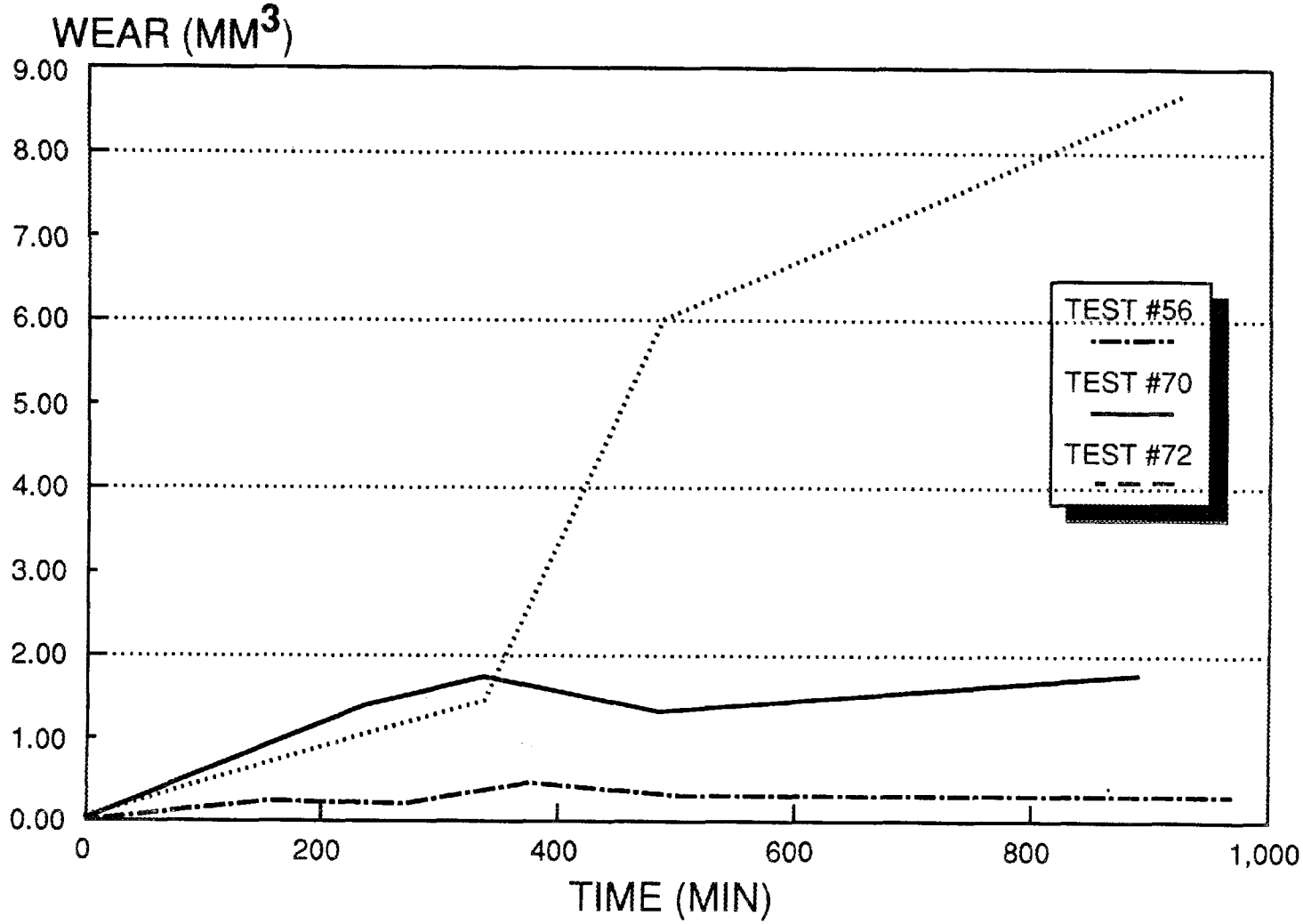

FIG. 1B: Wear Curve for Chromia-Silica Disk Running Against High Carbon Iron-Molybdenum Shoes

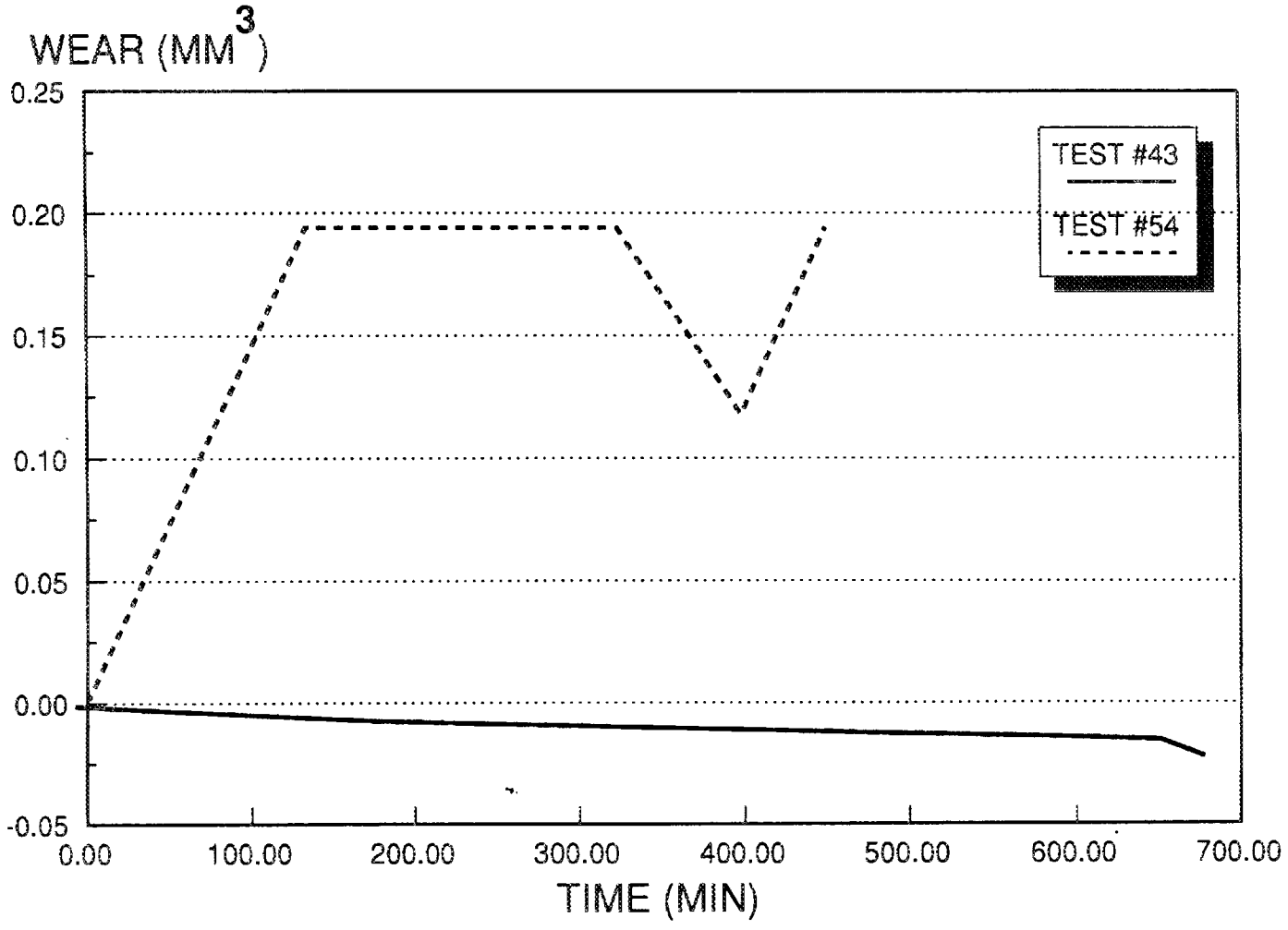

FIG. 2A: Wear Curve for High Carbon Iron-Molybdenum Shoes Running Against a Chrome Nitride Disk

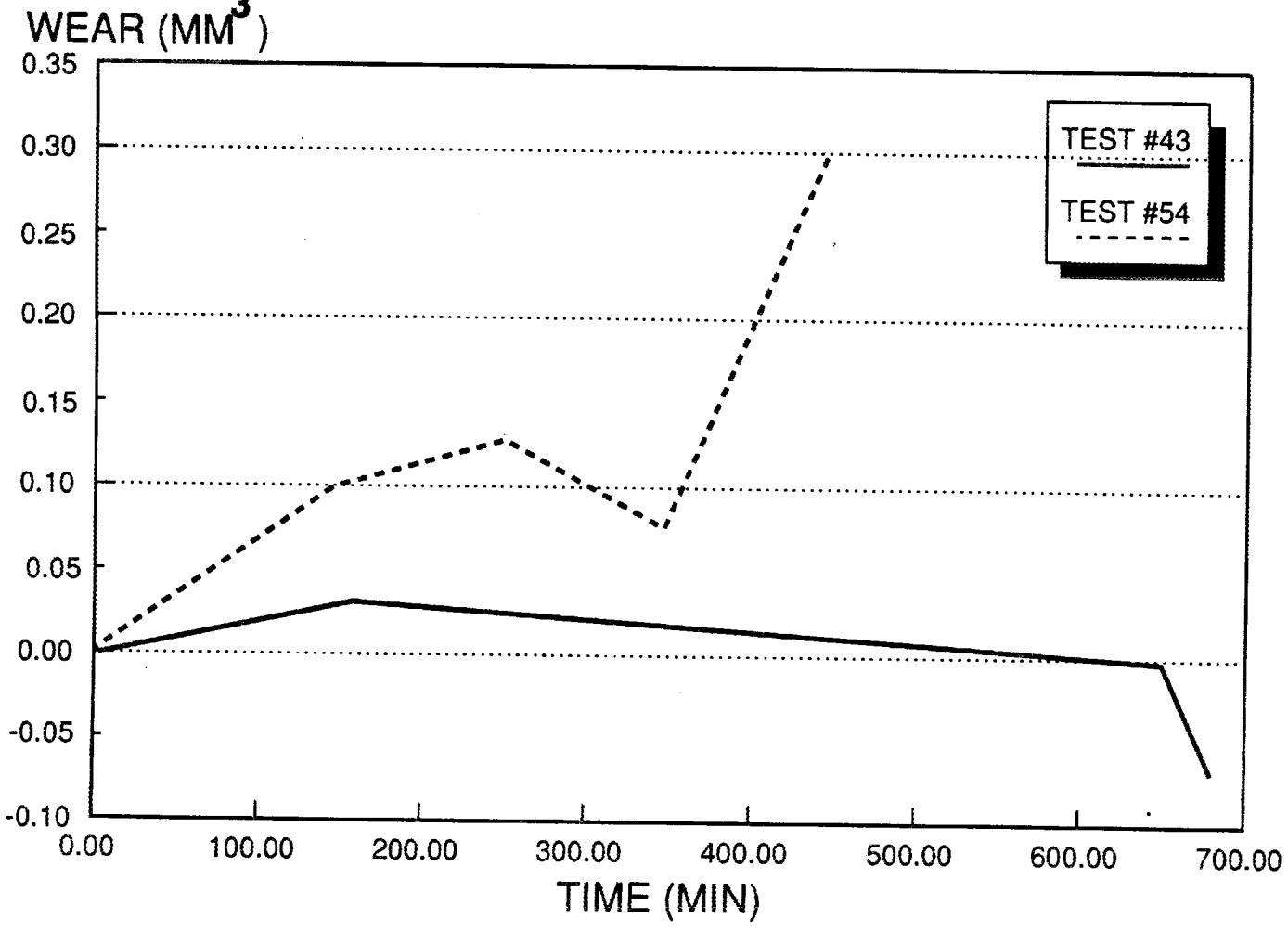

FIG. 2B: Wear Cuve for Chrome Nitride Disk Running Against High Carbon Iron-Molybdenum Shoes

1.4 JOINING

1.4.1 Ceramic-Metal Joints

Joining of Ceramics for Heat Engine Applications
M. L. Santella (Oak Ridge National Laboratory)

Objective/scope

The objective of this task is to develop strong reliable joints containing ceramic components for applications in advanced heat engines. Presently, this work is focused on the joining of silicon nitride by brazing. The technique (i.e., vapor coating ceramics to circumvent wetting problems) that was developed for brazing zirconia at low temperatures is being applied to brazing silicon nitride. The emphasis of this activity during FY 1991 will be on: (1) high-temperature brazing of silicon nitride and (2) correlating braze-joint microstructures with strength data to identify factors that influence joint strength.

Technical progress

Si_3N_4 joint tests: Flexure bars cut from joints of Ti-vapor-coated SN220 Si_3N_4 vacuum furnace brazed with Au-25Ni-25Pd wt % filler metal were tested at 700 and 800°C. Whereas at 600°C many joint test bars failed in the Si_3N_4 away from the joint, all of the bars tested above 600°C failed near the joint region. Most of the bars tested at 800°C broke under pre-loading conditions. Initial examination of the test bars suggested that failures were not occurring in the filler metal layer. A more detailed examination of the bars is continuing.

Table 1 contains the results from flexure testing the joints at 700 and 800°C. These data are also plotted in Fig. 1 with the data from previously reported testing at room temperature and 600°C. Figure 1 shows that, for this material combination, high-joint strength was maintained up to 700°C. However, a dramatic loss of joint strength occurred for specimens tested at 800°C. Because of this behavior, only a few bars were tested at the highest temperature.

Two separate points are plotted in Fig. 1 at 700°C because initial examination of these data suggested that the final thickness of the braze layer influenced joint strength. Table 1 shows that the braze layer thicknesses of specimens from two coupons (815 and 817) were in the range of 10 to 20 μm, and in the range of 40 to 50 μm for the remaining two (814 and 816). The data indicate that joint strength may be improved by reducing braze layer thickness. The bars were all taken from the same orientation relative to the original brazed coupon, and the layer thicknesses were measured on the faces loaded in tension during testing. The nominal thickness of the braze filler metal foil is 25 μm. The source of the variation in braze layer thickness and the apparent dependence of joint strength on the braze filler metal layer thickness are currently under investigation.

Si_3N_4 brazing: Several experiments were done to investigate the possibility of bonding Si_3N_4 with a higher-temperature filler metal than the Au-25Ni-25Pd wt % (T_m = 1100 to 1120°C) alloy currently being used for brazing Ti-vapor-coated Si_3N_4.

Table 1. Results of testing Ti-vapor-coated Si_3N_4 joints at 700 and 800°C

ID	Test temp., °C	Braze thick., μm	Bar width, mm	Bar thick., mm	Fracture Load, kg	Strength, MPa
814-1	700	50.8	3.068	2.456	31.9	322.3
814-2	700	44.5	3.094	2.479	30.2	296.4
814-3	700	44.5	3.035	2.484	30.4	303.1
814-4	700	44.5	3.142	2.494	32.7	312.1
814-5	700	44.5	3.056	2.487	30.4	300.5
814-6	700	47.6	3.112	2.502	33.1	317.6
815-1	700	9.5	3.048	2.512	38.6	374.5
815-2	700	9.5	3.056	2.522	43.1	414.5
815-3	700	12.7	3.023	2.527	39.7	384.1
815-4	700	9.5	3.119	2.530	43.1	403.3
815-5	700	15.9	3.073	2.527	39.7	377.7
815-6	700	25.4	3.101	2.540	37.2	347.3
816-1	700	50.8	3.043	2.537	---	---
816-2	800	41.3	3.066	2.540	2.3	21.4
816-3	700	41.3	3.081	2.540	29.2	274.1
816-4	800	41.3	3.023	2.548	1.4	13.0
816-5	700	41.3	3.117	2.548	32.7	301.6
816-6	700	44.5	3.043	2.535	35.5	339.3
817-1	700	12.7	3.084	2.499	42.2	409.1
817-2	800	9.5	3.061	2.502	2.3	22.1
817-3	700	9.5	3.094	2.517	46.5	443.1
817-4	800	12.7	3.084	2.517	10.4	99.3
817-5	700	15.9	3.053	2.527	51.1	489.3
817-6	700	12.7	3.081	2.530	48.1	455.9

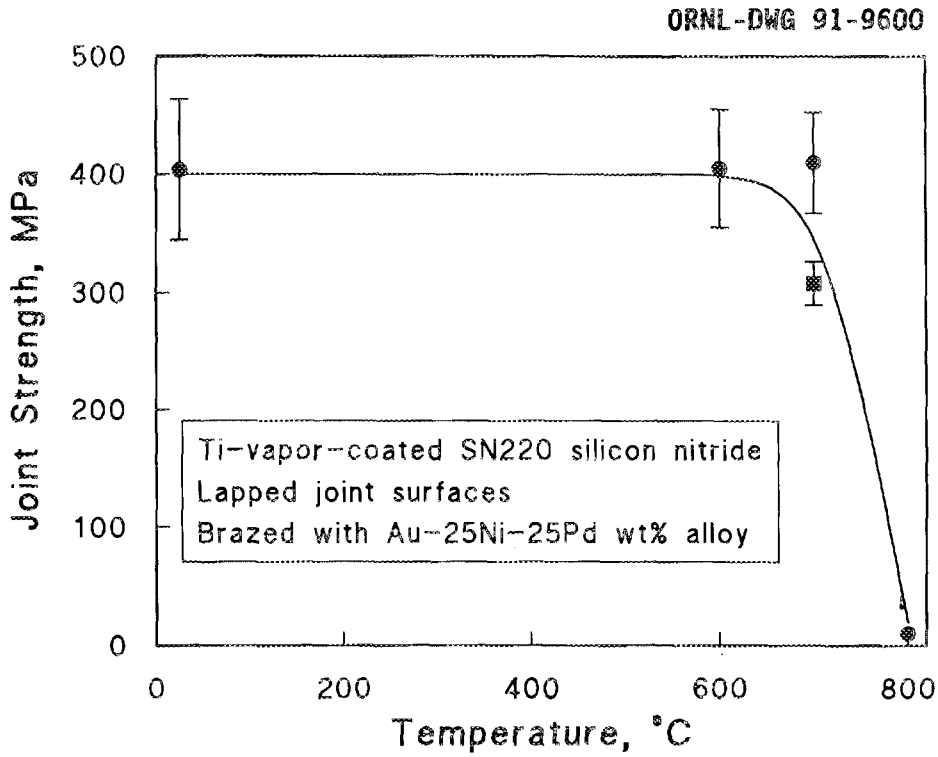

Fig. 1. Variation of joint strength with test temperature for Ti-vapor-coated SN220 Si_3N_4 brazed with Au-25Ni-25Pd wt % filler metal.

Published work on the strength of ceramics bonded with metals indicates that a thin-ductile metal layer with a thermal expansion coefficient higher than that of a ceramic is advantageous for bonding because edge fracture is suppressed. Thin-ductile, low-strength metal layers are also capable of sustaining tensile stresses in excess of their nominal yield strengths because of hydrostatic loading.

Based on this information, several ductile alloys were selected for evaluation as possible brazing filler metals for Si_3N_4. The alloys included pure platinum, Ni-20Cr wt %, and Pd-40Ni wt %. Platinum was selected because of its good oxidation resistance and high ductility. Both Ti-vapor-coated and uncoated SN220 Si_3N_4 specimens with 1 x 1-cm surfaces were bonded with 25-μm-thick Pt foils at temperatures of 1000, 1250, 1275, and 1300°C. (The melting temperature of Pt is 1769°C.) The bonding was done in vacuum, and the specimens were held together by applying a load that resulted in a pressure of 0.03 MPa during the bonding process. Bonding was achieved at all temperatures except for 1000°C. An optical micrograph of the bond made at 1250°C is shown in Fig. 2. No reaction layer was visible between the Pt and the Si_3N_4, but the filler metal layer was two-phased after bonding, and the appearance of the joint suggested that a liquid phase was present at 1250°C. These observations indicate that considerable decomposition of the Si_3N_4 occurred. Microchemical analysis in the scanning electron microscopy confirmed that the alloy layer was a mixture of Pt-Si solid solution and Pt-silicides after bonding. Figure 2 also shows that there were large voids at the bond layer/Pt

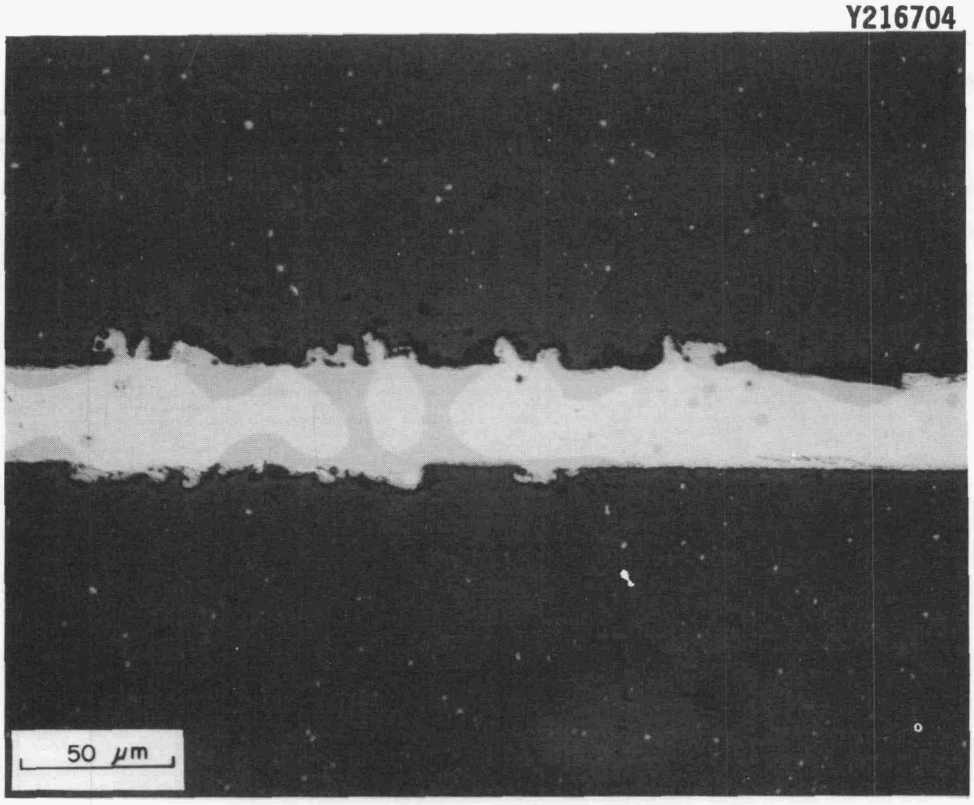

Fig. 2. Cross-sectional view of bond layer formed between SN220 Si_3N_4 and Pt at 1250°C.

interfaces and suggests that there was some intrusion of liquid phase into the Si_3N_4. The extent of reaction between the Si_3N_4 and the Pt foils was slightly less when the Si_3N_4 was coated with Ti and, in both cases, it increased with temperature. These observations indicate that Pt cannot be used for high-temperature bonding of Si_3N_4 unless reaction between the two materials can be inhibited, perhaps through the use of other coatings.

Another series of joints was made by brazing Ti-vapor-coated SN220 Si_3N_4 with a Ni-20Cr wt% alloy. The melting temperature of Ni-20Cr is in the range of 1400 to 1425°C, and brazing was done at 1450°C under vacuum and under slightly less than 1 atm of nitrogen. The exterior appearance of these joints was good. However, evidence of spraying of the liquid filler metal out of the bond layer was found on both, and both contained large areas of voids. Similar behavior was observed for the Pd-40Ni wt % alloy. The reaction of Ti-vapor-coated Si_3N_4 with these filler metals is being further investigated.

Status of milestones

Milestone 141109:

Complete initial evaluation of the use of indentation fracture testing for studying residual stresses in ceramic joints.

December 31, 1990 - Completed. A draft report is available.

Publications

None.

Analytical and Experimental Evaluation of Joining Silicon Nitride to Metal and Silicon Carbide to Metal for Advanced Heat Engine Applications - S. Kang (GTE Laboratories Incorporated)

Objective/Scope

The goal of Phase I is to demonstrate analytical tools for use in designing ceramic-to-metal joints, including the strain response of joints as a function of the mechanical and physical properties of the ceramic and metal, the materials used in producing the joint, the geometry of the joint, externally imposed stresses both of a mechanical and thermal nature, temperature, and the effects of joints exposed for long times at high temperatures in an oxidizing (heat engine) atmosphere. The maximum temperature of interest for application of silicon carbide to metal and silicon nitride to metal-containing joints is 950 °C. The initial joint-fabrication work shall include "experimental" joints whose interfacial area is not less than 2 cm^2. The work shall also include demonstration of the potential for scale-up of the joint size to interfacial areas of commercial significance, applicability of the analytical joint modeling tools, and the ability to use these tools to design and predict the mechanical and thermal behavior of larger joints. These joints, referred to as "scale-up" joints, shall have an interfacial area of at least 20 cm^2.

The goal of Phase II is to optimize materials systems and joint designs building on the results of Phase I. The work shall also include demonstration of the potential for scale-up of the joint size to interfacial areas of commercial significance, applicability of the analytical joint modeling tools and the ability to use these tools to design and predict the mechanical and thermal stability of the larger joints. These joints, referred to as "scale-up" joints, shall have the ceramic shaft at least 0.8 inches in diameter. The goal is to develop a system which can perform in an engine such as the ATTAP engine. The anticipated environment will be oxidizing and will have joint temperatures of 650°C or higher. Improved joint materials systems shall be developed to optimize the combination of competing properties which include ductility, yield strength, and creep resistance. The effect of each of these properties on joint performance shall be examined using the FEM model. Finally, a program of mechanical testing shall be carried out to confirm the effectiveness of the modeling program. This shall include torsion tests, thermal and mechanical fatigue, and creep testing. In addition, an analytical and experimental program in service life prediction will be undertaken.

Technical Progress

Materials System Design

Brazing Alloy Design

Search for Ni-based new brazing alloys with adequate melting points (about 1200°C) was continued. DTA has been completed for the alloys with metalloids or IB elements (>20% in wt.). In this reporting period, new braze alloys with higher percentages of Au, Cu, and Pd (10-20%) were characterized to find optimum compositions in terms of melting points and tensile properties.

Differential thermal analysis (DTA) of the alloys showed that the additions of 10-20% IB elements or Ge to the Ni-Cr-Mo system resulted in melting points of 1220-1310°C and 970-1260°C, respectively, while the same additions of IB or Ge to the Ni-Cr-Fe system reduced the melting points to 1280-1380°C and 980-1320°C, respectively. The effects of these alloying elements on the melting points of the Ni-Cr-Fe alloys were found to be about the same as on the Ni-Cr-Mo alloys. Ge reduced the melting points of the alloys significantly, even though the effect is not comparable with that of B or Si. The additions of Ge caused a broad melting range and multiple exothermic reactions near the melting points, implying the formation of various phases. This may limit the use of Ge as a component.

Table 1 summarized the tensile properties of the Ni-Cr-Mo alloys. Among those listed in the table, the Au-containing alloy exhibited the best properties. Combination of high ultimate tensile strength and extremely low yield strength of this alloy will provide the ability to accommodate the stress built between ceramic and metal during processing and service. Pd-containing alloys behave similarly to the Au-containing alloys. The Cu-containing alloys also resulted in reasonably good tensile properties, even if the properties degrade as the Cu content increases. The elastic moduli of the alloys are expected to be low as well. The Ni-Cr-Fe alloys in Table 2 showed a slightly lower strength level than that of Ni-Cr-Mo alloys. The addition of Au to the system again resulted in the best properties among the alloys.

The study performed in this period indicated that Incoloy 909, a typical structural alloy for this application, would lose its desirable mechanical properties if heat treated above 1200°C. Also, our braze/coating compatibility study revealed that severe degassing started around 1200°C from the Ti- or Zr-coated PY6 silicon nitride. The degassing can cause gas entrapment in the joining area, resulting in large unbonded area. Therefore, it is recommended that all brazing process be carried out below or at 1200°C.

Finite element analysis (FEA), summarized in the following section of this report, showed that brittle braze alloys such as alloys of intermetallic compositions increase the maximum tensile stress in the vicinity of the joint 5-7 times compared to a ductile braze alloy like Au-Pd-Ni. Also, the FEA study with various braze alloys and interlayer materials indicated that alloys with a high thermal expansion coefficient and low yield strength would perform better in handling the residual stress at the ceramic/metal interface than those with a low thermal expansion coefficient, high yield strength, and high Young's modulus. These results emphasize the significance of high ductility of the brazing alloys and interlayer materials.

Based on this information, new brazing alloys are being designed to have a liquidus temperature around 1150°C with a low yield strength. Also, it is important for the alloys to have as much Ni as possible to improve high temperature performance. Sixty additional brazing alloys categorized as Ni-Cr-Cu-Sn or In, Ni-Au-Cr-Mo, Au-Ni-Cr-Mo, and Au-Ni-Cu-Cr-Mo were produced, and some of them were characterized with differential thermal analysis (DTA), hardness test and tensile test.

Differential Thermal Analysis (DTA) showed that the addition of 10%Sn or 5-10% In to Ni-Cr-Cu alloys has been effective in lowering the melting points below 1200°C. The additions of 10%Sn or 5%In resulted in melting points of 915-1180°C and 1040-1210°C, respectively, for Ni-Cr-Cu alloys. Large temperature gap between solidus and liquidus (ΔTeq >150°C) was a setback of these alloys. Further, Rockwell hardness tests showed the values of R_B over 100, while useful ductility for Ni-Cr-Mo alloys was found around 90. Addition of less than 5% In or 7% Sn to the alloys resulted in the R_B below 100, indicating that the addition of Sn or In embrittled the base alloy significantly. Tensile tests performed with Ni-Cr-Cu-Sn or In demonstrated that the addition of Sn or In to Ni-Cr-Mo alloys not only embrittled the alloys, but weakened the strength in general.

Au-Ni-Cr-Mo and Au-Ni-Cu-Cr-Mo alloys were produced to meet the processing temperature and yield strength requirements with a moderate gain in high temperature creep strength. These alloys provided desirable melting temperatures (<1200°C) and ductility for ceramic-metal joints. They are expected to show improved high temperature performance compared to previous alloys like Au-Pd-Ni and Au-Ni due to the presence of 20-40% Ni-based super alloy in the system. Optimization of these alloys will be done by increasing Ni content and replacing Cr content with other solid solution strengtheners like Mo and Fe. Oxidation resistance which is obtained from Cr for Ni-based alloys will be maintained by the presence of Au in the system.

Table 1. Tensile properties of Ni-Cr-Mo-IB alloys

	UTS (ksi)	YS (ksi)	% Elongation
Ni-Cr-Mo-10Cu	94.9	13.3	105.0 (40)*
Ni-Cr-Mo-15Cu	65.8	16.1	43.0
Ni-Cr-Mo-20Cu	63.0	13.5	70.0
Ni-Cr-Mo-10Ge	75.7	18.0	30.0 (5)
Ni-Cr-Mo-10Au	106.2	15.6	104.0 (55)
Ni-Cr-Mo-10Pd	105.7	15.4	102.0 (47)

( )* Measured elongations from tested samples

Table 2. Tensile properties of Ni-Cr-Fe-IB alloys

	UTS (ksi)	YS (ksi)	% Elongation
Ni-Cr-Fe-10Cu	75.0	11.5	97.0 (46)*
Ni-Cr-Fe-15Cu	76.5	12.8	92.0 (54)
Ni-Cr-Fe-10Ge	98.6	15.7	79.0 (31)
Ni-Cr-Fe-10Au	97.1	-	101.0 (63)

( )* Measured elongations from tested samples

Braze/Coating Compatibility

Interactions between various combinations of coatings and brazing alloys were investigated in the temperature range of 1100-1250°C. It was concluded from this study that all joining process with Ni-based brazing alloys should be performed below 1200°C to suppress the nitrogen evolution from the coated silicon nitride surface.

For the experiment, the brazing alloys were placed on a coated substrate (PY6 silicon nitride) and heated in argon atmosphere. The wetting behavior and degassing phenomena were monitored using a video system. Preliminary results showed that the degassing started near 1200°C from all the Ti-, Hf-,or Zr-coated PY6 when a Au-Ni-Cr-Mo alloy was melted. When similar tests were done with pure Au and Ag-Cu alloys, little degassing was observed from the Ti- or Zr-coated PY6. Furthermore, the Au-Ni-Cr-Mo alloy did not cause degassing above 1200°C when the Al-coated silicon nitride (SNW1000) was used as a substrate. This implies that Ni in the braze alloy with those reactive coating materials causes nitrogen degassing. However, this degassing can be avoided or minimized by brazing below 1200°C. The result from this braze/coating compatibility study emphasizes the need of brazing alloys which melt below 1200°C.

System Components: Incoloy 909

There has been a concern over the effect of the high-temperature brazing process (>1000°C) on the mechanical properties of Incoloy 909 such as (1) the extent of degradation in the mechanical properties of Incoloy 909 after heat treatment at a high temperature (>1000°C), and (2) the possibility of the strength recovery of this alloy during the brazing process. In this study, the effects of high-temperature brazing on the mechanical properties of Incoloy 909 were evaluated after various heat treatments, and a post-heat treatment procedure was demonstrated to regain the strength of Incoloy 909.

Incoloy 909 has become a common choice as a structural alloy for ceramic-metal joints because it has a low thermal expansion coefficient as well as high strength. This precipitation-hardened Fe-based alloy (Fe-38Ni-13Co-5Nb-1.5Ti) has been used for gas-turbine casing, shrouds, vanes and shafts. According to the manufacturer, Huntington Alloys, the alloy is normally homogenized at 1200°C (2200°F), solution heat treated at 980°C (1800°F), and double aged at 750°C (1375°F) for 4 hours and at 620°C (1150°F) for 4 hours to strengthen it. Therefore, the use of Incoloy 909 is limited by the solution heat treatment (SHT) temperature. This alloy is also known to suffer oxygen embrittlement at high temperatures due to the lack of Cr in the alloy composition. In aircraft brazing applications (1050°C brazing), the manufacturer recommends overaging treatment along with solution treatment at 1050°C. Table 3 lists the manufacturer's specifications on the room-temperature and 650°C tensile properties of Incoloy 909, which was prepared by the regular heat treatment and overaging treatment.

In Phase I of the ceramic-metal joining program, PY6 silicon nitride was joined to Incoloy 909 via brazing at 1180°C with an Au-Pd-Ni alloy. For Phase II, new brazing alloys which have high-temperature creep strength at 600-650°C are being sought. As the application temperature of the joints increases, it is mandatory for a new braze alloy to have a high melting point.

For the experiments, Incoloy 909 was solution heat treated in vacuum at 1200°C for 30 minutes to exaggerate the brazing condition. The duration of brazing time at a brazing temperature does not normally exceed 10 minutes. In addition, the solution treated alloys were aging treated at the temperature range of 600-1000°C for 1-24 hours in air. Table 4 shows the results of hardness tests (R_B) after various aging heat treatments. The SHT at 1200°C for 30 minutes resulted in a reduction of R_B from 102 to 89 by putting precipitates back into solution. Subsequent aging treatments (AT) resulted in gradual gains in hardness, depending on aging temperature and time. Of these aging temperatures, a quick response was noted from AT at 600°C.

Table 3. Tensile Properties of Incoloy 909: Manufacturer's Specifications

Heat Treatment Conditions	Test Temp (°C)	UTS (ksi)	YS (ksi)	% Elongation
SHT at 980°C (1 hr.), AT at 750°C (4 hrs.) and at 620°C (4 hrs.)	RT 650	180 130	130 100	15 15
SHT at 1050°C (1 hr.), AT at 770°C (8 hrs.) and at 620°C (4 hrs.)	RT 650	115-120 125	100 90-95	10 10-15

Table 4. Rockwell B (R_B) Hardness of Incoloy 909 After Various Heat Treatments

Heat Treatment Conditions	Time for Aging Treatment (Hrs.) 0	1	2	3	4	8	12	24
As-received	102							
SHT at 1200°C (10 min.) in vac.	92							
SHT at 1200°C (30 min.) in vac.	89							
SHT at 1200°C (30 min.) in vac., AT at 600°C in air		92	95	98	100	100	95(?)	104
SHT at 1200°C (30 min.) in vac., AT at 800°C in air		89	90	89	91	107	108	112
SHT at 1200°C (30 min.) in vac., AT at 1000°C in air		87	87	87	86	-	-	-

Based on the hardness results, representative heat treatment conditions (600 and 800°C) were selected for Incoloy 909, and the tensile properties were measured using substandardized samples of 0.25" diameter. The results, an average of three tests for each condition, are listed in Table 5. Compared to the manufacturer's strength specifications, the properties of as-received Incoloy 909 were significantly low, while the elongation values were high. The solution heat treatment at 1200°C for 30 minutes reduced the tensile strength by 25% (from 132 ksi to 98.5 ksi) without a loss of ductility. It was the processing in vacuum (10^{-5} torr) that prevented the alloy's embrittlement. Aging at 600°C for 4-24 hours provided the regain of strength. As expected, aging treatments (AT) in air for 24 hours caused a reduction in ductility. Aging treatment at 800°C seemed to have caused overaging of the alloy as well as noticeable embrittlement. The AT's at 600°C and 800°C were done in air to simulate actual service conditions.

Table 5. Tensile Properties of Incoloy 909 After Various Heat Treatments

Heat Treatment Conditions	UTS (ksi)	YS (ksi)	% Elongation
As-Received	132	81	52
SHT*	99	52	58
SHT*, AT 600°C (4 hrs.) in air	121	89	48
SHT*, AT 600°C (24 hrs.) in air	139	107	33
SHT*, AT 800°C (4 hrs.) in air	88	51	37
SHT*, AT 800°C (24 hrs.) in air	105	-	11

*SHT (Solution Heat Treatment) was done at 1200°C for 30 min., subsequently followed by AT.

Attempts were made to see the impact of our current high temperature brazing at 1180°C for 10 minutes on the mechanical properties of Incoloy 909. Also, one-step high temperature brazing which could restore the strength of the alloy was developed by performing SHT at 1200°C for 10 or 30 minutes and subsequent AT at 600°C for 4 hours in vacuum. The results are shown in Table 6. Evidently, high temperature brazing at 1180°C lowered the tensile and yield strength of the alloy by 15 % and 20%, respectively, compared to that of as-received 909 without a loss of ductility. However, the subsequent AT at 600°C for 4 hours after SHT for 10 min. increased the yield strength of the alloy with some loss of the ductility. Metallography and tensile tests with the alloys showed that the high temperature processing, for example, SHT 1200°C for 30 min. and AT at 600°C for 4 hours, induced grain growth of the alloy from 250 μm to 350 μm, resulting in softening of the alloys.

Table 6. Tensile Properties of Incoloy 909 After One-Step Process

Heat Treatment Conditions	UTS (ksi)	YS (ksi)	% Elongation
1180°C for 10 min. (a typical brazing cycle)	111	65	52
1200°C for 10 min., 600°C for 4 hrs. in vac. (typical brazing & heat treatment)	135	101	44
1200°C for 30 min., 600°C for 4 hrs. in vac. (extended brazing time + heat treatment)	117	89	44

Overall results showed that high temperature brazing at 1200°C lowered the strength of the alloy as the brazing time at the temperature increased. However, it was confirmed that the strength loss caused by high temperature processing such as brazing could be minimized or avoided when proper post-heat treatment was used. Therefore, the service life of the alloy for 600-650°C application is more related to the intrinsic high-temperature properties of the alloy than to the processing history.

Design/Failure Analysis

Analysis of Joint by Probabilistic Approach

Work continued to develop a better method of predicting the strength of brazed joints. The previous method used was essentially a strength-of-materials approach and ignored the probabilistic nature of ceramic fracture. In the recently developed method, the probabilistic nature of ceramic fracture was included in the predicted joint strength. The present method involved several steps that are outlined below. First, the residual stress in the joint was calculated with the ABAQUS finite element code. Second, an applied torque was added to the residual stress field. The torque is added as a shear stress. When the torque was added to the residual stress field, the stress concentration due to the change in cross-section at the joint was included, along with the torque transfer between the ceramic and metal in the joint region. Figure 1 shows the torque distribution used in the prediction. Third, once the torque was added to the residual stress field, the combined stress field was used as input to the CARES probabilistic failure computer code. CARES was used to give the probability of survival for the joint at the applied torque level. This same procedure was followed for several different torques, resulting in several different probability-of-survival values. Once the analysis was completed, a Weibull plot was made of the torques and probability-of-survival values (Figure 2). This results in a predicted Weibull plot of the braze joint, and is a better measure of the joint's strength.

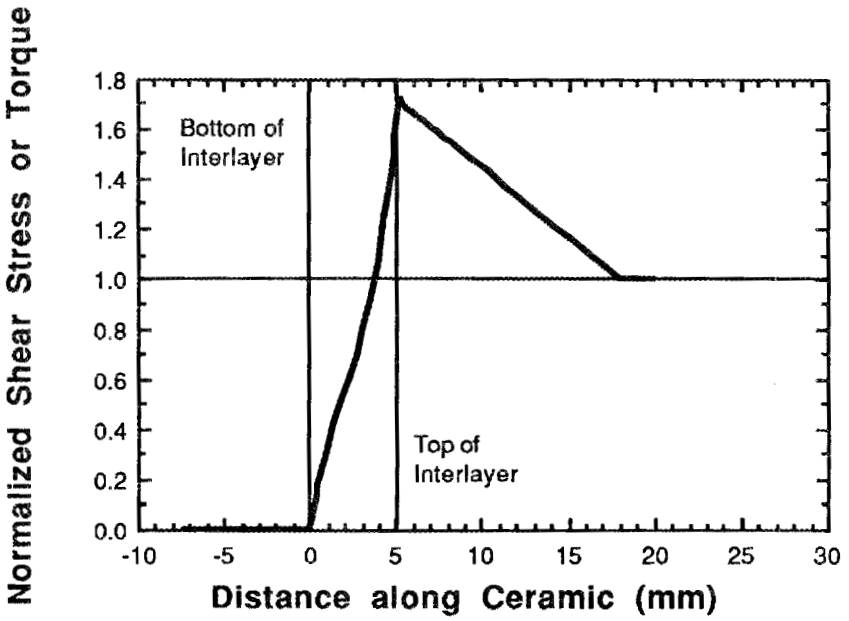

Figure 1. Plot of the torque distribution in the ceramic portion of the brazed joint. The Torque values are normalized to 1.0.

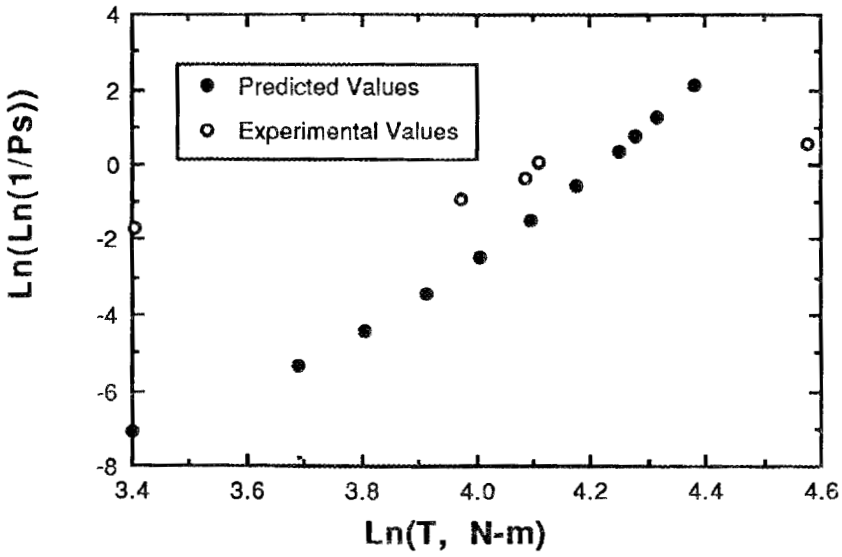

Figure 2. Plot of the predicted and experimental values of the brazed joint strength measured in torsion.

The final joint geometry from phase 1 of the program was studied by probabilistic failure analysis. This joint consisted of a 12.5 mm diameter ceramic, an interlayer with an inner diameter of 12.9 mm and an outer diameter of 16.08 mm, and a structural alloy with an inner diameter of 16.28 mm and an outer diameter of 19.46 mm. The effects of a nickel and a molybdenum interlayer on the probability of survival (P_s) of the joint were studied. Updated materials properties were used in the finite element model and in the CARES analysis: a normalized Weibull scale parameter of 471.35 MPa $m^{3/15.6}$, a crack density coefficient of 32.2, and a Weibull modulus of 15.6. The shear sensitive Shetty criterion with $\bar{C}$ = 0.82 and a penny-shaped crack were used. The joint with a nickel interlayer was found to have a Ps of 0.999955, while the joint with the molybdenum had a Ps of 0.997293. It is to be noted that high values of P_s are theoretical upper limits of the idealized joints used in the above calculations.

Analysis of Shrink Fit

To address the possibility of using a shrink fit joint as opposed to a brazed joint, the following study was carried out. A simple shrink fit joint between a 14 mm diameter PY6 Si_3N_4 ceramic and Incoloy 909 with a 2 mm wall thickness was assembled at several temperatures commonly suggested for this method and cooled to room temperature. After reaching room temperature, the stresses in the ceramic were used to calculate the P_S. For the joint mentioned above assembled at 600°C, the P_S was 0.80, and for this joint assembled at 500°C, P_S was 0.98.

Joints assembled at these two temperatures were studied to determine the torque as a function of reheat temperature. The torque, T, was calculated according to T = μPrA, where μ is the metal-ceramic friction coefficient (μ = 0.10), P is σ_{rr} calculated from finite element analysis, r is the radius of the ceramic (r = 7 mm), and A is the joint area. The calculated torques for the joints assembled at 500°C and 600°C, as a function of temperature, are shown in Figure 3. The maximum temperature that these joints can support 20 N-m is 270°C for the joint assembled at 500°C, and 360°C for the joint assembled at 600°C. It should be noted that the stress concentration associated with the change in cross-section from the metal to the ceramic was ignored and that by increasing the joint area the maximum torque would be increased. For the shrink fit joint geometry described above the maximum assemble temperature should be 500°C. This temperature corresponds to a probability of survival of 98% when cooled to 20°C. Higher assembly temperatures would result in significantly lower values of P_s. Therefore, the maximum use temperature of the shrink fit joint described above would be 270°C.

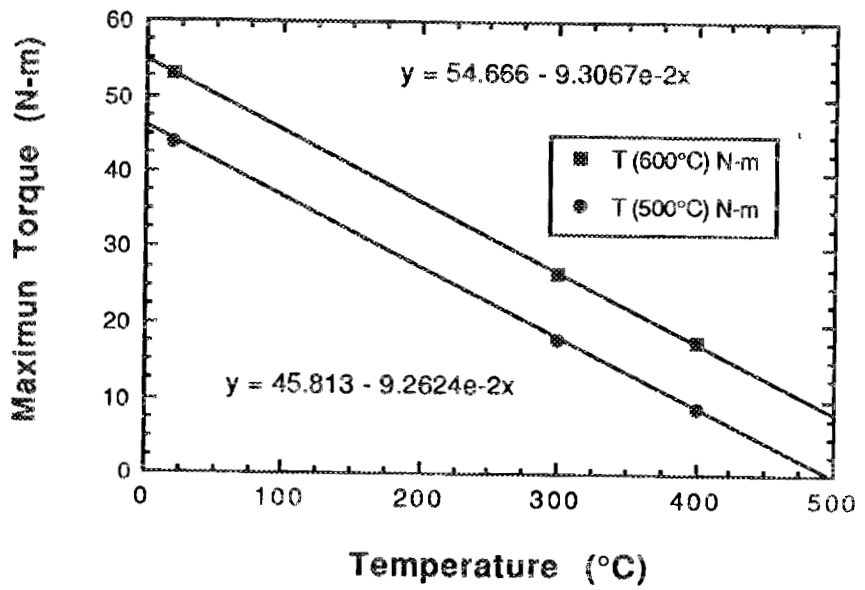

Figure 3. Plot of torque versus temperature for shrink fit joints assembled at 500°C and 600°C.

Analysis of Multi-interlayer

The effect of nickel, molybdenum, tantalum and a composite nickel-molybdenum on the probability of survival, P_S, and the shrink-fit stress was studied with finite element analysis and the CARES computer code. Table 7 shows the calculated P_S for each interlayer material at 20°C. In these joints the structural alloy was Incoloy 909 and the braze alloy was Au-5Pd-2Ni. The nickel and tantalum interlayers resulted in similar P_S values, and the molybdenum and Ni-Mo double interlayers had lower P_S values.

Table 7. Comparison between different interlayer materials and the P_S of the brazed joint at 20°C.

Interlayer Material	P_S
Nickel	0.9999549
Molybdenum	0.9972930
Ni & Mo	0.9884370
Tantalum	0.9999877

Figure 4 shows the stresses in the ceramic at the interlayer/ceramic interface. These stresses are analogous to the "shrink-fit" stresses. The stress plot for the nickel interlayer is symmetrical about the midpoint of the interlayer, while the other 3 stress plots are not symmetrical. The nonsymmetrical stress distributions are due to the nature of the deformations that occur in the joint. The low expansion interlayers, Mo, Ta and Ni-Mo, result in the bottom part of the interlayer being squeezed more that the top part of the joint. This is because these interlayers do not shrink much and are squeezed more by the structural alloy, and the structural alloy is more compliant at the top of the joint than at the bottom. Figure 5 shows the maximum principal stresses in the joint with Incoloy 909 structural alloy and the nickel-molybdenum composite interlayer after cooling from 1180°C to 20°C. This figure indicates that the molybdenum undergoes little deformation as compared to the nickel interlayer. From the above studies of interlayer materials, it was concluded that (1) the most important interlayer property is a low yield stress, and (2) the interlayer made of two different materials such as Ni and Mo is not clearly advantageous over a single interlayer. Therefore, there will be no further investigation with multi-interlayer for the joint component systems.

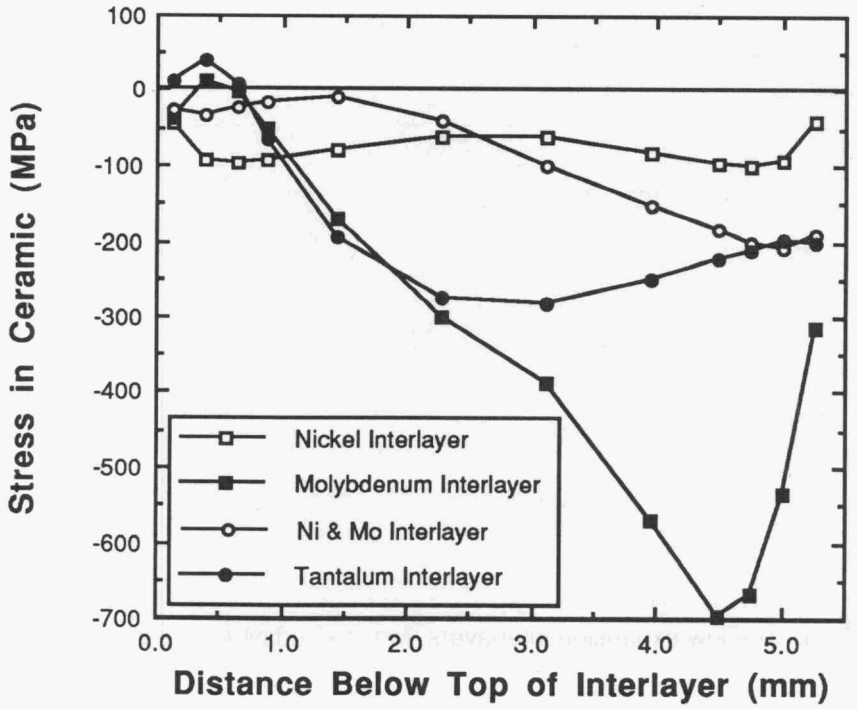

Figure 4. Plot of the shrink-fit for several different interlayer materials at 20°C.

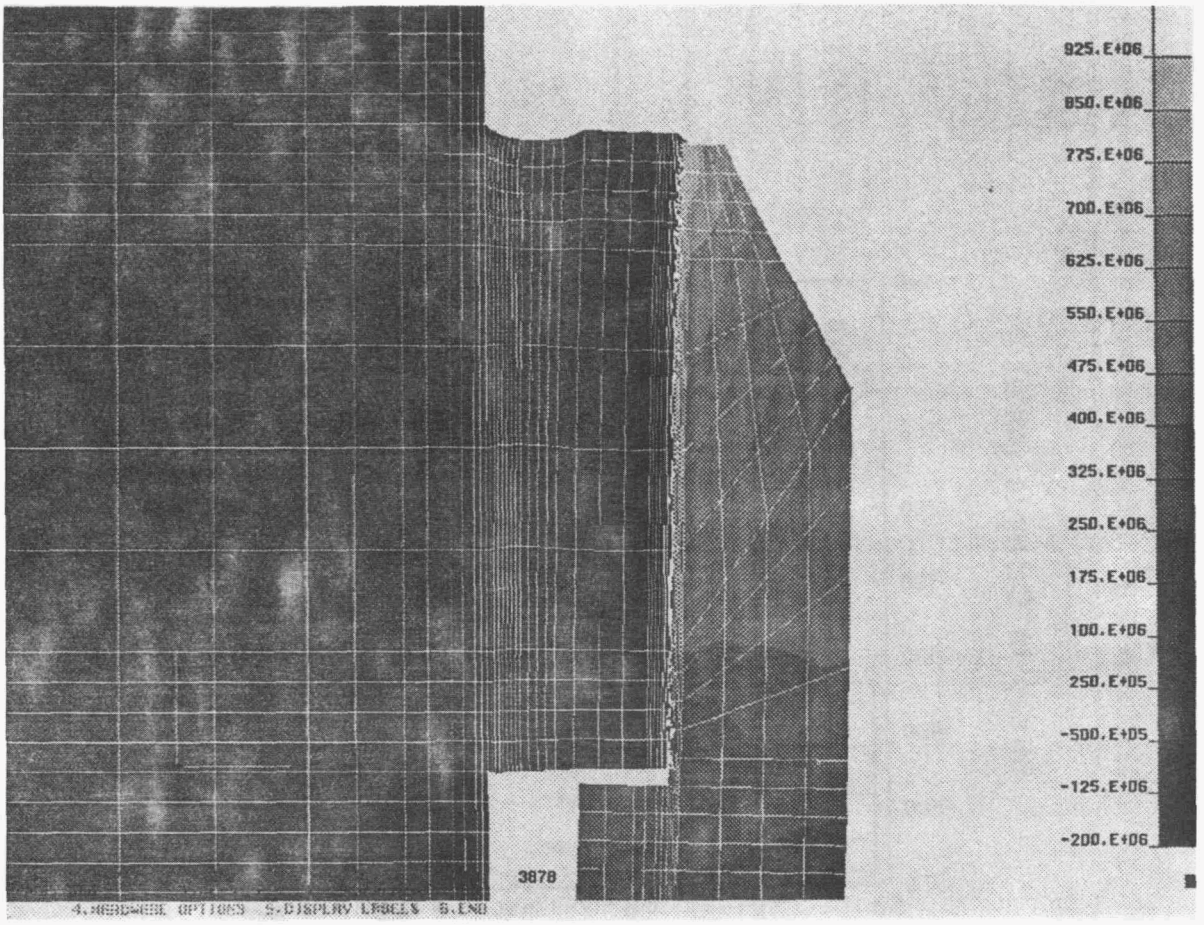

Figure 5. Max. principal stress contour of PY6/Au-Pd-Ni/Ni-Mo interlayer/Au-Pd-Ni/Incoloy 909 system

Note: The level of deformation occurred on Ni (left side) and Mo (right side) in interlayer.

Effect of Braze and Interlayer Properties on Residual Stress

There are two main components of the stress field in the joint, neglecting shear forces. Both of these components are due to the difference in the coefficients of thermal expansion of the joint materials. The first component is the compressive stress in the ceramic. This is mainly caused by the radial force applied by the structural alloy, which is transmitted through the braze and interlayer to the ceramic; this is analogous to the "shrink-fit". The second component is the tensile stress in the ceramic. This tensile stress is mainly caused by the metal components of the joint shrinking in a direction parallel to the long axis of the joint. The interlayer causes the largest part of this tensile stress because of its close proximity to the ceramic. The metal interlayer will shrink in the axial direction due to its much higher coefficient of thermal expansion as compared to Si_3N_4. Several finite element calculations have been carried out for the tapered cylindrical joint to determine the effect of the physical and mechanical properties of joint materials on the residual stress in the joint. The results of these finite element calculations can be used to identify important concepts in ceramic-to-metal joining.

The mechanical properties of the joint materials play an important part in determining the stresses in the joint. The basic effects of the material's properties on the stress in the joint are summarized in Tables 8 and 9. The braze layer supports a large part of the deformation. The yield strength of the braze layer plays a key role in transferring the stresses from the metal components to the ceramic. However, doubling the thickness of the braze layer between the ceramic and interlayer (from 0.02 cm to 0.04 cm) had a negligible effect on the magnitude of the stresses in the ceramic: the compressive stress decreased by 5%, while the tensile stress increased by 5%. Doubling the thickness of the braze layer between the interlayer and the metal alloy (from 0.0033 cm to 0.0066 cm) had a slightly larger effect on the stresses in the ceramic: the tensile stress increased by 5%, while the compressive stress was unchanged. The thickness of braze, 0.02 cm and 0.0033 cm, was the calculated sizes of the gaps among the joint components at 1180°C for the joint geometry and the dimensions used for Phase I. The Young's modulus of the braze alloy had a small effect on the stresses in the ceramic, similar to that of the interlayer Young's modulus. The thermal expansion coefficient of the braze alloy had a moderate effect on the stresses in the Si_3N_4 ceramic. The reason for the stress increase in the ceramic with a decrease in CTE is described below in conjunction with the interlayer properties.

The elastic and thermal properties of the interlayer contribute to the magnitude of the stresses in the ceramic. This was shown by the fact that at 20°C the maximum compressive stress in the ceramic was 100 MPa for the Si_3N_4/nickel/Incoloy 909 joint and 700 MPa for the Si_3N_4/molybdenum/Incoloy 909 joint. The high compressive stress with the molybdenum interlayer was attributed to high yield properties and a low coefficient thermal expansion (CTE). In a joint with a high CTE interlayer such as nickel, the interlayer and structural alloy contract during cooling from the brazing cycle, and there will be little interference between them. The main source of stress in the ceramic will stem from the interlayer, which in the case of nickel can deform easily. However, in a joint with a low CTE interlayer, the interlayer does not contract as much as the structural alloy on cooling from the brazing cycle. The contraction of the structural alloy is opposed by the interlayer, and this interference stress will be transferred to the ceramic. The structural alloy is more compliant at the top of the joint than at the bottom; this results in a hinging motion of the structural alloy. Therefore, the top of the interlayer is pulled away from the ceramic, and the radial stress (shrink-fit stress) at the top of the interlayer becomes tensile in sign. The tensile radial force induces a tensile force in the ceramic through the Poisson effect. This induced tensile force is added to the tensile force in the ceramic due to the axial shrinkage of the interlayer and structural alloy. These 2 tensile forces are additive and result in the large increase in tensile force in the ceramic listed in Table 8. It should be noted that this behavior is expected to be valid only for taper cylindrical joints.

Table 8. The effects of braze alloy properties on the maximum tensile stress and on the maximum compressive stress in the ceramic for PY6/braze/Ni/Braze/Incoloy 909 system. The properties of the Au-5Pd-2Ni braze alloy were used as the reference level for comparison with the associated properties of a nickel aluminide. Stresses at the centroid of the elements were used for comparison. The percentages are the magnitude of the change in the stresses as compared to their reference level.

Property of Braze Alloy	Maximum Tensile Stress in Ceramic	Maximum Compressive Stress in Ceramic
Low Young's Modulus (Au-Pd-Ni)	reference	reference
High Young's Modulus (Ni_3Al)	small increase (15%)	small increase (20%)
Low Thermal Expansion Coefficient (Ni_3Al)	small increase (20%)	moderate increase (40%)
High Thermal Expansion Coefficient (Au-Pd-Ni	reference	reference
Low Flow Strength (Au-Pd-Ni)	reference	reference
High Flow Strength (Ni_3Al)	large increase (125%)	very large increase (440%)

Table 9. The effects of interlayer properties of the maximum tensile stress and on the maximum compressive stress in the ceramic for PY6/Au-Pd-Ni/interlayer/Au-Pd-Ni/Incoloy 909 system. The properties of the nickel interlayer were used as the reference level for comparison with the associated properties of molybdenum. Stresses at the centroid of the elements were used for comparison. The percentages are the magnitude of the change in the stresses as compared to their reference level.

Property of Interlayer	Maximum Tensile Stress in Ceramic	Maximum Compressive Stress in Ceramic
Low Young's Modulus (Ni)	reference	reference
High Young's Modulus (Mo)	small increase (10%)	no change
Low Thermal Expansion Coefficient. (Mo)	moderate increase (25%)	very large increase (230%)
High Thermal Expansion Coefficient (Ni)	reference	reference
Low Flow Strength (Ni)	reference	reference
High Flow Strength (Mo)	large increase (65%)	very large increase (285%)

Comparing FEA predictions for joints with molybdenum interlayers and Incoloy 909 and Inconel 718, respectively, indicates that a high expansion, high flow stress structural alloy (Inconel 718) increased stresses in the ceramic. However, it is interesting to note that the compressive stress increased by 25% (from -700 MPa to -860 MPa), while the tensile stress only increased by 5% (from 220 MPa to 230 MPa). The properties of the structural alloy contribute mostly to the radial stress (shrink-fit) and only slightly to the axial forces.

This study showed that interlayers were effective in reducing the residual stresses in the ceramic. For joints between Si_3N_4 and typical metal superalloys, the ideal braze mechanical properties are low Young's modulus, high thermal expansion and a low flow stress; the ideal interlayer properties are high thermal expansion and low flow stress; and the ideal structural alloy has a low coefficient of thermal expansion.

Status of Milestones

On schedule.

Publications

S. Kang and J. Selverian submitted a paper entitled "Effect of Active Metal Coating on the Mechanical Properties of Silicon Nitride-based Ceramics" to *J. of Amer. Ceram. Soc.*, 12/11/90.

S. Kang, J. H. Selverian, D. O'Neil, H. J. Kim and K. Kim submitted a paper entitled "Analytical and Experimental Evaluation of Joining Silicon Nitride-to-Metal and Silicon Carbide-to-Metal for Advanced Heat Engine Applications" to the 28th Automotive Technology Development Contractor's Coordination Meeting, 1/11/91.

2.0 MATERIALS DESIGN METHODOLOGY

INTRODUCTION

This portion of the project is identified as project element 2 within the work breakdown structure (WBS). It contains three subelements: (1) Modeling, (2) Contact Interfaces, and (3) New Concepts. The subelements include macromodeling and micromodeling of ceramic microstructures, properties of static and dynamic interfaces between ceramics and between ceramics and alloys, and advanced statistical and design approaches for describing mechanical behavior and for employing ceramics in structural design.

The major objectives of research in Materials Design Methodology elements include determining analytical techniques for predicting structural ceramic mechanical behavior from mechanical properties and microstructure, tribological behavior at high temperatures, and improved methods for describing the fracture statistics of structural ceramics. Success in meeting these objectives will provide U.S. companies with methods for optimizing mechanical properties through microstructural control, for predicting and controlling interfacial bonding and minimizing interfacial friction, and for developing a properly descriptive statistical data base for their structural ceramics.

2.1 MODELING

2.1.1 Modeling

Microstructural Modeling of Cracks - J.A.M. Boulet (University of Tennessee, Knoxville)

Objective/scope

The goal of the study is to develop mathematical procedures by which existing design methodology for brittle fracture could accurately account for the influence of protrusion interference on fracture of cracks with realistic geometry under arbitrary stress states. To predict likelihood of fracture in the presence of protrusion interference, a simulation will be developed. The simulation will be based on a three-dimensional model of cracks with realistic geometry under arbitrary stresses.

Technical progress

The iteration software referred to in the previous report has been developed and is being verified by comparison with results from a two-dimensional code developed in previous work. The configuration being studied is a rectangular crack with a small jog at the center, loaded in shear. An edge view of the crack is shown in Figure 1. The iterator

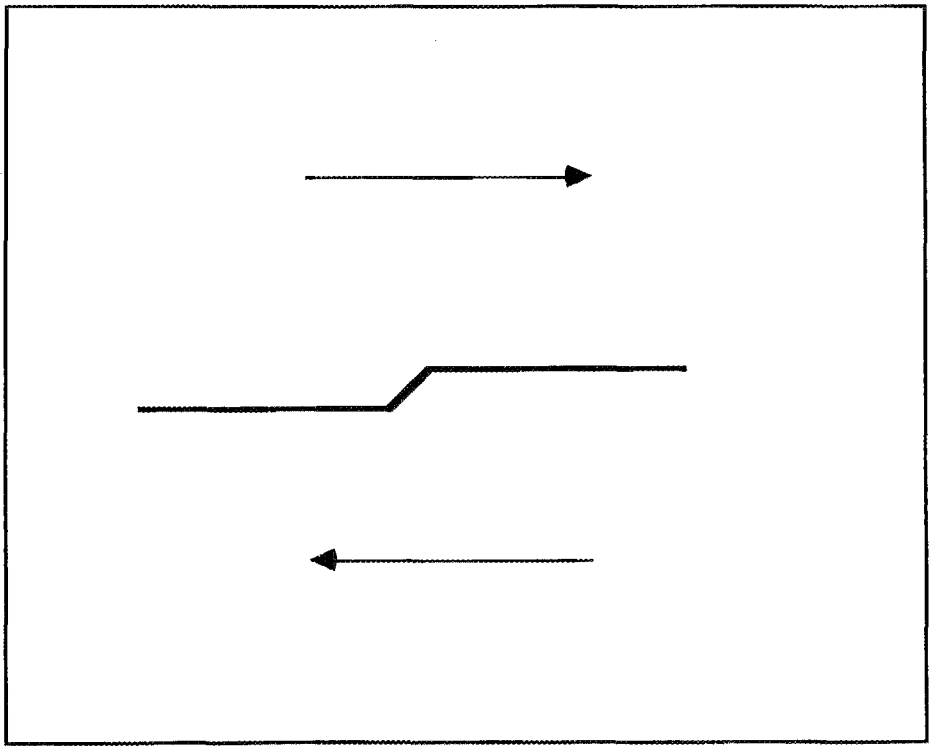

Fig.1 Edge View of Jogged Crack. The crack is much wider (perpendicular to page) than it is long. In plan view, its boundary is rectangular. The shear stress is applied at infinity.

detects crack-face interference as predicted by the three-dimensional (3-D) boundary element method (BEM) computer code referred to in previous reports and adjusts the nodal tractions to bring the interference to zero. Once the code's performance for this simple geometry is verified, more complicated geometries and loadings will be examined. These will include cracks with jagged cross sections and, eventually, cracks with bumps that do not extend over the full width of the rectangle. Whether or not circular or other nonrectangular cracks will be studied depends on the geometry of the fracture specimen on which we finally focus our attention.

The 3-D BEM code we are using is strictly for a crack in an infinite domain. The next step in the project is modify the computational model to accommodate the finite domain of some appropriate test specimen geometry. We plan to do this by using the existing code in conjunction with another 3-D BEM code that models uncracked, finite domains. The relevant mathematics is under development and will lead to a scheme for using the two codes together to model a cracked, finite domain. A suitable finite-domain code (BINTEQ) has been acquired and is being implemented on our computers.

The central difficulty in using the two codes referred to above to analyze the problem of a cracked, finite domain, is that the governing boundary integral equation (BIE) for each code is different. BINTEQ, the code that analyzes an uncracked, finite domain, is based on the "fundamental" BIE [1], while the code that analyzes a cracked, infinite domain is based on a "traction" BIE [1, 2]. Presently, the BINTEQ is programmed to account for only an external boundary, while the latter code is programmed to account for only an internal boundary. To analyze a cracked, finite domain, we must add sections to each of the codes that, in essence, "inform" each about the other kind of boundary. When this is completed, the iterator mentioned above will be used to drive both BEM codes.

References

1. T. A. Cruse, *Boundary Element Analysis in Computational Fracture Mechanics*, Kluwer Academic Publishers, The Netherlands, 1988.

2. T. A. Cruse and G. Novati, "Traction-BIE Solutions for non-planar and surface cracks," pp. ed. proceedings of presented at 22nd National Symposium on Fracture Mechanics, June 26-28, Atlanta, Georgia, 1990.

Status of milestones

Work is on schedule.

2.2 CONTACT INTERFACES

2.2.1 Static Interfaces

Elastic Properties and Adherence of Thin Films and Coatings

Debra Joslin, Dept. of Materials Science and Engineering
University of Tennessee, Knoxville, Tennessee 37996-2200

Objective/scope

The objective of this research is the examination of the effects of ion bombardment on the structure of thin ceramic films on ceramic substrates. The material combinations will include oxide films that have (a) no solid solubility, (b) limited solid solubility, and (c) complete solid solubility with the substrate material (also an oxide). Techniques for determination of elastic and plastic properties of thin films or coatings on ceramic substrates and for the determination of the strength of the bond between the film and substrate, which are currently being developed, will be used to determine the hardness, elastic modulus, and adherence of each material combination. The main testing techniques will be the ultra-low load microindentation tester (Nanoindenter), and thermal cycling tests.

Technical highlights

Two Al_2O_3 single crystals (c-axis oriented, previously annealed for 5 days in air) were implanted at room temperature with Cr at an energy of 300 KeV to a fluence of $1x10^{17}$ ions/cm^2. In order to allow oxygen in-diffusion, the samples were then annealed in air at 1500°C for 1.5 hr and 2 hr, respectively. Rutherford Backscattering Spectrometry (RBS) was performed on the samples before implantation, and before and after annealing to determine the range of the implanted ions, the damage evolution in the Al_2O_3, and the percent of Cr substitutional in the Al_2O_3 after annealing. According to the RBS results, the fraction of Cr in substitutional sites after annealing was about 0.90 for both annealing times. Spreading of the implanted layer by a few nanometers was also observed (data not presented here). Similar samples will be examined by transmission electron microscopy after annealing to determine the nature of the substitutional layer (eg. continuous Cr_2O_3 vs. coherent Cr_2O_3 precipitates).

These samples were then implanted with Au (3 MeV, $5x10^{14}$ ions/cm^2 on one portion of the sample; $5x10^{15}$ ions/cm^2 on another); one sample was implanted at room temperature, the other at 450°C. RBS was performed on these samples after implantation to determine the damage evolution in the sample. RBS spectra for the sample implanted at 450°C are shown in fig.1. No significant diffusion of the Cr resulted from either Au fluence at this temperature. The results for the room temperature implantations are similar in this respect. The RBS results shown in figs. 2 and 3 were obtained with the samples' c-axes aligned with the beam. The spectra show the aluminum peak from the sample after the Cr implantation and subsequent anneal, and after the Au implantations to each fluence. The spectra for the room temperature implantation are shown in fig. 2, and for the 450°C

implantation in fig.3. From this information, the fraction of disorder (minimum yield), χ_{min}, can be calculated for each set of fluence and temperature conditions. Note that $\chi_{min} = 1$ implies an amorphous material, while $\chi_{min} = 0$ denotes a perfect crystal. These data indicate that the damage induced is greater for the 450°C implantation than for the room temperature implantation. This result is somewhat unexpected; generally more damaged is induced by implantation at lower temperature. Transmission electron microscopy will be performed to determine the nature of the damage.

Also during this report period, two other c-axis oriented Al_2O_3 single crystals (same prior anneal) were implanted with Cr at an energy of 300 keV to a fluence of $1x10^{17}$ ions/cm^2. In a similar manner to the first two samples, these samples were then annealed in air at 1300°C for 1 hour. Rutherford Backscattering Spectrometry (RBS) results indicate that 90% of the Cr was in substitution in the Al sublattice following this treatment. The imbedded layer sits at a depth of about 325 nm with a spread of about 120 nm. These results are shown in figs.4 and 5; the curves are labelled "implanted Cr only."

These samples were then implanted with Si at an energy of 1.25 MeV to a fluence of $3x10^{16}$ ions/cm^2. One sample was implanted at room temperature; the other at 600°C. RBS measurements on these samples are shown in figs. 5 and 6. No significant diffusion of the Cr occurred at either temperature.

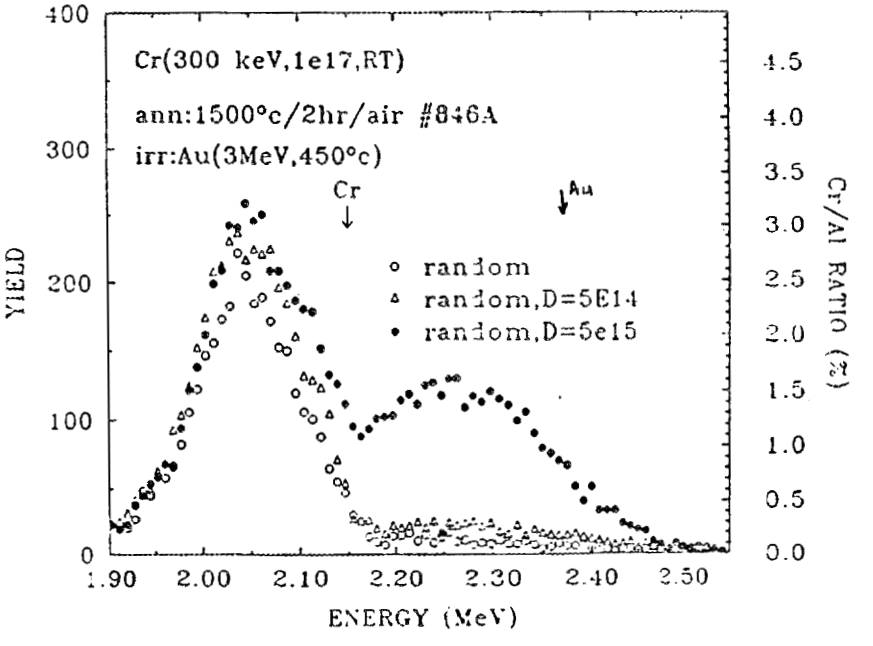

Figure 1. RBS spectra for Au implantation (3 MeV, $5x10^{14}$ ions/cm^2 or $5x10^{15}$ ions/cm^2, 450°C) into an Al_2O_3 specimen previously implanted with Cr (300 KeV, $1x10^{17}$ ions/cm^2, room temperature) and then annealed for 2 hr in air at 1500°C.

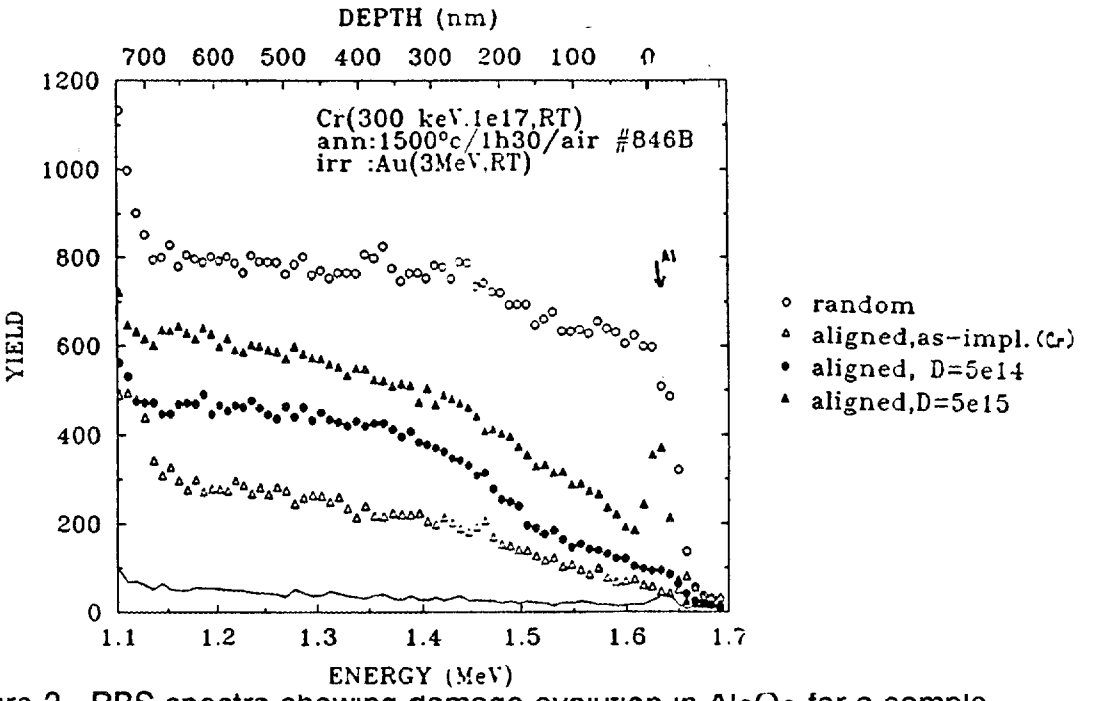

Figure 2. RBS spectra showing damage evolution in Al_2O_3 for a sample implanted with Au (3 MeV, $5x10^{14}$ ions/cm^2 or $5x10^{15}$ ions/cm^2, 450°C) after a previous Cr implantation (300 KeV, $1x10^{17}$ ions/cm^2, room temperature) and anneal (1.5 hr in air at 1500°C).

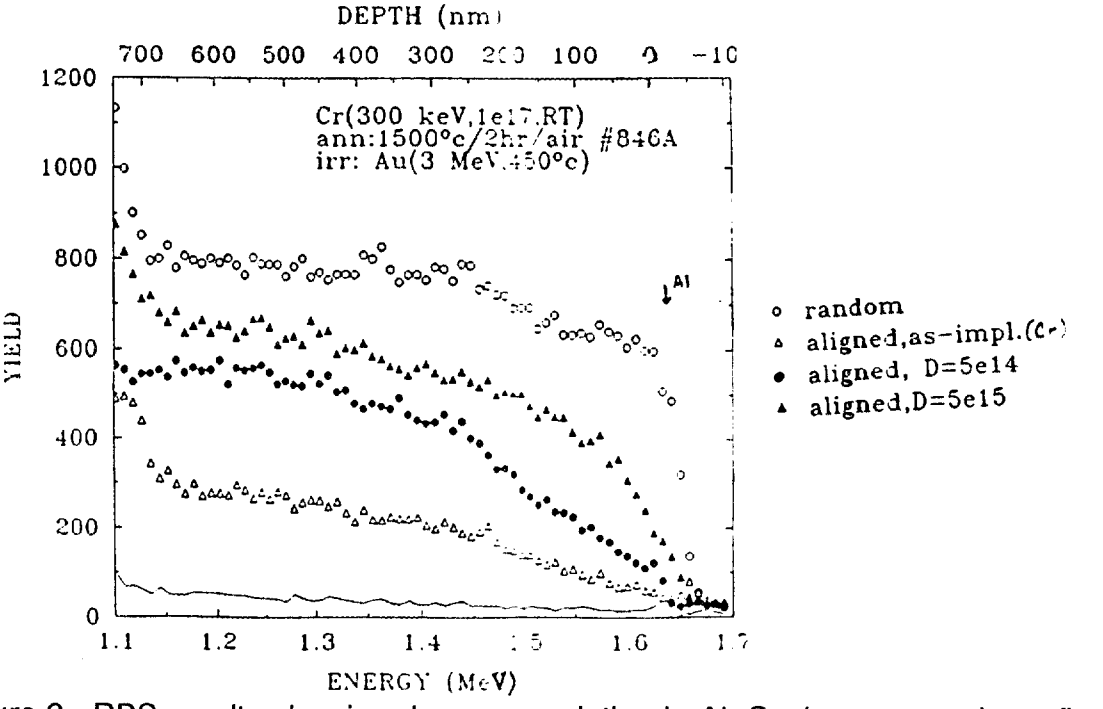

Figure 3. RBS results showing damage evolution in Al_2O_3 (same sample as fig.2)

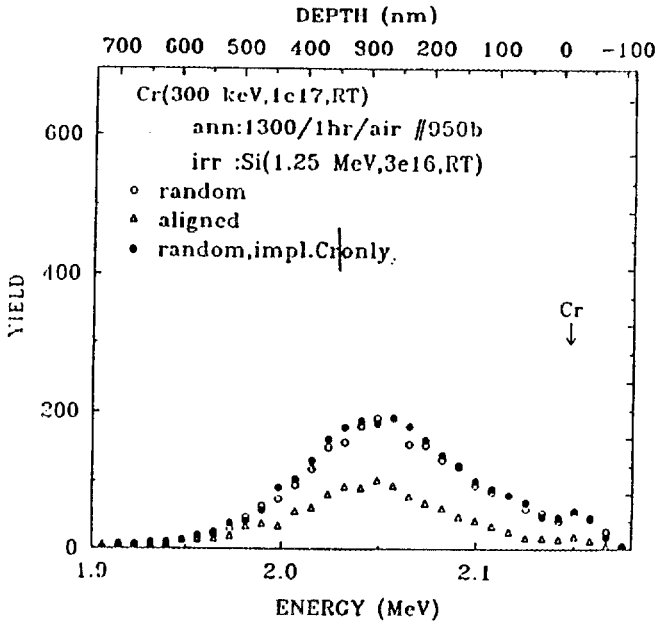

Figure 4. RBS results for the room temperature ion implantation of Si^+ (1.25 MeV, $3x10^{16}$ ions/cm^2). No significant diffusion of the Cr occurred.

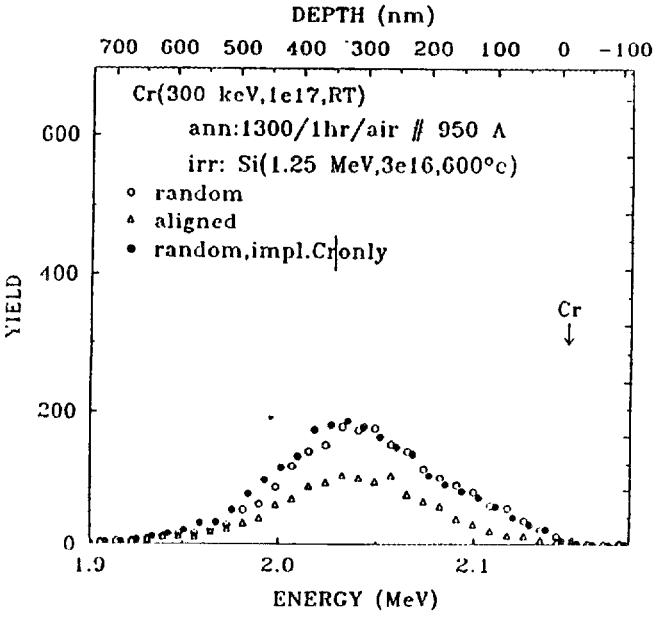

Figure 5. RBS results for the 600∞C ion implantation of Si (1.25 MeV $3x10^{16}$ ions/cm^2). No significant diffusion of the Cr occurred.

Status of milestones

N/A

Publications

None

2.2.2 Dynamic Interfaces

Studies of Dynamic Contact of Ceramics and Alloys for Advanced Heat Engines

P.A. Gaydos and K.F. Dufrane (Battelle)

Objective/Scope

The objective of the program is to develop an understanding of the friction and wear processes of ceramic interfaces based on experimental data. The supporting experiments are to be conducted at temperatures to 650 C under reciprocating sliding conditions reproducing the loads, speeds, and environment of the ring/cylinder interface of advanced engines. The test specimens are to be carefully characterized before and after testing to provide detailed input to the model. The results are intended to provide the basis for identifying solutions to the tribology problems limiting the development of these engines.

Technical Highlights

Apparatus

The apparatus developed for this program uses specimens of a flat-on-flat geometry, which facilitates specimen procurement, finishing, and testing. The apparatus reproduces the important operating conditions of the piston/ring interface of advanced engines. The specimen configuration and loading is shown in Figure 1. A crown with a 32 mm radius is ground on the ring specimen to ensure uniform contact. The ring specimen holders are pivoted at their centers to provide self-alignment. A chamber surrounding the specimens is used to control the atmosphere and contains heating elements to control the temperature. The exhaust from a 4500 watt diesel engine is heated to the specimen temperature and passed through the chamber to provide an atmosphere similar to that of actual diesel engine service. A summary of the testing conditions is presented in Table 1.

Materials

Ring and Cylinder Materials

The compositions of the various materials used in the study are presented in Table 2. A variety of monolithic and coating materials were selected to represent various chemical compositions and materials with previously demonstrated successful sliding performance.

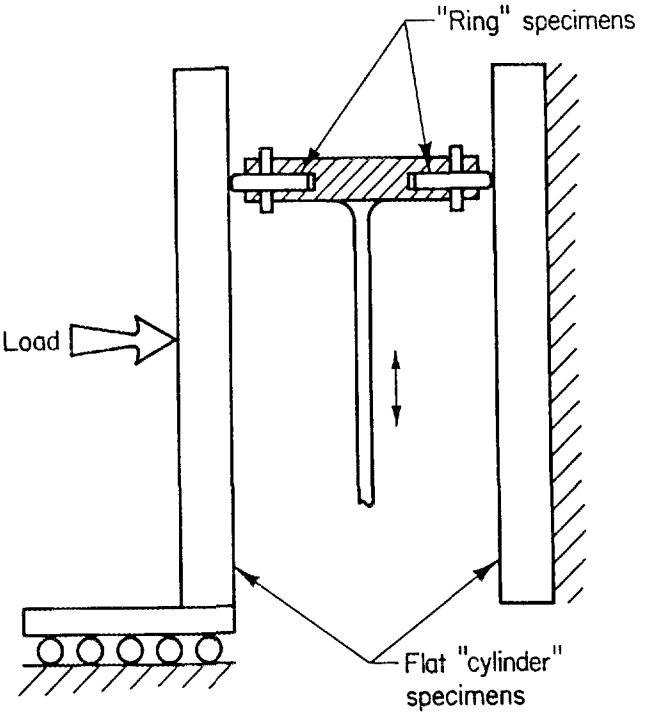

FIGURE 1. TEST SPECIMEN CONFIGURATION AND LOADING

TABLE 1. SUMMARY OF TESTING CONDITIONS

Sliding Contact:	Dual flat-on-flat
"Cylinder" Specimens:	12.7 x 32 x 127 mm
"Ring" Specimens:	3.2 x 19 x 19
"Ring" crown radius:	32 mm
Motion:	Reciprocating, 108 mm stroke
Reciprocating Speed:	500 to 1500 rpm
Average Specimen Speed:	1.8 x 5.4 m/s
Load:	to 950 N
Ring Loading:	to 50 N/mm
Atmosphere:	Diesel exhaust or other gases
Measurements:	Dynamic friction (during test) Specimen wear (after test)

TABLE 2. MATERIALS EVALUATED

Monolithic Ceramics	Coatings
YPSZ	Tribaloy 400
MPSZ	METCO 130 (13 TiO_2, 87 Al_2O_3)
ATTZ	METCO 501 (30 Mo, 12 Cr, bal Ni)
αSiC	Plasmalloy 312M ($MoSi_2$)
SiC/Al_2O_3	Cr_2O_3 (5 Cr, bal Cr_2O_3)
Sialon	Jet-Kote WC (12 Co, bal WC)
K162B (TiC - Ni/Mo)	Cr (Electroplated)
Si_3N_4	PS212 (Cr_3C_2 + BaF_2/CaF_2 + Ag)
	VR73 (WC/TaC/TiC/Co)
	VA 20 (WC/TaC/TiC/Ni)
	CA 815 (Cr_3C_2/Ni)
	Mo
	Duplex (WC and Mo)
	Ion Implanted (N in Cr_2O_3)
	Cr_2O_3 + S_iO_2
	High Carbon Fe + Mo

Wear Experiments

Caterpillar Wear Specimens

Caterpillar, Inc. supplied wear specimens prepared under Subcontract No. 86X-SA582C to be tested under conditions simulating the ring and cylinder liner interface in advanced engines. The ring specimens were sprayed with a chromia-silica coating and the cylinder liner specimens were coated with a high carbon ion-molybdenum. The tests thus far have produced ring wear rates that are among the lowest of all material combinations run in the previous two phases of this research. The average friction coefficients, however, are about twice as high as those of other material pairs run with the same lubricants at the same temperature.

The range of friction coefficients decreased slightly as the temperature increased from 260 to 315 C, and it is now comparable to the friction of other materials run in OS-80001H Lubricant at the same temperature. While the wear rate of the chromia-silica ring material at higher temperatures increased between 50 and 100 percent over the wear rate recorded at 260 C, no other material run above 300 C has shown lower wear rates.

Table 3 below shows the results from all of the tests run with the Caterpillar specimens.

TABLE 3. WEAR RATES OF CHROMIA-SILICA RING SPECIMENS AGAINST HIGH CARBON IRON-MOLYBDENUM CYLINDER SPECIMENS

Test I.D.	Lubricant	Temperature C	Run Duration Min.	Friction Coefficient Range	Average Ring Wear Factor $mm^3/N-m$
84	SDL-1	260	240	0.08 - 0.11	4×10^{-9}
84	SDL-1	260	240	0.09 - 0.13	2×10^{-8}
85	SDL-1	260	240	0.10 - 0.13	4×10^{-9}
85	SDL-1	260	240	0.07 - 0.10	2×10^{-8}
85	SDL-1	260	480	0.08 - 0.10	1×10^{-8}
86	OS-80001H	260	240	0.13 - 0.20	7×10^{-9}
86	OS-80001H	315	240	0.11 - 0.14	1×10^{-8}
86	OS-80001H	315	240	0.10 - 0.14	4×10^{-8}

Table 4 shows baseline data with conventional materials as well as wear rates of some previously evaluated advanced materials.

TABLE 4. WEAR OF OTHER MATERIAL PAIRS

Test I.D.	Lubricant	Temp. C	Ring/ Cylinder Material	Friction Coefficient Range	Average Ring Wear Factor $mm^3/N-m$
19	SAE 10	100	Cr/Cast Iron	0.03 - 0.04	3×10^{-9}
51	SDL-1	260	WC/Si_3N_4	0.03 - 0.07	1×10^{-9}
64	SDL-1	260	Cr_2O_3/Cr_2O_3	0.03 - 0.07	2×10^{-8}

M.S.U. Ion Implantation

Michigan State University has demonstrated the feasibility of implanting ^{7}Be and ^{22}Na ions in ceramic materials for the purpose of wear studies. The intensity of low-level γ radiation emitted from the wear surface of the ion-implanted material can be correlated to the depth of wear. This method is said to be capable of resolving wear as low as 50 nm.

Wear tests were conducted to determine if the implantation itself would influence the wear rate of the material. M.S.U. supplied a number of control Si_3N_4 ring specimens as well as some that were implanted with six doses of 10^{12} particles of ^{20}Ne. This non-radioactive ion is similar in size to ^{22}Na and should produce similar radiation damage. The dosage was 2 to 3 orders of magnitude higher than required for using ion-implantation as a wear diagnostic tool so that any damage would be intensified. Each of the six doses was implanted to different depths, which ranged from less than 5 μm to about 10 μm. Any damage, characterized by an increase in wear rate, would be located in the region between these depths.

Two tests were run with control specimens and two with implanted ones for a total of four tests. Each test, furthermore, consisted of three portions, a one-hour break-in followed by two two-hour runs. The tests were halted after each portion for wear measurements and to ensure that the wear was confined to the first 10 μm. Finally, two specimens were run simultaneously during each test in the rig's T-shaped slider arm for a total of 24 wear measurements.

The results are presented in Table 5. All 24 of the wear rates measured are within an order of magnitude of each other (between 5×10^{-9} and 4×10^{-8} $mm^3/N-m$). This amount of data scatter is typical in wear tests, and the results indicate that there is no significant

difference in the wear performance of the control and implanted specimens. As the test results for the left and right hand specimens running simultaneously are averaged, the test results fall within a half an order of magnitude. Continuing to average all the data from each of the four tests shows the differences becoming smaller. Finally, the average of all 12 of the control tests and all 12 of the implanted tests are virtually the same.

TABLE 5. WEAR RATES OF SILICON NITRIDE RING SPECIMENS AGAINST PLASMA SPRAYED CHROMIA CYLINDER SPECIMENS (mm^3/N-m)

(SDL-1 lubricant, room temperature, 12.3 N/mm ring load, 500 cpm)

^{20}Ne Ions?	Test Number & Portion	Run Duration Min.	Wear of Specimen in Left Position	Wear of Specimen in Right Position	Average Wear of Both test Specimens	Average Wear of Both Specimens and all Test Portions
No	88a	60	2×10^{-8}	4×10^{-8}	3×10^{-8}	2×10^{-8}
	b	120	1×10^{-8}	2×10^{-8}	2×10^{-8}	
	c	120	2×10^{-8}	1×10^{-8}	2×10^{-8}	
Yes	89a	60	2×10^{-8}	3×10^{-8}	2×10^{-8}	2×10^{-8}
	b	120	2×10^{-8}	3×10^{-8}	2×10^{-8}	
	c	120	2×10^{-8}	1×10^{-8}	2×10^{-8}	
Yes	90a	60	3×10^{-8}	3×10^{-8}	3×10^{-8}	2×10^{-8}
	b	120	2×10^{-8}	8×10^{-9}	1×10^{-8}	
	c	120	2×10^{-8}	2×10^{-8}	2×10^{-8}	
No	91a	60	1×10^{-8}	1×10^{-8}	1×10^{-8}	9×10^{-9}
	b	120	5×10^{-9}	6×10^{-8}	6×10^{-9}	
	c	120	1×10^{-8}	1×10^{-8}	1×10^{-8}	
Average Wear of all Control Specimens						2×10^{-8}
Average Wear of all Implanted Specimens						2×10^{-8}

The evaluation performed during this reporting period showed that implanting ^{20}Ne ions in silicon nitride does not affect the wear performance of the material. Since these ions are similar in size to ^{22}Na ions, it is expected that their effects on silicon nitride would be equally benign.

Status of Milestones

The study is progressing in accordance with the overall milestone schedule.

Publications

Gaydos, P.A., "Self-Lubricating Materials for High Temperature Ring/Cylinder Application", SAE Paper 910455, 1991.

2.3 NEW CONCEPTS

Advanced Statistical Concepts of Fracture in Brittle Materials
C. A. Johnson and W. T. Tucker (General Electric Corporate Research and Development)

Objective/Scope

The design and application of reliable load-bearing structural components from ceramic materials requires a detailed understanding of the statistical nature of fracture in brittle materials. The overall objective of this program is to advance the current understanding of fracture statistics, especially in the following four areas:

- Optimum testing plans and data analysis techniques.
- Consequences of time-dependent crack growth on the evolution of initial flaw distributions.
- Confidence and tolerance bounds on predictions that use the Weibull distribution function.
- Strength distributions in multiaxial stress fields.

The studies are being carried out largely by analytical and computer simulation techniques. Actual fracture data are then used as appropriate to confirm and demonstrate the resulting data analysis techniques.

Technical Highlights

Phase II of this contract is scheduled to be completed on April 30, 1991. In preparation for that date, work during this reporting period concentrated on documentation of many Phase II results and conclusions, plus completion of various efforts described in previous bimonthly and semiannual reports that had "loose ends" still needing attention. These wrap-up efforts fall in the following areas: confidence and tolerance bounds, bias correction, statistical efficiency of estimators, and multiaxial approaches to probabilistic failure prediction. The following two sections describe work on ranking methods for linear regression and statistical efficiency.

I. Comparison of Ranking Methods in Linear Regression

Comparisons were made of biased and unbiased estimates of Weibull parameters from six variations of linear regression estimator. These variations included three different ranking methods used to assign probabilities of failure and two different directions of regression. Surprisingly, it was found that unbiased estimates of Weibull parameters and unbiased confidence bounds on those parameters were independent of the ranking method used.

Bootstrap analyses of confidence and tolerance bounds for Class IV problems (where the fracture data include strengths from multiple specimen sizes and loading geometries, while the component of interest may be of yet a different size and loading configuration) have been described in earlier semi-annual reports. Bootstrap analyses utilize estimators such as maximum likelihood and linear regression to digest a set of fracture strengths and estimate quantities such as the Weibull parameters and/or the probability of failure of a component at any quantile of interest (at any probability of failure of interest). As with most estimators, these Weibull estimators have the property of yielding offset or "biased" estimates. Strength estimates are particularly prone to large bias errors, especially if the strength is being estimated for a specimen or component with a much larger (or smaller) effective size than the test specimens. This large bias after size extrapolation can generally be traced to bias in the estimate of m. Of course, a small error in m will lead to progressively larger errors in predicted strength as one extrapolates farther and farther from the effective size of the test specimen data.

Although not normally utilized, bootstrap simulations for estimation of confidence and tolerance bounds contain information about the magnitude of bias introduced by the estimator. This information is now being used within the bootstrap analysis computer program to yield estimates of distribution parameters, strengths and confidence and tolerance bounds that have been corrected for bias.

The fracture data used herein is the same set of 137 bend strengths of sintered beta SiC used in prior reports for various purposes. The specimens were fabricated in the three Mil Std 1942MR specimen sizes: A, B, and C. Specimens of each size were tested in both 3-point and 4-point bending, thus resulting in a total of six different specimen sizes and geometries. Each of the six groups consisted of approximately 18 specimens except for the 4-point B group which consisted of 48 specimens. Fractography indicated that fracture was initiated predominately from surface-related defects, therefore all size scaling is carried out using surface areas.

Six variations of linear regression estimator were compared with each other The six regression estimators were similar but differed from each other in two respects--ranking scheme and direction of regression. Three different ranking schemes were used:

$$P = i/(N + 1)$$

$$P = (i - 0.3)/(N + 0.4)$$

$$P = (i - 0.5)/N$$

where P is the cumulative probability of failure assigned to the i-th specimen of a group of N specimens that are ordered in strength from weakest to strongest. All three ranking schemes have been proposed and used in the statistical and materials literature. The third ranking method is typically used in the linear regression

estimators within our contract effort (including the WeibEst program, version 2.0).

The other variation of regression estimator that was studied was the direction of regression. Conventional regression estimators regress the probability on the strength. That is, the sum of squared-errors between the "observed" and the estimated probabilities of failure is minimized. On conventional Weibull probability paper, this corresponds to minimizing the vertical sum of squared-distances between the data points and the best-fit straight line. This again is referred to as regression of the probability on the strength. The other direction is to regress the strength on the probability of failure where the sum of squared-errors between the observed and estimated strengths is minimized. (Both directions of regression are available in WeibEst).

Comparisons of these six variations of linear regression were made both for a simple Class I problem that involved 48 bend specimens of a single size and loading geometry (4-point B configuration) and for a more complex Class IV problem that involved 137 specimens of six different combinations of size and geometry (3-point and 4-point bending of A, B, and C geometries). The results are summarized in Figures 1-8. Figures 1-4 describe the dependence of Weibull modulus on the estimator; while Figures 5-8 do the same for the second Weibull parameter, sigma zero. Figures 1, 2, 5, and 6 are for the Class I problem; while Figures 3, 4, 7, and 8 are for the Class IV problem. Figures 1, 3, 5, and 7 regress probability on strength; while Figures 2, 4, 6, and 8 regress strength on probability.

All eight figures use a similar format. In each figure, the Weibull modulus and 95 percent confidence bounds on the modulus are plotted for the three ranking schemes being considered. For each ranking scheme, both the biased (uncorrected for bias) and unbiased estimates of the Weibull modulus and the bounds are included.

Comparison of biased estimates in Figure 1 (circles and associated error bars) shows that different ranking schemes result in different estimates of m as well as different bounds. Even with 48 strengths in the data set, the use of the "wrong" ranking method incurs a bias error of approximately 1 part in 15. The bias corrected m's and associated bounds (squares and associated error bars), however, are virtually identical for the three ranking schemes. Therefore, if bias correction is carried out, there is no "best" ranking method for this Class I problem. The least bias of uncorrected estimates in this Class I problem is incurred when the third ranking scheme is used. This observation is consistent with earlier observations on Class I estimators. As shown below, however, this ranking method does not always yield the smallest bias.

Figure 2 still considers the Class I problem but compares the three ranking schemes for regression of strength on probability. Conclusions are similar to those above. Biased estimates are dependent on ranking scheme. Unbiased estimates of m and bounds on m are independent of ranking scheme. The unbiased m and bounds are slightly different than those on Figure 1, but regression in the opposite direction results in a different estimator with different properties. It should not be surprising

that two different estimators result in different estimates of parameters when analyzing the same data set. Finally, the least bias in m was created by the second ranking method in this case.

Figure 3 uses the estimators of Figure 1 but analyzes the Class IV problem with 137 strength measurements. The results are plotted on the same scale as Figure 1 to illustrate that the bounds of both biased and unbiased estimates of m are smaller for this larger data set. This is expected since the larger data set contains more information about the true value of m. Characteristics of the bias are quite different relative to Figure 1. The bias is larger, especially when compared in proportion to the size of the bounds. The bias in m is as large as 1 part in 10. Bias in confidence bounds seems even more severe as illustrated by the extreme asymmetry of the error bars, especially for the first ranking method. The bias corrected estimates, however, are in very good agreement. Again, this suggests that bias corrected estimates of m and associated confidence bounds are independent of ranking scheme.

Figure 4 uses the same Class IV data but regresses in the other direction. Bias in both m and bounds is less than in Figure 3. The second ranking scheme causes the least bias. Again, the bias corrected estimates are in good agreement with each other.

Figure 5 is the first of four figures that illustrates the properties of estimates of the second Weibull parameter, sigma zero. Figure 5 is for the same data set and direction of regression as Figure 1. As in Figure 1, bias is present in all uncorrected estimates but is least for the third ranking method. Bias correction again results in virtually perfect agreement from the three ranking schemes. Similar statements can be made about Figures 6-8.

Several summarizing statements can be made concerning these studies:

- After bias correction, there is virtually no difference in estimated parameters from different ranking schemes. The m values of the different ranking schemes agreed within 0.3 percent. The sigma zero values agreed within 0.1 percent. There is no apparent equivalence of estimates from different ranking schemes prior to bias correction. Therefore bias errors are the primary source of differences that, in the past, have been attributed to different ranking schemes.
- After bias correction, there is very little difference in confidence bounds on estimated parameters from different ranking schemes. A corollary of this statement is that the different ranking schemes yield equivalent efficiencies. (As described in the section to follow, for a given data set, the narrower the confidence bounds, the more efficient the estimator must have been in using the available information.) The small dependence of the width of the confidence bounds on ranking method slightly favors the use of the third ranking method.

- The degree of bias present in uncorrected estimates of Weibull parameters varies with the ranking method chosen. Unfortunately, no single ranking method seems to consistently yield the smallest bias for all problems of interest. Since the best ranking method cannot be identified until after they are compared to bias corrected estimates, it is recommended that estimates always be corrected for bias.

II. Statistical Efficiency of Weibull Estimators

In the area of statistical efficiency, quantitative comparisons were made of the efficiency of maximum likelihood versus the six variations of linear regression estimators described in the previous section. It was found that maximum likelihood is substantially more efficient than linear regression in extracting information from a given set of fracture data. This is important from a practical standpoint because an inefficient estimator results in larger confidence intervals than a more efficient one. Therefore, use of an inefficient estimator is statistically equivalent to ignoring (not analyzing) some fraction of the original fracture data. In light of the cost and difficulty of measuring fracture strengths, it is undesirable to waste any of the information available in the data set.

The relative efficiency of two estimators can be measured by comparing the widths of confidence intervals on estimates from those estimators. Qualitatively, the more efficient an estimator, the smaller the confidence interval when used to analyze identical data sets. For instance, if two Weibull estimators are used to estimate the Weibull modulus, m, then the more efficient of the two will yield the smaller confidence interval on m at any level of confidence quoted.

In order to quantitatively describe the relative efficiency of different estimators, we take advantage of the relationship that the width of a confidence interval is approximately proportional to the inverse square root of the number of observations. From the invariance property of the distribution of $\hat{m}/m$ in the Weibull distribution, it can be shown that the interval in m values should be measured on a logarithmic scale, not on a linear scale. Therefore, in the case of the 95% confidence bounds on the Weibull modulus:

$$\log m_{0.975\ app} = \log m_{0.025} = \frac{C}{\sqrt{N}} \tag{1}$$

where C is a proportionality constant characteristic of the estimator and the quoted confidence interval. From Eq. 1, if one quadruples the number of strength measurements, N, then the width of the resulting confidence interval (plotted on a log scale) is expected to decrease by a factor of approximately two.

The efficiency of different estimators could be evaluated by comparing the proportionality constants. A smaller value of C is associated with a smaller interval and, therefore, a higher efficiency. An alternate method of comparing efficiencies involves use of Eq. 1 to calculate relative numbers of specimens necessary to result in comparable intervals from different estimators. This latter approach has an advantage in ease of interpreting the results and is therefore used here.

The statistical literature has proven for conditions of regularity that maximum likelihood estimators are at least as efficient as any other estimator. Therefore, we have chosen to normalize the efficiency of estimators to that of maximum likelihood. As an example, consider two estimators analyzing the same data set to estimate m and confidence bounds on m. One estimator is maximum likelihood and the other will be referred to as the "alternate" estimator. For this example, let us say that the 95 percent confidence bounds on m for the alternate had a width (on a log scale) that was twice that of maximum likelihood. From the inverse square root relationship of Eq. 1, we can state that maximum likelihood could have resulted in the same width of bounds as the alternate estimator by analyzing only one-quarter of the full data set. Conversely, the alternate estimator must have used only 25 percent of the information that was extracted by maximum likelihood. Using Eq. 1, this "relative efficiency" of the alternate estimator in using all available information is defined by:

$$\textit{Relative Efficiency} = \left[\frac{\log m_{ML,\,0.975} - \log m_{ML,\,0.025}}{\log m_{Alt,\,0.975} - \log m_{Alt,\,0.025}}\right]^2 \tag{2}$$

The relative efficiency defined above is calculated using the 95% confidence interval. Use of different intervals (70, 90, 95, 98 and 99%) in both the numerator and denominator was found to make no significant difference. A relationship similar to Eq. 2 can be generated for other estimated quantities such as the second Weibull parameter and the estimated strength of a component of interest. In the case of strength estimates and/or the second Weibull parameter, the invariant used to derive the equivalent of Eq. 2 is $(\hat{\sigma}/\sigma)^m$.

The efficiency as measured by Eq. 2 has been determined for two directions of linear regression, for two different "Classes" of problem and for both Weibull parameters. The results for all eight combinations are included in Table 1. As described in the previous section, the width of the confidence bounds and therefore the efficiency of linear regression estimators has been found to be largely independent of the ranking scheme used. Therefore the efficiencies quoted in Table 1 are the average of the efficiencies from the three ranking relationships described earlier.

The two directions of regression estimator are those described in the previous section. Two Classes of problem were analyzed to determine if the relative efficiency was a function of the type of problem. Both analyses used data from the study of the strength of sintered beta SiC. As an example of a Class I problem, only the 48 4-point B specimens were analyzed. As an example of a Class IV problem, the full 137

specimens from six different combinations of bend specimen size and geometry were analyzed.

As can be seen in Table 1, the eight measures of efficiency ranged from 0.40 to 0.63. Therefore, even in the best case, it is concluded that some 40 percent of the useful information that is available to maximum likelihood is unrecovered and wasted when linear regression is used. Regression of strength on probability (unconventional direction of regression) may be incrementally more efficient than the opposite direction of regression. Also, it appears that linear regression is even less efficient in Class IV problems than it is in Class I problems. Caution should be exercised in making conclusions from small differences in efficiencies form Table 1. Repetition of the bootstrap analysis was carried out for selected cases of Table 1. Due to random sampling error during the bootstrap simulations, the resulting efficiency varied slightly from repetition to repetition with a standard deviation of approximately 0.03. Despite this small variability in our knowledge of the efficiencies, the first conclusion of this paragraph is still valid and significant. As a result, we strongly recommend that maximum likelihood be used for the final analysis of fracture data.

TABLE 1

Efficiency of Weibull Estimators Relative to Maximum Likelihood
(Fraction of specimens needed in maximum likelihood for equivalent 95% interval)

	Class I Problem (48 4-pt bend)		Class IV Problem (137 3- and 4-pt bend)	
Estimator	m	σ_0	m	σ_0
Regression of P on σ	0.59	0.44	0.52	0.40
Regression of σ on P	0.63	0.52	0.53	0.44

Status of Milestones

On schedule.

Publications

Article submitted to ASM Engineered Materials Handbook, Volume 4: Ceramics and Glasses. Article is entitled "Advanced Statistical Concepts of Fracture in Brittle Materials."

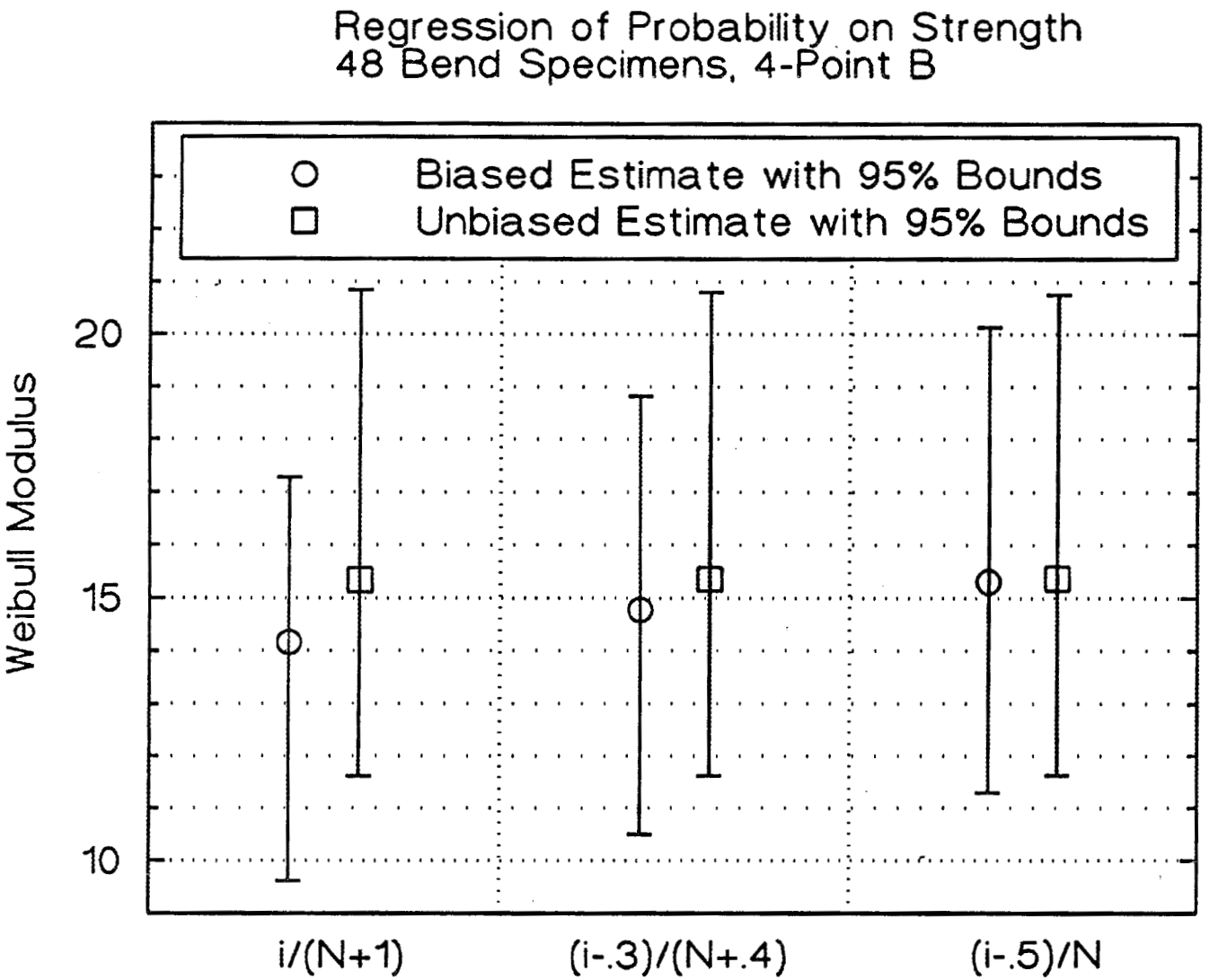
Regression of Probability on Strength
48 Bend Specimens, 4-Point B
Biased Estimate with 95% Bounds
Unbiased Estimate with 95% Bounds
Weibull Modulus
20
15
10
i/(N+1)
(i-.3)/(N+.4)
(i-.5)/N

Figure 1

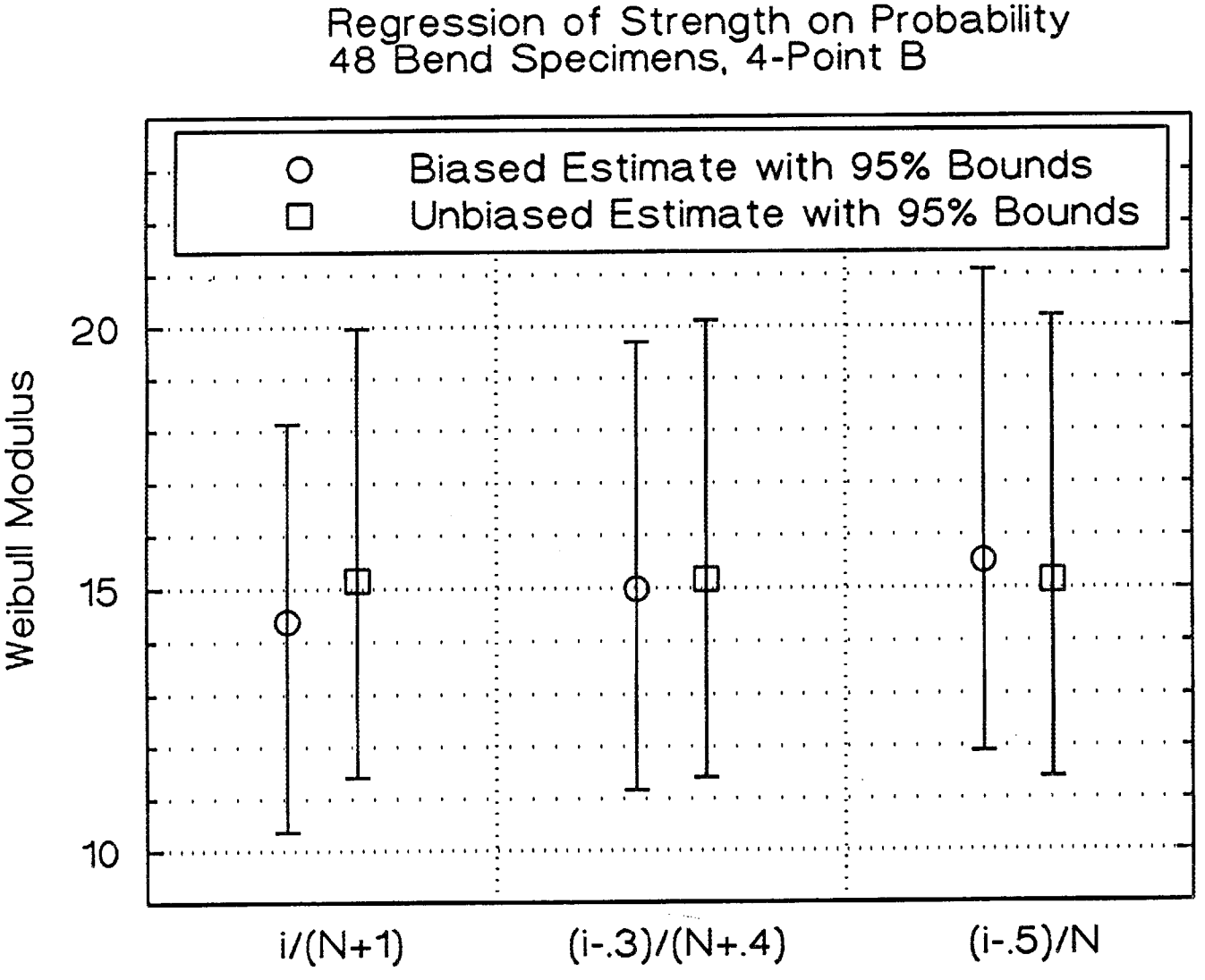
Regression of Strength on Probability
48 Bend Specimens, 4-Point B
Biased Estimate with 95% Bounds
Unbiased Estimate with 95% Bounds
Weibull Modulus
20
15
10
i/(N+1)
(i-.3)/(N+.4)
(i-.5)/N

Figure 2

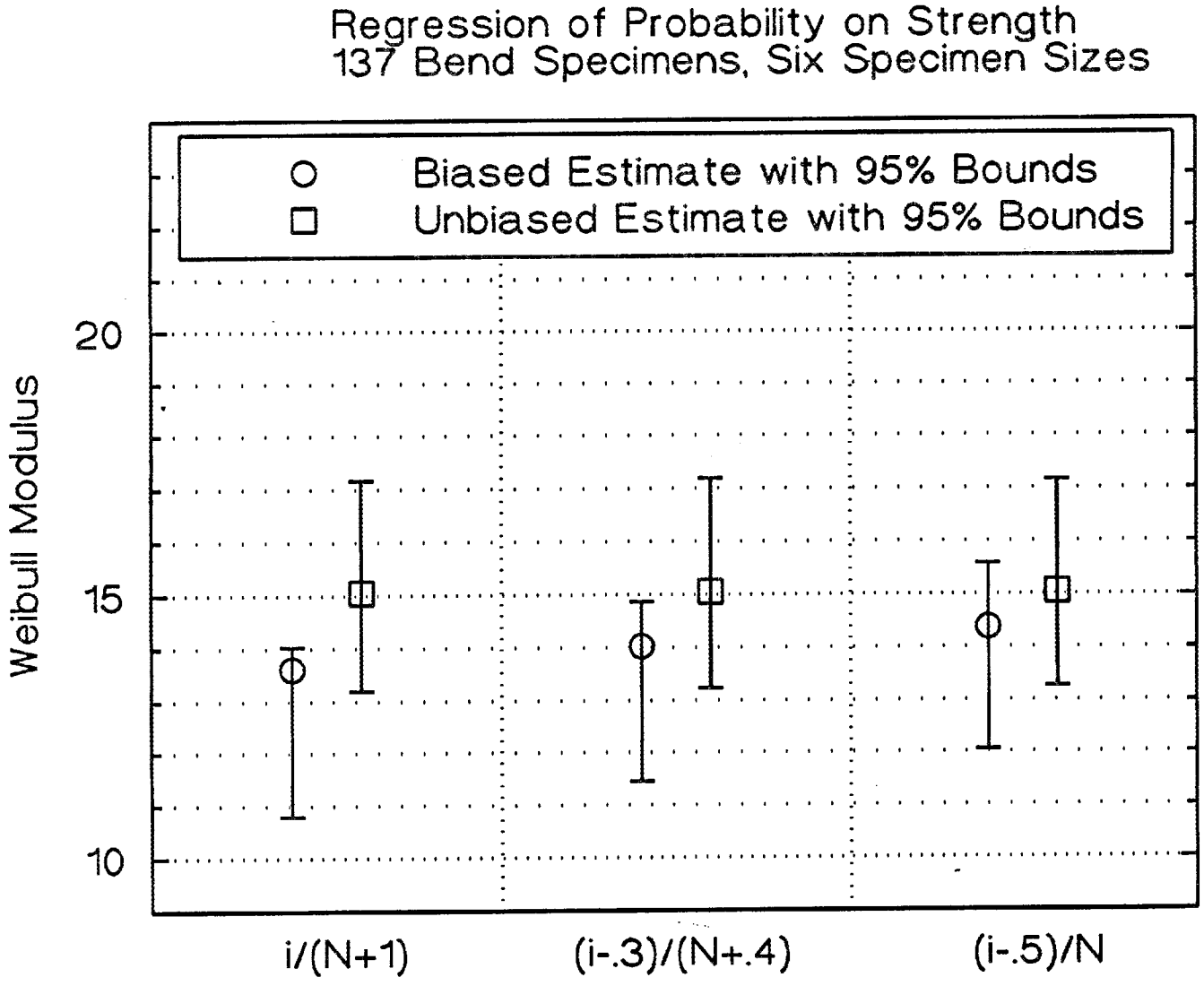
Regression of Probability on Strength
137 Bend Specimens, Six Specimen Sizes
Biased Estimate with 95% Bounds
Unbiased Estimate with 95% Bounds
Weibull Modulus
20
15
10
i/(N+1)
(i-.3)/(N+.4)
(i-.5)/N

Figure 3

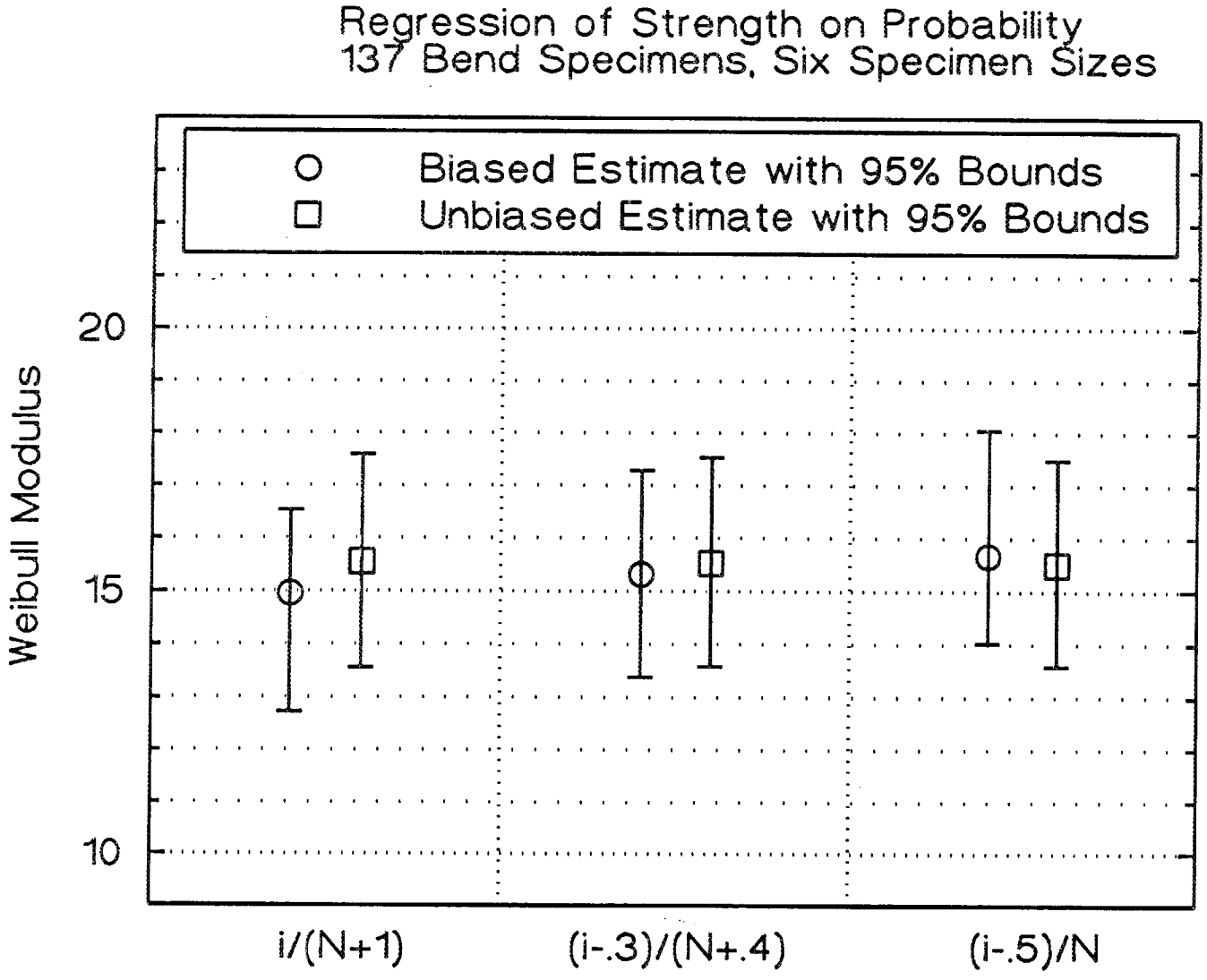
Regression of Strength on Probability
137 Bend Specimens, Six Specimen Sizes
Biased Estimate with 95% Bounds
Unbiased Estimate with 95% Bounds
Weibull Modulus
20
15
10
i/(N+1)
(i-.3)/(N+.4)
(i-.5)/N

Figure 4

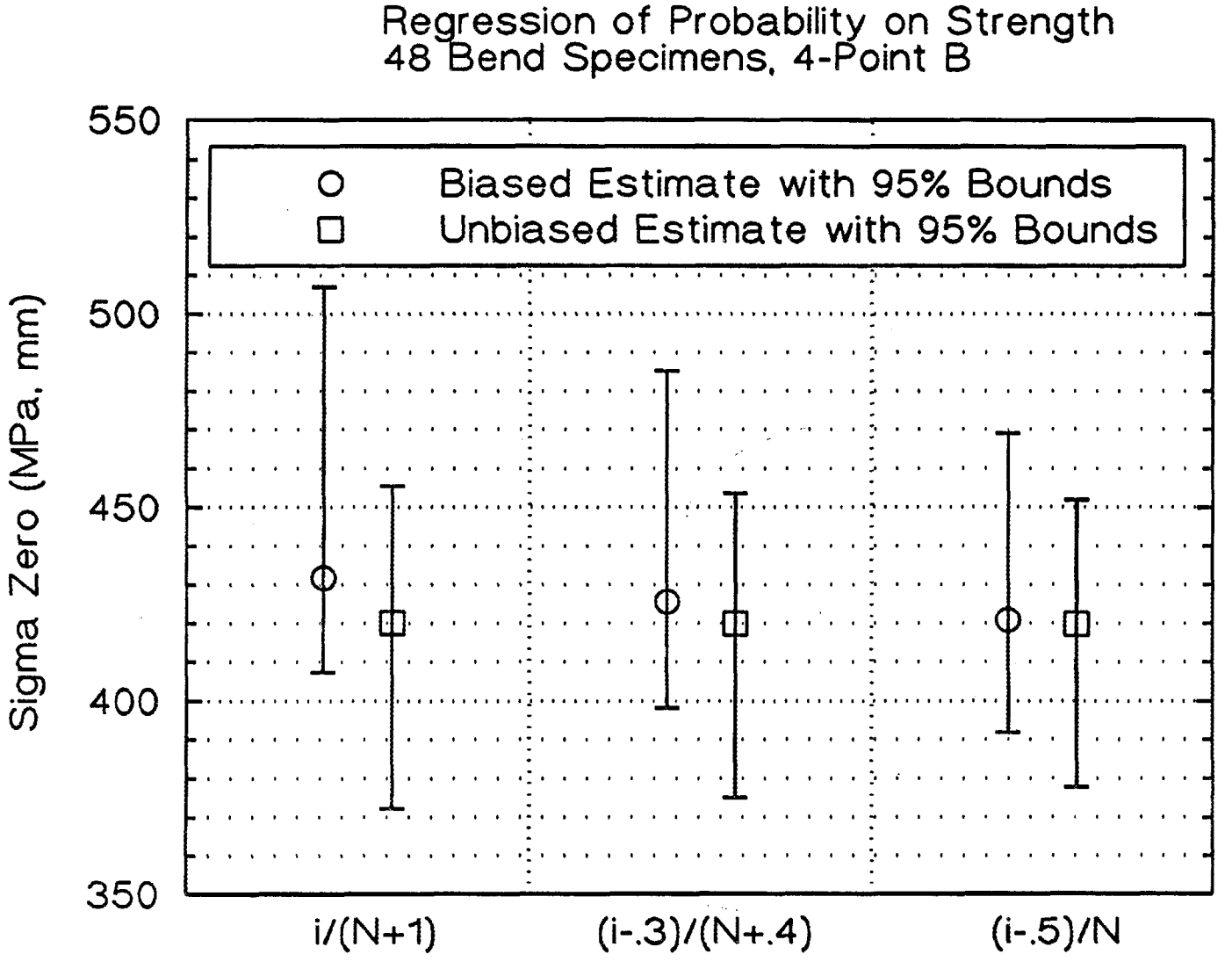
Regression of Probability on Strength
48 Bend Specimens, 4-Point B
Biased Estimate with 95% Bounds
Unbiased Estimate with 95% Bounds
Sigma Zero (MPa, mm)
550
500
450
400
350
i/(N+1)
(i-.3)/(N+.4)
(i-.5)/N

Figure 5

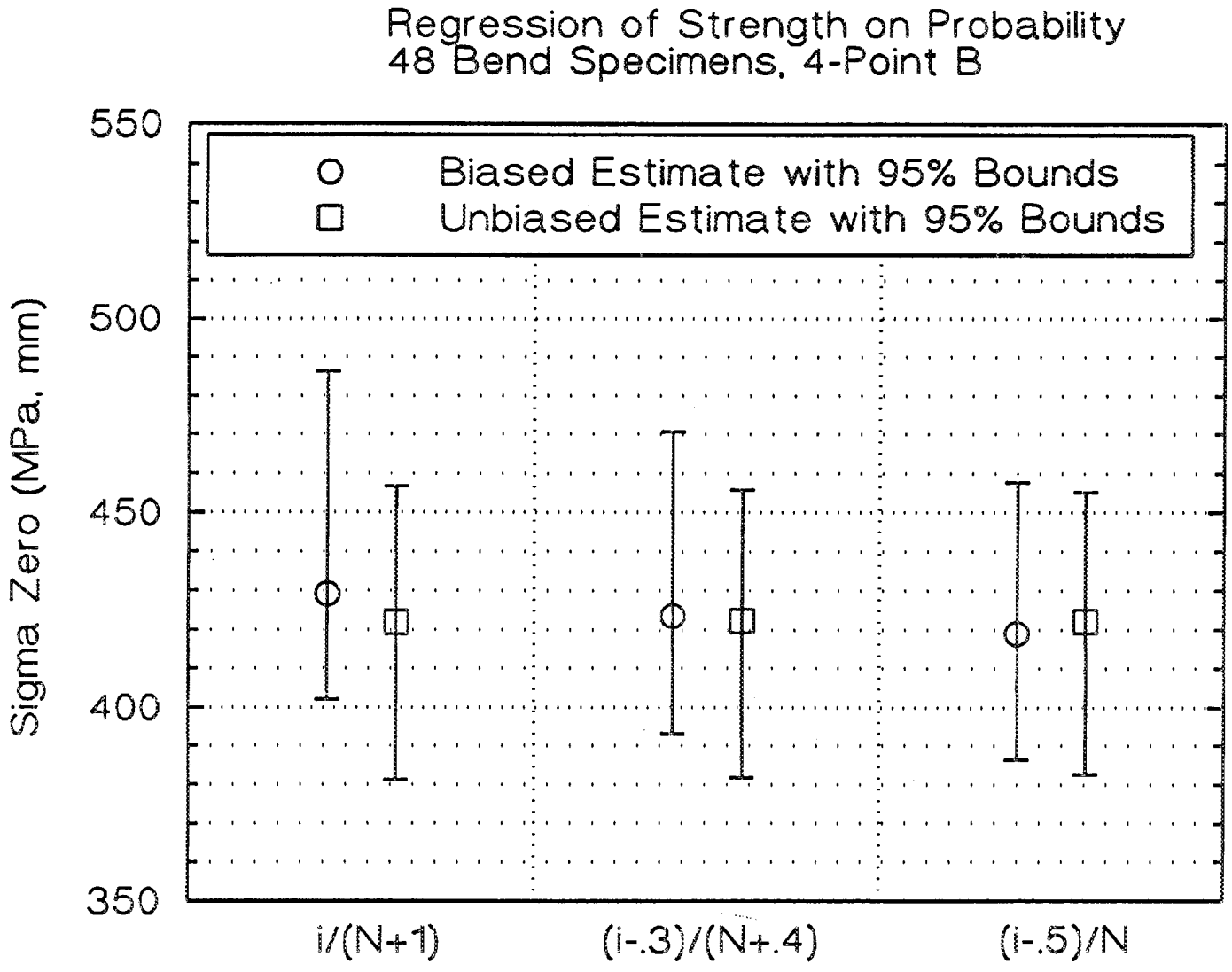
Regression of Strength on Probability
48 Bend Specimens, 4-Point B
Biased Estimate with 95% Bounds
Unbiased Estimate with 95% Bounds
Sigma Zero (MPa, mm)
550
500
450
400
350
i/(N+1)
(i-.3)/(N+.4)
(i-.5)/N

Figure 6

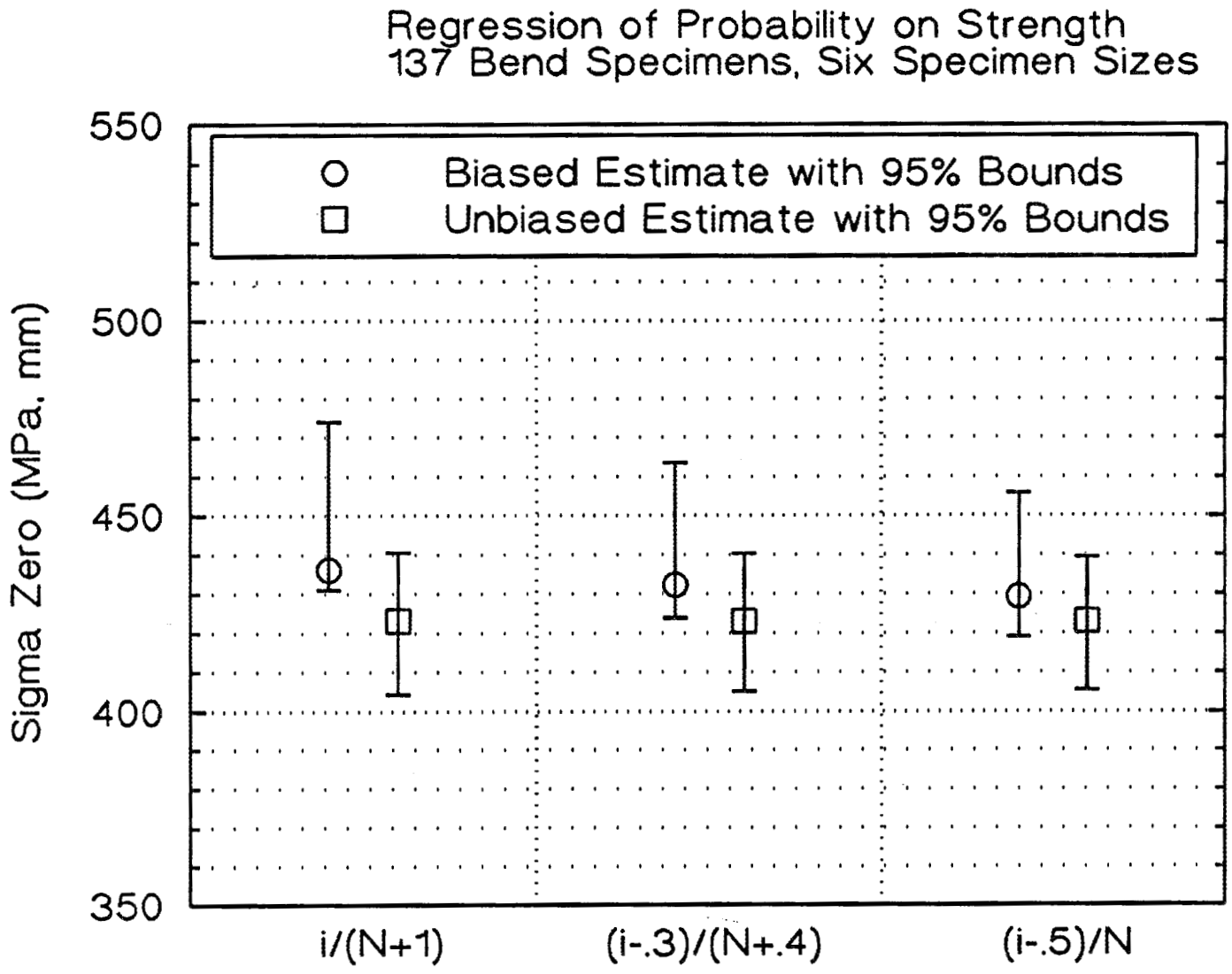
Regression of Probability on Strength
137 Bend Specimens, Six Specimen Sizes
Biased Estimate with 95% Bounds
Unbiased Estimate with 95% Bounds
Sigma Zero (MPa, mm)
550
500
450
400
350
i/(N+1)
(i-.3)/(N+.4)
(i-.5)/N

Figure 7

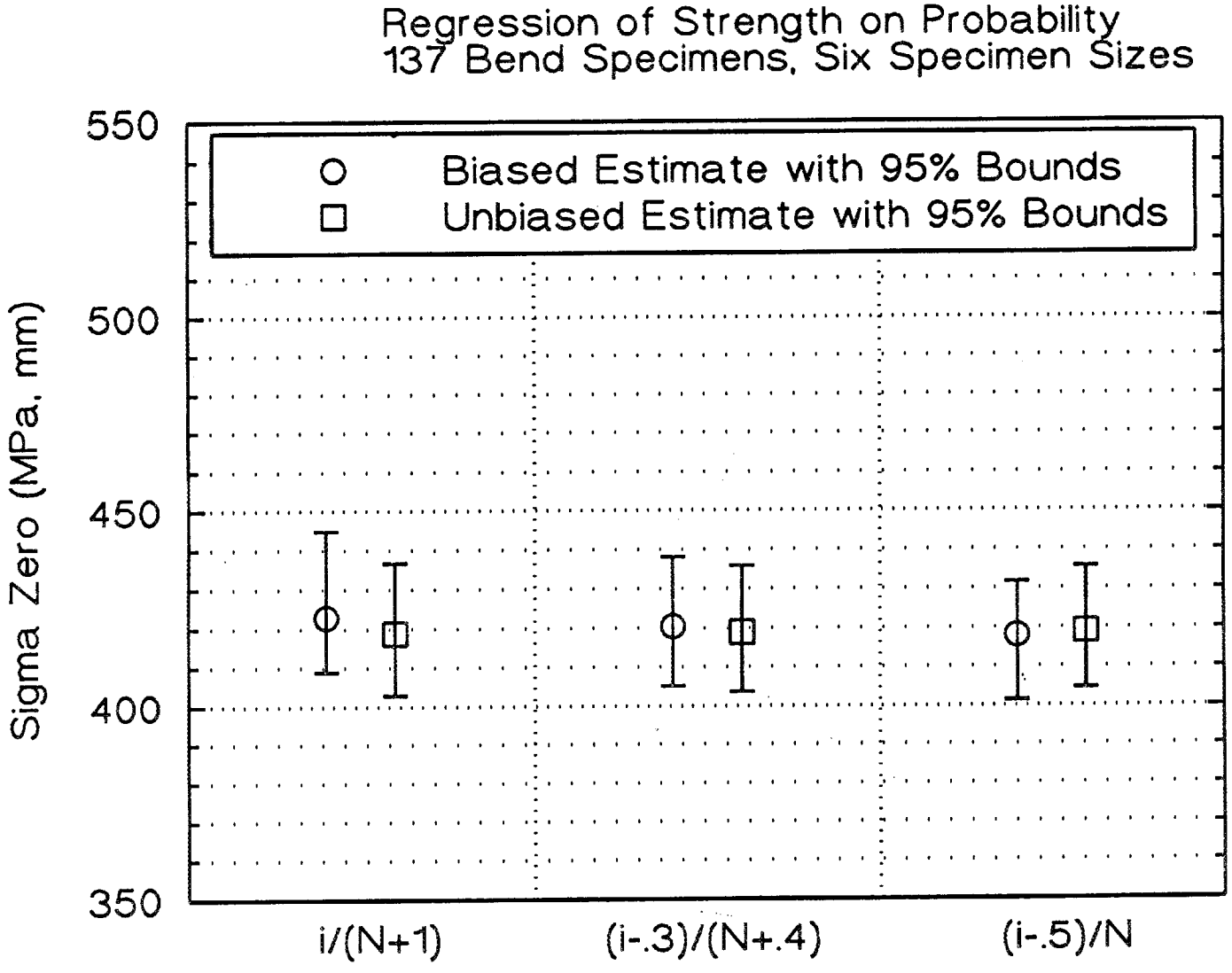
Regression of Strength on Probability
137 Bend Specimens, Six Specimen Sizes
Biased Estimate with 95% Bounds
Unbiased Estimate with 95% Bounds
Sigma Zero (MPa, mm)
550
500
450
400
350
i/(N+1)
(i-.3)/(N+.4)
(i-.5)/N

Figure 8

3.0 DATA BASE AND LIFE PREDICTION

INTRODUCTION

This portion of the project is identified as project element 3 within the work breakdown structure (WBS). It contains five subelements, including (1) Structural Qualification, (2) Time-Dependent Behavior, (3) Environmental Effects, (4) Fracture Mechanics, and (5) Nondestructive Evaluation (NDE) Development. Work in the Structural Qualification subelement includes proof testing, correlations with NDE results and microstructure, and application to components. Work in the Time-Dependent Behavior subelement includes studies of fatigue and creep in structural ceramics at high temperatures. Research in the Environmental Effects subelement includes study of the long-term effects of oxidation, corrosion, and erosion on the mechanical properties and microstructures of structural ceramics. Work in the fracture mechanics subelement includes development of techniques for measuring the tensile strength and creep resistance of ceramic materials at high temperatures, and testing ceramic materials at high temperatures under uniaxial tension. Work in the NDE development subelement is directed at identifying approaches for quantitative determination of conditions in ceramics that affect their structural performance.

Major objectives of research in the Data Base and Life Prediction project element are understanding and application of predictive models for structural ceramic mechanical reliability, measurement techniques for long-term mechanical property behavior in structural ceramics, and physical understanding of time-dependent mechanical failure. Success in meeting these objectives will provide U.S. companies with the tools needed for accurately predicting the mechanical reliability of ceramic heat engine components, including the effects of applied stress, time, temperature, and atmosphere on the critical ceramic properties.

3.1 STRUCTURAL QUALIFICATION

Microstructural Analysis of Structural Ceramics

B. J. Hockey and S. M. Wiederhorn (National Institute of Standards and Technology)

Objective/Scope

The objective of this part of the program is to identify mechanisms of failure in structural ceramics subjected to mechanical loads at elevated test temperatures. Of particular interest is the damage that accumulates in structural ceramics as a consequence of high temperature exposure to stresses normally present in heat engines.

Design criteria for the use of ceramics at low temperature differ from those at high temperature. At low temperature ceramics are elastic and brittle; failure is controlled by a distribution of flaws arising from processing or machining operations, and the largest flaw determines the strength or lifetime of a component. By contrast, at high temperature where ceramics are viscoelastic, failure occurs as a consequence of accumulated, or distributed damage in the form of small cavities or cracks that are generated by the creep process. This damage effectively reduces the cross-section of the component and increases the stress that must be supported. Such increases in stress are autocatalytic, since they increase the rate of damage and eventually lead to failure as a consequence of loss in cross section. When this happens, the individual flaw loses its importance as a determinant of component lifetime. Lifetime now depends on the total amount of damage that has occurred as a consequence of the creep process. The total damage is now the important factor controlling lifetime.

Recent studies of high temperature failure of the non-oxide ceramics intended for use for heat engines indicates that for long term usage, damage accumulation will be the primary cause of specimen failure. Mechanical defects, if present in these materials, are healed or removed by high temperature exposure so that they have little influence on long term lifetime at elevated temperature. In this situation, lifetime can be determined by characterizing the damage and the rate of damage accumulation in the material at elevated temperatures. In ceramic materials such as silicon nitride and SiAlON, such characterization required high resolution analyses because of the fine grain size of these materials: hence the need for transmission electron microscopy as an adjunct to the mechanical testing of ceramics for high temperature applications is apparent.

In this project, the creep and creep-rupture behavior of several ceramic materials will be correlated with microstructural damage that occurs as a function of creep strain and rupture time. Materials to be studied include: SiAlON; hot-pressed silicon nitride; sintered silicon carbide. This project will be coordinated with WBS 3.4.1.3, Tensile Creep Testing, with the ultimate goal of developing a test methodology for assuring the reliability of structural ceramics for high temperature applications.

Technical Highlights

During the past six months, microstructural characterization studies were continued on Norton NT-154, Hip'ed silicon nitride to determine the effect of microstructure on tensile creep behavior. As this study is nearly completed, an effort was made to correlate the results on NT-154 with those from earlier studies on GTE AY6 silicon nitride and on a SiC whisker reinforced grade of AY6. This report provides a summary comparison the microstructural analyses of three different silicon nitride, whose tensile creep/creep rupture behavior were investigated under Task 2. As mentioned, two of these materials were from GTE and were similarly hot-pressed with yttria (6 w/o) and alumina (1.5 w/o) as sintering aids; one, W/YAS, was reinforced with 30 v/o SiC whiskers, while the other, YAS, was not. The third material was from Norton (NT-154)-here designated as YS - and was HIP'ed with yttria (4.0 w/o) as the sole sintering aid. The aim of this review is to identify and compare those microstructural characteristics which appear to strongly influence the creep of these materials.

Experimental Technique

The bulk of the results obtained in this project were obtained by analytical transmission electron microscopy. Observations were made on the materials in both the as-received and post-crept conditions. Test samples selected for examination covered the range of creep conditions and included samples that failed after times ranging from 4 to ~300 hrs., depending on applied stress and temperature. Specimens from interrupted tests that survived for over 4000 hrs were also examined. In all cases, the gage sections of crept specimens were cut parallel to the stress axis to obtain both the near-surface and mid-plane sections. Prior to final TEM specimen preparation, these sections were examined optically for evidence of distributed creep cavitation or crack damage.

Results and Discussion

Although different in detail, the microstructures of all three materials can be described as "composite-like". Each contained distributions of equiaxed, submicron Si_3N_4 grains together with either, Fig. 1, highly acicular SiC whisker (W/YAS) of variable length (1-20 μm) or Fig. 2, distributions of both blocky and acicular ß-Si_3N_4 grains of 1 to 5 μm dimensions (YAS and YS). In the as-received state, intergranular glass is present at multi-grain junctions (eg. Fig. 1) and along most two-grain interfaces. For both YAS and YS, the glass compositions were consistent with reactions between silica and the sintering aid oxides; for W/YAS, however, the glass also contains minor concentrations of calcia, apparently leached from the SiC whiskers.

During creep testing in air at elevated temperatures, devitrification of the intergranular glass occurs. Crystallization

within the multi-grain junctions is particularly rapid, Fig. 3, and results primarily (but not exclusively) in the formation of: monoclinic y-$Y_2Si_2O_7$ in W/YAS; orthorhombic δ-$Y_2Si_2O_7$ in YAS, both at 1200-1250°C; triclinic α-$Y_2Si_2O_7$ and hexagonal N-Apatite (yttrium-silicon oxynitride) at 1300-1400°C within YS. Even after prolonged periods at these temperature (e.g. 2500 hrs.), complete devitrification does not occur and residual glassy interfaces (1-10 mm thick) remain between the crystalline secondary phases and the matrix grains, Fig. 4a. More importantly, devitrification is not found to occur within the narrow interfaces separating adjacent Si_3N_4 grains. Although these interfaces vary in thickness, ranging from roughly 10nm down to interplanar dimensions, (Fig. 4b), most are in the 1 to 5 nm range (Fig. 4c) and contain residual glass.

In comparing the different materials, only a qualitative assessment of interfacial morphologies can be made. In this regard, interfaces in YS tended to be more irregular and interfacial separations ranged from unit cell dimensions (as in Fig. 4b) to estimated values of 1-2 nm, whereas in YAS interfaces tended to be more uniform (as in Fig. 4c) due to an apparent increased tendency for grain facetting, and interfacial separations tended to range upwards to roughly 5nm. In W/YAS, residual glass in primarily concentrated along the SiC whiskers and resulted in continuous glassy interfaces of variable widths (~1nm to ~5nm).

Although devitrification, being primarily restricted to multi-grain junctions, does not affect interfacial separation distances, it does bring about an associated change in residual glass composition. These changes, while not always directly verifiable by EDS, can be deduced from the fact each of the secondary phases ($Y_2Si_2O_7$, Y_2SiO_7, and N-Apatite) are essentially "pure" and all have Y/Si concentration ratios larger the that of the original glasses. As a consequence of devitrification then, the residual glasses in each material become depleted in yttria or alternatively silica enriched; for YAS, there is additionally an enrichment of alumina, while for W/YAS there is an enrichment in both alumina and calcia.

The effect of devitrification on creep behavior can be considered in relation to tensile creep test results, which show varying degrees of improved creep resistance (and lifetime) upon pre-annealing. In addition, these materials exhibit transient creep behavior, indicative of progressive "work hardening". Here, considering that creep is primarily governed by "grain boundary" sliding involving viscous flow of residual glass and diffusive processes involving interfacial transport, the reduction in the amount of residual glass due to devitrification should lead to enhanced creep resistance. While the specific effect of a volume reduction in residual glass can be deduced from current viscous flow or interfacial transport models only by artificially introducing a volume term, the alternative, ie. assuming the rate of deformation is enhanced by an increase in residual glass content, is untenable. Moreover, while all applicable creep models predict a strong relationship between creep behavior and interfacial glass properties, the change in properties due to the associated change in residual glass composition upon devitrification cannot be

defined. At best, it can only be speculated that the relative decrease in Y/Si concentration ratio that occurs in YS upon devitrification results in a change in glass properties that further enhance creep resistance. For YAS and W/YAS, however, the depletion in yttria is accompanied by an enrichment of alumina or alumina and calcia so that the ultimate effect of glass composition changes could conceivably be contradictory to creep behavior. Finally, comparison of the devitrification behavior of these three materials showed that residual glass composition affected not only the nature of the secondary crystalline phase (generally, in fact, offsetting the expected temperature dependence), but the rate of crystallization as well. For YS, nearly complete devitrification of multi-grain junctions, regardless of size, occurred rapidly throughout the test samples, in that no significant difference in the extent of apparent devitrification was found in samples from tests of 4 to over 4000 hours duration. In contrast, devitrification in both YAS and, particularly, W/YAS appeared to occur more gradually, in that small multi-grain junctions often remained glassy after more than 100 hours at temperature.

Most significantly, the structure and composition of interfaces was found to have a profound effect on cavitation, which occurs in these materials during tensile creep and which is ultimately responsible for creep rupture. In general, the density and distribution of cavitation damage was highly stress dependent, and quantitive correlations with strain, strain rate, or lifetime await more systematic study. As such, we consider only the general aspects of cavity formation and growth, which is found to occur primarily within the narrow glassy interfaces separating adjacent matrix grains oriented for tensile stress

In W/YAS, the cavitation process was dominated by the presence of the SiC whiskers. In this material, residual glass is primarily concentrated along the whisker interfaces. During creep, preferential cavity nucleation occurs at tensile oriented whiskers. Rapid growth along the whisker interface results in distributed microcracks, Fig. 5, which link up to cause failure at relatively low stresses.

While YAS similarly exhibited preferential cavity nucleation and growth along the larger acicular or blocky grains in this material, cavity growth along the interfaces to full facet dimensions and the formation of creep crack segments, Fig. 6a, was controlled, and only gradually evolved just prior to failure. From Fig. 6b, the blunted morphology of cavities with widths exceeding the interfacial thicknesses suggest that in YAS cavity growth involves both surface diffusion and intergranular transport. The nucleation process, Fig. 7a, however, appears to involve viscous rupture of the interfacial glassy layer.

In YS, cavitation was found to occur in a completely different manner. In this material, cavitation is preceeded by fluctuations in the average width of tensile oriented interfaces due to the accumulation of glass into discrete "droplets". These droplets, which invariably exhibit a discernable concentration of chlorine, provide the nucleating sites for interfacial cavities Fig. 7b. Continued

growth, apparently by bulk diffusion, leads to distributions of non-interacting ellipsoidal cavities, whose widths (up to 100 nm) clearly exceed the interfacial separation distances between Si_3N_4 grains, Fig. 8.

The results suggest that crack formation and creep rupture in both W/YA and YAS are controlled by cavity growth, whereas in YS they are determined by the nucleation of cavities to a critically density. The observed differences in cavitation behavior clearly relate to the inherent differences in the morphologies, thicknesses, and compositions of the glass interfaces present within these materials. As opposed to YS, the interfaces in both YAS and W/YAS tend to be somewhat wider and more uniform, characteristics that are not only less inhibiting to interfacial sliding but which are also more favorable to accelerated cavity growth along the interface by both viscous flow or interfacial transport processes. By contrast, the highly irregular and narrower interfaces found in YS provide a natural impediment to interfacial sliding as such rigid body displacements will be limited by grain to grain contact (grain interlocking). Thus, while interfacial sliding may contribution to the nucleation of cavities, both continued deformation and/or cavity growth must proceed by localized diffusive transport. In this regard, the nature of the cavities produced in YS further suggests that rapid diffuse transport along the interfaces in inhibited, presumably as a consequence of the interfacial glass film thickness and composition. This tentative conclusion, however, ignores the possible effect of chlorine on cavity growth and therefore, cavity morphology. While detectable concentrations were repeatedly found within the glass "droplets" that form prior to cavity nucleation, Fig. 7b, the origin of chlorine and it's role in cavitation is yet to be determined.

Status of Milestones

All milestones are on schedule.

Publications

D. C. Cranmer, B. J. Hockey, S. M. Wiederhorn, and R. Yeckley, "Creep and Creep Rupture of Hip'ed Si_3N_4" Ceram. Eng. Sci. Proc., 1991. In Press.

B. J. Hockey and S. M. Wiederhorn, "Tensile Creep of Y-Si_3N_4: I. Microstructure" and "Tensile Creep of Y-Si_3N_4: II. Cavitation" Proc. 49th Annual Mtg. EMSA, 1991. In Press.

S. M. Wiederhorn, B. J. Hockey, D. C. Cranmer, and R. Yeckley, "Transient Creep of Hot Isostatically Pressed Silicon Nitride" To be submitted to J. Mater. Sci., 1991.

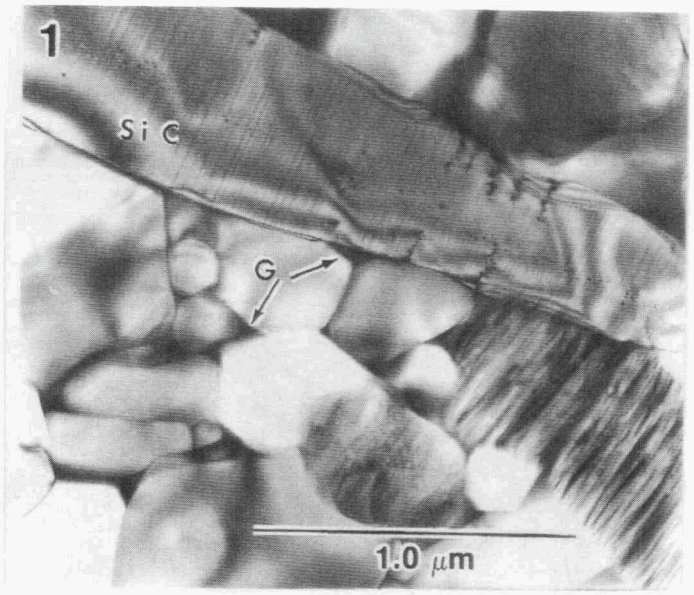

Figure 1. Representative view of as-received W/YAS, showing randomly oriented SiC whiskers distributed within matrix of equi-axed Si_3N_4 grains. Glass is present at multi-grain junctions (e.g. G) and along two-grain interfaces.

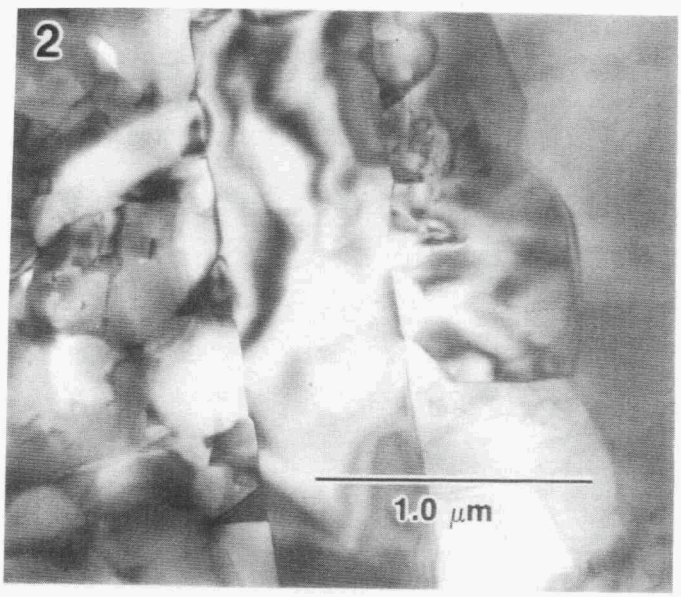

Figure 2. Representative view of YAS, illustrating heterogeneous nature of microstructure. YS exhibited a similar distribution in ß-Si_3N_4 grain size and morphology.

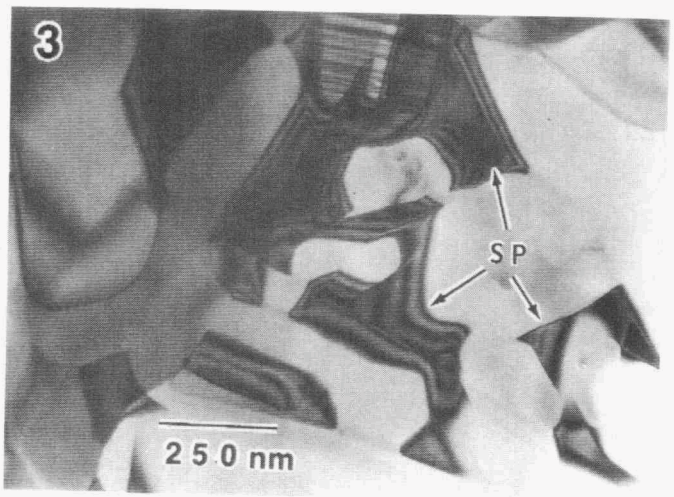

Figure 3. Illustrative view of crystalline secondary phase formation (SP) at multi-grain junctions in W/YAS after creep testing. Similar devitrification of glass at multi-grain junctions also occurs in YAS and YS. Primary phases identified in text.

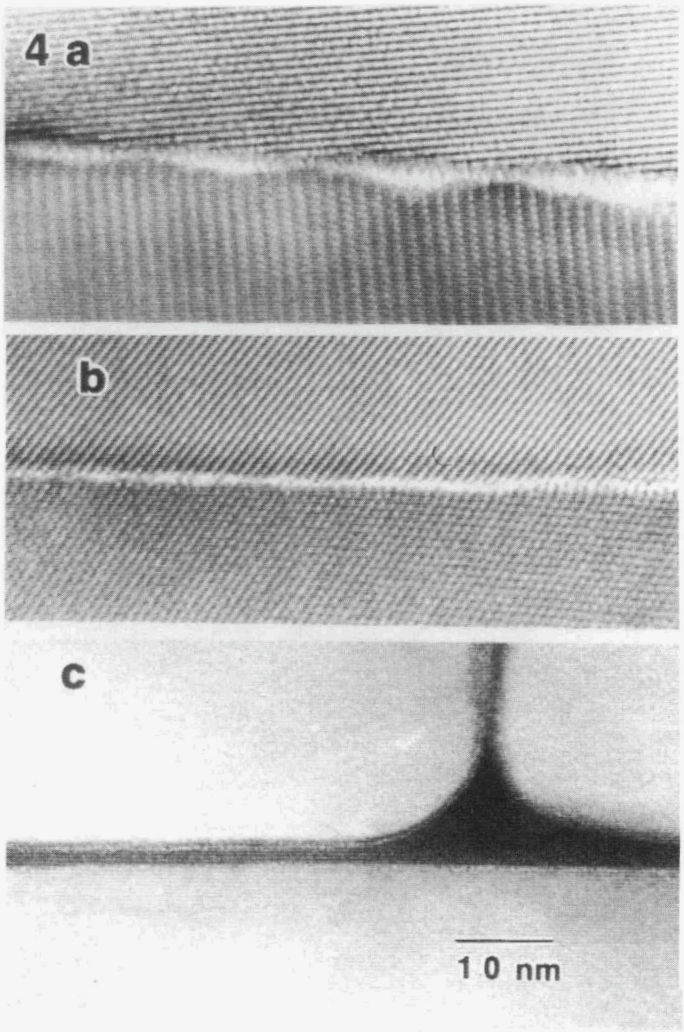

Figure 4. Representative views of narrow interfaces separating crystalline phases after creep testing. a) Glass interface between Si_3N_4 (top) and δ-$Y_2Si_2O_7$ (bottom) in YAS. Lattice fringe spacing in Si_3N_4 = 0.66 nm. b) Interface separating adjacent Si_3N_4 grains in YS. Contrast change across interface appears to indicate glassy film of interplanar dimensions. Fringe spacing in top Si_3N_4 grain = 0.66 nm. c) Glassy interface and triple junction in YAS. Time dependent devitrification eventually results in crystallization of triple junctions, but not within interfacial glass layers less than 10nm thick.

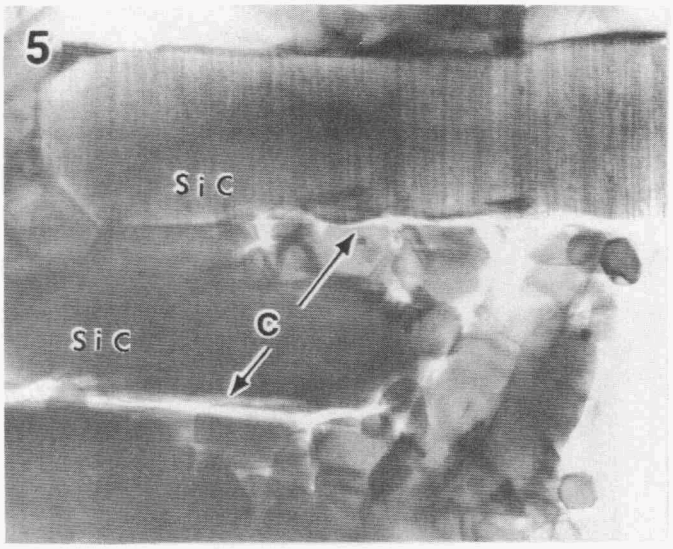

Figure 5. Microcracks (C) produced in W/YAS by rapid cavity growth along tensile oriented SiC whiskers during creep.

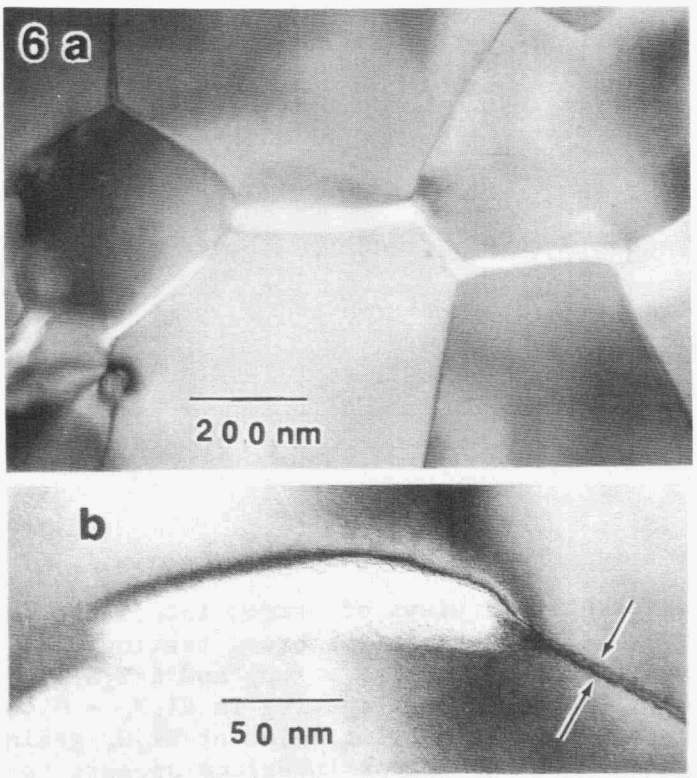

Figure 6. a) Microcrack development in YAS due to cavity growth along narrow interfaces separating Si_3N_4 grains. Note, however, the blunt morphology at points of arrest. b) Isolated crack-like cavity in YAS, again illustrating blunt morphology of advancing tips. Note, also, cavity width exceeds projected interfacial width (arrowed).

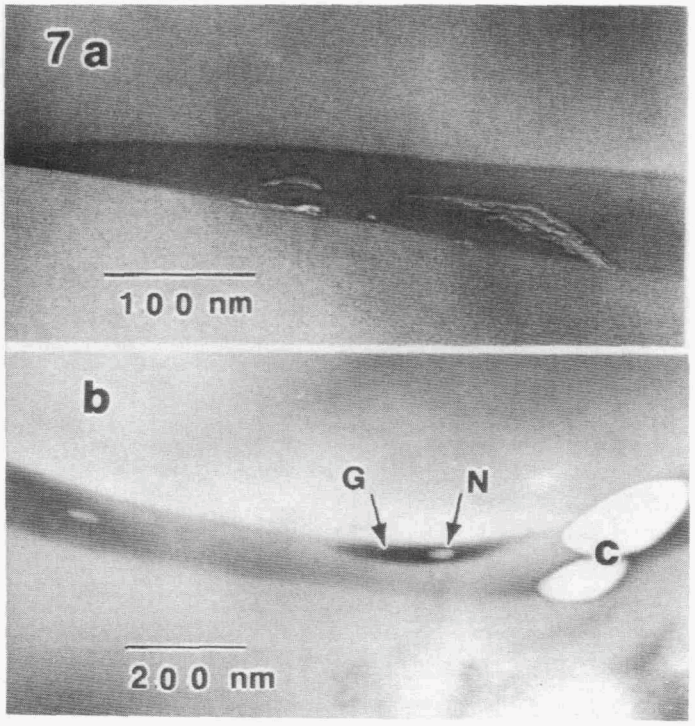

Figure 7. Cavity nucleation in YAS, (a), and YS, (b). a) In YAS, ruptures develop within the glassy film in tensile oriented interfaces. Diffusive growth along the interface leads to the formation of crack-line cavities, as in Fig. 2b. b) In YS, cavity nucleation (N) occurs with discrete "pockets" of glass (G), which develop at an earlier stage. Diffusive growth into the adjacent Si_3N_4 leads to the formation of ellipsoidal cavities (C).

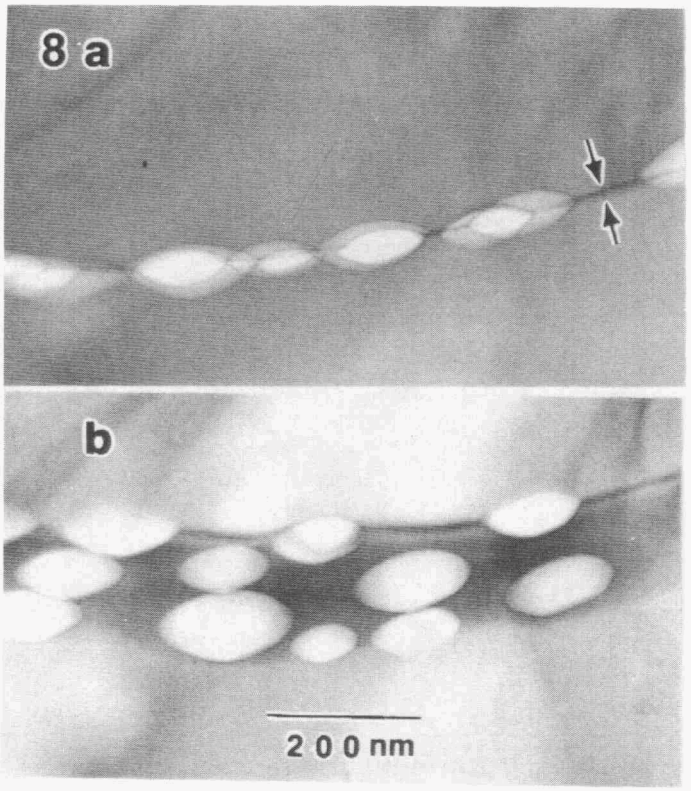

Figure 8. Two views of the same interface in YS illustrating the distribution of ellipsoidal cavities produced during tensile creep. In a) the interface is viewed nearly edge-on, and despite image overlap, cavity widths are seen to exceed the projected interfacial widths. In b) the interface is seen in projection to reveal the distribution of the non-interactive cavities. Presumably, rapid interactive growth or rupture eventually occurs once a critical density of cavities is produced.

Microstructural Characterization

Karren L. More (Oak Ridge National Laboratory)

Objective/scope

The objective of the research is to use analytical and high-resolution electron microscopy (HREM) to characterize the microstructure of a chemically vapor deposited (CVD) Si_3N_4 material and a SiC whisker-reinforced Si_3N_4 ceramic composite before and after creep deformation. This work represents a collaboration with North Carolina State University and GTE Laboratories.

Technical progress

Work during this reporting period focussed on the characterization and creep behavior of a CVD Si_3N_4 material. The Si_3N_4 was supplied by Union Carbide. Deposition was performed at 1720 K and 1 torr pressure and the reactant gases were $SiCl_4$ and NH_3. The methods used were similar to those described by Niihara and Hirai.[1]

The CVD Si_3N_4 was identified as pure α-Si_3N_4 by both electron diffraction and X-ray diffraction. The material was polycrystalline with an extremely large average grain size (20 to 100 μm). A transmission electron microscope (TEM) image showing the typical microstructural features observed in the as-grown CVD material is shown in Fig. 1. The sample was found to have many grown-in dislocation loops as well as other planar defects (arrowed) within the grains. Loops have been observed in neutron- and electron-irradiated ceramics[2,3] and in deformed sapphire.[4] They are rarely observed in as-grown CVD materials and have not been identified in Si_3N_4. In order to identify the nature of the loops and the planar defects frequently observed, a Kikuchi map was made using a MAC-based program called DIFFRACT to assist with tilting experiments.

The weak beam, dark field image of Fig. 2 shows that there are several different loop variants, labelled A, B, C (nearly invisible) and D (D loops are edge-on in image), existing in the structure and that the loops are typically faulted. The loops were analyzed using standard $\mathbf{g} \cdot \mathbf{b}$ analysis and inside/outside contrast techniques. The exact habit planes and corresponding Burgers vectors for the four variants observed are as follows:

Habit plane	Burgers vector	Loop type
(1121)	$\frac{1}{3}$[1123]	A
(2111)	$\frac{1}{3}$[2113]	B
(2111)	$\frac{1}{3}$[2113]	C
(1211)	$\frac{1}{3}$[1213]	D

YP11955

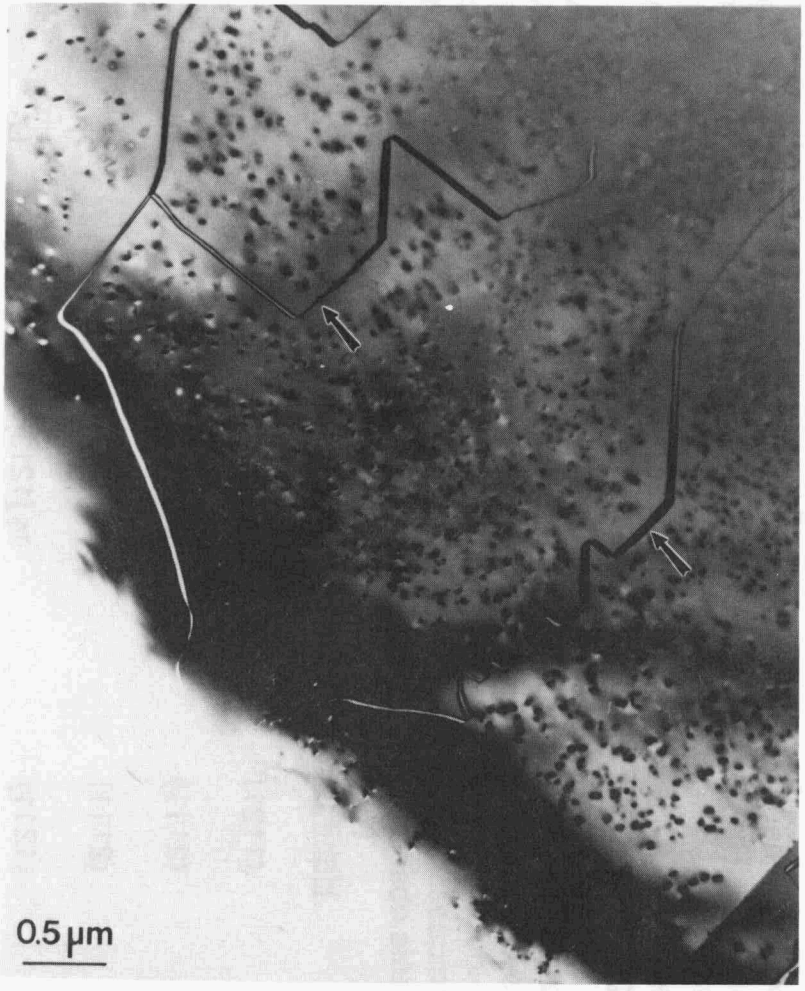

Fig. 1. Low magnification TEM image of CVD α-Si_3N_4 microstructure showing high concentration of dislocation loops and planar defects within the grains (arrowed).

YP11954

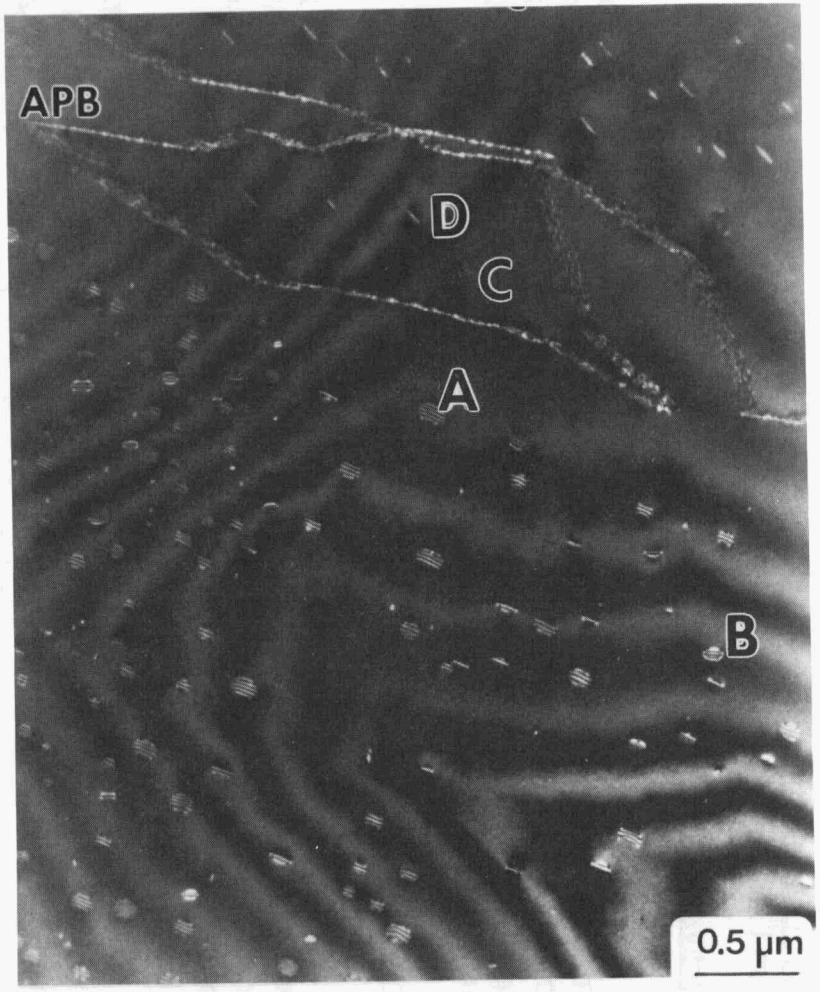

Fig. 2. Weak beam, dark field image showing the four variants (labelled A, B, C, and D) of faulted dislocation loops, which were identified in CVD α-Si_3N_4. The D loops are edge-on and the C loops are nearly invisible under these conditions.

There are two other variants of this type that were not observed, but it is anticipated that they also exist in the structure and are:

(1211) $\frac{1}{3}$[1213]

(1121) $\frac{1}{3}$[1123]

The loops were identified as vacancy loops and were pure edge in nature since the Burgers vector was normal to the habit plane.

The planar defects (exhibiting symmetrical fringe contrast) observed "swirling" through the grains were difficult to identify. There are three possible types of planar defects that exhibit symmetrical fringe contrast: (1) an enantiomorphic boundary (a boundary that separates regions of left- and right-handed symmetry); (2) an anti-phase domain boundary (separates regions of a crystal in which atoms occupy opposite sites and is usually associated with a displacement across the interface); and (3) an inversion domain boundary across which an inversion or 180° rotation occurs in a crystal without a center of symmetry (a particular type of antiphase domain boundary). Enantiomorphic boundaries are not possible in α-Si_3N_4 since a mirror plane exists in the structure (space group *P*31*c*). Antiphase domain boundaries have been identified in polar materials such as CVD β-SiC,[5] GaAs,[6] and AlN[7] using a technique described by Tafto.[8] However, α-Si_3N_4 is not a polar material and, thus, this particular technique is not applicable. HREM was employed to determine if there was an actual displacement across the interface. The displacement vector cannot be determined by this method since a high-resolution image reflects a projection in only one direction. However, the actual displacement in that projection can be determined.

A near edge-on boundary existing in an extremely thin region of the α-Si_3N_4 crystal was necessary for HREM, as shown in Fig. 3. A <1123> HREM image of the boundary (each end of the boundary is arrowed) together with a simulated image under comparable conditions is shown in Fig. 4. In the atomic representation of the <1123> projection [shown inset Fig. 4(*b*)], the small circles represent nitrogen and the large circles represent silicon. The HREM image shows a definite displacement across the boundary [drawn in black in Fig. 4(*a*)], the direction of which is arrowed in the corresponding simulated image. This displacement can be seen clearly in the oblique view of the HREM image (Fig. 4) shown in Fig. 5 (the boundary is arrowed). The displacement in this particular orientation was determined to be $\frac{1}{3}$<1100> and corresponds to a "shift" from one row of nitrogen atoms to the next across the boundary. The boundary is, thus, a type of antiphase domain boundary since the nature of the bonding has changed across the boundary and the boundary is associated with an atomic displacement. Work is ongoing to completely characterize the boundaries.

The CVD α-Si_3N_4 material was subjected to constant compressive stress creep in a manner similar to that used for the creep of a SiC whisker-reinforced

YP12266

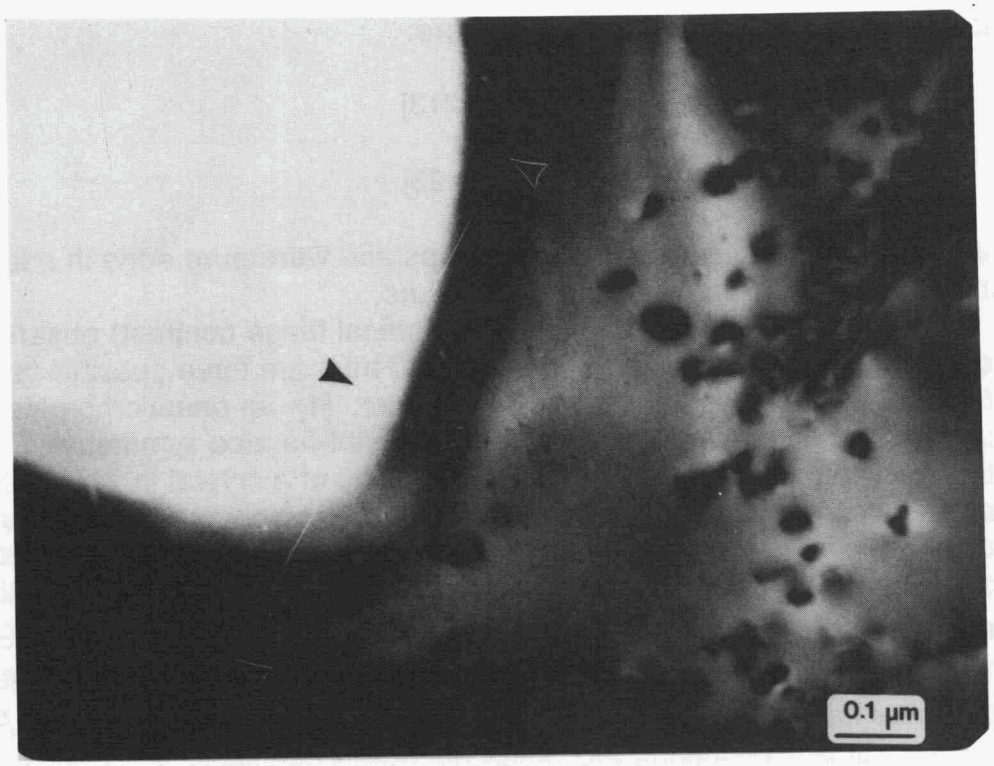

Fig. 3. A near edge-on boundary in a very thin region of the CVD α-Si_3N_4 crystal.

Si_3N_4 composite. Creep was conducted in nitrogen under temperature and stress conditions of 1920 to 2045 K and 50 to 350 MPa, respectively. The CVD material, however, did not creep. Steady-state conditions could not be reached before the specimens fractured. The material was examined by TEM following creep and no changes in microstructure were observed.

Work during this reporting period has also focussed on completing the study of the creep behavior of a SiC whisker-reinforced Si_3N_4 composite in air. As described in previous reports, the creep behavior of the composite in air was similar to that observed in nitrogen in that a bilinear stress dependence was observed at temperatures $\geq$ 1570 K. In the low stress regime, the stress exponent, **n**, was less than one, whereas in the high stress regime, **n** was greater than one. Creep in air resulted in higher creep rates than were observed for creep in nitrogen.

When crept in air, the morphology of the specimen surface was completely different than that observed following creep in nitrogen, as shown in Fig. 6. X-ray diffraction results showed only β-Si_3N_4 during a scan of the specimen surface following creep at both 1570 and 1620 K. There was little microscopic evidence for the formation of additional crystalline or glassy phases on the surface, except for

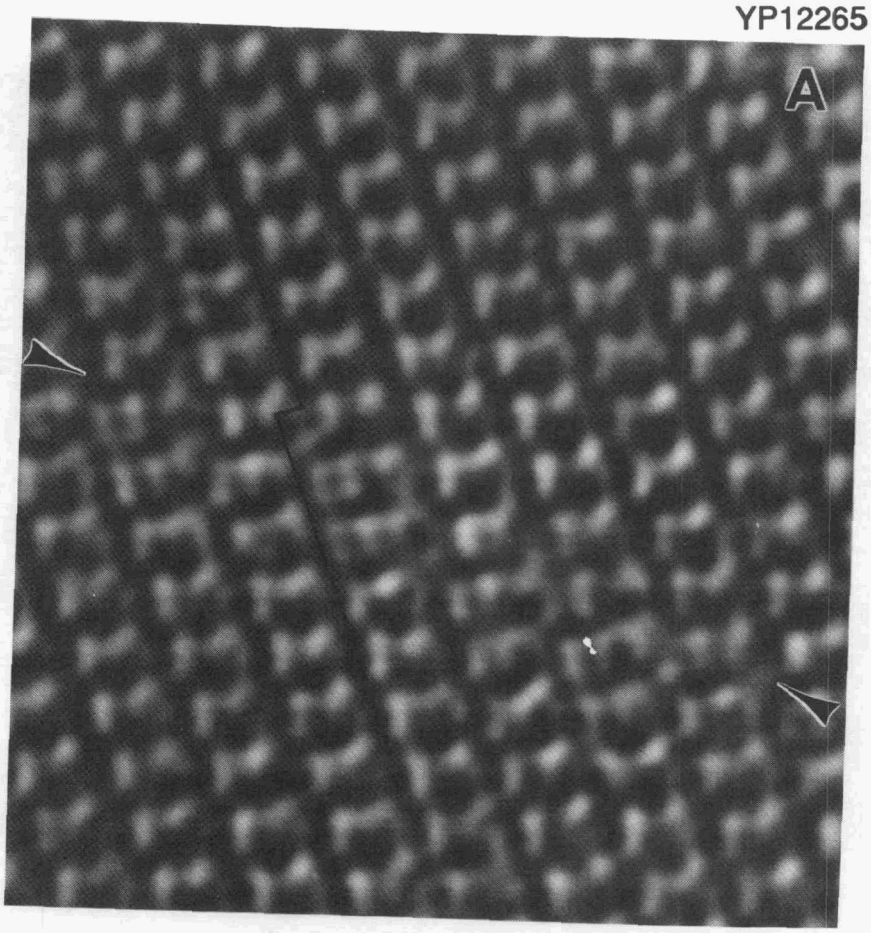

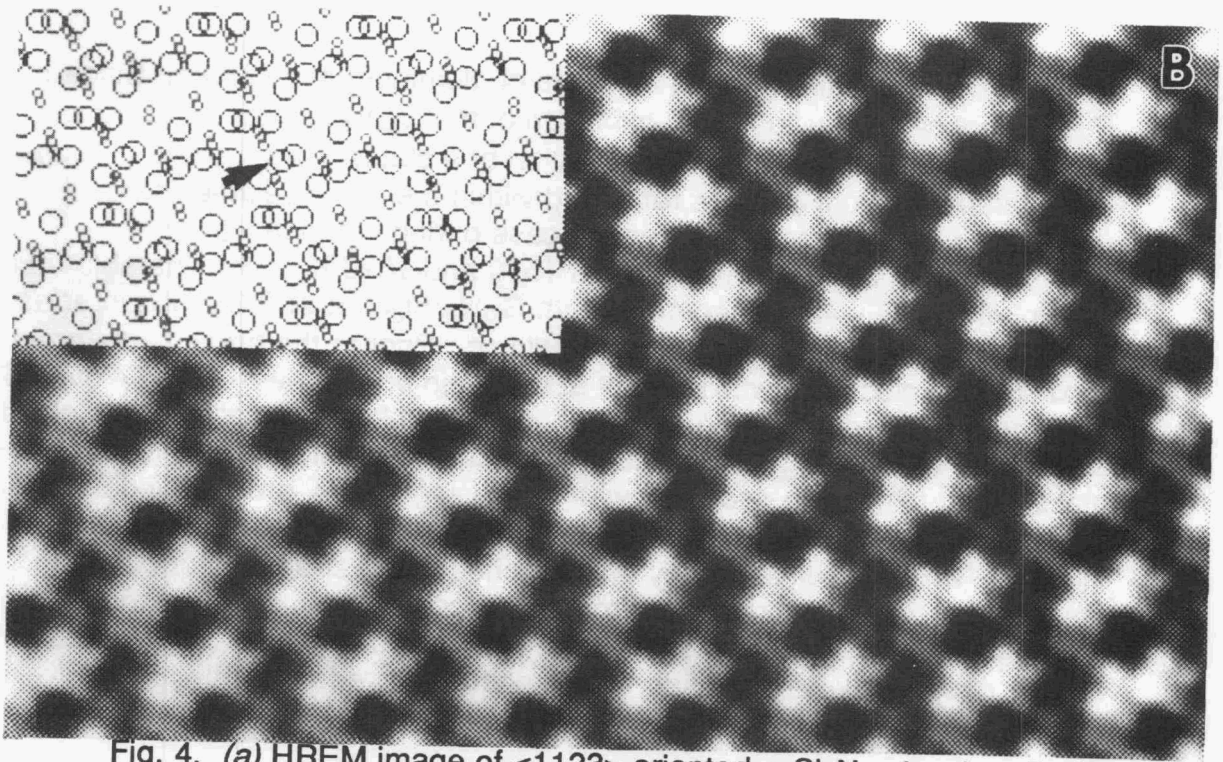

Fig. 4. *(a)* HREM image of <1123> oriented α-Si_3N_4 showing displacement across boundary and *(b)* corresponding simulated image with an atomic overlay inset.

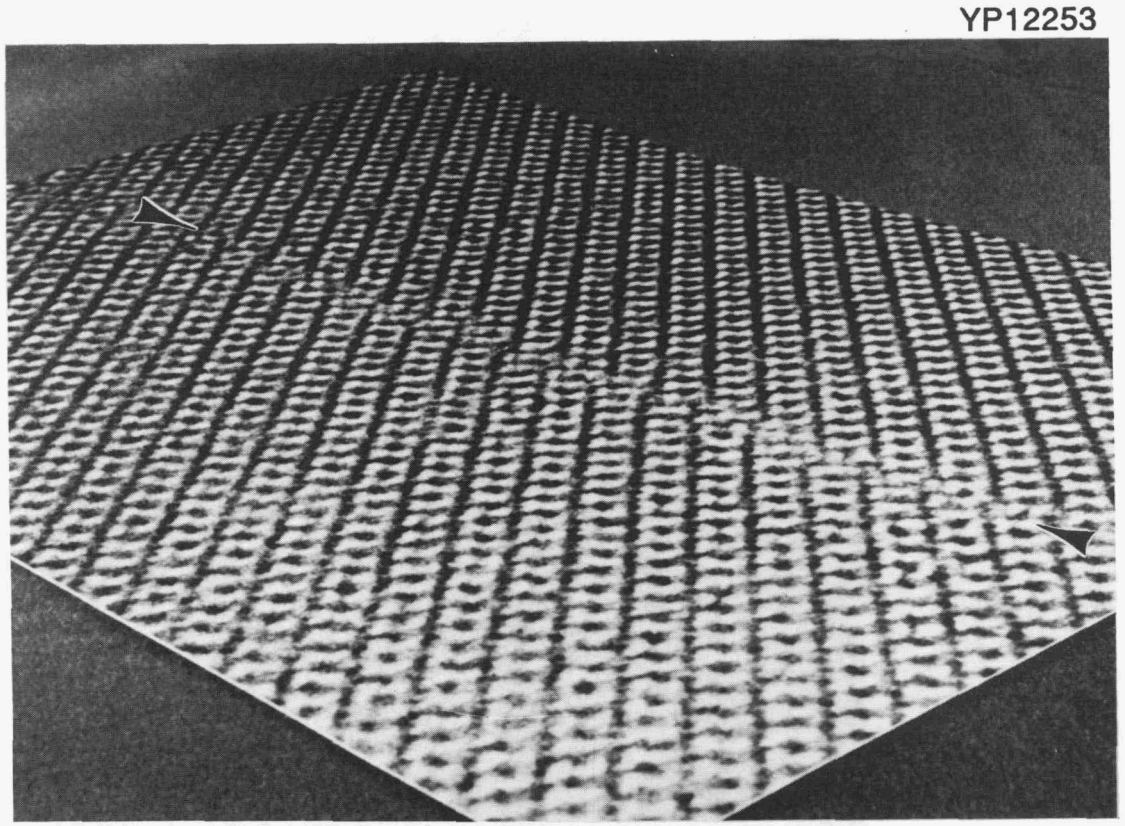

Fig. 5. Oblique view of same HREM in Fig. 4*(a)* clearly showing the displacement across boundary (arrowed).

isolated areas containing small amounts of aluminum and yttrium. Since pO_2 >> 81 Pa, it is not clear why "passive" oxidation of the Si_3N_4 surface does not occur under these conditions, resulting in the formation of a stable "oxide" scale.[9] Thus, a considerable amount of glass remained within the bulk specimen since it was not transported to the surface (as was the case during creep in nitrogen).

Following full creep runs at both 1570 and 1620 K, a considerable number of "strain whorls"[10] were observed at both Si_3N_4/Si_3N_4 and SiC/Si_3N_4 interfaces indicating the onset of grain-boundary sliding. Prior to the break in the creep curve, a continuous glass film was present at the grain boundaries. At the elevated temperatures used for the creep experiments, the lower viscosity of the glass film allowed for enhanced grain-boundary sliding. However, as the thickness of the glass film continued to decrease with increasing stress, grain-boundary sliding was inhibited by the closer proximity of Si_3N_4 grains and ledge asperities locking the structure, which is evidenced by the presence of the strain centers at grain boundaries. The glass retracted from these contact points into relatively large glass pockets (not to the specimen surface). The most significant microstructural feature observed was cavitation, which occurred predominantly along SiC

YP12001

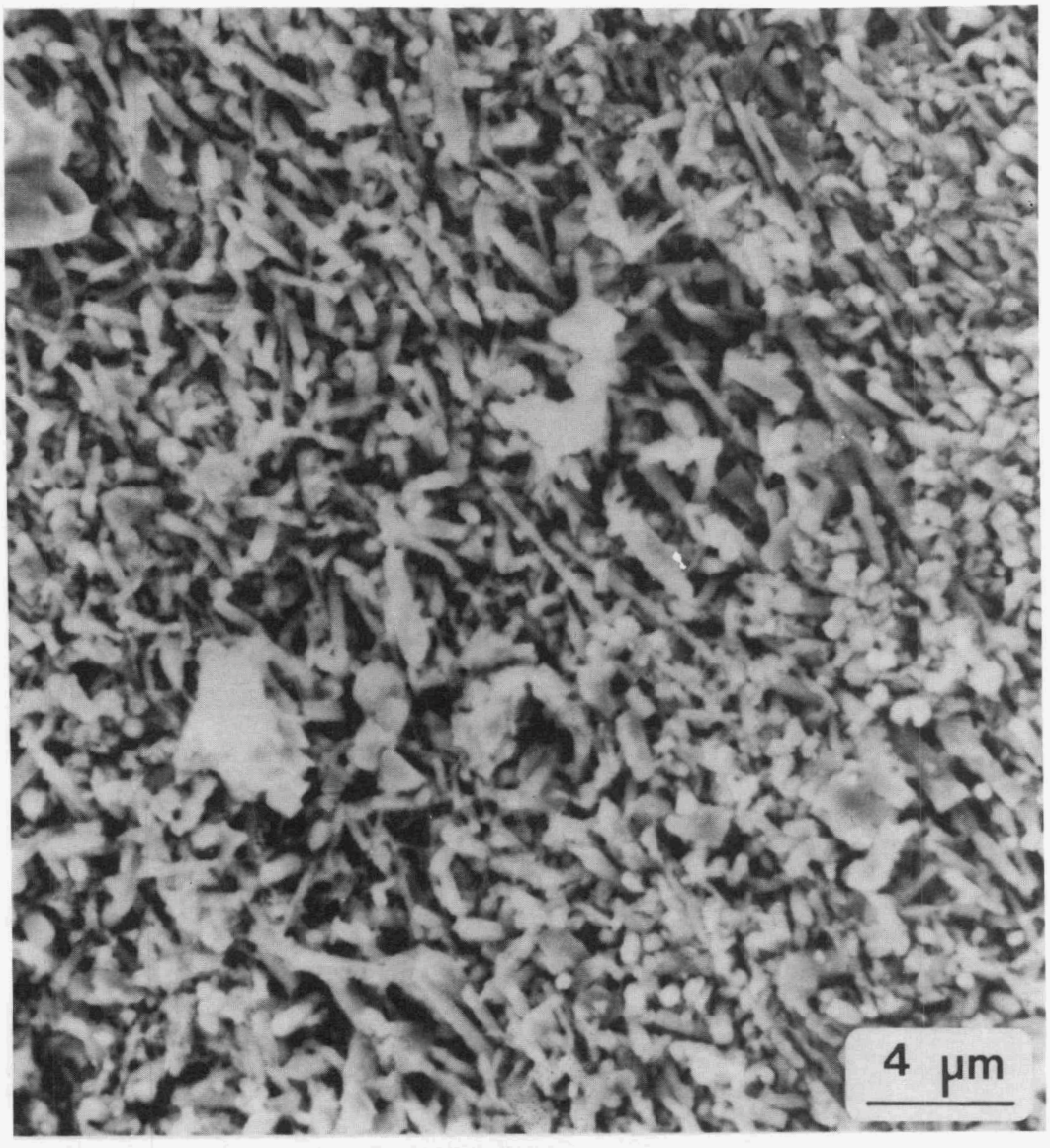

Fig. 6. Surface of cylinder following creep of SiC whisker-reinforced Si_3N_4 in air at 1570 K showing small, acicular β-Si_3N_4 grains covering surface.

whiskers, as shown in Fig. 7. The cavities formed within residual glass pockets throughout the microstructure. In fact, a glassy layer outlined many of the cavities (Fig. 8). Thus, creep in air occurred by a different mechanism than creep in nitrogen. Before the break in the creep curve (in the low stress regime), "non-steady state" creep was observed as a result of the presence of a significant amount of glass throughout the microstructure. During creep in air, much of the

YP12004

Fig. 7. Significant cavitation was observed following creep in air at 1570 to 1620 K.

YP12005

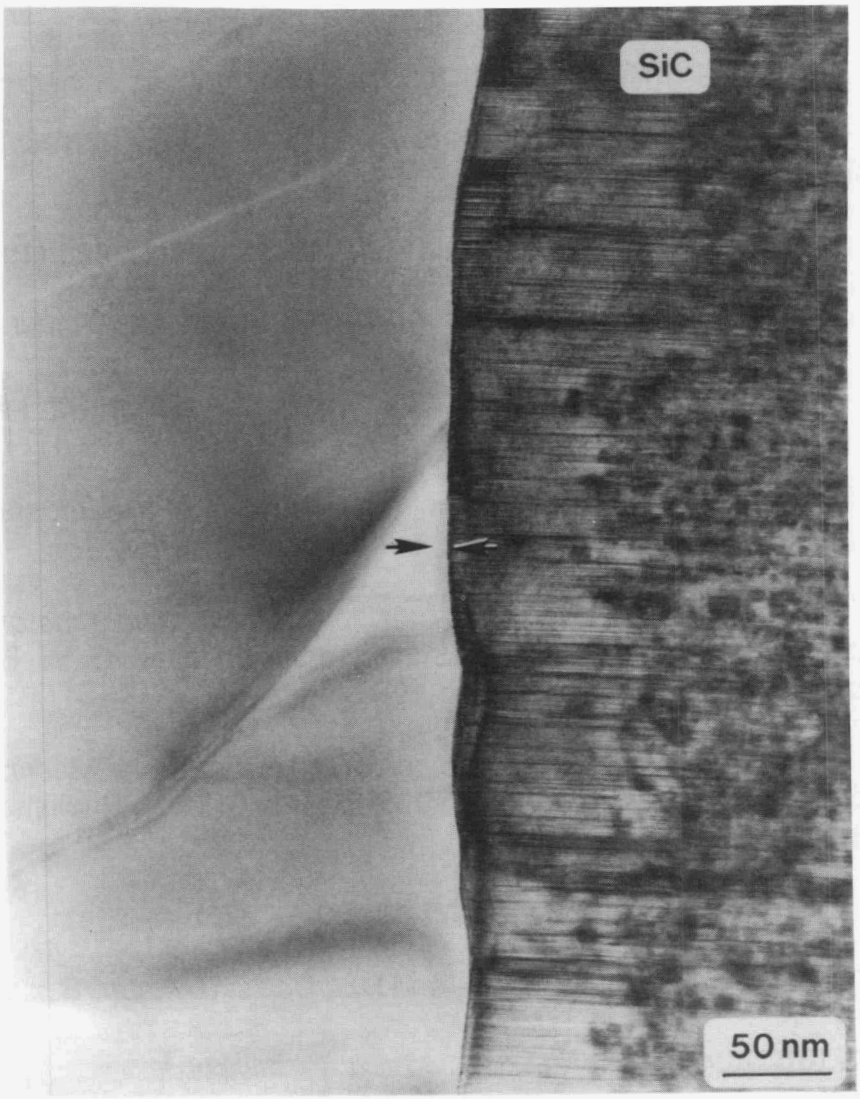

Fig. 8. Residual glass was found surrounding many of the cavities.

glass was removed from grain boundaries and segregated to large, isolated pockets rather than to the surface, as occurred during creep in nitrogen. Grain-boundary sliding occurred but was inhibited by ledge asperities meeting and locking the structure. Cavitation occurred in the high stress regime within residual glass pockets.

References

1. K. Niihara and T. Hirai, *J. Mater. Res.*, **11,** 593 (1976) .

2. F. W. Clinard, Jr., G. F. Hurley, and L. W. Hobbs, *J. Nucl. Mater.* **108-109,** 655 (1982).

3. D. G. Howitt and T. E. Mitchell, *Phil. Mag.* **44**(1), 229 (1981).

4. B. J. Pletka, T. E. Mitchell, and A. H. Heuer, *Acta Metall.* **30**, 147 (1982).

5. P. Pirouz, C. M. Chorey, and J. A. Powell, *Appl. Phys. Lett.* **50**(4), 221 (1987).

6. N. H. Cho, B. C. DeCooman, C. B. Carter, R. Fletcher, and D. K. Wagner, *Appl. Phys. Lett.* **47**(8), 879 (1985).

7. S. McKernan and C. B. Carter, p. 432 in *Proceedings of the 47th Annual Meeting of the Electron Microscopy Society of America*, ed. G. W. Bailey, San Francisco Press, San Francisco 1989.

8. J. Tafto, p. 154 in *Proceedings of the 39th Annual Meeting of the Electron Microscopy Society of America*, ed. G. W. Bailey, Claitor's Publishing Division, Baton Rouge, La., 1981.

9. S. C. Singhal, *J. Mater. Sci.* **11,** 500 (1976).

10. F. F. Lange, D. R. Clarke, and B. I. Davis, *J. Mater. Sci.* **15,** 615 (1980).

Status of milestones

The program on schedule.

Publications

1. K. L. More, D. A. Koester, and R. F. Davis, "Microstructural Characterization of a Creep-Deformed SiC Whisker-Reinforced Si_3N_4 Composite," presented at the Frontiers of Electron Microscopy in Materials Science Meeting, May 20–24, 1990, Oak Brook, Ill. (accepted for publication in *Ultramicroscopy).*

2. K. L. More, D. A. Koester, and R. F. Davis, "The Role of Interfaces in the Creep-Deformation of a SiC Whisker-Reinforced Si_3N_4 Composite," p.382 *in Electron Microscopy 1990*, Vol. **4**, ed. L. D. Peachey and D. B. Williams, San Francisco Press, San Francisco, 1990 382.

3. K. L. More, "Defect Characterization in a CVD α-Si_3N_4," to be presented at the Annual Meeting of the Electron Microscopy Society of America, August 4-9, 1991, San Jose, Calif. To be published in the conference proceedings.

4. D. A. Koester, K. L. More, and R. F. Davis, "Deformation and Microstructural Changes in SiC Whisker-Reinforced Si_3N_4 Composites," accepted for publication in *Journal of Materials Research.*

Project Data Base
B. L. Keyes (Oak Ridge National Laboratory)

Objective/scope

The objective of this task is to develop a comprehensive computer database containing the experimental data on properties of ceramic materials generated in the total effort. This computer system should provide a convenient and efficient mechanism for the compilation and distribution of the large amounts of data involved. The database will be available in electronic form to all project participants. In addition, periodic hard-copy summaries of the data, including graphical representation and tabulation of raw data, will be issued to provide convenient information sources for project participants.

Technical progress

The data base contains 6093 test results on over 360 different batches of ceramic materials. Approximately 48% of these are on zirconia-based ceramics, 7% are on silicon carbides, 22% are on silicon nitrides, 6% are on whisker-reinforced silicon nitrides, 15% are on alumina-based ceramics (including whisker-reinforced aluminas and mullites), and 2% are on other ceramics. Table 1 gives a detailed breakdown, by material class, of the data stored in the system. A list of materials within a material class is available on request.

Work during this semiannual period included sending the data base to several requestors, including Phillips Petroleum in Oklahoma, the U.S. Bureau of Mines, NIST, and NASA Lewis Research Center. To date, 18 full sets of data base disks have been distributed.

After working with a small user community for several months now, a need has arisen to facilitate specific material searches in the data base. One problem with ceramics is that a material may go by several different names (a company-assigned name and a generic name, for example). No standardization in the industry appears to exist. Since information in the data base is stored using the material name as a guide, the potential problems are immediately obvious. Another aspect to this problem involves accessing a material by creation process or heat treatment. All processing history data are stored in a text file (sentence-type structure), and accessing such information requires more specialized techniques that are readily available in dBASE IV. Possible solutions to these problems will be investigated in the next semi-annual period.

Data base personnel attended the Fall meeting of ASTM E49 - Committee on Computerized Materials Properties Data bases held November 9-11, 1990, in San Antonio, Texas. One of the objectives of this committee is to develop lists of fields, and definitions where necessary, that sufficiently describe the material being tested and the results of the tests being performed. Important information may be

Table 1. Ceramic Technology for Advanced Heat Engines data base summary as of April 30, 1991

Material class	Brazed specimens						Cyclic fatigue	Density	Dynamic fatigue	Elasticity
	MOR 4	Shear str.	Toughness	Torsion	Tor fatigue	Creep				
Alumina							15		9	28
Alumina + reinforcing fibers								7		
Alumina + zirconia										
Mullite										2
Mullite + reinforcing fibers										11
Silicon Carbide		12						10	13	15
Silicon Nitride	69	48		15	7	37	19	28	16	24
Silicon Nitride + reinforcing fibers							15	2		16
Zirconia	160	58	2				51	158		119
Zirconia + reinforcing fibers										
Other										
Totals	229	118	2	15	7	37	100	205	38	215

Material class	Fracture toughness	Hardness	Interrupted fatigue	MOR 3 Pt bend	MOR 4 Pt bend	Oxidation rate	Poisson's ratio	Shear modulus	Tensile	Thermal conductivity
Alumina	39	4			411				28	3
Alumina + reinforcing fibers	39				144				11	34
Alumina + zirconia					7					
Mullite				1	4					
Mullite + reinforcing fibers	16			9	22					
Silicon Carbide	24	27			235					
Silicon Nitride	94	112		10	647	1	2	1	73	9
Silicon Nitride + reinforcing fibers	53				144	3	17	16	86	9
Zirconia	347	24	239		1554				50	
Zirconia + reinforcing fibers					2				36	
Other	3	25			59					
Totals	615	192	239	20	3229	4	19	17	284	55

Table 1. Ceramic Technology for Advanced Heat Engines data base summary as of April 30, 1991 (continued)

Material class	Thermal contraction	Thermal diffusivity	Thermal expansion	Thermal shock	Torsion	X-ray diffraction	Wear resist	Material char.	Chemistry
Alumina			1	2				13	14
Alumina + reinforcing fibers		18	4	6				94	
Alumina + zirconia	23		21					8	
Mullite								2	
Mullite + reinforcing fibers								24	
Silicon Carbide			23			17		9	57
Silicon Nitride		10	44		3	49	2	50	6
Silicon Nitride + reinforcing fibers		17	14					52	
Zirconia						72		37	44
Zirconia + reinforcing fibers								5	
Other					4			18	2
Totals	23	45	107	8	7	138	2	312	123
Grand Total (test data only)	5970								

easily overlooked when creating a data base, since the builder is often not the person running the tests or analyzing the data. Details, such as type of testing facility (testing rig, testing machine); batch number of the material; specimen geometry; and post-processing history, are examples of essential information often not reported but definitely factors that could influence the test results. Composite materials present even more problems, since the industry-wide accepted definition of a composite is just too vague. Working with this committee has already proved to be beneficial to the Ceramic Technology for Advanced Heat Engines data base by shedding light on some of these potential problems while they still can be averted and by making contacts with others interested in ceramic/advanced materials data bases.

Status of milestones

Time constraints placed on data base personnel have hampered efforts to produce a semiannual data base summary during this reporting period. Data collected in preparation for the semiannual data base summary report planned for May 1991 (rescheduled from March 1991) will be used in the report due at the end of September 1991.

Publications

None during this period.

3.2 TIME-DEPENDENT BEHAVIOR

Characterization of Toughened Ceramics
J. J. Swab (U.S. Army Materials Technology Laboratory)

Objective/scope

To evaluate and characterize toughened ceramic matrix composite (CMC) materials for potential high temperature structural applications. This includes all classes of CMC materials. There will be no CMC materials produced as part of this project. At the present time four-point flexure testing is being used to determine the high temperature performance of these CMCs.

Technical progress

Two CMC materials from Ceramatec, Inc. were evaluated during the past six months. One was a Ce-TZP/30 vol% Al_2O_3 with and without $SrZrO_3$ and the other was a SiC-fiber reinforced silicon nitride.

1) In the first material SrO reacts with the Al_2O_3 which leads to the in-situ formation of $SrO{\cdot}6Al_2O_3$ platelets ($\approx$0.5 μm wide and 5-10 μm long) creating a material with good room temperature properties.[1] High temperature fast fracture in four-point flexure was done at 500, 750, 1000 and 1250°C. The results are summarized in Table 1 below. Five bars were used for each temperature.

Table 1.

Material	A	B
T = 500°C		
Mean Strength (MPa)	417	459
Standard Deviation	14	41
T = 750°C		
Mean Strength (MPa)	316	332
Standard Deviation	45	28
T = 1000°C		
Mean Strength (MPa)	291	336
Standard Deviation	39	36
T = 1250°C		
Mean Strength (MPa)	256	285
Standard Deviation	56	27

A - NO PLATELETS; B - WITH PLATELETS

The formation of the platelets does not significantly improve the high temperature fast fracture of this zirconia

material. As a result it was decided that stress rupture type testing was not appropriate at this time.

2) The second CMC has a silicon nitride matrix reinforced with ≈30-50 vol% SCS-6 SiC-fibers (the fibers are produced by Textron Specialties Materials, Lowell, MA). The matrix cracking stress, as measured in three-point flexure at Ceramatec is ≈460 MPa. The material is being developed as part of the DoE Fossil Energy Materials Program. Figure 1 is the stepped-temperature stress-rupture plot of this material. A comparison of this plot with that generated for a similar CMC produced by Textron[2] shows that the Ceramatec CMC is currently better in the 1000-1400°C temperature range. The reason for this is the addition of 5 vol% mullite to the composite. The mullite addition enhances the likely hood of fiber pull-out and fiber/matrix debonding at elevated temperatures.

References:

1. R.A. Cutler, R.J. Mayhew, K.M. Prettyman and A.N. Virkar, "High Toughness Ce-TZP/Al_2O_3 Ceramics with Improved Hardness and Strength," J. Am. Ceram. Soc., 74 [1] 179-86 (1991).

2. J.J. Swab, G.D. Quinn and D.J. Snoha, "Mechanical Behavior of a SiC-Fiber/Si_3N_4 Composite," MTL TN 90-2, September 1990.

Status of Milestones:

Milestones are difficult to set and keep on schedule when CMC materials are so difficult to obtain.

Publications:

1. J.J. Swab, G.D. Quinn and D.J. Snoha, "Mechanical Behavior of a SiC-Fiber/Si_3N_4 Composite," MTL TN 90-2, September 1990.

STEPPED-TEMPERATURE STRESS-RUPTURE

CERAMATEC COMPOSITE

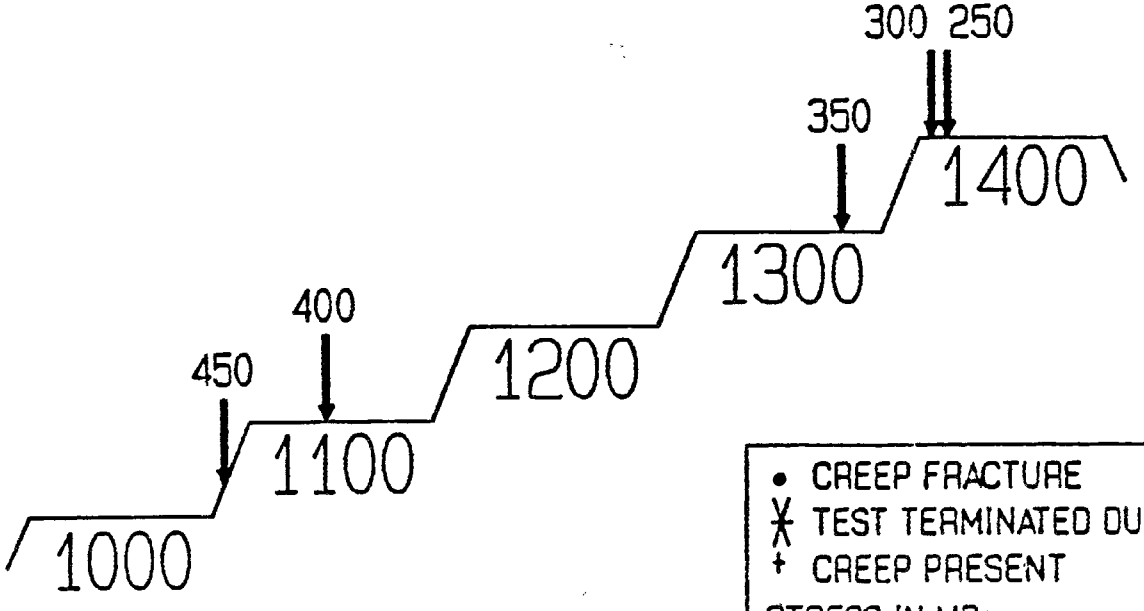

- • CREEP FRACTURE
- ¥ TEST TERMINATED DUE TO CREEP
- + CREEP PRESENT

STRESS IN MPa
TEMPERATURE IN °C
24 HOUR HOLD AT EACH STEP
10 MINUTES BETWEEN STEPS

Fracture Behavior of Toughened Ceramics

H. T. Lin, P. F. Becher, and W. H. Warwick (Oak Ridge National Laboratory)

Objective/scope

Ceramic composites, such as fiber- and whisker-reinforced ceramics, particulate phase composites, and ceramics with similar grain structures, offer important advantages for heat engine applications. Chief among these is the improved fracture toughness, which can be achieved by appropriate design of microstructural and material parameters. Previous studies show that these materials often exhibit substantial improvements in damage, thermal shock, and slow crack growth resistances. However, design of such systems must also consider those factors influencing their performance at elevated temperatures.

In response to these needs, studies are conducted to determine the mechanical properties (e.g., creep, delayed failure, strength, and toughness) at elevated temperatures for these toughened ceramics. Particular emphasis is placed on understanding how microstructure and composition influence the mechanical performance at elevated temperatures and the stability of these properties for extended periods at these temperatures. The knowledge gained from these studies provides input on how to modify materials to optimize their mechanical properties for the temperature ranges of interest.

Technical progress

During the past six months, flexure creep studies in air of toughened Si_3N_4 and SiC ceramics were undertaken at temperatures from 1200 to 1400°C, respectively. The objective of these two studies was to understand the microstructural dependence of high-temperature creep resistance of advanced ceramic systems.

Self-reinforced silicon nitride ceramics

This part is a continuing study of the creep study of Si_3N_4 ceramics containing elongated grains, which have been reported in the previous semi-annual report.[1] The experimental self-reinforced Si_3N_4 ceramics (designated SN0112 and SN141, respectively) supplied by Allied-Signal contain highly developed acicular (whisker-like) grains and were formulated with identical chemical compositions. SN0112 was manufactured by a gas-pressure-sintered (GPS) process, while SN141 was processed via a hot-isostatically-pressed (HIP) process. Both Si_3N_4 ceramics contain amorphous phases at grain boundaries. Note that the size (both diameter and length) of SN0112 is approximately 10 times that of SN141. The objective of this study was to investigate the effects of elongated grain structures and grain size on the creep resistance of self-reinforced Si_3N_4 ceramics.

Figure 1 shows the creep data of SN0112 subject to 4-point flexure loading (19-mm inner span vs 38-mm outer span) at temperatures of 1350 and 1400°C at stress levels ranging from 50 to 300 MPa in air. Results[2] of Norton NT154 Si_3N_4, which contains acicular but finer grains, tested under flexure stresses from 100 to 300 MPa at 1370°C in air are also included for comparison of creep properties. The creep data indicate that SN0112 has a

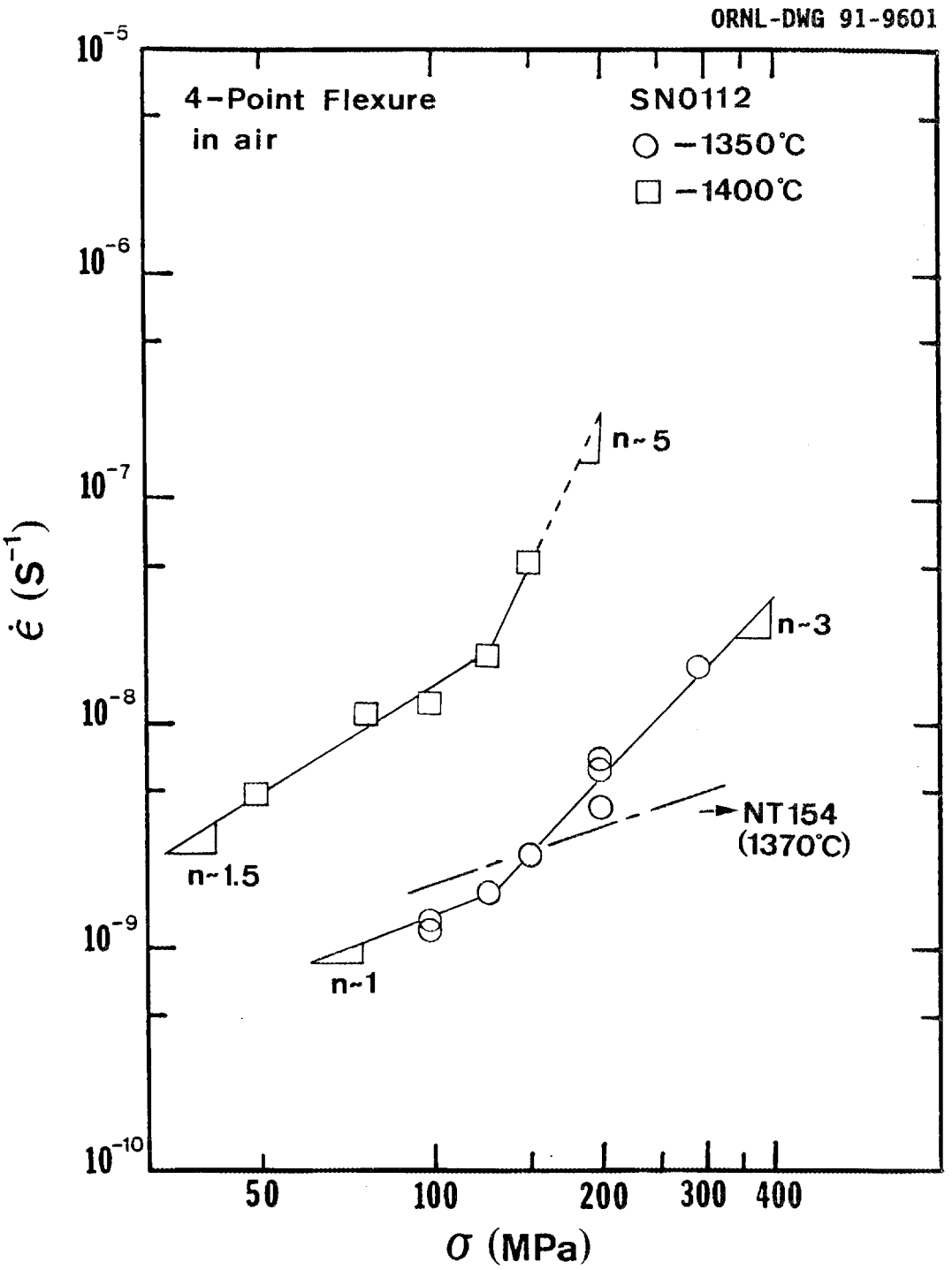

Fig. 1. Creep rate vs applied stress curves of gas-pressure-sintered silicon nitride (SN0112) containing high-developed acicular grains.

creep resistance comparable to that of NT154 at about 1370°C and at stresses ≤ 200 MPa. The results show that the creep rate vs stress curves of SN0112 exhibit an inflection at both 1350 and 1400°C. Both curves have stress exponents of approximately 1 and 1.5 at stress ≤ 125 MPa and, then, transition to higher exponent values of 3 and 5, respectively, at higher stress levels. As reported previously,[1] the creep stress exponent of this material at temperatures of 1200 and 1300°C was approximately 1. A stress exponent of 1 for Si_3N_4 ceramics containing intergranular glassy phases can be attributed to diffusional or viscous creep mechanisms. The higher stress exponents, plus higher creep rates, at stress > 125 MPa resulted from extensive creep cavitation. A similar transition in stress exponents, with increasing the stresses, was observed in siliconized silicon carbide under both tension and compression[3] and was also attributed to creep damage (cavitation). Note that NT154 exhibits a stress exponent of approximately 1 over the stress range employed at 1370°C. In addition, the creep data indicate that the creep rates of SN0112 at 1400°C are substantially faster, by approximately one order of magnitude, as compared with those at 1350°C. The enhanced creep deformation at 1400°C was found to be associated with enhanced oxidation reactions and more extensive creep cavitation.

The flexure creep data of HIP fine-grained Si_3N_4 (SN141) in air at temperatures from 1200 to 1350°C under selected stress levels are given in Fig. 2. The creep data of GPS coarse-grained Si_3N_4 (SN0112) at 1200 and 1300°C are also included for comparison. In general, the fine-grained Si_3N_4 (SN141) exhibits creep rates, which are approximately 4 to 8 times that of the coarse-grained Si_3N_4 (SN112) under the same test conditions employed. This indicates that the creep resistance in air of self-reinforced Si_3N_4 ceramics is greatly enhanced by the increased grain size. Additionally, SN141 exhibits a creep stress exponent (n) of 1 at 1200°C and, then, transitions into a higher stress exponent (1.7) at both 1300 and 1350°C. As stated above, the creep mechanism corresponding to n = 1 is attributed to diffusional or viscous creep. The higher stress exponent of SN141 at 1300 and 1350°C may be attributed to the increased number density of creep cavitation and/or to enhanced oxidation as compared to that at 1200°C.

Toughened SiC ceramic

Creep tests in 4-point loading configuration (12.7-mm inner span to 25.4-mm outer span) were conducted on a sintered SiC ceramic (designated CL3) in order to characterize its creep resistance at elevated temperatures and selected stress levels in air. CL3 is a sintered α-SiC material provided by Carborundum Company that has a grain size of approximately 3 μm and contains a second phase at grain-boundary, triple-grain junctions. At 1200°C, a 4-point flexure strength of approximately 600 MPa was obtained for a stressing rate of 30 MPa/s and a span ratio of 6.35 mm to 19.05 mm for this material. Figure 3 shows the creep data for CL3 subjected to flexure stresses of 100 to 213 MPa at temperatures ranging from 1200 to 1400°C in air. The results indicate that CL3 exhibits very promising creep resistance under the test conditions employed in this study. For instance, at an applied stress of 150 MPa, the creep rates are 6.8×10^{-10} s^{-1} and 3.6×10^{-9} s^{-1} at 1300 and 1400°C, respectively, which are comparable to a creep rate of 2.8×10^{-9} s^{-1} at an applied stress of 150 MPa at 1370°C for

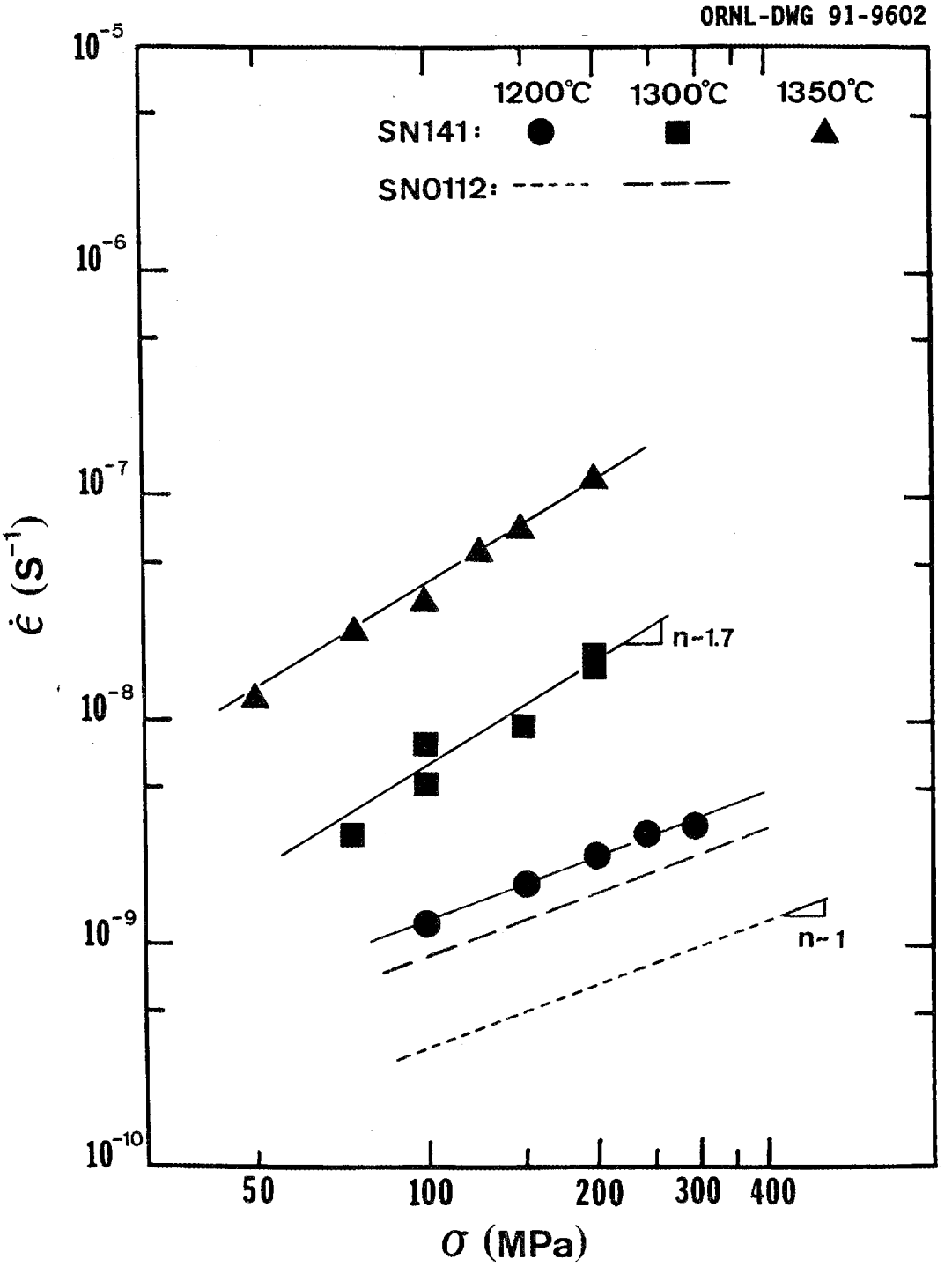

Fig. 2. Creep rate vs applied stress curves of hot-isostatically-pressed silicon nitride (SN141) with elongated grain structures.

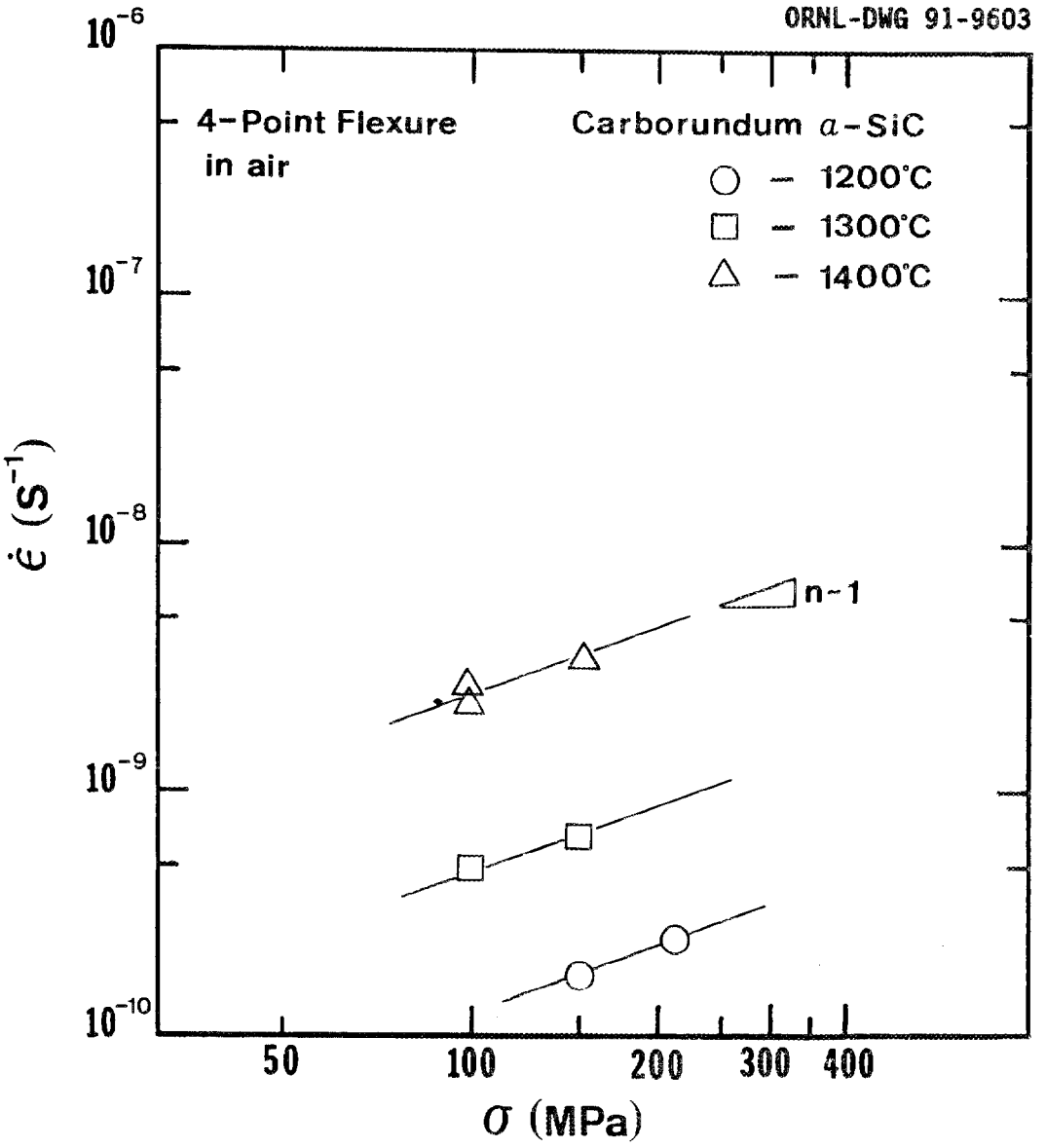

Fig. 3. Creep rate vs applied stress curves for a sintered α-SiC material.

the Norton NT154 Si_3N_4. In addition, CL3 maintains a creep stress exponent (n) of approximately one at ≤ 1400°C under the stress levels employed. The activation energy (Q) for creep of CL3 is calculated to be 302 kJ/mol for an applied stress of 150 MPa. The activation energy (302 kJ/mol) obtained for CL3 is intermediate to the activation energy for lattice diffusion of silicon (322 kJ/mol)[4,5] and the activation energy for grain-boundary diffusion of carbon (296 kJ/mol).[6] Additionally, the values of Q and n for CL3 are similar to that noted by Coble et al. for crept, hot-pressed, polycrystalline SiC.[6,7]

Status of milestones

Milestone 321309: Creep studies of Si_3N_4 ceramics with elongated grains and toughened SiC ceramics were completed.

A modification of Milestone 321310 was requested in March 1991 with a new target date of September 1991 and a new Milestone No. of 321311. The request was due to the difficulty in obtaining Si_3N_4 materials from external sources. A new Milestone 321310 was initiated to investigate the compressive creep of SiC whisker-reinforced alumina and alumina in order to compare creep behavior under different stress loading conditions.

Publications

None

References

1. H. T. Lin, P. F. Becher, and W. H. Warwick, "Fracture Behavior of Toughened Ceramics," pp. 308–14, in *Ceramic Technology for Advanced Heat Engines Project Semiannual Progress Report*, ORNL/TM-11719, Martin Marietta Energy Systems, Inc., Oak Ridge Natl. Lab., December 1990.

2. H. T. Lin and P. F. Becher, unpublished results.

3. S. M. Wiederhorn, D. E. Roberts, T.-J. Chuang, and L. Chuck, "Damage-Enhanced Creep in a Siliconized Silicon Carbide: Phenomenology," *J. Am. Ceram. Soc.* 71(7), 602–8 (1988).

4. R. N. Ghoshtagore and R. L. Coble, "Self-Diffusion in Silicon Carbide," *Phys. Rev.* 143(2), 623–26 (1966).

5. J. D. Hong, R. F. Davis, and D. E. Newbury, "Self-Diffusion of Silicon-30 in α-SiC Single Crystals," *J. Mater. Sci.* 16, 2485–92 (1981).

6. P. L. Farnsworth and R. L. Coble, "Deformation Behavior of Dense Polycrystalline SiC," *J. Am. Ceram. Soc.* 49(5), 264–68 (1966).

7. T. L. Francis and R. L. Coble, "Creep of Polycrystalline Silicon Carbide," *J. Am. Ceram. Soc.* 51(2), 115–16 (1968).

Cyclic Fatigue of Toughened Ceramics

K. C. Liu, J. L. Ding, H. Pih, C. O. Stevens, and C. R. Brinkman
(Oak Ridge National Laboratory)

Objective/scope

The objective of this task is to develop, design, fabricate, and demonstrate the capability to perform tension-tension dynamic fatigue testing on a uniaxially loaded ceramic specimen at elevated temperatures. Four areas of research have been identified as the main thrust of this task: (1) design, fabrication, and demonstration of a load train column that truly aligns with the line of specimen loading; (2) development of a simple specimen grip that can effectively link the load train and test specimen without complicating the specimen geometry and, hence, minimize the cost of the test specimen; (3) design and analysis of a specimen for tensile cyclic fatigue testing; and (4) conduct cyclic tests on a number of candidate ceramic materials in order to establish a data base.

Technical progress

Cyclic fatigue behavior of SiC (Hexoloy-SA)

A series of tensile and cyclic fatigue tests was completed on SiC at 1300 and 1400°C. The tensile tests were run at a stressing rate of 21 MPa/min and the fatigue tests at 21,000 MPa/min in a tension-tension mode. Some tests were cycled from low to high stress in steps until failure occurred, a test mode generally known as coaxing. Test parameters and results are given in Table 1 and data are plotted in Figs. 1 and 2. Because this material was extremely sensitive to residual surface flaws caused by machining, particularly to those at the root radius of buttonhead (which have caused a number of buttonhead failures), several specimens were annealed at 1500°C for 150 h before testing. To further avoid buttonhead failure, tapered copper collets were utilized. Subsequently, no buttonhead failures occurred. The collets were made of a dispersion-strengthened copper (GLIDCUP AL-15) for strength at high temperature. Although some degree of surface oxidation was observed after about 1100 h of fatigue testing, no visible physical deterioration was noticed. Therefore, the fixture was refurbished and reused. In Figs. 1 and 2, closed symbols indicate the end of the tests and that fractures occurred within the gage section. Open symbols indicate the intermittent life of the specimen at the indicated test condition. They were linked together by a broken line to indicate the loading history until specimen failure finally occurred at the end, as shown by a closed symbol. The short arrows attached to the open symbols imply that the lifetime would have been higher if the specimens had not failed outside the gage section.

Cyclic fatigue at 1300°C

Oak Ridge National Laboratory (ORNL) fatigue data were compared with UDRI fatigue data[1] in Fig. 1. Data were bracketed in a band to approximate the fatigue behavior. Half-filled symbols indicate residual tensile strength of UDRI specimens after they were precycled for 450,000 cycles.

Table 1. Summary of tensile and cyclic fatigue tests of Hexoloy-SA SiC tested at elevated temperatures

Specimen	Tensile strength MPa	Cyclic stress to failure MPa	Intermediate cyclic stress MPa	Number of cycles at intermediate cyclic loading	Number of cycles to failure	Locations of fractures
			Temperature = 1300°			
1 - 9	220				1	
1 - 3		199			2	
1 - 1		204			165	
1 - 4			189	239,361	(239,361)[a]	BH & SHNK[b]
1 - 2			187	231,000	(231,000)	
			200	193,800	(424,800)	
			208	394,000	(818,800)	
			222	352,513	(1,171,313)	
		235			1,171,415	
4 - 4			189	551,960	(551,960)	
			202	596,901	(1,148,861)	
			215	567,000	(1,715,861)	
		228		75,647	1,791,508	
			Temperature = 1400°C			
2 - 2	243				1	
4 - 1			169	1	(1)	BH
4 - 2			172	1	(1)	BH
5 - 1			189	1	(1)	BH
2 - 4		194			167	
3 - 4			206	433	(433)	BH & SHNK
2 - 1			193	185,299	(185,299)	BH & SHNK
3 - 1			188	1,032,500	(1,032,500)	
			202		(1,032,618)	SHNK
5 - 2			182	523,900	(523,900)	
			196	541,100	(1,065,000)	
			210	457,000	(1,522,000)	
			224	638,900	(2,160,900)	
			239	364,500	(2,525,400)	
			253	479,300	(3,004,700)	
			268	524,700	(3,529,400)	
			281	548,600	(4,078,000)	
		295		209,527	4,287,527	
5 - 3			185	141,625	(141,625)	
			199	113,087	(254,712)	
			214	393,648	(648,360)	
			228	169,195	(817,555)	
			241	108,145	(925,700)	
			255	228,585	(1,154,285)	
			269	109,468	(1,263,753)	
		283		77,160	1,340,913	
5 - 4			227	71,459	(71,459)	
		241		103,233	174,692	
6 - 2			257	101,812	(101,812)	
			271	122,973	(224,785)	
			284	183,482	(408,267)	
			298	123,323	(531,590)	
		310		60,867	592,457	
6 - 3	207				1	
6 - 4	249				1	

[a]Number of cycles accumulated at the end of intermediate loading.
[b]BH = Buttonhead failure; SHNK = shank failure.

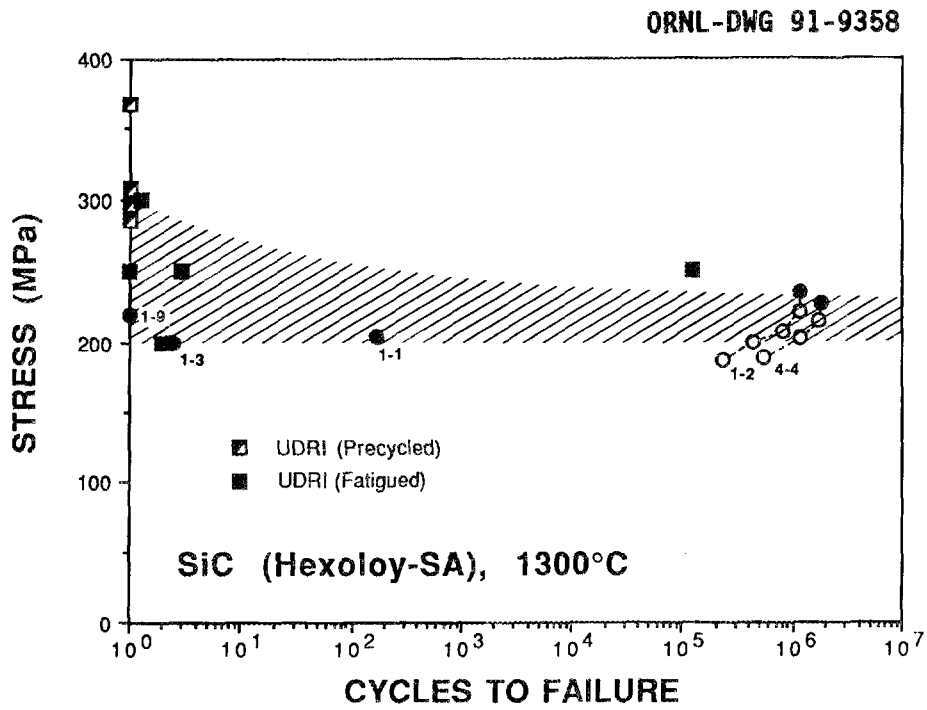

Fig. 1. Comparison of UDRI and ORNL cyclic fatigue data of SiC (Hexoloy-SA) tested at 1300°C.

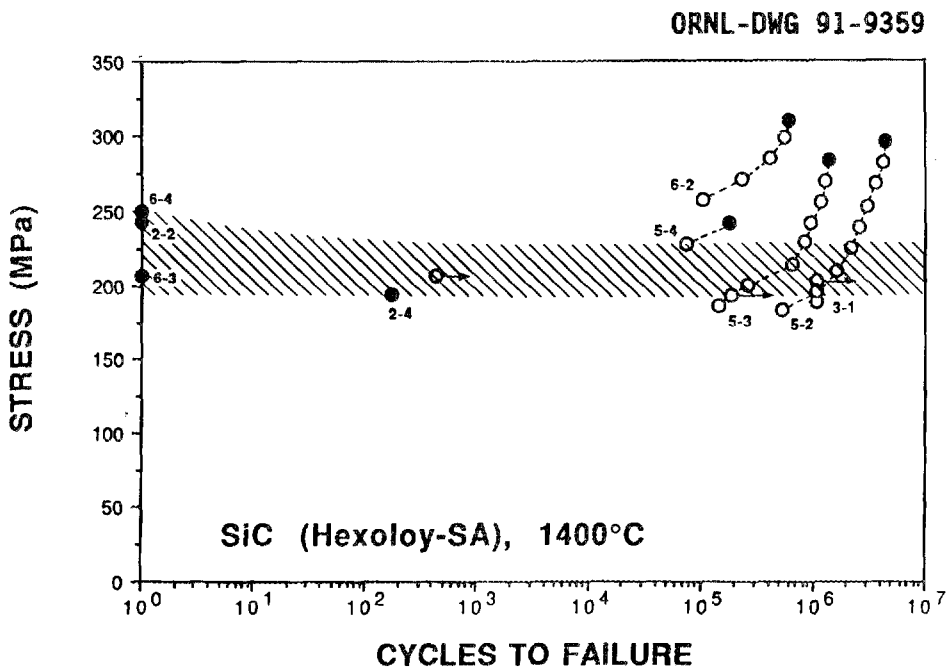

Fig. 2. Cyclic fatigue behavior of SiC (Hexoloy-SA) tested at 1400°C.

The UDRI lot showed fatigue resistance of the material generally to be higher than the ORNL lot by about 15 to 35%. However, the lowest fatigue strength determined by both laboratories was about the same. ORNL tests showed that coaxing increased the fatigue resistance of the material, but the resultant effect on fatigue strength was not comparable to that exhibited by the UDRI material. This observation and the high residual tensile strength exhibited by partially fatigued UDRI specimens (450,000 cycles) suggested that the ORNL lot might be somewhat inferior compared to the UDRI lot.

Cyclic fatigue at 1400°C

Several attempts were made to determine the low-cycle fatigue behavior (between 10^1 to 10^4 cycles) of this material at 1400°C (Fig. 2). In most cases, specimens either failed in the initial loading leg as a monotonic tensile test or showed fatigue lives in excess of 10^4 cycles. Those tests that went beyond 5×10^4 cycles or more were then cycled to higher peak stresses in steps until failure. Results showed that coaxing at this temperature was extremely beneficial to the fatigue resistance of this material. A total number of cycles to failure in excess of 4.2 million was achieved in specimen 5-2, which also showed that the enhanced fatigue strength exceeded the tensile strength by about 20%.

To ascertain the beneficial effect of coaxing exhibited by specimen 5-2, specimen 5-3 was used to duplicate the test conditions, except that the first two loading segments were abbreviated. Although the fatigue strength of specimen 5-3 fell just one little step below that of specimen 5-2, the beneficial effect was clearly discernable in this case also.

Coaxing usually starts with initial cycling from a peak stress amplitude below the fatigue endurance limit of the material. Significant improvement in fatigue strength was demonstrated when specimens 5-2 and 5-3 were cycled from a stress amplitude below the banded fatigue curve in the high-cycle range. To evaluate the effectiveness of coaxing relative to the starting peak stress amplitude, specimens 5-4 and 6-2 were cycled starting from stress levels on or above the fatigue curve, respectively, as shown in Fig. 2. Mixed results were obtained. However, general observations appeared to indicate that coaxing was beneficial at any starting stress level. Failure to enhance the fatigue resistance in other cases was probably due to the competing crack growth of large preexisting flaws in the specimens. It was further observed that the fatigue strength of Hexoloy-SA SiC at 1300 and 1400°C was about the same, except that coaxing at 1300°C was not as effective as that at 1400°C.

Acoustic Emission Studies of Ceramic Fatigue

Various mechanisms have been proposed as acoustic emission (AE) sources such as crack nucleation and propagation, moving dislocations, twinning, grain-boundary sliding, fracture and decohesion of inclusions, and phase transformations. However, a unified method to identify the type of AE does not exist as yet. Nevertheless, significant progress has been made in AE techniques to analyze not only the profile of AE activities but also to determine the location of AE sources with reasonable accuracy, mainly due to the advance in both hardware and software of personal computers developed in recent years.

When ceramic materials are subjected to load, latent defects may enlarge by deformation, defect enlargement, or propagation, and fracture resulting in spontaneous release of transient elastic energy that may be audible by sensitive instruments. It is believed that applications of the AE technology in determining flaw location and crack growth in ceramic materials in real time could enhance the understanding of crack nucleation and propagation, fatigue, and fracture mechanisms that are unique in brittle materials.

We have made a preliminary AE study of an Al_2O_3 tensile specimen subjected to cyclic loading at room temperature. Figure 3 shows a schematic of the experimental setup used. A detailed discussion of the equipment and

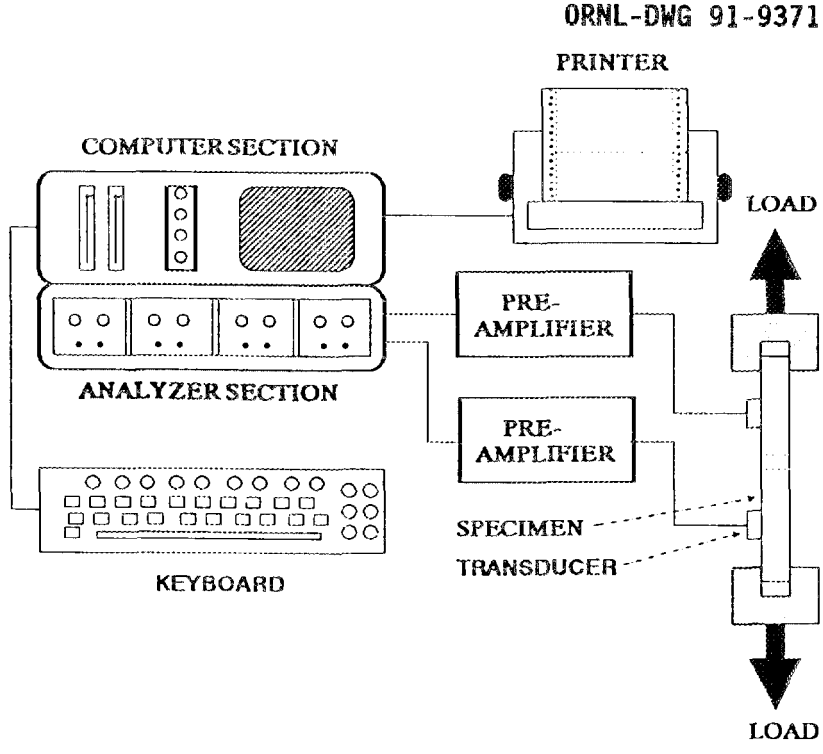

Fig. 3. A schematic of the experimental setup.

test procedure is found elsewhere.[2] To locate AE sources within the gage section, at least two sensors are required. The relative arrival time from an AE event is monitored at the two transducers and the event location is computed by the AE analyzer. In this experimental work, two sensors were set 50 mm apart on the reduced section of the tensile specimen with a high-viscosity vacuum grease and held in place by rubber bands. Artificial AE events were imposed by striking with a thin knife blade on the specimen surface at three locations: the midpoint between the transducers (25 mm from each transducer) and points on both sides of the midpoint offset by 10 mm. This procedure was used to determine the key AE parameters such as

parity of transducer sensitivity, threshold amplitude, velocity of AE signal, and signal gain, etc. The specimen was then loaded under a static stress of 5 MPa for about 68 h. A total of 50 AE events were recorded as shown in Fig. 4, which is a graph of AE events vs distance X measured from transducer No. 1. An AE event was defined as an AE activity accompanied with a signal amplitude greater than a preset value, which was set at 45 dB in this case. It shows most events occurred at two locations, X = 25 and 33 mm.

ORNL-DWG 91-9372

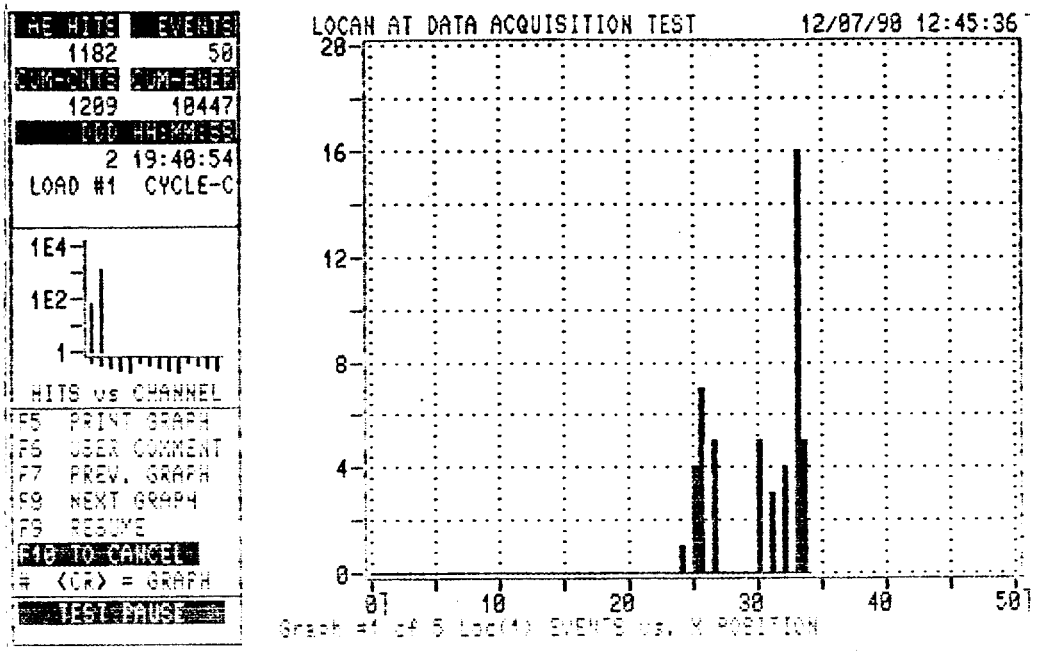

Fig. 4. A graph showing number and locations of AE events occurring in an Al_2O_3 tensile specimen subjected to a static stress of 5 MPa.

The Al_2O_3 tensile specimen was then cycled in tension-tension to a peak stress of 150 MPa, equivalent to 50% of the tensile fracture strength of the material at a rate of 1 Hz. Figure 5 showed the frequency of AE events that have occurred at the position indicated, after about 92 h of testing when the test was momentarily interrupted. Most AE events were determined to have occurred in two zones, A and B, centered at X = 26 and 37 mm, respectively. Several more events were scattered over the gage span. The scatter was not unexpected since the noises from the hydraulic and mechanical systems and the changes in wave mode can be misinterpreted by the AE analyzer. The locations where high incidence of AE activities occurred would be potential sites of fracture failures. Subsequently, the test was restarted and run for 51.3 h until failure. Additional AE events

ORNL-DWG 91-9373

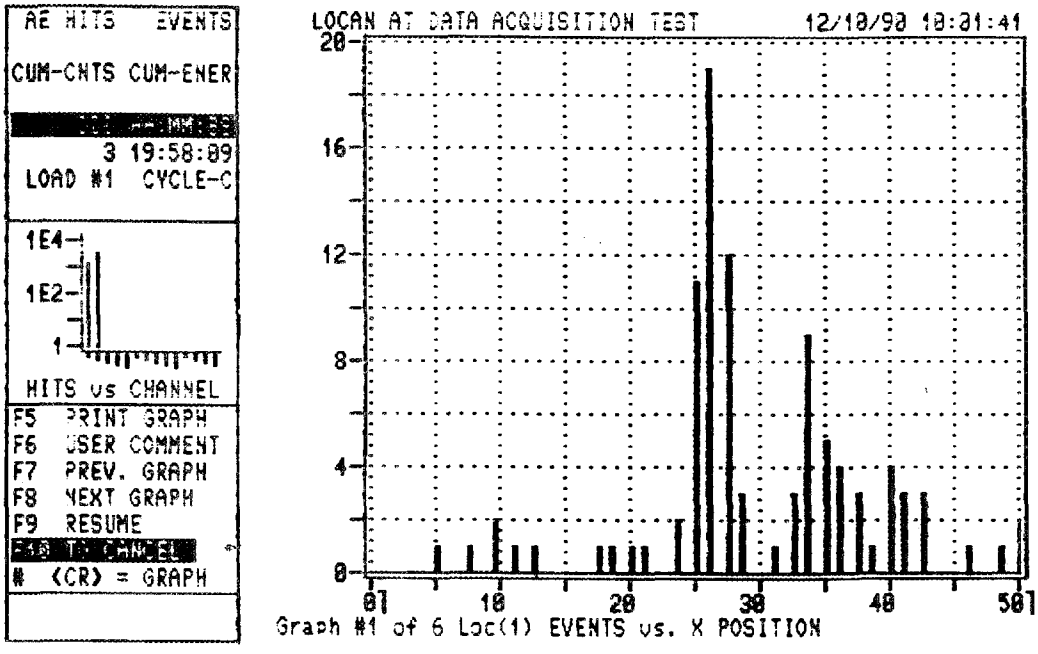

Fig. 5. A graph showing number and locations of AE events occurring in an Al_2O_3 tensile specimen subjected to tension-tension cyclic fatigue loading to a peak stress of 150 MPa for 92 h.

recorded after the restart were compiled separately and results are summarized in Fig. 6, which also shows that most AE events were detected to have occurred in either of the two zones. The frequency distribution of zone A was narrow and peaked, whereas that of zone B was wide and relatively flat. Several reasons for the differences can be cited. Firstly, an event location is computed based on relative arrival time monitored at two sensors, using a linear equation. Material inhomogeneity, wave path, interferences, sensor mismatch, end effect, wave velocity, and other factors can invalidate the simple linear relationship, resulting in various degrees of error. Secondly, severity of the error depends on the event location relative to the sensor position. Since the relative arrival time from an AE event occurring at central locations is very short due to the symmetry of the sensor positions, the error is minimal. In contrast, the error range is likely to be amplified as the AE event location moves toward one of the sensors. Actual fatigue failure occurred at X = 37 mm.

The same technique was used to investigate the cyclic fatigue behavior of SiC (whisker)/Al_2O_3 matrix composite material subjected to tension-tension cyclic loading. An exploratory specimen was used to establish the AE parameters of the composite material, since little was known. Cyclic fatigue loading was applied to the specimen in increasing steps beginning from 345 MPa (about 80% of tensile strength) until failure. This exploratory test showed that the AE characteristics of the composite material were

ORNL-DWG 91-9374

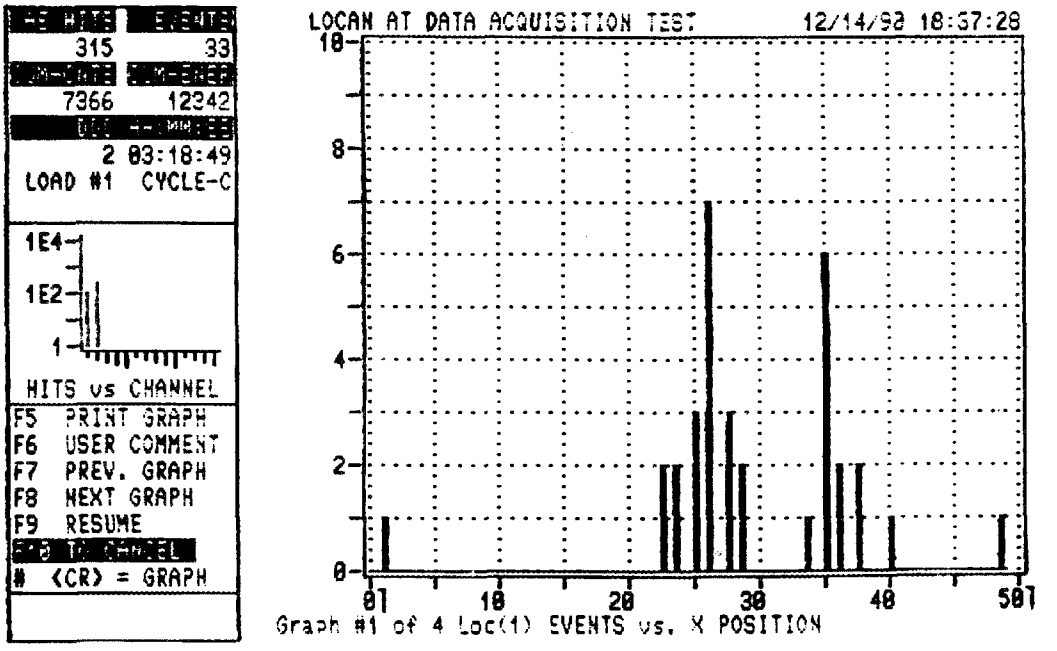

Fig. 6. A graph showing frequency and locations of AE events detected in an Al_2O_3 tensile specimen subjected to tension-tension cyclic fatigue loading to a peak stress of 150 MPa for 51.3 h following the initial 92 h testing. Specimen fracture occurred at X = 37 mm, 2 mm off to the right of the second high peak.

different from those of monolithic Al_2O_3 investigated previously, apparently due to the presence of whiskers in the composite. A high number of AE activities in counts (but lower amplitude in AE signal intensity) was detected in the composite compared to those monitored in the monolithic specimen. The lower intensity in AE signal signified that crack growth was effectively suppressed by the whiskers even though the composite was cycled to a peak stress amplitude twice as high as that used in the cyclic testing of the monolith. Because of the decrease in signal intensity, it was necessary to lower the threshold setting to 42 dB, which allowed most of the major events occurring in the composite to be detected. As a result, the locations of AE events determined from the detected signals were somewhat scattered probably due to the rise in number of detectable AE activities.

To produce a meaningful number of clear AE signals for determining locations of AE events, a second composite specimen was cycled initially under an applied peak stress of 420 MPa, which was estimated to fall above 95% of the tensile strength. A distribution of 456 AE events detected after 3000 cycles of testing is shown in Fig. 7. Although it showed five or six competing peaks, they were more or less evenly distributed. Since the number of AE events detected per block of cycles decreased as cycling continued, the cyclic stress was increased to 432 MPa after about 35,000

ORNL-DWG 91-9375

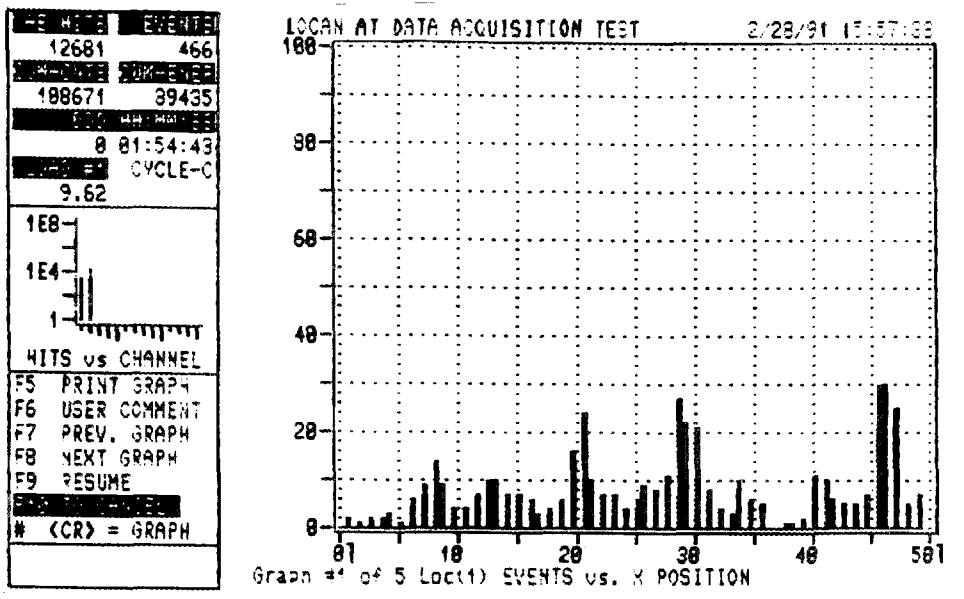

Fig. 7. A graph showing number and locations of AE events occurring in a SiC whisker-reinforced Al_2O_3 tensile specimen subjected to tension-tension cyclic fatigue loading to a peak stress of 420 MPa after 3000 cycles of testing.

cycles of testing. The specimen failed at 48,316 cycles. A new distribution of all AE events detected at the end of the test is shown in Fig. 8. It shows three high peaks at X = 14, 20, and 29 mm measured from the location of sensor #1. Two low peaks are discernable at X = 41 and 46 mm locations. Actual fatigue failure occurred at X = 40 mm. This exploratory study demonstrated that potential fatigue sites in the composite material can be detected using AE techniques. However, a pinpoint prediction of the final fracture location based on the highest frequency of AE events apparently would not be reliable. A wealth of test data obtained from this experiment is being analyzed for understanding of the in-situ fatigue behavior and slow crack growth under cyclic loading.

Creep Testing of NT-154 Si_3N_4

Experimental efforts were continued on creep testing of NT-154 Si_3N_4. Activities that occurred during this reporting period follow.

Creep behavior at 1200°C

Since 1200°C is the temperature of many practical applications of NT-154, six specimens were evaluated under various stresses ranging from 200 to 350 MPa. Results are summarized in Figs. 9 and 10. Open arrows indicate that the tests are continuing.

Specimen 20-42 (annealed at 1370°C for 150 h): Tested initially under 200 MPa. Creep strain rate decreased to about 3.2×10^{-10}/s after 1000 h

ORNL-DWG 91-9376

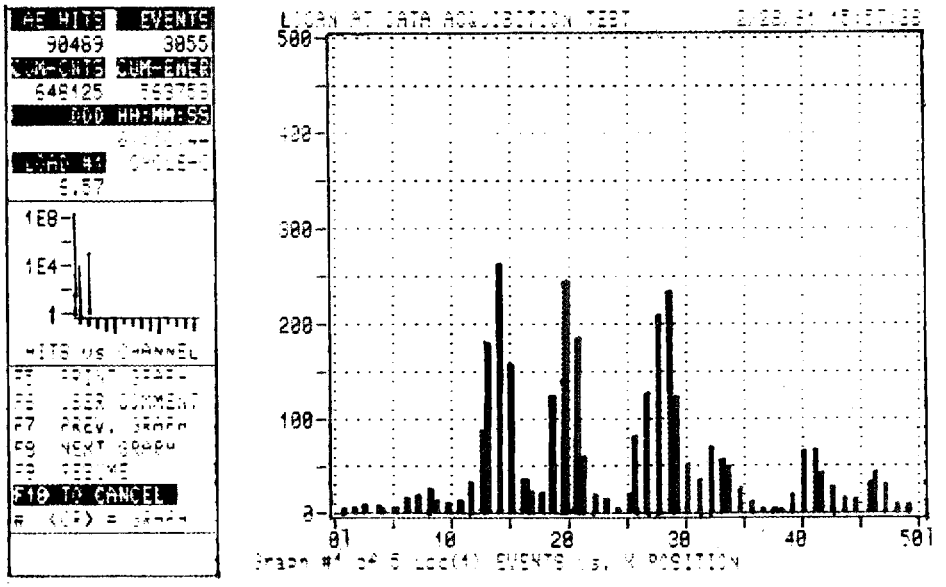

Fig. 8. A graph showing frequency and locations of AE events detected in the same ceramic composite specimen subjected to tension-tension cyclic fatigue loading to a peak stress of 432 MPa, when it ruptured at 48,316 cycles. Actual specimen fracture occurred at X = 40 mm.

ORNL-DWG 91-9360

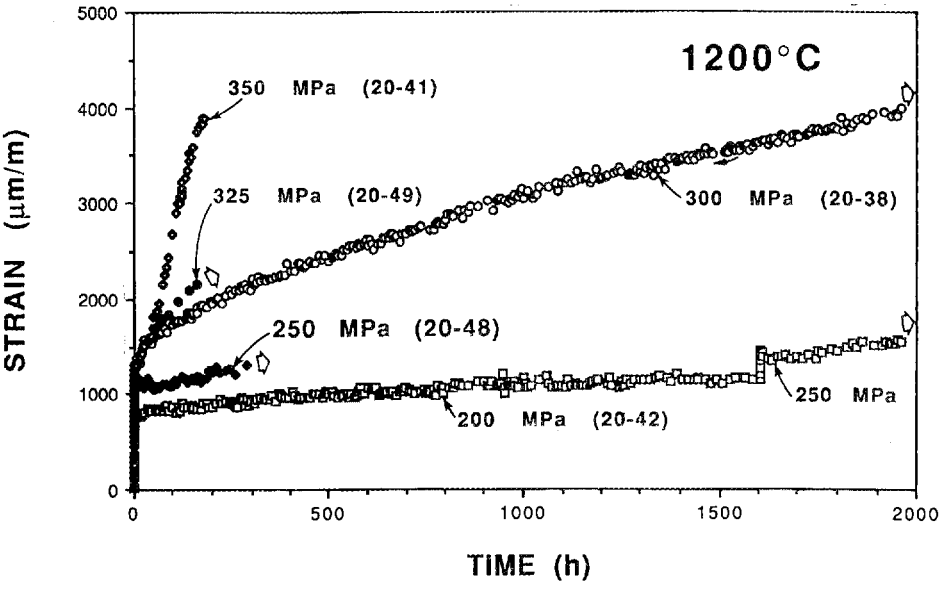

Fig. 9. Creep curves of NT-154 Si_3N_4 tested at 1200°C under applied stresses ranging from 200 to 350 MPa.

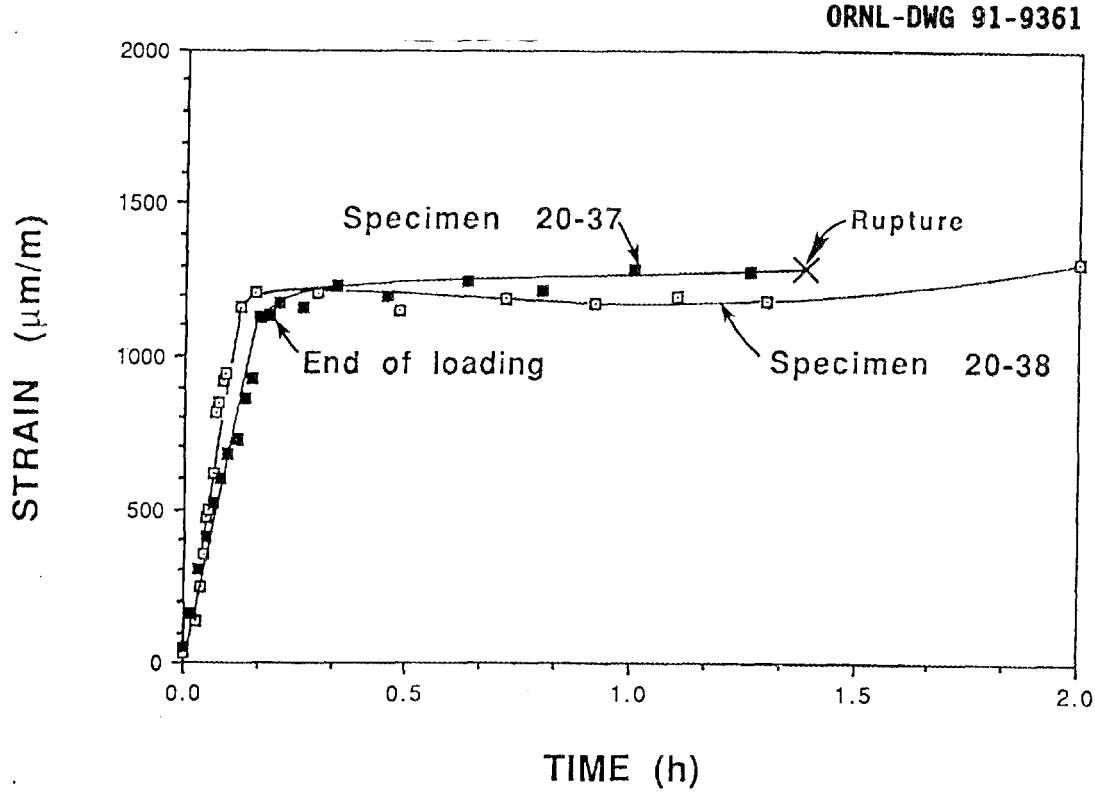

Fig. 10. Comparison of creep behavior of unannealed (specimen 20-37) and that of annealed (specimen 20-38) NT-154 Si_3N_4 tested at 1200°C under 300 MPa.

of testing. The stress was raised from 200 to 250 MPa after completing 1600 h of testing.

Specimen 20-48 (annealed): Tested at 250 MPa for about 270 h. This segment of the creep curve showed a remarkable similarity to the second leg of the creep curve of specimen 20-42 tested under the same stress.

Specimen 20-38 (annealed): Tested at 300 MPa for nearly 2000 h. Transient creep dominated the entire test period and the test is continuing.

Specimen 20-49 (annealed): Tested at 325 MPa for about 160 h and the test is continuing. The creep curve fell slightly above that of specimen 20-38.

Specimen 20-41 (annealed): Tested at 350 MPa for 150 h with a total of about 0.3% creep strain accumulated to date.

Specimen 20-37 (unannealed): Tested at 300 MPa and ruptured after 1.4 h of testing. The rupture time was far shorter than that of specimen 30-38, which was an annealed specimen. Figure 10 shows creep curves of both specimens are about the same. The cause of the premature failure will be determined from the results of microstructural analyses.

Creep behavior at 1300°C

Creep behavior of NT-154 at 1300 °C was investigated and test results were reported previously for two specimens 20-06 and 20-13 tested in unannealed and partially fatigued conditions, respectively. To investigate the effects of prethermal aging on creep behavior, an annealed specimen 20-30 was tested under an applied stress of 120 MPa. To facilitate comparison, all three sets of creep data are plotted in Fig. 11. The solid arrow indicates that the specimen ruptured outside the gage section due to the contraction of specimen gripping fixtures when a laboratory power outage occurred. Therefore, the actual rupture time of the specimen would be somewhat higher than the total creep test time indicated.

Annealing was shown to be effective in reducing the initial transient creep by a factor of about three compared to that of the unannealed specimen. The transient creep was extensive for the annealed specimen. However, from the viewpoint of practical engineering applications it is not unreasonable to assume that the transient creep ended after about 500 to 600 h of testing as was the case observed in the creep curve of the unannealed specimen. On the basis of this approximation, the creep rate in the range following the transient creep was practically the same for all of the three specimens. This observation indicates that the transient creep behavior was sensitive to the initial microstructural state of the grain-boundary phase present. However, as the microstructure of the grain-boundary phase underwent changes through thermal exposure at appropriate temperatures (with or without external stimulus such as cyclic loading) for certain periods of time, the creep behavior became predictable.

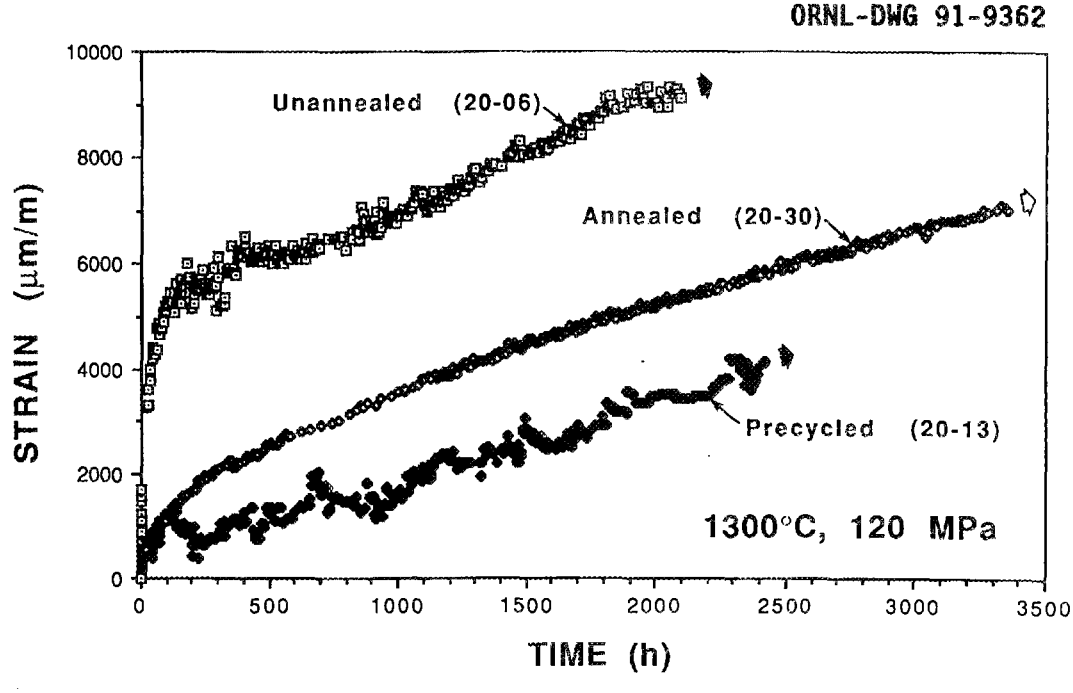

Fig. 11. Comparisons of three creep curves of NT-154 Si_3N_4 tested at 1300°C under applied stresses of 120 in unannealed, annealed, and precycled conditions.

Creep behavior at 1370°C

Specimen 20-09 (precycled): The test was interrupted again by a laboratory power outage after about 3200 h of testing. The specimen was reheated and reloaded to 100 MPa but fractured in the gage section after about 700h of testing since the second reloading. The creep curve with nearly 4000 h of testing is shown in Fig. 12. A brief transient creep was discernable immediately following reloading. This observation confirmed the previous finding that the behavior was real. Without the transient creep, the last segment of the creep curve would have continued as if no interruption had occurred.

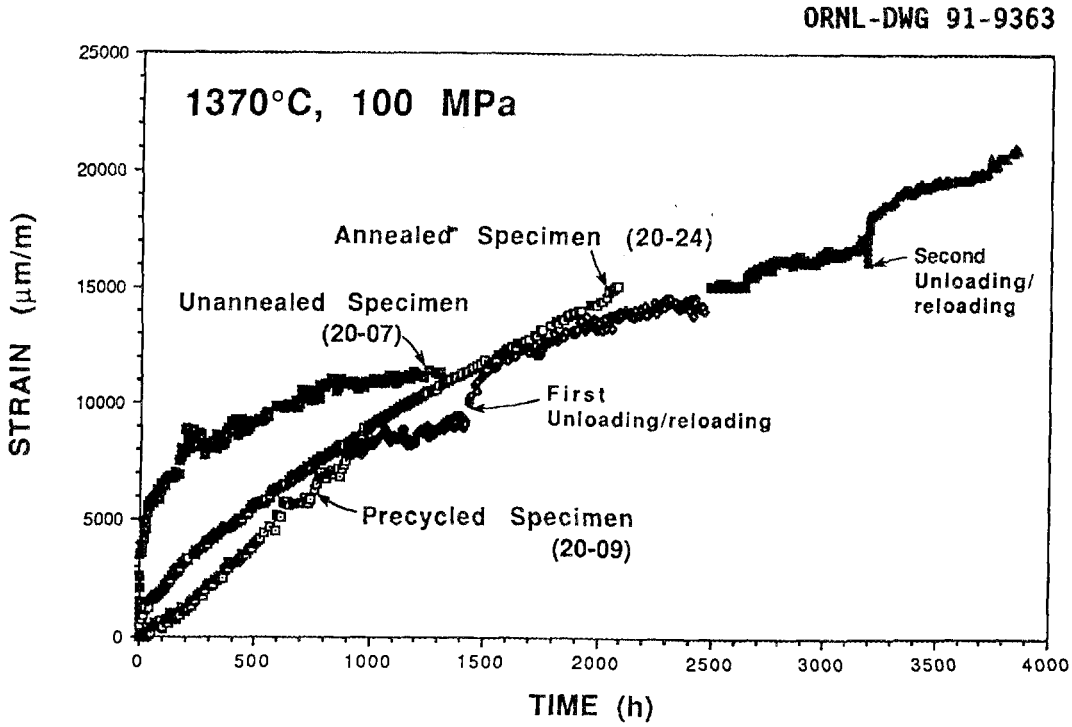

Fig. 12. Annealing and precycling of specimens at 1370°C can dramatically modify the initial transient creep behavior and enhance the creep rupture time of NT-154 Si_3N_4.

Specimen 20-24 (annealed): The test was completed after 2100 h of testing with a total creep strain of about 1.5%. Neither steady-state creep nor tertiary creep range can be defined unambiguously due to the dominance of the extensive transient creep exhibited by the creep curve shown in Fig 13. A hint of tertiary creep was discernable near the end of the test but the existence of the behavior remained dubious.

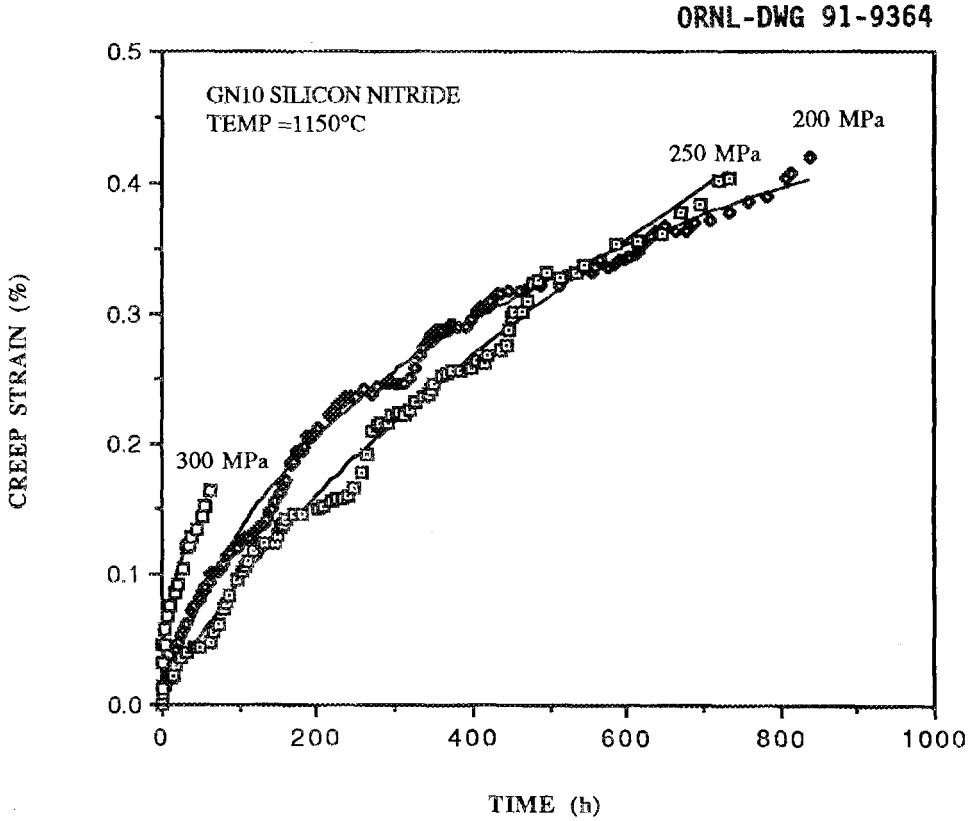

Fig. 13. Comparisons of calculated and experimental creep curves of GN-10 Si_3N_4 tested at 1150°C. Solid lines are calculated from Eq. (4) using the values of constants A, B, and C given in Table 3.

Creep Testing of GN-10 Si_3N_4

Upgrading of the mechanical extensometer

To minimize the problems of transducer signal drift due to the change of the ambient temperature in the proximity of the high-temperature furnace, new chassis made of Invar were used in all of the mechanical extensometers. Invar is a low-expansion alloy of iron and nickel. Performance was evaluated for the extensometers after the modification. Results indicated that the extensometers performed at the grade level between class A and class B1 of the ASTM standards. The drift problems were virtually eliminated by this change and meaningful test results were obtained.

Creep behavior of GN-10 Si_3N_4

A test matrix summarizing the status of ongoing and completed creep tests on GN-10 Si_3N_4 is shown in Table 2. A few creep curves were selected

Table 2. A matrix summarizing the status of creep tests on GN-10 Si_3N_4

	1150°C	1200°C	1250°C	1300°C
70 MPa				YC (2001.9 h)[c]
100 MPa			XC (1029.5 h)[c]	YC (19.5 h); XP (>1035 h)
125 MPa		XC (>1030.9 h)[a]	XP (>2220 h)	XC (15.2 h)
150 MPa		YC (1203.6 h)	XC (135.9 h); YC (58.6 h)[d]	YC (0.2 h)
175 MPa		YP (>1820 h)	XP (25.5 h)	
200 MPa	XC (840.9 h)	YP (240.3 h); XC (62.4 h)[b]		
225 MPa		XC (96.3 h)		
250 MPa	XC (733.8 h)	YC (7.5 h)		
275 MPa				
300 MPa	XC (62.0 h)[c]			

X indicates tests initiated during this reporting period, Y continued from the last period, P ongoing, and C completed.

[a]Stress increased to 225 MPa after 1030.9 h of testing. Specimen failed at buttonhead after 5.4 h of testing at 225 MPa.

[b]Does not indicate true lifetime due to premature failure caused by surface damage due to extensometer probe.

[c]Specimen fracture outside the gage section.

[d]Tested at 1230°C.

for illustration in Figs. 13 through 16 for specimens tested at 1150, 1200, 1250, and 1300°C, respectively.

Figure 17 compares the transient creep behavior of a virgin specimen tested at 1200°C under an applied stress of 225 MPa with that of a precrept specimen (at 125 MPa for 1030.9 h prior to the application of additional stress to 225 MPa) tested under the same condition. Both curves have been replotted so that they start at zero time to facilitate comparison. The enhancement of creep resistance exhibited by the precrept specimen was very dramatic. Because the total creep strain accumulated during the low stress creep was very low (less than 0.05%), the strengthening was most likely attributed to thermal aging instead of strain history.

Creep rupture of GN-10 Si_3N_4

The minimum commitment model and the Larson-Miller model discussed in the last progress report have been updated with additional rupture data. Comparisons between experimental data and predictions are shown in Figs. 18 and 19. Neither model showed clear superiority to the other in terms of the degree of fitting within the data range, which remained too limited for definitive model development.

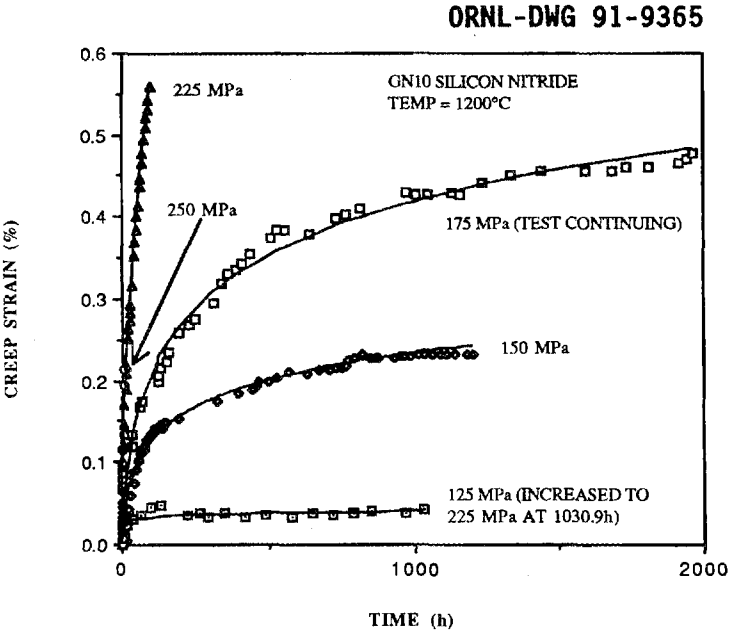

Fig. 14. Comparisons of calculated (solid lines) and experimental creep curves of GN-10 Si_3N_4 tested at 1200°C. The bottom curve shows the first leg of the creep curve before the applied stress was increased from 125 to 225 MPa at 1030.9 h. The second leg is shown in Fig. 17.

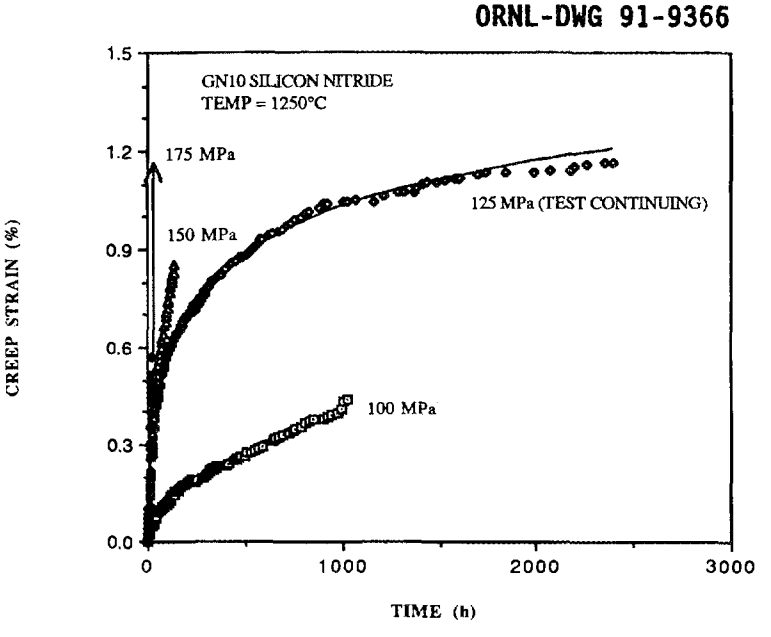

Fig. 15. Comparisons of calculated (solid lines) and experimental creep curves of GN-10 Si_3N_4 tested at 1250°C.

ORNL-DWG 91-9367

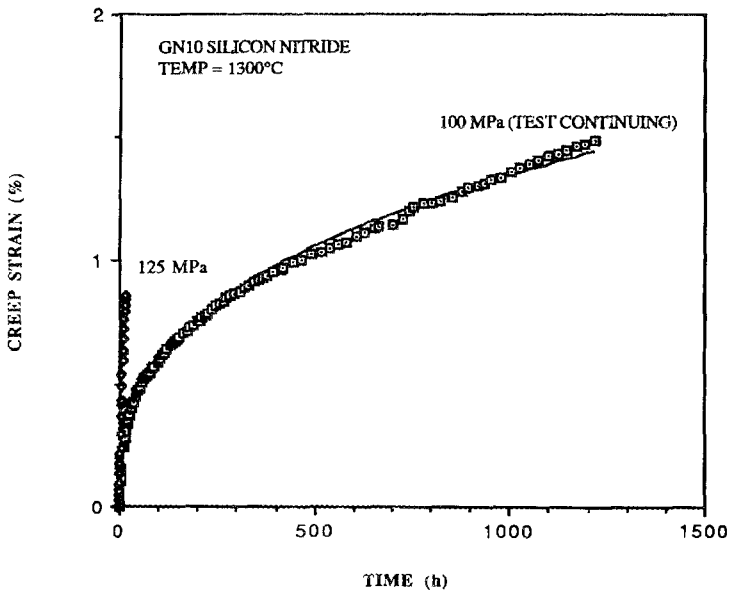

Fig. 16. Comparisons of calculated (solid lines) and experimental creep curves of GN-10 Si_3N_4 tested at 1300°C.

ORNL-DWG 91-9368

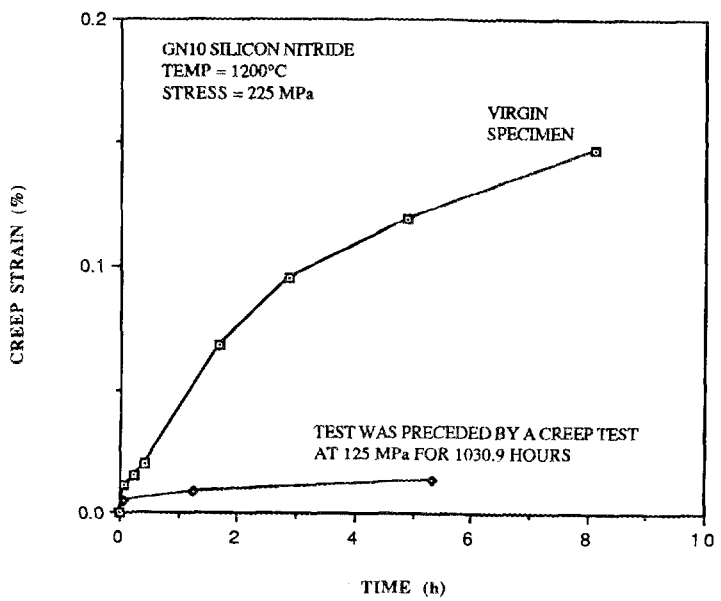

Fig. 17. Comparison of initial transient creep behavior of a virgin specimen and that of a specimen precrept at 125 MPa for 1030.9 h.

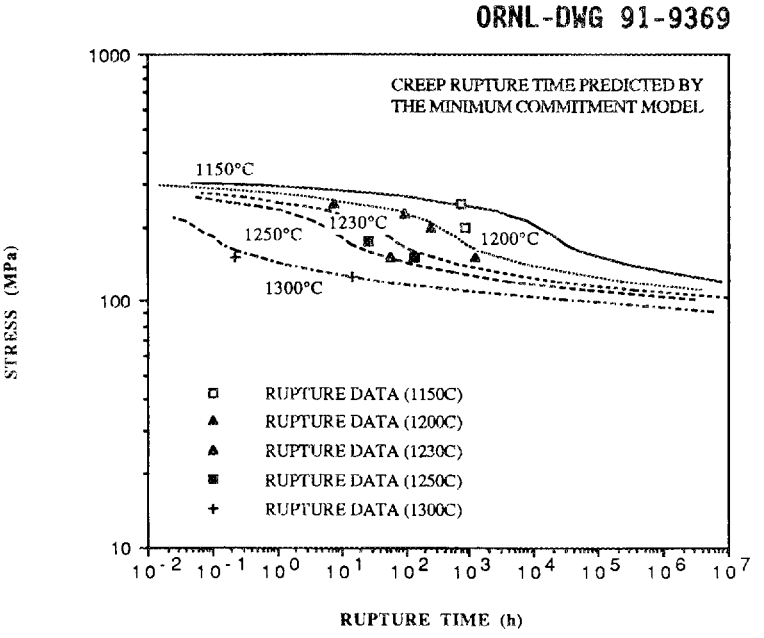

Fig. 18. Comparison of creep rupture times and predictions based on the minimum-commitment model.

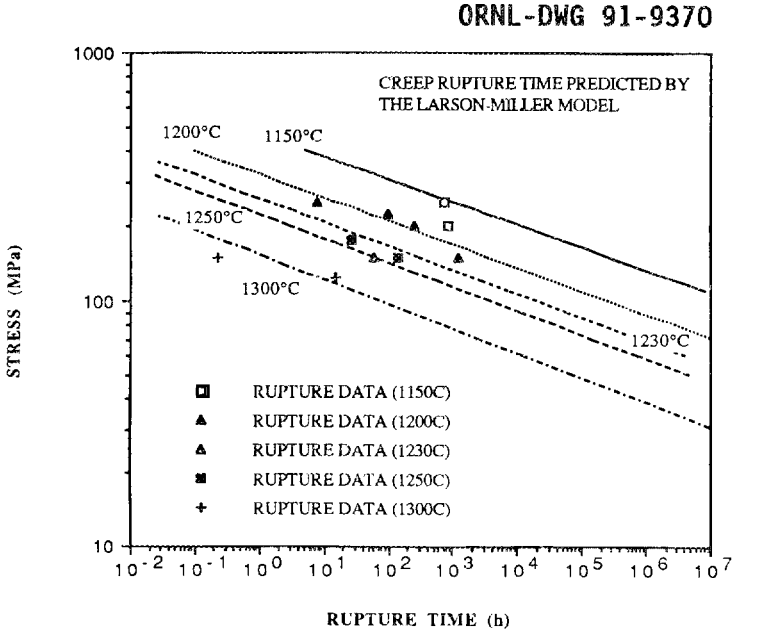

Fig. 19. Comparison of creep rupture times and predictions based on the Larson-Miller model.

Development of a deformation and life-prediction model

Based on the experimental data obtained to date, a deformation and life-prediction model in its preliminary form has been developed. Three evolution rules associated with the model are postulated as follows:

$$\dot{\varepsilon} = \frac{\dot{\varepsilon}_o (\sigma / \sigma_o)^n e^{-\frac{Q_\varepsilon}{RT}}}{D^q} , \tag{1}$$

$$\dot{D} = \dot{D}_o (D_o / D)^m e^{-\frac{Q_D}{RT}} , \tag{2}$$

and

$$\dot{\omega} = \dot{\omega}_o \frac{(\sigma / \sigma_o)^{\frac{\nu}{T}} e^{\frac{-Q_\omega}{RT}}}{(1 - \omega)^\psi} , \tag{3}$$

where ε is the creep strain with $\dot{\varepsilon}_o$ as its initial creep rate at a reference stress σ_o; σ, the applied stress; D, a material parameter that represents the level of crystallinity with D_o and $\dot{D}_o$ as its initial value and initial evolution rate, respectively; ω, a damage parameter that has a range between 0 and 1 with 1 representing the ruptured state; $\dot{\omega}_o$, the initial damage evolution rate; T, the absolute temperature; R, the gas constant; Q_ε, Q_D, Q_ω, ν, ψ, m, and n are constants.

Although the above evolution rules need further refinement, the proposed model in the present form is capable of delineating qualitatively the behavioral features consistent with the observed physical phenomena showing that creep strain rate increased with increased stress and temperature but decreased as the level of crystallinity increased due to devitrification occurring in the grain-boundary phase. While the creep behavior was governed by the grain-boundary material, fracture in some cases could be controlled by a separate phenomenon strictly due to the slow crack growth initiating from defects preexisting in the material. The equations can be easily applied to problems involving general thermomechanical loading conditions and integrated into a numerical code (e.g., finite element code) for engineering analyses.

It can be shown that integration of Eqs. (1) and (2) under constant stress condition will lead to the following equation:

$$\varepsilon = A [(1 + Bt)^C - 1] , \tag{4}$$

where t is the creep time and A, B, and C are constants that can be correlated to those used in Eqs. (1) and (2). Under the constant-stress creep conditions, Eq. (3) can lead to the Larson-Miller rupture model.

model. Therefore, the constants in Eq. (3) are determined from the creep rupture data.

A computer program has been developed to determine the values of constants A, B, and C used in Eq. (4). Excellent fitting between experimental data and calculations (solid lines) is demonstrated in Figs. 13 through 16, using the values tabulated in Table 3.

Table 3. Values of constants A, B, and C of Eq. 4 for calculating the creep curves shown in Figures 13 to 16.

Temp. (°C)	Stress (MPa)	A	B	C
1150	200	8.255	0.01216	0.01970
1150	250	0.06558	0.03059	0.6268
1150	300	0.005114	122.2	0.3853
1200	125	3.161	126.9	0.001096
1200	150	41.58	0.1135	0.001186
1200	175	19.36	0.07596	0.004918
1200	225	0.01444	15.8	0.5015
1200	250	0.0003598	61940	0.4808
1250	100	0.0003194	915.7	0.5196
1250	125	62.61	0.1637	0.003169
1250	150	0.1571	0.7278	0.4005
1250	175	0.00001269	7328	0.8830
1300	100	0.06431	10.59	0.3330
1300	125	35.57	0.1249	0.02248

Important findings and observations

Although test results are very preliminary, the AE techniques may be used to detect potential fracture initiation sites in ceramic materials.

Status of milestone

Milestone 321411 (complete technical report covering results of tests on an advanced, toughened ceramic material) was completed.

Publications

1. K. C. Liu, H. Pih, C. O. Stevens, and C. R. Brinkman, "Tensile creep behavior and cyclic fatigue/creep interaction of hot-isostatically-pressed Si_3N_4," has been submitted for inclusion in the *Proceedings of the Twenty eighth Automotive Technology Development Contractors' Coordination Meeting* at Dearborn, Michigan, October 22–25, 1990 (in press).

2. H. Pih and K. C. Liu, "Laser Diffraction Methods for High Temperature Strain Measurements," Experimental Mechanics, pp. 60–4, vol. 31, No. 1, March 1991.

References

1. N. L. Hecht, "Environmental Effects in Toughened Ceramics," pp. 94–100 in *Ceramic Technology for Advanced Heat Engines Project Bimonthly Technical Progress Report* to DOE Office of Transportation Technologies, October–November 1990, ORNL/CF-90/385, Martin Marietta Energy Systems, Inc., Oak Ridge Natl. Lab., December 31, 1990.

2. F. A. Moslehy, "Applications of Acoustic Emission to Flaw Detection in Engineering Materials," Experimental Techniques, Vol. 14, No. 1, 1990, pp. 31–33.

Rotor Data Base Generation

M. K. Ferber and M.G. Jenkins Oak Ridge National Laboratory (ORNL)

Objective/scope

The goal of the proposed research program is to systematically study the tensile strength of a silicon nitride ceramic as a function of temperature and time in an air environment. Initial tests will be aimed at measuring the statistical parameters characterizing the strength distribution of three sample types (two tensile specimens and one flexure specimen). The resulting data will be used to examine the applicability of current statistical models as well as sample geometries for determining the strength distribution.

In the second phase of testing, stress-rupture data will be generated by measuring fatigue life at a constant stress. The time-dependent deformation will also be monitored during testing so that the extent of high-temperature creep may be ascertained. Tested samples will be thoroughly characterized using established ceramographic, scanning electron microscopy (SEM), and transmission electron microscopy (TEM) techniques. A major goal of this effort will be to better understand the microstructural aspects of high-temperature failure including:

(1) extent of slow crack growth,
(2) evolution of cavitation-induced damage and fracture,
(3) transition between brittle crack extension and cavitation-induced growth, and
(4) crack blunting.

The resulting stress-rupture data will be used to examine the applicability of a generalized fatigue-life (slow crack growth) model. If necessary, model refinements will be implemented to account for both crack blunting and creep damage effects. Insights obtained from the characterization studies will be crucial for this modification process. Once a satisfactory model is developed, separate stress-rupture (confirmatory) experiments will be performed to examine the model's predictive capability. Consequently, the data generated in this program will not only provide a critically needed base for component utilization in automotive gas turbines, but also facilitate the development of a design methodology for high-temperature structural ceramics.

Technical progress

Studies of the high-temperature mechanical properties of a high-performance silicon nitride (PY6) were continued this reporting period.* The PY6 material is fabricated by hot isostatic pressing (HIP) using 6 wt % yttria as

*PY6 silicon nitride, GTE Laboratories, Inc., Waltham, Mass.

the densification aid. The microstructure typically consists of 1 to 6-μm-long acicular grains surrounded by equiaxed grains 0.1 to 1.0 μm in diam. This morphology leads to a relatively dense microstructure. The silicon nitride grains, which are generally in the form of β-Si_3N_4, are separated by relatively thin layers of an amorphous yttrium silicate. The intergranular phase is also present in the triple points as a crystalline yttrium silicate. The exact phase composition of these intergranular compounds depends upon the HIP conditions.

Testing of this material involved the measurement of (1) the fast-fracture strength as a function of temperature and (2) the creep/fatigue behavior at temperatures in the range of 1150 to 1400°C. Data were generated using both 4-point flexure (3 x 4 x 50 mm) and button-head tensile specimens (6.35-mm gage diam and 35-mm gage length). The majority of the flexure specimens were machined from injection-molded and HIP'ed bars having approximate fired dimensions of 4 x 6 x 50 mm. The tensile specimens were machined to the specifications given in Fig. 1 from isopressed and HIP'ed rods 160-mm-long

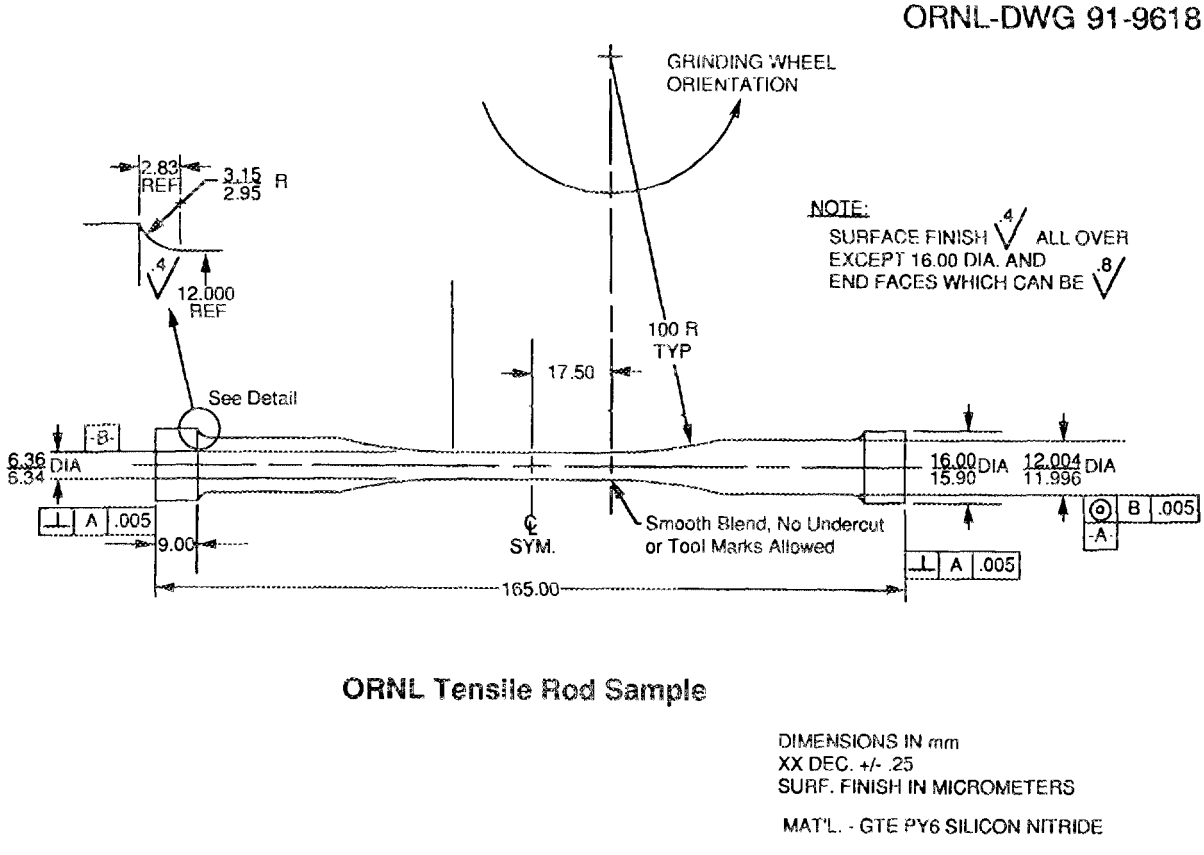

Fig. 1. Dimensional Specifications for the button-head tensile specimen. Note the gage diameter is 6.35 mm and the total gage length is 35 mm.

and 22-mm in diam. In order to examine the effect of green state processing (i.e., injection molding versus isopressing) upon mechanical behavior, a limited number of flexure specimens were also machined from the as-received tensile rods.

The strength and creep/fatigue flexure tests were conducted using the Flexure Test Facility (FTF) shown in Fig. 2. This equipment consists of a load frame capable of testing up to three separate flexure samples concurrently. The test fixtures have inner and outer spans of 20 and 40 mm, respectively. The loads are generated by pneumatically driven air cylinders located at the top of the

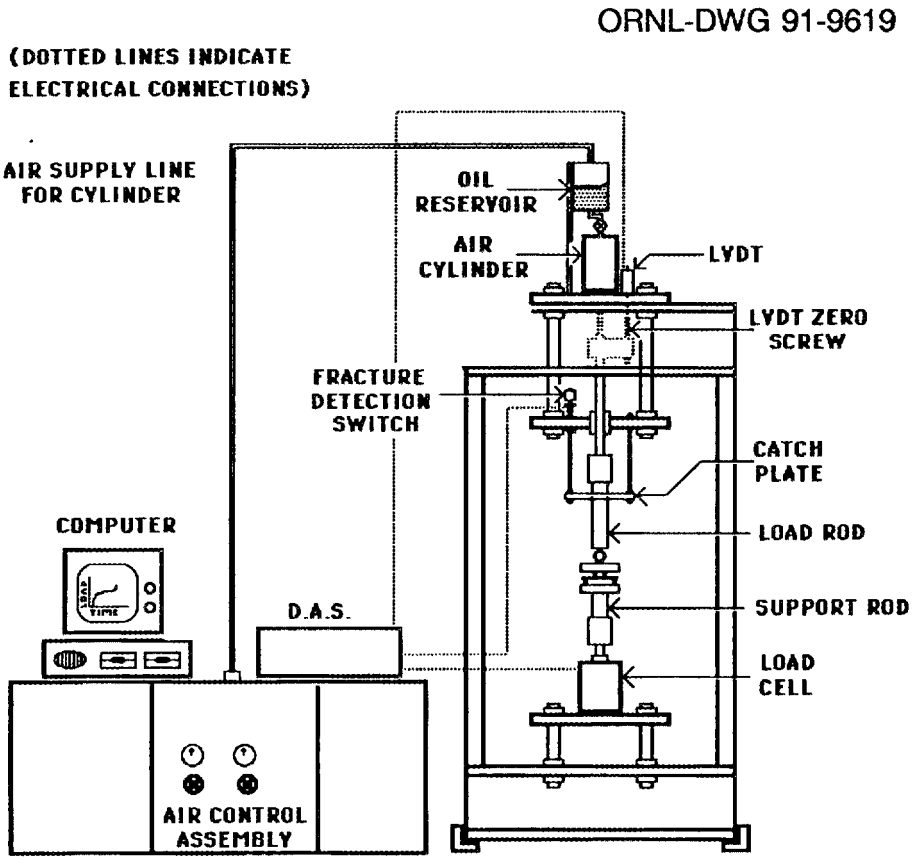

Fig. 2. Schematic illustration of the Flexure Test Facility.

support frame. In order to minimize impact problems normally encountered during fracture, a hydraulic fluid is used as the working medium in the cylinder. The mechanical loads are transmitted into the hot zone of the furnace through SiC rods. Each of the bottom three SiC rods are also attached to a load cell which monitors the applied force as a function of time. During a test, a linear variable differential transformer (LVDT) tracks the downward displacement of the load ram. The computer monitors this displacement, as well as the load on each specimen, and provides necessary adjustments in the air pressure (via the

electro-pneumatic transducer) such that the desired stress level is maintained. The applied load can be specified as a function of time through the computer software. The required test temperature is maintained by a resistance-heated box furnace.

The time dependence of the flexural creep deformation was determined using two methods. The first involved the measurement of the load-point deformation, y_l, which was based upon the LVDT readings (see Fig. 3 for reference). In order to account for the effects of thermal fluctuations upon the

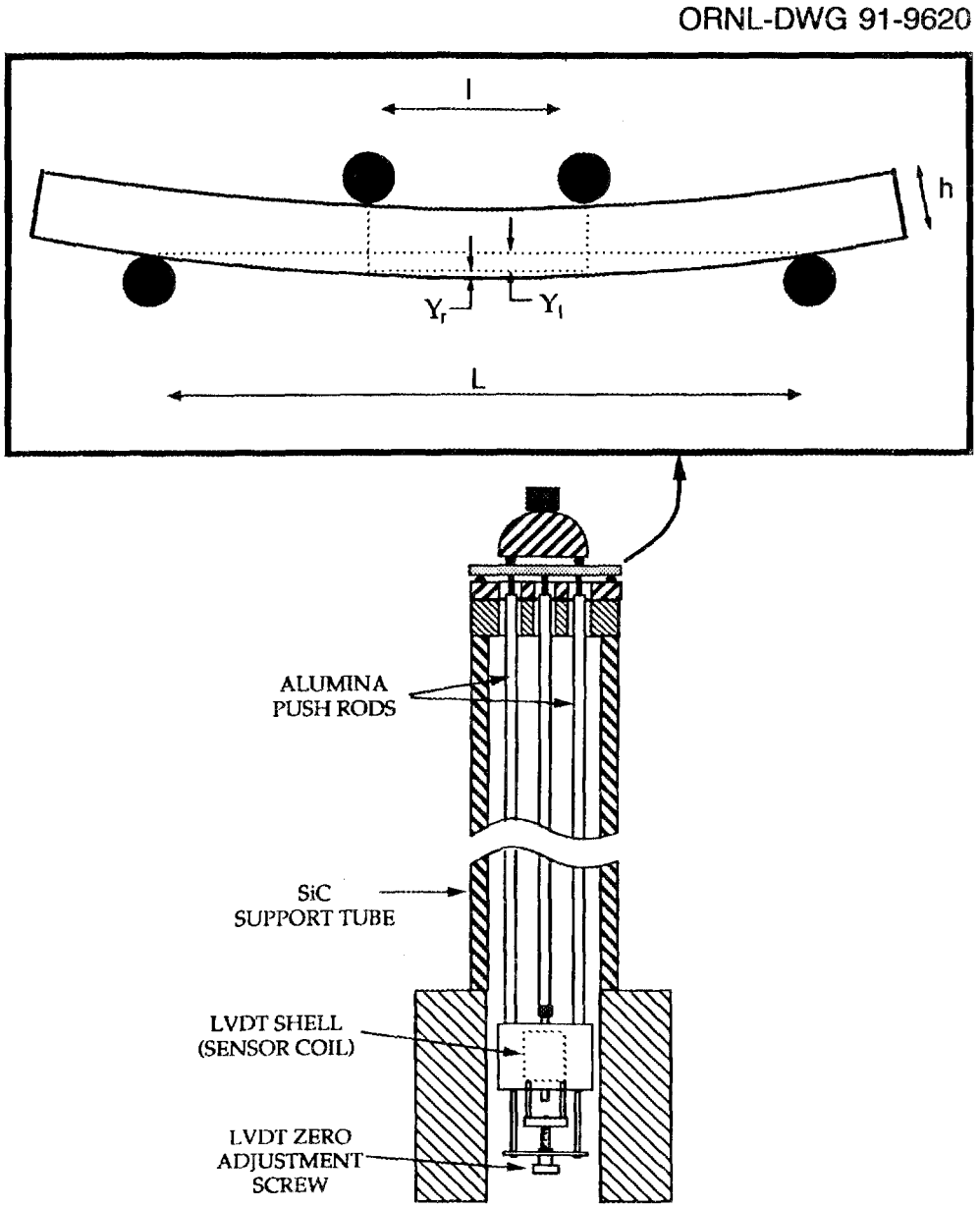

Fig. 3. Triple-point deflectometer used for measurement of creep deformation. Inset illustrates definitions of y_r and y_l.

displacement data, the front load station in each test frame was "dead" loaded (i.e., specimen removed from fixture). The resulting displacement-time data, which were indicative of the background thermal fluctuations, were used to correct the y_l-t profiles for the two adjacent load stations. In the second method, a triple-point deflectometer, adapted to the FTF (Fig. 3), was used to measure the outer fiber displacement at the center of the specimen relative to the inner load points (y_r). The resolution of these displacement measurements was approximately 5 μm. Samples not failing during the creep testing were examined with an optical comparator to obtain independent estimates of y_r and y_l.

The tensile strength and creep tests were conducted on commercial electromechanical load machines having both load- and strain-control capabilities.* The desired load (strain)-time profile was controlled by a trapezoidal function generator. The specimen grips, which were configured for button-head specimens, were located outside the compact, two-zone, resistance-heated furnace capable of generating a maximum temperature of 1600°C. The grips were attached to the load frame through hydraulic couplers to minimize bending moments. Specimen displacement was measured with a direct-contact capacitance extensometer (Fig. 4). By carefully controlling the temperatures of both the measurement hardware and grip cooling water,[1] a resolution < 0.5 μm could be achieved with this extensometer. A computer was used to monitor and store various output signals including displacement, load, load error, and testing temperature. All tensile creep/fatigue tests were conducted in ambient air under electronic load control. Specimens were strain gaged and the percent bending measured at room temperature to ensure that minimum bending was imposed at the lower loads and stresses imposed during the creep tests. In all cases bending at the anticipated creep stresses was < 3%.

Table 1 gives the number of flexure and tensile specimens tested and the corresponding test temperatures for the strength and creep/fatigue measurements. The loading rate range for all fast-fracture strength tests was 35 to 37 MPa/s. In the case of the elevated temperature tensile strength tests, the load-displacement curves were recorded at each test condition. Displacement was measured over a 25-mm gage length at a resolution of ~0.5 μm using the aforementioned contacting extensometer. Least-squares fits of the linear portions of the resulting stress-strain curves yielded the average elastic moduli at each temperature.

Tensile and flexure creep/fatigue tests of the PY6 material were conducted in the temperature range of 1150 to 1400°C. The lowest temperature examined, 1150°C, is believed to be near the critical temperature for softening of the secondary intergranular phase. The fatigue behavior at this temperature should be dominated by slow crack growth since creep damage mechanisms are limited by kinetic considerations. The remaining two test temperatures examined, 1260 and 1370°C, are the component design and ultimate use temperatures, respectively. At temperatures above 1260°C, the evolution of creep damage is expected to control the fatigue behavior.

*Instron Model 1380 Low Cycle Creep Fatigue Machine, Instron Corporation, Canton, Mass.

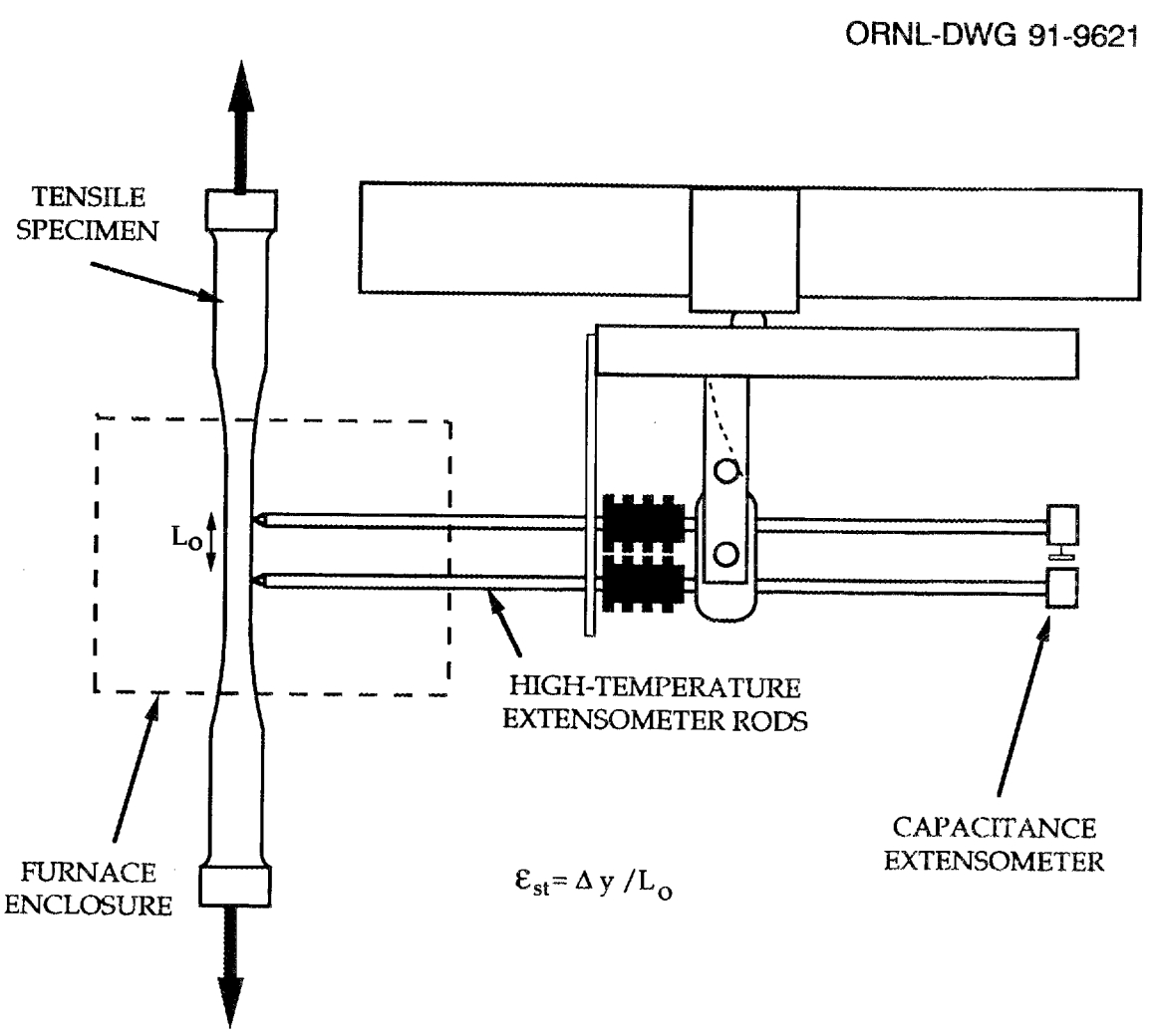

Fig. 4. Capacitance extensometer used for measurement of creep strain in button-head tensile specimens.

Table 1. Test Matrix for PY6 strength and creep/fatigue measurements. All tests were conducted in ambient air.

	Tension		Flexure	
Test type	T (°C)	No. tested	T (°C)	No. tested
Strength	25	26	25	49
	1000	3	1100	50
	1260	3	1300	44
	1370	2		
Creep/fatigue	1150	6	1150	*
	1260	6	1260	*
	1370	5	1370	*

*Testing under way.

Several characterization techniques were used to examine both the as-received and tested specimens. For example, in order to observe the microstructure of the as-received PY6 material, several specimens were polished to a 0.25-μm finish and subsequently etched in molten potassium hydroxide for 1 to 4 min. The grain size and morphology were then determined with SEM.

The fracture surfaces resulting from the strength and creep/fatigue tests were routinely examined with a low-power optical microscope. These observations were used to determine the general location of the failure origin for the strength specimens and the nature of the fatigue process (slow crack growth versus creep damage) for the crept specimens. Unfortunately, in the case of the specimens tested at elevated temperatures, observations of the fracture surfaces made at higher magnification with SEM were obscured due to surface oxidation. However, it was possible to examine the cavitation process with SEM by generating secondary fracture surfaces in the gage section at room temperature (Fig. 5).

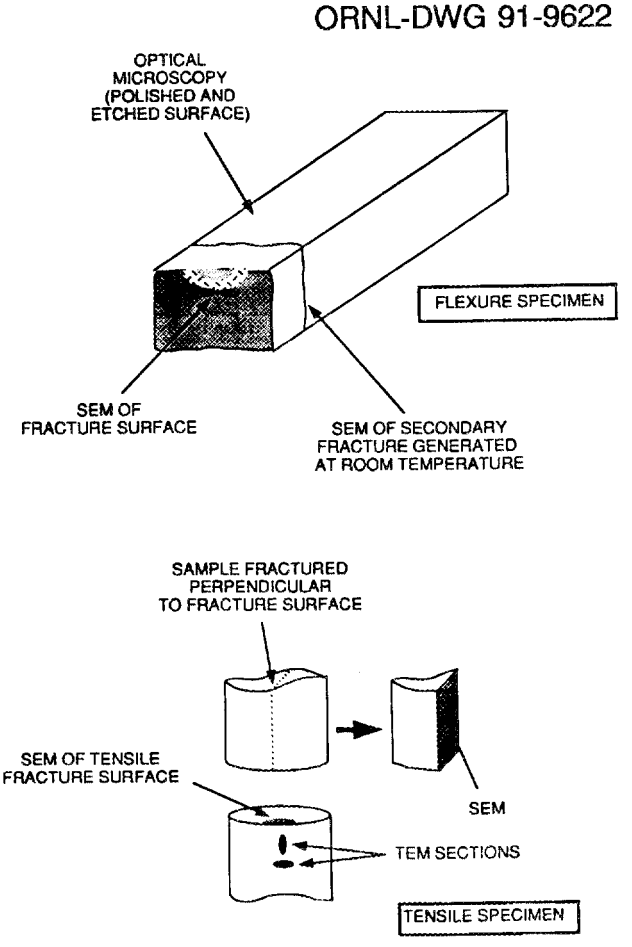

Fig. 5. Schematic illustration of specimen section for SEM and optical microscopy.

Variations in the phase composition (including both the silicon nitride and intergranular compounds) of the as-received PY6 were measured by X-ray diffraction. This technique was also used to examine changes in the phase composition resulting from the long-term creep exposures. In the case of the tensile creep tests, these changes could be detected directly from the tested specimen by comparing the diffraction profile obtained from the gage section with that from the button-head region. Note, because the button head remained relatively cool during the test, the phases determined by X-ray diffraction should be representative of the as-received material. This approach minimized uncertainties arising from specimen-to-specimen variations in phase compositions.

The flexure and tensile strength data (for sample sizes exceeding 25) were used to estimate the Weibull parameters m and s_o in the expression

$$P_f = 1 - \exp\,[-B\,(\sigma_s/\sigma_o)^m], \qquad (1)$$

where P_f is the failure probability, σ_s is the failure stress (strength) in the flexure specimen and the gage-section failure stress in the tensile specimen, and B is a load factor.[2] The value of B depends upon the loading geometry and the flaw location. For tensile loading, B is simply equal to the gage-section volume and gage-section surface area, for volume and surface flaws, respectively. In the case of the flexure specimen, B is given as

$$B = V\,K_V = V\,(l_i\,m/\,l_o + 1)/[2(m+1)^2] \qquad (2a)$$

for volume flaws and

$$B = A\,K_S = A\,K_V\,(w\,m/(w+h) + 1) \qquad (2b)$$

for surface flaws. In Eqs. (2a) and (2b), V is the flexural bar volume, A is the surface area, b is the specimen width, h is the specimen height, and l_i and l_o are the inner and outer span lengths, respectively, of the four-point loading fixture.

The Weibull parameters were estimated for each data set using both least - squares (LS) and maximum likelihood estimate (MLE) techniques.[3] In the former method, the strength values were first sorted in ascending order. The failure probability P_f was determined from the expression, $P_f = (n-0.5)/N$, where N is the total number of data points and n is the rank of the corresponding strength value (n = 1 for the least strength to n = N for the greatest strength). The least-squares estimates of m and σ_o parameters were then obtained from the familiar logarithmetic form of the Weibull equation:

$$\ln \ln\,(1-P_f)^{-1} = m \ln\,(\sigma_s/\sigma_{exp}), \qquad (3a)$$

where

$$m \ln (\sigma_{exp}) = m \ln (\sigma_o) - \ln (B). \quad (3b)$$

In the MLE method, m and σ_o were determined using an iterative technique discussed in Ref. 3. A major advantage of the MLE method over the LS method is that it does not require the assignment of failure probabilities.

The creep and fatigue data generated from the flexure and tensile tests were described by the respective equations:[4]

$$d\varepsilon_s/dt = A_0 (\sigma_a/\sigma'_0)^n \exp(-Q/RT), \quad (4a)$$

$$t_f = B (\sigma_a/\sigma'_0)^N, \quad (4b)$$

where $d\varepsilon_s/dt$ is the steady-state (or minimum) creep rate, n is the creep exponent, Q is the activation energy, T is the absolute temperature, σ'_0 is a normalizing parameter (=1 MPa), t_f is the fatigue life, N is the fatigue exponent and A_0 and B are pre-exponential factors. The experimental data were also used to examine the applicability of the modified Monkman-Grant equation, which describes the relationship between fatigue life and creep rate:

$$t_f = C (d\varepsilon_s/dt)^m, \quad (5)$$

where C and m are constants. By combining Eqs. (4a) and (4b), one can show that $N = n \cdot m$.

The calculation of the tensile creep strain from the y_I-t and y_F-t flexure data was initially based upon the formulation of Hollenburg.[5] This formulation assumes that the creep rate is independent of the sign of the applied creep stress. Unfortunately, creep studies of similar silicon nitrides[6,7] and silicon carbides[8] have shown that, at a given stress, the creep rates in tension are much greater than those in compression. Consequently, the application of a more rigorous evaluation[6,9,10] accounting for differences in the compression and tension creep rates was also investigated.

1. Strength behavior of PY6

Figure 6 illustrates the temperature dependence of the tensile and flexural strengths (designated σ_{st} and σ_{sf}, respectively) measured for the PY6 material. Similar data reported by University of Dayton Research Institute (UDRI)[11] are included for comparison. In the room-temperature tensile tests, all specimens were tested with four strain gages located circumferentially at the midpoint of the gage section to monitor bending for the entire loading sequence to failure. The percent bending for all the tests ranged from 0.4 to 4.3 with a mean of 2.4 and a standard deviation of 1.1. A least-squares fit of the stress-strain curves yielded

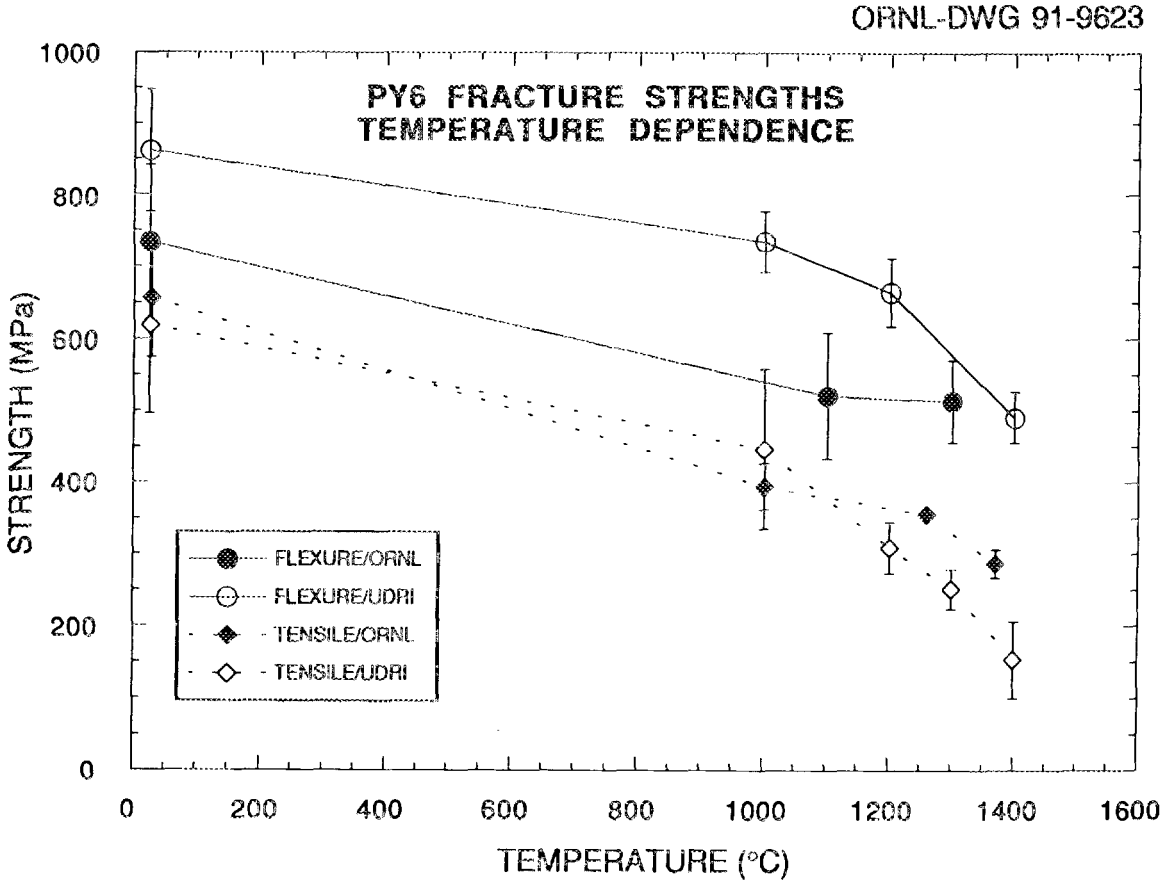

Fig. 6. Temperature Dependencies of the Flexure and Tensile Strengths for the PY6 Silicon Nitride. Data generated in the present study (ORNL) are compared with that reported by UDRI (Ref. 11).

the average elastic modulus at room temperature of 305 GPa with a standard deviation of 3.5 GPa.

As shown in Fig. 6, the strength values generally exhibited a gradual drop as the temperature was increased to 1000°C. With the exception of the ORNL flexure data, both σ_{st} and σ_{sf} dropped sharply as the temperature exceeded 1100°C. However, the ORNL flexure strength values increased slightly as the temperature was raised from 1100 to 1300°C. As discussed below, this behavior may have resulted from enhanced creep-assisted crack blunting in the ORNL flexure specimens due to the high α-Si_3N_4 content in the starting material. The presence of α-Si_3N_4 may have also been responsible for the poor agreement between the flexure strengths measured at UDRI and ORNL.

In the case of the tensile specimens, the agreement was considerably better. The slight divergence of the tensile data for temperatures above 1200°C probably reflects slight differences in the testing conditions (e.g., loading rate, soak time at

temperature, etc.).* For example, in the UDRI study, each specimen was held under a constant preload (4454.55 N) at temperature prior to testing in order to deform the copper collets in the grip ends, whereas in the ORNL study, all tests were initiated from a load of 150 N after deformation of the copper collets at a load of 6000 N applied at room temperature. For test temperatures exceeding 1200°C, the high, sustained preload in the UDRI study may have led to creep damage, which decreased the resulting strength.

As indicated in Fig. 6, the UDRI flexural strength values were consistently greater than those measured in the present study. These differences may have several possible explanations. One possible explanation is that, in the UDRI study, the stressing rate was approximately four times greater than that used for the ORNL flexure specimens. However, a high stressing rate would be expected to increase the measured strength only at temperatures exceeding 1000°C, since this temperature regime exhibits the greatest load-rate sensitivity.[11,12] This expectation is contrary to the empirical results in Fig. 6, which show better agreement between the UDRI and ORNL data at elevated temperatures.

A second possible explanation is that the the flexure test samples used in the respective studies were machined differently. Surface profilometry studies are currently under way to better quantify the roughness variations in the flexure specimens used in both the UDRI and ORNL studies.

Batch-to-batch material variations represent a third possible explanation for the measured differences in flexure strengths. To better quantify the material consistency, X-ray diffraction was used to identify the crystalline phases in both the UDRI and ORNL flexure samples. As shown in Fig. 7, the major phase in UDRI material was β-Si_3N_4 (indicated by asterisks). Although some secondary compounds were detected, their concentration was very low (< 5%). However, the specimens used in the ORNL tests exhibited a significant number of secondary phases not associated with the β-Si_3N_4. These phases were identified as α-Si_3N_4, yttrium silicon oxynitride, and yttrium silicate. Furthermore, the relative amounts of these phases varied considerably from sample to sample. In the case of the room-temperature strength samples, there was no clear correlation between the nature of secondary phase present and the measured strength value.

The presence of α-Si_3N_4 in the ORNL flexure specimens suggests that the α-to-β transformation was not completed during the HIPing process. It is likely that the grain size of the residual α-Si_3N_4 was relatively small compared with the

---

* Differences in the UDRI and ORNL tensile strengths arising from variations in material consistency were not expected since the HIPed tensile rods used in each study were manufactured during the same time frame.

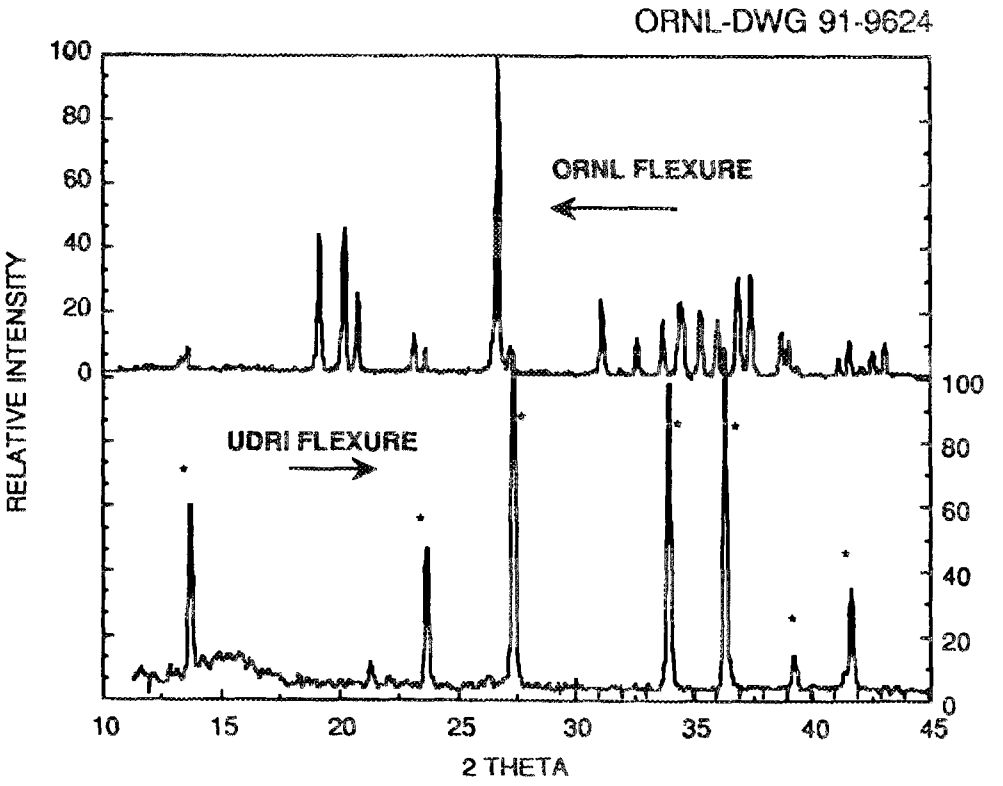

Fig. 7. Diffraction profiles for UDRI (Ref. 11) and ORNL flexure specimens.

β-Si_3N_4 grains. These small grains would lead to higher creep rates, thereby facilitating creep-assisted crack blunting at elevated temperatures. This would, in turn, result in a strength increase as the temperature was raised into the creep regime. Such behavior is reflected by the data shown in Fig. 6.

Additional X-ray diffraction profiles generated for the tensile rods used by both UDRI and ORNL indicated that β-Si_3N_4 was the major phase. The respective diffraction profiles were similar to that generated for the UDRI flexure specimen (Fig. 7). This result is consistent with the close agreement between the respective strength-temperature curves (Fig. 6).

The MLE Weibull parameters are summarized in Table 2. Note that m measured for the ORNL flexure specimens at 1300°C was substantially higher than the values determined at 25 and 1100°C. This increase in m at 1300°C may again reflect the effects of creep-assisted crack blunting discussed above. The fact that the m values measured for the ORNL tensile and flexure specimens were similar would suggest that the overall flaw populations were similar. However, fractographic analyses indicated that the predominate defects in the flexure specimens were machining flaws, while both machining and volume defects were responsible for failure in the tensile specimens. To account for the surface (S) and volume (V) defect populations in the tensile specimens, censoring

Table 2. Summary of maximum likelihood Weibull parameters

T (°C)*	m	s_{exp} (MPa)	K_V	s_0 (V) (MPa)	K_s	s_0 (S) (MPa)
25 (f)	8.46	779	0.0292	91.9	0.1709	261
1100 (f)	6.66	558	0.0369	38.2	0.1787	140
1300 (f)	11.54	538	0.0215	109	0.1646	240
25 (f)**	12.31	899	0.0202	201	0.1622	422
25 (t)	8.98	692	1.0000	150	1.0000	308
25 (t)†	10.52	743	-------	-------	1.0000	372
25 (t)††	7.37	767	1.0000	119	-------	-------

*(f)-flexure and (t)-tension.
**UDRI data (Ref. 11).
†Surface defect estimators for ORNL tensile specimens.
††Volume defect estimators for ORNL tensile specimens.

techniques[3] were used to estimate the respective Weibull parameters (see Table 2). As shown in Fig. 8, the P_f values for the volume defects were higher than those for surface defects for $\sigma_{st} < 690$ MPa. This indicates that failure in the low-strength regime was dominated by volume flaws while surface defects controlled the strength for $\sigma_{st} > 690$ MPa.

As shown in Fig. 6, σ_{st} measured at a given temperature was significantly lower than σ_{sf}. Assuming that the lower tensile strength was a result of either an increased surface area or gage volume, one would expect Weibull statistics to adequately describe these strength differences. To verify this conclusion, the temperature dependence of σ_{st} was predicted from the flexure data using the expression:

$$\sigma_{st}\,(est) = \sigma_{sf}\,(B_f/B_t)^{1/m}\,, \qquad (6)$$

where B_f and B_t are the respective load factors for the flexure (Eq. 2) and tensile specimens. Values of σ_{st} (est) were calculated for both surface- and volume controlled failure using the flexure Weibull parameters associated with the ORNL flexure data (Table 2). In all cases, σ_{sf} was equal to the average strength measured at a fixed temperature.

Figure 9 illustrates the predicted temperature dependency of σ_{st}. The curve based upon the surface flaw flexure Weibull estimators (K_s and σ_o (S)) provides a reasonably good description of the experimental data for T< 1100°C. This is somewhat surprising in view of the differences in starting phase composition. However, for temperatures above 1100°C, the deviation between the experimental and predicted curves may again reflect the differences in starting phase composition.

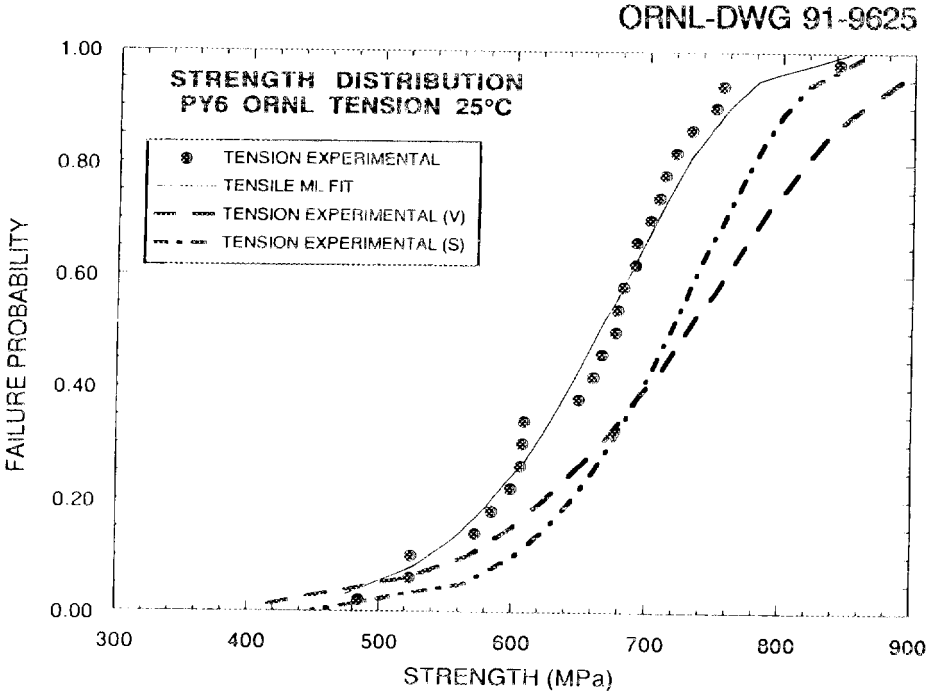

Fig. 8. Weibull strength distributions for the surface and volume defect populations in the ORNL tensile specimens tested at 25°C.

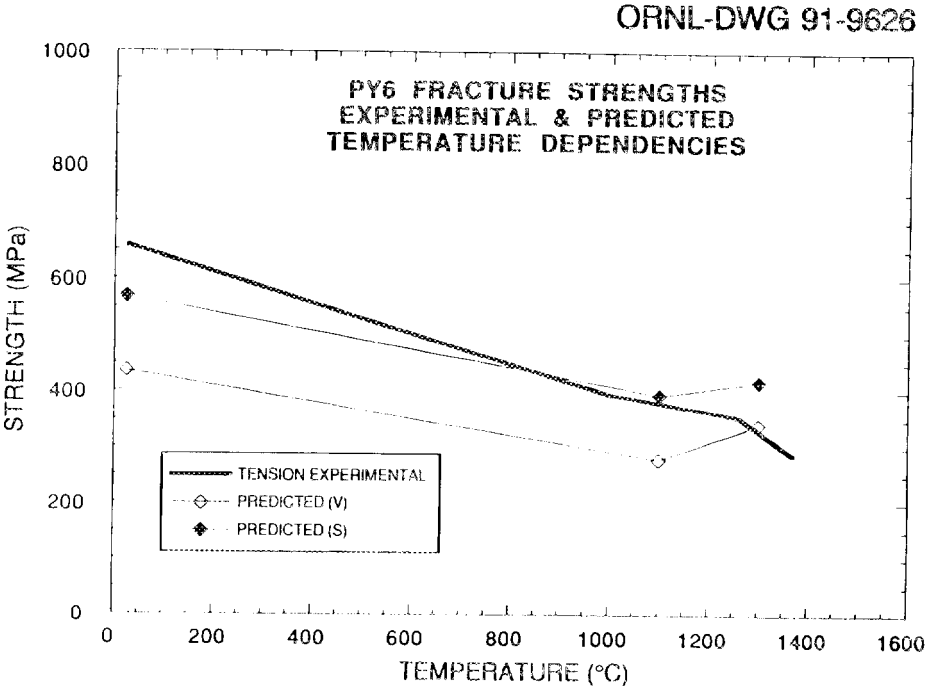

Fig. 9. Temperature dependency of the ORNL tensile strengths predicted from flexure strength data and corresponding Weibull parameters.

A major problem with such comparisons is that the tensile specimens failed from both volume and surface defects while the flexure specimens failed primarily from surface flaws. Consequently, the Weibull analysis based upon the flexure data should be restricted to the prediction of the tensile strength distribution for surface flaws only [σ_{st} (S)]. The results of such an analysis are illustrated in

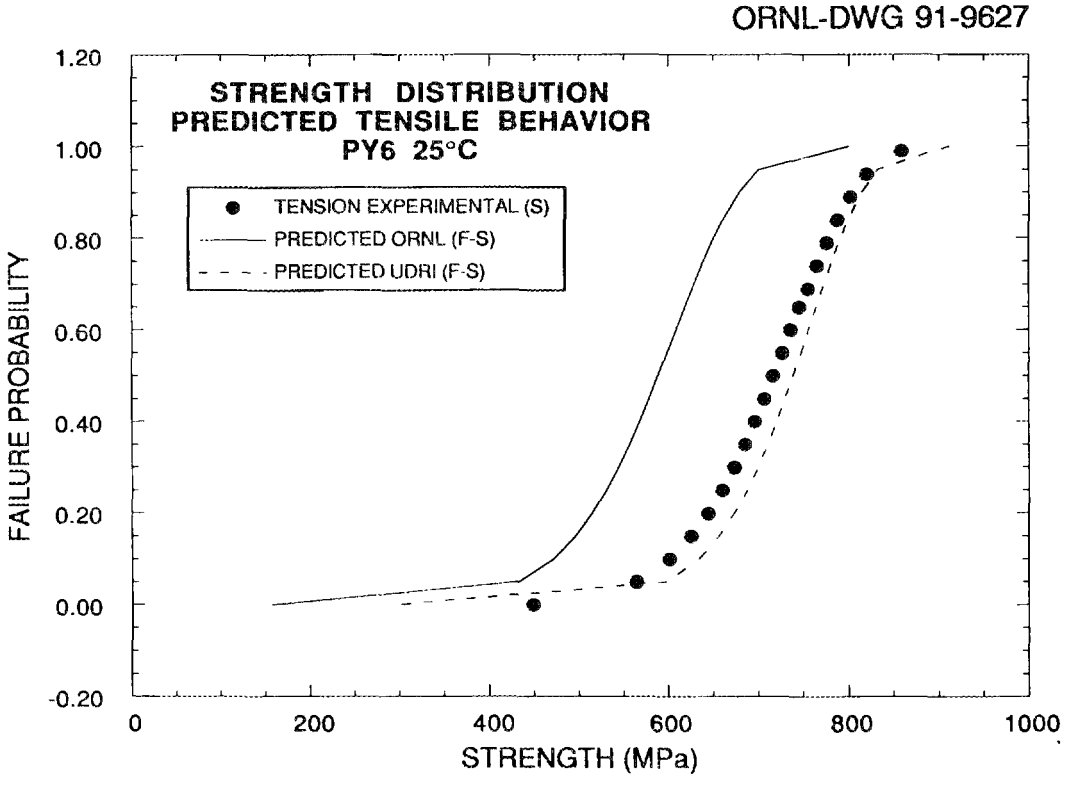

Fig. 10. Comparison of experimental tensile strength distribution for flaws (25°C) and distributions predicted from the ORNL and UDRI flexure data.

Fig. 10. This figure compares the room temperature distribution of σ_{st} (S) calculated from the censored Weibull analysis discussed previously (Table 2) with the tensile strength distributions predicted from the ORNL and UDRI flexure data [using values of K_s and σ_o (S) in Table 2]. In this case, the ORNL flexure data provide a very poor description of the tensile strength distribution. However, the predicted strength distribution based upon the UDRI data is quite comparable with the experimental data. This result is as expected on the basis of similar starting phase compositions in the UDRI flexure and ORNL tensile specimens. New studies are under way in which flexure bars are being machined from ORNL tensile rods to eliminate effects of compositional variations and green state processing (injection molding versus isopressing).

2. Creep/fatigue behavior of PY6

The total strain was measured as functions of time and applied tensile stress at 1150, 1260, and 1370°C. The data generated at 1370°C exhibited a clear trend of increasing strain rate with increasing stress. However, as shown in Fig. 11, the creep curves for the 1260°C tests were somewhat erratic in nature. In particular, the data generated at applied stresses of 125 and

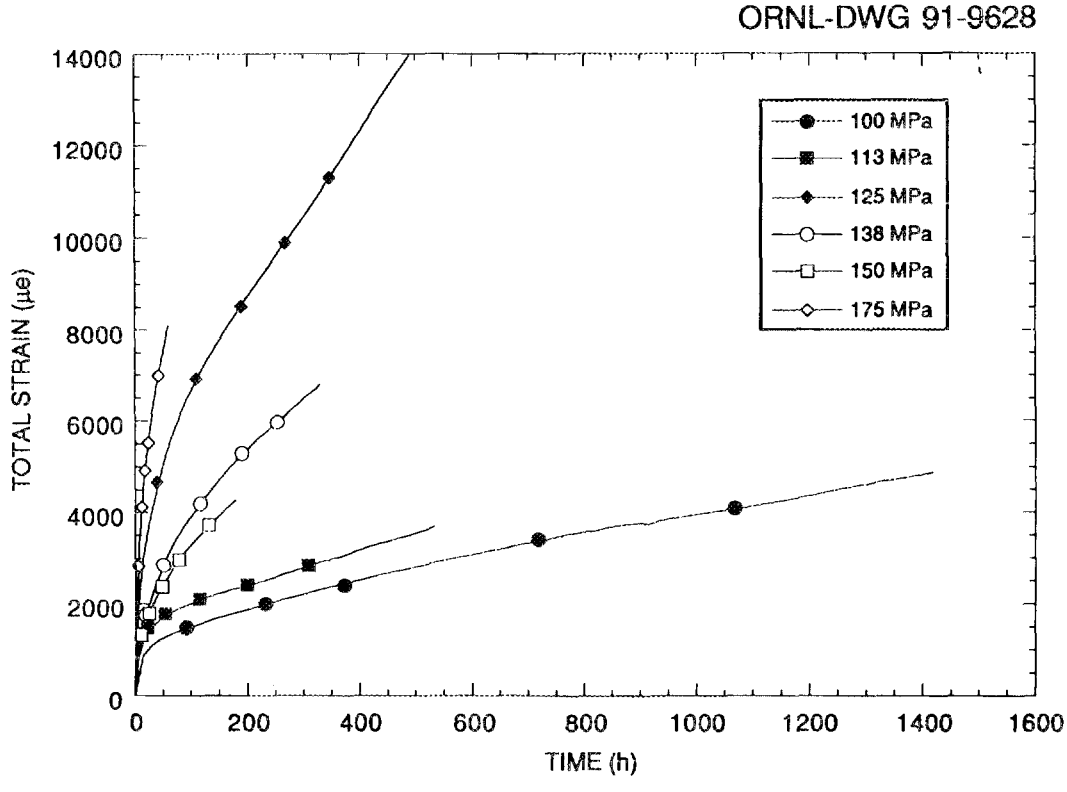

Fig. 11. Stress and time dependencies of creep strain measured at 1260°C.

150 MPa did not follow the trend of increasing creep strain rate with increasing stress. This behavior, which was also apparent in the strain rate versus stress curve (Fig. 12), is thought to be a result of specimen-to-specimen variations in the crystallinity of the intergranular phase. For a given stress level, samples containing an amorphous intergranular phase would be expected to creep at faster rates than samples containing a highly crystallized grain boundary phase.

In order to measure the crystallinity of the intergranular phase, X-ray diffraction studies of the button-head and gage regions were conducted on

samples tested at both 125 and 175 MPa (specimen designators P13 and P16, respectively). Because the tensile button head experienced relatively low temperatures (~200°C) during creep testing, the resulting X-ray diffraction data were expected to be representative of the starting composition. The major phase in all analyzed samples was β-Si_3N_4. However, the intergranular phase in sample P13 prior to testing was amorphous in character. X-ray diffraction results obtained from the gage section indicated that, during the creep test, this amorphous phase crystallized into a yttrium silicate ($Y_2Si_2O_7$). The intergranular phase in sample P16 prior to testing was already in the form of a crystallized $Y_2Si_2O_7$ phase. Exposure to the creep conditions had no measurable effect upon the nature of this phase. These results suggest that the presence of the amorphous grain-boundary phase in sample P13 was responsible for the high creep rate. These specimen-to-specimen variations in the grain-boundary phase crystallinity may have resulted from variations in the HIPing cycle.

Figure 12 shows log-log plots of the steady-state (or minimum) creep strain rate, $d\varepsilon_c/dt$, versus applied stress, σ_a. It is interesting that the stress dependence of the strain rate associated with the 1150°C tests was even less

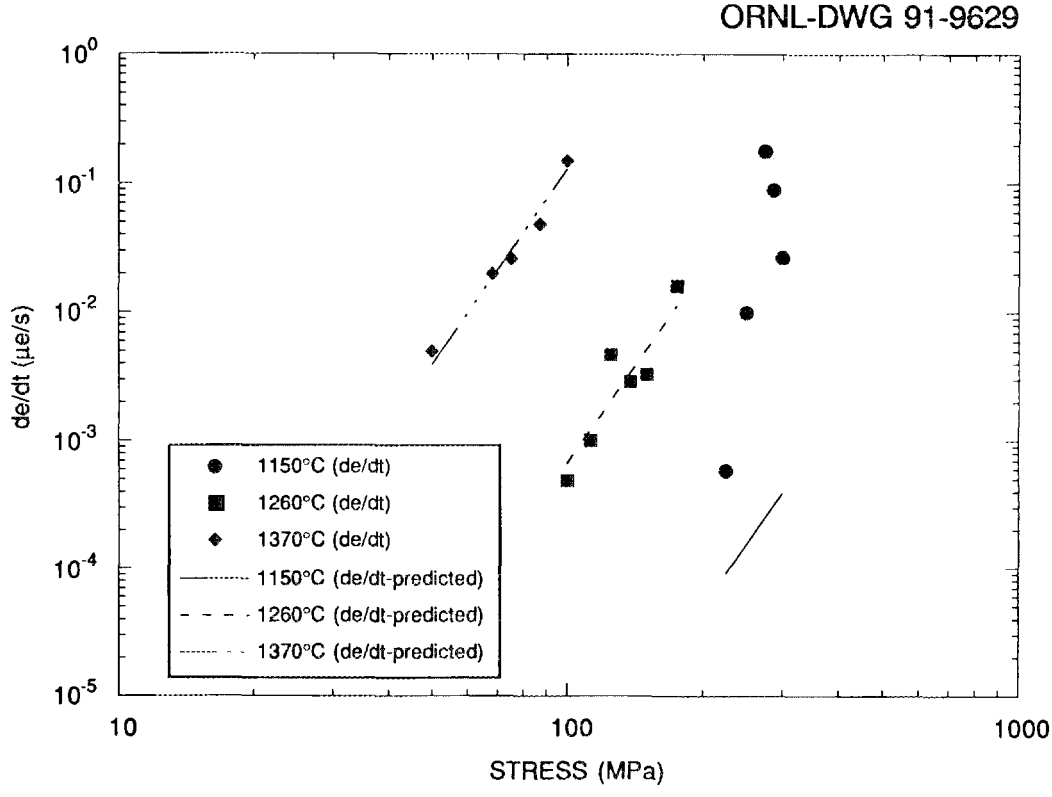

Fig. 12. Stress and temperature dependencies of the secondary (minimum) creep strain rate. The solid and dashed lines represent the "best fit" of the experimental data (excluding the 1150°C results) to Eq. (4a).

predictable than that measured at 1260°C. As discussed below, the increased scatter in the 1150°C data was not due to variations in intergranular phase crystallinity but rather a change in failure mechanism.

The n values Eq. (4a) calculated for each curve from separate regression analyses were 16.1 at 1150°C, 5.6 at 1260°C, and 4.7 at 1370°C. The creep exponents for the 1370 and 1260°C tests are consistent with those expected for diffusion-assisted cavitation processes.[4] The presence of these cavities was confirmed by SEM studies. The high value of n measured at 1150°C suggests a change in failure mechanism with decreasing temperature. Based upon results for other HIPed silicon nitrides,[6,11] one would expect slow crack growth of pre-existing flaws or defects to control failure in the temperature range of 1000 to 1200°C. As shown below, additional support for this conclusion was provided by the fatigue-life characteristics.

Values of Q and n in Eq. (4a) were estimated from a multiple linear regression analysis of the data in Fig. 12. The results obtained at 1150°C were excluded from this analysis since they were associated with a different failure mechanism. The resulting estimates of n and Q were 5.0 and 1102 kJ/mole, respectively. As shown by the solid lines in Fig. 12, these values provided a good description of the 1260°C and 1370°C data. Activation energies measured for other silicon nitride ceramics[13,14] are typically in the range of 550 to 700 kJ/mole. The high value obtained in the present study may be a consequence of time-dependent crystallization of the intergranular phase during the creep exposure.

In order to examine the fatigue behavior, all creep tests were continued until the samples failed. The resulting fatigue curves are shown in Fig. 13. The

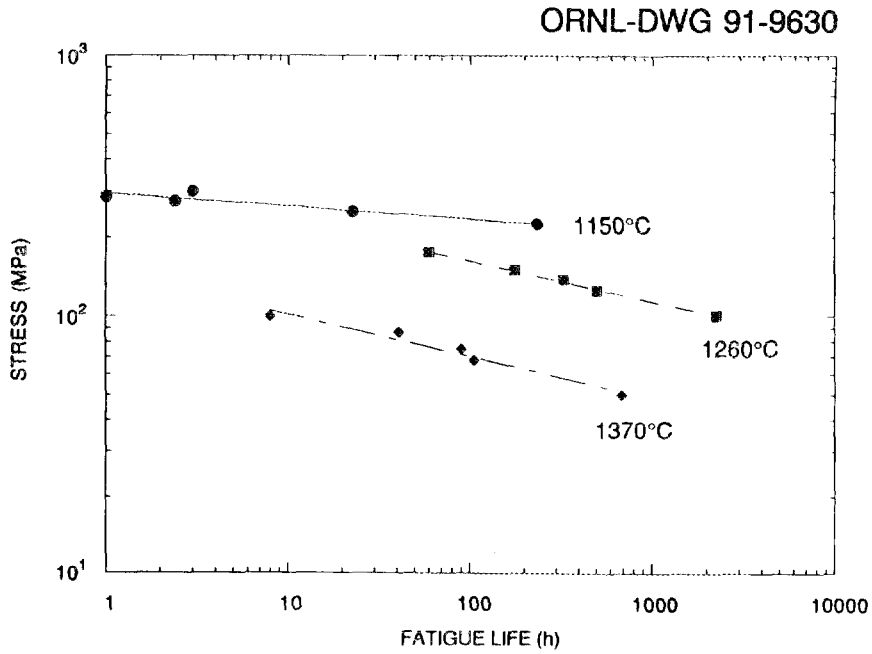

Fig. 13. Fatigue behavior of PY6 silicon nitride tested at 1150, 1260, and 1370°C.

fatigue exponents [N in Eq. (4b)] estimated from linear regression analyses were 18.0 at 1150°C, 6.4 at 1260°C, and 6 at 1370°C. The values of N for the 1260 and 1370°C tests are indicative of failure by a creep damage accumulation mechanism. Observations of the fracture surfaces of the corresponding test specimens revealed the existence of two distinct fracture regimes: a region of high surface roughness, the size of which increased with decreasing applied stress, and a relatively smooth area. The formation of the rough region was attributed to a damage zone evolution, which involved extensive creep cavitation. Once this zone reached a critical size, the sample failed catastrophically, thus forming a smooth, fast-fracture surface. The fracture surfaces for the 1150°C samples were more characteristic of catastrophic failure involving a slow crack growth process. This result is consistent with the high N value obtained for the 1150°C data.

The data in Figs. 12 and 13 indicate that, at a given temperature, the creep and fatigue exponents (n and N, respectively) were similar. This relationship, which suggests that the failure mechanisms were controlled by creep-related processes, is conveniently illustrated by expressing t_f as a function of $d\varepsilon_s/dt$ [i.e., the modified Monkman-Grant relationship in Eq. (5)]. An application of the experimental data to this relationship is shown in Fig. 14(*a*). Note that the data for the 1260 and 1370°C tests fall within a narrow band, indicating that the fatigue mechanisms were identical. Based upon preliminary SEM observations, the failure process probably involved the time-dependent accumulation of creep damage (in the form of cavities). Although the slope of the Monkman-Grant curve at 1150°C was similar to that of the higher temperature data, the curve was displaced to lower fatigue-life values. This result implies that the fatigue mechanism, while still controlled by the creep resistance, was altered as the temperature was lowered. The fact that the fracture surfaces at 1150°C gave evidence of slow crack growth suggests that a localized creep crack extension process was responsible for the fatigue behavior.

Values of m estimated from the data in Fig. 14(*b*) were relatively independent of temperatures and in the range 0.98 to 1.15. Taking $m \approx 1$, which is consistent with values for other structural ceramics,[6] leads to the prediction that $N = n \cdot m$ or, in this case, $N \approx n$ in agreement with experimental observations. It is also interesting to note that fatigue-life/strain rate dependence recently measured for a second HIPed silicon nitride (NT 154)* was quite similar to that for the PY6 [see Fig. 14(*b*)]. This result implies that the failure mechanisms operating at temperatures exceeding 1200°C were similar for both materials.

---

* NT 154 silicon nitride, Norton Co., Worcester, Massachusetts.

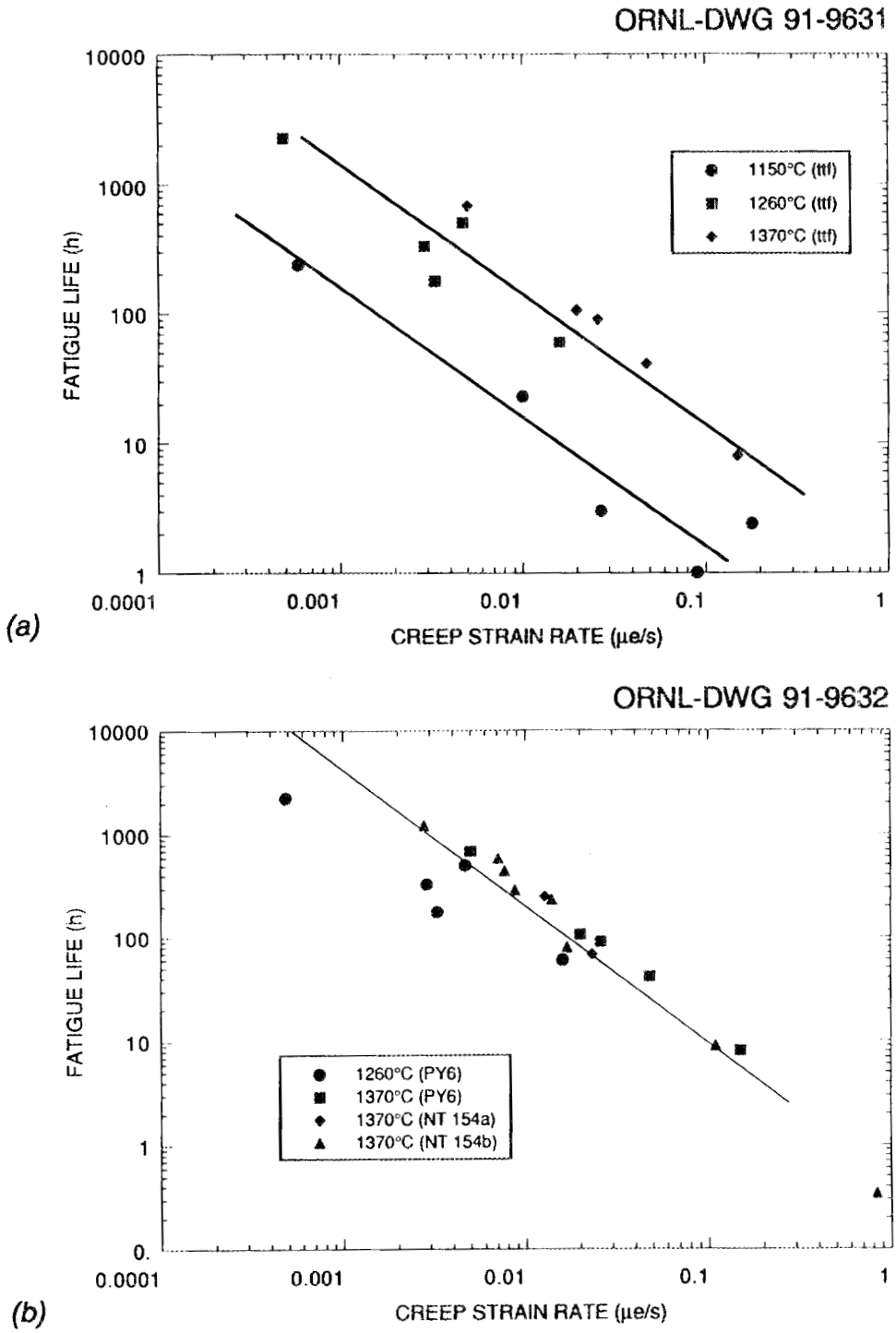

Fig. 14. Dependence of fatigue life upon creep strain rate. The modified Monkman-Grant relationship provided a good description of the strain rate dependence of the fatigue life for the PY6 material tested at 1260 and 1370°C (*a*). Trends in the fatigue life/strain rate data for the NT 154 were similar (*b*). Note the NT 154b was crystallized while the NT 154a was crystallized and annealed following the machining of the tensile samples.

Status of milestones

The final version of the report describing the results of the button-head grip comparison has been reviewed and has been submitted to the ORNL publications office for printing and distribution. All editorial changes have been made.

Publications

M.G. Jenkins, M.K. Ferber , and J.A. Salem, "Determination of the Stress Distributions in a Ceramic, Tensile Specimen Using Numerical Techniques," published in the *Proceedings of the 1990 ASME International Computers in Engineering Conference and Exposition.*

M. K. Ferber, M. G. Jenkins, T. A. Nolan, and R. Yeckley, "Creep-Fatigue of Structural Ceramics: I, Comparison of Flexure, Tension, and Compression Testing," to be published in the *Proceedings of the Thirty-Seventh Sagamore Conference on Structural Ceramics*, Plymouth, Mass., Oct. 1-4, 1990.

M.K. Ferber, T. N. Tiegs, and M. G. Jenkins, "Effect of Post-Sintering Microwave Treatments Upon the Mechanical Performance of Silicon Nitride," to be published in *Proceedings of the 15th Annual Conference on Composites and Advanced Ceramic Materials*, American Ceramic Society, Westerville, Ohio.

References

1. M. K. Ferber and M. G. Jenkins, "Rotor Data Base Generation," p 361–71 in *Ceramic Technology for Advanced Heat Engines Project Semiannual Progress Report for October 1988 Through March 1989*, ORNL/TM-11239, Martin Marietta Energy Systems, Inc., Oak Ridge Natl. Lab., August 1989.

2. C. A. Johnson, "Fracture Statistics in Design and Application,"Report 79-CRD 212, General Electric Co., Schenectady, New York, 1979.

3. R.B. Abernethy, J.E. Breneman, C.H. Medlin, and G.L. Reinman, *Weibull Analysis Handbook*, Report Number AFWAL-TR-83-2079, Aero Propulsion Laboratory, United States Air Force, Wright-Patterson AFB, Ohio, 1983.

4. H. Riedel, *Fracture at High Temperatures*, Springer-Verlag, Berlin, Heidelburg, 1987.

5. G. W. Hollenburg, G. R. Terwilliger, and R. S. Gordon, "Calculation of Stresses and Strains in Four-Point Bending Creep Tests." *J. Am. Ceram. Soc.* **54**[4], 196–99 (1971).

6. M. K. Ferber, M. G. Jenkins, T. A. Nolan, and R. Yeckley, "Creep-Fatigue of Structural Ceramics: I, Comparison of Flexure, Tension, and Compression Testing," to be published in the *Proceedings of the Thirty-Seventh Sagamore Conference on Structural Ceramics,* Plymouth, Mass, Oct. 1–4, 1990.

7. D. C. Cranmer, B. J. Hockey, S. M. Wiederhorn, and R. Yeckley, "Creep and Creep-Rupture of HIP-ed Si_3N_4," to be published in *Proceedings of the 15th Annual Conference on Composites and Advanced Ceramic Materials,* American Ceramic Society, Westerville, Ohio.

8. D. F. Carroll, T-J Chuang, and S. M. Wiederhorn, "A Comparison of Creep Rupture Behavior in Tension and Bending," p. 635–41 in *Ceram. Eng. Sci. Proc.,* Vol. **9** [7-8], American Ceramic Society, Westerville, Ohio, 1988.

9. T. Chuang, "Estimation of Power-Law Creep Parameters from Bend Test Data," *J. Mater. Sci.* **21**, 165–75 (1986).

10. R. F. Krause, Jr., "Comparison of Flexural Creep Ratre with that Predicted from the Power-Law Parameters for the Compressive and Tensile Creep," submitted to the *J. Am. Ceram. Soc.* for publication.

11. N.L. Hecht, "Environmental Effects in Toughened Ceramics-Final Report," UDR-TR-91-15, February 1991.

12. N. L. Hecht, "Environmental Effects in Toughened Ceramics," pp 254–381 in *Ceramic Technology for Advanced Heat Engines Semiannual Progress Report for April 1987 Through September 1987,* ORNL/TM-10705, Martin Marietta Energy Systems, Inc., Oak Ridge Natl. Lab., March 1988.

13. J. A. Todd and Zhi-Yue Xu, "The High-Temperature Creep Deformation of Si_3N_4-$6Y_2O_3$-$2Al_2O_3$," *J. Mater. Sci.* **27**, 4443–52 (1989).

14. M. K. Ferber and M. G. Jenkins, Oak Ridge Natl. Lab., unpublished work (1991).

TOUGHENED CERAMICS LIFE PREDICTION

J. A. Salem and S. R. Choi (NASA Lewis Research Center)

Objective/scope

The purpose of this research is to understand the room temperature and high temperature [>1370°C(2500°F)] behavior of *in situ* and SiC-whisker toughened Si_3N_4 ceramics as the basis for developing a life prediction methodology. A major objective is to understand the relationship between microstructure and the mechanical behavior of a limited number of materials. Another objective is to determine the behavior as a function of time and temperature.

Specifically, the room temperature and elevated temperature strength and reliability, the fracture toughness, slow crack growth and the creep behavior will be determined for the as-manufactured material. The same properties will also be evaluated after long-time exposure to various high temperature isothermal and cyclic environments. These results will provide input for parallel materials development and design methodology development programs. Resultant design code will be verified.

Technical progress

The crack growth resistance of two *in situ* toughened silicon nitride materials were experimentally measured and a model quantifying the enhancement of Weibull modulus by crack growth resistance was derived.

One of the *in situ* toughened materials was commercially produced[1], whereas the other material was developed at NASA Lewis[2]. Fractography of crack trajectories through the toughened materials was performed and compared to that of a material without crack growth resistance. Microstructures of the materials are shown in Figure 1.

Test Procedures

Room temperature R-curve behavior was estimated using the indentation strength technique proposed by Krause [1]. The test specimens were 3 x 5.6 x 25 mm MOR bars. The center of the tensile surface was polished and indented with a Vickers microhardness indenter at loads ranging from 49 to 196 N. The subsequent strength tests of the indented samples were conducted using a four-point bend fixture with 9.5 and 20 mm spans and a displacement rate of 0.2 mm/min in

---

1 Kyocera SN251.

2 Designated "8SC."

room temperature air. Three specimens were tested at each indentation load.

Weibull modulus, fracture toughness, elastic modulus and thermal properties of the commercial material were previously reported [2,3].

Crack Growth Resistance

Damage or flaw tolerance that results from an increasing resistance to stable crack propagation is a desirable property for structural ceramics. Krause [1] has shown that R-curve behavior can be evaluated from indentation strength data, assuming that the fracture resistance (K_r) is related to the crack length (c) by a power-law relationship. The fracture resistance and the indentation strength (σ_f) relations are expressed by

$$K_r = kc^{\tau} \tag{1}$$

$$\sigma_f = [k(3+2\tau)/(4\beta)_o][4P\Gamma/(k(1-2\tau))]^{2\tau-1/2\tau+3} \tag{2}$$

where k and τ are constants, Γ and β are the dimensionless quantities associated with the residual contact stress intensity and the crack geometry (defined in $K_I = \beta\sigma\sqrt{c}$, where K_I is the mode I stress intensity factor and σ is the applied stress) respectively, and P is the indentation load. When $\tau = 0$, Equation (2) reduces to the case of no crack resistance toughening. Also, $K_r = K_{IC}$ for $\tau = 0$. The parameter τ was evaluated from the best-fit slope of the Log σ_f-Log P data shown in Figure 2. The constant k was evaluated from Equation (1) with the estimated τ and the toughness value obtained with the indentation strength method [4] for a crack size of c = 102 μm.

The R-curve estimation for the materials is presented in Figure 3, where the fracture resistance curves are plotted as a function of the crack size based on Equation (1). For illustrative purposes, the fracture resistance curve for a silicon nitride[3] with an equiaxed microstructure (see Figure 4) is included [5]. It can be seen from Figure 3 that the *in situ* toughened materials exhibit R-curve behavior with toughening exponents of $\tau = 0.126$ and 0.08 for the commercial and NASA developed materials, respectively. The material with an equiaxed microstructure exhibits a flat R-

---

3 Norton 6% yttrium Si_3N_4, reference [5].

curve with a negligibly small exponent of $\tau = 0.027$, and a lower level of K_r.

The elongated grain morphology of the *in situ* toughened materials not only increased the fracture toughnesses, but imparted crack growth resistance. Similar observations of rising R-curve behavior ($\tau = 0.1$ to 0.22) and improved fracture toughness were found in other *in situ* toughened silicon nitrides [6, 7].

R-Curve Behavior and its Relation To Weibull Modulus

Ceramics with a rising R-curve have been experimentally shown to exhibit a higher Weibull modulus as compared to ceramics with a flat R-curve. Kendall et al [8], Cook and Clarke [9], and Shetty and Wang [10] made attempts to develop closed form solutions for the modified Weibull parameters based on fracture mechanics principles and two-parameter Weibull statistics. A similar derivation of the modified Weibull parameters for the R-curve enhanced material, based on the procedure used by Shetty and Wang [10], was made in this study and found to yield

$$m_r = \frac{m_o}{1-2\tau} \tag{3}$$

and

$$\sigma_r = \frac{k K_{IC}^{2\tau-1}}{\sigma_o^{2\tau-1}\,\beta^{2\tau}} \tag{4}$$

where m_r and σ_r are the Weibull modulus and characteristic strength of the material with R-curve behavior, respectively, and m_o and σ_o are the Weibull modulus and characteristic strength for the flat R-curve material with the same flaw distribution. The Weibull modulus m_r is the same as that derived by Kendall et. al [8] or Shetty and Wang [10]. However, the characteristic strength, σ_r is different from the one derived by Shetty and Wang [10] by a factor of $(\pi\beta^2/4)^{-\tau}$.

Note that when $\tau = 0$ the parameters reduce to the m_o and σ_o for the flat R-curve material. It also should be noted that the characteristic strength σ_r in equation (4) is not an explicit function of the given material, but rather depends on the functional form that is chosen to represent K_{IC}.

Equation (3) shows that the Weibull modulus increases with increasing toughening exponent. For the previously evaluated exponent $\tau = 0.126$ and surface Weibull modulus of $m_r = 18.36$ for the commercial material, the Weibull modulus

of a flat R-curve material with the same surface flaw distribution is back-calculated as $m_o = 14$, a value typical of the upper range for monolithic silicon nitrides. This indicates that the R-curve behavior increased the Weibull modulus by 34 % as compared to a material with the same flaw distribution and a flat R-curve. The Weibull modulus for surface flaws, $m_r = 18.36$, was used in the above calculation because the value of τ was derived from surface indentations cracks, and the R-curve is not considered unique for crack extension from different flaws. However, if the value of τ associated with stable crack extension from volume flaws is known (the same growth pattern), then the analysis should be applicable to volume flaws as well as surface flaws.

Although several simplifying assumptions were made in the above analysis, this approach gives a quantitative insight to the increased Weibull modulus observed for materials with rising R-curves.

Crack Trajectory

In an attempt to explain the greater room temperature fracture toughness and crack growth resistance of the *in situ* toughened materials relative to the silicon nitride with an equiaxed microstructure, indentation cracks (Vickers indentation load = 98 N) were placed in polished sections of the commercial materials. The crack trajectories, as observed by SEM, are shown in Figure 5. The cracks traversed through the equiaxed microstructure with little deflection, but occasional bridging was apparent. In the *in situ* toughened material, however, the cracks followed a very tortuous path through the microstructure.

The crack path relative to the grain boundaries of the commercial *in situ* toughened material is illustrated in Figure 6. The crack passed through the boundaries of small grains as well as large grains oriented at low angles, resulting in crack deflection, interlocking, and bridging behavior analogous with whisker pullout. Note the wedging of the elongated grain relative to surrounding material (arrow A), and the resultant, secondary cracking (arrow B). Long grains oriented at large angles to the crack path were cleaved (arrow C). This crack interaction with the elongated grain structure may account for the improved fracture toughness and rising crack growth resistance of the *in situ* toughened materials relative to the material with an equiaxed microstructure.

Conclusions

Silicon nitrides with an elongated microstructure exhibited good crack growth resistance and a high Weibull modulus. However, ultimate strength of the materials was limited by excessively large grains and pores. The excessively long grains were developed by a nonuniform distribution of sintering additives.

For the commercially developed, *in situ* toughened material, room temperature crack growth resistance ranged from 6.5 to 9 MPa$\sqrt{m}$ within a 300 μm crack extension. This resulted in a 34 %, estimated enhancement of the Weibull modulus. The NASA developed material exhibited a rise in crack growth resistance form 6.5 to 8.7 MPa$\sqrt{m}$ within a 300 μm crack extension.

The improved fracture toughness, crack growth resistance and Weibull modulus were attributed to the elongated grain structure, which resulted in significant crack deflection and bridging, as compared to that of a material with an equiaxed microstructure.

References

1. K. F. Krause, "Rising Fracture Toughness for the Bending Strength of Indented Alumina Beams," J. Am. Ceram. Soc. 71(5), 338 43 (1988).

2. "Mechanical Behavior and Failure Phenomenon of an In Situ-Toughened Silicon Nitride," J.A. Salem, S.R. Choi, M. Freedman, and M.G. Jenkins, NASA TM 103741, May 1991.

3. "Toughened Ceramic Life Prediction" J.A. Salem and S.R Choi, in Ceramic Technology of Advanced Heat Engines Semiannual Contractors Report, ORNL/TM-11586, April, 1990.

4. P. Chantikul, G.R. Anstis, B.R. Lawn, and D.B. Marshall, "A Critical Evaluation of Indentation Techniques for Measuring Fracture Toughness: II, Strength Method," J. Am. Ceram. Soc.. 64[9] 539-43 (1981).

5. J. A. Salem "Strength and Toughness of Monolithic and Composite Silicon Nitrides," NASA Technical Memorandum 102423, 1990.

6. C. W. Li and Y. Yamanis, "Super-Tough Silicon-Nitride with R-curve Behavior," Ceram. Eng. Sci. Proc. 10(1989) 632.

7. J. E. Ritter, S. R. Choi, K. Jakus, P. J. Whalen, and R. G. Rateick, "Effect of Microstructure on the Erosion and Impact Damage of Sintered Silicon Nitride," to be published in J. Mater. Sci. (1991).

8. K. Kendall and N.M. Ashford, S.R Tan, and J.D. Birchall "Influence of Toughness on Weibull Modulus of Ceramic Bending Strength," J. Mater. Research 1[1], 120-123 (1986).

9. R.F. Cook and D.R. Clarke, "Fracture Stability, R-Curves and Strength Variability," Acta Metall. 36[3] 555-562 (1988).

10. D.K. Shetty and J.S. Wang, "Crack Stability and Strength Distribution of Ceramics that Exhibit Rising Crack-Growth Resistance (R-Curve) Behavior," J. Am. Ceram. Soc. 72[7] 1158-62 (1988).

Status of Milestones

Milestones on time.

Publications

1. "Mechanical Behavior and Failure Phenomenon of an In Situ-Toughened Silicon Nitride," J. A. Salem, S. R. Choi, M. Freedman, and M. G. Jenkins, NASA TM 103741, May 1991.

2. "Comparison of Dynamic Fatigue Behavior Between SiC Whisker-Reinforced Composite and Monolithic Silicon Nitrides," S.R. Choi and J.A. Salem, NASA TM 103707, February, 1991.

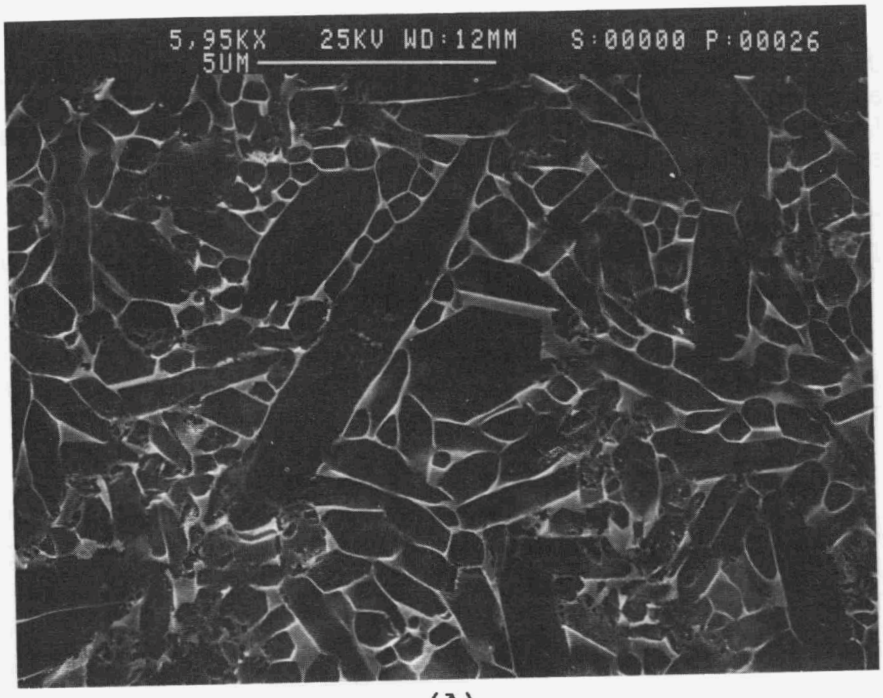

(A)

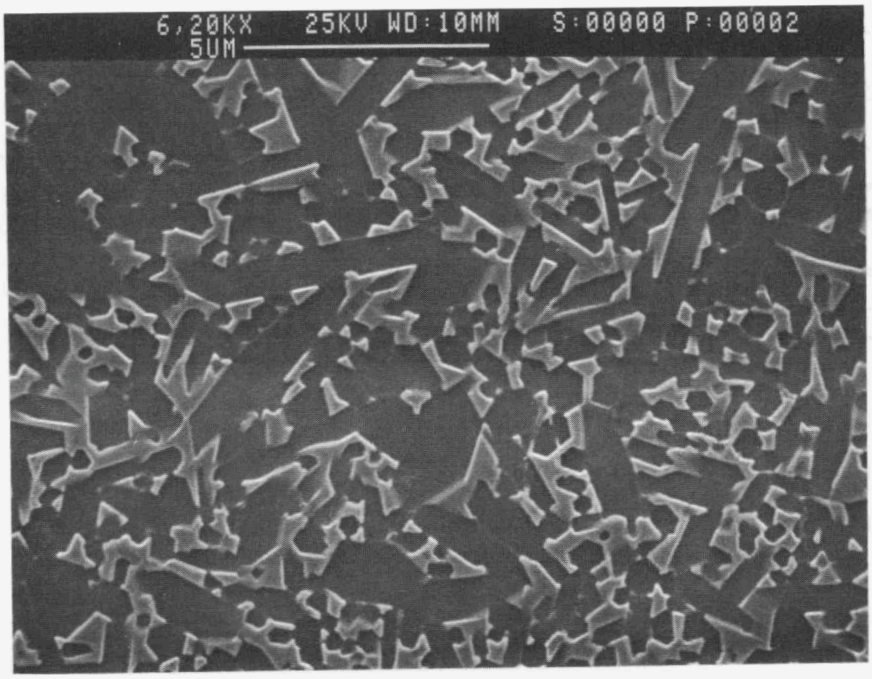

(B)

Figure 1. Etched microstructures of *in situ* toughened silicon nitrides: (A) Kyocera SN251 and (B) 8SC material developed at NASA Lewis.

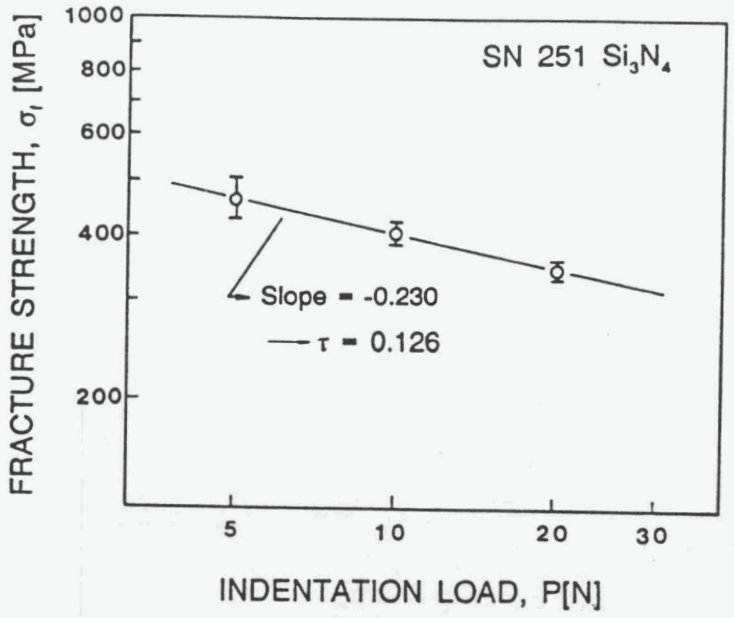

Figure 2. Fracture strength as a function of indentation load for SN251. Error bar indicates % 1.0 standard deviation.

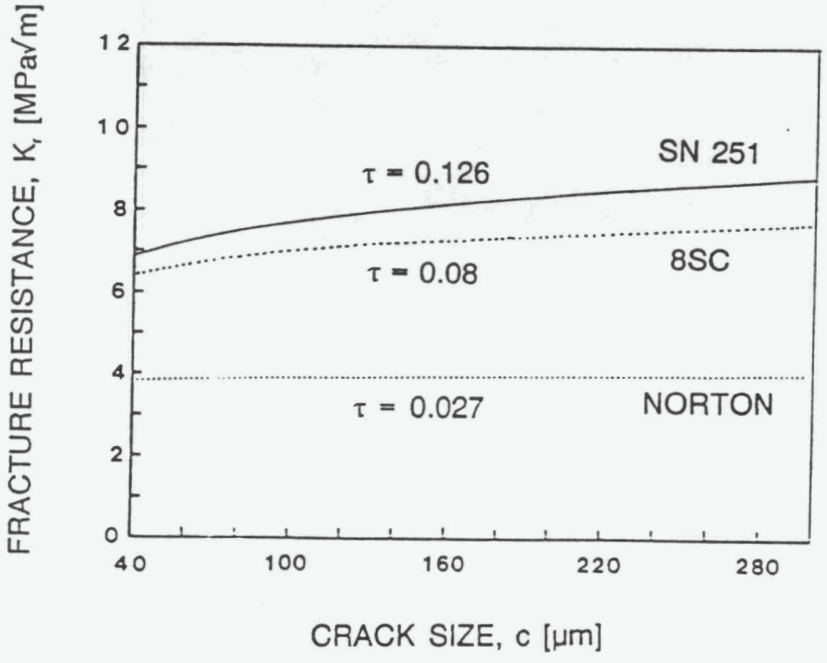

Figure 3. Predicted fracture resistance curves for *in situ* toughened materials and material with an equiaxed microstructure.

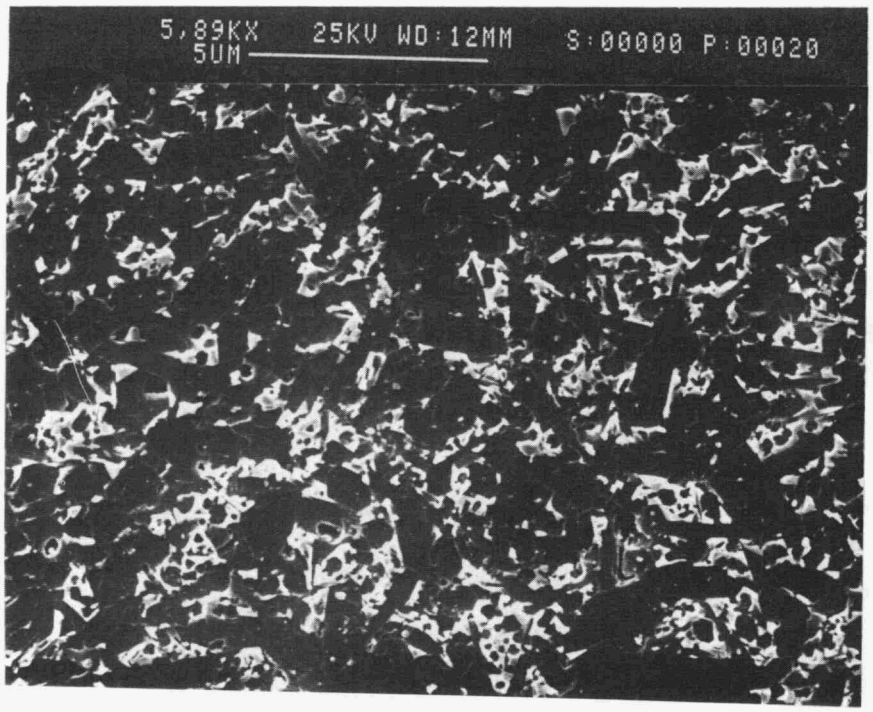

Figure 4. Plasma etched microstructure of a 6% yttrium silicon nitride with an equiaxed grain structure.

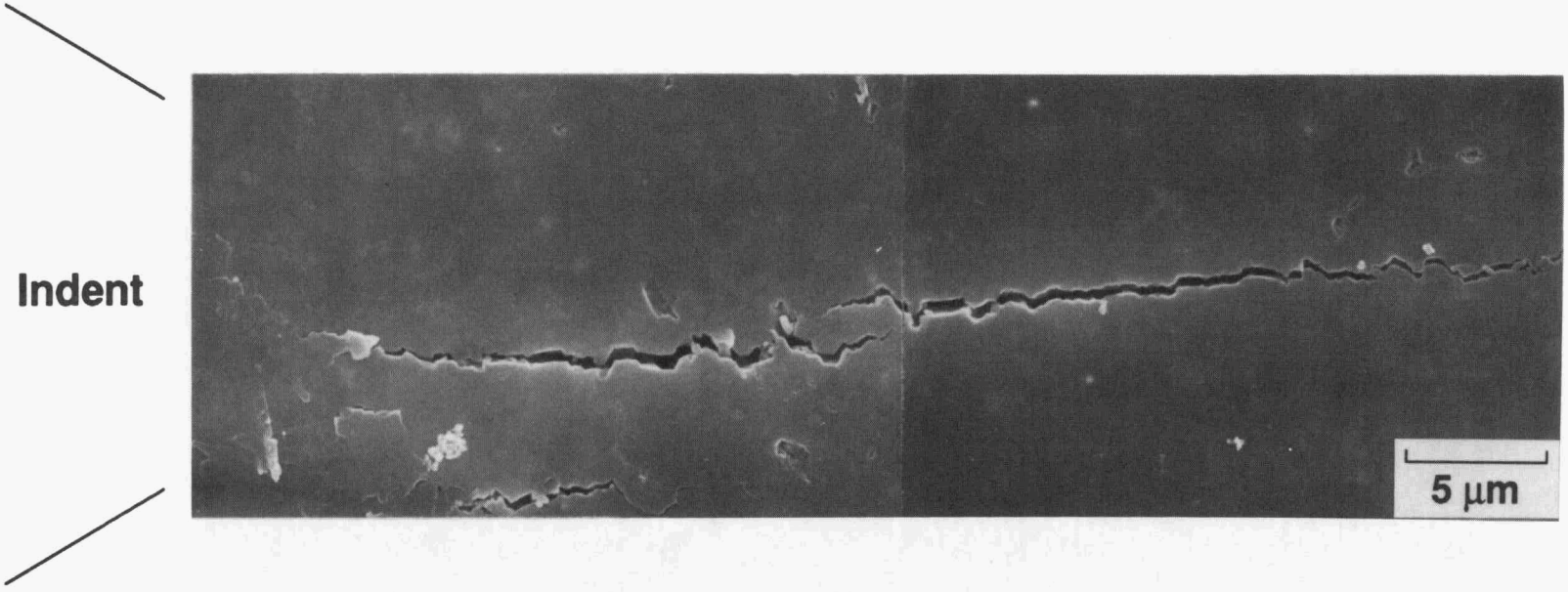

Figure 5A. Indentation crack trajectory in silicon nitride with an equiaxed microstructure (6% yttrium).

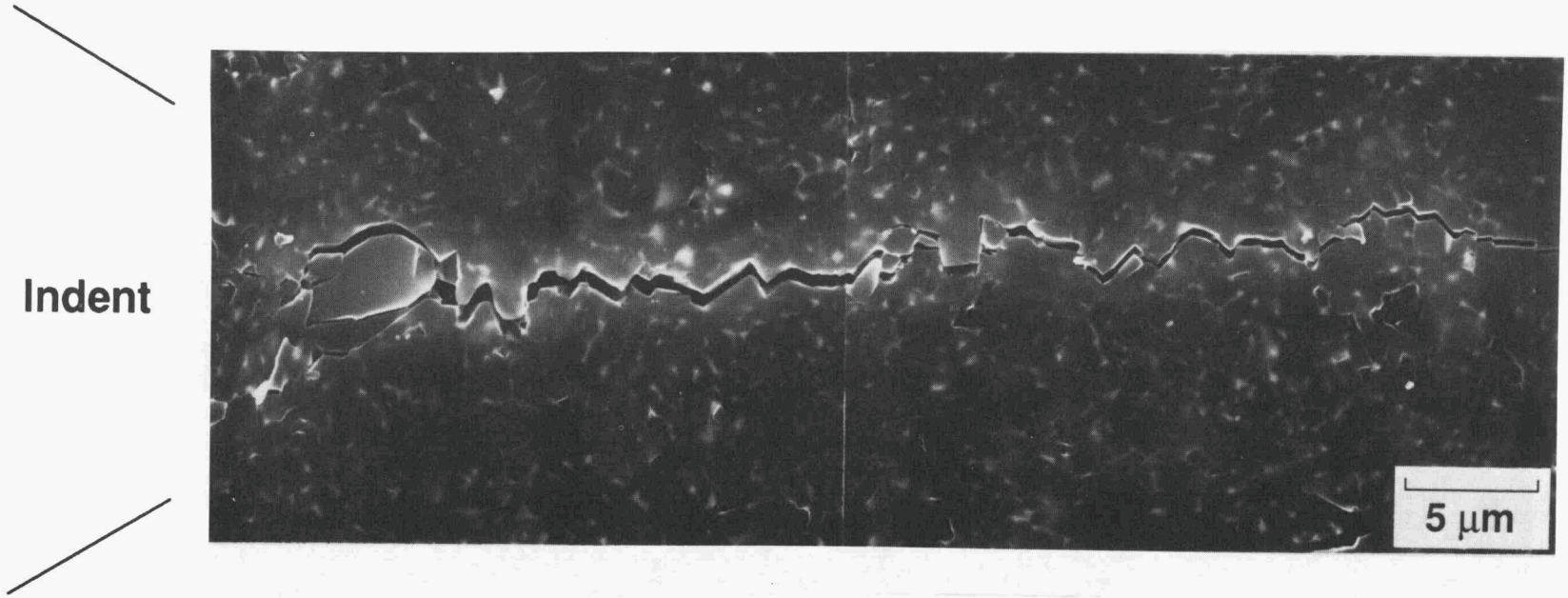

Figure 5B. Indentation crack trajectory in commercial *in situ* toughened silicon nitride (SN251).

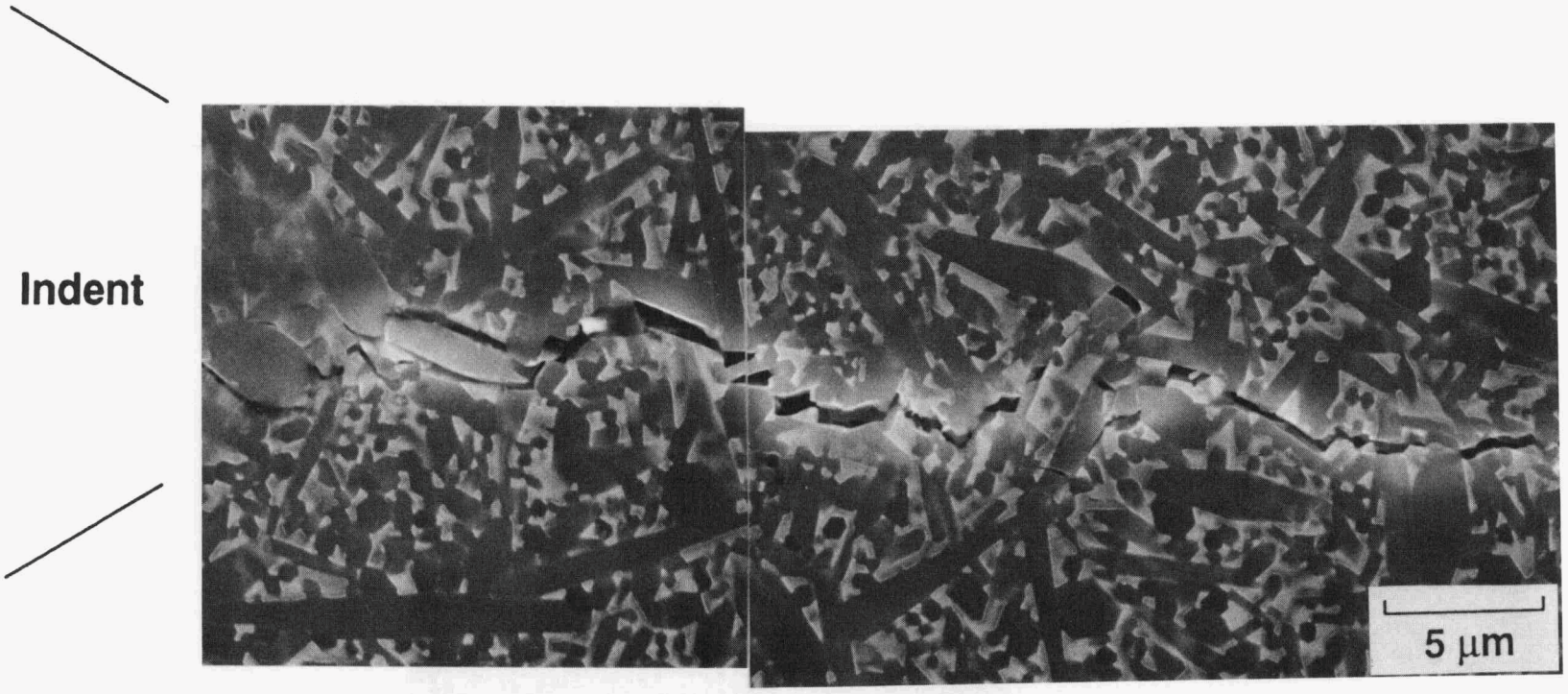

Figure 5C. Indentation crack trajectory for *in situ* toughened silicon nitride developed at NASA Lewis (8SC).

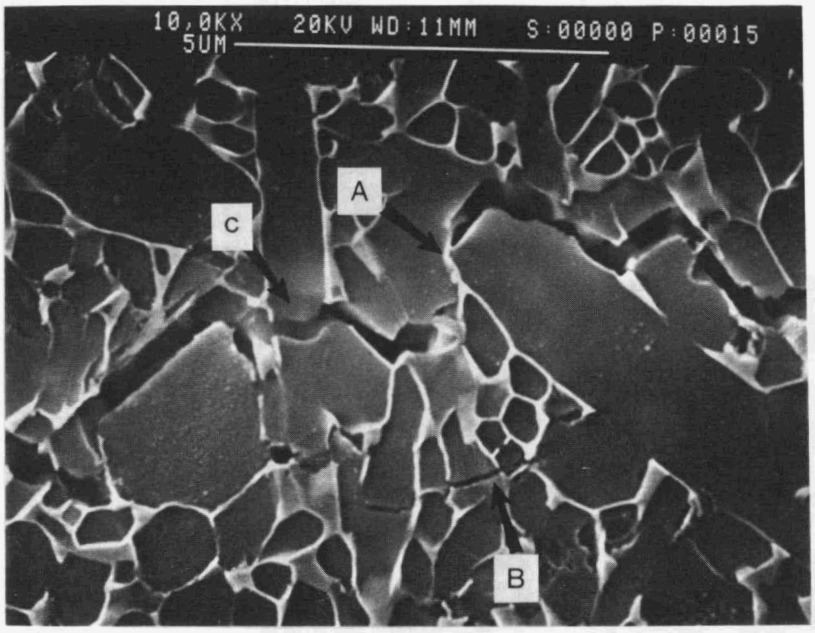

Figure 6. Indentation crack trajectory for etched, *in situ* toughened silicon nitride.

Life Prediction Methodology

D. L. Vaccari and P. K. Khandelwal (Allison Gas Turbine Division of General Motors Corporation)

Objective/scope

The objective of this project is to develop and demonstrate the necessary nondestructive examination (NDE) technology, materials data base, and design methodology for predicting useful life of structural ceramic components of advanced heat engines. The analytical methodology will be demonstrated through confirmatory testing of ceramic components subject to thermal-mechanical loading conditions similar to those anticipated to occur in actual vehicular service. The project addresses fast fracture, slow crack growth, creep, and oxidation failure modes.

Technical progress

Thermophysical properties

Samples of PY6 material were submitted for thermophysical property testing during this reporting period. Specific heat was measured using a differential scanning calorimeter. Results are shown in Figure 1. Bulk density values were determined from the samples' geometries and masses. The average density was 3.2429 g/cm^3. Thermal diffusivity was measured using the laser flash technique with results shown in Figure 2. Thermal conductivity was calculated from these quantities and is shown in Figure 3. Thermal expansion values were determined using a dual push rod dilatometer and are reported in Figure 4.

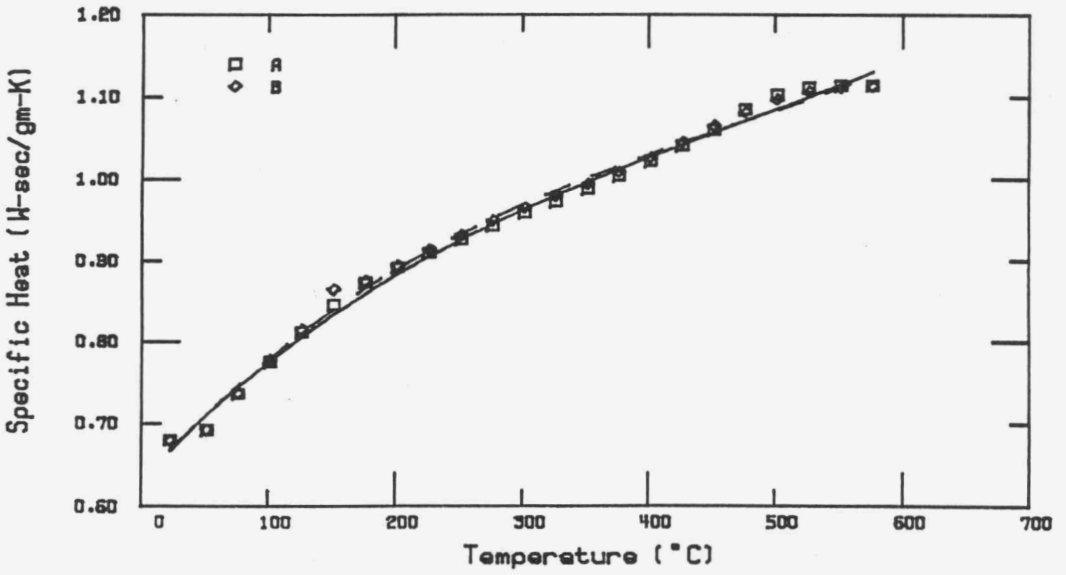

Figure 1. Specific heat measurements for PY6 material.

Modulus of rupture bars

The initial modulus of rupture (MOR) results obtained from room temperature testing during the last reporting period indicated a higher percentage of chamfer failures than expected. Although the

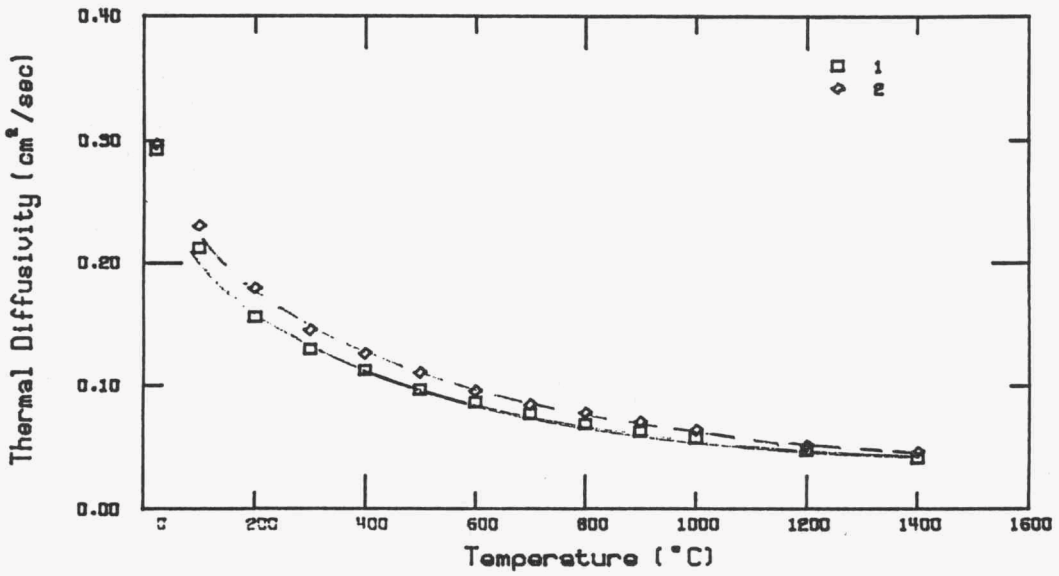

Figure 2. Thermal diffusivity measurements for PY6 material.

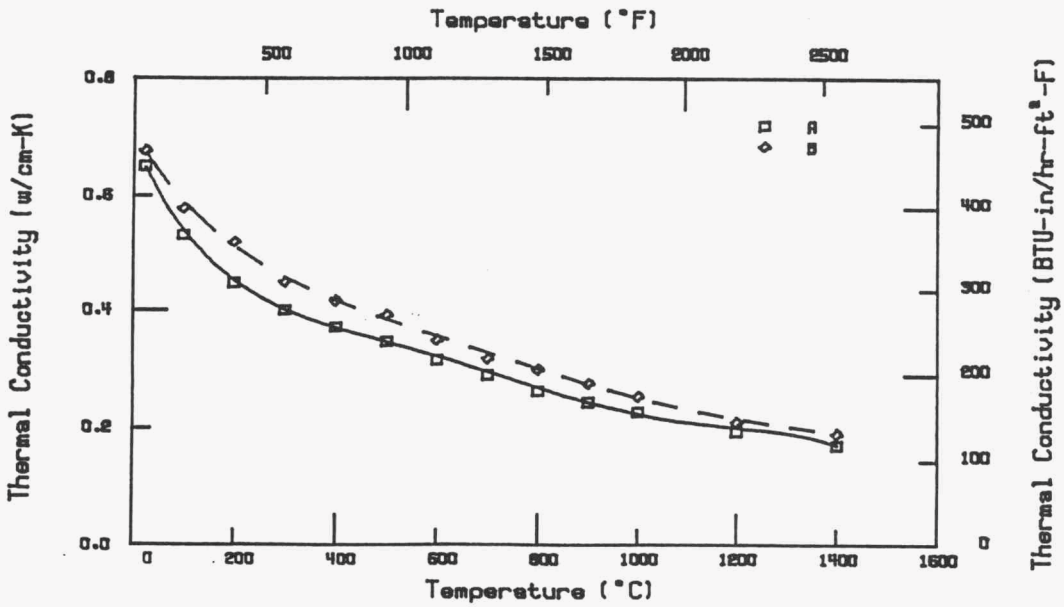

Figure 3. Thermal conductivity for PY6 material.

bars that failed in the chamfer did not have strengths appreciably different from the other bars, an understanding of the failures was desired. Additional untested bars from the same lot were examined for machining irregularities. The bars had been longitudinally machined using a 400 grit diamond wheel by Bomas Speciality, Waltham, Mass. Surface roughness of 40 MOR bars was measured to assess the reproducibility and distribution of the surface finish. A Model PRS-2 precision surface measurement system manufactured by Sheffield Measurement Division, Dayton, with a 10 micron (0.0004 in.) radius stylus was utilized. Figure 5 shows a histogram of the measured

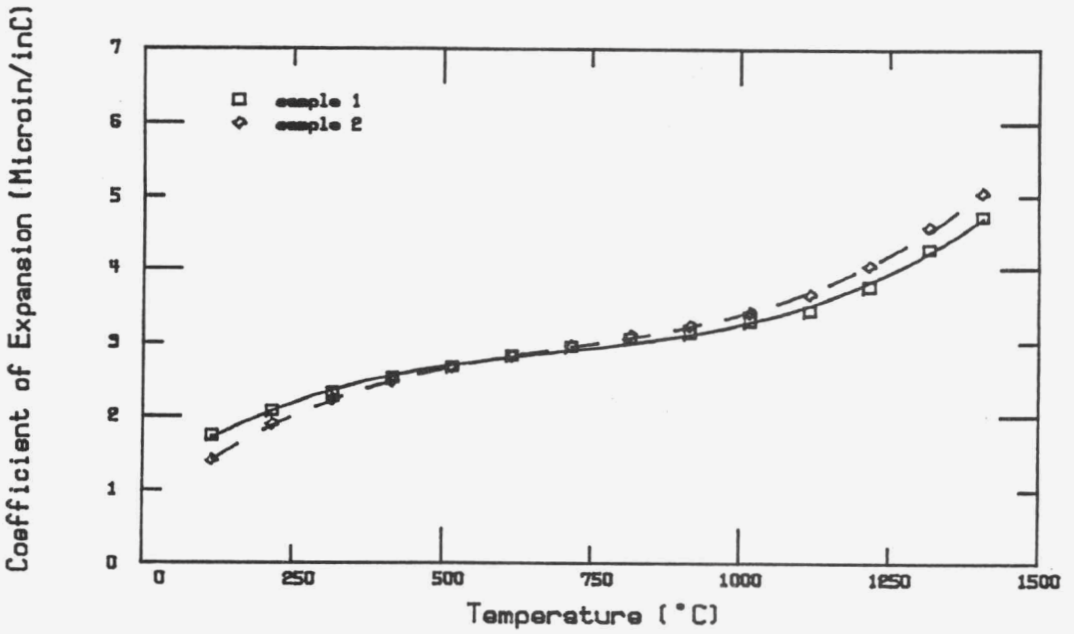

Figure 4. Coefficient of thermal expansion for PY6 material.

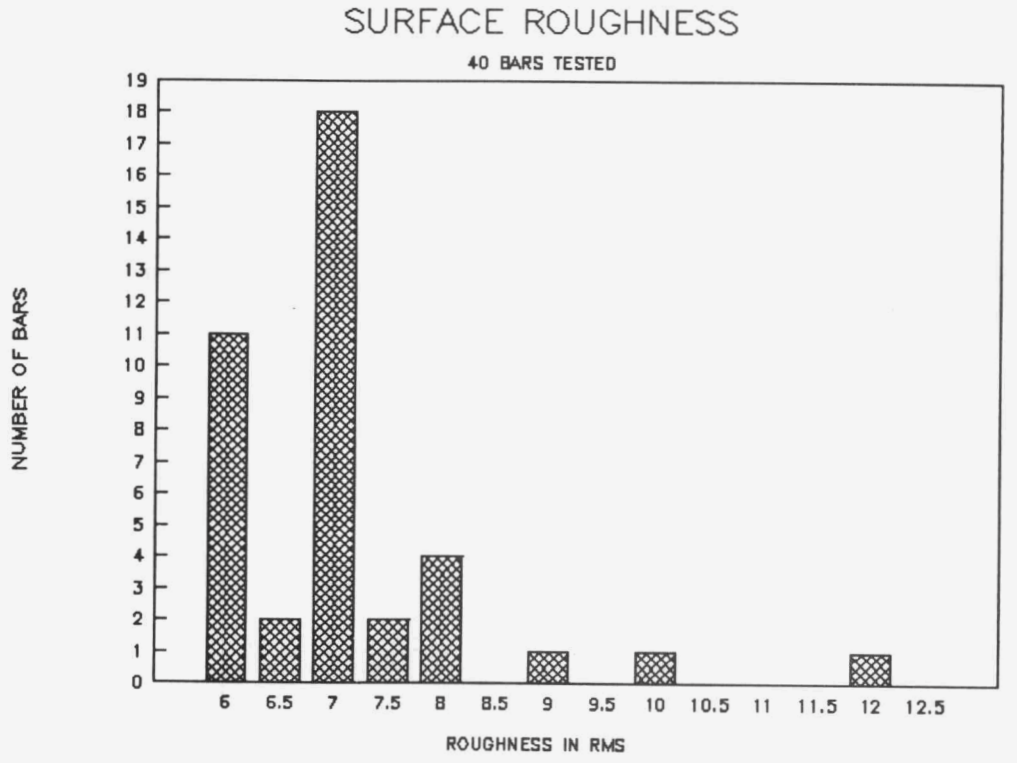

Figure 5. Surface finish of MOR bars.

surface roughness with the stylus moving transverse to the machining direction. The average surface finish was between 6 to 7 microinches rms. It was concluded that the bar's surface finish was acceptable. The test fixture was also checked out to insure no extraneous bending was being introduced.

Additional PY6 MOR bars were tested at both room and elevated temperatures during this reporting period. The specimens are nominally 3 X 4 X 50 mm with an inner load span of 20 mm and an outer span of 40 mm. The results are shown in Tables 1 through 3. The testing at room and

Table 1. Room temperature MOR test results.

Specimen number	Test temp--°C	Strength-- MPa	Strength-- ksi
34.1946	20	1086.9	157.6
34.1947	20	1059.1	153.6
34.1948	20	797.2	115.6
34.1949	20	898.9	130.4
34.1950	20	992.9	144.0
34.1951	20	939.4	136.2
34.1952	20	768.6	111.5
34.1953	20	1114.9	161.7
34.1954	20	762.8	110.6
34.1955	20	849.2	123.2
34.1956	20	841.4	122.0
34.1957	20	829.5	120.3
34.1958	20	989.1	143.4
34.1959	20	978.4	141.9
34.1960	20	1029.7	149.3
34.1961	20	844.5	122.5
34.1962	20	1008.3	146.2
34.1963	20	872.7	126.6
34.1964	20	910.9	132.1
34.1965	20	575.7	83.5

Table 2. MOR test results at 1000, 1100, and 1200°C.

Specimen number	Test temp--°C	Strength-- MPa	Strength-- ksi
34.1526	1000	666.9	96.7
34.1527	1000	636.2	92.3
34.1528	1000	610.6	88.6
34.1529	1000	835.7	121.2
34.1530	1000	769.4	111.6
34.1531	1100	536.3	77.8
34.1532	1100	547.0	79.3
34.1533	1100	516.6	74.9
34.1534	1100	587.4	85.2
34.1535	1100	557.6	80.9
34.1426	1200	625.7	90.7
34.1427	1200	593.0	86.0
34.1428	1200	694.8	100.8

Table 2 (cont)

Specimen number	Test temp--°C	Strength-- MPa	Strength-- ksi
34.1429	1200	716.7	103.9
34.1430	1200	577.4	83.7
34.1510	1200	705.2	102.3
34.1511	1200	649.9	94.3
34.1512	1200	630.9	91.5
34.1513	1200	684.2	99.2
34.1514	1200	599.2	86.9
34.1515	1200	549.2	79.7
34.1521	1200	659.4	95.6
34.1522	1200	598.9	86.9
34.1523	1200	588.5	85.3
34.1524	1200	548.3	79.5
34.1536	1200	697.3	101.1
34.1537	1200	698.6	101.3
34.1538	1200	608.5	88.3
34.1539	1200	604.7	87.7
34.1540	1200	531.5	77.1

Table 3. MOR test results at 1300 and 1400°C.

Specimen number	Test temp--°C	Strength-- MPa	Strength-- ksi
34.1421	1300	572.8	83.1
34.1422	1300	598.3	86.8
34.1423	1300	583.7	84.7
34.1424	1300	572.2	83.0
34.1425	1300	606.4	88.0
34.1541	1300	623.2	90.4
34.1542	1300	615.0	89.2
34.1543	1300	490.3	71.1
34.1544	1300	561.6	81.5
34.1545	1300	601.7	87.3
34.1416	1400	484.3	70.2
34.1417	1400	474.6	68.8
34.1418	1400	557.2	80.8
34.1419	1400	518.6	75.2
34.1420	1400	536.6	77.8
34.1500	1400	453.0	65.7
34.1501	1400	499.3	72.4
34.1502	1400	471.5	68.4
34.1503	1400	437.7	63.5
34.1504	1400	502.5	72.9
34.1505	1400	598.8	86.8
34.1506	1400	508.4	73.7
34.1507	1400	470.3	68.2
34.1508	1400	483.7	70.2
34.1509	1400	490.3	71.1

Table 3 (cont)

Specimen number	Test temp--°C	Strength-- MPa	Strength-- ksi
34.1546	1400	439.2	63.7
34.1547	1400	477.6	69.3
34.1548	1400	447.1	64.9
34.1549	1400	541.5	78.5
34.1550	1400	491.2	71.2

1000°C still had some chamfer failures, but this was not a problem at 1100°C and higher. Although the chamfer failures do not seem to be affecting the measured strength values, it is not understood why we are having a high frequency of these failures at low test temperatures. Fractography does not indicate appreciable machining damage at the fracture origins, as shown in Figure 6. Testing will continue per plan.

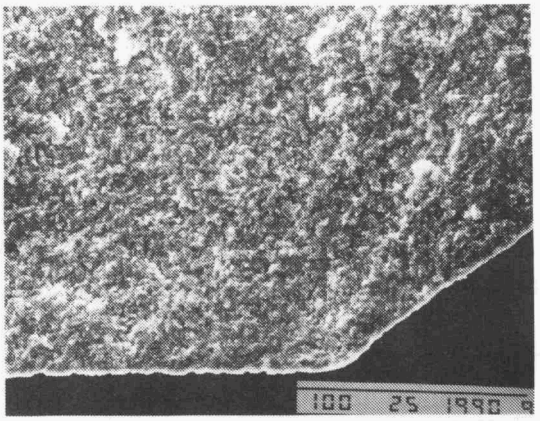

Figure 6. Scanning electron micrograph of MOR bar chamfer failure.

This period also marked the beginning of assessing the dynamic fatigue behavior of the PY6 material. MOR bars were tested at a slower loading rate. A cross-head speed of 0.0508 mm/min (0.002 in./min) was used as opposed to the standard rate of 0.508 mm/min (0.020 in./min). The initial results are shown in Table 4. Additional dynamic fatigue testing will be performed at various loading rates to explore the material's behavior.

Testing has commenced for determining the effect of oxidation on the PY6 material. Five MOR bars were oxidized in an air furnace at 1400°C for 50 hr and another five were oxidized for 200 hr. The bars were then weighed to determine weight gain and subsequently tested in four-point bending. Table 5 shows the strengths that were recorded. Fractography indicated an oxide thickness of approximately 2.3 microns for the 50-hr exposure bars and 2.8 microns for 200-hr exposure. However, the 200-hr exposure bars also indicated a new flaw population of surface pores from which the failures originated, as shown in Figure 7.

Tensile bars

Elevated temperature tensile testing of the PY6 material was initiated this reporting period. The specimen is an injection-molded, cylindrical button-head bar having a 55.9 mm (2.20 in.) long gage section with a 4.762 mm (0.1875 in.) diameter. Testing is being performed by Southern Research Institute. Limited testing at several temperatures was performed to check out test apparatus and procedures. Table 6 shows these as well as some additional room temperature test results. Everything seems to be fine. The thermal gradients in the specimens were acceptable and the

Table 4. MOR test results with slower loading rate.

Specimen number	Test temp--°C	Strength-- MPa	Strength-- ksi
34.1440	1000	769.4	111.6
34.1441	1000	754.9	109.5
34.1442	1000	400.1	58.0
34.1443	1000	658.6	99.4
34.1444	1000	659.9	95.7
34.1455	1200	625.7	90.7
34.1456	1200	593.0	86.0
34.1457	1200	694.8	100.8
34.1458	1200	716.7	103.9
34.1459	1200	577.4	83.7
34.1470	1400	362.0	52.5
34.1471	1400	394.5	57.2
34.1472	1400	419.1	60.8
34.1473	1400	349.5	50.7
34.1474	1400	388.8	56.4

Table 5. Room temperature MOR oxidation test results.

Specimen number	Oxidation condition	Strength-- MPa	Strength-- ksi
34.1445	1400°C/50 hr	509.0	73.8
34.1446	1400°C/50 hr	745.6	108.1
34.1447	1400°C/50 hr	765.8	111.1
34.1448	1400°C/50 hr	750.1	108.8
34.1449	1400°C/50 hr	722.8	104.8
34.1450	1400°C/200 hr	600.7	87.1
34.1451	1400°C/200 hr	748.2	108.5
34.1452	1400°C/200 hr	679.9	98.6
34.1453	1400°C/200 hr	679.9	98.6
34.1454	1400°C/200 hr	671.4	97.4

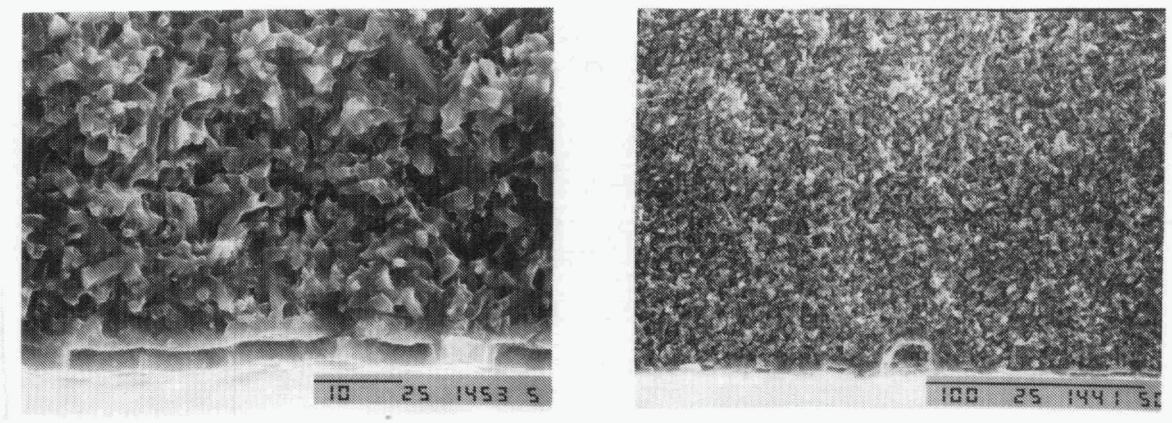

Figure 7. Failure surface of oxidized MOR bar.

Table 6. PY6 tensile test results.

Specimen number	Test temp--°C	Strength-- MPa	Strength-- ksi
66B	20	304.8	44.2
68A	20	420.2	60.9
90B	20	399.8	58.0
104A	20	479.6	69.6
105A	1000	461.9	67.0
95B	1000	469.8	68.1
97A	1200	377.2	54.7
94B	1300	309.6	44.9
67B	1400	149.1	21.6

failures occurred in the gage section, resulting in valid data. In addition to more tensile testing, future work will consist of setting up creep frames and checking out the creep strain measurements.

Circular disks

A series of experiments was undertaken to measure the mixed-mode fracture toughness of the PY6 material by Battelle Laboratories in Columbus, which was put under contract to do this research. The chevron-notched disks were loaded at room temperature by diametral compression. The specimen was placed with the notch at an acute angle to the load line, with the proportions of tensile and shear stress on the crack being controlled by choice of angle. Preliminary results, summarized in Figure 8, indicate a fracture toughness value of 6.4 MPa$\sqrt{m}$, which is on the high side of recent literature data for silicon nitride. This effort marks the accomplishment of one of the program formal milestones.

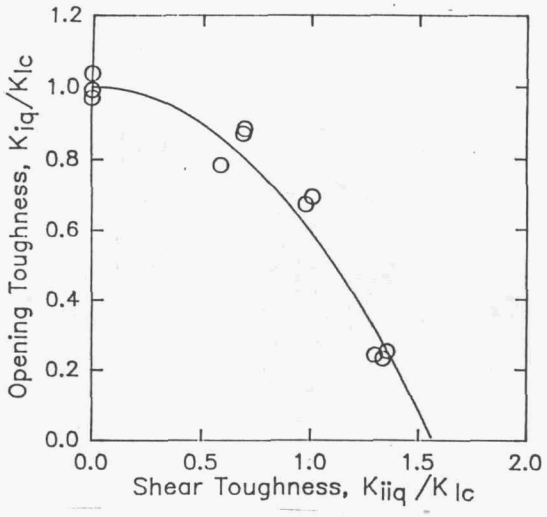

Figure 8. Biaxial fracture toughness test results.

NDE laboratory enhancement

The development of the NDE techniques continued during this reporting period. The real time X-ray imaging and processing system was integrated with the Feinfocus microfocus system and is now operational at Allison. The Image-Pro video processing software manufactured by Cybernetics has been installed and is operating in conjunction with the Data Translation frame grabber and processor.

A parametric study was conducted to optimize the microfocus X-ray image contrast to detect small flaws. Two PY6 silicon nitride bars were taped together in a step manner and radiographed at various accelerating voltages (Kv) at 10x. The film density in the region of one bar was kept constant to around 2.7 by changing the current and film exposure. The film density of the two bar region was measured as a function of Kv. The difference in the film density at two successive Kv's was determined. Figure 9 shows that there is an optimum Kv at which there is maximum density difference, i.e., maximum contrast, which is required for detecting small fracture controlling flaws in structural ceramic materials. All future MOR specimens will be characterized using the optimum setup.

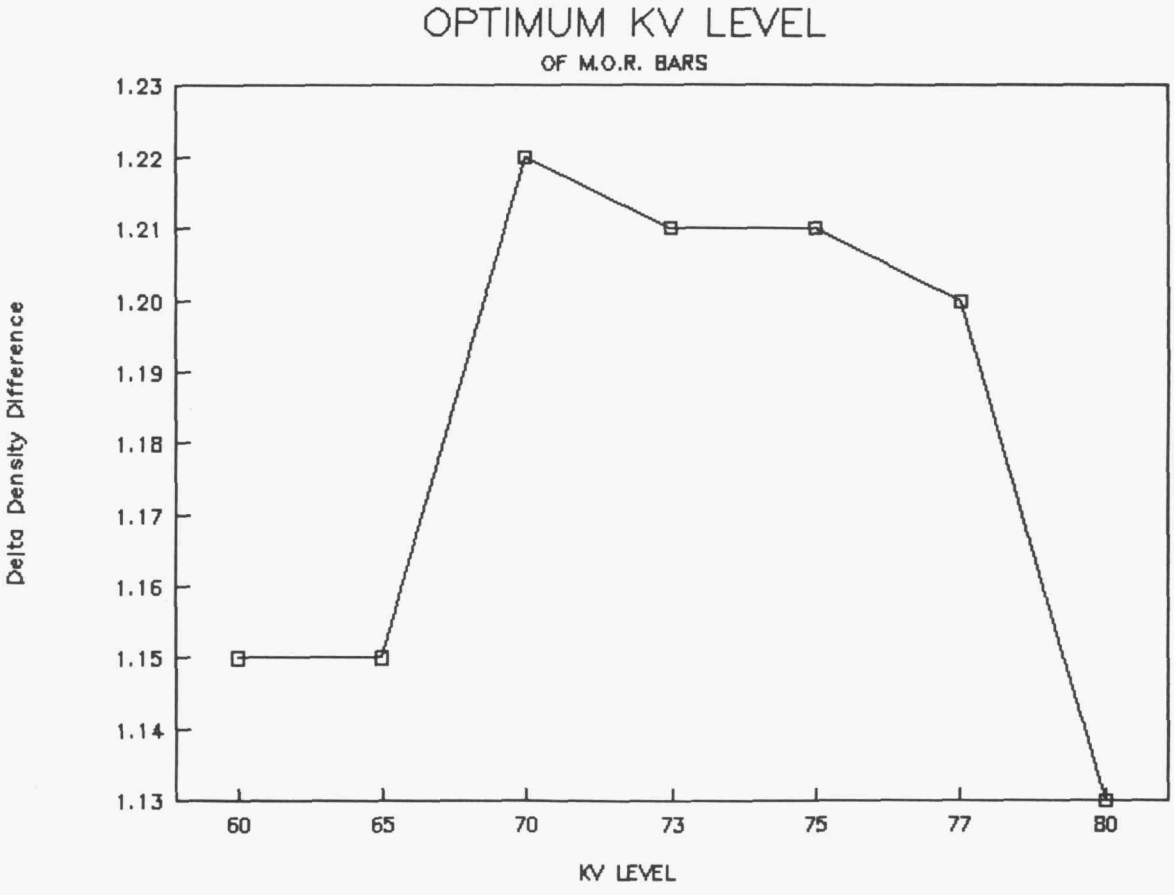

Figure 9. Optimization of X-ray image contrast.

Status of milestones

322201: Computer Implementation of Initial Failure Models--complete.
322202: Initiation of MOR Testing--complete.
322203: Initiation of Tensile Testing--complete.

322204: Initiation of Biaxial Testing--accomplished this reporting period.
322205: Initiation of Confirmatory Testing--on schedule.
322206: Completion of All Specimen Testing--on schedule.
322207: Finalization/Verification of Computer Code--on schedule.
322208: Draft Final Report--on schedule.
322209: Final Report--on schedule.

Publications

None.

Life Prediction Methodology

J. Cuccio and A. Reese
(Garrett Auxiliary Power Division, Allied-Signal Aerospace Company)

Objective/Scope

Garrett Auxiliary Power Division (GAPD) has defined a program to develop the methodology required to adequately predict the useful life of ceramic components used in advanced heat engines. GAPD's approach to ceramic life prediction consists of comprehensive testing of various specimen geometries under both uniaxial and multiaxial loads at different environmental conditions to determine the strength-controlling flaw distributions and to identify various failure mechanisms. This information will be used to develop the flaw distribution statistical models and material behavior models for fast fracture, slow crack growth, creep deformation, and oxidation. As sub-routines, these models will be integrated with stress and thermal analyses into a failure risk integration analytical tool to predict the life of ceramic components. The methodology developed will be verified (for completeness and accuracy) by analytically predicting the life of several ceramic components and testing these components under stress and temperature conditions encountered in ceramic turbine engines.

Technical Highlights

Material Testing and Analysis
H. Fang

Material Testing

Test specimen deliveries from Norton/TRW Ceramics (NTC) are on schedule. Table 1 summarizes the specimens ordered and their current status. All specimens are NT154 silicon nitride, processed under identical conditions and finish machined and heat treated by NTC. Selected specimens will be notched and precracked for testing. All specimens will be subjected to visual inspection, laser marking, and NDE (which may include fluorescent penetrant, radiography, and ultrasonic inspection) before testing.

NTC delivered four prototype or "first article" specimens, for each of the complicated specimen geometries. The purpose was twofold: (1) to allow NTC to demonstrate machining capability for these complex shapes, and (2) to allow GAPD to identify any potential problems before the entire specimen order was machined. The four prototype specimens included two flaw growth specimens and two notch sensitivity confirmatory specimens (Figure 1).

GAPD has initiated an investigation with NTC to determine the cause of these flaws and whether they are part of the underlying flaw population inherent to the standard fabrication procedure. The criteria used to decide whether to test these flawed specimens will be based on the nature and cause(s) of the flaw(s), rather

TABLE 1. CERAMIC TEST SPECIMEN STATUS

Type of Test	Specimens Received	Specimen Status
4-Point Bend	Yes	Visual Inspection and NDE
Chevron Notch	Yes	Ready for Testing
Diametral Compression	Yes	Ready for Testing
Plate Bending	Yes	Visual Inspection
Tensile (Fast Fracture and S/R)	Yes*	Visual Inspection and NDE
Pre-cracked Tension/Torsion	Yes	NDE
Unnotched Tension/Torsion	No	On Order
Notched Tensile	No	On Order
Rectangular Flaw Growth	No	On Order
Square Flaw Growth	No	On Order
Spin Disk	No	On Order
*Partial Shipment Received		

8491(04)-1B

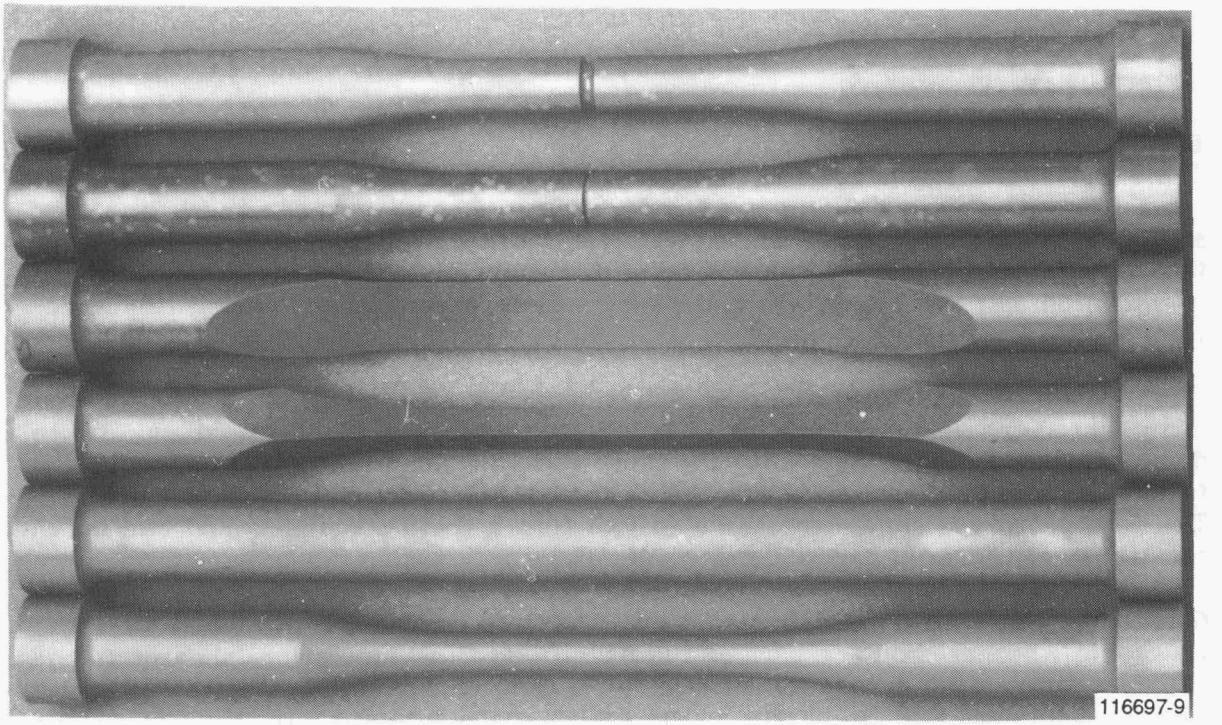

Figure 1. Prototype Specimens Demonstrate Machining Capabilities and Identify Potential Problems.

Visual inspection showed that the notch-root surface finish is different for the two notch sensitivity specimens (Figure 2). The larger notch-root radius ($K_T = 2$) is smoother than the smaller notch ($K_T = 3$). This is unacceptable, as the purpose of these specimens is to compare the stress concentration (K_T) effect due to the notch geometry only, assuming the same surface and volume flaw distributions between specimens. Any significant difference in surface finish means a change in surface flaw distribution, which cannot be accounted for within the scope of this program. Since the difference in surface finish is thought to be due to use of separate diamond notching wheels, the specimens were redesigned. The difference in K_T between specimens will be achieved by changing the diameter of the specimens and the depth of the notches. The notch radius will be the same for both redesigned specimens.

Visual inspection of the buttonhead tensile specimen using a stereo microscope at 7-40X magnification revealed some flaws that will likely affect the test results. Approximately 10 percent of the 100 specimens inspected thus far have surface flaws of concern. The largest group (7 total) of flawed specimens have grind marks or scratches on the specimen gage section. The flaws are either transverse or near-transverse marks in the longitudinal machining direction of the gage section. Based on prior GAPD test experience with NT154, these marks or scratches are believed to be severe enough to cause failure, which is unacceptable for the purpose of these specimens.

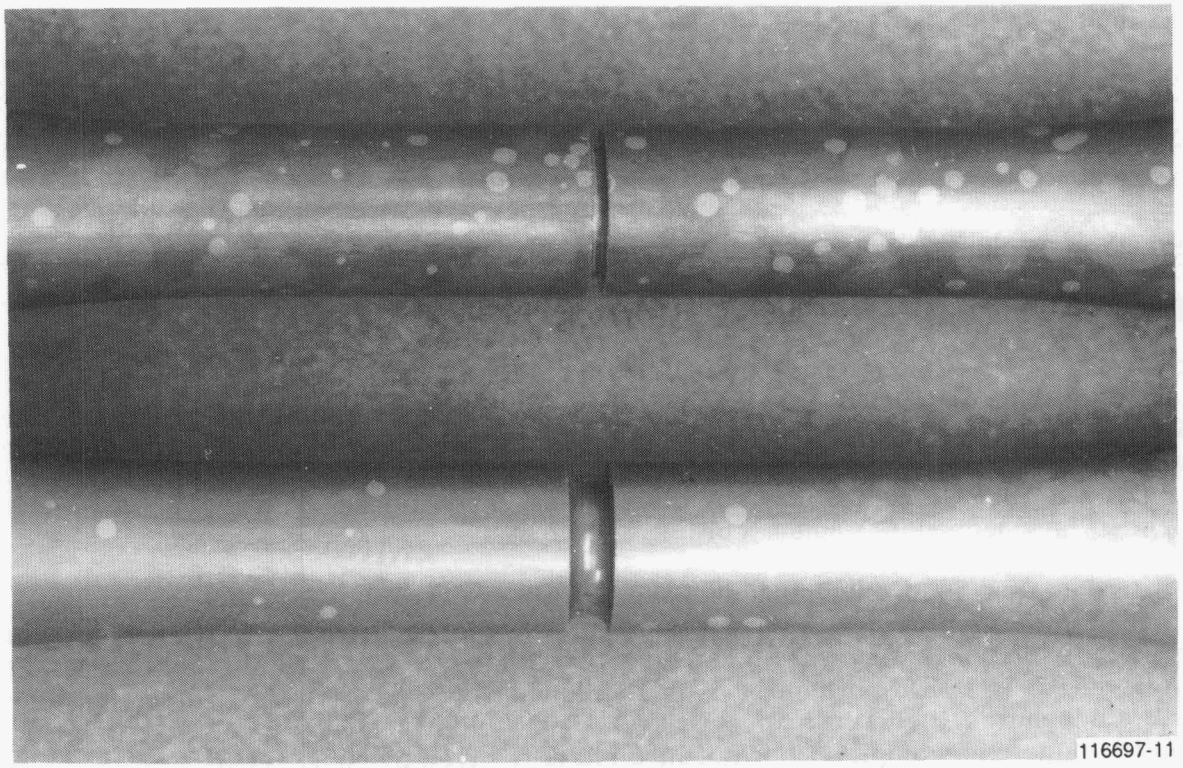

Figure 2. Notched Sensitivity Tensile Specimens Have Different Surface Finishes in the Notch Radius.

than the severity of the flaw(s). For example, if the scratches discussed above are a result of the standard machining procedure, the specimens will be tested; whereas, if the scratches originated from some aberration not typical of the machining process, they will not be tested.

Data Analysis and Methodology Development
J. Cuccio, A. Peralta, D. Wu, and N. Menon

Methodology development includes three main areas:

(1) Data analysis
(2) Probabilistic risk integration
(3) Behavior modeling, including:

  (a) Fast fracture
  (b) Slow crack growth
  (c) Creep
  (d) Oxidation

Under data analysis, statistical methods are being developed to predict the Weibull parameters for a material. The methods will also include confidence limit and bias correction calculations. The goal is to predict confidence limits on component reliability predictions. Data analysis includes the evaluation of results from specimen testing.

Probabilistic Risk Integration will incorporate recent advancements in multiaxial risk integration and link them with statistical methods to provide confidence limits on component reliability. These methods will be developed for isotropic and anisotropic flaw populations and for multiple failure modes.

Behavior modeling includes studies of the phenomenology of each failure mode and the development of mechanistic models. These models will be combined with the probablistic risk integration and statistical methods.

Current efforts have concentrated on statistical methods development and on specimen randomization to establish the planned tensile specimen test matrix. Under statistical methods development, the goal is to develop capabilities to encompass the complications, outlined in Table 2, of predicting Weibull parameters, confidence limits, and associated bias corrections. Table 2 is split into primary and secondary goals according to priority.

Statistical methods development is based on the assumption that the strength distribution of a material is independent of the specimen size, shape, stress gradients, or multiaxial state of stress. It is further assumed that the distribution of strength is a two-parameter Weibull distribution and that the Weibull parameters depend on the failure theory used. The Weibull probability density function that includes the complications outlined above is given by equation [1].

TABLE 2. LIST OF COMPLICATIONS BEING ADDRESSED IN THIS PROGRAM

Primary Goal	Secondary Goal
Size Effect	Flaw Anistropy
Multiaxial Stress	Fast Fracture Versus Temperature
Multiple Flaws	Time-Dependent Mechanisms
Confidence Interval	
Bias Correction	

8491(04)-3A

$$f(\sigma_i) = mV_i\, I_i \sigma_o^{-1} \left(\frac{\sigma_i}{\sigma_o}\right)^{m-1} \exp -\left\{V_i\, I_i \left(\frac{\sigma_i}{\sigma_o}\right)^{m}\right\} \qquad [1]$$

where the variables are defined as follows:

- i, Subscript specifying the ith specimen
- m, First Weibull parameter or Weibull modulus, a material constant
- σ_o, Second Weibull parameter, a material constant
- σ_i, Specimen fracture strength
- V_i, Specimen size (volume, area, or length)
- I_i Specimen multiaxial stress and stress gradient factor as a function of m, as defined by Evans/Lamon [1,2]* or Batdorf/Heinisch [3]

As equation [1] shows, any specimen size, type, and loading condition may be combined to predict the Weibull parameters. A benefit of representing the Weibull distribution in this form is that the calculated Weibull parameters are material constants. A second benefit is the more accurate estimate of the Weibull parameters by the combination of data from specimens and components with multiple sizes.

*References in parentheses ( ) are given at the end of this report.

The estimate of the Weibull parameters is performed by using maximum likelihood estimation techniques; the derived equations have already been incorporated into a computer code. The results of the analysis of six different data sets is shown in Figures 3 and 4. Figure 3 shows the results that would be obtained if a conventional Weibull analysis was used; as can be seen, every data set has its own set of Weibull parameters. In contrast, Figure 4 shows the data analyzed by using equation [1]; only one set of Weibull parameters are obtained from the analysis. The silicon carbide (SiC) material data used in these figures was provided by Drs. C. Johnson and W. Tucker of the General Electric Corporate Research Center (GE-CRC)[4]. These data will be reanalyzed when censoring techniques are completed, to account for the surface and volume failures that are both present.

Confidence limit calculation equations have ben derived for the Weibull parameters, reliability prediction, and component design stress. The maximum likelihood ratio and bootstrap methods are being used to predict confidence limits under the technical direction of Drs. C. Johnson and W. Tucker. The confidence limits for the reliability prediction are shown in Figure 4 and for the design stress level in Figure 5.

The probabilistic risk integration efforts are in progress. An approach has been defined to incorporate the previously noted complications. The Evans/Lamon and Batdorf/Heinisch methods are under consideration for computational benefits and capabilities to handle the complications.

Behavior modeling is on hold, pending availability of specimen test data. Specimen testing is in progress. The specimen test matrix is the result of extensive planning to reduce the risk of concentrating processing problems in only one or a few sets of data which could then render the test matrix useless. Randomization is particularly important for the 270 tensile specimens that will be used for the fast fracture, slow crack growth, and creep testing. In addition to randomization, the tensile specimens will be blocked according to hot isostatic pressing (HIP) batches.

The HIP batches were identified as the most likely source of processing inconsistencies, if any occur. The plan to block the HIP batches for the 18 sets of tensile specimen tests is shown in Figure 6. Three HIP batches are common to all the test sets. Other HIP batches will be blocked according to the test sets that will be correlated for model development. Specimens within each block will be randomized.

NDE Methods Development and Application
J. Wade

The NDE activities for Milestone 3 - NDE Calibration are complete.

Acoustic Microscopy

Surface wave inspection evaluations were performed on laser-drilled hole targets using 25, 50, 75, and 100 MHz unidirectional surface waves, to determine the transducer to be used for surface wave inspections. The inspections included 12 to 125 micron diameter holes ranging from 6.4 to 125 microns in depth. In addition, 50 MHz converging surface waves were also used, to quantify the loss in sensitivity caused by noise from typical component surface finishes. Based on these inspections, the 50 and 75 MHz unidirectional surface wave inspections have been selected for component inspection. The results from these two frequencies will be compared during the early component inspections before selecting a single frequency.

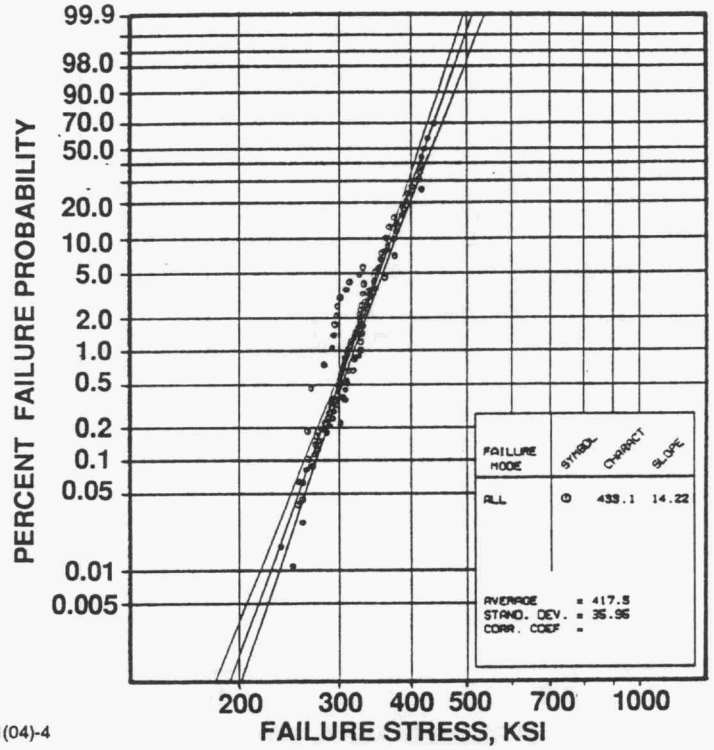

Figure 3. Data From Specimen Sets of Various Specimen Sizes Produces Multiple Estimates of Weibull Parameters.

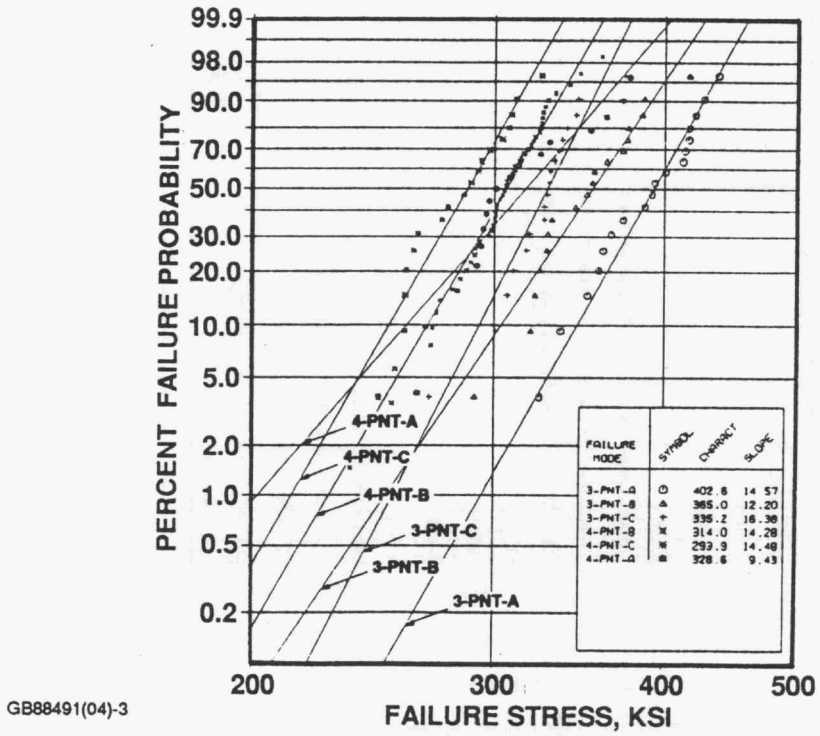

Figure 4. Material Weibull Parameters Predicted From Combined Sets of Specimens of Multiple Sizes Listed in Figure 3.

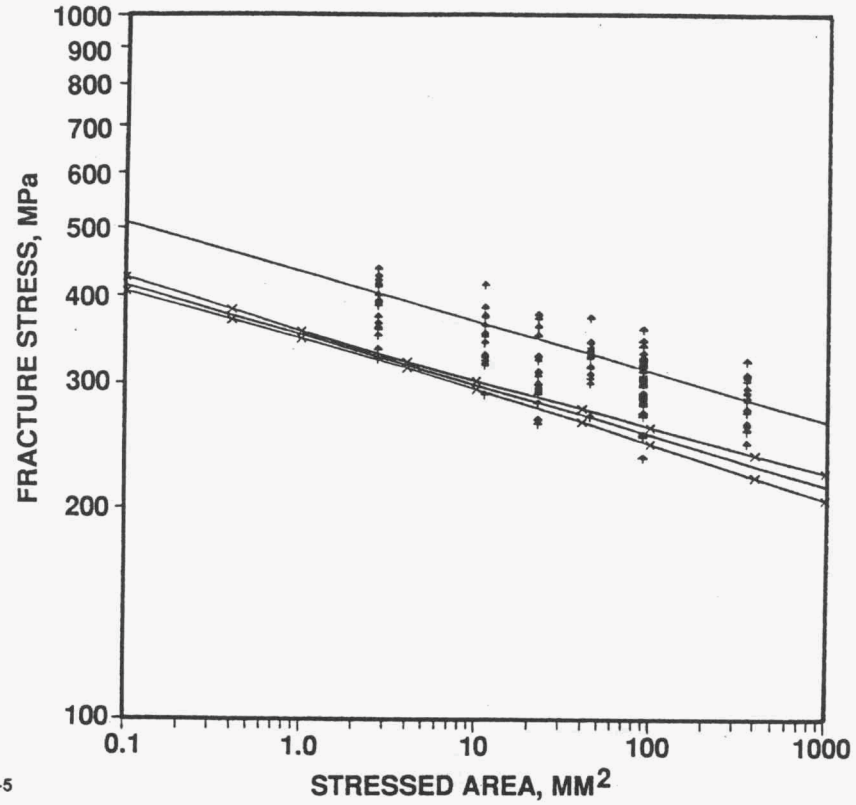

Figure 5. Predicted Component Design Stress Level and Confidence Limits Based on Data From Multiple Specimen Sizes.

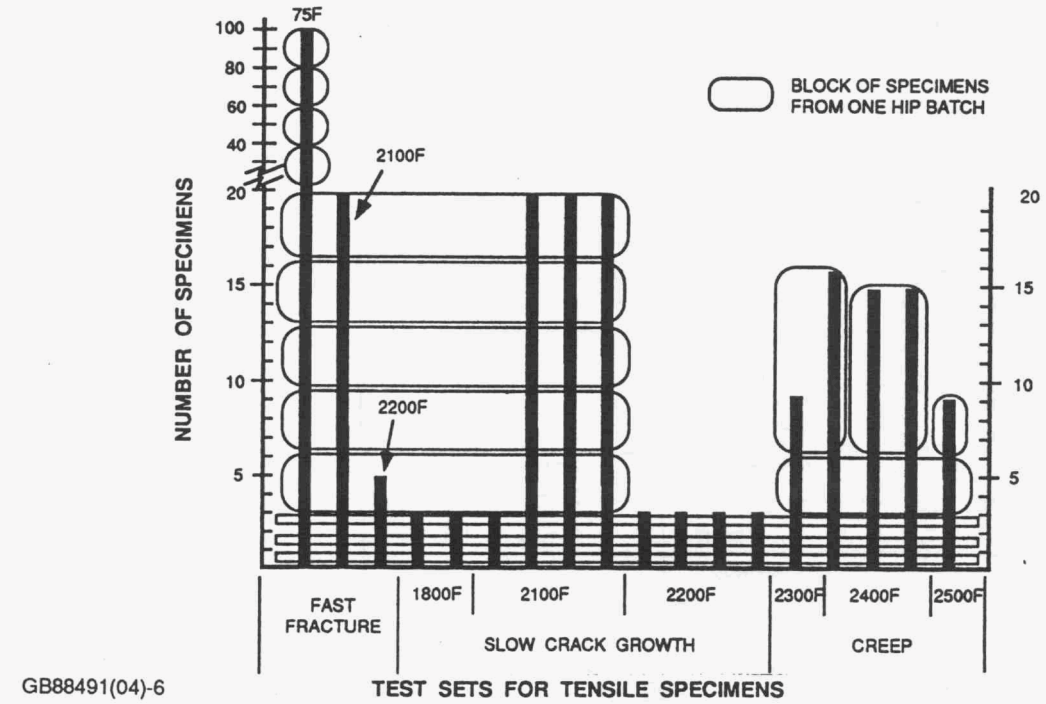

Figure 6. Specimens Will Be Blocked According to HIP Batches, Then Randomized Within Each Block to Minimize the Influence of Potential Processing Inconsistencies.

Resolution standards have been fabricated successfully by the University of California at Berkeley (UC Berkeley). The NDE standards will facilitate the determination of surface and bulk resolution capabilities for ultrasonic inspection. The standards were fabricated using a photolithographic etching process and bonding technique developed by UC Berkeley. The resolution standards were fabricated from zero-degree sapphire because it is transparent and because sapphire supports longitudinal, shear, and surface wave velocities that are very similar to silicon nitride. The acoustic similarity between silicon nitride and sapphire produces acoustic beam geometries which are almost identical. Using the sapphire resolution standards permits optical examination without destructive analysis and avoids the development time required to fabricate a silicon nitride resolution standard.

The resolution standards (Figure 7) were fabricated using the MIL-STD-150 line pair pattern, which permits determination of resolution as a function of transducer frequency and depth. The largest element in the target used is Group 0, starting with a 1 mm line-space pair (each 0.5 mm wide); the line pairs decrease in size in six equal steps until the spacing of Group 1 is reached. The largest Group 1 element contains two line-space pairs per mm.

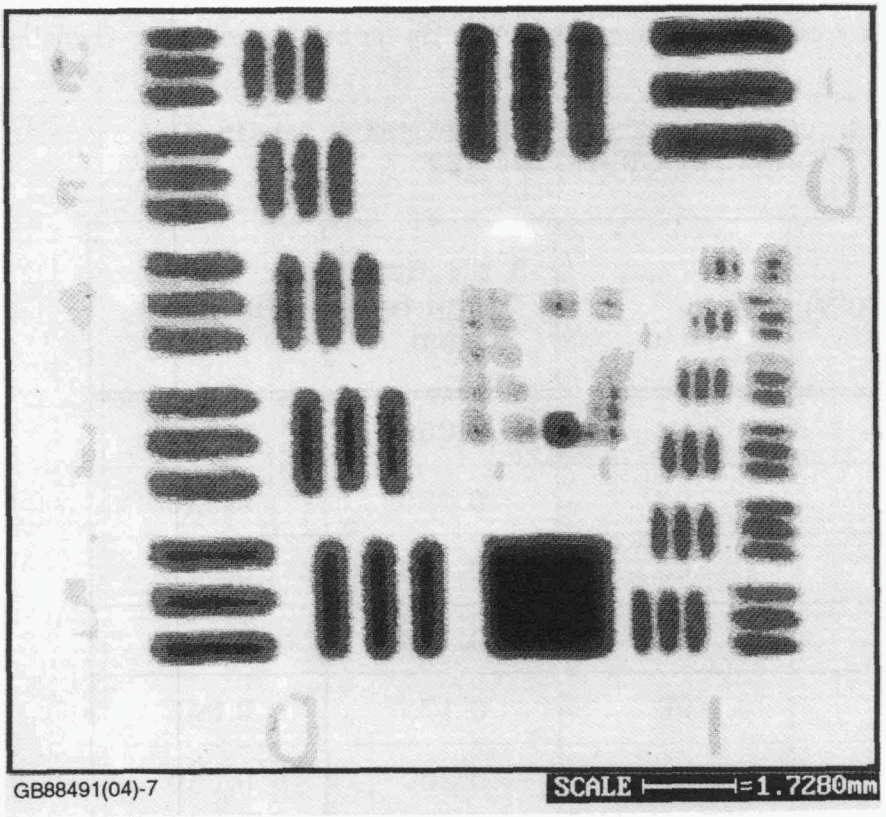

Figure 7. Acoustic Scan of Sapphire Resolution Target.

The -3dB diameter, ε_{x1}, produced by a circular lens of diameter d focusing a pulse of wavelength λ at a distance F has been shown to be:

$$\varepsilon_{x1} = 1.03\ \lambda\ F/d \qquad [2]$$

Provided that the refracted angle is less than 30 degrees of arc, the corresponding -3dB depth of focus, ε_{x2}, is:

$$\varepsilon_{x2} = 4\ \lambda\ (F/d)^2 \qquad [3]$$

Using these equations, the beam diameters for several transducers were calculated and are given in Table 3.

The ability of an acoustic beam to detect a void and to resolve and/or image the void are different. For low-noise materials in the vicinity of the near-field limit of an unfocused transducer, or when focused in the focal zone, voids can be detected that have a diameter equal to 25 percent of the wavelength or the beam diameter, whichever is smaller. The longitudinal velocity in both sapphire and silicon nitride is 11.2 mm/microsecond and therefore the wavelength at 50 MHz is 0.224 mm. A 1/4-wavelength void is therefore 56 microns in size. Table 3 shows that the detection capability can be improved significantly below 1/4-wave by focusing the beam.

TABLE 3. TRANSDUCER BEAM DIAMETERS AND VOID DETECTION CAPABILITY

Frequency, MHz	F/d	-3 dB Beam Diameter, mm	Void Diameter, mm
100	f/4	0.060	0.015
75	f/4	0.080	0.020
50	f/3	0.100	0.025
50	f/4	0.125	0.030
50	f/6	0.175	0.045
50	f/8	0.200	0.060
25	f/8	0.400	0.125

8491(04)-2

The resolution inherent in a raster-scanned image is controlled by:

- o The diameter of the scanned beam
- o The spacing of the scan lines
- o The acoustic pulse spacing along the scan line.

The line-pulse spacing determines the pixel size making up the image. Nyquist's theorem states that the minimum spatial resolution of a 2-D array of points is twice that point spacing. Therefore, the spatial resolution of the beam is twice its -3dB diameter. In order to support the -3dB diameters listed in Table 2, these beams must be scanned at less than half of their diameter. The beam, however, cannot resolve objects closer than twice the beam diameter from the resolution target at a depth of 2 mm, as shown in Figure 7.

The first laser-drilled, blind (as opposed to through-drilled) hole standards were received during this reporting period from Resonetics, Inc., and evaluation of the standards was initiated. The standards were inspected with a range of transducers to determine the detection sensitivity of each transducer at various material depths. At this time, the goal of 50 micron detection has not been achieved for all depths required for component inspection.

The water path has a much greater effect on the inspection sensitivity than originally anticipated, so the maximum water path has been reduced from 25 mm to 12 mm. In addition, the inspection sensitivity seems to be degraded in the 0.2 to 2.5 mm range. This condition is being studied further and two alternate inspection approaches have been identified:

- o Inspect the 0.2 to 2.5 mm range using more tightly focused transducers
- o Inspect from both sides to achieve uniform sensitivity

Computer Tomography (CT)

CT parameter selection was completed, using the CT resolution and detection gages which were delivered in early January 1991. These standards allowed the evaluation of system performance by varying key system parameters, measuring system response, and selecting the combination of parameters that provides the best results. The following variables were evaluated:

- o Tube voltage (420, 320, 220 kV)
- o Views-per-image (1500, 3000)
- o Integrations (4, 8)
- o Detector Pressure (1000, 900, 800, 600 psi)
- o Detector collimator size (0.25 mm, 0.13 mm)

The parameters which provided the best imaging results were:

- o Tube voltage = 320 or 220 kV
- o Views-per-image = 3000
- o Integrations = 4
- o Detector pressure = 900 psi
- o Detector collimator size = 0.25 mm

Digital filtering (high-pass and low-pass) was also performed on those images which displayed good detectability (see Figure 8). In some cases, the filtering helped to smooth out the image and decrease the system noise. Although image viewing was easier, system detectability was not increased. Inspections will use both filtered and non-filtered images.

Figures 8(a) and 8(c) show how ring artifacts contribute significantly to the image noise. These artifacts make it difficult to identify smaller defects. Although these artifacts may be reduced by eliminating uncharacterized variations between detector elements, it is unlikely that they will be eliminated entirely. Since most of the samples to be inspected are small in cross-sectional area, they will be placed in the fixture away from the center of rotation of the system. This will avoid most if not all of the ring artifacts. For the larger samples the parts can be imaged twice, moving the part between scans in order to adequately inspect the entire cross-section. Additionally, it appears that digital filtering reduces the effect of the rings.

Based on the results of the NDE development effort, an inspection matrix for all test specimens has been developed. The test matrix concentrates inspection coverage where the specimens are expected to fail and will help minimize the inspection time required for each specimen. For example, on the A- and B-sized MOR bars, failures are expected to occur primarily from the surfaces, so internal inspections on these components will be minimized and high-resolution surface inspections will be concentrated on the tensile surfaces of the bars. Inspection of tensile rods and B-size MOR bars has begun.

Status of Milestones

Milestone No. 3, NDE Calibration Complete, was successfully completed. Milestone No. 4, All Specimens Delivered, has been delayed two months.

Publications

A paper entitled "Progress in Life Prediction Methodology for Ceramic Components of Advanced Heat Engines" was submitted for publication by the Society of Automotive Engineers (SAE).

References

1. A.G. Evans, "A General Approach for the Statistical Analysis of Multiaxial Fracture," J. Am. Ceram. Soc., 7-8, pp. 302-308 (1978).

2. J. Lamon and A.G. Evans, "Statistical Analysis of Bending Strengths for Brittle Solids: A Multiaxial Fracture Problem, "J. Am. Ceram. Soc., Vol. 66, No. 3, pp. 177-182 (1983).

3. S.B. Batdorf H.L. Heinisch, "Weakest Link Theory Reformulated for Arbitrary Failure Criterion, "J. Am. Ceramic Soc., 61, 7-8, pp. 355-358 (1978).

4. C. Johnson and W. Tucker, private communications.

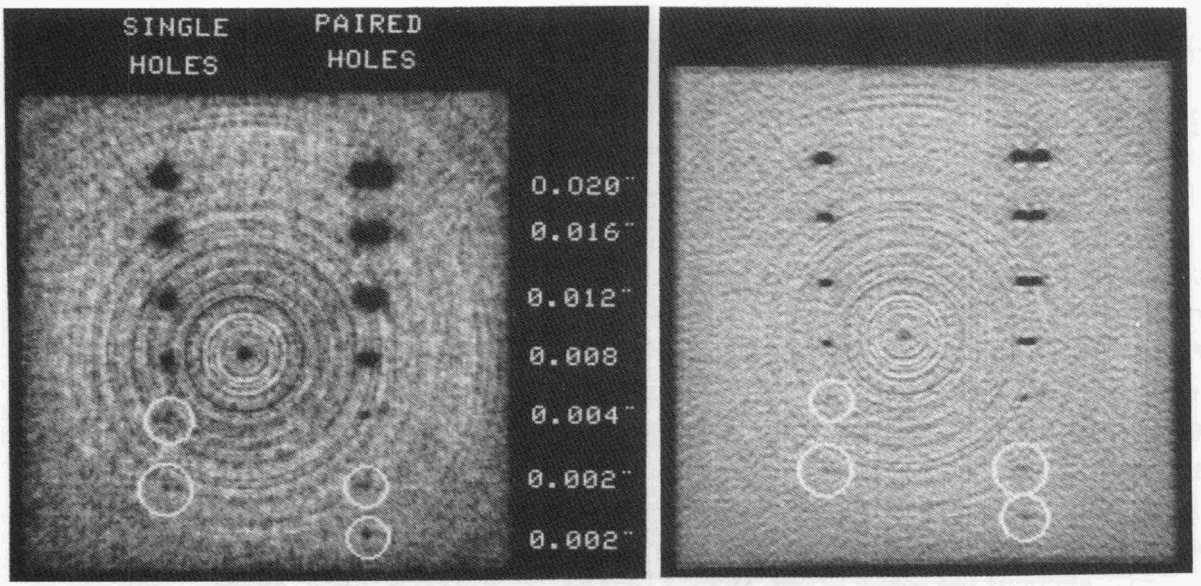

(a). Raw Data-CT Resolution Gage (b). Filtered Data-CT Resolution Gage

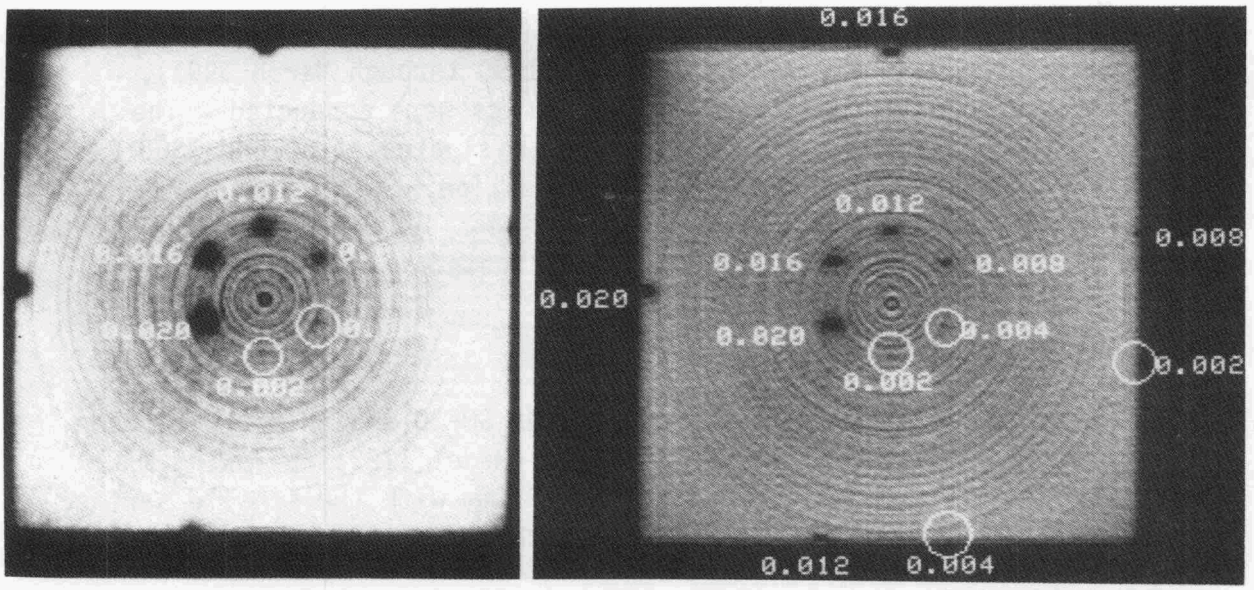

(c). Raw Data-CT Detection Gage (d). Filtered Data-CT Detection Gage

Figure 8. Computed Tomography Images Show Ring Artifacts and Improvements Achieved by Digital Image Filtering.

3.3 ENVIRONMENTAL EFFECTS

Environmental Effects in Toughened Ceramics

Norman L. Hecht (University of Dayton)

Objective/scope

Since December 1984, the University of Dayton has been involved in a four-phase project to investigate the effects of environment on the mechanical behavior of commercially available ceramics being considered for heat engine applications. In the first phase of this project, the effects of environment on the mechanical behavior of transformation-toughened ZrO_2 ceramics were investigated. In the second phase, two Si_3N_4 ceramics (GTE PY6 and Norton/TRW XL144) and one SiC ceramic (Hexoloy SA) were evaluated. In the third phase, the tensile, flexural, and fatigue strength of nine SiC and Si_3N_4 ceramics were evaluated at temperatures ranging from 20 to 1400°C. Microstructure, chemistry, and physical properties were also investigated. In the fourth phase, the flexural strength and fatigue behavior of two additional Si_3N_4 ceramics (Kyocera SN-260 and Garrett GN-10) are being investigated. In addition, the tension/compression cyclic fatigue behavior of one Si_3N_4 ceramic (NT-154) is being investigated.

During the past six months (October 1990 through March 1991), evaluations of one SiC and three Si_3N_4 ceramics were conducted. The flexural strength and dynamic fatigue were evaluated at 20 and 1300°C for SN-260 and GN-10 Si_3N_4 ceramics. In addition, the failure behavior of the Hexoloy SA SiC and NT-154 Si_3N_4 specimens subject to tensile cyclic fatigue at 1300°C was further investigated.

Experimental Procedures

The flexural strength measurements for GN-10 and SN-260 were made using an Instron Universal Testing Machine (Model 1123) following MIL-STD-1942(A). Test specimens were 3 x 4 x 50 mm with the tensile surface ground and polished to a 16-microinch finish. The test specimens

---

*Research sponsored by the U.S. Department of Energy, Assistant Secretary for Conservation and Renewable Energy, Office of Transportation Systems, as part of the Ceramic Technology for Advanced Heat Engines Project of the Advanced Materials Development Program under Contract DE-AC05-840R21400 with Martin Marietta Energy Systems, Inc., Work Breakdown Structure Subelement 3.3.1.4.

were stressed at both fast and slow loading rates (machine crosshead speeds of 0.004 and 0.00004 cm/s). For the measurements made at elevated temperatures an ATS #3320 high-temperature furnace and four-point bend fixture of SiC was used.

In addition to flexural strength, density, elastic modulus, and fracture toughness were measured for both Si_3N_4 ceramics. The density of five specimens was determined by the immersion method. Elastic modulus of five specimens was measured using a Grindo-Sonic (Model MR35T) transient impulse/elastic modulus apparatus. Fracture toughness was measured by the controlled flaw and micro-indent methods. Using the microindent method five GN-10 specimens were evaluated with a Zwick 3213 hardness testing machine at an indent load of 10 Kg and 20 SN-260 specimens were evaluated at indent loads of 5, 10, 30, and 50 Kg. Five specimens of each Si_3N_4 were used to determine fracture toughness by the controlled flaw method using 10 kg load indents to create the flaw. The specimens were evaluated at 20°C using a three-point load fixture at a cross-head speed of 0.02 in/min.

The flexural strength data for the GN-10 and SN-260 was statistically evaluated, and the fracture surfaces examined microscopically. The microstructure and chemistry of these two Si_3N_4 ceramics were investigated. The chemical composition was determined by low magnification compositional backscatter SEM imaging. Microstructure was determined from observations of polished and etched sections using the SEM. SN-260 specimens were both acid (HF for 20 min at 100°C) and plasma etched for these examinations.

The flexural strength data obtained for SN-260 and GN-10 were evaluated to determine the Weibull parameters. Maximum likelihood estimates of the shape parameter m (modulus) and the scale parameters βo (the 63rd percentile for the distribution of breaking strength) and So (the surface area adjusted parameter) were determined. The goodness of fit of the Weibull distributions for GN-10 and SN-260 were tested by using S test.

During this reporting period the NT-154 and Hexoloy SA specimens tested in tension/tension cyclic fatigue (see UDR-TR-90-113, October 1990 Semiannual Progress Report) were examined microscopically to determine fracture origin and the cause of

failure. In addition, the cyclic fatigue failure data obtained was further analyzed.

Technical progress

Results for the Evaluation of GN-10 and SN-260

During this reporting period GN-10 and SN-260 were evaluated. GN-10 is a sintered and HIP Si_3N_4. SN-260 is a β-Si_3N_4 fabricated by pressure gel casting and positive pressure sintering. SN-260 contains additions of Y_2O_3 and Yb_2O_3 and the sintering process is controlled to promote in-situ "whisker" reinforcement by growth of the β-Si_3N_4 phase. The strength, toughness, and physical properties measured for GN-10 and SN-260 are compiled in Table 1.

Table 1. Summary of Property Values Measured for GN-10 and SN-260 Si_3N_4 Ceramics

Property	GN-10	SN-260
1. Flexural Strength (MPa)		
a) 20°C (loading rate 0.004 cm/s)	779±83* (m⁺=12)	619±54 (m=17)
b) 1300°C (loading rate 0.004 cm/s)	563±40 (m=23)	607±41 (m=20)
c) 1300°C (loading rate 0.00004 cm/s)	444±63 (m=11)	589±60 (m=12)
2. Fracture Toughness ($MPa\sqrt{m}$)		
a) Controlled flaw (10 Kg load)	3.6±0.2	3.1±0.3
b) Micro Indent		
10Kg	5.5	5.7
5Kg	-	6.2
30Kg	-	5.3
50Kg	-	5.6
3. Density (g/cc)	3.33	3.37
4. Elastic Modulus (GPa)	283	315
5. Vickers Hardness (Kg/mm^2)	1431	1604

⁺m = Weibull modulus

*Data for GN-10 at 20°C is based on an average for 20 test specimens, all other strength data is based on the average for 10 test specimens.

The results of the Weibull analysis of the flexural strength data for GN-10 and SN-260 are summarized in Table 2 and displayed graphically in Figures 1 and 2.

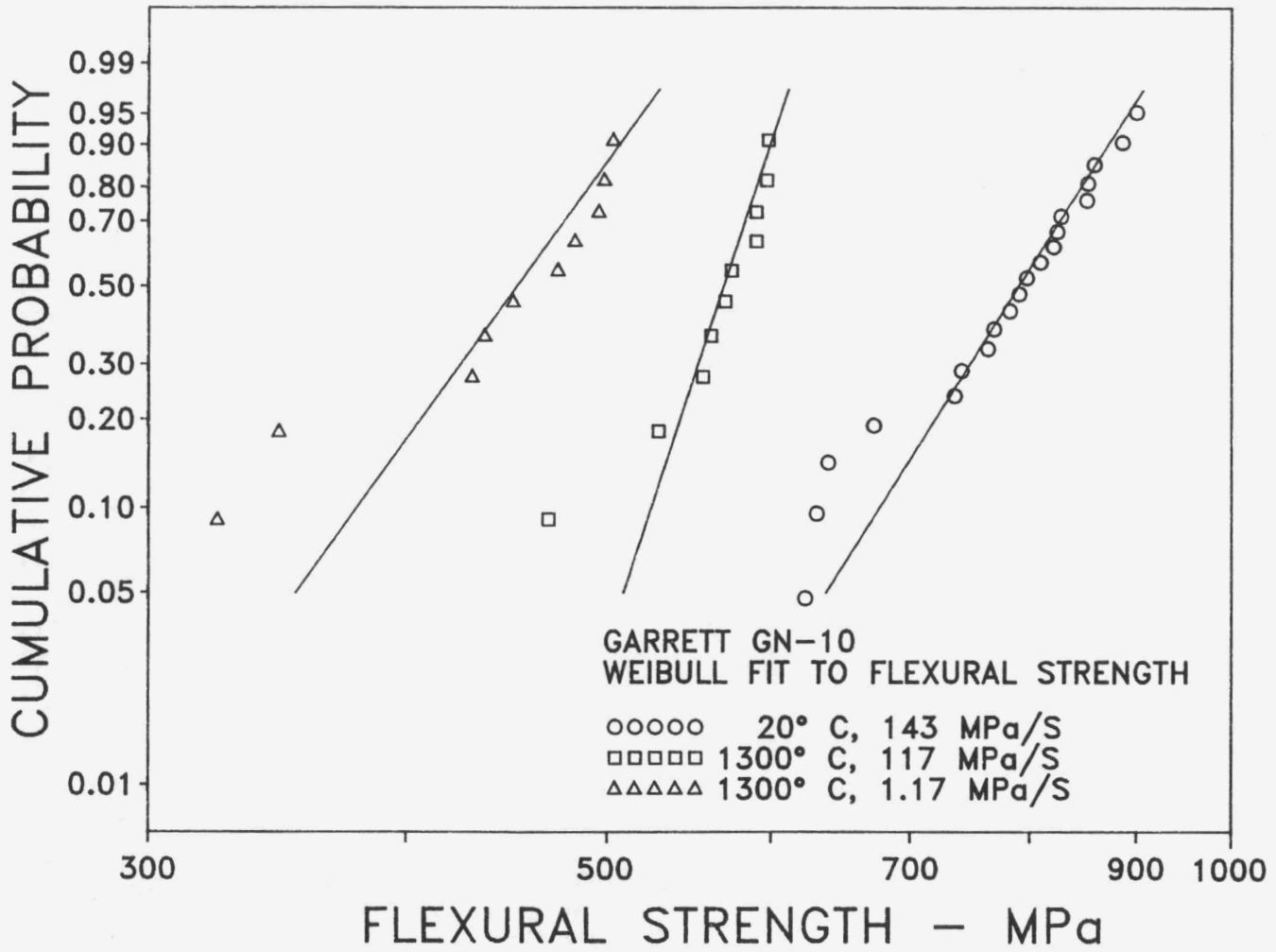

Figure 1. Garrett GN-10 Weibull fit to flexural strength data.

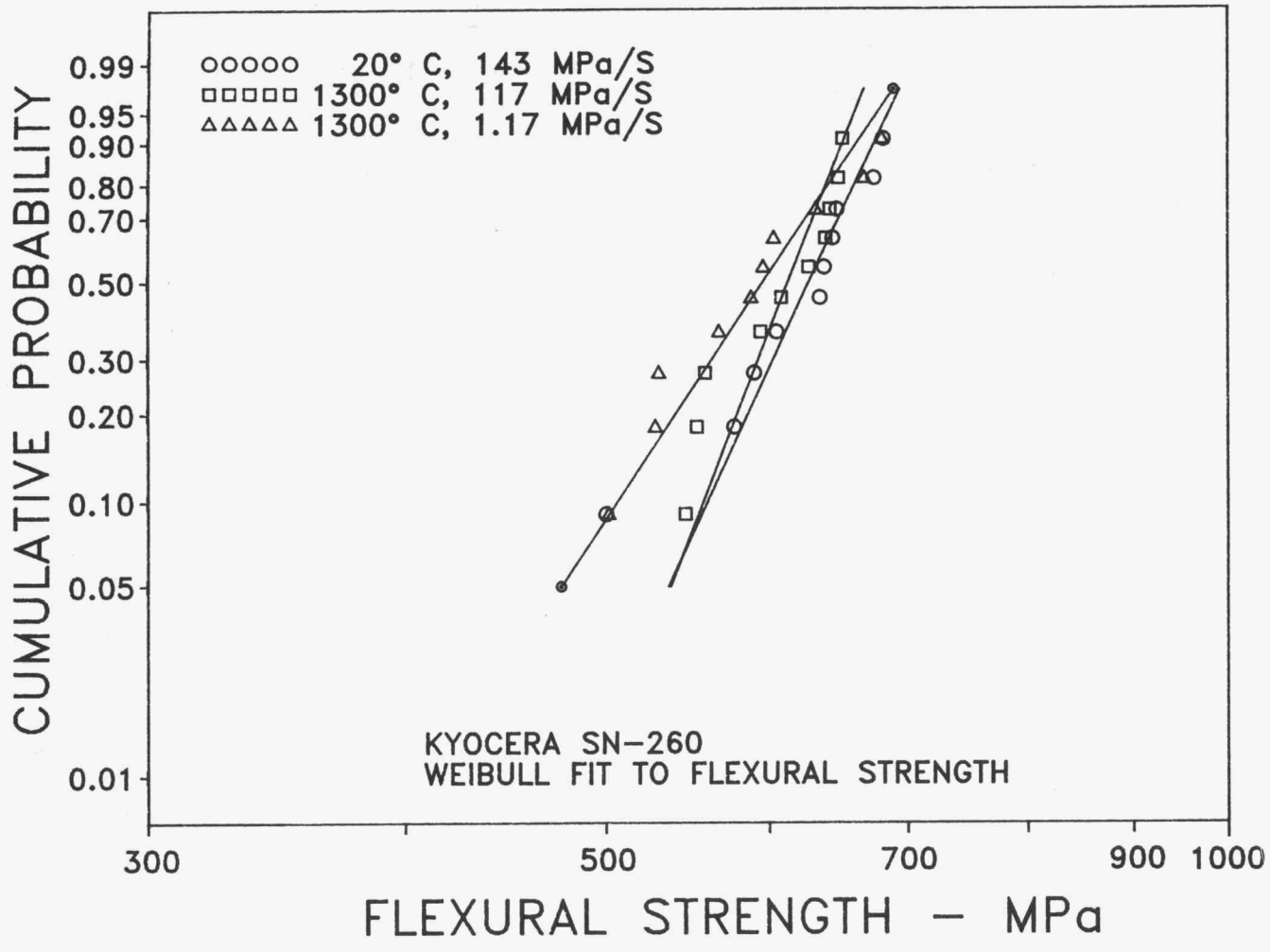

Figure 2. Kyocera SN-260 Weibull fit to flexural strength data.

Table 2. Summary of the Weibull Analysis Results Based on the Flexural Strength Data for GN-10 and SN-260

Material Designation	Temp. (°C)	Loading Rate MPa/S	Weibull Modulus m	Weibull Scale-data β_o-MPa	Weibull Scale-area S_o-MPa	Sample Size
Garrett	20	143	12.11	814	387	20
GN-10	1300	1.17+	10.57	468	200	10
	1300	117	23.27	578	393	10
Kyocera	20	143	16.55	641	372	10
SN-260	1300	1.17+	11.52	615	282	10
	1300	117	19.78	624	396	10

+The slow loading rate ($\dot{\sigma}$) at 1300°C is determined from the relationship

$$\dot{\sigma} = \frac{SEd}{L^2}\left(\frac{dy}{dt}\right)$$

where S = flexural strength
E = Youngs modulus
L = lower knife edge span
d = bar thickness, and

$\left(\frac{dy}{dt}\right)$ = crosshead speed (0.00004 cm/s)

This calculation does not include an adjustment for the effects of plastic deformation rate (creep) which could result in lower loading rates at elevated temperatures.

Dynamic fatigue analysis was conducted by using the strength values measured at fast and slow loading conditions for both Si_3N_4 ceramics at 1300°C. This comparison is shown graphically in Figure 3. As shown in Figure 3 the GN-10 has an n (corrosion coefficient) of 18, and SN-260 has an n approaching ∞. The GN-10 behaved similarly to the other Si_3N_4 evaluated displaying slow crack growth due to creep phenomena at 1300°C. GN-10 also displayed a loss of flexural strength (~30%) from 20-1300°C. The SN-260, unlike the other Si_3N_4 ceramics examined, did not display any significant change in strength with either temperature or loading rate.

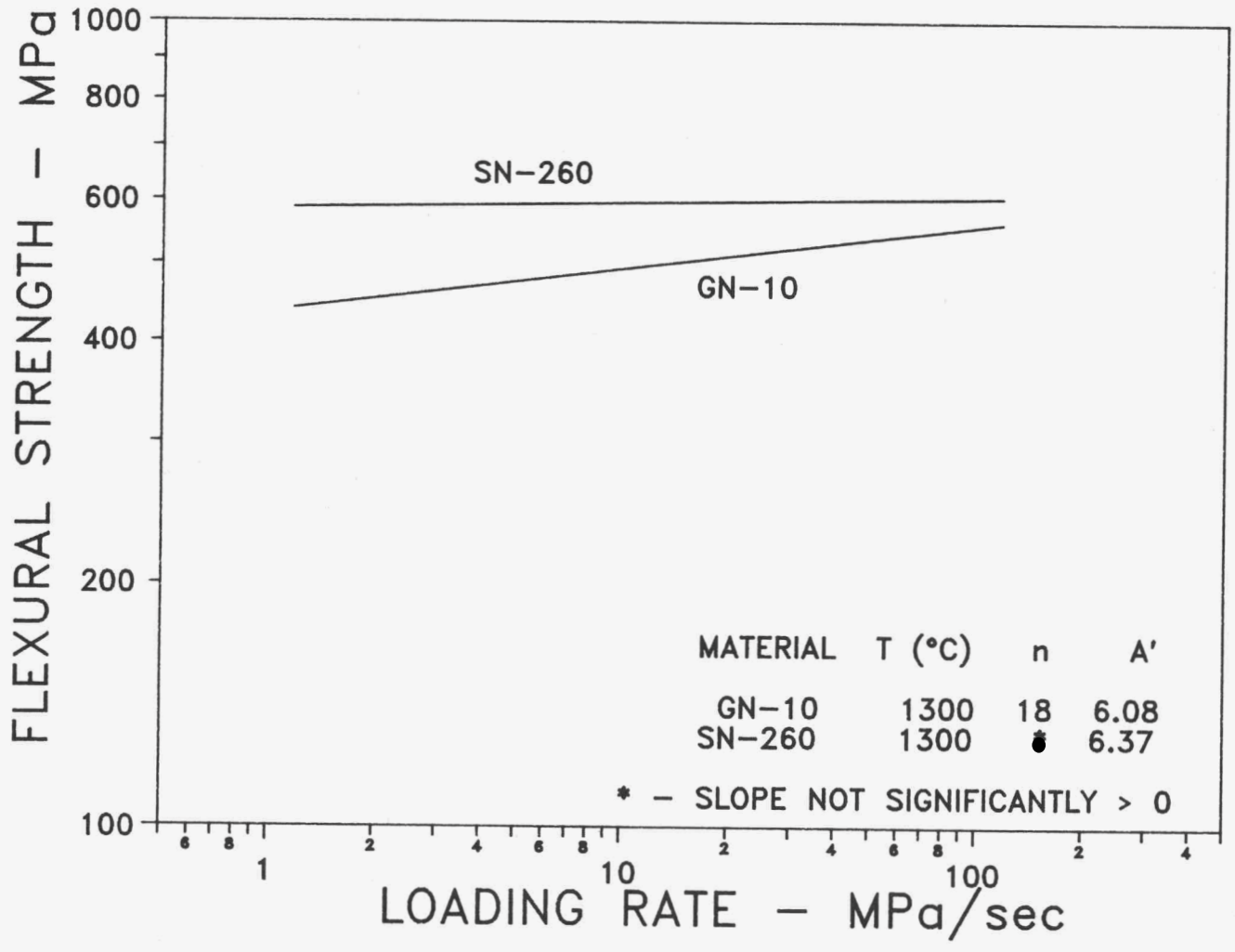

Figure 3. Dynamic fatigue behavior of SN-260 and GN-10 at 1300°C.

The applicability of the two parameter Weibull distribution to the GN-10 and SN-260 flexural strength was evaluated by the S Test.* The S Test is based on differences in the observed order statistics as compared to the expected differences under the Weibull hypothesis. The S Test for the two parameter Weibull has been shown to be more powerful than the Kolmogorov-Smirnov, and other common goodness of fit test against the normal, lognormal, and three parameter Weibull alternatives. More powerful means that there is a larger probability of rejecting the Weibull distribution when one of the above alternatives is true. The test statistics and their percentiles for the six data sets are shown in Table 3.

Table 3. Summary of the S Test on the Weibull Distribution for GN-10 and SN-260

Material	Temp. (°C)	Load Rate (MPa/s)	S Static	S Percentile	Sample Size
GN-10	20	143	0.432	<0.75	20
	1300	1.17	0.220	<0.75	10
	1300	117	0.325	<0.75	10
SN-260	20	143	0.345	<0.75	10
	1300	1.17	0.535	<0.75	10
	1300	117	0.263	<0.75	10

The S test statistics are entirely consistent with the assumption of a Weibull distribution for the observed flexural strengths of each data set. Goodness of fit tests failed to reject the Weibull distribution in all of the above test sets.

The fracture surfaces of all the flexural specimens tested were examined to determine fracture origin. For GN-10 most of the specimens tested at the fast loading rate failed at surface flaws. Thirty-five percent of these surface flaws were metallic inclusions. The fracture origin of the GN-10 specimens tested at 1300°C at the slow loading rate were difficult to determine due to the large degree of slow crack growth from surface flaws. A typical fracture surface for GN-10 is shown in Figure 4(a-c). Almost all the SN-260 flexural specimens tested failed at surface flaws. Two specimens failed at subsurface pores (Figure 5).

---

* Mann, N. R., Scheuer, E. M., and Fertig, K. W., "A New Goodness-of Fit Test for the Two-Parameter Weibull or Extreme-Value Distribution with Unknown Parameters," Communications in Statistics, 1973, Vol. 2, pp. 383-400 or Mann, N. R., Schafer, R. E., and Singpurwalla, N. D., Methods for Statistical Analysis of Reliability and Life Data, John Wiley & Sons, New York, 1974, pp. 339-349.

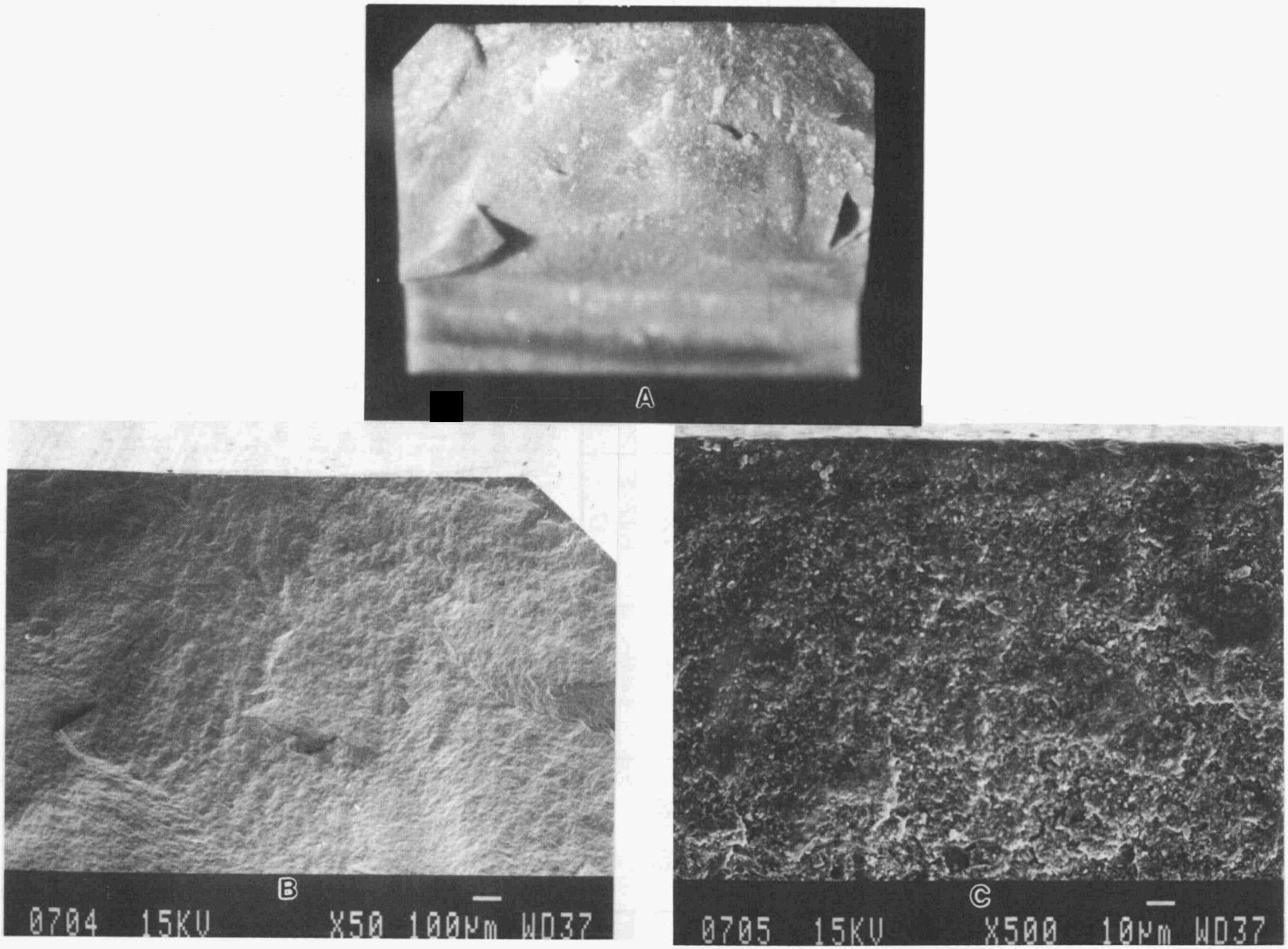

Figure 4. Typical surface fracture of a GN-10 specimen.

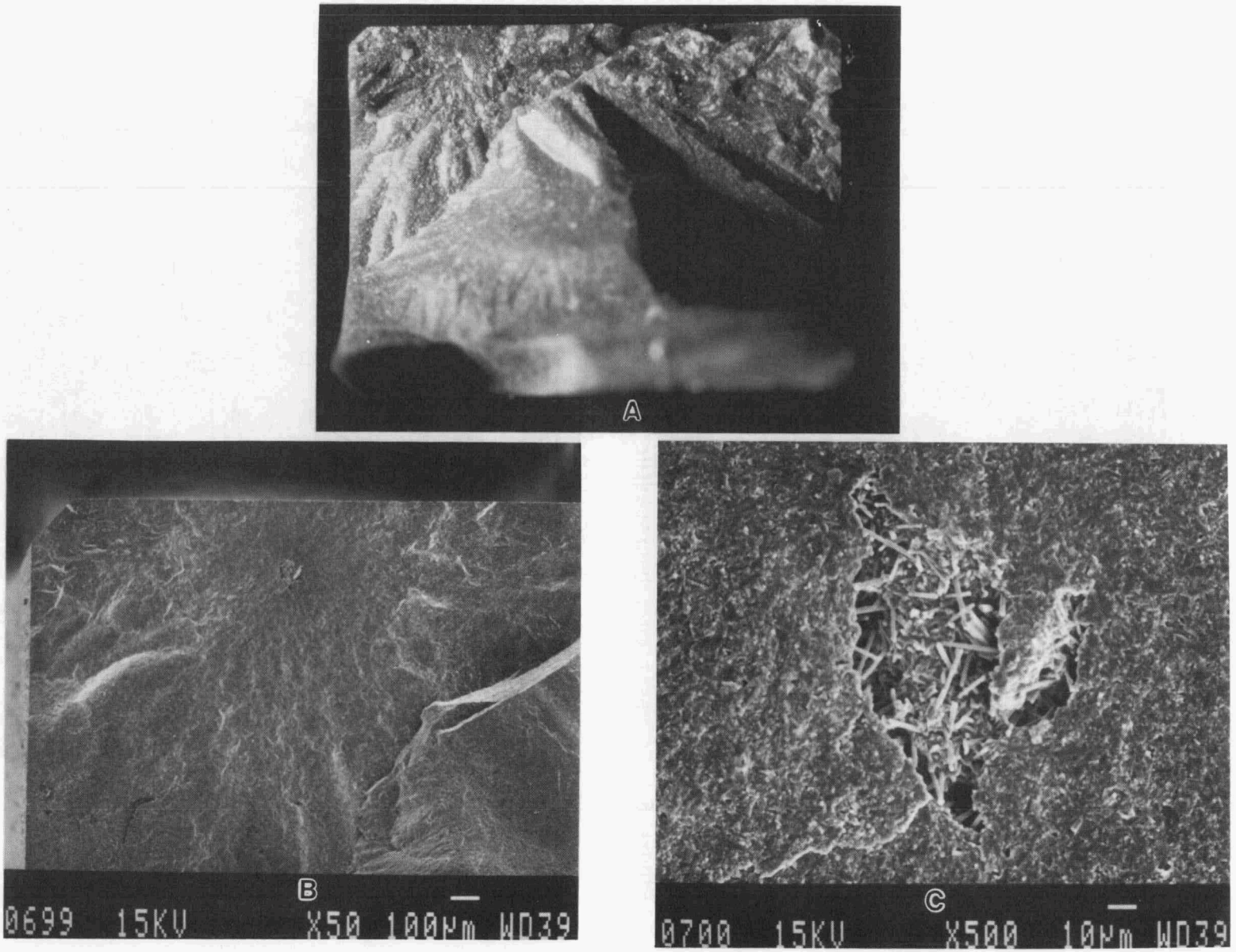

Figure 5. Fracture surface of a SN-260 specimen which failed at a subsurface pore.

The compositional backscatter SEM of a polished cross-section of GN-10 is presented in Figure 6. The gray phase is Si_3N_4 and the white phase is Y_2O_3 and SrO. The black phase is pores in the as-received microstructure.

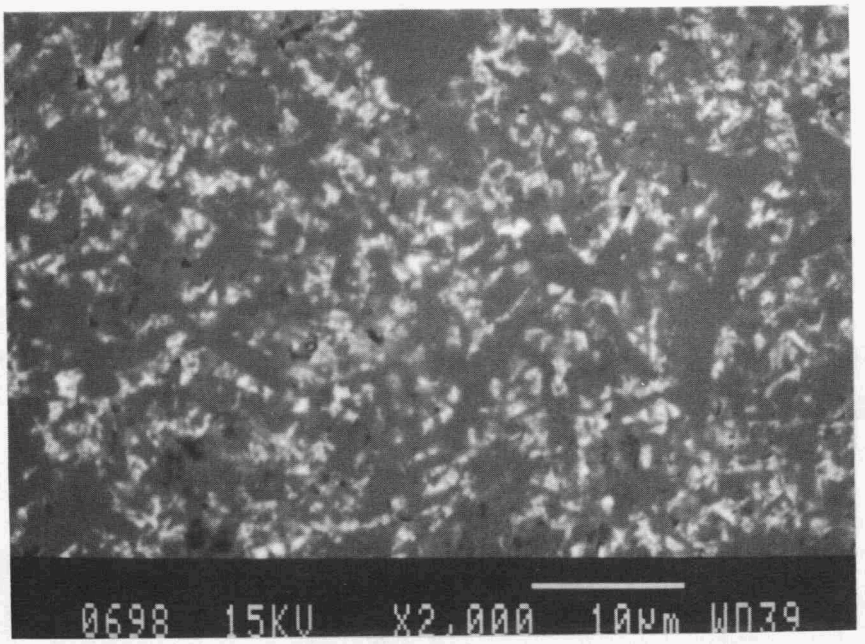

Figure 6. Compositional backscatter SEM of GN-10.

The compositional backscatter SEM photo-micrograph of a polished cross-section of SN-260 is presented in Figure 7. The gray phase is Si_3N_4 and the white phase is a mixture of Y_2O_3 and Yb_2O_3.

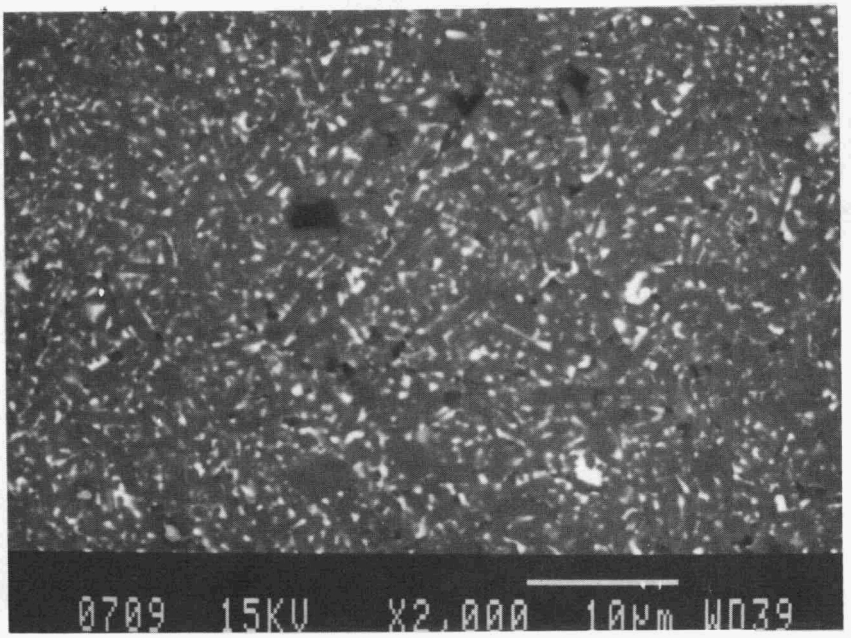

Figure 7. Compositional backscatter SEM of a polished cross-section SN-260.

A polished and HF etched SN-260 Si_3N_4 specimen is shown in Figure 8. This photomicrograph shows a network of elongated β-Si_3N_4 grains in the microstructure of SN-260. A polished and plasma etched specimen of SN-260 is shown in Figure 9. The photomicrographs provides a much more effective picture of the elongated grain structure and the nature of the intergranular phase in the microstructure of SN-260.

Figure 8. Polished and etched photomicrograph of SN-260.

Results for the Continued Evaluation of the Cyclic Tensile Testing

As reported in the last semiannual report cyclic tensile testing was conducted on 10 Hexoloy SA and 16 NT-154 tensile specimens. During this reporting period the fractured surfaces of the tested specimens were examined microscopically and the strength data collected for NT-154 was re-examined. It was observed that fracture initiated at both surface and volume sites for both NT-154 and Hexoloy SA specimens. For NT-154, fracture initiated at a pore or an agglomeration of pores. For Hexoloy SA fracture appeared to be due to the growth of surface flaws (pores). Failure of NT-154 due to cyclic tensile testing appears to be by a void nucleation and coalescence

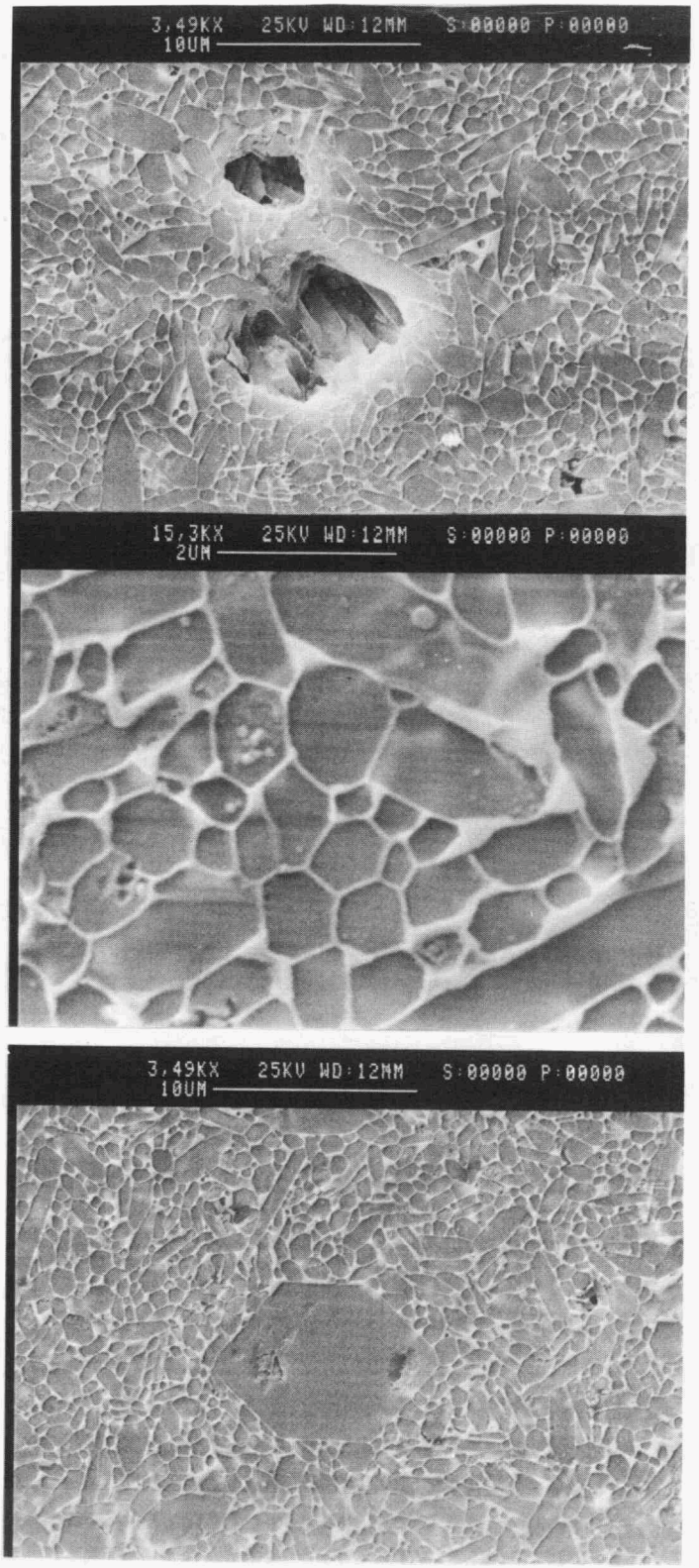

(a)

(b)

(c)

Figure 9. Polished and plasma etched SN-260 Si_3N_4.

mechanism similar to that observed in tensile stress rupture. Typical failure surfaces obtained from cyclic tension testing of NT-154 and Hexoloy SA are presented in Figures 10 and 11, respectively.

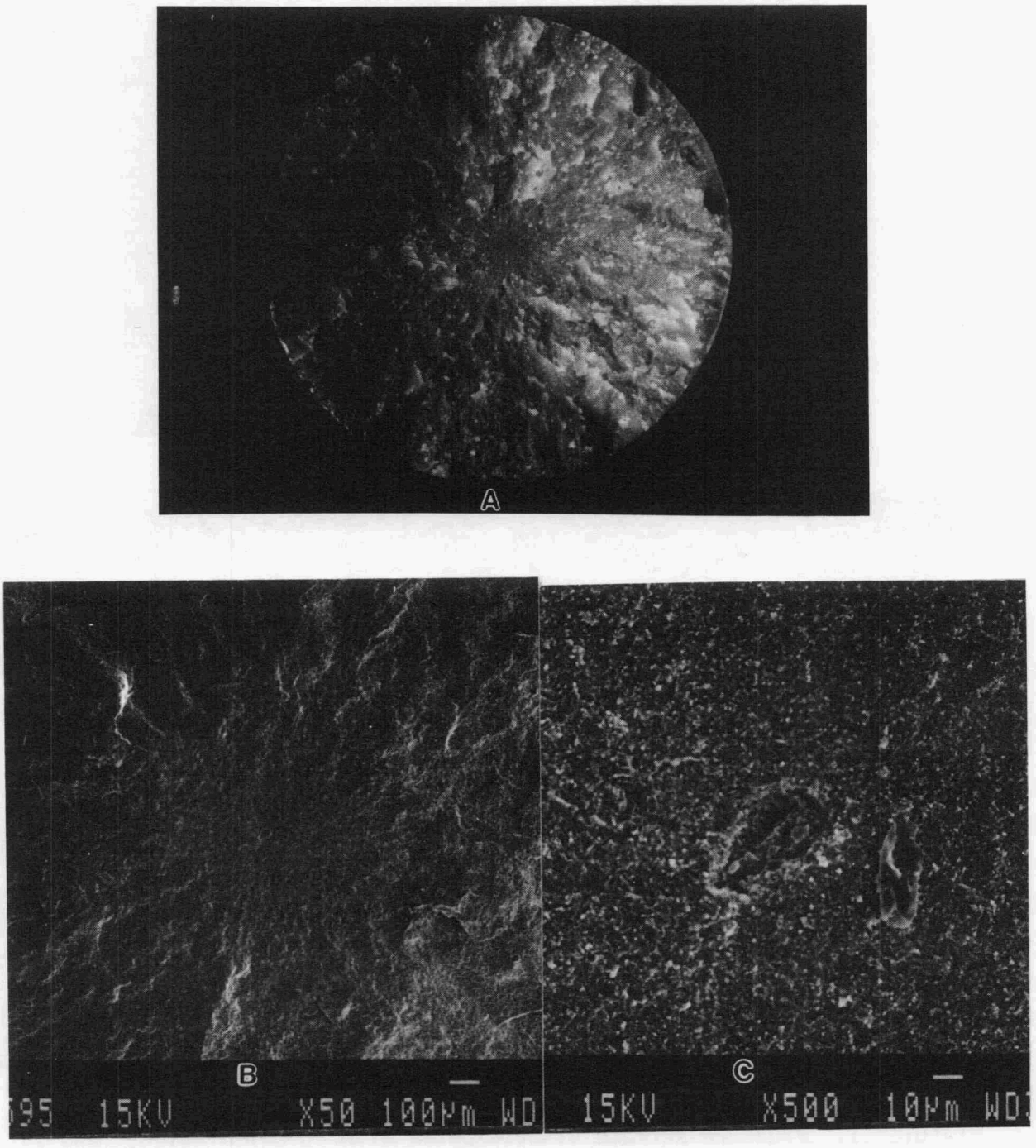

Figure 10. Fracture surface of NT-154 after cyclic fatigue tension testing.

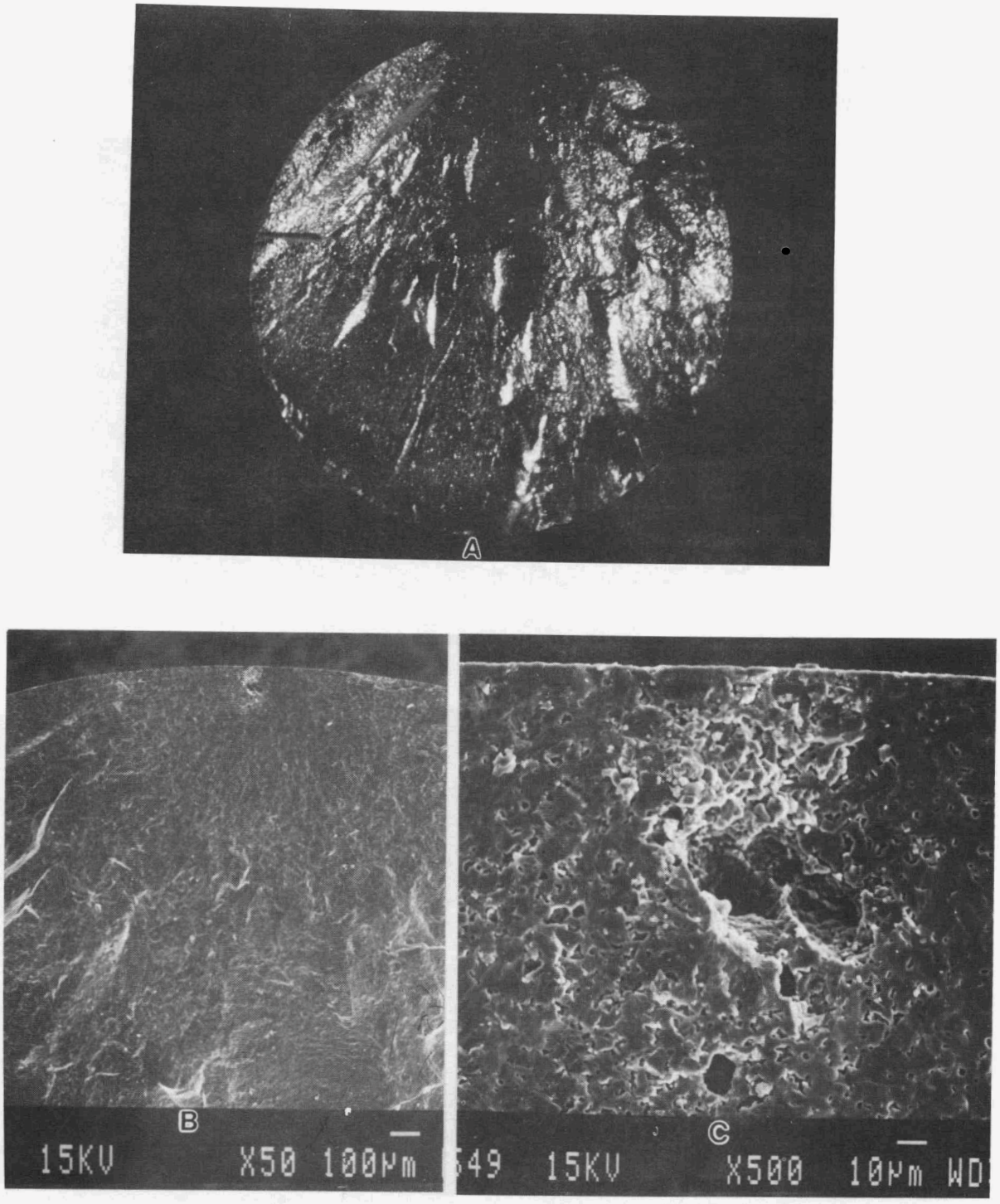

Figure 11. Fracture surface of Hexoloy-SA after cyclic fatigue tension testing.

The results of the tension-tension cyclic fatigue tests for NT-154 are compiled in Table 4. Three specimens failed within 200 cycles at an applied stress of 400 MPa. At 350 MPa applied stress, the range of cycles to failure was from 5 to 246,381. At 300 MPa applied stress, only one of the five specimens survived the 450,000 mechanical cycles and had a residual strength of 456 MPa. The remaining four specimens tested at 300 MPa failed in the range from 767 to 103,432 cycles.

Table 4. Tension-Tension Cyclic Fatigue Results

Applied Stress, MPa	Cycles to Failure	Failure or Residual Strength, MPa
400	190	400
400	2	400
400	2	400
350	724	350
350	4617	350
350	5	350
350	8370	350
350	246381	350
300	450000	456
300	7253	300
300	30239	300
300	103432	300
300	767	300
200	450000	364
200	450000	341
200	450000	417

At an applied stress of 200 MPa, all three specimens survived the 450,000 cycles (equivalent to 100 hours). The residual strengths measured for the surviving specimens ranged from 341-417 MPa. The results of the tensile stress rupture studies conducted earlier in this project showed that the measured residual strength after 100

hours at an equivalent maximum applied stress of 200 MPa were 450, 469, 470, and 506 MPa. Although the number of tested specimens was too small for statistical comparison, the lower residual strengths measured after cyclic fatigue testing were significant, implying that low-frequency mechanical cyclic fatigue can cause long-term strength degradation.

All three specimens tested at 400 MPa applied stress failed from volume defects. One of the three defects was identified as a foreign inclusion. At 350 MPa applied stress, two specimens failed from surface defects and the other three failed from volume defects. The eight specimens tested at 300 and 200 MPa applied stresses failed from volume defects. The fatigue failure data for NT-154 is plotted in Figure 12, and the distributions are presented on a linear number of cycles to failure.

The tension-tension cyclic fatigue specimens show bimodal failure similar to that reported for the tensile rupture specimens. From Figure 12 the bimodal distribution can be more easily seen since the data are separated and the individual distributions are compressed. Threshold failure separation occurred at approximately 10, 10,000, and 100,000 cycles for 400, 350, and 300 MPa applied stress, respectively. The specimens surviving these preliminary threshold number of cycles probably fail from a different mechanism or combination of failure mechanisms. The tension-tension cyclic test, results reported by Liu and Brinkman* for NT-154 also showed similar bimodal failure behavior.

Fracture analysis of the specimens tested in cyclic fatigue resulted in some interesting observations. In the SEM micrograph a specimen tested at 300 MPa, an impression of a possible whisker was observed (Figure 13) at the fracture origin. There were no foreign remnants on the fracture surface for chemical examination. In the SEM micrograph (Figure 14) of a specimen tested at 300 MPa a similar "whisker" void impression was observed; however, as shown in low and high magnification, this void was not the origin of fracture. The fracture plane happened to be on the same plane as the "whisker" void impression. The origin of these "whisker" impressions is not known.

---

* Liu, K. C. and Brinkman, C. R., "High Temperature Tensile and Fatigue Strengths of Silicon Nitride," Proceedings of the Twenty-Seventh Automotive Technology Development Contractor's Coordination Meeting, Dearborn, MI, October 1989; SAE Publication, pp. 230, 1990.

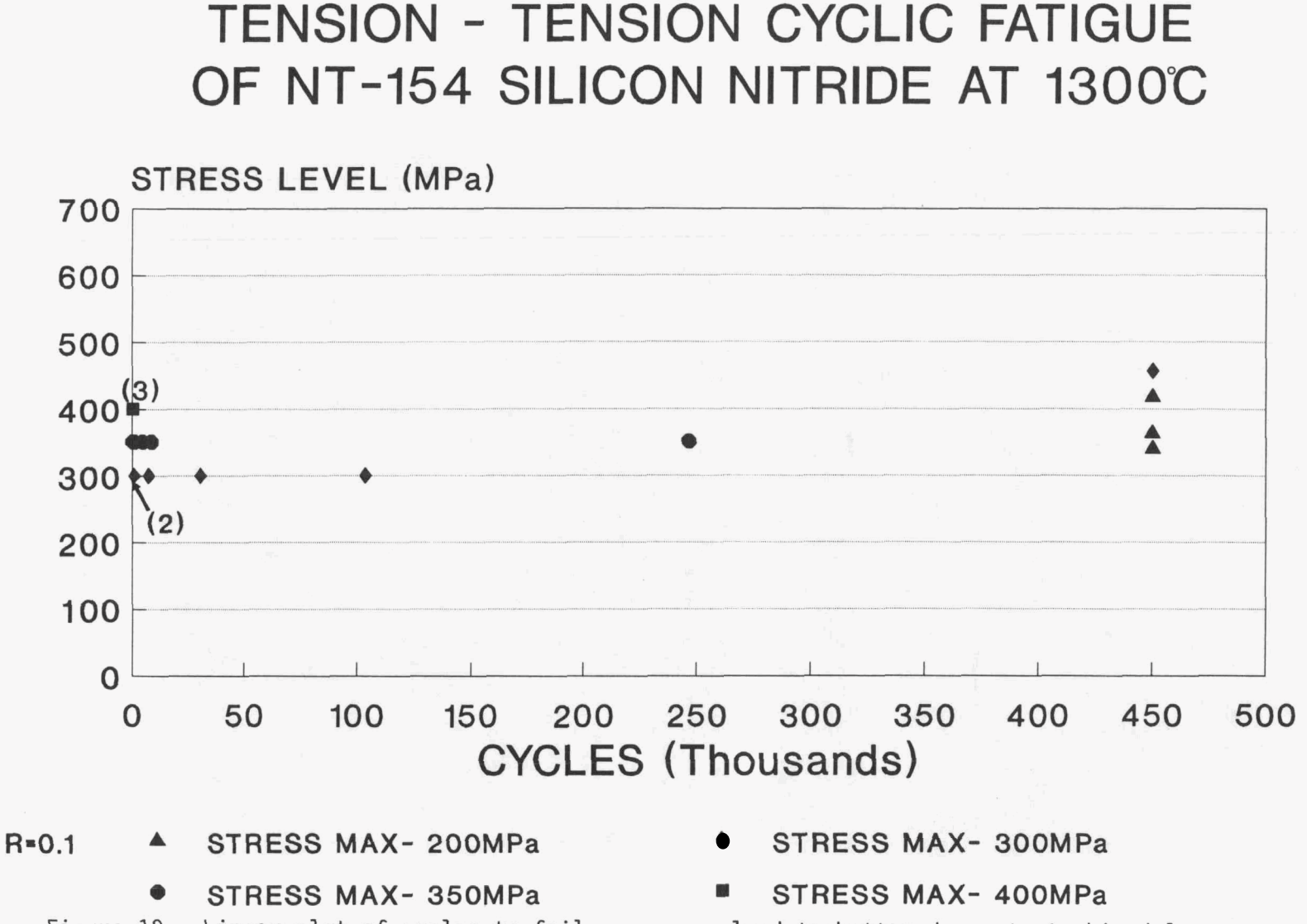

Figure 12. Linear plot of cycles to failure versus load to better demonstrate bimodal distributions of cycles to failure.

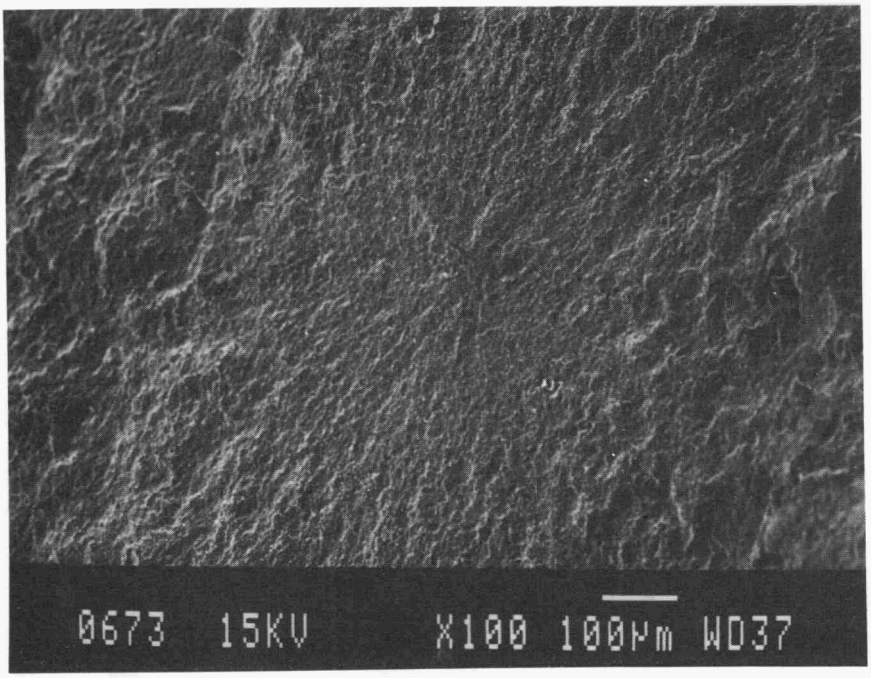

(a)

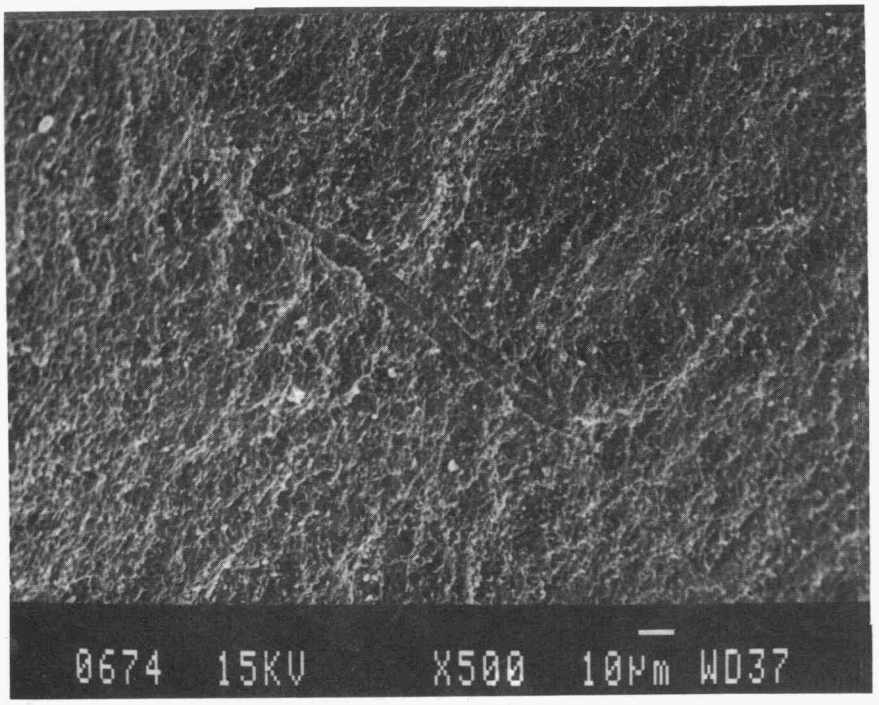

(b)

Figure 13. Low (a) and high (b) magnification SEM fractographs of a specimen after surviving 450,000 cycles at a peak stress of 300 MPa at 1300°C in air. The measured residual strength is 456 MPa. The fracture origin is the "whisker" void impression.

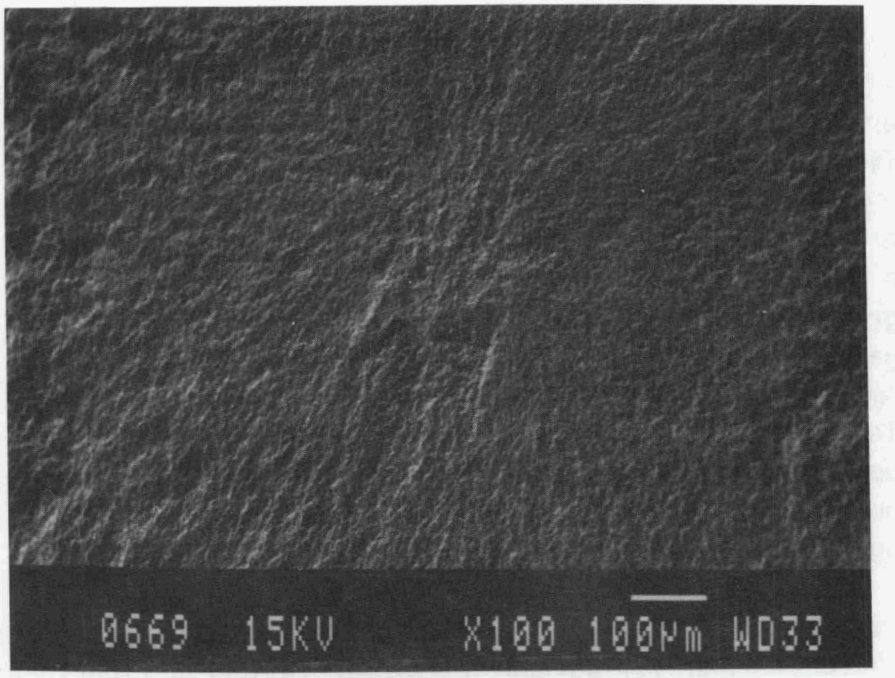

(a)

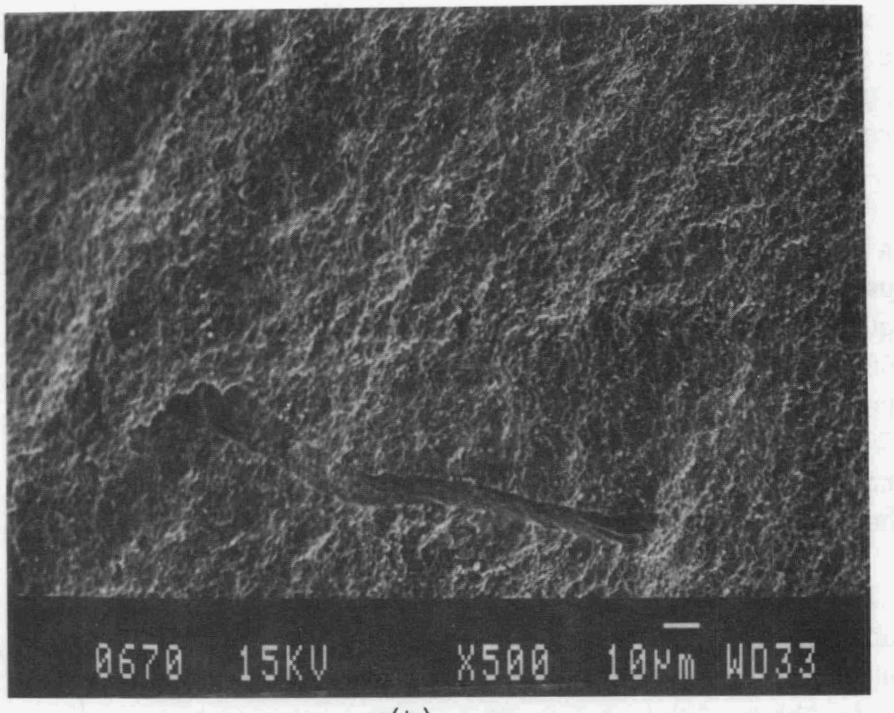

(b)

Figure 14. Low (a) and high (b) magnification SEM fractographs of a specimen that failed after 246,381 cycles at an applied cyclic stress of 350 MPa at 1300°C in air. The "whisker" void impression is not the fracture origin.

The majority of fractured specimens failed from mechanical cyclic fatigue crack growth as typified by the specimen shown in Figure 15. Two regions on the fracture surface are identified for further study. Regions 1 and 2 are shown in Figure 16 at high magnification. The diameter of the cyclic fatigue crack growth in region 2 is approximately 450 to 500 μm in size. As shown in Figure 16, region 2 has a slightly rougher surface texture than region 1. Fatigue debris are apparent in both regions. However, only grain cleavages were observed in region 1 from rapid crack propagation. The fracture surface of this cyclic fatigue specimen was compared to a stress rupture (static fatigue) test specimen. Cavities are evident on both fracture surfaces; however, the cyclic fatigue surface has a considerable amount of debris. This debris is from dislodged grains generated by the mechanical opening and closing of the crack during cyclic fatigue.

It is hypothesized that cavity nucleation and coalescence would have to occur for mechanical cyclic fatigue action to cause grain pullout, rotation, and grain grinding to form debris as the crack surfaces opened and closed. The threshold time under tensile cyclic fatigue loading is considered minimal to cause cyclic fatigue crack growth. More systematic testing and detailed analysis are required to confirm this hypothesis.

Polished cross sections of the gage section, perpendicular to the fracture surface of two specimens subject to tensile cyclic fatigue, were examined (Figures 17 and 18). The specimen examined in Figure 17 was fast fractured at 341 MPa after being exposed to 450,000 cycles at 200 MPa maximum applied tensile cyclic stress. The specimen shown in Figure 18 failed after 246,381 cycles at 350 MPa maximum applied tensile cyclic stress. The top edges of the fracture surface for these two specimens are shown in profile, and the applied tensile stress was normal to the fracture surface.

In Figure 17 a montage of optical photographs was used to show the subsurface damage and crack propagation patterns below the main fracture surface. The fine crack path patterns were not always normal to the applied stress field. The polished gage section lengths examined were nominally 10 to 11 mm. It is not known why these crack propagation patterns were only seen immediately below

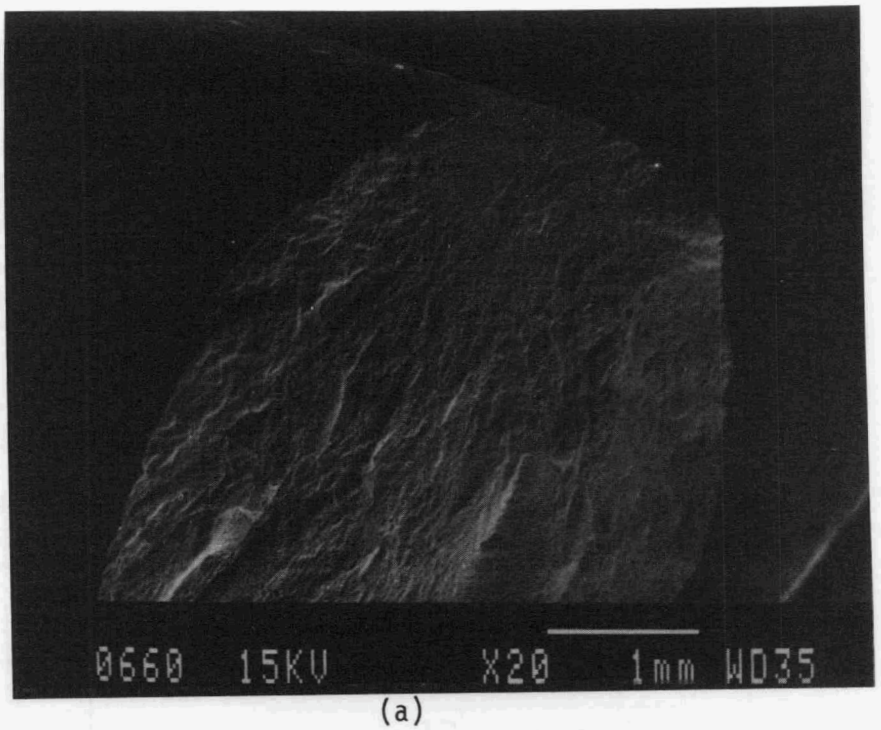

(a)

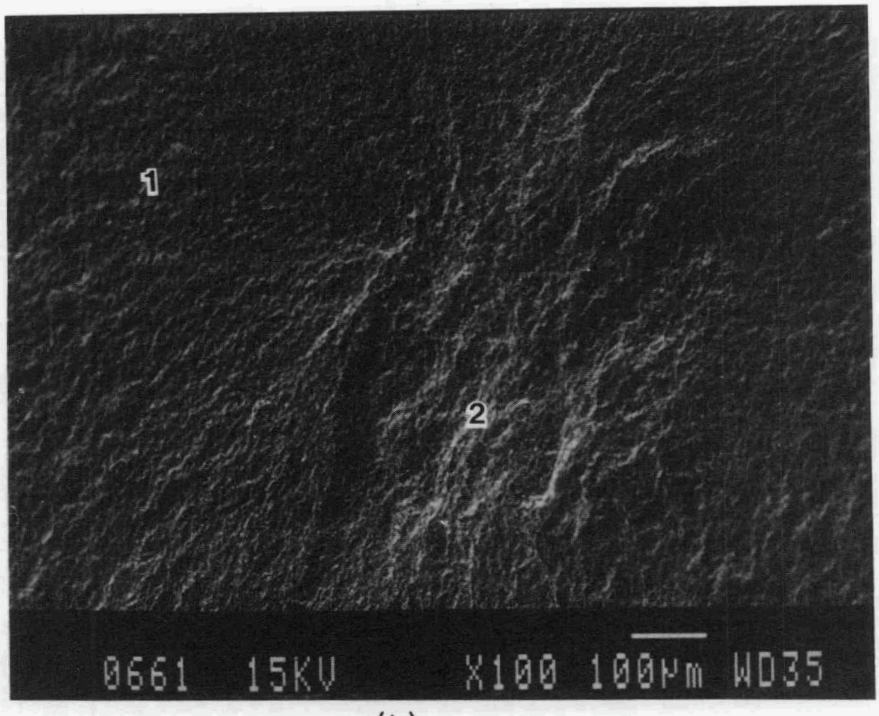

(b)

Figure 15. Low (a) and high (b) magnification SEM fractographs of a specimen that failed after 103,432 cycles at an applied cyclic stress of 300 MPa (typical fracture surface for specimens subject to cyclic fatigue). Rapid crack propagation occurred in region 1. Region 2 is identified as mechanical cyclic fatigue crack growth fracture surface.

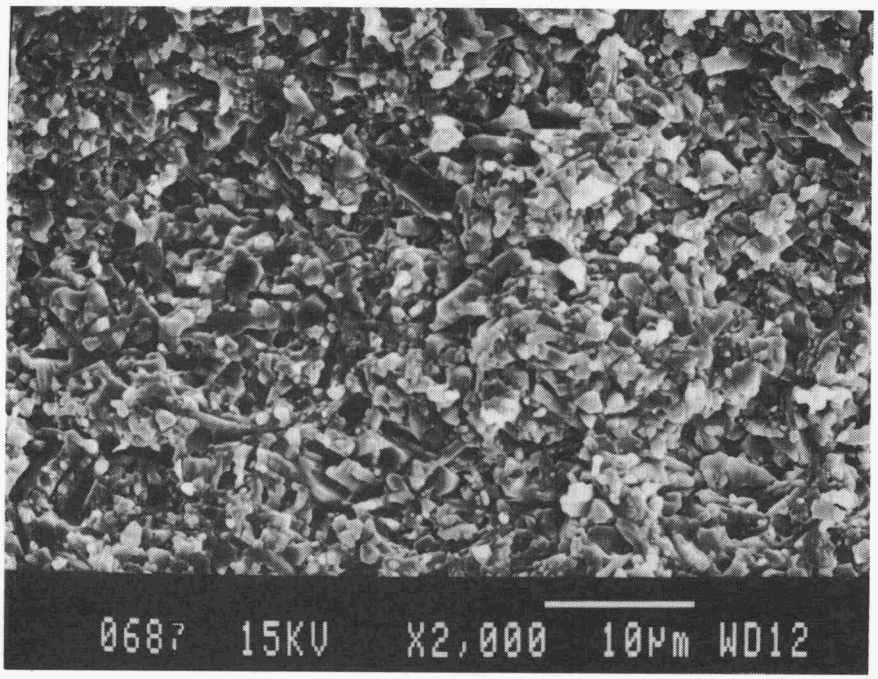

(a)

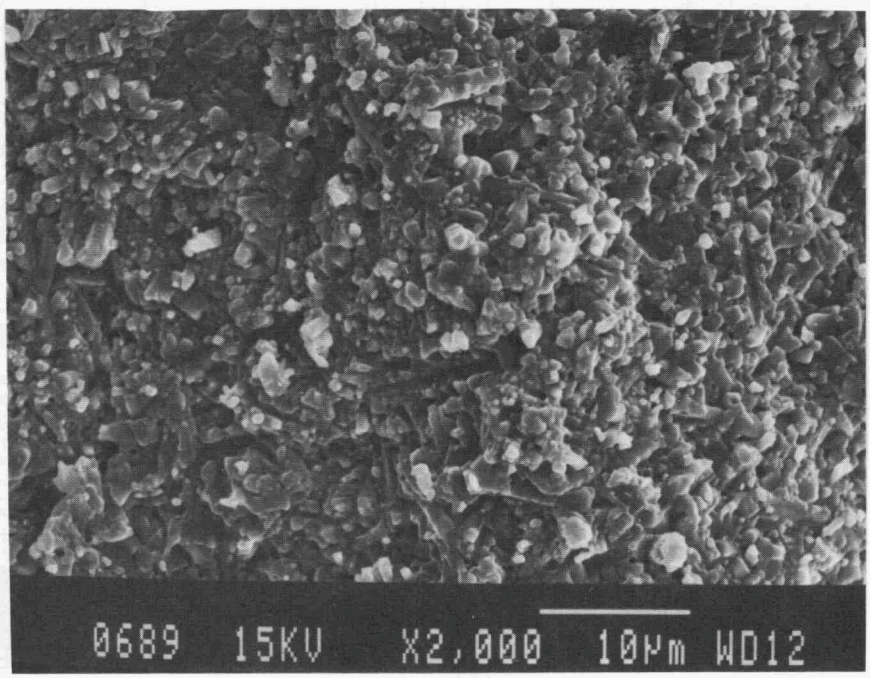

(b)

Figure 16. Increased magnification of region 1 (a) denoted by cleaved silicon nitride grains and fatigue debris, and region 2 (b) denoted by cavities and fatigue debris (no cleaved grains are observed).

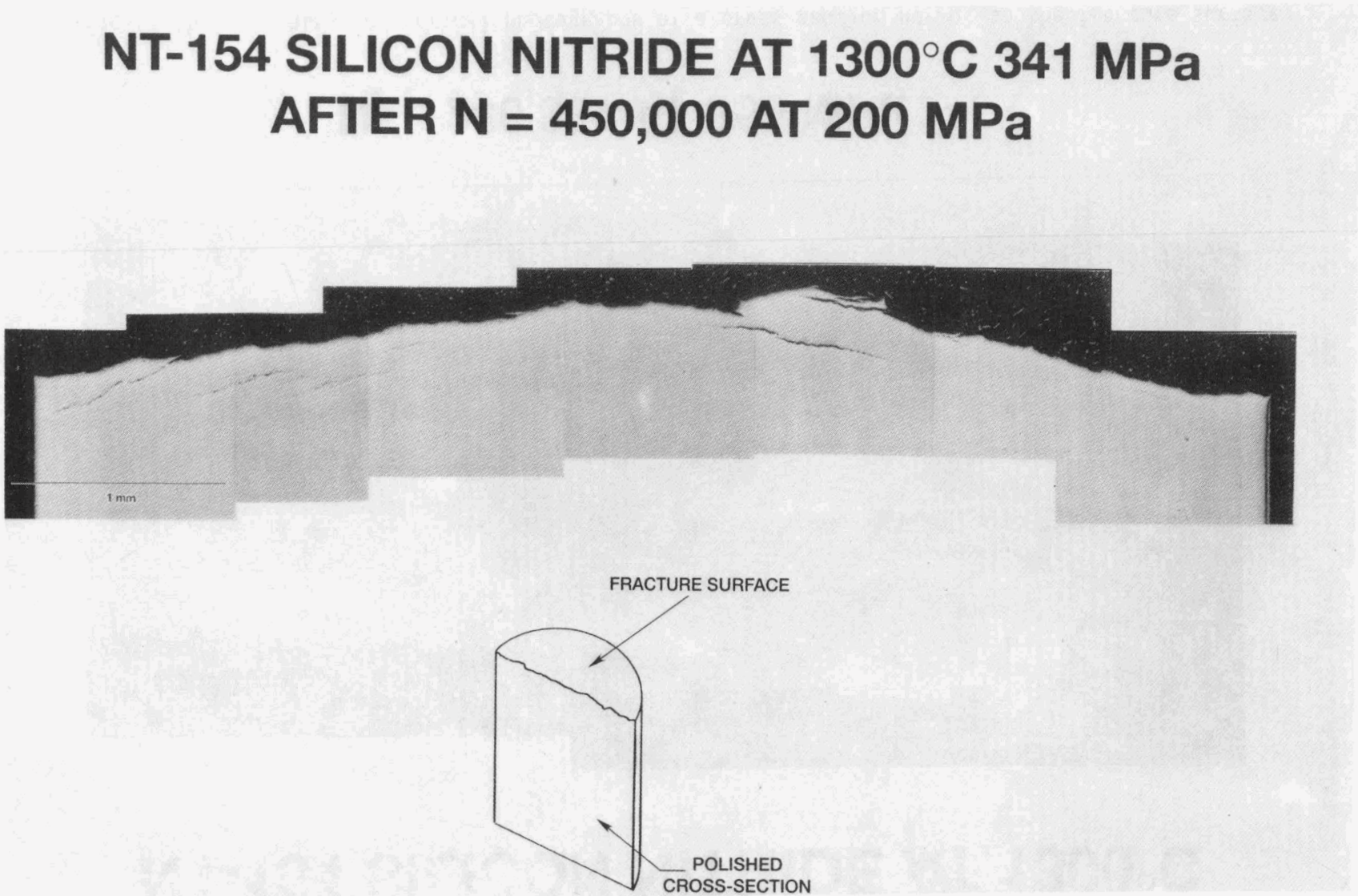

Figure 17. A montage of optical photographs to demonstrate local subsurface damage and crack propagation patterns below the main fracture surface.

NT-154 SILICON NITRIDE AT 1300°C

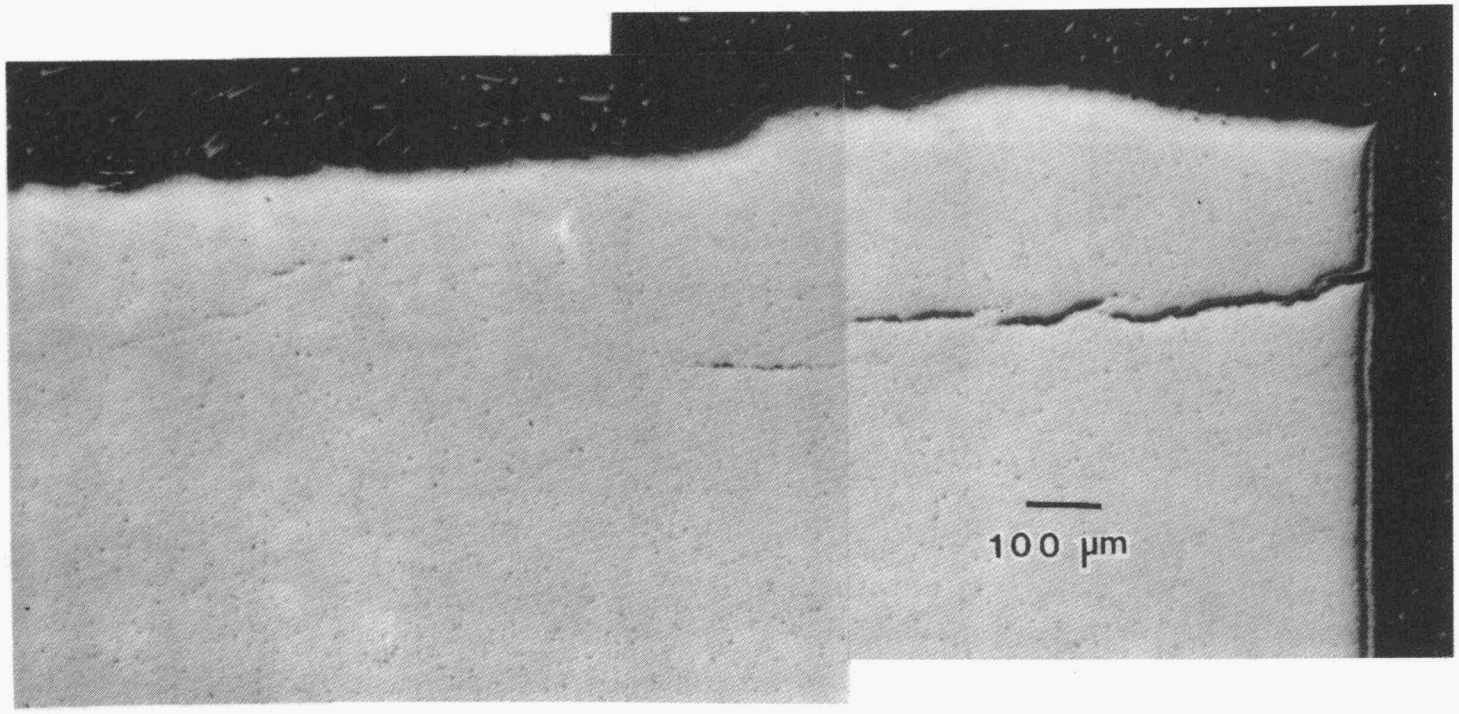

N_f = 246,381 AT 350 MPa

Figure 18. A montage of optical photographs of a cross section normal to the fracture surface. A large cyclic fatigue crack developed below the main fracture surface.

the main fracture surface. However, this may be due to secondary cracking of the weakened and cavitated microstructure or to interactions with the high-energy stress wave generated at fracture. Interactions with the stress wave are not as likely since the crack opening of the subsurface cracks are large for this event time.

Below the main fracture surface, shown in Figure 18, a large cyclic fatigue crack developed from the surface. Crack patterns were only seen immediately below the fracture surface. The number of cavities developed could not be accurately determined because of grain pullout during polishing.

Status of milestones

Milestones 331410, 331411, and 331412 have been completed, and milestones 331413 and 331414 are in progress.

3.4 FRACTURE MECHANICS

Testing and Evaluation of Advanced Ceramics at High Temperature in Uniaxial Tension

J. Sankar, A. D. Kelkar, and S. Krishnaraj (Department of Mechanical Engineering, North Carolina A&T State University, Greensboro, NC 27411)

Objective/Scope

The purpose of this effort will be to test and evaluate advanced ceramic materials at temperatures upto 1200° C in uniaxial tension. Testing may include fast fracture strengths, stepped static fatigue strength, and creep strength along with the analysis of fracture surfaces by scanning electron microscope. This effort will comprise of the following tasks:

Task 1. Specifications for testing machine and controls + (procurement) for creep testing.
Task 2. Identification of test material(s) for the present year + (procurement of specimens).
Task 3. Identification of test specimen configuration.
Task 4. Identification and procurement of test grips, high temperature extensometer, and furnace for the creep machine.
Task 5. High temperature fatigue-creep interaction study and tensile testing.
Task 6. Reporting(periodic).
Task 7. Final report.

It is anticipated that this program will help in understanding the behavior of ceramic materials at very high temperatures in uniaxial tension.

Technical Progress

For the present year's work, October 1990 to October 1991, two(2) materials have been identified namely SNW1000 and PY6 Si_3N_4, both from GTE. During the last year, uniaxial creep testing were conducted on the SNW1000 and this year we are planning to conduct fatigue-creep interaction studies on the same material.

During the reporting period two(2) creep machines were transferred from ORNL to A&T, and they are being installed now. The machine will have a suitable furnace and a laser extensometer set up. Presently we are working on these subtasks and are also in contact with the GTE personnel regarding the fifty(50) PY6 Si_3N_4 samples. The sample configuration is slightly modified from our normal SNW1000 test specimen to accomodate the GTE's manufacturing routines. The new configuration used will be similar to that of the Advanced Processing Program. Anticipated due date for the samples is mid May 1991.

During the semi-annual period, some of the creep tested samples (SNW1000 Si_3N_4) of the last year's effort were characterized for their internal porosity distribution. Figure 1A shows pores in an untested specimen, while Figure 1B shows pores in a creep tested specimen. The sample for the creep tested specimen was taken 2mm away from the fractured surface of the creep tested sample. It can be clearly seen that the pores in the creep

Figure 1. GTE SNW-1000 untested (A) and creep tested (B) specimen

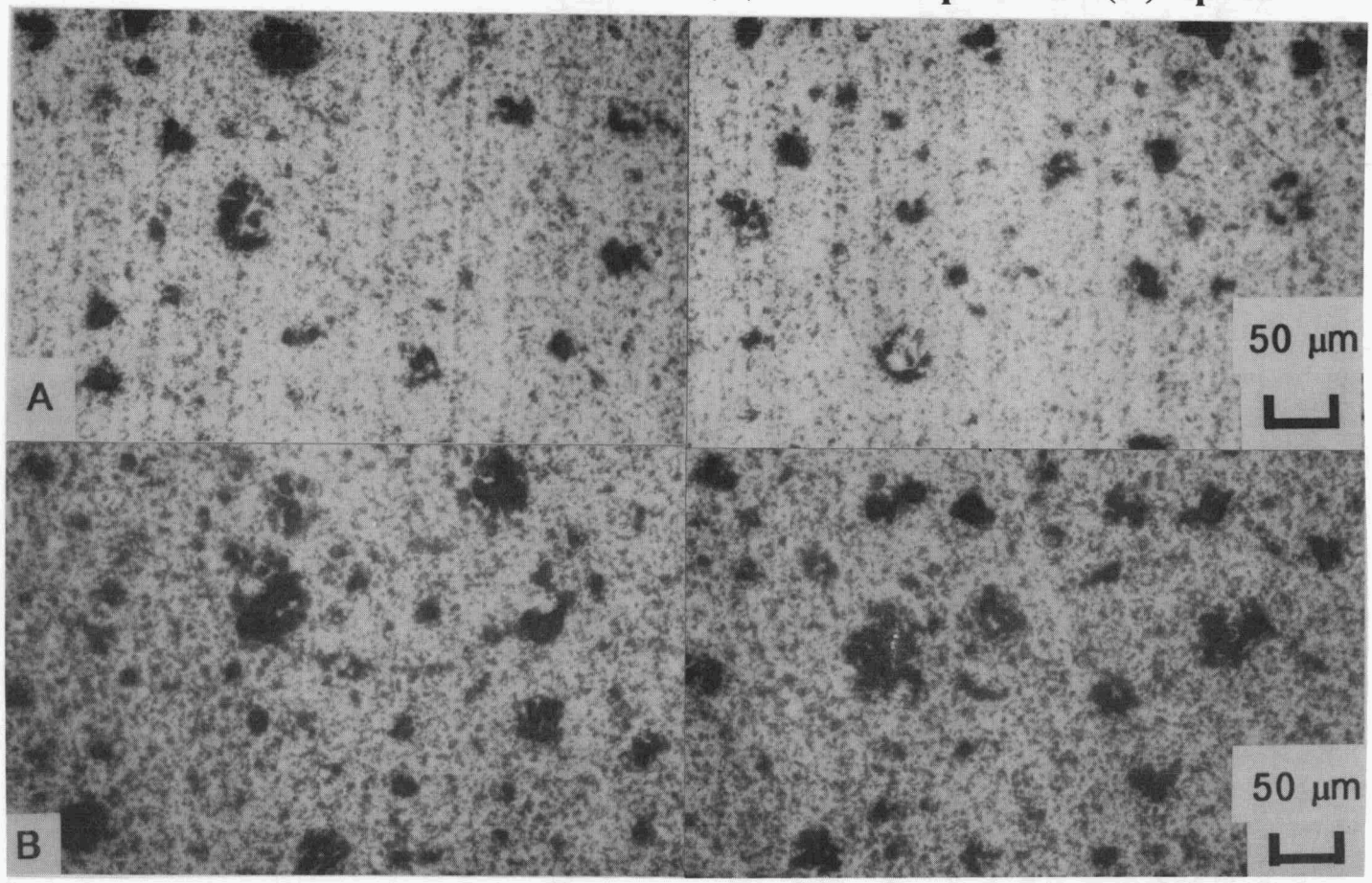

(A) Polished microstructure surface of untested specimen, showing pores.

(B) Polished microstructure surface of one of the specimen, 1200^{o}C, 138 MPa. Observe the distribution of the pores.

tested specimen is larger and also their distribution density is much higher compared to the untested sample. This type of evidence is present throughout the observed area and we feel that the pre-existing pores from processing starts to grow and start to appear distinctly in the tested samples. Further, there are evidence for the creep induced cavities and their linking up process during creep testing resulting in long fissure (Figure 2). Note that the cavities do not show any β-Si_3N_4 whiskers inside.

As far as the fatigue-creep interaction study of SNW1000 Si_3N_4 is concerned, we have ten(10) samples of this material and presently a computer program is being developed for testing the samples in fatigue.

Cyclic fatigue tests will be performed for a specified number of cycles in constant amplitude tension-tension loading using a triangular waveform at 0.5 Hz. All tests will be carried out at 1200° C, with a maximum stress of 75% or less of the fatigue strength of the material at 1200° C. Number of cycles will be varied in such a way that the specimen will not fail during fatigue testing.

Tensile creep tests will be performed on fatigued specimens at 1200° C. Different percentage of the Tensile Strength load of the material at 1200° C will be used. During the test, strain will be calculated with respect to time based on the extension monitored by the laser extensometer.

Status of Milestones
On schedule

Publications and Presentations
None

Research sponsored by the U. S. Department of Energy under prime contract DE-AC05-840R21400 with the Martin Marietta Energy Systems, Inc., subcontract 19X-89867C

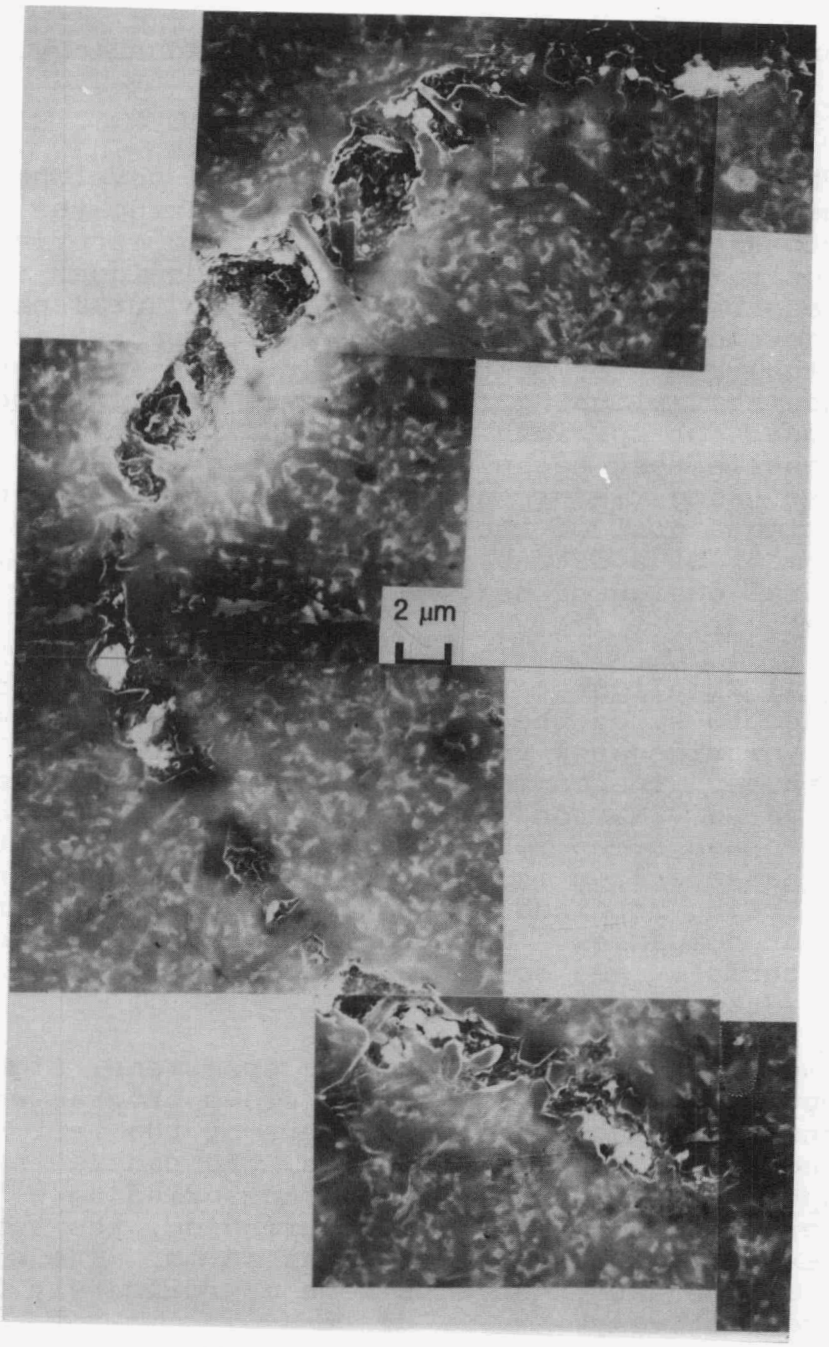

Figure 2. GTE SNW-1000 creep tested specimen, 1200^{o} C, 138 MPa. Magnified images showing part of the cavities.

Standard Tensile Test Development

S. M. Wiederhorn, D. C. Cranmer, D. A. Kauffman, R. F. Krause, Jr., and D. E. Roberts
(National Institute of Standards and Technology)

Objective/Scope:

This project is concerned with the development of test equipment and test procedures for measuring the tensile strength and creep resistance of ceramic materials at elevated temperatures. Inexpensive techniques for measuring the creep behavior and strength of structural ceramics are being developed and will be used to characterize the mechanical behavior of these materials. The test methods will use self-aligning fixtures, and simple grinding techniques for specimen preparation. Creep data obtained with tensile test techniques will be compared with data obtained using flexure and compressive creep techniques. The ultimate goal of the project is to assist in the development of a data base and a test methodology for the structural design of heat engines for vehicular applications.

Technical Highlights - During the past six months, we have continued to study the creep and creep rupture behavior of silicon nitride as a function of applied tensile stress and temperature. Two commercial grades of material are being investigated: Norton/TRW NT-154, and Allied-Signal GN-10. The creep and creep rupture behavior of these materials are being characterized in tension and compression and a data base is being obtained to compare materials manufactured by different companies. This report presents data collected on both materials, and compares their behavior based on a Monkman-Grant description.

Experimental Technique - Dog-bone specimens, figure 1, developed as part of our tensile creep program were used in this study. To assure that failure of the test specimens occurred within the gauge section, the central section of each specimen was reduced by surface grinding with a 38 mm diameter grinding wheel. After grinding, the total thickness of the gauge section was ≈2 mm. The width and length of the gauge sections were approximately 2.5 mm and 14 mm respectively.

Creep tests were conducted using the tensile equipment developed in an earlier phase of the project. The gauge length of each test specimen was monitored by placing small α-SiC flags on the central portion of the test specimen. The position of the flags were monitored as a function of time with a laser extensometer, which was capable of an

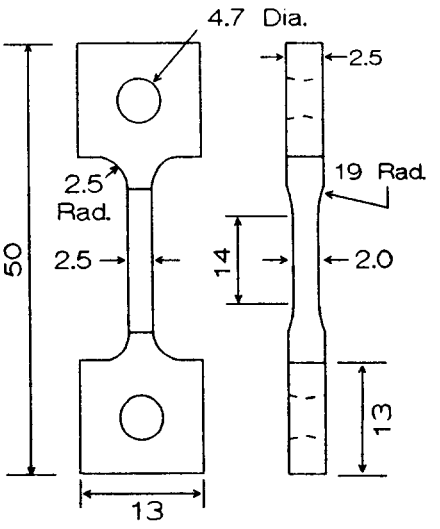

Figure 1. Specimen configuration. All dimensions are in mm. Note the double reduction in specimen gauge section. Also, the holes are tapered at an angle of ≈15°.

accuracy of better than ±1 μm in the measurement of distance between the two flags. This level of accuracy resulted in a precision of ±2 μm in the displacement measurements during the evaluation of creep curves for each specimen. Details of the experimental apparatus were published previously [1].

In studies on NT-154, the test temperature ranged from 1330°C to 1430°C. Tests were conducted in air, with a short ≈24 hour anneal to assure thermal equilibrium within the test furnace prior to application of the stress. Applied stresses ranged from 75 to 175 MPa. NT-154 is a HIP-ed grade of Si_3N_4 using 4 weight percent Y_2O_3 as a sintering aid. The billets used were made specifically for this study, and do not relate to billets used on other parts of the DOE heat engine program. As transient effects were observed in the creep of the NT-154 during a previous six-month period, long-term creep measurements were carried out on two specimens to clarify the effect of time at temperature on the creep rate. Data were then expressed in terms of a Monkman-Grant curve in which the creep rate was plotted as a function of the time to failure.

Similar experiments and analyses have been conducted on the GN-10. For this material, temperatures ranged from 1200 to 1350°C and applied stresses ranged from 75 to 150 MPa. GN-10 is also a HIP-ed Si_3N_4, but contains a total of about 8 weight percent sintering aids (Y_2O_3 plus other). Transient effects like those seen in NT-154 were not

observed in GN-10, although steady-state creep was not generally achieved in this material either.

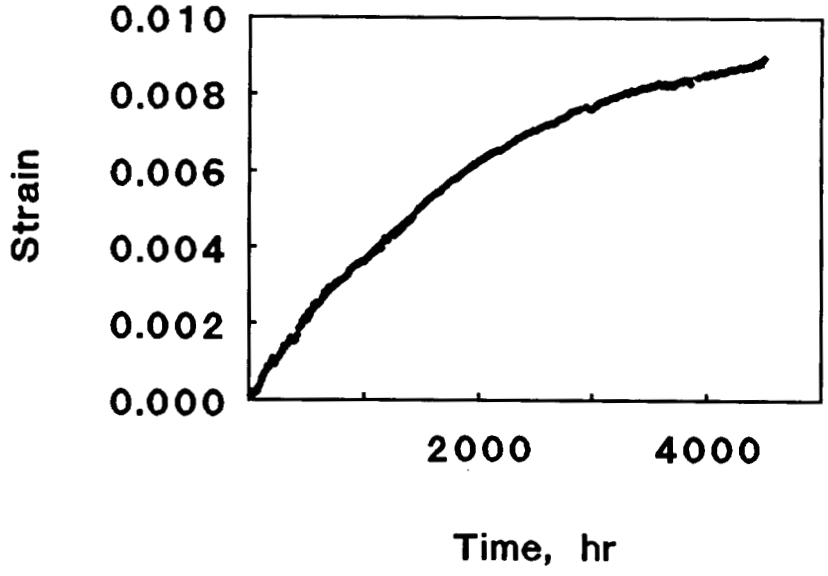

Figure 2. Extended creep curve for NT-154. Note that transient creep occurs over the entire creep period. The minimum creep rate was determined by a least squares fit over the last 200 hr of the creep curve.

Results and Discussion

NT-154: Initial tests on the NT-154, as reported in the previous mid-year report indicated the presence of long term transient creep behavior for this material. This has now been confirmed on long term creep specimens. As illustrated in Figure 2, transient creep is observed for the full test period (>4500 hr). Both specimens exhibit creep rates of less than 2×10^{-9} s^{-1}. In all, 14 creep and creep rupture tests were conducted. For all conditions studied, transient creep dominated the deformation behavior. Transient creep occurred as a consequence of devitrification of the intergranular bonding phase in this material.

The long transient behavior suggests that the microstructure of the material is slowly modified by exposure to elevated temperatures. Similar observations were made earlier on AY6 (made by GTE), in which case the increase in creep resistance of the material was attributed to devitrification of the glass phase at Si_3N_4 grain interfaces. The devitrification process was slow, and only

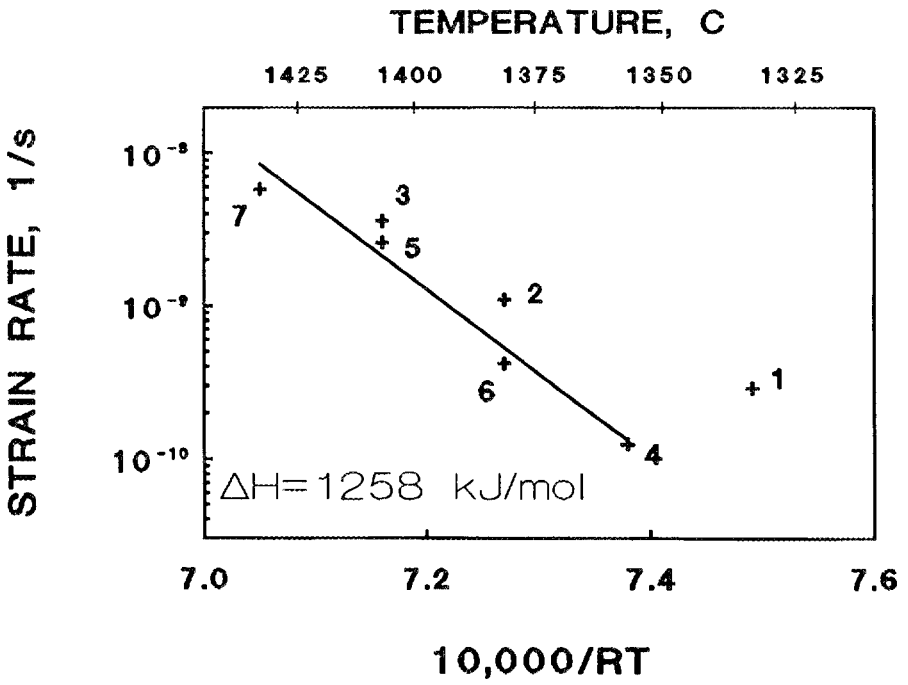

Figure 3. Activation energy for creep of NT-154 silicon nitride.

affected the creep rate when the narrowest boundaries between the grains became devitrified.

Using the data at one applied stress over a range of temperatures, we determined the activation energy for creep as 1,250 kJ/mol, as shown in Figure 3. Because the apparent activation energy for creep, ≈1,250 kJ/mol, is greater than the heat of formation of Si_3N_4, 744.8 kJ/mol [2], creep in this material is probably not controlled by any of the normal creep mechanisms (diffusion, climb of dislocations, etc.) used to explain the creep of ceramic materials. This high apparent activation energy may be a consequence of cavity formation in the silicon nitride, which has been reported by a number of investigators for NT-154 [3,4]. TEM studies at NIST and elsewhere have confirmed the formation of cavities in NT-154. Cavities in Si_3N_4 usually form in the glass that surrounds the Si_3N_4 grains, so the estimation of the activation energy for cavitation given here is specific for cavity formation in glass. From the work of Raj and Ashby, the activation energy for cavity formation is $16 \cdot \pi \cdot \Gamma^3 / 3 \cdot \sigma^2$, where Γ is the surface tension of the cavity, and σ is the local stress. By assuming Γ=0.3 J/m^2 (a normal value for glass at high temperature) and σ= 1 to 2 GPa (i.e. the cohesive stress of glass) an activation energy ranging

from 600 to 2400 J/mol can be calculated. This range of activation energies is consistent with those measured in the present experiment, tending to support our assumption that creep is a cavitation controlled process.

From a practical point of view, the high apparent activation energy for creep indicates a sharp transition in the performance of this material at elevated temperatures. Based on other creep studies conducted at NIST on structural ceramics, the only material that has better creep behavior is α-SiC. However, this material has a lower fracture toughness (≈2 MPa-$m^{\frac{1}{2}}$ for the SiC compared to ≈6 MPa-$m^{\frac{1}{2}}$ for the Si_3N_4), which increases its susceptibility to thermal shock and to foreign particle damage.

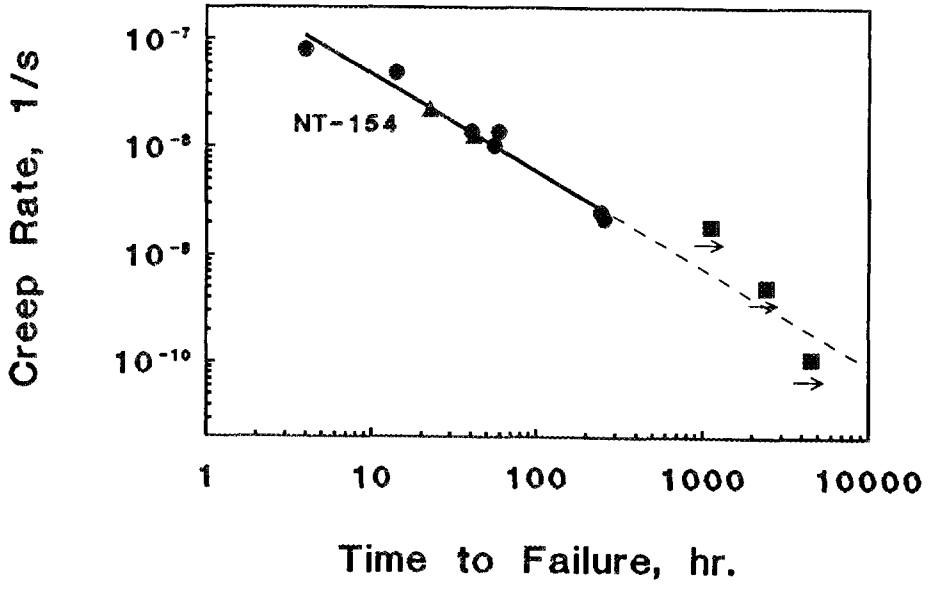

Figure 4. Creep rupture data: minimum creep rate as a function of the time to failure for NT-154. Time-to-failure seems to be determined uniquely by the rate of creep.

To determine the susceptibility of the NT-154 to stress rupture, nine specimens were crept to failure. Both the time to failure and the creep rate were measured during these experiments. A tensile creep stress exponent (n) of 6.9 has been determined from the data over the range of applied stresses from 75 to 150 MPa. As can be seen in Figure 4, all of the creep rupture data fall on a single

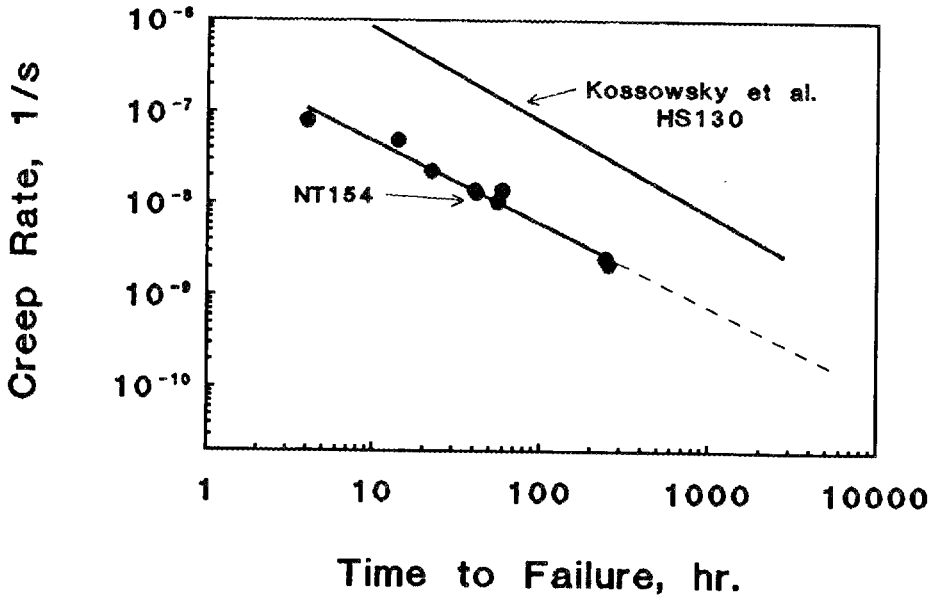

Figure 5. A comparison of Monkman-Grant curves for NT-154 and NC-130 (Kossowsky et al.).

curve when the creep rate is plotted as a function of the time to failure, a so-called Monkman-Grant curve. Regardless of test temperature or level of applied load, the time to rupture can be represented as a power function of the creep rate, $t_f = B \cdot \dot{\varepsilon}^{-m}$, figure 4. The power law exponent of this material, 1.12, was slightly greater than 1, in contrast to metallic alloys which are equal to or slightly less than 1. Most other ceramic materials studied by the group also have a stress exponent, m, slightly greater than 1.

The possibility of a creep rupture threshold at creep rates less than 2×10^{-9} s^{-1} is suggested by the fact that no failures were observed for exposure times exceeding ≈250 hr. Two specimens exhibiting minimum strain rates slightly greater than 2×10^{-9} s^{-1} failed at ≈250 hr, while a third specimen with a minimum creep rate of slightly less than 2×10^{-9} s^{-1} survived for over 1000 hr. Furthermore, the strain at failure for the two specimens, 0.41% and 0.58%, was considerably less than the strain, 1.3% of the surviving specimen. Although we suspect a change in the fracture mechanism at the threshold, no significant differences in microstructure were observed in the course of the study.

The Monkman-Grant representation of creep rupture behavior was first applied to silicon nitride (HS-130, a magnesia doped material) by Kossowsky et al., who showed that the strain exponent of the Monkman-Grant curve had a value of -1, compared to -1.12 in the present study, Figure 5. The two sets of data are displaced from one another, indicating a factor of ≈10 increase in time-to-failure at the same strain rate for the HS-130. Therefore, the strain-to-failure is greater for the HS 130, i.e. it is more ductile than NT-154. The creep rate for the NT-154 is, however, so much better than that of the HS-130, that at a given stress the failure time of the NT-154 is several orders of magnitude better than that of the HS-130. For example, at 1385°C and 70.5 MPa the HS-130 creeps at a rate of $\approx 4.7 \times 10^{-7} s^{-1}$, while at the same temperature and stress, the NT-154 creeps at a rate of $\approx 3.5 \times 10^{-10} s^{-1}$. Referring to the Monkman-Grant curves for these materials, the expected lifetime of the NT-154 is ≈2500 hr, while that for the HS-130 is ≈12 hr. Thus, even though the NT-154 is less ductile than the HS-130, its greater resistance to creep makes it the superior material with regard to failure by creep rupture. This curve, in combination with creep curves, can be used to establish stress allowables for high temperature applications. This is shown in Figure 6, where lifetime predictions for NT-154 are shown. The predictions indicate that the material can withstand a combined stress and temperature of about 75 MPa and 1370°C for a period of about 1 year.

GN-10: Tensile creep tests on Garrett's GN-10 have also been conducted at temperatures from 1200 to 1350°C, and applied stresses from 75 to 150 MPa. The creep rates range from approximately 5×10^{-9} to $10^{-7} s^{-1}$ over these conditions. The activation energy for creep of this material is ≈1230 kJ/mol, as determined from the plot shown in Figure 7, and is virtually identical to that obtained for the NT-154. Times to failure taken from eight of these specimens range from 3 to 850 hrs, and, when plotted in a Monkman-Grant fashion, exhibit a slope of 0.96, as shown in Figure 8. This value is very close to that obtained previously on the NT-154 material, although the amount of data is limited. As with the NT-154, the GN-10 satisfies a Monkman-Grant curve when the strain rate is plotted as a function of the failure time. A comparison of Monkman-Grant curves for the NT-154, GN-10, and HS-130 (Figure 8) indicates that, although the three curves are not identical, they are similar enough that all three materials can be represented by the same Monkman-Grant curve. When this happens, the material exhibiting the greatest resistance to creep also exhibits the greatest resistance to creep rupture, in this case the NT-154. Again, referring to the Monkman-Grant curves for these

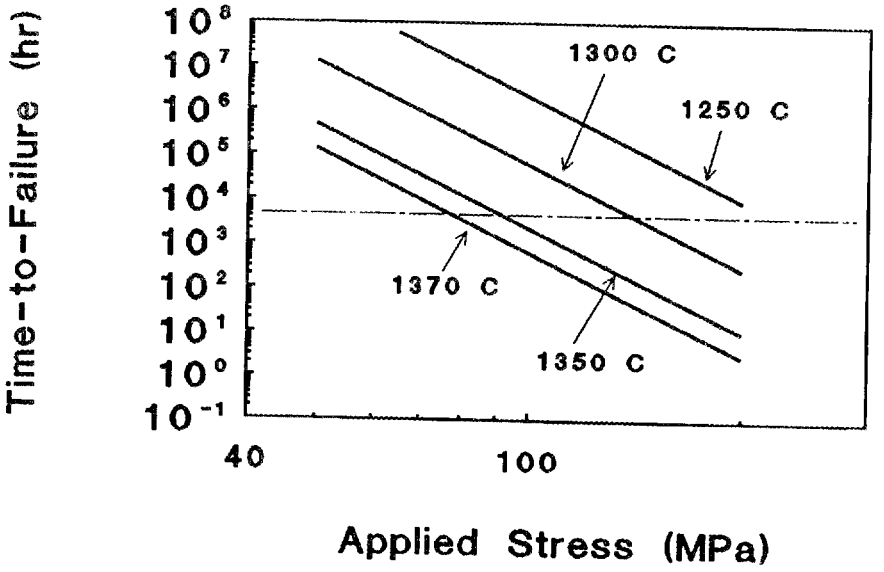

Figure 6. Lifetime predictions for NT-154 silicon nitride. This material is expected to survive combined stress and temperature of 75 MPa and 1370°C for 1 year.

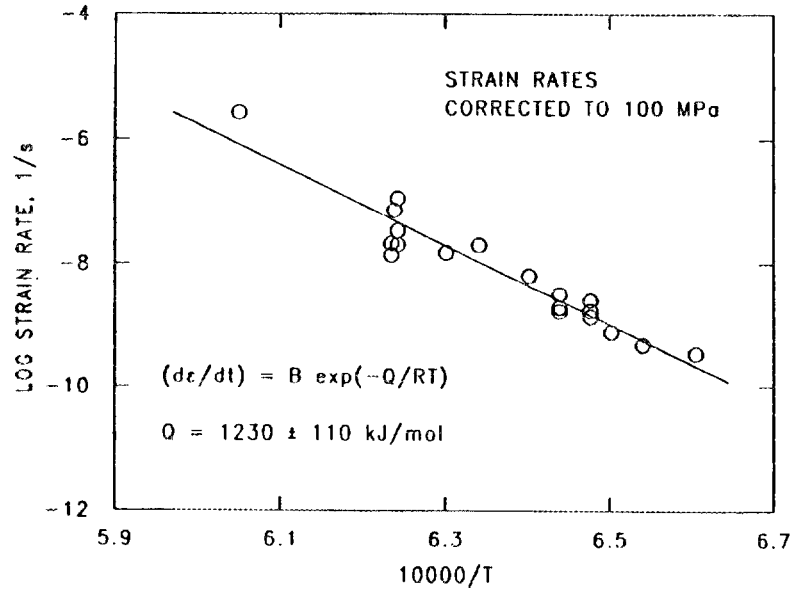

Figure 7. Activation energy for creep for GN-10 silicon nitride.

materials, the expected lifetime of the NT-154 is ≈2500 hr, for GN-10 is ≈15 hr, while that for the HS-130 is ≈12 hr.

As above for the NT-154, the Monkman-Grant curve for GN-10, in combination with creep curves, can be used to establish stress allowables for high temperature applications. This is shown in Figure 9, where lifetime predictions for this material are shown. A comparison of lifetimes for NT-154 and GN-10 are shown in figure 10. The superior high temperature behavior of the Nt-154 is evident.

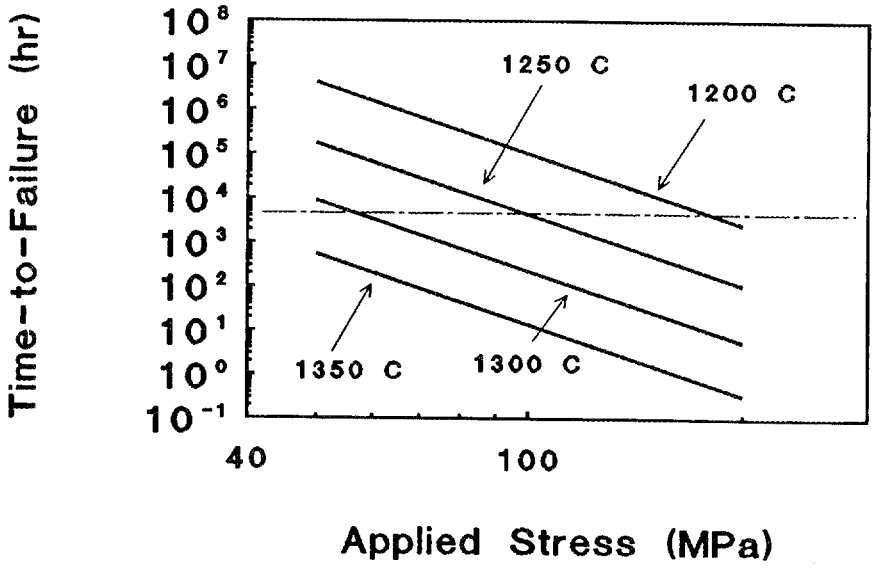

Figure 8. Lifetime predictions for GN-10 silicon nitride, based on Monkman-Grant curve and creep curves.

Both NT-154 and GN-10 exhibit similar activation energies for creep. NT-154 is the more creep-resistant material but GN-10 has a higher strain-to-failure for a given temperature. The data collected on the GN-10 and a comparison with the NT-154 has been presented at the Annual Meeting of the American Ceramic Society, April 27 to May 2, 1991, Cincinnati, OH.

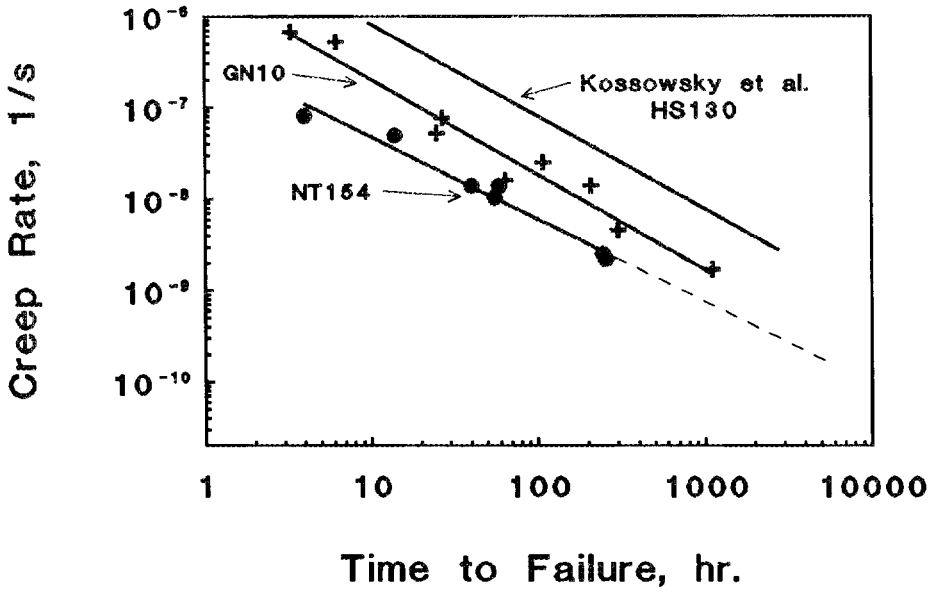

Figure 9. Comparison of Monkman-Grant behavior of NT-154, GN-10, and HS-130.

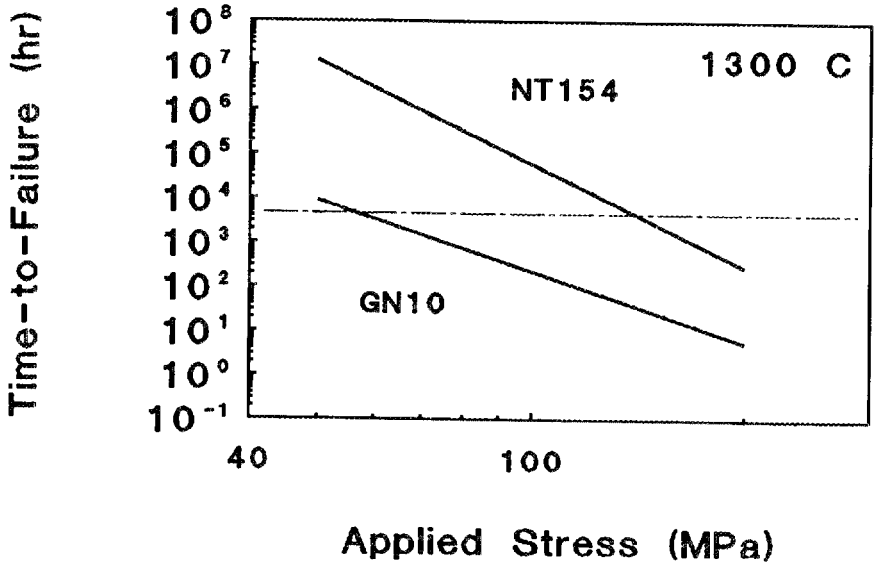

Figure 10. Comparison of lifetime predictions for NT-154 and GN-10 silicon nitrides.

In the coming months, additional studies will be conducted on NT-154 in order to determine the effect of annealing on the creep behavior. This work is being conducted in collaboration with Annette Reese (Comfort) at Allied-Signal. The objective of the work will be to determine if annealing is a viable procedure for improving creep resistance in silicon nitride. A similar program will be started later in the year with Bernie Busavne of the Garrett Processing Division. In this research, we will be investigating GN-10 instead of NT-154. A second program will be started to characterize the creep and creep rupture behavior of PY6, a grade of silicon nitride made by GTE. This work is being done in collaboration with Pramod Khandelwal of Allison Gas Turbine. In this program we hope to obtain a complete evaluation of the creep and creep rupture behavior of PY6. Studies on the NT-154 and PY6 are being conducted as part of the DOE Reliability program.

Status of Milestones

All milestones are on schedule.

Publications

B. J. Hockey, S. M. Wiederhorn, W. Liu, J. G. Baldoni and S.-T. Baljan, "Tensile Creep of Whisker Reinforced Silicon Nitride", J. Mat. Sci.

S. M. Wiederhorn and B. J. Hockey, "High Temperature Degradation of Structural Composites", to be published in Proceedings of the Seventh Cimtec World Ceramics Congress, 1990.

S. M. Wiederhorn, B. J. Hockey and T.-J. Chuang, "Crack Growth, Creep, and Creep Rupture at High Temperatures", to be published in *Toughening Mechanisms in Quasi-Brittle Materials*, 1990.

S. M. Wiederhorn, "Creep and Creep Rupture of Ceramic Matrix," to be published in FLIGHT-VEHICLE MATERIALS, STRUCTURES AND DYNAMICS TECHNOLOGIES-ASSESSMENT AND FUTURE DIRECTIONS, Edited by Ahmed K. Noor and Samuel L. Venneri

D. C. Cranmer, B. J. Hockey, S. M. Wiederhorn and R. Yeckley, "Creep and Creep-Rupture of HIP-ed Si_3N_4," Ceram. and Eng. Sci. Proc. (1991) in press.

Talks

D.C. Cranmer, S.M. Wiederhorn and B.J. Hockey, "Tensile Creep and Creep Rupture of Silicon Nitride," 93rd Annual Meeting of the American Ceramic Society, Cincinnati, OH, April 27 to May 2, 1991

S.M. Wiederhorn and B.J. Hockey, "Creep of Granular Ceramics at High Temperatures," 93rd Annual Meeting of the American Ceramic Society, Cincinnati, OH, April 27 to May 2, 1991

References

1. D. F. Carroll, S. M. Wiederhorn and D. E. Roberts, J. Am. Ceram. Soc., 72 [9] 1610-1614 (1989).

2. JANAF Thermochemical Tables, 2nd ed., U.S. Govt. Printing Office, Washington, DC, 1971.

3. D. C. Cranmer, B. J. Hockey, S. M. Wiederhorn and R. Yeckley, "Creep and Creep-Rupture of HIP-ed Si_3N_4," Ceram. and Eng. Sci. Proc. (1991) in press.

4. T.A. Nolan, L.F. Allard, D.W. Coffey, M.K. Ferber and K.L. More, "Microstructural Characterization of Tensile and Flexural Creep Deformation and Fatigue in a Si_3N_4 Ceramic," Presented at the 93rd Annual Meeting of the American Ceramic Society, Cincinnati, OH, April 27 to May 2, 1991.

5. R. Raj and M. F. Ashby, Acta Metall., 23 653 (1975).

6. R. Raj, Acta Metall., 26 995 (1978).

Development of a Fracture Toughness Microprobe

G. M. Pharr and D.S. Harding (Rice University)

Objective/scope

The objective of this study is to develop a technique for measuring fracture toughness in thin films and small volumes on a spatially resolved basis using the Mechanical Properties Microprobe at ORNL (MPM or Nanoindenter). The MPM is currently used to measure both hardness and elastic modulus with a spatial resolution of better than 1 μm. Once developed, the technique will be useful in probing toughness at the scale of the microstructure and thus in establishing important relations between microstructure and fracture behavior.

Technical progress

The method we are pursuing is based on the cracking which occurs when brittle materials are indented by a sharp indenter, such as a Vickers diamond. The indentation cracking method has been developed by several investigators over the last 15 years[1-12]. A critical review of its predictive capabilities has been presented by Anstis et al.[7], who have applied the method to a wide variety of ceramics and glasses and found its accuracy to be better than 40%.

The basis of the method is to compute the fracture toughness, K_c, from the length of the cracks, c, through the semi-theoretical relation[7]

$$K_c = \alpha \left(\frac{E}{H}\right)^{1/2} \left(\frac{P}{c^{3/2}}\right) \qquad (1)$$

Here, α is an empirically determined geometric constant (for a Vickers indenter, its value is about 0.016 [7]), P is the indentation load, and E and H are the elastic modulus and hardness of the material, respectively. One attractive feature of applying this method with the MPM is that, in addition to being able to produce very small indents with very precise positioning, the load-displacement data provided by the instrument can be used to establish the local modulus and hardness. Since a knowledge of both these quantities is needed for the computation of toughness, the MPM provides a simple and convenient means for obtaining *all* the data needed to measure toughness on a spatially resolved basis.

To date, the indentation cracking method has been applied to indents which, by MPM standards, are fairly large. The indents typically used in the indentation cracking method are produced at loads of 1000 grams or greater, and the cracks are of the order of 100 μm or so in length. Since the size of the cracks sets a limit on the spatial resolution of the technique, much of the work in

the program is concerned with how indent size can be reduced without having the method break down or become impractical.

The main issue addressed during the last semi-annual reporting period dealt with the fact there are often well defined loads below which indentation cracking does not occur. For example, for a Vickers indenter, cracking thresholds in most ceramics are about 25 gms or more[13,14]. Since the indents associated with these loads are relatively large (several microns wide), cracking thresholds place severe restrictions on the spatial resolution which can potentially be achieved.

We have now established that cracking thresholds can be substantially reduced by using indenters with non-standard geometries. The indenter we have chosen for further studies has the geometry of the corner of a cube. With this indenter, cracking thresholds can be reduced to loads of 0.5 grams or less in most brittle materials (corresponding to sub-micron sized indents). The objective of our current work is to establish if Eqn. (1) works as well for the cube corner indenter as it does for the Vickers indenter, and if so, to establish a value for the geometric constant, α.

A great deal of work during this period dealt with setting up the equipment needed to assess the usefulness of the cube corner diamond in the measurement of fracture toughness. A number of model brittle materials were obtained and testing machines were set up to measure their toughness using the indentation method and, for independent verification, the chevron notch method. Local experts at the University of Houston were consulted on how to obtain meaningful results from the chevron notch test. The testing will be carried out in our Instron machine using a three-point bend bend fixture which was designed during this period and is now in the final stages of construction. Three model brittle materials - fused quartz, soda-lime glass, and pyrex glass - were obtained in polished sheet form to be used in our initial studies, and arrangements have been made to machine chevron notch specimens from these materials using special grinding equipment at the University of Houston. The equipment is capable of mass producing specimens in lots of approximately 12. To perform the hardness testing, our Buehler microhardness tester was modified to accommodate a cube corner diamond.

In the next few months, the toughness of the model materials will be measured, first with the chevron notch method, and then using the indentation method and the cube corner diamond. The results will be used to determine how well the method works and what the value of α in Eqn. (1) is for the cube corner diamond. Once the assessment of these materials is complete, other materials will be tested to expand the assessment of the method.

Another effort undertaken during this period involved the construction of a simple acoustic emission sensor which was incorporated into the Nanoindenter to explore whether acoustic emission can be used in the identification of indentation cracking thresholds. An exploratory study was undertaken in which acoustic emissions were monitored from fused silica, soda lime glass, sapphire, silicon, and tungsten. A minor problem was encountered in that noise levels were relatively high, making identification of thresholds difficult. The noise appears to originate in the Nanoindenter head, which is

driven by an analog signal having a characteristic frequency related to the clock rate in the D-A converter. After consulting the with the manufacturer, it appears that this problem can be resolved in future work by changing the capacitor which damps the signal.

Our study of the 5 materials listed above indicated that all are acoustically active when indented with the cube corner indenter. While this was expected for fused silica, soda lime glass, sapphire, and silicon, it was somewhat of a surprise for tungsten, since tungsten does not crack. Our suspicion is that the tungsten emissions, whose magnitude is small in comparison to those from the brittle materials, are caused by stick-slip of the diamond. This will be examined in the future work by using blunter indenters to minimize frictional effects. Despite this, the preliminary work suggests that the sensor has the ability to detect cracking at very small indentation loads, and the sensor will be used in future work to explore the utility of acoustic emission in identifying cracking thresholds. This could lead to an alternative means for measuring toughness.

Work was also undertaken during this period to establish the morphology of cracks which form underneath very small indents produced by the Nanoindenter. While the morphology of the surface traces of cracks in a variety of materials was established in earlier work, of particular interest here was to study the *sub-surface* crack structure of at least one brittle material. A method by which this could be accomplished was developed and applied to silicon. A jig was built on which a thin silicon wafer was mounted with bonding resin and then cracked by applying 4-point bending to the plate on which the wafer was mounted. This produced a very straight cleavage crack through the thickness of the specimen. The crack was subsequently closed by removing the bending forces, and numerous indentations were made on and around the crack with the Nanoindenter. The two halves of the wafer were then separated along the cleavage crack to be viewed edge-on in the SEM, thus revealing a cross-section of the structure underneath the indent.

The technique worked extremely well, and we have now developed a complete picture of the surface and subsurface cracking which occurs in silicon. One of the most interesting features of it is how the surface and subsurface cracks are linked - the radial, median, and lateral cracks are all interconnected in a way which suggests that they do not develop independently. We also found that for the Berkovich indenter, there is a load below which no cracking - either surface or subsurface - occurs. This cracking threshold load is around 1 gm.

Status of milestones

All milestones are proceeding on schedule.

Publications

A short paper entitled "New Evidence for a Pressure-Induced Phase Transformation During the Indentation of Silicon" was accepted for publication

in the *Journal of Materials Research*. This paper results from SEM observations of cracked indents in silicon. It is now in press.

A second paper dealing with the sub-surface cracking observations in silicon is in preparation.

References

1. A.G. Evans and E.A. Charles, "Fracture Toughness Determinations by Indentation", J. Am. Ceram. Soc. **59**, 371 (1976).
2. B.R. Lawn, T. Jensen, and A. Arora, "Brittleness as an Indentation Size Effect", J. Mater. Sci. Let. **11**, 573 (1976).
3. B.R. Lawn and A.G. Evans, "A Model for Crack Initiation in Elastic/Plastic Indentation Fields", J. Mater. Sci. **12**, 2195 (1977).
4. B.R. Lawn and D.B. Marshall, "Hardness, Toughness, and Brittleness: An Indentation Analysis", J. Am. Ceram. Soc. **62**, 347 (1979).
5. T.P. Dabbs, D.B. Marshall, and B.R. Lawn, "Flaw Generation by Indentation in Glass Fibers", J. Am. Ceram. Soc. **63**, 224 (1980).
6. B.R. Lawn, D.B. Marshall, and P. Chantikul, "Mechanics of Strength-Degrading Contact Flaws in Silicon", J. Mater. Sci. **16**, 1769 (1981).
7. G.R. Anstis, P. Chantikul, B.R. Lawn, and D.B. Marshall, "A Critical Evaluation of Indentation Techniques for Measuring Fracture Toughness: I, Direct Crack Measurements", J. Am. Ceram Soc. **64**, 533 (1981).
8. P. Chantikul, G.R. Anstis, B.R. Lawn, and D.B. Marshall, "A Critical Evaluation of Indentation Techniques for Measuring Fracture Toughness: II, Strength Method", J. Am. Ceram Soc. **64**, 539 (1981).
9. J. Lankford, "Indentation Fracture in the Palmqvist Regime: Implications for Fracture Toughness by the Indentation Method", J. Mater. Sci. Let. **1**, 493 (1982).
10. K. Niihara, "A Fracture Mechanics Analysis of Indentation Induced Palmqvist Crack in Ceramics", J. Mater. Sci. Let. **2**, 221 (1983).
11. M.T. Laugier, "Palmqvist Cracking in WC-Co Composites", J. Mater. Sci. Let. **4**, 207 (1984).
12. M.T. Laugier, "Palmqvist Indentation Toughness in WC-Co Composites", J. Mater. Sci. Let. **6**, 897 (1987).
13. J. Lankford and D.L. Davidson, "The Crack-Initiation Threshold in Ceramic Materials Subject to Elastic/Plastic Indentation", J. Mater. Sci. **14**, 1662 (1979).
14. J. Lankford, "Threshold-Microfracture During Elastic/Plastic Indentation of Ceramics", J. Mater. Sci. **16**, 1177 (1981).

3.5 NONDESTRUCTIVE EVALUATION DEVELOPMENT

Nondestructive Characterization
D. J. McGuire (Oak Ridge National Laboratory)

Objective/scope

The purpose of this program is to conduct nondestructive evaluation (NDE) development directed at identifying approaches for quantitative determination of conditions (including both properties and flaws) in ceramics that affect the structural performance. Those materials that have been seriously considered for application in advanced heat engines are all brittle materials whose fracture is affected by structural features whose dimensions are on the order of the dimensions of their microstructure. This work seeks to characterize those features using high-frequency ultrasonics and radiography to detect, size, and locate critical flaws and to measure nondestructively the elastic properties of the host material.

Technical progress

Ultrasonics - W. A. Simpson, Jr., and K. V. Cook

We have received three large ceramic tiles for nondestructive determination of the elastic moduli. Two of these tiles are made of fused silica and the third is alumina. The tiles are approximately 0.42 m square and 76 mm thick and weigh about 27 kg (silica) and 46 kg (alumina). Initial ultrasonic examination revealed that the silica was far too attenuative to perform conventional pulse-echo velocity measurements using either pulse-overlap or pulse-digital techniques. Through-transmission measurements indicated that reasonable signal levels could be achieved at frequencies up to 2.5 MHz for compressional waves and 1 MHz for shear waves. The lack of two or more echoes with this approach, however, would necessitate some form of nonconventional processing in order to provide accurate results.

After considerable experimentation, two possible approaches were selected. In both methods, a signal propagated through the sample is acquired and digitized. The time from the beginning of the record to the signal of interest is the sum of the propagation time through the sample and an (unknown) offset time from the beginning of the record to the issuance of the elastic wave from the transmitting transducer. A second signal is then acquired on a sample of known thickness and for which the velocity is known from independent measurements. This record also contains the same unknown offset time. The difference in these records is thus independent of the offset time and dependent only on the propagation time of the wave through the differential thickness of the sample of interest.

The differences in the two techniques are centered on how the differential propagation time is determined. In the first technique, the records are Fourier transformed and the cross correlation computed. This record peaks at the shift corresponding to the time difference between the two signals. In the second technique, the differential propagation time is measured directly using pulse digital methods. The former technique, which

is equivalent to digital pulse-overlap, gave better results when quasi-monochromatic radiation was used. The latter approach requires relatively broadband radiation.

For both techniques, the velocity in the unknown sample is easily determined from the differential propagation time and the velocity in the known standard. Several materials for which the velocity was measured by conventional means were used as the "unknown" sample. Both techniques yielded virtually identical results, which agreed well with the conventional measurements. Because the cross-correlation approach requires additional processing time, all subsequent measurements were made using the pulse-digital technique.

Measurements were made at four locations on each of the two silica blocks. The variation observed was more than four times larger than the computed error for a single measurement (several measurements were also made at each location to confirm these computations). This suggests a considerable variation in the point-to-point density of the samples. It is easy to show that the fractional variation in the density is twice that of the observed compressional or transverse wave velocities. The latter were consistent and averaged about 4% (the single-measurement error was about 1%).

Although four measurements are not sufficient to provide a highly accurate estimate of the mean velocities, our results suggest a point-to-point density variation of about 8%. This is not surprising in light of the method of fabrication of these blocks.

The mean values for the elastic properties of the two silica blocks were: shear modulus - 7.5 GPa, Young's modulus - 16.1 GPa, and Poisson's ratio - 0.07.

These measurements represent the first time that we have had to deal with ceramic materials that were either too attenuative or too thick for application of standard velocity measuring techniques. The results obtained are believed to be accurate to about 1% and extend our capabilities to materials that are too difficult for conventional analysis.

The third tile was made of alumina. The weight of 46 kg gives it a density of about 86% of the theoretical value. Surprisingly, the tile is sufficiently transmissive to permit conventional pulse-echo determination of the elastic wave velocities. This is in contrast to the previous tiles, where a special through-transmission measurement technique had to be developed in order to determine the wave velocities. As before, measurements were made at four points on the tile. The mean values for the elastic properties were: shear modulus - 90 GPa, Young's modulus - 223 GPa, and Poisson's ratio - 0.24.

We are engaged in construction of a system to implement high-frequency synthetic aperture ultrasonic inspection of structural ceramics. Our previous work has shown that this approach has considerable potential for inspection of "thick" ceramics (i.e., those having a thickness greater than the 3-mm penetration depth obtainable with conventional focused transducers). Good results were obtained when using ultrasonic energy focused on the surface of the sample with subsequent processing of the data to improve the signal-to-noise ratio and to "focus" the desired internal plane of the ceramic. These results were obtained using manual positioning of the ultrasonic transducer, which is clearly untenable for rapid inspection.

In order to automate this process, however, it is necessary to build or purchase hardware capable of integrating the functions of generating the requisite transducer motion and acquiring the resulting data. We have already written the software necessary to perform the data processing.

Two approaches are possible for solving the hardware problems. The first involves design and construction of the circuitry necessary to position the ultrasonic transducer using one of our existing scanners without modification. The second approach is to purchase suitable modifications to our scanner from an outside vendor. Both avenues are being investigated.

A commercial, general purpose I/O board has been obtained for our 386-based computer. This board has 48 I/O lines, which are software selectable as input or output in groups of 8 bits, more than sufficient for the problem at hand. A primitive interrupt handler has been written and demonstrated, which will permit the board to respond to signals generated by the ultrasonic hardware. A minicomputer software package for controlling the high-speed digitizer, effecting temporal averaging, and transferring the acquired data to magnetic tape was available from our previous ceramics work. This package is being rewritten for a PC with the magnetic tape drive replaced by a high-speed ram disk. Because of the rate at which data must be acquired and processed for a viable synthetic aperture technique, all programming has been done in assembly language for maximum speed.

Most of the software for controlling the ultrasonic scanner, digitizing the full analytic signal from the ceramic, and transferring the data to high-speed ram disk has now been written for a PC. Programs for controlling the commercial I/O board have also been developed and tested. A preliminary test of the system indicated that some modifications to the scan tank controller will have to be made because of the characteristics of the PC interrupt system. (Unlike our minicomputer interrupt hardware, the PC requires that the interrupt signal be asserted until the CPU acknowledges the interrupt.)

To our surprise, relatively long data cables could be driven directly by the controller and PC hardware without the need for line drivers at either end of the cable. In a preliminary test of the system, however, the PC was able to read correctly the transducer position counters in the controller, but the system was not responding reliably to the interrupt signals generated by the ultrasonic hardware. This appears to be a simple problem of pulse distortion in the connecting cable, which can be corrected by installing line drivers at both ends of the interrupt cable. We are not yet sure of this, however, as the response of the PC to an interrupt request is fundamentally different from that of our minicomputer, for which the scan controller was originally built.

Using a separate pulse generator to simulate an interrupt request on the PC, we have been able to read data asynchronously from the scan tank controller at a rate commensurate with that generated by the ultrasonic hardware and to store the acquired data on a high-speed ram disk. This result suggests that the system should work well for the acquisition of synthetic aperture data when we can reliably interrupt the PC with the ultrasonic signals.

We have also located two commercial vendors capable of upgrading our 4-bit, high-speed digitizer to a full 8-bit unit. One provides a board-level flash digitizer, which may be mounted in and controlled by a PC.

The second is a variable range option for our existing hardware, which permits the voltage range over which the ultrasonic signal is digitized to be compressed, thus yielding effective 8-bit (or greater) discretization. The latter system is much less expensive but may have some drawbacks for our current work. Neither vendor can supply the software necessary to implement synthetic aperture techniques, but both are willing to make available the source code for their controller software for modification by us. It is not clear that the direct cost and modification time involved would achieve the desired goal more efficiently than our present *ab initio* approach.

Computerized Tomography - B. E. Foster

A triangle of silicon nitride has been used to produce beam-hardening correction tables. Most of the beam-hardening artifacts previously observed in the larger ceramic samples have now been corrected. The Exebyte (8-mm) tape drive developed an internal short circuit and has been repaired by the vendor, reinstalled, and is operating properly. The auxiliary TK-50 tape drive is being used for backing up data. During the evaluation of three ceramic (one SiC and two Si_3N_4) rotors with the CT System, a circular artifact was noted within the area of interest with a decrease in signal-to-noise ratio and failure to reconstruct a large data file of approximately 40 MB. The manufacturer recently installed an updated version of reconstruction and display software, which corrected everything except the circular artifact within the area of interest. As a temporary solution, we will use a slightly larger ray spacing (a little loss in resolution) until we determine the cause.

A 760 MB-hard disk drive that was procured to double the disk space (380 MB) of our user disk was found to be defective during installation in December 1990. The installation of the replacement drive included formatting, transfer of necessary data and system files from tapes, and evaluation of the success of the installation. This larger disk capacity enables us to do the requested detailed scanning of several ceramic rotors.

Three ceramic rotors (two Si_3N_4 and one SiC) were scanned with the CT System. Several different scanning parameters were varied in attempts to optimize detection of any voids larger than about 0.2- to 0.3-mm diam. After final selection of the appropriate parameters (e.g., aperture, ray-spacing, scanning speed, and filter), approximately 20 CT slices at 1-mm increments were made of each rotor.

The images were reconstructed using the recently completed beam-hardening correction tables obtained with the Si_3N_4 wedge. The scans from the two Si_3N_4 rotors were uniform in density (good correction for beam hardening); however, as might be expected, the SiC rotor showed evidence of inadequate correction for beam hardening. An SiC wedge will be obtained to prepare a separate beam-hardening correction table. A few voids with diameters on the order of 0.2 mm were confirmed with repeat scans.

Milestones

All milestones are on schedule.

Publications

W. A. Simpson, Jr., and R. W. McClung, "An Ultrasonic Evaluation of Silicon Carbide Whisker-Reinforced Ceramic Composites," to be published in *Mater. Eval.*

R. W. McClung, W. A. Simpson, Jr., and D. R. Johnson were invited contributors to a chapter entitled, "Ultrasonic Tests for Advanced Structural Ceramics," *Section 15, UT Applications in Advanced Materials and Processes*, in the ASNT Nondestructive Testing Handbook on Ultrasonic Testing, in press.

B. E. Foster and F. Hopkins (Scientific Measurement Systems, Inc.), "High Resolution Imaging of Ceramic Materials With Digital Radiography, Computed Laminography, and Computed Tomography," published in the abstracts of The WATTEC Conference, February 20–23, 1990, Knoxville, Tenn.

NDE Standards for Advanced Ceramics

R. W. McClung (Oak Ridge National Laboratory)

The development of standards is important for the establishment of reliability and acceptance of advanced structural materials. Committee C-28 on Advanced Ceramics has been organized in the American Society for Testing and Materials (ASTM) to address this issue. One of the activities of the C-28 committee is nondestructive examination (NDE). The Task Group on NDE is reviewing existing standards (primarily developed for metals) to determine potential applicability for ceramics. Use of existing or modified standards is more efficient than generation of new documents and will assure the input of a large body of NDE expertise. Close liaison has been established with ASTM Committee E-7 on Nondestructive Testing, and documents are in various stages of review, recommendations for change, modification, and balloting. R. W. McClung is a member of both committees and the official liaison.

Liaison and technical support have been continued between ASTM Committees C-28 and E-7. To date, 26 E-7 NDE standards have been reviewed in detail with recommendations made to E-7 for modifications. Successful action is complete on 13 documents and E-7 balloting action is in progress on 8 items; the others require action by C-28. A table of ultrasonic velocities in typical ceramic materials was prepared and sub-mitted to E-7 for incorporation into an existing NDE standard. At a meeting in January 1991, approval was obtained for an E-7 subcommittee ballot on this item. A document on fabrication of seeded voids in pressureless sintered ceramics was balloted in C-28 at the subcommittee level in December 1990. Comments received during the ballot will be processed for approval at the May 1991 meeting of C-28 prior to further ballot action. A guideline document that describes available approved standards and their applicability for examination of ceramics was successfully balloted at both subcommittee and committee levels of C-28; it subsequently was approved in the January 1991 Society ballot. A Task Group advisory ballot is being conducted on five new E-7 standards covering specific techniques of liquid penetrant examination. Future actions in the Task Group on NDE include preparation of reference standards and procedures for ultrasonic examination of ceramics. R. W. McClung was appointed chairman of Subcommittee C28.02, Design and Evaluation, which now includes both NDE and Probabilistic Design.

X-ray Computed Tomographic Imaging

W. A. Ellingson, N. Gopalsami (Argonne National Laboratory), and T. Luethi (visiting Scientist, EMPA Laboratory, Zurich, Switzerland)

Objective/scope

The objective of this program is to develop X–ray computed tomographic (CT) imaging technology for application to structural ceramic materials. This technique has the potential for mapping short–range (<5 mm) and long–range (>5 mm) density variations (to perhaps 0.5–1%), detecting and sizing high– and low–density inclusions, and detecting and sizing (within limits) cracks in green–state and densified ceramics. Use of 3-D CT imaging allows the capability of interrogating the full volume of a component and is noncontacting. It is also relatively insensitive to part shape and thus can be used to inspect components with complex shapes, such as turbocharger rotors, rotor shrouds, and large individual turbine blades.

Technical progress

The work this reporting period covers two applications of X-ray computed tomography using Argonne National Laboratories 3-D microfocus system: (1) Phase II application to monolithic injection molded Si_3N_4 (Garrett's GN-10) with an emphasis on detection of density variations perhaps induced by nonuniformity of binder distribution and (2) initial work on phase III of this research program relative to detection of whisker distributions (likely to be manifested and detected as density variations) in as-cast pressure slip-cast $Si_3N_4(w)Si_3N_4$ (also Garrett's GN-10 material). This a continuing joint project between Argonne National Laboratory and Garrett Ceramic Components of Allied-Signal Aerospace Corporation of Torrance, California.

The potential of modifying real-time microfocus X-ray imaging systems, now presently available in almost all ceramic component processing facilities, into computed tomography systems is beginning to show significant promise and benefit. There are several reasons for this: (1) the availability of faster, higher storage-capacity micro computers, (2) the availability of very high resolution video cameras—especially CCD-array cameras (i.e., 1024 by 1024 and even 2048 by 2048), (3) the availability of higher speed Analog to Digital (A/D) converters and necessary software for higher dynamic range conversions which allow more density discrimination sensitivity and (4) the availability of very user friendly image display software which runs very well on currently available microcomputers and which contains a surprising amount of image processing capability. With the advent of so-called region of interest reconstruction software codes, there also is getting to be less part-shape limitations caused by complex shapes. In addition, cooled X-ray heads (microfocus systems) are becoming available and thus the problem of low-flux at small focal spot sizes (causing extremely long data acquisition times) are also slowly being eliminated.

For ceramic process development activities, which is the focus of this applied research on use of computed tomography, there is no real problem with component size limitation as most test components tend to be in the 25-50 mm size. In addition, the work in this project has exclusively to date, been concerned with characterizing green-state ceramics and thus the problem of high density and large size (implying the need for higher X-ray energies) has not required attention.

Phase II. Injection molding: Monolithic Si_3N_4

Part 1: Detection of binder-concentration induced density variations

1) Injection Molding

We reported earlier[1] that we had obtained X-ray CT data on inserts in the Garrett T-25 turborotor fabricated by injection molding of Garrett's GN-10 Si_3N_4 material. We did not have complete data at that time on the density, porosity and relative volume fractions of components used in processing. These data have now been obtained and are presented below in Table 1.

Table 1

Molded Insert Specimen and Turbo-Rotor Data

Fabrication Method	Insert Identification	Measured Density, g/cm3	Weight % Binder	Volume % Binder	Volume % Powder	Volume % Porosity
Cold pressed	A	2.552	9	24.64	69.53	5.83
Cold pressed	B	2.519	10	27.02	67.87	5.11
Cold pressed	C	2.492	11.5	30.75	66.02	3.23
Cold pressed	D	2.422	13.5	35.08	62.73	2.19
Cold pressed	E	2.415	14.5	37.57	61.81	0.62
Cold pressed	F	2.383	15.5	39.63	60.28	0.09
Injection molded	Rotor 6	2.380	12.5	31.925	62.36	5.72
Injection molded	Rotor 9	2.384	12.5	31.973	62.45	5.88

When the organic binder content is plotted in Wt.% as a function of X-ray CT image gray scale, one obtains the relationship shown in Fig. 1.

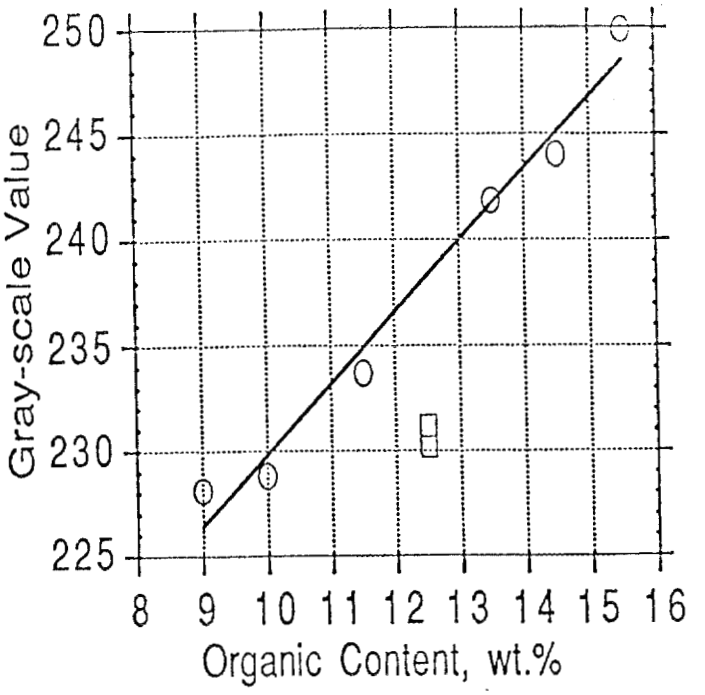

Fig. 1. Plot of X-ray computed tomography gray scale as a function of Wt.% organic in cold pressed Si_3N_4 inserts inside as-molded (injection molded) T-25 turborotors

The relationship between gray scale value and organic content is excellent for the cold-pressed samples. However, if these calibration data are then used to predict the organic content of injection molded turborotors, the correlation does not hold. The known injection molding mix organic concentration is 12.5 Wt.%. However, the corresponding gray scale value does not correlate. Clearly the ratio of volume fraction of powder to binder changes dramatically between injection molding and cold pressing and further, there is a sensitivity of X-ray CT data to these changes of about 5%.

When the volume % organic binder content is plotted as a function of X-ray CT image gray scale, one obtains the relationship shown in Fig. 2. What is important to note is that the X-ray computed-tomographic image gray scale value, is directly proportional to the volume fraction of polymeric binder and is not dependent upon the process methods; i.e., cold-pressed or injection molded. On the other hand, when one plots volume fraction of powder as a function of X-ray CT image gray scale value, one sees a definite change in sensitivity to process method, i.e., cold-pressing or injection-molding. This is shown in Fig. 3. Reasons for this will be further pursued and will be reported on in future reports.

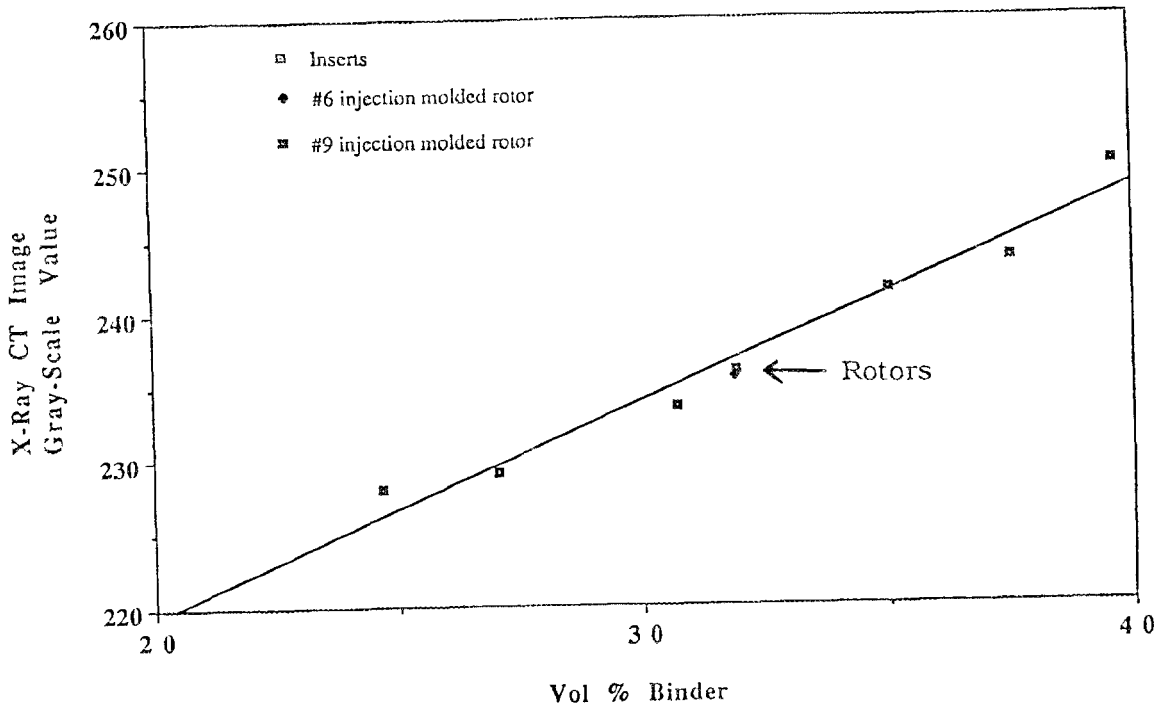

Fig. 2. Correlation between 3-D X-ray computed tomographic image gray-scale value and volume fraction of polymeric binder in Garrett's GN-10 Si_3N_4 material. Note that for volume % binder, the X-ray CT image is independent of process method and depends only on binder content.

Phase III. Pressure Slip-cast: Si_3N_4(w)Si_3N_4
Part 1: Detection of density variations as a function of whisker concentration

In this part of the program, Garrett Ceramic Components of Allied-Signal Aerospace will provide for X-ray CT analysis the specimens shown in Table 2.

Table 2.

Green-state Pressure-slip-cast Cylindrical Specimens

L/D ratio	Wt.% SiC whiskers
1.5	20, 23, 27, 30
3.0	20, 23, 27, 30

We completed 3-D X-ray microtomography data acquisition on the first L/D ratio set (L/D ≈ 1.5) using 256 X 256 reconstructions with 2 mm thick sections over the entire length of the 20 and 23 wt.% SiC(w)/Si_3N_4 (American Matrix SiC whiskers and Garrett's GN-10 Si_3N_4 material). As we noted in our last report, we had trouble maintaining the shape of

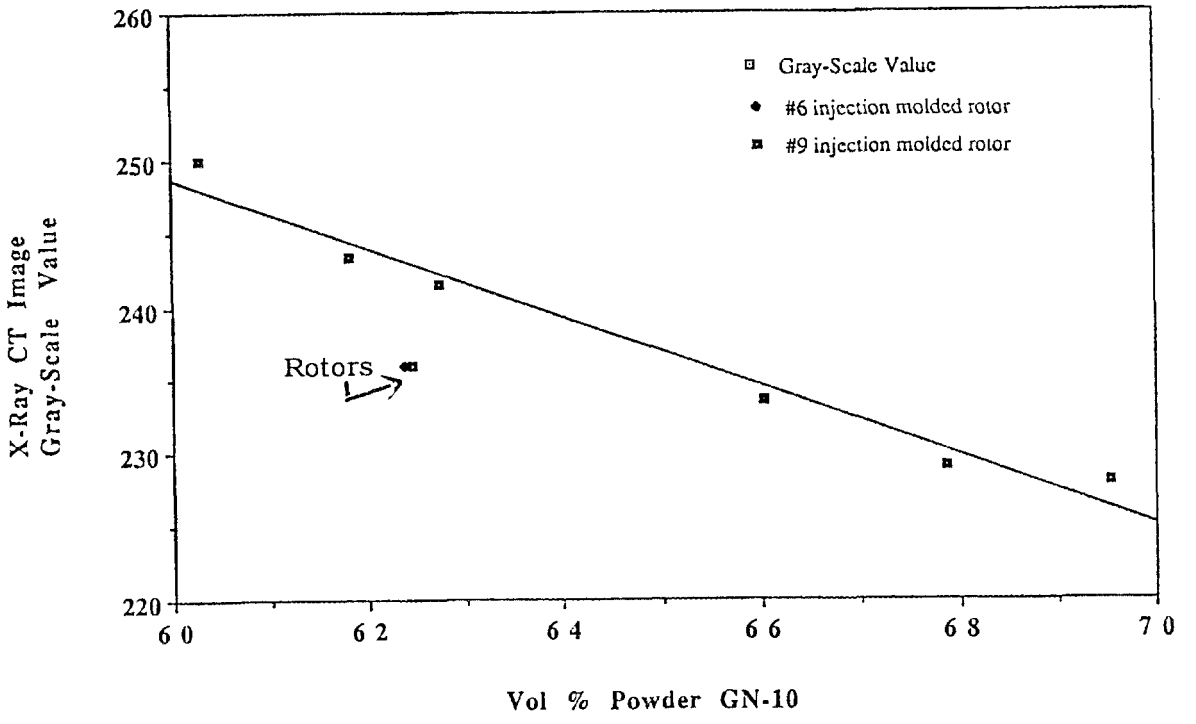

Fig. 3. Correlation between 3-D X-ray microfocus computed tomographic image gray scale value and Garrett's GN-10 S_3N_4 powder loadings for two processes: cold-pressing and injection-molding. Note that the X-ray CT data appears to be process method dependent.

the specimens for the 27 and 30 wt.% whisker loadings and they will need to be remade. We are working now with Garrett Ceramics to establish how best to handle these samples.

The slip casting parameters are given below for each of the 20, 23, 27 and 30 wt.% SiC whisker specimens.

Table 3

Slip Casting Parameters

Specimen Identification	Whiskers Wt.%	Content Wt.%	Casting Solids Pressure, psi	Slip Viscosity, cps	Density at time of demolding, g/cc
91A-013	20	69.9	40	135	2.07
S910002	23	68	40	93	2.47
S910006	27	65	40	65	2.18
91A-031	30	63	40	107	2.36

For initial diagnostic purposes, we have chosen to analyze transaxial cross-sections at 14 mm below the top surface, 21 mm below the top surface and 40 mm below the top surface.

We have selected 3 parameters for initial comparison of the various whisker loadings. These are: (a) the diameter of the low density inner core (see Fig. 4); (b) the relative gray scale values of the outer rim versus the inner core region (we see three distinct regions typically as shown in Fig. 4.) and (c) the relative S/N ratio of a diametral densitometer trace across the plane of section. This may begin to give information on uniformity of whisker distribution.

Table 4 shows the diameters of the "inner", lowest density "core" as measured for the 3 sections and for each of the 2 whisker loadings studied to date. Because the center core was not axisymmetric, we measured the diameter of the core at two diametral positions. The data in the Table thus shows the average of the two values.

Table 4

Diameter of apparent lowest density inner core of pressure slip-cast SiC(w)/Si_3N_4 as measured using 3-D microfocus X-ray computed tomography

	Diameter	
Plane of Section	20 Wt.% whisker (mm)	23 Wt.% whiskers (mm)
7	7.11	5.94
11	10.19	4.14
22	10.42	7.21

In order to establish differences in density we measured the relative gray scale of the image at three azimuthal positions in the outer region on each planes of section as well as in the middle of the central "core". These relative gray scale values, are shown in Table 5.

Table 5

Relative gray scale (density) values between the outer rim region and central core of the pressure slip-cast SiC(w)/Si_3N_4

Plane of Section	Gray-Scale				Ratio (inner/outer)	
	20 wt.%		23 wt.%		20 wt.%	23 wt.%
	Inner	Outer	Inner	Outer	Inner	Outer
7	90.1	102.3	139.2	167.1	.833	.881
11	88.8	101.2	140.6	167.6	.839	.877
22	89.2	100.5	139.3	172.4	.808	.887

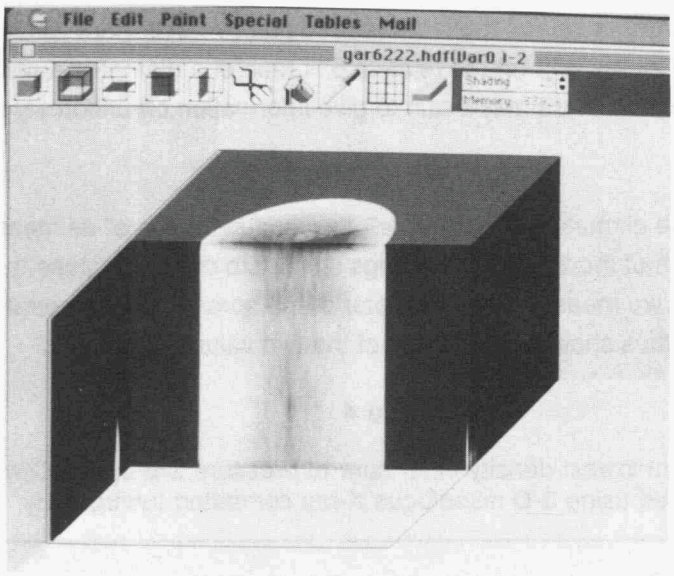

(a)

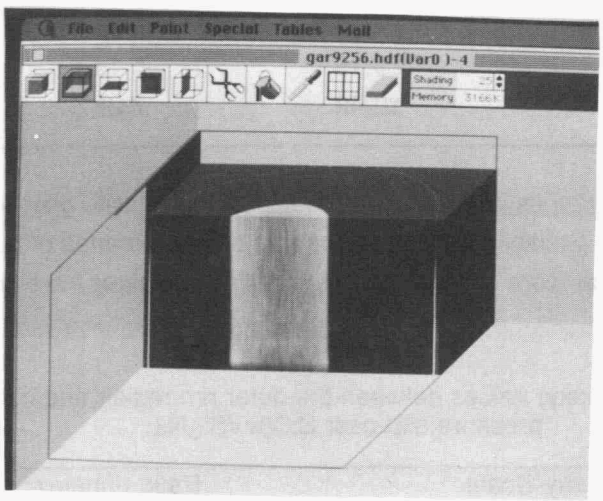

(b)

Fig. 4. 3-D X-ray computed tomographic sectioned images showing axial and radial density variations in pressure slip cast SiC(w)/Si_3N_4. test samples, (a) 20 wt.% whiskers, (b) 23 wt.% whiskers

To be noted here is that in all planes of section, the inner core has a gray scale value of about 0.88 of the outer shell for the 20 wt.% whisker but for 23 wt.% whiskers the inner core has a gray scale value of about .81 – .83 of the outer shell. If the gray scale can be related to density, then there is a 12% difference in the 20 wt.% core and 17–19 difference in the 23 wt.% core.

We are working now on developing better diagnostic methods for better defining the measurable differences between the whisker loading.

We are now making individual planes of section diagnostics on noise measurement and will report on these shortly.

References

1. Ceramic Technology for Advanced Heat Engines Project: Semi-Annual Progress Report for April 1990 through September 1990, Oak Ridge National Laboratory Report ORNL/TM-11719, dated December 1990, pp. 421-426.

Nuclear Magnetic Resonance Imaging

A. C. Raptis, W. A. Ellingson, R. E. Botto (Argonne National Laboratory), H. Yeh, and J. P. Pollinger (Garrett Ceramic Components Division of Allied-Signal Aerospace Corporation)

Objective/scope

The objectives of this program are to: utilize NMR imaging techniques developed at ANL to study the distribution of whiskers and other possible variations in composite green-state (as cast) billets; perform 3-D X-ray (in a related activity (3.5.1.5)) and optical microscopic analysis (to be performed by Garrett Ceramic Components a Division of Allied Signal Corp.) of the composite billets; correlate the results obtained from the NMR imaging techniques with those obtained from both the 3-D X-ray and the optical microscopy.

Technical progress: Part A-NMR studies

The previous work has establishing the utility of two-dimensional (2-D) back-projection NMR imaging techniques for nondestructive evaluation of semi-solid organic distributions in injection-molded green-state ceramics. In this work, three-dimensional (3-D) back-projection NMR imaging techniques were developed for imaging green-state slip-cast composites. The 3-D NMR imaging technique employed here offers several advantages over conventional slice-selection imaging techniques. The 3-D back-projection technique provides (1) contiguous data sampled in three dimensions over the volume of interest, (2) higher resolution in the third dimension, (3) higher signal-to-noise ratio in the reconstructed image, and (4) equal applicability to fluid systems (such as water in slip-cast materials), semi-rigid materials (such as the semi-solid organic binders), and solids.

In a conventional 2-D NMR back-projection tomographic experiment, one applies a linear magnetic field gradient in a plane at numerous projection angles. For each angle, the Fourier transform of the data represents a planar integral of the proton density normal to the gradient vector. Similarly, in the 3-D back-projection experiment, by varying the gradient vector in order to sample the entire 3-D space, one obtains a 3-D Radon transform of the proton density. The inversion of this transform can be obtained by double differentiation and back projection.

The 3-D back-projection technique was demonstrated by imaging the distribution of organic additive (2.5 Wt.% polyethylene glycol) in a cold-pressed green-state Si_3N_4-whisker-reinforced Si_3N_4 matrix composite specimen. This specimen, which measured 7 x 7 x 3 mm, was chosen because it was both extremely stable and experimentally challenging. Conventional ceramic processing techniques were employed in sample preparation.

Three-dimensional NMR imaging data were acquired by using 128 complex data points, and a total of 1024 projections about a spherical volume surrounding the sample. A

gradient strength of 35 G/cm and a sweep width of 100 kHz were used. A total of 128 averages were acquired by using an approximate 90^{o} pulse and a recycle delay time of 0.25 S. A resolution, of $175_x \times 175_y \times 175_z\ \mu m^3$ was achieved as calculated from the spectroscopic full-width-at-half-maximum peak width.

Three-dimensional NMR and X-ray images displayed via surface rendering techniques are presented in Fig. 1. Surface rendering is performed by applying a user-adjusted threshold intensity to define a minimum intensity that is used to calculate the contiguous surface. The particular threshold chosen for the X-ray image resulted in an accurate representation of the sample's topology. The NMR surface, however, was reconstructed with a minimal threshold intensity that was chosen to suppress structures having low proton density near the sample surface. This threshold level essentially eliminated two corners of the sample from the rendered object (as indicated in Fig. 1A). The remainder of the NMR image, however, is similar to the one acquired by X-ray, Fig. 1B.

Thin 2-D sections (or "slices") of the 3-D NMR and X-ray CT reconstructed images taken from identical spatial locations within the specimen is shown in Fig. 4. Three types of localized intensity indications can be observed in Fig. 2: (a) areas of low NMR and low X-ray intensity stemming from voids, cracks, or low-density inclusions having little or no discernible protons; (b) areas of high ceramic density; and (c) areas of high organic concentrations. Use of these techniques for the measurement of whisker or fiber distributions in as-cast composites should provide superior results than those achieved on the low concentration of polymeric material in this specimen. NMR probe modifications are currently underway, and application of this technique to as-cast specimens will commence shortly.

Developments in this reporting period include design and implementation of a new RF resonator specifically designed to provide high B_1 homogeneity, cylindrical sample access, and low signal sensitivity. The resonator was designed to provide a cylindrical "working" volume of 28mm in diameter by 30mm in height. The composite specimens which are to be used in this study are approximately 25mm in diameter and 41mm in length.

The sensitivity of the coil was tested by imaging a button head of a green-state tensile specimen (provided by Norton Advanced Ceramics) using the 3-D imaging method reported in the previous reporting period. A 3-D surface reconstruction and 2-D slice is presented in Fig. 3A and 3B, respectively. Initial indications suggest that the coil provides sufficient sensitivity and homogeniety for the experiments on the composite specimens.

The development of the coil and the 3-D method imaging reported in this reporting period provides the key components necessary to successfully image the distribution of whiskers and other possible variations in composite green-state (as cast) billets. These imaging experiments should be completed in the upcoming reporting period.

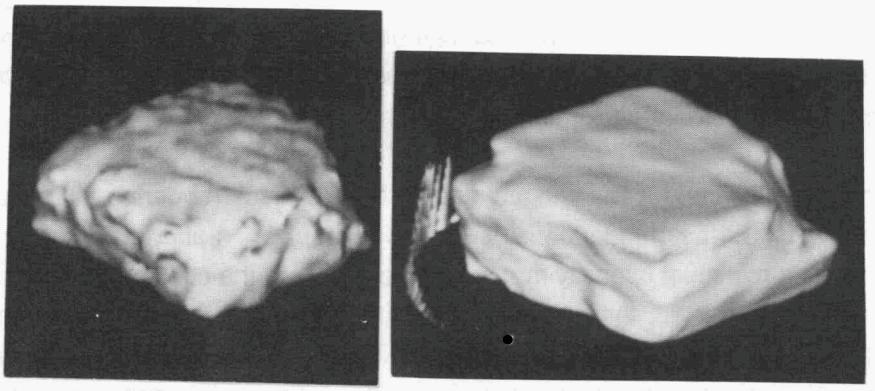

(A) (B)

Fig. 1. Surface reconstructed (A) 3-D NMR image and (B) 3-D X-ray CT image of a green-state Si_3N_4-whisker reinforced Si_3N_4 composite specimen.

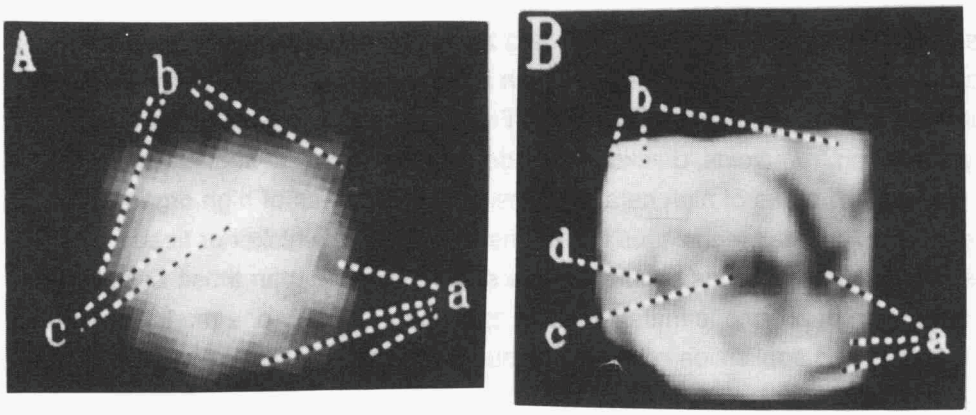

(A) (B)

Fig. 2. Internal thin 2-D sections of 3-D (A) NMR image and (B) X-ray CT image of the composite specimen shown in Fig. 3.

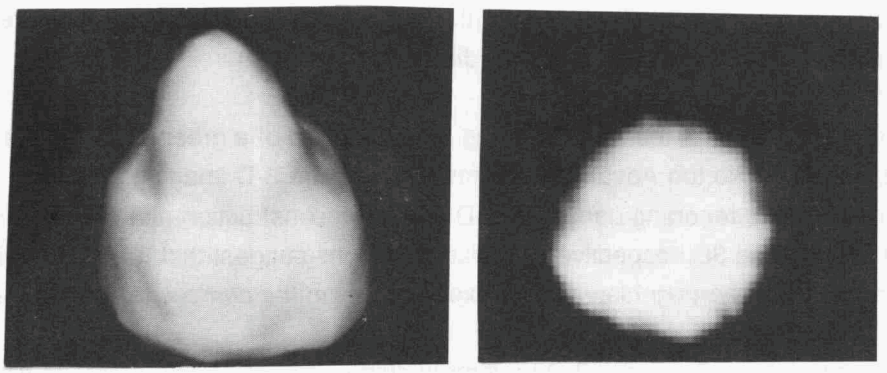

(A) (B)

Fig. 3. (A) Three-dimensional NMR surface reconstruction and (B) a 2-D slice through the button end of a green-state Si_3N_4 tensile specimen obtained from Norton Advanced Ceramics.

Physicochemical Characterization and Surface Modification of Silicon Nitride Ceramic Powders

Prof. Marc A. Anderson (University of Wisconsin - Madison)

Objective/scope

This project is designed to fulfill two primary objectives:

1. characterization of the aqueous surface chemistry of silicon nitride, which also requires the development of a standard for mobility measurements and participation in a round-robin characterization of this standard; and
2. spectroscopic characterization of aqueous suspensions of silicon nitride.

Technical progress

Our work in the past six months has focused on two areas:

1. perform a third round robin with the "benchmark" material, phosphated goethite, and analyze the results; and
2. continue investigating the kinetics of hydrolysis for silicon nitride powder (Ube E-10) as a function of pH.

Round Robin Analysis of Mobility Measurements:

A. SAMPLE PREPARATION AND MEASUREMENT PROTOCOL: Fifteen different suspensions (with each participant receiving five subsamples of each suspension) were prepared and distributed for the GEMS 3 (for Goethite Electrophoretic Mobility Study) round robin mobility measurements. All samples were aqueous suspensions of phosphated goethite at a phosphate concentration of 100 μmol/g goethite and a goethite concentration of 100 mg/L (.0023% by volume). Due to problems in dispensing goethite from the stock suspension, the actual goethite concentration was somewhat less than given above, thus the phosphate loading was somewhat higher than calculated. However, the actual values should be within 10% of the desired values.

Each suspension was prepared in bulk (either 3.6 or 4 L, depending on the container size) at one of five nominal pH values (3.5, 4.4, 5.2, 6.1 or 7.0) and one of three ionic strengths (0.001, 0.01 or 0.05 M KNO_3). To prepare the 0.001 M KNO_3 suspension at pH 3.5, the final pH was assumed to be exactly 3.50 due solely to HNO_3, then the additional amount of solid KNO_3 needed to give a total ionic strength of 10^{-3} M was added to the system. For all other suspensions, the final ionic strength was assumed to be due solely to the added KNO_3. In practice, the conductivity of the 10^{-3} M suspension at pH 3.5 was nearly double the conductivities of the 10^{-3} M suspensions at the other pH values due to the high mobility of the proton.

The pH values of the bulk suspensions were adjusted by adding either HNO_3 or KOH to the suspension, allowing the suspension to equilibrate at room temperature for at least 3 h (usually overnight), pouring a subsample of the suspension into a 30 mL container, and measuring the pH. All pH 3.5 and 4.4 samples readily equilibrated near the desired pH values, as did the two higher ionic strength samples at pH 5.2. However, pH adjustment of the remaining samples proved very difficult, probably due to a combination of solid aging and CO_2 absorption effects at the higher pH values. During the round robin, measured values of pH for the nominal pH 7.0 samples were consistently between pH 6.5 and 6.7. Similar behavior had also been observed during the previous round robin measurements, GEMS 2.

Once a reasonable pH value had been attained, the bulk suspension was divided among 20 separate pre-cleaned clear HDPE Nalgene containers (I-Chem Research), then capped. A stream of dry nitrogen was blown over the surface of the pH 7 samples for 30 sec before capping in order to remove most of the CO_2 present in the container.

Two days were allotted for performing each of four sets of measurements for GEMS 3: Nov. 29 & 30, Dec. 3 & 4, Dec. 10 & 11 and Dec. 17 & 18. All measurements were conducted according to the following protocol:

SAMPLE PREPARATION

1. Sonicate each sample in its sample bottle with the cap on for 15 min in bath sonicator. Sonicate each sample individually rather than doing 2 or 3 samples together.
2. Let samples stand at least 10 min at room temperature before making pH measurements. (Ignore this step if pH measurements are made using automatic temperature compensation.)

pH METER STANDARDIZATION

1. Standardize using pH 4 and 7 (or near 7) buffers. Change the pH 7 buffer at least weekly.
2. The pH value should be stable to within 0.01 pH unit (0.6 mV) for at least 1 minute.
3. Restandardize the electrode every 4 h.
4. Condition the electrode to the samples by placing the electrode in a sample for 10 min, then discarding the sample. Do not record the pH value. (Ignore this step if your first sample is at pH 3.5 or 4.4).

pH MEASUREMENTS

1. Transfer some sample to a container which minimizes contact between the sample and the surrounding air.
2. Set stirring speed roughly between 100 and 150 rpm.
3. Record pH value only after it is stable to within 0.01 pH unit (0.6 mV) for 30 sec. It will probably take several minutes for the higher pH samples to stabilize.

MOBILITY MEASUREMENTS

1. Condition chamber by exposing it to some sample and flushing it with a fresh loading of that sample before making a measurement.

2. For a given sample, record mobility values for 5 fresh loadings of that sample. More measurements may be taken if desired but must be reported separately. [In practice, when one mobility value appeared significantly different from the other four, extra measurements were taken.]

B. RESULTS: The conclusions given below must be considered preliminary. They are based on mean values of mobility for a given pH and ionic strength which are obtained by averaging five separate mobility measurements for that system. Statistical analysis of the data based on the individual mobility values is planned but has not yet been performed. Because mobilities for this material are pH dependent, this study required concurrent measurements of pH and mobility. Thus, the conclusions are listed for three separate areas: pH measurements; mobility measurements; and isoelectric point (IEP) for the phosphated goethite. The IEP determination incorporates both of the other measurements. Note that aging of the samples was not observed.

pH MEASUREMENTS

1. The variation in measured pH values for a given sample depends on the pH and ionic strength of that sample. In poorly buffered systems (pH near neutral and low ionic strength - 0.001 M KNO_3), the difference between the highest and lowest reported pH values was as much as 0.70 pH units. In more highly buffered systems (pH below 5 and high ionic strength - 0.05 M KNO_3), this difference dropped to 0.10 pH units.

2. Part of this variation may be attributable to differences in the behavior of the pH electrodes used by the various groups for this study. All pH measurements in all 0.001 and 0.01 M KNO3 systems by one group were noticeably lower than the pH values measured for the same systems by the other groups. This difference does not appear to be caused by errors in measuring the pH because all groups reported similar pH values in all 0.05 M KNO_3 systems. However, it is still not known if these differences are statistically significant.

3. While we still recommend the use of Ross Sure-Flow electrodes (Orion #8172BN) for pH measurements in aqueous suspensions, problems exist in operating these electrodes. If the ground glass joint at the base of the electrode is not seated tightly, the reference electrode filling solution can leak fast enough to seriously compromise pH measurements. Also, the electrode is rather fragile, as the electrical connections within the electrode break frequently.

MOBILITY MEASUREMENTS

1. The variation in average mobility values measured for a given sample appears to be independent of pH and ionic strength. Differences between the highest and lowest average mobility values were 0.30 to 0.40 x 10^{-8} $m^2V^{-1}sec^{-1}$ for almost all samples.

2. These variations may be worse in the 0.001 M KNO_3 systems. Possible outlier values were observed in all of these systems. The statistical significance of these possible outliers must still be determined.

IEP DETERMINATIONS

1. IEP values (pH at which the particles are uncharged) have been estimated for these phosphated goethite systems from graphs of average mobility vs. pH and are reported in Table I to the nearest 0.05 pH unit.

2. We consider this agreement to be quite good, as all IEP values fall within 0.25 pH units of pH 4.75 and all but two of the values fall in the range pH 4.75 ± 0.2.

3. In GEMS 2, it was suggested that there might be a small dependence of the IEP on the type of instrument used for the mobility measurements. This dependence is less clear in GEMS 3 and may be due to the variations in pH measurements noted above.

4. A separate experiment was performed to determine if shipping the samples had any effect on their properties. Extra samples at nominal pH 7.0, which should be most seriously affected by CO_2 leakage into the bottles, were shipped from Wisconsin to Oak Ridge and then shipped back to Wisconsin. Measurements on these samples did not differ noticeably from measurements performed on samples of the same systems which had not been shipped. Note that covers of all sample bottles were hand tightened as tightly as possible before shipping.

TABLE I. Measured IEP Values for Phosphated Goethite

	I = 0.001	I = 0.01	I = 0.05
Rutgers	4.60	4.70	4.75
	4.65	4.70	4.75
	4.50	4.70	4.75
	4.55	4.65	4.70
Wisconsin	4.80	4.75	4.60
	4.75	4.80	4.70
	4.80	4.80	4.60
	4.80	4.80	4.55
Oak Ridge	5.00	4.90	4.75
	4.85	4.80	4.70
	4.85	4.80	4.70
	4.80	4.80	4.70

These results demonstrate that pH and mobility measurements can be performed reproducibly by workers at different sites if the measurement conditions are carefully controlled. Phosphated goethite might even serve as a useful mobility standard for both the ceramics and colloid chemistry communities. However, the next round robin will determine if similar reproducibility can be obtained for measurements in aqueous silicon nitride suspensions. Such measurements have begun, with samples prepared at each site from bulk suspensions supplied by Rutgers Univ. After samples are prepared, measurements are obtained using the same protocols as for phosphated goethite.

Aging of Aqueous Suspensions of Silicon Nitride: It was shown previously that measurable amounts of dissolved silica were obtained when Ube E-10 silicon nitride powder was exposed to aqueous solutions at different pH values. While this observation has been noted in previous studies, it has usually been explained as hydrolysis of the silicon nitride, which would be expected to exhibit a pH dependence. However, this explanation does not adequately account for two further observations made during our studies. (1) Dissolved ammonia concentrations in these systems are considerably less than dissolved silica concentrations, by as much as an order of magnitude, even when efforts are made to minimize loss of ammonia to the atmosphere. This behavior is observed when the powder is first exposed to the hydrolysis system. (2) If the powder is separated from the supernatant after the first hydrolysis and then hydrolyzed a second time, the dissolved silica concentration decreases significantly.

A better explanation for these phenomena is that the silicon nitride powder has hydrolyzed in air, forming patches of silica on the surface. (IEP measurements do not support the idea that the silicon nitride powder is completely covered with a layer of silica.) These patches of silica dissolve during hydrolysis, causing the unexpectedly high dissolved silica concentrations. By continually replacing the hydrolysis solutions, a more pristine silicon nitride surface can be obtained. Thus, we have suggested that these powders be washed in alkaline solutions before being used for further studies.

At present, a detailed study is being conducted of the kinetics of hydrolysis of alkaline-washed silicon nitride powders. Results of this study will be presented once all of the data have been obtained and analyzed.

CIR-FTIR Spectroscopy of Silicon Nitride Suspensions: No further work has been performed because no silicon nitride powder with an acceptably high surface area is available. Efforts to find a suitable powder are continuing.

Status of Milestones

1. Complete round robin characterization of "benchmark" colloid. Complete.

2. Complete initial round robin mobility testing of silicon nitride. Expected completion: Apr. 30, 1991. On schedule.

3. Complete round robin mobility testing of silicon nitride. Expected completion: Oct. 31, 1991. Further delayed to allow possible industrial participation in at least one round robin.

4. Complete peak assignments for CIR-FTIR spectra of aqueous suspensions of silicon nitride. Expected completion: Nov. 30, 1991. On schedule.

Publications

None.

Surface Adsorption

J. H. Adair (University of Florida)

Objective/scope

This project represents a coordinated effort among ORNL and three university laboratories (WBS Elements 3.5.1.7, 3.5.1.8, 3.1.5.9, and 3.5.2.0). The purpose of this project (WBS 3.1.5.9) is to study the surface chemical interaction of silicon nitride powders in aqueous and nonaqueous enviroments and to study surface chemical modification of the material, and, in particular, to understand the acid - base nature of the silicon nitride - solvent interface.

Background

As a heat resistant material, silicon nitride has applications or potential applications in ceramic engines, heat exchangers, turbine blades, and high frequency combustion crucibles. The variety of current and potential applications for silicon nitride require a range of forming operations to fabricate the specific components. Most of the forming processes to achieve the range of shapes for silicon nitride components require the use of organic additives. For example, precombustion chambers for diesel engines and turbine blades are usually injection molded using highly filled thermoplastic polymers while tubular heat exchangers are extruded with less polymer as binder and usually the binder is significantly different in terms of functional groups and properties than those polymers used for injection molding.

Ceramic processing often involves the suspension of ceramic powders in an organic solvent rather than water to promote separation or dispersion of the ceramic particles during forming operations. The use of nonaqueous solvents is particularly important in the processing of nonoxide ceramics such as silicon carbide, silicon nitride, and aluminum nitride because these compounds are subject to reactions with water to form oxides or hydroxides surface groups or, in the case of aluminum nitride, uniform transformation to the hydroxide. Yet little fundamental data exists on the interaction of ceramic particle surfaces with the organic species in organic solvents. Furthermore, the role that the surface composition of the ceramic particle plays in the dispersion and interaction of particles in solvents is not well established. The current study is designed to determine the nature of the surface interactions of silicon nitride with organic solvents and solutes.

Approach

There are four participants in the overall project: ORNL and three universities, the University of Florida (UF), the University of Wisconsin, and Rutgers University.

The UF project is composed of two distinct elements:

1. Participation in a round robin characterization of electrophoretic mobility and acid-base character in aqueous suspension to be conducted by all participants.

2. Special projects at UF composed of the following activities:

The UF workplan is based on five tasks: Task 1 to participate in round-robin particle electrophoretic mobility measurements, Task 2 to determine the nature of reactive sites on the silicon nitride surface, Task 3 to modify the chemistry of the silicon nitride interface using organic species, Task 4 to determine the rheological and dispersion properties of the nonaqueous silicon nitride suspensions, and Task 5 to ensure transfer technology to ORNL via meetings and reports.

Technical progress

FY 1989

Round Robin - Electrophoresis - Goethite standards prepared at Wisconsin were evaluated as part of the UF participation in the round robin.

Reactions at the Silicon Nitride - Solution Interface - A study was conducted to determine the extent of aqueous reactions at the silicon nitride - water interface. It was demonstrated that up to 27 days are required to stabilize reactions at the interface as indicated by pH and particle electrophoresis measurements. A semi-automatic titrator was also purchased and set-up to use acid - base titrations to study the silicon nitride - solvent interface. A particular emphasis of this work was on the non-aqueous potentiometric and conductometric titration to determine the relative strength of acid and base sites on the silicon nitride surface.

FY 1990

Round Robin - Electrophoresis and pH measurements - The round robin electrophoresis on the goethite standards prepared at Wisconsin indicated several interesting features. The isoelectric points determined by each of the participants in the round robin were similar, but measured pH values displayed considerable scatter at higher pH (e.g., pH 8). The suspected influence of dissolved CO_2 and adducts and methods to overcome the effect of these dissolved species are currently under investigation at UF.

Reactions at the Silicon Nitride - Solution Interface - The use of potentiometric titrations in non-aqueous solvents indicates that there are several different kinds of acid and base sites on the silicon nitride depending on the prior enviromental history of the powder. The results are generally consistent with potentiometric titrations used to evaluate the silicon dioxide surface. Future work will focus on further potentiometric as well as conductometric titrations on silicon nitride as well as model systems such as silicon dioxide.

FY 1991

Round robin - The first test of the silicon nitride powders was completed and evaluated. The University of Florida team did not participate in this round because of instrument problems. A second round of tests on silicon nitride have been conducted and are currently being evaluated at Rutgers. The final, approved test procedure will be written. Industrial participation will be invited.

Reactions at the Silicon Nitride - Solution Interface - The strengths of the acid and base sites at the silicon nitride surface are being estimated based on calculated relative bond strengths and the non-aqueous titrations. The surface of silicon nitride has also been modified used metal oragnic coatings selected to ensure both dispersion and inhibition of oxidation reactions.

Preliminary particle electrophoresis in isopropanol indicates that measureable surface charge is present on the surfaces of silicon nitride in as-received isopropanol. Initial particle electrophoresis of as-received silicon nitride (UBE E-10) indicates that the particles are positively charged with zeta potentials of approximately 3 mV. The contribution of the electrostatic forces toward dispersion of the silicon nitride in this nonaqueous solvent are currently being estimated as are the effects trace amounts of water have on the formation of surface charge in the nonaqueous solvents.

Current work is directed toward studies to better understand the surface chemical interactions that control the dispersion of silicon nitride particles in nonaqueous solvents such as isopropanol and toluene. Thus, X-ray photon spectroscopy, nonaqueous potentiometric titrations, electrophoretic mobility determinations and theoretical calculations that predict particle dispersion for specific systems are being used to evalaute the relative contribution of various dispersion mechanisms. These studies combined with novel dispersion techniques are being used to develop guidelines for the dispersion of silicon nitride particles in nonaqueous solvents.

Status of milestone

The program is on schedule.

Physicochemical Characterization and Surface Modification of Silicon Nitride Ceramic Powders

J.-F. Wang, R. E. Riman, and D. J. Shanefield (Rutgers University)

Objective/scope

The purpose of this effort is to (1) identify and characterize those aspects of the chemistry and physics of the ceramic powder and powder/solvent interface that control processing, (2) develop standard methods of analysis for item (1), and (3) develop procedures for writing specifications for ceramic powders to include any methods of analysis developed in this project.

Technical progress

The work that has been done or under investigation in the past six months is summarized as follows:

(1) The third electrophoretic mobility (μ) round robin study on phosphated goethite (GEMS 3) was made. In general, the agreement in pH and μ measurements for GEMS 3 was good. The reproducibility of μ measurement from lab to lab increased as the ionic strength increased from 0.001 to 0.05 M KNO_3 solution. All the isoelectric points (IEP) for 0.001, 0.01, and 0.05 M KNO_3 solutions fell in the range of pH 4.75±0.25, which was about 0.4 pH unit lower than that obtained from the GEMS 2. The deviation of the IEP could be due to the different amount of adsorbed phosphate groups on goethite or due to the different solids loading applied. The agreement in pH measurement increased as the ionic strength increased and decreased as pH approached neutrality. The pH measurement was also found to be electrode dependent.

(2) The surface property of silicon nitride powder (UBE E-10) was studied as a function of aging and sample preparation history. The IEP of UBE E-10 increased as the aging time increased. The freeze-dried and isopropanol(IPA)-ball-milled powders have lower IEP's than as-received powder.

(3) The doping of yttrium and aluminum compounds on the surface of UBE E-10 powder has been conducted in both aqueous and nonaqueous media. The surface property of the doped UBE E-10 changed significantly starting from pH 4.5 using either aluminum nitrate or aluminum tri-sec-butoxide (ASB) and from pH 7.0 using either yttrium nitrate or yttrium isopropoxide (YIP) in aqueous or in IPA solution, respectively.

(4) The first electrophoretic mobility round robin study on UBE E-10 suspension (SEMS 1), which was prepared by the Rutgers University, has been conducted starting from March 27, 1991. In total, four simultaneous measurements, on various days among four participating laboratories, will be taken. A reconstitution procedure for the μ measurement from the 5 vol% suspension was given.

Electrophoretic mobility round robin study on phosphated goethite:

The third electrophoretic mobility round robin study on phosphated goethite (GEMS 3) was investigated. The GEMS 3 was started on November 29, 1990 and ended on December 18, 1990; totally, four scheduled measurements have been conducted. All the GEMS 3 samples were prepared and distributed by Dr. Walter A. Zeltner in the University of Wisconsin at Madison. The solids loading used for GEMS 3 is 100 mg/L (~0.0023 vol%), which is two and a half times more dilute than that used in the GEMS 2 (~0.0058 vol%). Three buffer electrolyte (KNO_3) concentrations were utilized in GEMS 3 (i.e., 0.001, 0.01, and 0.05 M) instead of the single one (i.e., 0.01 M) used in GEMS 2. For a given electrolyte concentration, five samples with different pH values were examined (i.e., nominal pH 3.5, 4.4, 5.2, 6.1, and 7.0).

The sample was sonicated in its sample bottle with the cap on for 15 minutes in a bath sonicator. Then the sample was allowed to stand at least 10 minutes at room temperature before making pH and μ measurements. The pH value was recorded only after it was stable to within 0.01 pH units for at least 30 seconds. For a given sample, the μ was measured after conditioning the sample chamber. Conditioning was accomplished by exposing the cell to the sample and flushing it with a fresh loading of that sample. Then, μ values for 5 fresh loadings of that sample were then recorded.

The four measurements conducted on four different dates (i.e., 11/29, 12/3, 12/10, and 12/17) were summarized in Figures 1 to 3, respectively, which show μ as a function of pH and electrolyte concentration. The measurements were quite consistent especially at pH lower than 5.5 and at higher electrolyte concentrations (i.e., 0.01 and 0.05 M) and gave an IEP of 4.75±0.25. The pH value measured using the Metrohm electrode (Rutgers) at low electrolyte concentrations was consistently lower than that obtained from the Ross electrode (University of Wisconsin and ORNL), especially at 0.001 M KNO_3 solution (Figures 1 to 3). According to the small descripancies observed for both pH and μ measurements, the sample with nominal pH at 3.5 and in 0.01 or 0.05 M KNO_3 solution will be chosen as the referencing suspension for the silicon nitride round robin studies.

The effect of solids loading on the μ measurement using a laser light scattering instrument was reported in our semi-annual report which was

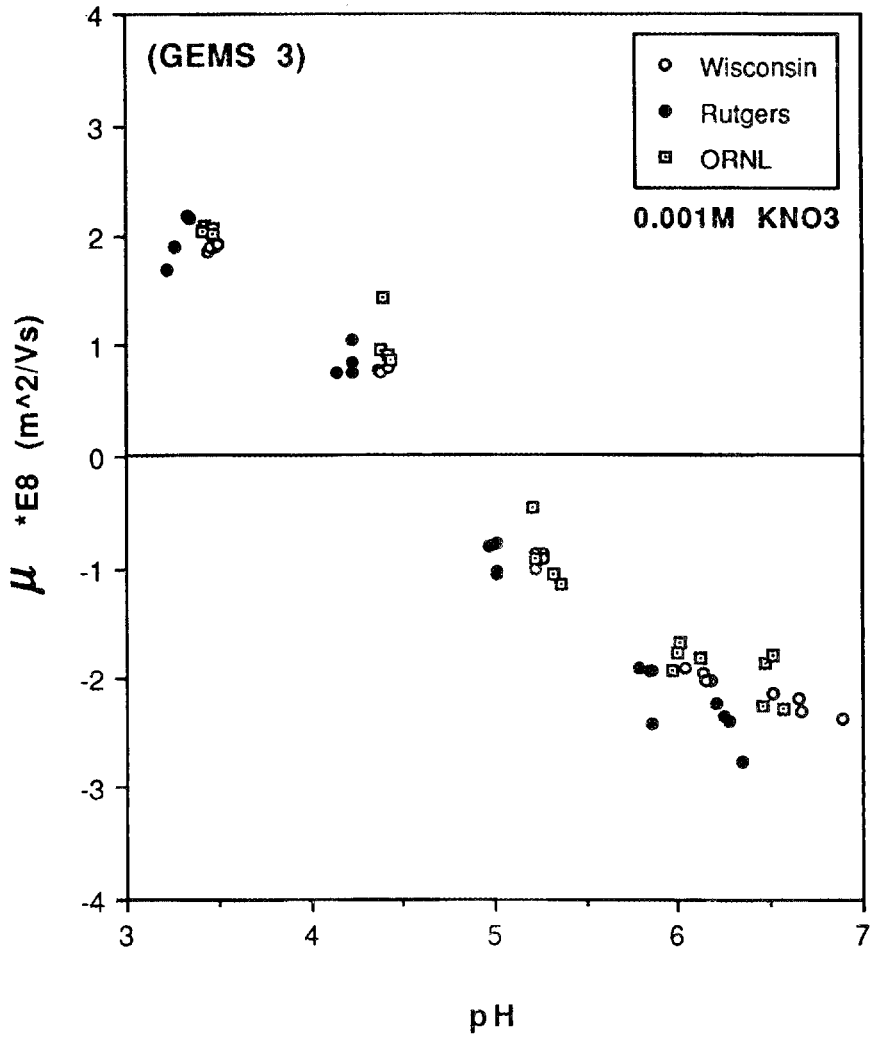

Figure 1. The electrophoretic mobility of 100 mg/L phosphated goethite in 0.001 M KNO_3 solution as a function of pH of GEMS 3.

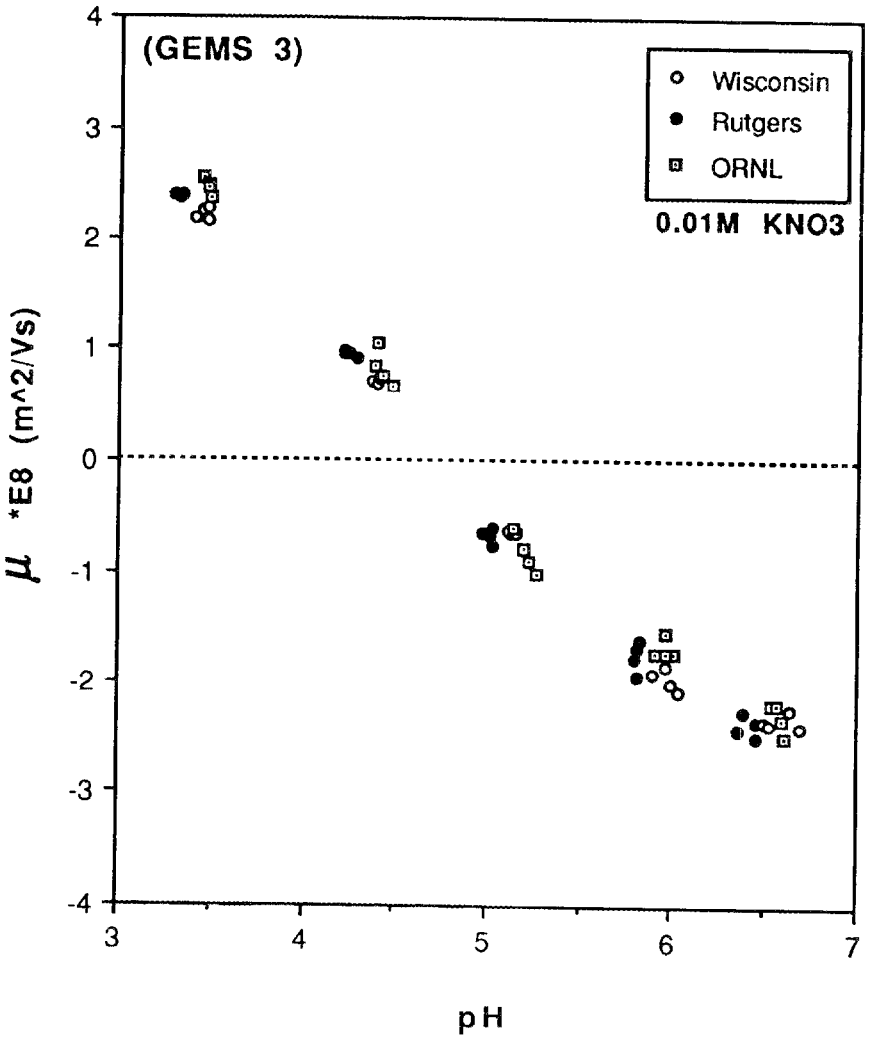

Figure 2. The electrophoretic mobility of 100 mg/L phosphated goethite in 0.01 M KNO_3 solution as a function of pH of GEMS 3.

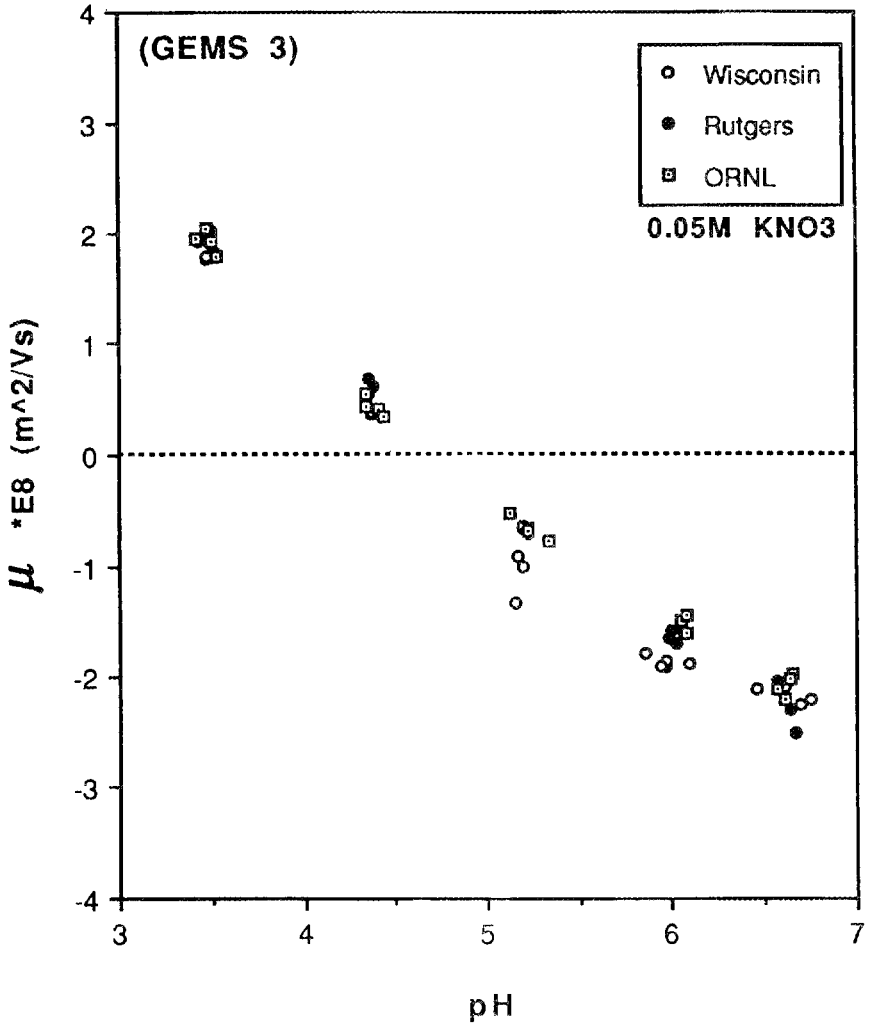

Figure 3. The electrophoretic mobility of 100 mg/L phosphated goethite in 0.05 M KNO_3 solution as a function of pH of GEMS 3.

dated May 25, 1990. We found that a solids loading greater than 0.005 vol% was required before a constant μ could be obtained. Since the particle concentration used for the GEMS 3 was only 0.0023 vol%, the examination of the solids loading effect to understand the deviation of the IEP (Figure 4) was therefore necessary.

The phosphated goethite used for investigating the solids loading effect was synthesized in our lab but not from GEMS 3. The characteristic and the μ measurement of our phosphated and non-phosphated goethite were reported in the last semi-annual report (November, 1990). The phosphated goethite was prepared in different solids loadings such as 0.001, 0.0025, 0.005, and 0.01 vol%. All of the samples were diluted in 0.01M KNO_3 solutions and aged for a day before the μ measurement.

The pH value of the suspension was found to be proportional to the solids loading. Thus, it is impossible to obtain a simple graph such as solids loading versus μ at constant pH. A graph with three components (μ, pH, and solids loading) is therefore necessary to present the experimental results (Figure 5). The solid line in the Figure 5 was obtained from the μ measurement of the Rutgers phosphated goethite using as a μ reference. It was noticed that the lower the solids loading the more the μ decreases at its corresponding pH. When the solids loading is greater than 0.005 vol%, the measurements begin to converge. This is the same finding as we obtained from the polystyrene latices and the UBE E-10 silicon nitride powder.

Even though we now understand that the solids loading effect has certain influence on the μ measurement, we still do not have enough data to explain why the IEP obtained from GEMS 3 is lower than that from GEMS 2. The shift of the IEP towards lower pH value was also noticed by the other contractors (University of Wisconsin and ORNL). The possible explanation for the shift could be due to the combination of different amount of adsorbed phosphate groups on goethite surfaces and the effect of solids loading .

Sample preparation history:

Figure 6 shows that the surface properties of the non-doped silicon nitride powder were greatly influenced by the sample preparation history. The one day aged and as-received UBE powder gives the highest isoelectric point (IEP) compared to those for freeze-dried and IPA-ball-milled UBE E-10 powders. It is believed that the leaching of silica (e.g., silanol groups) from the silicon nitride powder surfaces during aging in aqueous solution gives relatively more amino groups (e.g., $-SiNH_2$ or $-Si_2NH$) than silanols and causes the shift of IEP towards a higher value.

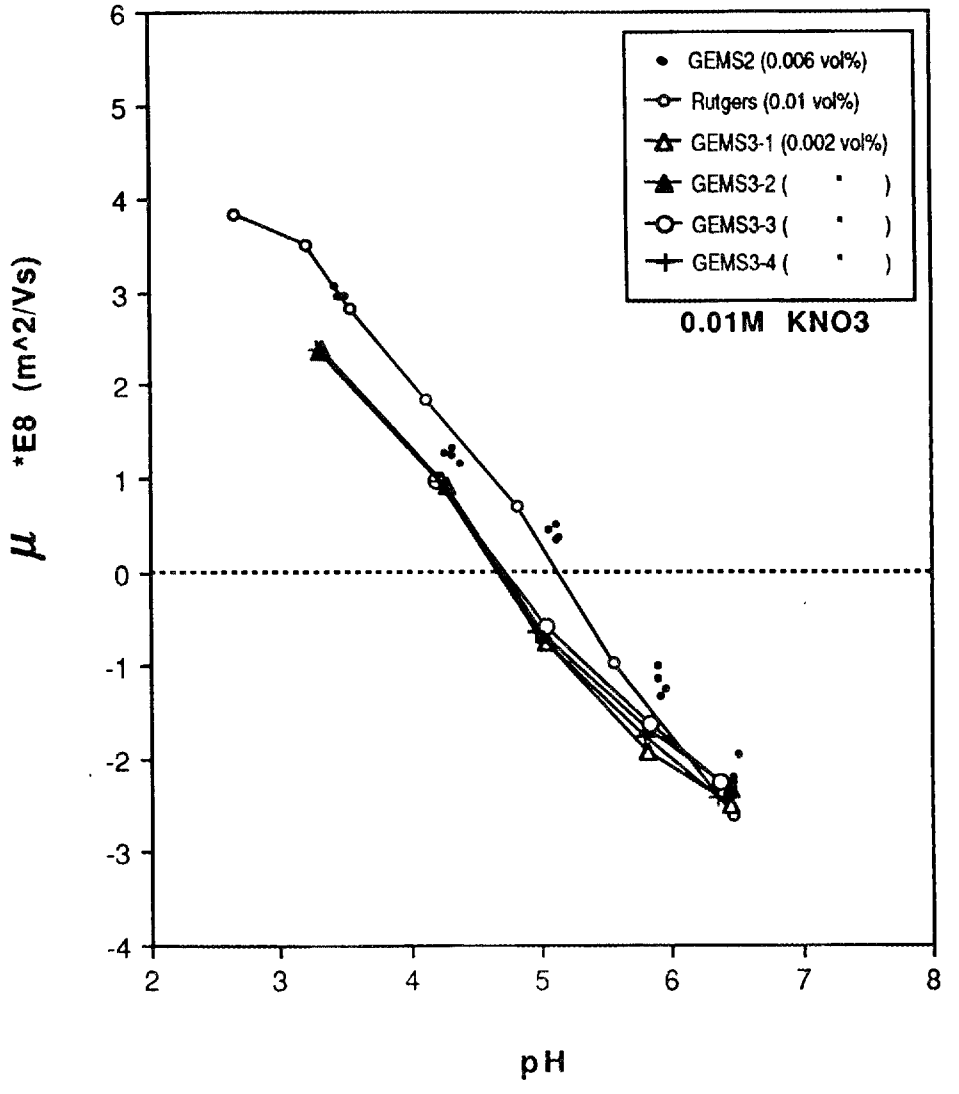

Figure 4. The electrophoretic mobility of phosphated goethite in 0.01 M KNO_3 solution as a function of pH, solids loading, and sources.

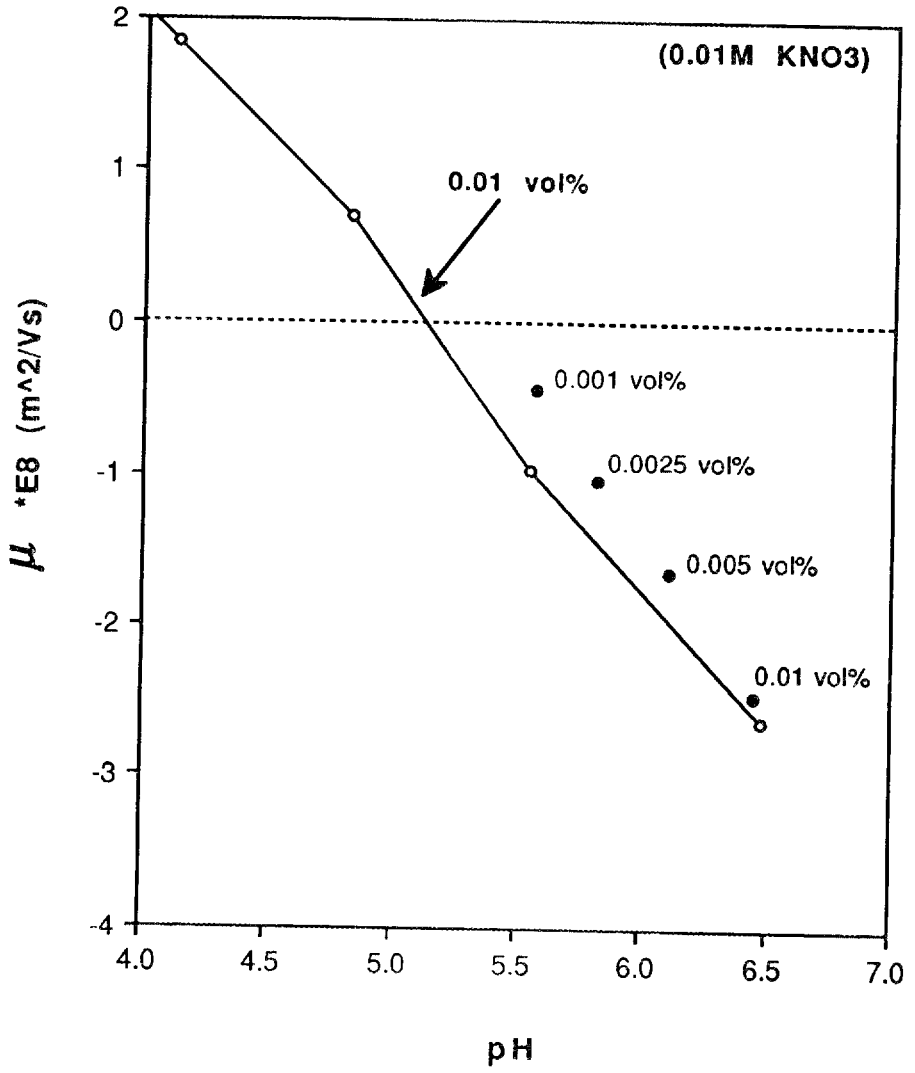

Figure 5. The electrophoretic mobility of Rutgers phosphated goethite in 0.01 M KNO_3 solution as a function of pH and solids loading.

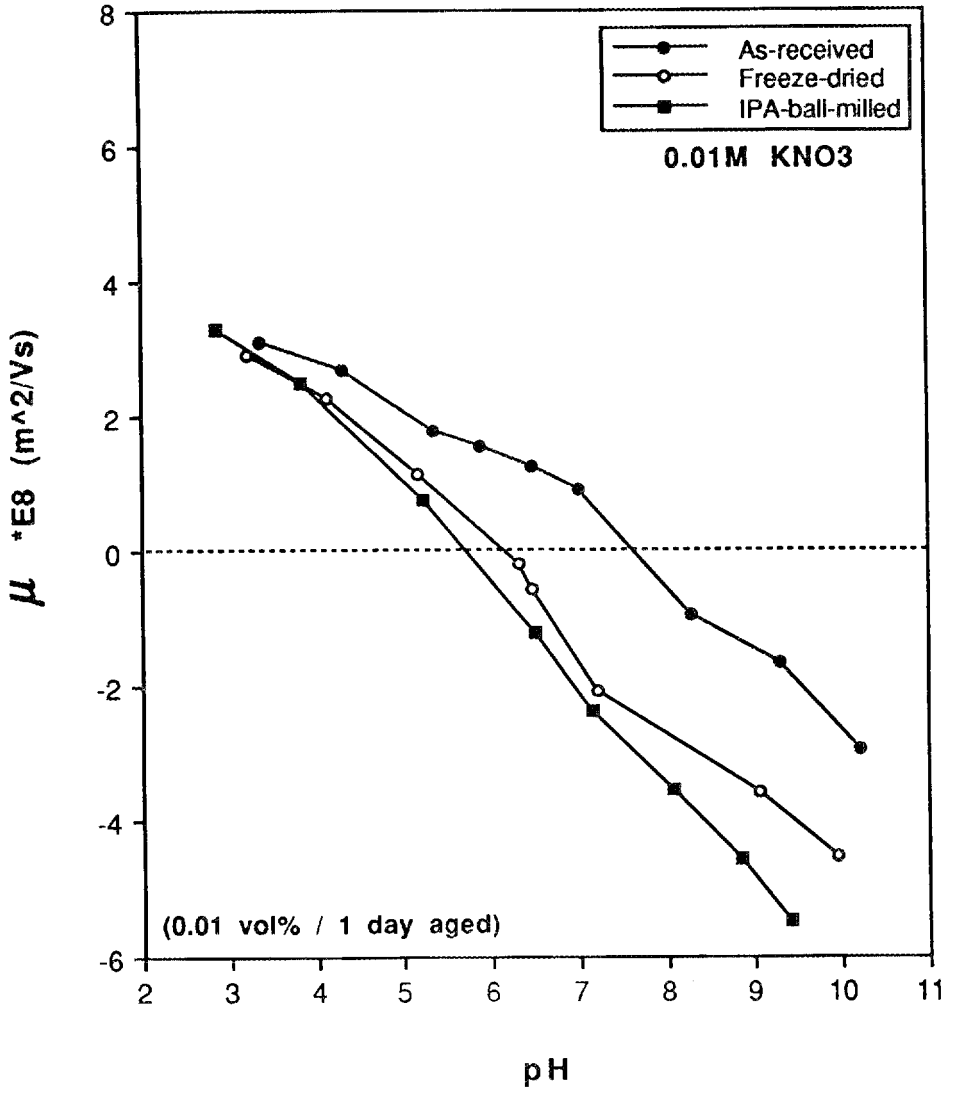

Figure 6. Electrophoretic mobility of 0.01 vol% UBE E-10 powder in 0.01 M KNO_3 solution as a function of preparation history.

The supersaturation of silica species during the freeze-drying of concentrated slurry could cause the reprecipitation of the leached silica back on the UBE E-10 powder surfaces. The amount of reprecipitated silica might change the surface composition to have relatively more silanols than amino groups. This might explain why the freeze-dried powder exhibits a lower IEP than the as-received one after one day of aging in aqueous solution. If the freeze-dried powder is aged in aqueous solution for longer times, it is expected that its IEP should coincide with that of the as-received powder. The IPA-ball-milled UBE E-10 powder gives the lowest IEP that could be explained by the esterification of the powder surface by the adsorbed IPA molecules . This prevents severe leaching of the silica from powder surface since hydrolysis of surfaces occurs slowly.

Doping of UBE E-10 silicon nitride powder:

The doping of yttrium and aluminum compounds on the surface of UBE E-10 powder has been conducted in both aqueous and nonaqueous phases. The adsorption of the dopant was studied using the microelectrophoresis. Yttrium and aluminum nitrates were used as dopants in the aqueous system, while the YIP and ASB precursors were employed in a nonaqueous system using IPA as the solvent.

In the aqueous system, a 10 vol% UBE E-10 powder in deionized water was prepared. The amount of dopant added versus the weight of powder was controlled to be equivalent to 1 wt% of yttria or alumina. The dopant containing suspension was sonicated for 15 minutes in an ultrasonic bath. The well-mixed and large agglomerate-free suspension was then allowed to stand for another 15 minutes for equilibration before freeze-drying. The freeze-dried powder was used to prepare the dilute suspension (0.01 vol%) for aqueous electrophoretic mobility measurements.

In IPA, the UBE E-10 powder and the silicon nitride grinding balls were added prior to the doping procedure. The addition of YIP and ASB precursor was performed in a pre-evacuated and nitrogen-purged glove box to avoid the hydrolyzation of the alkoxides during the sample preparation. The weight percentage of the dopant versus powder was also calculated to be equivalent to 1 wt% of yttria or alumina. The UBE E-10 powder with dopant(s) was then ball-milled in IPA for 24 hours to break down the large agglomerates and to get uniform coating of the precursor on powder surfaces by hydrolysis and condensation reactions.

The ball-milled slurry was transferred to an open aluminum pan and stirred to dry at room temperature. The hydrolysis of the coated precursor took place during the drying process while the slurry was exposed to the atmosphere. The dried and doped powder was ground lightly and used for aqueous electrophoretic mobility measurement. In addition,

a mobility reference of non-doped UBE E-10 sample was prepared for each aqueous and nonaqueous system.

A significant μ change was observed for μ-pH curves starting from pH 4.5 for aluminum and from pH 7 for yttrium compound doped UBE E-10 powders (Figures 7 and 8). An example of showing good reproducibility of the μ measurement on doped system was given by varying the molar ratio of the dopants and using the same doping weight percentage (Figure 7). The doping of yttrium and aluminum compounds regardless of synthesis method showed the mobility curves typical of adsorption of hydrolyzable metal ions at the oxide-water interface[1]. At higher pH values, the μ-pH curve followed the curve of the corresponding hydroxides precipitating from the solutions on silicon nitride powder surfaces.

All the μ-pH curves observed for the corresponding hydroxides give similar trends regardless of the different sample preparations (Figure 9). The difference of the μ-pH curves at higher pH values could be due to the different surface properties through different powder preparation methods (Figure 6). For aqueous doping freeze-drying was used while for nonaqueous systems IPA-ball-milling was applied. In addition, the various chemical routes may have provided the formation of different types hydroxy compounds through different doping routes could be the other possible explanation for this deviation.

According to the mobility curves obtained (Figures 7 and 8), the working pH range for co-precipitating aluminum and yttrium compounds should fall in the value of 6.5 to 7.5.

Electrophoretic mobility round robin study on UBE E-10 silicon nitride powder (SEMS):

The first electrophoretic mobility round robin study on UBE E-10 silicon nitride powder (SEMS 1) has been conducted starting from 3/26 and 3/27/91. Four round robin measurements were scheduled to be taken in four consecutive weeks. The 5 vol% suspensions for SEMS 1 were prepared in Rutgers University and sent out by overnight delivery to the other three participating institutes on 3/22. A reconstitution procedure for the μ measurement from the concentrated 5 vol% suspension was made by consulting with the other participants. Prior to the suspension preparation, the scale-up acid/base titration curves using three smaller quantities of suspensions were made in order to achieve the target pH values for the actual and larger size suspensions to be prepared. The variation of pH in time of the no acid or base added 5 vol% suspension was investigated.

The preparation of 5 vol% UBE E-10 suspension and the followed reconstitution procedure at each pH and ionic strength are given as follows.

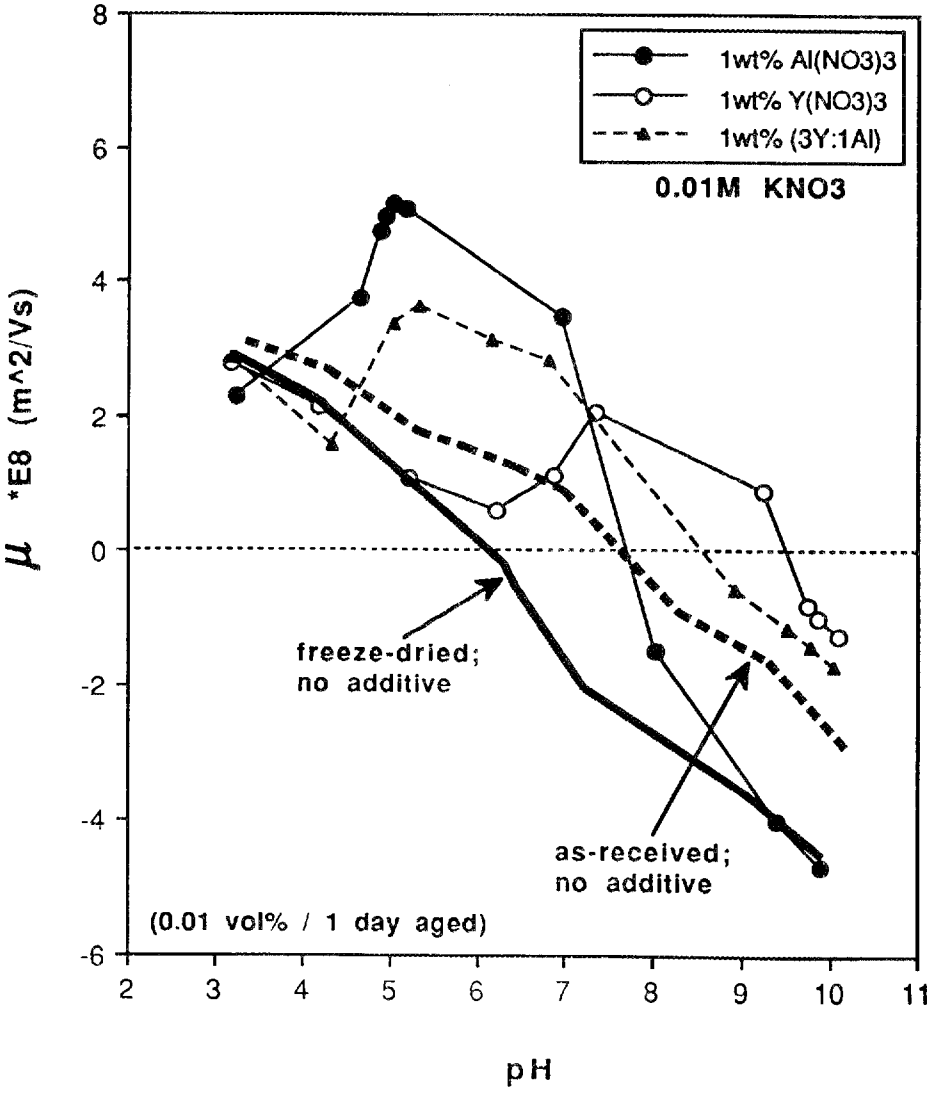

Figure 7. Electrophoretic mobility of 0.01 vol% UBE E-10 powder in 0.01 M KNO_3 solution as a function of aqueous dopant.

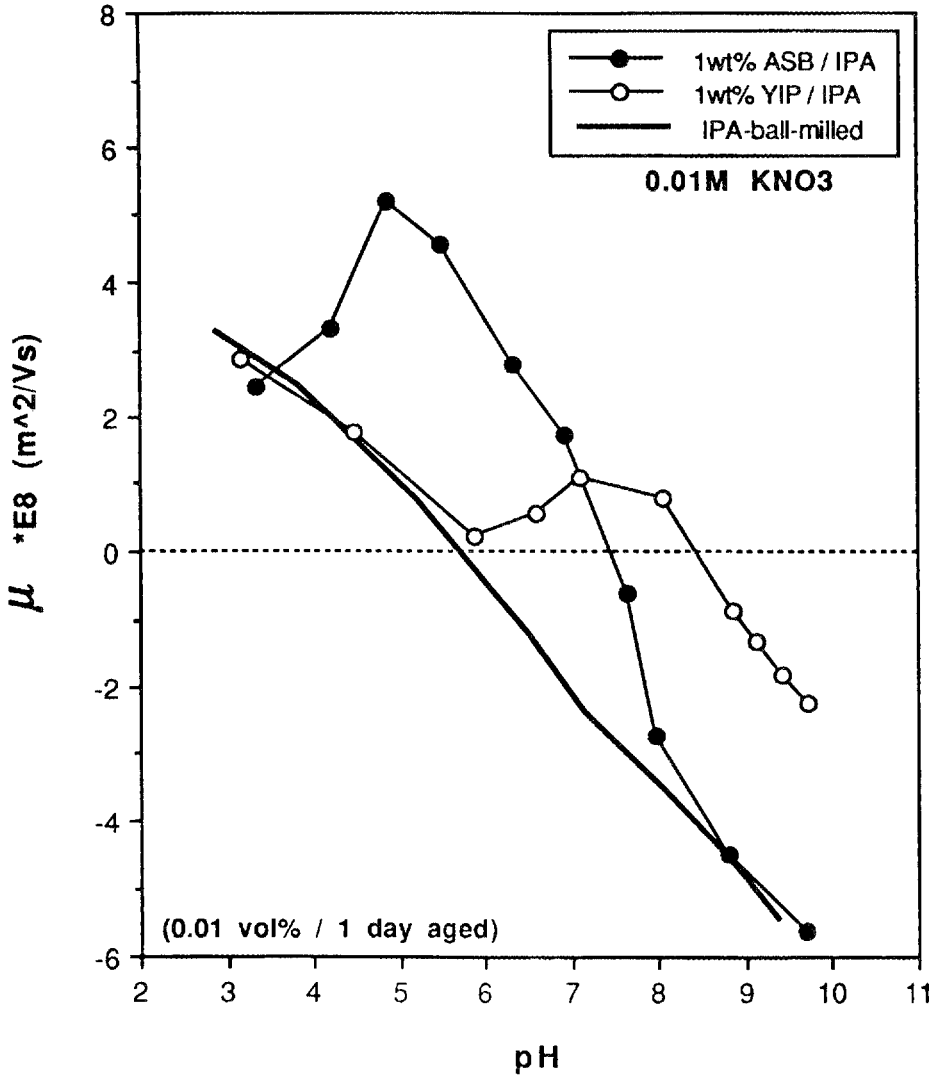

Figure 8. Electrophoretic mobility of 0.01 vol% UBE E-10 powder in 0.01 M KNO_3 solution as a function of nonaqueous dopant.

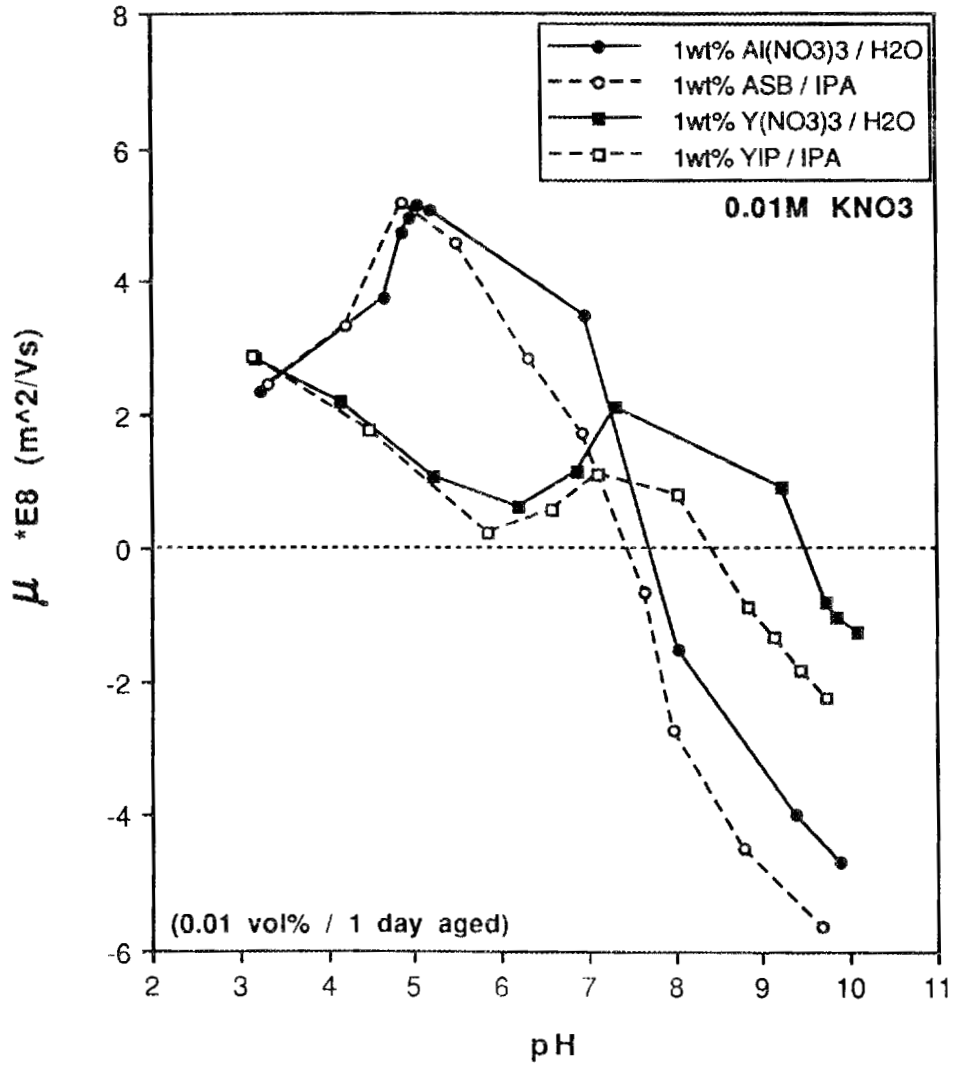

Figure 9. Comparison of electrophoretic mobilities of 0.01 vol% aqueous and nonaqueous doped UBE E-10 powders in 0.01 M KNO_3 solution as a function of pH and dopant.

PREPARATION OF 5 VOL% SUSPENSION

Five pH values (e.g., 3.5, 5.0, 6.5, 8.0, and 9.5) and two ionic strengths (e.g., 0.01 and 0.05 M) were used for the suspension preparation. Therefore, a total of 10 batches of suspensions were prepared.

1. Mix 666 g silicon nitride (ρ = 3.16 g/cc) in 4,000 ml KNO_3 solution (5 vol% suspension) for 10 minutes in a 2-gal plastic container using a Fisher Stedfast Lab Stirrer or a similar device.

2. Add 1 N HNO_3 or KOH to achieve target pH after aging and mix the suspension for another 10 minutes.

3. Load aliquot of the suspension (~200 ml) into a precleaned plastic bottle by siphoning from the stirred mixing container. (Totally 20 bottles were filled for each batch: 4 labs and 5 samples for each round robin measurement.) (The suspension was siphoned from the bottom center of the container towards the edge between the suspension level and the container for each bottle.)

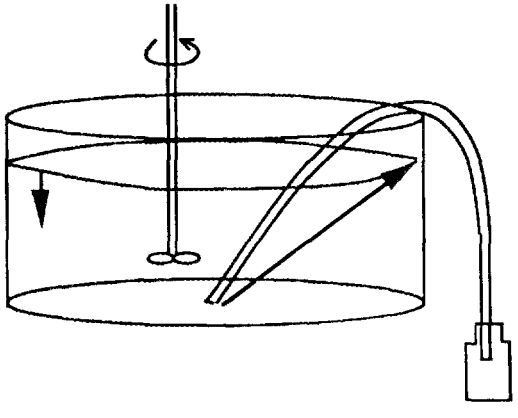

4. Seal. Package. Ship by UPS overnight delivery to the labs for μ and pH measurement. (The proposed schedule: 3/20/91 -- sample preparation; 3/22 -- sample delivery; 3/26 & 3/27 -- 1st measurement; 4/1 & 4/2 -- 2nd measurement; 4/8 & 4/9 -- 3rd measurement; 4/15 & 4/16 -- 4th measurement; 5/6 & 5/7 -- 5th measurement (if necessary)).

RECONSTITUTION PROCEDURE

(Use the first day for the reconstitution work and the second day for the pH and μ measurements.

The time spent on the reconstitution for a single sample is somewhat similar to that for pH and μ measurements. In order to maintain the same aging time for each sample, **the sampling order for reconstitution should be same as that for μ and pH measurements** --- starting from the sample with 0.01M ionic strength and the lowest pH; afterwards complete the all five samples with different pH values; then do the samples with 0.05M ionic strength with the same pH sequence.

1. Redisperse the 5 vol% suspension by magnetic stirring for 5 minutes (drop a magnetic stirrer in the bottle). During the stirring, the bottle should be capped to avoid CO_2 adsorption.

2. Transfer 0.3 ml of the 5 vol% suspension from the middle region of the bottle to an empty and precleaned 250 ml capped-bottle while stirring. Close the latter bottle.

3. Centrifuge the remaining 5 vol% suspension at 7,000 rpm for 20 minutes at 25 °C. (If temperature control is not available, the centrifugation should be done at room temperature.)

4. Transfer the centrifuged supernatant carefully to a scaled container (e.g., a graduated cylinder).

5. Transfer 150 ml of the centrifuged supernatant to the bottle having 0.3 ml of the 5 vol% suspension to make 0.01 vol% suspension for pH and μ measurements.

6. Repeat the procedure 1 to 5 until finish all 10 samples.

μ AND pH MEASUREMENTS

1. A referencing point of μ measurement will be taken using a GEMS 3 phosphated goethite sample (nominal pH 3.5 and 0.01M KNO_3) prior to the SEMS 1. (The measurement of pH of the goethite sample is also required.)

2. The protocols for these two measurements will follow the previous description for GEMS by Dr. Zeltner (e.g., for a given sample, record μ values for 5 fresh loadings of that sample; conduct μ measurement right after the loading; a pH value only be recorded when it is stable to 0.01 pH unit for 30 sec, etc.).

3. The μ measurement will not be conducted until 10 minutes of relaxation time is given after the 15 minutes of sonication for the 0.01 vol% suspension, which is also suggested by Dr. Zeltner.

The suspensions used for titration work were prepared in 0.05 M KNO_3 solution. The titration and pH measurement of the suspension were conducted after 30 minutes of homogenization on a stirring plate (Figure 10). The pH measurement was made by Metrohm pH electrode. An Eppendorf Digital Micropipette was used for the acid or base addition during titration.

In order to conserve powder and conduct the pH measurement more easily, three smaller sizes of 5 vol% suspensions (e.g., 37.5g in 225mL, 75g in 450mL, and 150g in 900mL supernatant) than a desired size (666g in 4,000mL) were used. The density of the UBE E-10 powder, 3.16 g/c.c., was measured using a He gas pycnometer.

Five pH values (e.g., 3.5, 5.0, 6.6, 8.0, and 9.5) were selected for the scale-up titration study. Prior to the addition of acid or base, an average pH of 6.59±0.06 for five out of six 5 vol% suspensions used for the titration study. The exception was the one for base titration with 150g in 900mL supernatant, which had the initial pH of 6.07. The scale-up titration curves were prepared using pH=6.60 as the starting and referencing point. All the curves for different pH values showed linear relationships between the amount of the titrant added and the volume of the supernatant used (Figure 11) indicating that similar suspension conditions could be maintained while increasing the size of suspension.

We found that the initial suspension pH of the UBE powder was dependent on the exposure time to air. For shorter the exposure times, higher suspension pHs were observed. The primary powder used for the titration work was taken from a sealed bag of the powder spin-riffled five months ago and stored in capped-plastic containers. The powder for the suspension with the initial pH at 6.07 may have been obtained from a container which was exposed to the air for a longer time.

The powder used for monitoring the pH change in time was taken just before the 5 vol% suspension (37.5g in 225mL 0.05 M KNO_3 solution) preparation from the same powder bag. The suspension pH measured after 15 minutes of mixing for the one completely open to air was 7.73 and for the one closed to air was 7.89. However, strictly speaking, the closed

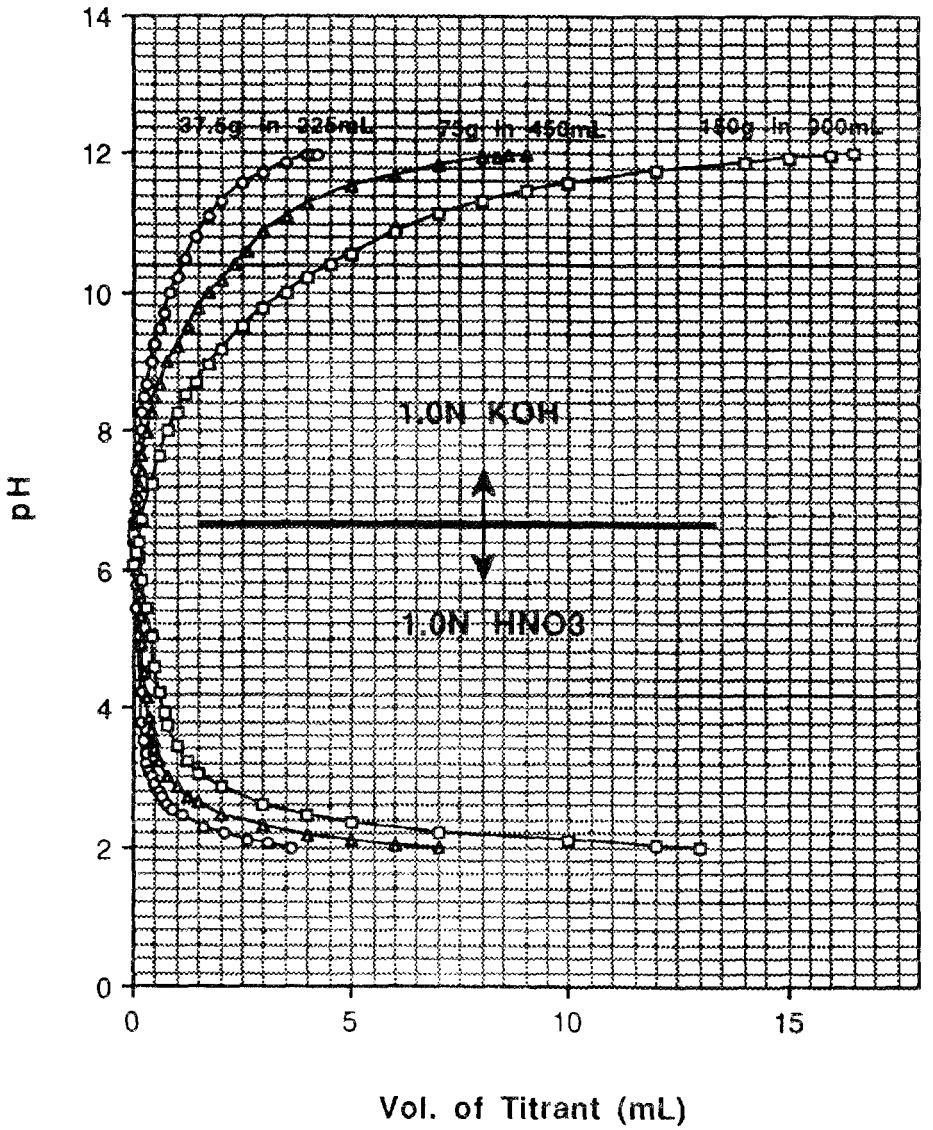

Figure 10. Titration curve of 5 vol% UBE E-10 powder in 0.05 M KNO_3 solution as a function supernatant volume.

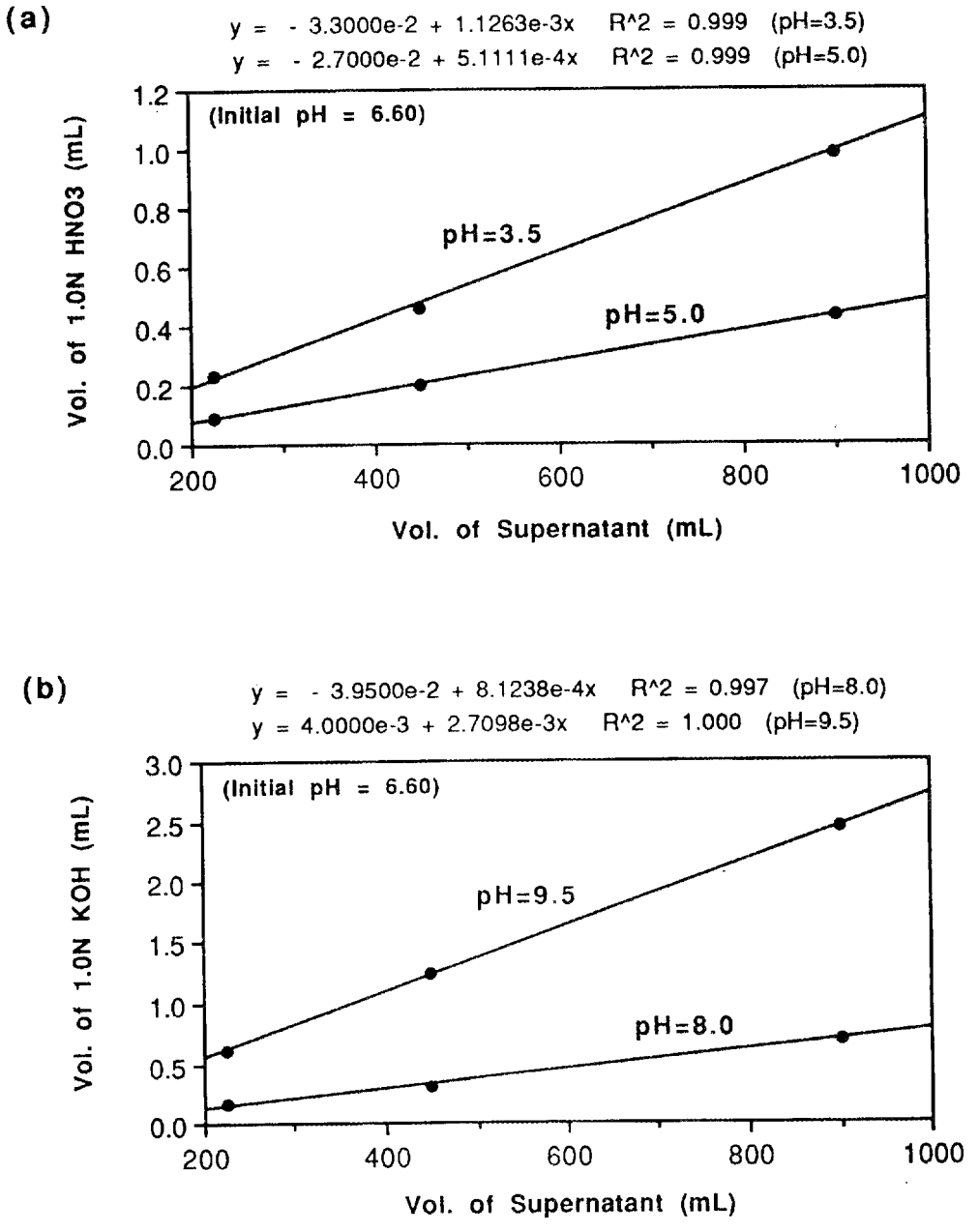

Figure 11. Linear relationships between the amount of the (a) acid or (b) basic titrant and the volume of the supernatant for 5 vol% UBE E-10 in 0.05 M KNO_3 solution.

system was exposed to air whenever the pH measurement was conducted. The suspension pH did not show significant change in the first 24 hours for either case. Even after 3 days of aging, the variation of pH was not over 0.2 pH units for both cases (Figure 12).

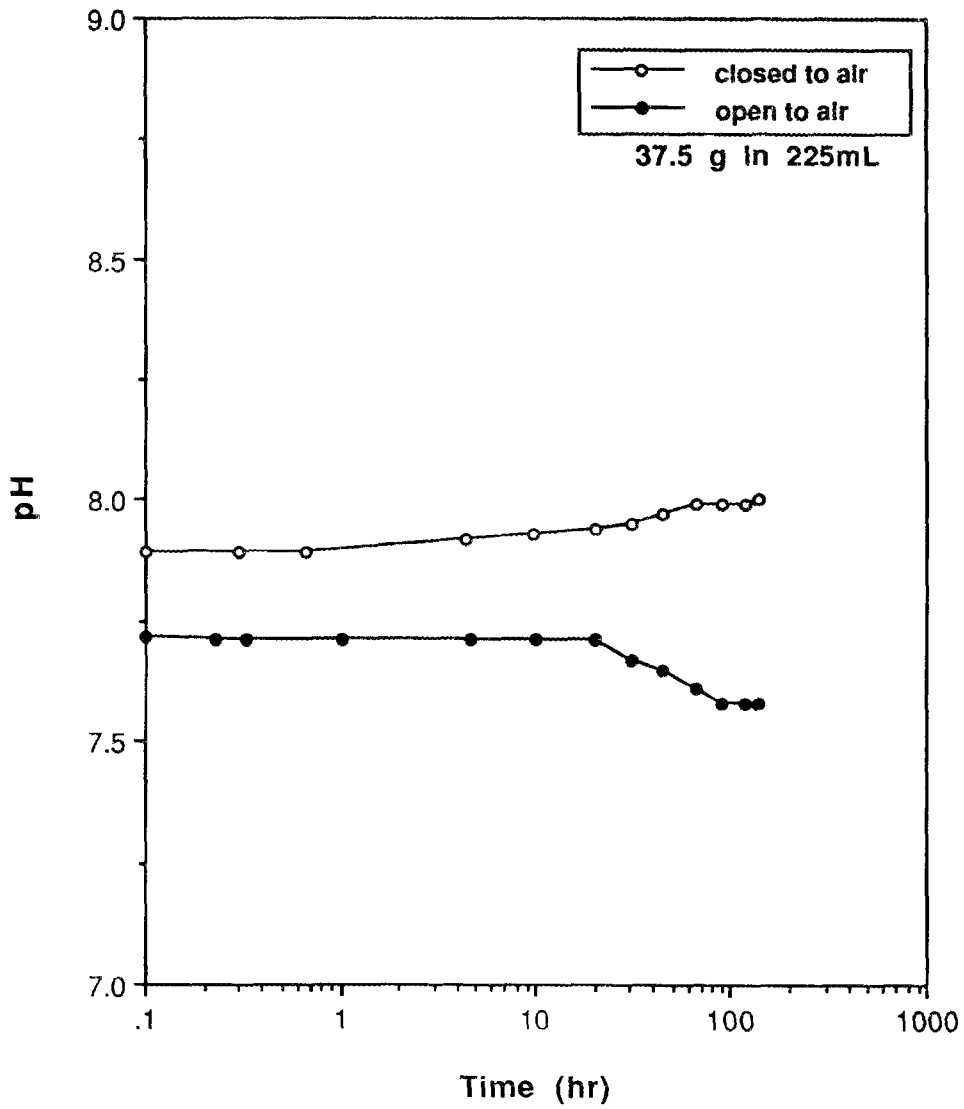

Figure 12. The suspension pH of 5 vol% UBE E-10 in 0.05 M KNO_3 solution as a function of aging condition and time.

References

1. R. O. James and T. W. Healy, Journal of Colloid and Interface Science, Vol. 40, No.1, pp.53-64, July, 1972.

Status of milestones

Milestone 352007---complete the round robin mobility testing of silicon nitride---the first round robin study is expected to be completed on 5/7/91.

Publications

1. J.-F. Wang, R. E. Riman, and D. J. Shanefield, "Reliable Electrokinetic Characterization Procedures for Ceramic Powders," pp.293-298 in the Proceedings of the Better Ceramics Through Chemistry IV of Materials Research Society, San Francisco, CA, 1990.

2. J.-F. Wang, R. E. Riman, and D. J. Shanefield, "Electrokinetic Characterization of Ceramic Powders," to appear in the Proceedings of Symposium III- Forming Science and Technology for Ceramics of the 93rd Annual Meeting of the American Ceramic Society, Cincinnati, OH, April 29-May 2, 1991.

4.0 TECHNOLOGY TRANSFER

4.1 TECHNOLOGY TRANSFER

4.1.1 Technology Transfer

Technology Transfer
D. R. Johnson (Oak Ridge National Laboratory)

Technology transfer in the Ceramic Technology Project is accomplished by a number of mechanisms including the following:

Trade Shows - A portable display describing the program has been built and has been used at numerous national and international trade shows and technical meetings.

Newsletter - A Ceramic Technology Newsletter is published regularly and sent to a large distribution.

Reports - Semiannual technical reports, which include contributions by all participants in the program, are published and sent to a large distribution. Informal bimonthly management and technical reports are distributed to the participants in the program. Open-literature reports are required of all research and development participants.

Direct Assistance - Direct assistance is provided to subcontractors in the program via access to unique characterization and testing facilities at the Oak Ridge National Laboratory.

Workshops - Topical workshops are held on subjects of vital concern to the ceramics community.

International Cooperation - This program is actively involved in and supportive of the cooperative work being done by researchers in West Germany, Sweden, the United States, and, most recently, Japan under an agreement with the International Energy Agency. This effort is ultimately aimed at development of international standards and includes physical, morphological, and micro-structural characterization of ceramic powders and dense ceramic bodies, and mechanical characterization of dense ceramics.

IEA Annex II Management

V. J. Tennery (Oak Ridge National Laboratory)

Objective/scope

The purpose of this task is to organize, assist, and facilitate international research cooperation on the characterization of advanced structural ceramic materials. A major objective of this research is the evolution of measurement standards for key material properties. This task, which is managed in the United States by Oak Ridge National Laboratory (ORNL), now includes a formal IEA Annex agreement identified as Annex II between the United States, the Federal Republic of Germany, Sweden, and Japan. The original annex included four subtasks: (1) information exchange, (2) ceramic powder characterization, (3) ceramic chemical and physical characterization, and (4) ceramic mechanical property measurements. The research in Subtasks 2, 3, and 4 is now completed. For the new Subtasks 5 and 6, there are 35 and 45 laboratories participating, respectively. During CY 1990, agreements were reached for Japan to join the Annex and for research in two new subtasks to be initiated. These include Subtask 5, Tensile and Flexural Properties of Ceramics, and Subtask 6, Advanced Ceramic Powder Characterization.

The Executive Committee agreed at the Cocoa Beach conference on January 17, 1991, that the next Executive Committee meeting will be held at the Japan Fine Ceramics Center in Nagoya, Japan, on October 15, 1991. The Executive Committee approved a change in the completion date for Amended Annex II from December 31, 1991, to December 31, 1993. At a future Executive Committee meeting, the Executive Committee may elect to establish further subtasks within Annex II.

Technical progress

Subtask 5, Flexural and Tensile Properties of Ceramics

United States

Compiling of the strength and loading data from the strain gages and conducting Weibull and other statistical analyses for the completed ambient- and high-temperature measurements have been completed. Preliminary results of the flexure strength data from both the ambient- and high-temperature measurements were analyzed to determine the most probable value of α and β for the Weibull distribution function representing each data set. Values of α were determined using both linear regression and maximum likelihood methods. Values of β were determined using the maximum likelihood method. The β values ranged from 881.1 to 851.9. The ambient-temperature flexural strength data have been analyzed using both maximum likelihood and linear regression methods. The maximum likelihood results provided α values ranging from 14.3 to 9.1. Similarly, linear regression provided values ranging from 14.0 to 6.5. These results were further analyzed using Johnson's[1] Monte Carlo simulation results for sampling from Weibull distributions. Using the maximum likelihood estimator for α, all of the 10 sets of data were located between the 90th and 10th percentiles. Results for seven of the laboratories were located between the 80th and

20th percentiles, which indicates that within the sampling errors expected from a Weibull distribution, the ambient-temperature data represent reasonable values for the estimator. Results for the linear regression estimator for α were not as well behaved; however, results from seven of the laboratories were located between the 80th and 20th percentiles.

Preliminary analyses of the U.S. flexure data were completed in December 1990 and, in general, were found to be within the expected range of variation, assuming that the strengths came from a Weibull distribution. Examples of these analyses are shown in Figs. 1 and 2.

In both Figs. 1 and 2, the Weibull modulus m (or α) for each data set is shown in terms of a ratio of the measured m value for the set to the expected true value, which is assumed to be equal to the Gaussian average of all 10 values of m for the material determined for that temperature. This ratio is plotted in a diagram derived by Johnson on which the percentiles for the modulus are shown based upon his extensive Monte Carlo sampling study. Only the analyses for the maximum likelihood method for determining m will be discussed here. Similar analyses were also performed

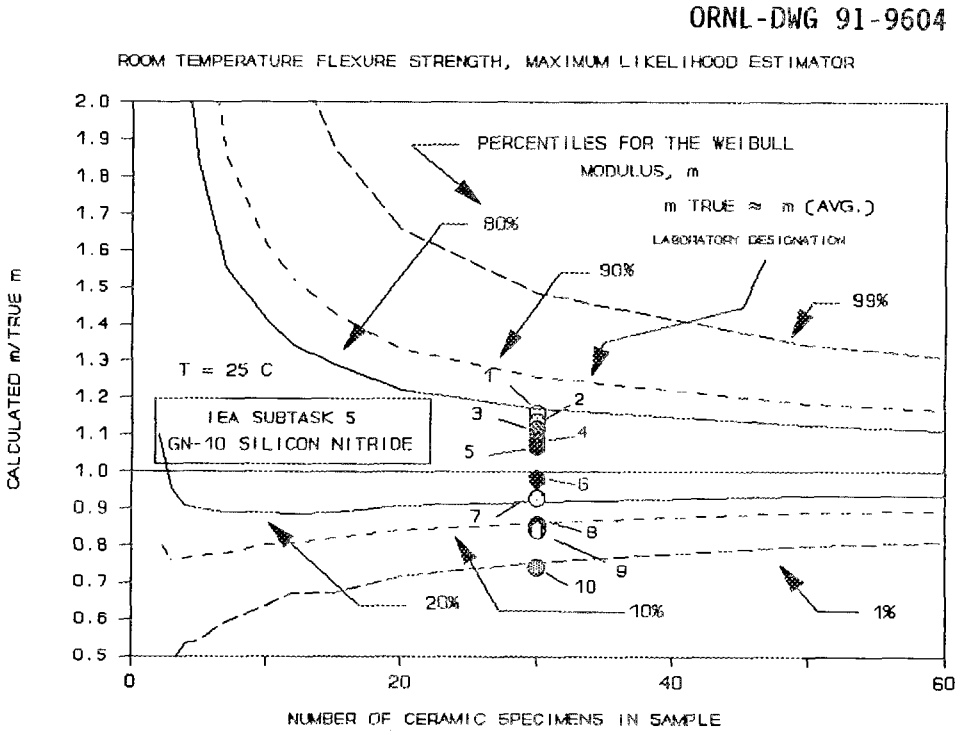

Fig. 1. Maximum likelihood analysis, 25°C flexure strength, GN-10 (10 U.S. laboratories, Subtask 5).

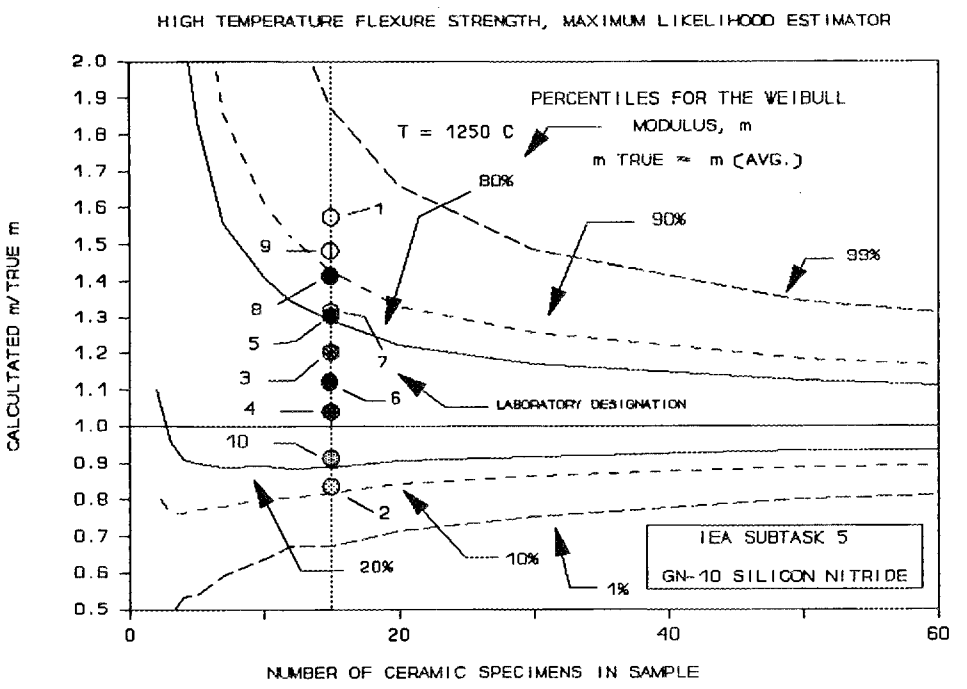

Fig. 2. Maximum likelihood analysis for 1250°C flexure strength of GN-10 silicon nitride from 10 U.S. laboratories, Subtask 5.

using the linear regression method for determining the value of m. Values of β were also determined for each data set from each laboratory, but these analyses are not included here. Figure 1 shows that the m ratios all fall between the 10th and 90th percentiles expected from a Weibull distribution for sample sizes of 30 specimens. The values for laboratories 9 and 10 fall outside this range. These results are considered to be very consistent with the variation in m expected from a random sampling of the strength from a Weibull distribution. Figure 2 shows the results of an analysis similar to Fig. 1, but is for the strength values measured at 1250°C and for a sample size of 15 specimens. As expected, the scatter in the m ratios is much greater at N = 15 than it is for N = 30. However, all of the data sets fall within the range of the 10th and 90th percentiles, except for laboratories 1 and 9. Further analyses of these data will be conducted next year.

The flexure specimen strain-gage data have been analyzed. Preliminary results indicate that many of the participants' high-temperature flexure fixtures were subject to frictional effects, which caused the true specimen stress to be lower than the stress calculated by the elastic beam formula. A letter was sent to the U.S. participants on the status of the flexural strength measurements.

Analysis of the flexural strength data is proceeding. To date we have not received the fractography data from Corning, Ford, Carborundum, and General Electric. Corning has not indicated when fractography data will be

provided. Ford has promised the data by the end of April 1991, General Electric has promised the data by the end of May 1991, and Carborundum will send the data by the end of April 1991.

The status of the U.S. tensile specimens is as follows. A total of 175 tensile specimen blanks to be machined (120 straight collet and 55 tapered collet) were delivered to Chand/Kare Technical Ceramics, Worcester, Massachusetts, on October 16, 1990. The finished specimens are returned to ORNL in increments of 25 with the requirement for a complete inspection before final machining starts on the remaining specimens. The inspection procedure includes a total of 104 dimensional measurements on each specimen using shadowgraph comparator techniques. Machining by Chand/Kare was completed except IEA tensile specimen sequence Nos. 161-175 were returned because they did not meet the specification for the button-head radius. Fortunately, the button-head radius was too large and, thus, material was available for further machining. The specimens were returned to Chand/Kare and all specimens were machined to the required specification. This machining results in essentially a 100% yield. All dimensional analysis has been completed on all specimens except Nos. 161-175. These will be completed in April 1991.

Discussions were held with members of ASTM Subcommittees C-28.01, Properties and Performance, and C-28.02, Design and Evaluation, at the San Antonio meeting of C-28 in November 1990 to review the plans for strain gaging the tensile specimens. At an earlier meeting in Dearborn, Michigan, the advantages of using 9 gages per specimen were reviewed, in addition to the substantial cost. The conclusion of the C-28.01 and C-28.02 discussions has resulted in a basic agreement to use 7 gages on 172 specimens, with 9 gages used on 3 specimens, which will be loaded to fracture in the High Temperature Materials Laboratory (HTML) under highly controlled conditions. The results will then be directly usable by Committee C-28 for preparing a tensile strength standard. The present plan is to complete all of the tensile specimen measurements in the United States by the end of CY 1991, in order that the results can be used as input for drafting a structural ceramic tensile strength measuring standard during the first quarter of 1992. A formal recommendation from representatives of ASTM C-28, John S. Cuccio and Curtis Johnson, was received recommending use of seven strain gages in a particular configuration for all of the IEA tensile specimens. A nine-gage configuration should be used on three specimens and tested at the HTML. Additional funds for this gage intensive activity were requested and approved January 28, 1991.

The first 25 IEA tensile specimens were sent March 4, 1991, to HiTec Corporation, Westford, Massachusetts, for application of strain gages at seven (7) locations in the gage section of each specimen. These first 25 specimens were returned at the end of March 1991, and gage placement verification was completed by our staff and found to meet the specification. An important fact learned during this trial set of 25 specimens was that trace amounts of cutting fluids on the surface of the silicon nitride specimens made it very difficult to properly attach the strain gages to the specimens. As a result of this observation, our staff rigorously cleaned all of the tensile specimens before they were sent to HiTec Corp. This detail will later be included in a draft tensile strength standard.

Germany

A copy of the German grinding procedure for the tensile specimens to be done by the firm of Wemhöner and Popp was received on October 4, 1990. Notification was received October 2, 1990, from Dr. Faul stating that Dr. Vierkorn-Rudolph will no longer be involved with the IEA Annex II project. Dr. Eberhard Seitz is the new German representative.

The subgroup, "Mechanical Characterization of Structural Ceramics," met on November 19, 1990, at the KFA to update the joint working plan and time schedule for Germany and Sweden. Dr. Lenard Carlsson, Swedish Testing and Research Institute, was the Swedish coordinator at this meeting. We received a letter from Dr. Seitz giving the results of their national subgroup meeting of November 19, 1990. The major points are as follows: (1) manufacturing of preshaped glass ceramics by Schott Glaswerke will be completed early in December 1990 and the specimens will be mailed to Wemhömer & Popp for machining by the end of December 1990; (2) the first HIP-cycle of ESK preshaped silicon nitride will be completed early in February 1991 with blanks mailed to Wemhömer & Popp for machining by the end of February 1991, and the second HIP-cycle of nitride by ESK will be completed by early March 1991 with mailing to Wemhömer & Popp completed by the end of March; and (3) mailing of "finished" samples and start of fracture strength measurements by mid April 1991.

We received notification from Dr. Seitz that, due to budget cuts in Sweden, the number of specimens produced by ABB-Cerama has been reduced. The number of ASCERA tensile specimens will now be 25 (both Sweden and Germany) instead of 30, 4-point flexure specimens will be 150 (both Sweden and Germany) instead of 200, and the number of ball-on-ring specimens will be 25 (Sweden only) instead of 30.

V. J. Tennery provided to the German team the thirty (30) GN-10 flexure specimens, which are part of our IEA Annex II exchange in Subtask 5, at the Executive Committee meeting in Cocoa Beach on January 17, 1991.

Sweden

Notification was received November 26, 1990, that funds have been approved for the IEA cooperation.

V. J. Tennery provided to the Swedish team the thirty (30) GN-10 flexure specimens, which are part of our IEA Annex II exchange in Subtask 5, at the Executive Committee meeting in Cocoa Beach on January 17, 1991.

Japan

Colleagues in Japan started ambient-temperature fracture of their flexure specimens in October 1990. On October 17, 1990, we sent our 30 GN-10 exchange flexure specimens to Japan, and on November 14, 1990, we received in return 30 SSN-H silicon nitride flexure specimens from Mr. Awaji of the JFCC.

At the Executive Committee meeting in Cocoa Beach, preliminary ambient-temperature flexure strength data were provided from the participating Japanese laboratories for the Kyocera silicon nitride, SSN-H. Use of a strain-gaged calibration specimen in the fixtures before and after specimen measurement and use of the calibration specimen data were used to

provide a strength correction factor for each laboratory, which reduced the laboratory-to-laboratory variation in measured strengths.

Subtask 6, Advanced Ceramic Powder Characterization

Major responsibility for this subtask in the United States is at the National Institute of Standards and Technology (NIST), and a detailed report of progress on this subtask is provided in the section of this report submitted by NIST. Only a brief summary is provided here.

Analysis of powder samples in all four participating countries is progressing. Data from three countries arrived in January 1991. The participants have not experienced significant problems in the interpretation of powder analysis procedures. Most of the questions received until now have been about the surface chemical methods. The methods of surface chemical analysis were provided only as a guide, leaving sufficient flexibility to the participants to adopt their standard practices. This is in contrast to the procedures for physical and bulk chemical analysis, which were described in sufficient detail to avoid misinterpretations.

At NIST, two additional activities are in progress: development of software programs for data entry and analysis of powder samples. Several programs are being developed to facilitate data entry and data retrieval. All five powders are being analyzed for physical and surface chemical properties. These data are being used to test the data-entry programs.

Analysis of the powder samples in the participating countries is progressing at various stages. Japan's participants have completed analysis of all powders and procedures to fulfill their commitment. The participants in Germany have completed physical properties analysis, while the bulk chemical analysis is expected to be completed by March 1991. Sweden's participants have completed most of their analyses. The analysis activity in the United States is approximately 75% complete, while the remaining is expected to be completed by the middle of March 1991.

Data entry activity was initiated at NIST in January 1991. Approximately 65% of the total data has been sent to NIST. Of this data, we have com-pleted entry of a major portion. Data entry was completed in March 1991. Preliminary analysis of the data shows that most participants have followed the agreed-to procedures, though a few exceptions exist, particularly in the area of powder dispersion methods used prior to sedimentation analysis for particle size distribution.

A meeting of the technical leaders was held at the Cocoa Beach conference on January 17, 1991, to discuss technical issues and future plans. Professor Hausner, Technical leader from Germany, was unable to attend this meeting. Steve Hsu, Chairman of Subtask 6, made a presentation to the IEA Executive Committee on the status of the activities at this meeting.

Several discussions were held with the technical coordinator of this task at NIST. A meeting of the U.S. members of the working group is scheduled for April 22, 1991, at NIST to analyze all of the ceramic powder characterization data that have been received and to recommend data sets for inclusion for the statistical analysis. Working group members will attempt to identify those data sets that should be excluded from the final data set subjected to statistical analysis. No data have been received from Germany, but it is hoped that data will be received by May 15, 1991,

to allow time for preliminary analysis prior to the working group meeting planned for June 13, 1991, in Göteborg, Sweden.

Reference

"Advanced Statistical Concepts of Fracture in Brittle Materials," C. Johnson and W. Tucker, pp. 208-23 in *Ceramic Technology for Advanced Heat Engines Project, Semiannual Report*, ORNL/TM-10079, Martin Marietta Energy Systems, Inc., Oak Ridge Natl. Lab., March 1986.

Status of milestones

(Milestone No. 411508 - January 31, 1991)
The ambient- and high-temperature testing on the flexure specimens by the participating laboratories has been completed.
Other milestones are on schedule.

Publications

V. J. Tennery, oral presentation, "Cooperative International Program on Mechanical Strength Measurements of Ceramics," at Annual Automotive Technology Development Contractors' Coordination Meeting, Dearborn, Michigan, October 22–25, 1990, to be published in the *Proceedings of the Twenty-Eighth Annual Automotive Technology Development Contractors' Coordination Meeting.*

V. J. Tennery, invited presentation, "The Maximum Likelihood Method for Determining Weibull Distribution Function Estimators of Ceramic Materials," at ASTM Committee C-28 Meeting, Advanced Ceramics - Probabilistic Procedures Task Group, San Antonio, Texas, November 14–16, 1990.

V. J. Tennery presented preliminary results on the status of the flexure strength measurements in the United States at the Executive Meeting in Cocoa Beach entitled, "Status of U.S. Research in Subtask 5 - IEA Annex II."

Characterization of Ceramic Powders

S. G. Malghan, L.-S. Lum, J. F. Kelly, E. Begley and S. M. Hsu
(National Institute of Standards and Technology)

Objective/Scope

Ceramics have been successfully employed in engines on a demonstration basis. The successful manufacture and use of ceramics in advanced engines depends on the development of reliable materials that will withstand high, rapidly varying thermal stress loads. Improvement in the characterization of ceramic starting powders is a critical factor in achieving reliable ceramic materials for engine applications. The production and utilization of such powders require characterization methods and property standards for quality assurance.

The objectives of the NIST program are (1) to assist with the division and distribution of five ceramic starting powders for an international round-robin on powder characterization; (2) to provide reliable data on physical (dimensional), chemical and phase characteristics of powders; and (3) to conduct statistical assessment, analysis and modeling of round-robin data. This program is directed toward a critical assessment of powder characterization methodology and toward establishment of a basis for the evaluation of fine powder precursors for ceramic processing. This work will examine and compare by a variety of statistical means the various measurement methodologies employed in the round-robin and the correlations among the various parameters and characteristics evaluated. The results of the round-robin are expected to provide the basis for identifying measurements for which Standard Reference Materials are needed and to provide property and statistical data which will serve the development of internationally accepted standards.

Technical Progress

The technical progress covered in this report includes description of three major activities--samples analyses, data compilation and data analyses.

Samples Analyses. During the period October-December 1990, major effort was expended in the analyses of powder samples. Most of the participants were involved in Group I (Physical Properties-- particle size distribution, surface area, x-ray diffraction) and Group II (Bulk Chemical Analysis-- major impurities, C, O, N, F, Cl, and free C in SiC) measurements. The Group III (Surface Chemistry) properties were studied in all four participating countries, on an optional basis. No problems were experienced in the interpretation of analysis procedures that were sent along with the powder samples. Very few incidences of sample vials breakage was reported by the participants.

At NIST, all five powders were tested by a number of measurement methods, such as x-ray absorption during gravity sedimentation in Sedigraph, laser-diffraction by stream scanning in Horiba LA-500, scanning electron microscopy, specific surface area by single and

multipoint BET, specific gravity by helium pycnometer, electrokinetic sonic amplitude by Matec 8050, phase composition by nuclear magnetic resonance spectroscopy, surface chemistry by Auger spectroscopy and X-ray diffraction. Most of the procedures for these methods were used in as-developed form. In only a few cases, minor changes were made to the procedures.

Data Compilation. This activity involved the development of data entry modules and entry of the data. Data acquisition forms that were distributed to the participants served as the basis for the computerized data entry module. The module consisted of eight distinct templates corresponding to the fifteen data acquisition forms. The listing of fifteen data acquisition forms was provided in a previous bimonthly report. The data entry program contains additional codes to support and manipulate the templates so that behind the scene operations can be carried out to provide an interface to the data entry function. This program was used to complete the data entry activity.

The data were received from the participants in U.S., Japan and Sweden only. The German data has not been received at the time of writing of this progress report. The primary reason for the delay is slow progress in samples analyses, and adverse effect of sluggish economy. The German data are expected to arrive at NIST by May 15, 1991, and their compilation is expected to be completed within three weeks of their receipt.

The data received until now has been compiled and two reports have been prepared. The first report contains data only in a tabulated format. The data are organized according to the procedure by which each powder was analyzed. The participants names are identified by number codes. In the first version of this data-report all the data sent by the participants are included. Where data are not provided, blanks are left. One of the future activities is to obtain the missing information by contacting each participant. The computer program is written in such a way as to present the data in a different format for comparison. For example, the concentration of calcium in silicon nitride powder by inductivity coupled plasma, direct coupled plasma and atomic absorption spectroscopy can be tabulated. The second report is a compilation of comments by the participants on the procedures. In this report every detail provided by the participant is entered in accordance with the data acquisition module. Some of the problems we observed in preparing this report were lack of information from the participants and information provided in a different format than asked for. The computer program had to be modified as we came across the problems. In general, most of the participants made an effort to meet the guidelines. This report has approximately 1400 pages. Therefore, it is not distributed to the participants unless they specifically request for a copy. Both reports are necessary in order to provide interpretation of discrepancies in the data. The first report was distributed to all the participants in Japan, Sweden, and the U.S. Both reports are available on a diskette or a hard copy.

Data Analysis. The compiled data are being examined by the participants. The U.S. participants met at NIST on April 22-23, 1991 to review the data. At this meeting, each data set was examined critically and reasons for discrepancies were recorded. In many cases, the participants did not provide enough information. As a result, detailed data analysis could not be carried out. At this meeting detailed questions were developed for participants whose data did not accompany sufficient information. Through these questionnaires, more information will be collected.

Preliminary evaluation of the data shows that lab to lab comparison of data for a given analysis method was good for participants who followed the recommended procedure. For every analysis method, there were some participants who did not follow the recommended procedure. Reasons for not following the procedure are either lack of required equipment and/or no familiarity with the procedure. In most cases, it is very easy to identify outliers, because the data from non-recommended procedures are fairly well separated from the rest. Since the experimental design called for at least six laboratories using the same procedure, the data analysis will focus on identifying the outliers and reasons for the difference.

Future activities will be devoted to the compilation of data from Germany, technical and statistical analysis of the data, and preparation of draft conclusions.

Status of Milestones

On target, except for compilation of German data.

Publication

Two reports on data and procedure comments were released to IEA participants.

S. G. Malghan - Co-authored a chapter on Powder Characterization to the ASM Handbook

Ceramic Mechanical Property Test Method Development

George D. Quinn
(National Institute of Standards and Technology)

Objective/Scope

This is a new task with a focus on developing mechanical test method standards in support of the Ceramic Technology for Advanced Heat Engines and Advanced Turbine Technology Applications Programs. The prime DOE contractors and subcontractors will be surveyed by on-site visits to assess their needs and capabilities. Test method development should also consider the general USA structural ceramics community as well as foreign laboratories and companies, but emphasis will be placed on the needs of the DOE community.

Draft recommendations for practices or procedures shall be developed based upon the needs identified above and circulated within the DOE ceramics heat engine community for review and modification. Round robins will be conducted as necessary, but shall be well-focussed, limited in scope and not interfere with ongoing IEA round robins. Procedures developed in this program shall be presented as ATTAP or CTAHE "standard procedures." Alternatively, (and eventually) these will be advanced for final standardization by ASTM or by the U.S. Army as possible MIL STD's.

Technical Highlights and Results

A chapter entitled "Strength and Proof Testing" for the new ASM Handbook of Ceramics and Glasses was completed and delivered to ASM. The chapter reviews the state-of-the-art of the scientific know-how and test procedures at a level that "shirtsleeve engineers" and newcomers to the field can appreciate.

Flexure fixtures are being fabricated by the NIST machine shop that will permit fast fracture strength and fracture toughness evaluation by any of the standards in place or under development. These include ASTM C1161, DIN 51-110 Part 1, JIS R 1601, MIL STD 1942(MR). These standards have sufficiently similar features, that only minor modifications are necessary for specimen size and/or fixtures. The same style fixtures can be used for fracture toughness tests as well.

A set of handout fliers have been revised and are available on a simple room temperature flexure test fixture that can be machined by any competent shop at a reasonable cost. A draft of a similar set of design notes is being prepared for a rolling pin high temperature flexure fixture. Guidelines such as these will enable DOE contractors to develop competent testing capabilities if they are unable or unwilling to purchase off-the-shelf commercial fixtures.

The whole issue of what flexure testing is and is not good for needs to be defined once and for all. To that end, a draft manuscript: "Design Data for Engineering Ceramics: A Review of the Flexure Test" was finished and copies sent to Dr. R. Morrell in the National Physical Laboratory in England (the U.K. analogue of NIST).

The paper is a comprehensive review of the topic of whether flexure testing can be used for design. There are wide ranging opinions on this issue. The literature has wildly mixed results. The findings of the review are surprising. In brief summary, for flexure testing to be useful for design, a number of assumptions must be met. For example, both the average microstructures and the extreme microstructural features, the defects, must be identical in the test specimens and the components. Consistency is the key issue. In most instances, one or more of the assumptions are not met, and the flexure data has limited applicability. Unfortunately, many of the assumptions apply equally well to direct tension data as well and there is a risk that even tension data will be misleading. The assumptions are listed in a checklist fashion in the manuscript such that they can be addressed for each problem a designer may confront. There is some cause for optimism however, since the literature review showed that there were at least several dozen instances where flexure data scaled quite well to uniaxially stressed components.

The manuscript includes sections on flexural creep, stress rupture and corrosion/erosion testing. A primary conclusion reached is that although flexural studies may be satisfactory for qualitative assessments of creep, it is not recommended for quantitative measurements. The results of flexural creep studies are compromised by the assumptions necessary on the constitutive equations. Direct tension testing is strongly preferred. The manuscript is currently being condensed, since a preliminary review showed it to be too long.

A draft standard "Flexure Strength of Advanced Ceramics at Elevated Temperatures," was prepared and presented at the San Antonio, Nov. 1990 meeting of C-28. This draft is a clone of the ASTM C-28 room temperature flexure standard, C 1161, but with the necessary high temperature features added in. The author is leading a task group comprised of Mike Foley of Norton, Matt Ferber of ORNL, Terry Richardson of Garrett Engine Company and Leon Chuck of the University of Dayton Research Institute. After that meeting, a draft standard was prepared and has been sent out for a C-28.01 Properties and Performance subcommittee ballot. This ballot will be complete prior to the C-28 May, 1991 Philadelphia meeting. One key aspect of this standard is that it permits either rolling loading pins or fixed pins to be used, but with a strong preference for the rolling pin scheme. This is because the fixed pin scheme will incur a friction error, estimated to be 5-15%. We are allowing the fixed pin arrangement as a concession to experimental difficulties in conducting high temperature testing. Another major change over the room temperature standard is the specification of a time-to-failure criterion for the rate of loading, as opposed to the strain rate criterion in the room temperature standard. These two issues will undoubtedly be discussed in some detail in Philadelphia and may in fact elicit some negative ballots. That is not a problem, since the balloting process is meant to stimulate such revisions or discussions.

A draft standard for elastic modulus determination has been developed in cooperation with Dr. S. Gonczy of Allied Signal and Mr. John Helfinstine of Corning. This draft standard is a modification to

ASTM standards already on the books as ASTM standards (Whitewares and Glass Ceramics) but has been modernized and adapted to make it suitable for advanced ceramics. It is based upon the well known beam resonance methods. A review of the equations had to be made and extended back through 70 years of the literature to Timoshenko. (The Japanese elastic moduli standard for advanced ceramics: JIS R 1604 includes this method). The draft has been submitted for an ASTM C-28 Main and Subcommittee ballot.

Reviewer's responses have been coming in on the draft standard for fractographic analysis of strength limiting defects in advanced ceramics. Several technical presentations have been given to highlight the objectives and approach that this standard will have. General guidelines for fractographic analysis will be given including procedures for mechanical testing, specimen preservation, visual examination, optical microscopic and scanning electron microscopic examination. The goal of the standard is to develop common guidelines for the detection and characterization of strength limiting defects in advanced ceramics. We project that there will be major revisions to the draft standard. The following Table illustrates the required characterization and reporting scheme, for strength limiting defects. It is mandatory to report the first two aspects of a defect; the third is optional. Very careful distinction must be made with respect to whether a flaw was distributed in the volume or the surface, and where the specific flaw was actually located in the particular specimen. For example, volume distributed pores may be located (in any one specimen) in the bulk (volume), at the surface, or at an edge.

FLAW CHARACTERIZATION SCHEME

FLAW TYPE	FLAW LOCATION	FLAW SIZE
Pore, Volume Distributed	Surface	120 μm
Inclusion, Vol. Dist.	Volume	50 μm
Machining Damage, Surf.	Surface	30 μm

This project was commenced while the author was still with the U.S. Army Materials Technology Laboratory and is in collaboration with Mr. Jeffrey Swab and Mr. Michael Slavin. A preliminary draft standard was sent to approximately 40 experts in the fractography field and some excellent constructive criticism has been obtained. Major revisions to the draft standard are now being written. The original thrust to characterize strength limiting defects has to be modified somewhat. In older structural ceramics, strength was limited by gross microstructural aberrations such as pores or inclusions. The remarkable improvements in structural ceramics over the last decade have led to new materials which no longer fail from such defects, but from "mainstream microstructural features." This latter phrase

(coined by Roy Rice) refers to microstructural features such as large grains or zones of slightly irregular structure (i.e. microporosity) which are part of the "normal" range of the microstructure. It is a matter of semantics as to whether these features can be considered "defects." From a fracture mechanics standpoint, they are; but from a materials processing perspective, they are not. Another issue that was uncovered (by Bruce Adams) is the legal ramifications of using the words "defect" or "flaw." Such words are avoided in the glass industry. We must consider the consequences of using these words if we evision using ceramics in general structural applications. In view of these two issues, it has been decided that the fractography standard will focus on characterization of "fracture origins", but will include a discussion of defects. It is now envisioned that the document will become a MIL HDBK (Military Handbook). Ultimately, it is the goal to have interrelated standards for mecahnical testing, fractography and statistical interpretation as illustrated below:

MECHANICAL TEST	FRACTOGRAPHIC STANDARD
Flexure ASTM C1161 or MIL STD 1942 or Tension ASTM XXXX	MIL HDBK XXXX

WEIBULL STATISTICAL ANALYSIS
ASTM Std XXXX

The test method standards are either on the books or are in development. The fractography standard is targeted for a 1991 approval as a MIL HDBK and will then be brought into the ASTM C-28 forum for consideration. The Weibull Statistical Analysis standard is being developed in ASTM Committee C-28.

The Weibull statistical analysis draft standard is beginning to take shape in the Design and Evaluation Subcommittee C28-02. The author prepared a strawman draft standard whose function was to propose one scheme, but more importantly, to provoke action by that subcommittee and to focus its work. The latter objectives were successful and the subcommittee is now industriously working towards a draft standard. Dr. Steven Duffy of NASA-Lewis has the lead in this initiative and a new draft will be presented at the Philadelphia meeting in May. The author has received a German draft standard: "Testing of Advanced Technical Ceramics: 4-Point Bending Test; Statistical Evaluation; Determination of tghe Weibull parameters." This document has already been approved in the German Standards Body DIN and assigned a number DIN 51-110 Part 3. The author is translating the document and will bring it to the ASTM Philadelphia meeting. It calls for a Maximum likelihood analysis (and forbids the least squares regression method) but also mandates that the results be plotted on a conventional Weibull graph with the double natural log

ordinate axis and the natural log stress abscissa. In light of this, and also considering new statistical analyses conducted as part of the DOE Life Prediction programs by Dr. C. Johnson of G.E., it now appears that the Maximum Likelihood analysis should become the DOE and ASTM standards. The Least Squares analysis should be abandoned.

Standardization of fracture toughness testing remains elusive. This is a very contentious issue since very strong preferences and opinions have developed over the years. There is at the moment, only a small amount of actual work ongoing on optimizing or refining the measurement of fracture toughness. The likelihood of standardizing a specific method within ASTM is hard to anticipate, but it will be a difficult process. The author is currently touring the DOE contractors and subcontractors and is assessing their needs and preferences. The indented flexure strength and chevron notch methods are surpisingly popular. There is a fair to good prospect that DOE guidelines for toughness testing can be prepared as part of this program in 1991 or early 1992.

The author has committed to measure the fracture toughness of the zirconia and silicon nitride specimens furnished by the Japan Fine Ceramics Center as part of the 1989 round robin organized under the auspicies of VAMAS. The methods include indentation fracture, indentation strength and the single edge precracked beam (bridge indentation) methods.

During this interval, Mr. Quinn was appointed international leader of VAMAS (Versailles Advanced Materials and Standards) Technical Working Area #3, Ceramics. At the moment, there is intensive work on fracture toughness evaluation and two round robins are underway. This work is relevant to the DOE programs since the new round robin includes the chevron notch method. A fractography round robin is a possible task for this group in 1991 and 1992.

Status of Milestones

All milestones are on schedule with the exception that the author has had to withdraw from the Goteburg, June 1991 conference.

Publications/Presentations

1. Chapter 8H "Strength and Proof Testing," Submitted to ASM for the Handbook on Ceramics and Glasses.
2. Flier Sheets: "Guidelines for Flexure Testing of Advanced Ceramics, Room Temperature," Jan. 1991
3. ASTM Draft Standard: "Dynamic Young's Modulus, Shear Modulus, and Poisson's Ratio for Advanced Ceramics by Sonic Resonance," by S. Gonczy, G. Quinn and J. Helfinstine.
4. ASTM Standard C1161-90 "Standard Test Method for Flexural Strength of Advanced Ceramics at Ambient Temperature," Adopted Dec. 27, 1990, Published Feb. 1991.
5. ASTM draft standard: Standard Test Method for Flexural Strength of Advanced Ceramic at Elevated Temperature," Draft 2, Nov. 1990; Draft 3, March 1991.

6. U.S. Army MIL STD 1942(A), "Flexure Strength of High Performance Ceramics at Ambient Temperature," adopted Nov. 1990. (An update of the original 1983 standard. The update incorporates minor technical revisions, is more consistent with the ASTM standard, and is a triservice standard).
7. U. S. Army draft standard: "Standard Practice for Characterizing Strength Limiting Defects in Advanced Structural Ceramics", with M. Slavin and J. Swab, Nov. 1990.

ORNL/TM-11859

INTERNAL DISTRIBUTION

1-2. Central Research Library
3. Document Reference Section
4-5. Laboratory Records Department
6. Laboratory Records, ORNL RC
7. ORNL Patent Section
8-10. M&C Records Office
11. L. F. Allard, Jr.
12. L. D. Armstrong
13. R. L. Beatty
14. P. F. Becher
15. R. F. Bernal
16. T. M. Besmann
17. P. J. Blau
18. A. Bleier
19. E. E. Bloom
20. K. W. Boling
21. R. A. Bradley
22. C. R. Brinkman
23. V. R. Bullington
24. R. S. Carlsmith
25. P. T. Carlson
26. G. M. Caton
27. R. H. Cooper, Jr.
28. S. A. David
29. J. H. DeVan
30. J. L. Ding
31. M. K. Ferber
32. F. M. Foust
33. W. Fulkerson
34. R. L. Graves
35. D. L. Greene
36. E. E. Hoffman
37. C. R. Hubbard
38. M. A. Janney
39. M. G. Jenkins
40. A. F. Johnson
41-45. D. R. Johnson
46. W. F. Jones
47. D. Joslin
48. R. R. Judkins
49. M. A. Karnitz
50. B. L. Keyes
51. H. D. Kimrey, Jr.
52. T. G. Kollie
53. K. C. Liu
54. E. L. Long, Jr.
55. W. D. Manly
56. R. W. McClung
57. D. J. McGuire
58. J. R. Merriman
59. A. J. Moorhead
60. B. J. Moses
61. T. A. Nolan
62. J. L. Rich
63. C. R. Richmond
64. J M Robbins
65. M. Rohr
66. M. L. Santella
67. A. C. Schaffhauser
68. S. Scott
69. G. M. Slaughter
70. E. J. Soderstrom
71. D. P. Stinton
72. R. W. Swindeman
73. V. J. Tennery
74. T. N. Tiegs
75. J. R. Weir, Jr.
76. B. H. West
77. F. W. Wiffen
78. S. G. Winslow
79. J. M. Wyrick
80. C. S. Yust

EXTERNAL DISTRIBUTION

81. James H. Adair
University of Florida
Materials Science & Engineering
323 MAE Bldg.
Gainesville, FL 32611-2066

82. Donald F. Adams
University of Wyoming
Mechanical Engineering Department
P. O. Box 3295
Laramie, WY 82071

83. Jane W. Adams
Corning Glass Works
SP-DV-21
Corning, NY 14831

84. Jalees Ahmad
AdTech Systems Research
1342 North Fairfield Road
Dayton, OH 45432

85. Yoshio Akimune
NISSAN Motor Co., Ltd.
Materials Research Laboratory
1 Natsushima-Cho
Yokosuka 237
JAPAN

86. Mufit Akinc
Iowa State University
322 Spedding Hall
Ames, IA 50011

87. R. G. Alexander
BASE
26 Malvern Close
Kettering Northants NN16 AJP
UNITED KINGDOM

88. Richard L. Allor
Ford Motor Company
Material Systems Reliability Department
20000 Rotunda Drive
Post Office Box 2053
Room S-2031
Dearborn, MI 48121-2053

89. Richard T. Alpaugh
U.S. Department of Energy
Office of Transportation Technologies
1000 Independence Avenue, S.W.
Forrestal Building CE-322
Washington, DC 20585

90. Joseph E. Amaral
Instron Corporation
Corporate Engineering Office
100 Royale Street
Canton, MA 02021

91. Edward M. Anderson
Anderson & Associates
4300 Pyles Ford Road
Centreville, DE 19807

92. Norman C. Anderson
Ceradyne, Inc.
Ceramic-to-Metal Division
3169 Redhill Avenue
Costa Mesa, CA 92626

93. H. Arbabi
Brunel University
Department of Materials Technology
Uxbridge Middlesex UB8 3PH
UNITED KINGDOM

94. Thomas Arbanas
G.B.C. Materials Corporation
580 Monastery Drive
Latrobe, PA 15650-2698

95. Frank Armatis
3M Company
3M Center/60-1N-01
St. Paul, MN 55082

96. William H. Atwell
Dow Corning Corporation
3901 South Saginaw Road
MS:540
Midland, MI 48686-0995

97. V. S. Avva
North Carolina A&T State University
Department of Mechanical Engineering
Greensboro, NC 27411

98. Michel Badia
Embassy of France
4101 Reservoir Road, S.W.
Washington, DC 20007-2176

99. Kirit J. Bahnsali
U.S. Army Materials Technology Laboratory
SLCMT-EMM
405 Arsenal Street
Watertown, MA 02172

100. Sunggi Baik
Pohang Institute of Science & Technology
Department of Materials Science and Engineering
P.O. Box 125
Pohang 790-600
KOREA

101. John M. Bailey
Caterpillar Inc.
Research Department
Technical Center
Building L
Post Office Box 1875
Peoria, IL 61656-1875

102. Bob Baker
Ceradyne, Inc.
3169 Redhill Avenue
Costa Mesa, CA 92626

103. Frank Baker
Aluminum Company of America
Alcoa Technical Center
Alcoa Center, PA 15069

104. J. G. Baldoni
GTE Laboratories Inc.
40 Sylvan Road
Waltham, MA 02254

105. Clifford P. Ballard
Allied-Signal, Inc.
Ceramics Program
P.O. Box 1021
Morristown, NJ 07962-1021

106. M. Balu
Amoco Performance Products Inc.
4500 McGinnis Ferry Road
Alpharetta, GA 30202

107. B. P. Bandyopadhyay
University of North Dakota
University Station
Box 8214
Grand Forks, ND 58202

108. P. M. Barnard
Ruston Gas Turbines Limited
Metallurgical Laboratory
P. O. Box 1
Lincoln LN2 5DJ
ENGLAND

109. Harold N. Barr
Hittman Corporation
9190 Red Branch Road
Columbia, MD 21045

110. Martin L. Bartlett
Southwest Research Institute
Materials and Mechanics Department
6220 Culebra Road
P.O. Drawer 28510
San Antonio, TX 78228-0510

111. Renald D. Bartoe
Vesuvius McDanel
510 Ninth Avenue
Box 560
Beaver Falls, PA 15010-0560

112. Donald M. Bartos
Dow Corning Corporation
Advanced Ceramics Program
Midland, MI 48686-0995

113. Donald F. Baxter, Jr.
ASM International
Advanced Materials and Processes
Materials Park, OH 44073-0002

114. Robert Beck
Teledyne CAE
Materials Engineering/Programs
1330 Laskey Road
P.O. Box 6971
Toledo, OH 43612

115. John C. Bell
Shell Research Limited
Thornton Research Centre
P.O. Box 1
Chester, Ch1 3SH
ENGLAND

116. Albert H. Bell, III
General Motors Technical Center
30200 Mound Road
Engineering Building/W3 Turbine
Warren, MI 48090-9010

117. A. L. Bement, Jr.
TRW, Inc.
23555 Euclid Avenue
Cleveland, OH 44117

118. M. Bentele
Xamag, Inc.
259 Melville Avenue
Fairfield, CT 06430

119. Larry D. Bentsen
BF Goodrich Company
R&D Center
9921 Brecksville Road
Brecksville, OH 44141

120. Joseph C. Bentz
ENCERATEC
2525 Sandcrest Drive
Columbus, IN 47203

121. Louis Beregszazi
Defiance Precision Products
P.O. Drawer 428
Defiance, OH 43512

122. Tom Bernecki
Northwestern University
BIRL
1801 Maple Avenue
Evanston, IL 60201-3135

123. Charles F. Bersch
Institute for Defense Analyses
1801 North Beauregard Street
Alexandria, VA 22311

124. Ram Bhatt
NASA Lewis Research Center
21000 Brookpark Road
Cleveland, OH 44135

125. Deane I. Biehler
Caterpillar Inc.
Engineering and Research Materials
Technical Center, Building E
Post Office Box 1875
Peoria, IL 61656-1875

126. John. W. Bjerklie
Consolidated Natural Gas Service Co., Inc.
Research Department
CNG Tower
Pittsburgh, PA 15222-3199

127. William D. Bjorndahl
TRW
One Space Park
Building 01, Room 2040
Redondo Beach, CA 90278

128. Keith A. Blakely
Advanced Refractory Technologies, Inc.
699 Hertel Avenue
Buffalo, NY 14207

129. Keith Blandford
Boride Products, Inc.
2879 Aero Park Drive
Traverse City, MI 49684

130. Paul N. Blumberg
Ricardo-ITI
645 Blackhawk Drive
Westmont, IL 60559

131. Bruce Boardman
Deere and Company Technical Center
3300 River Road
Moline, IL 61265

132. Russell Bockstedt
Hoechst Celanese Corporation
150 JFK Parkway
Short Hills, NJ 07078

133. M. Boehmer
DLR German Aerospace Research Establishment
Postfach 90 60 58
D-5000 Koln 90
GERMANY

134. Lawrence P. Boesch
EER Systems Corp.
1593 Spring Hill Road
Vienna, VA 22182-2239

135. Donald H. Boone
Boone & Associates
2412 Cascade Drive
Walnut Creek, CA 94598-4313

136. Tom Booth
Allied-Signal Aerospace Company
AiResearch Los Angeles Division
2525 West 190th Street
Torrance, CA 90509-2960

137. Tibor Bornemisza
Sundstrand Power Systems
4400 Ruffin Road
San Diego, CA 92186-5757

138. J. A. M. Boulet
University of Tennessee
Department of Engineering Science and Mechanics
310 Perkins Hall
Knoxville, TN 37996-2030

139. H. Kent Bowen
Massachusetts Institute of Technology
77 Massachusetts Avenue
Room E40-434
Cambridge, MA 02139

140. Leslie J. Bowen
Materials Systems
53 Hillcrest Road
Concord, MA 01742

141. Steven C. Boyce
Air Force Office of Scientific Research
AFOSR/NA Bldg. 410
Bolling AFB DC 20332-6448

142. Gary L. Boyd
CEC
400 Howell Avenue, No. 4
Warland, WY 82401

143. Steve Bradley
UOP Research Center
50 East Algonquin Road
Des Plaines, IL 60017-6187

144. Michael C. Brands
Cummins Engine Company, Inc.
P.O. Box 3005
Mail Code 50179
Columbus, IN 47201

145. Raymond J. Bratton
Westinghouse Science and Technology Center
1310 Beulah Road
Pittsburgh, PA 15235

146. John J. Brennan
United Technologies Corporation
Research Center
Silver Lane, MS:24
East Hartford, CT 06108

147. Jeff D. Bright
Ceramatec, Inc.
2425 South 900 West
Salt Lake City, UT 84108

148. Terrence K. Brog
Coors Ceramics Company
Corporate Development and Technology
4545 McIntyre Street
Golden, CO 80403

149. Gunnar Broman
317 Fairlane Drive
Spartanburg, SC 29302

150. Al Brown
High-Tech Materials Alert
P.O. Box 882
Dayton, NJ 08810

151. Jesse Brown
Virginia Polytechnic Institute and State University
Center for Advanced Ceramic Materials
Blacksburg, VA 24061-0256

152. S. L. Bruner
Ceramatec, Inc.
2425 South 900 West
Salt Lake City, UT 84119

153. Adolfo Brusaferro
Keramont Corporation
4231 South Fremont Avenue
Tucson, AZ 85714

154. W. Bryzik
U.S. Army Tank Automotive Command
R&D Center
Propulsion Systems Division
Warren, MI 48397-5000

155. S. T. Buljan
GTE Laboratories Inc.
40 Sylvan Road
Waltham, MA 02254

156. S. J. Burden
GTE Valenite
1711 Thunderbird
Troy, MI 48084

157. Curt V. Burkland
AMERCOM, Inc.
8928 Fullbright Avenue
Chatsworth, CA 91311

158. Bill Bustamante
AMERCOM, Inc.
8928 Fullbright Avenue
Chatsworth, CA 91311

159. Oral Buyukozturk
Massachusetts Institute of Technology
77 Massachusetts Avenue
Room 1-280
Cambridge, MA 02139

160. John M. Byrne, Jr.
PPG Industries, Inc.
Corporate Development Department
One PPG Place
Pittsburgh, PA 15272

161. David A. Caillet
Ethyl Corporation
451 Florida Street
Baton Rouge, LA 70801

162. Frederick J. Calnan
Heany Industries, Inc.
249 Briarwood Lane
P.O. Box 38
Scottsville, NY 14546

163. Donald J. Campbell
Air Force Wright Aeronautical Laboratory
AFWAL/POX
Wright-Patterson AFB, OH 45433

164. Roger Cannon
Rutgers University
Department of Ceramics
Post Office Box 909
Piscataway, NJ 08855-0909

165. Scott Cannon
P.O. Box 567254
Atlanta, GA 30356

166. Harry W. Carpenter
19945 Acre Street
Northridge, CA 91324

167. David Carruthers
Allied-Signal Aerospace Company
Garrett Auxiliary Power Division
2739 East Washington Street
Phoenix, AZ 85010-5227

168. Calvin H. Carter, Jr.
Cree Research, Inc.
2810 Meridian Parkway
Durham, NC 27713

169. J. David Casey
35 Atlantis Street
West Roxbury, MA 02132

170. Jere G. Castor
J. C. Enterprise
5078 North 83rd Street
Scottsdale, AZ 85250

171. James D. Cawley
Case Western Reserve University
Materials Science and Engineering Department
Cleveland, OH 44106

172. Thomas C. Chadwick
Den-Mat Corporation
P.O. Box 1729
Santa Maria, CA 93456

173. Ronald H. Chand
Chand Kare Technical Ceramics
2 Coppage Drive
Worcester, MA 01603

174. Frank C. Chang
U.S. Army Materials Technology Laboratory
AMTL-EMM
405 Arsenal Street
Watertown, MA 02172

175. Robert M. Chapman
Allied-Signal Aerospace Company
1530 Wilson Boulevard, 10th Floor
Arlington, VA 22209

176. William Chapman
Williams International Corporation
2280 West Maple Road
Walled Lake, MI 48390-0200

177. Albert A. Chesnes
U.S. Department of Energy
Office of Transportation Technologies
1000 Independence Avenue, S.W.
Forrestal Building CE-30, 6B-094
Washington, DC 20585

178. Kaiyin Chia
Carborundum Company
P.O. Box 832
Niagara Falls, NY 14302

179. Frank Childs
EG&G Idaho, Inc.
Idaho National Engineering Laboratory
P.O. Box 1625
Idaho Falls, Id 83415-3527

180. Gilbert Y. Chin
Bell Telephone Laboratories
R&D
Murray Hill, NJ 07974

181. Melvin H. Chiogioji
U.S. Department of Energy
Office of New Production Reactors, NP-3
1000 Independence Avenue, S.W.
Washington, DC 20585

182. William J. Chmura
Torrington Company
59 Field Street
Torrington, CT 06790-4942

183. Tsu-Wei Chou
University of Delaware
Center for Composite Materials
201 Spencer Laboratory
Newark, DE 19716

184. R. J. Christopher
Ricardo Consulting Engineers
Bridge Works
Whoreham-By-Sea West Sussex BN43 5FG
ENGLAND

185. Eugene V. Clark
Turbine Metal Technology, Inc.
Technology Engineering
7327 Elmo Street
Tujunga, CA 91042-2204

186. Joel P. Clark
Massachusetts Institute of Technology
Room 8-409
Cambridge, MA 02139

187. William L. Cleary
ORI, Inc.
1375 Piccard Drive
Rockville, MD 20850

188. W. J. Clegg
ICI Advanced Materials
Post Office Box 11
The Heath, Runcorn Cheshire
WA7 4QE
ENGLAND

189. William C. Connors
Sundstrand Aviation Operations
Materials Science and Engineering Department
4747 Harrison Avenue
P.O. Box 7002
Rockford, IL 61125-7002

190. Stephen Copley
University of Southern California
Materials Science Department
Los Angeles, CA 90089-0241

191. John A. Coppola
Carborundum Company
Post Office Box 156
Niagara Falls, NY 14302

192. Normand D. Corbin
Norton Company
Advanced Ceramics
Goddard Road
Northboro, MA 01532-1545

193. Douglas Corey
Allied-Signal Aerospace Company
2525 West 190th Street
MS:T52
Torrance, CA 90504-6099

194. John M. Corwin
Chrysler Motors Corporation
Advanced Materials Technology
703 Mt. Vernon Boulevard
Royal Oak, MI 48073

195. George A. Costakis
General Motors Corporation
Technical Center, WO-Turbine
30200 Mound Road
Warren, MI 48090-9010

196. Keith P. Costello
Chand/Kare Technical Ceramics
2 Coppage Drive
Worcester, MA 01603-1252

197. Anna Cox
Mitchell Market Reports
P.O. Box 23
Monmouth Gwent NP5 4YG
UNITED KINGDOM

198. Thomas Coyle
Unocal Corporation
Unocal Science & Technology Division
376 South Valencia Avenue
Brea, CA 92621

199. Art Cozens
Instron Corporation
3414 Snowden Avenue
Long Beach, CA 90808

200. Charles H. Craig
Naval Surface Warfare Center
Code R35
Dahlgren, VA 22448-5000

201. Mark Crawford
New Technology Week
4604 Monterey Drive
Annandale, VA 22003

202. Richard A. Cree
Markets & Products, Inc.
P.O. Box 14328
Columbus, OH 43214-0328

203. Les Crittenden
Vesuvius McDanel
Box 560
Beaver Falls, PA 15010

204. William J. Croft
U.S. Army Materials
Technology Laboratory
405 Arsenal Street
Watertown, MA 02172

205. M. J. Cronin
Mechanical Technology, Inc.
968 Albany-Shaker Road
Latham, NY 12110

206. Gary M. Crosbie
Ford Motor Company
1430 Culver Avenue
Dearborn, MI 48121-4036

207. Floyd W. Crouse, Jr.
U.S. Department of Energy
Morgantown Energy
Technology Center
Collins Ferry Road
Post Office Box 880
Morgantown, WV 26505

208. John Cuccio
Garrett Auxiliary Power
Division
2739 East Washington Street
P.O. Box 5227, MS:1302-2Q
Phoenix, AZ 85010

209. Raymond Cutler
Ceramatec, Inc.
2425 South 900 West
Salt Lake City, UT 84119

210. David A. Dalman
Dow Chemical Company
Central Research, Organic
Specialties Laboratory
1776 Building
Midland, MI 48674

211. James I. Dalton
Reynolds Metals Company
Metallurgy Laboratory
Fourth and Canal Streets
Post Office Box 27003
Richmond, VA 23219

212. Stephen C. Danforth
Rutgers University
Ceramic Engineering Department
Post Office Box 909
Piscataway, NJ 08855-0909

213. Sankar Das Gupta
Electrofuel Manufacturing Co., Ltd.
9 Hanna Avenue
Toronto Ontario MGK-1W8
CANADA

214. Charles Davis
Sverdrup Technology, Inc., MSFC
620 Discovery Drive
Huntsville, AL 35806

215. Robert F. Davis
North Carolina State
University
Materials Engineering
Department
229 Riddick Laboratory
Post Office Box 7907
Raleigh, NC 27695

216. Thomas DeAngelis
Carborundum Company
Niagara Falls R&D Center
P.O. Box 832
Niagara Falls, NY 14302

217. George DeBell
Ford Motor Company
Material Systems Reliability Department
20000 Rotunda Drive
P.O. Box 2053, Room S-2023
Dearborn, MI 48121-2053

218. Michael DeLuca
AMP-AKZO
West Lane
Aquebogue, NY 11931

219. Gerald L. DePoorter
Colorado School of Mines
Metallurgical and Materials Engineering Department
Golden, CO 80401

220. J. Franklyn DeRidder
Omni Electro Motive, Inc.
12 Seely Hill Road
Newfield, NY 14867

221. Nick C. Dellow
Materials Technology Publications
40 Sotheron Road
Watford Herts WD1 2QA
UNITED KINGDOM

222. L. R. Dharani
University of Missouri-Rolla
224 M.E.
Rolla, MO 65401

223. John Dodsworth
Vesuvius Research & Development
Technical Ceramics Group
Box 560
Beaver Falls, PA 15010

224. B. Dogan
Institut fur Werkstofforschung
GKSS-Forschungszentrum Geesthacht GmbH
Max-Planck-Strasse
D-2054 Geesthacht
GERMANY

225. Jean-Marie Drapier
FN Moteurs S.A.
Material and Processing
B-4041 Milmort (Herstal)
BELGIUM

226. Robin A.L. Drew
McGill University
Department of Mining and Metallurgical Engineering
3450 University Street
Montreal Quebec H3A 2A7
CANADA

227. Winston H. Duckworth
Battelle Memorial Institute
Columbus Division
505 King Avenue
Columbus, OH 43201-2693

228. Keith F. Dufrane
Battelle Columbus Laboratories
505 King Avenue
Columbus, OH 43201

229. Edmund M. Dunn
Texel Company
6 Third Street
Lexington, MA 02173

230. Jeremy D. Dunning
Indiana University
Industrial Research Liaison Program
Bloomington, IN 47405

231. Bill Durako
Sundstrand Aviation Operations
Department 789-6
4747 Harrison Avenue
P.O. Box 7002
Rockford, IL 61125-7002

232. Sunil Dutta
NASA Lewis Research Center
21000 Brookpark Road
MS:49-3
Cleveland, OH 44135

233. Ernest J. Duwell
212 Elm Street
Hudson, WI 54016

234. Chuck J. Dziedzic
Coors Ceramics Company
Structural Products Group
17750 West 32nd Avenue
Golden, CO 80401

235. Robert J. Eagan
Sandia National Laboratories
Department 1840
Post Office Box 5800
Albuquerque, NM 87185

236. Jeffrey Eagleson
Lanxide Corporation
1001 Connecticut Avenue, N.W.
Washington DC 20036

237. Harry E. Eaton
United Technologies Corporation
Research Center
Silver Lane
East Hartford, CT 06108

238. Christopher A. Ebel
Carborundum Company
Technology Division
P.O. Box 337
Niagara Falls, NY 14302

239. J. J. Eberhardt
U.S. Department of Energy
Office of Advanced
Transportation Materials
1000 Independence Avenue, S.W.
Forrestal Building CE-34
Washington, DC 20585

240. Jim Edler
Eaton Corporation
P.O. Box 766
Southfield, MI 48037

241. William A. Ellingson
Argonne National Laboratory
Materials Science Technology
Division
9700 South Cass Avenue
Argonne, IL 60439

242. Glen B. Engle
Nuclear & Aerospace Materials
Corporation
16716 Martincoit Road
Poway, CA 92064

243. Jeff Epstein
Ceramic Technologies, Inc.
2107 Jamara Lane
Houston, TX 77077

244. Kenneth A. Epstein
Dow Chemical U.S.A.
Ceramics and Advanced Materials
800 Building
Midland, MI 48667

245. Art Erdemir
Argonne National Laboratory
Materials and Components
Technology Division
9700 South Cass Avenue
Argonne, IL 60439

246. Kenji Esaki
Toyota Technical Center
U.S.A., Inc.
2000 Town Center, Suite 500
Southfield, MI 48075

247. Jose L. Escalante
Anglo-Mex-Tech. Inc.
3923 N.W. 24th Street
Miami, FL 33142

248. Charles D. Estes
U.S. Senate
Committee on Appropriations
SD-152 Dirksen Senate
Office Building
Washington, DC 20510

249. John N. Eustis
U.S. Department of Energy
Office of Industrial
Technologies
1000 Independence Avenue, S.W.
Forrestal Building CE-221
Washington, DC 20585

250. Peggy Evanich
National Aeronautics
and Space Administration
Energy Systems Office
Washington, DC 20546

251. Anthony G. Evans
University of California
College of Engineering
Santa Barbara, CA 93106

252. Robert C. Evans
NASA Lewis Research Center
Terrestrial Propulsion Office
21000 Brookpark Road, MS:86-6
Cleveland, OH 44135

253. W. L. Everitt
Kyocera International, Inc.
8611 Balboa Avenue
San Diego, CA 92123

254. Gordon Q. Evison
332 South Michigan Avenue
Suite 1730
Chicago, IL 60604

255. John W. Fairbanks
U.S. Department of Energy
Office of Transportation
Technologies
1000 Independence Avenue, S.W.
Forrestal Building CE-322,
5G-042
Washington, DC 20585

256. Rolf Fasth
Chem Systems, Inc.
303 South Broadway
Tarrytown, NY 10591

257. Tim Fawcett
Dow Chemical Company
Central Research, Advanced
Ceramics Laboratory
1776 Building
Midland, MI 48674

258. Robert W. Fawley
Sundstrand Power Systems
Division of Sundstrand
Corporation
4400 Ruffin Road
P.O. Box 85757
San Diego, CA 92186-5757

259. John J. Fedorchak
GTE Products Corporation
Hawes Street
Towanda, PA 18848-0504

260. Jeff T. Fenton
Vista Chemical Company
900 Threadneedle
Houston, TX 77079

261. Larry Ferrell
Babcock & Wilcox
Old Forest Road
Lynchburg, VA 24505

262. Raymond R. Fessler
BIRL
Industrial Research Lab
1801 Maple Avenue
Evanston, IL 60201

263. Michelle Finch
E. I. DuPont de Nemours &
Company, Inc.
Experimental Station
Information Center E302/301
Wilmington, DE 19898

264. Arthur D. Fine
United Technologies Corporation
Pratt & Whitney Aircraft
400 Main Street
MS:163-10
East Hartford, CT 06108

265. Ross F. Firestone
Ross Firestone Company
188 Mary Street
Winnetka, IL 60093-1520

266. Sharon L. Fletcher
Arthur D. Little, Inc.
15 Acorn Park
Cambridge, MA 02140-2390

267. H. W. Foglesong
Dow Corning Corporation
3901 South Saginaw Road
Midland, MI 48686

268. Thomas F. Foltz
Avco Corporation
Special Materials Division
Two Industrial Avenue
Lowell, MA 01851

269. Renee G. Ford
Materials and Processing Report
P.O. Box 72
Harrison, NY 10528

270. John Formica
Supermaterials
2020 Lakeside Avenue
Cleveland, OH 44114

271. Edwin Frame
Southwest Research Institute
Division 2
P.O. Drawer 28510
San Antonio, TX 78284

272. Armanet Francois
French Scientific Mission
4101 Reservoir Road, N.W.
Washington DC 20007-2176

273. Robert G. Frank
Technology Assessment Group
10793 Bentley Pass Lane
Cincinnati, OH 45140

274. David J. Franus
Forecast International
22 Commerce Road
Newtown, CT 06470

275. Marc R. Freedman
NASA Lewis Research Center
21000 Brookpark Road
MS:49-3
Cleveland, OH 44135

276. Douglas W. Freitag
LTV Missiles Division
Post Office Box 650003
MS:WT-21
Dallas, TX 75265-0003

277. Brian R.T. Frost
Argonne National Laboratory
9700 South Cass Avenue
Building 900
Argonne, IL 60439

278. Lawrence R. Frost
Instron Corporation
100 Royall Street
Canton, MA 02021

279. George A. Fryburg
Norton/TRW Ceramics
7A-4 Raymond Avenue
Salem, NH 03079

280. Xiren Fu
Shanghai Institute of Ceramics
Chinese Academy of Sciences
1295 Ding-xi Road
Shanghai 200050
CHINA

281. J. P. Gallagher
University of Dayton Research Institute
300 College Park, JPC-250
Dayton, OH 45469-0120

282. Tom Garritano
University of Tennessee
Science Alliance
101 South College
Knoxville, TN 37996-1328

283. Joy A. Garwood
Norton Company
Advanced Ceramics
Goddard Road
Northboro, MA 01532-1545

284. H. Maury Gatewood
Reynolds Metals Company - Corporate R&D
P.O. Box 27003
Richmond, VA 23261

285. L. J. Gauckler
ETH-Zurich
Sonneggstrasse 5
CH-8092 Zurich 8092
SWITZERLAND

286. Peter A. Gaydos
Battelle Columbus Laboratories
505 King Avenue
Columbus, OH 43201

287. George E. Gazza
U.S. Army Materials
Technology Laboratory
Ceramics Research Division
405 Arsenal Street
Watertown, MA 02172-0001

288. Bruce W. Gerhold
Phillips Petroleum Company
R&D
91-G, PRC
Bartlesville, OK 74004

289. D. Gerster
CEA-DCOM
33 Rue De La Federation
Paris 75015
FRANCE

290. John Ghinazzi
Coors Technical Ceramics
Company
1100 Commerce Park Drive
Oak Ridge, TN 37830

291. Robert Giddings
General Electric Company
Research Laboratory
P.O. Box 8
Schenectady, NY 12301

292. Charles M. Gilmore
George Washington University
Dept. of Civil, Mechanical, and
Environmental Engineering
Washington, DC 20052

293. A. M. Glaeser
University of California
Materials Science and Mineral
Engineering
Lawrence Berkeley Laboratory
Hearst Mining Building
Berkeley, CA 94720

294. Paul Glance
Concept Analysis
R&D
950 Stephenson Highway
Dupont Automotive Development
Building
Troy, MI 48007-7013

295. Fred M. Glaser
U.S. Department of Energy
Office of Fossil Energy
FE-14 GTN
Germantown, MD 20545

296. Joseph W. Glatz
Naval Air Propulsion Test
Center
Systems Engineering Division
Post Office Box 7176, PE24
Trenton, NJ 08628

297. W. M. Goldberger
Superior Graphite Company
R&D
2175 East Broad Street
Columbus, OH 43209

298. Allan E. Goldman
U.S. Graphite, Inc.
907 West Outer Drive
Oak Ridge, TN 37830

299. Stephen T. Gonczy
Allied Signal Research
P.O. Box 5016
Des Plaines, IL 60017

300. Jeffrey M. Gonzales
GTE Products Corporation
Hawes Street
Towanda, PA 18848-0504

301. Robert J. Gottschall
U.S. Department of Energy
ER-131, MS:G-236
Washington, DC 20545

302. Earl Graham
Cleveland State University
Department of Chemical Engineering
Euclid Avenue at East 24th Street
Cleveland, OH 44115

303. William A. Graham
Lanxide Corporation
P.O. Box 6077
Newark, DE 19714-6077

304. Kenneth Green
Coors Ceramics Company
17750 West 32nd Street
Golden, CO 80401

305. Robert E. Green, Jr.
Johns Hopkins University
Materials Science and Engineering Department
Baltimore, MD 21218

306. Lance E. Groseclose
Allison Gas Turbine Division-GMC
Post Office Box 420, MS:W-5
Indianapolis, IN 46206

307. Mark F. Gruninger
Union Carbide Corporation
Specialty Powder Business
1555 Main Street
Indianapolis, IN 46224

308. Ernst Gugel
Cremer Forschungsinstitut GmbH&Co.KG
Deslauer Strasse 35
D-8633 Roedental 8633
GERMANY

309. Donald L. Guile
Corning Glass Works
SP-DV-1-9
Corning, NY 14831

310. P. Ulf Gummeson
Hoeganaes
R&D
River Road and Taylors Lane
Riverton, NJ 08077

311. Bimleshwar P. Gupta
Solar Energy Research Institute
Mechanical and Industrial Technology Division
1617 Cole Boulevard
Golden, CO 80401

312. M. D. Gurney
NIPER
Post Office Box 2128
Bartlesville, OK 74005

313. John P. Gyekenyesi
NASA Lewis Research Center
21000 Brookpark Road, MS:6-1
Cleveland, OH 44135

314. J. J. Habeeb
Esso Petroleum Canada
Research Division
Post Office Box 3022
Sarina Ontario N7T 7MI
CANADA

315. Nabil S. Hakim
Detroit Diesel Corporation
13400 West Outer Drive West
Detroit, MI 48239

316. Philip J. Haley
Allison Gas Turbine Division
Vehicular Engineering
P.O. Box 420, MS:T12A
Indianapolis, IN 46236

317. Judith Hall
Fiber Materials Inc.
Biddeford Industrial Park
5 Morin Street
Biddeford, ME 04005

318. Y. Harada
IIT Research Institute
Nometallic Materials and Composites
10 West 35th Street
Chicago, IL 60616

319. Friedrich Harbach
Asea Brown Boveri AG
Department of Functional Ceramics
Eppelheimer Strasse 82
D-6900 Heidelberg 1
GERMANY

320. Kay Hardman-Rhyne
DARPA
1400 Wilson Boulevard
Arlington, VA 22209

321. R. A. Harmon
25 Schalren Drive
Latham, NY 12110

322. Amy Harmon-Barrett
Martin Marietta Laboratories
1450 South Rolling Road
Baltimore, MD 21227

323. Alan Hart
Dow Chemical Company
Advanced Ceramics Laboratory
1776 Building
Midland, MI 48674

324. Pat E. Hart
Battelle Pacific Northwest Laboratories
Ceramics and Polymers Development Section
P.O. Box 999
Richland, WA 99352

325. Stephen D. Hartline
Norton Company
Advanced Ceramics
Goddard Road
Northboro, MA 01532-1545

326. Michael H. Haselkorn
Caterpillar Inc.
Engineering Research Materials
Technical Center, Building E
Post Office Box 1875
Peoria, IL 61656-1875

327. N. B. Havewala
Corning Inc.
SP-PR-11
Corning, NY 14831

328. John Haygarth
Teledyne WAA Chang Albany
P.O. Box 460
Albany, OR 97321

329. Norman L. Hecht
University of Dayton Research Institute
300 College Park
Dayton, OH 45469-0172

330. S. S. Hecker
Los Alamos National Laboratory
Material Science and Technology Division, G-756
Post Office Box 1663
Los Alamos, NM 87545

331. Peter W. Heitman
Allison Gas Turbine Division-GMC
Post Office Box 420, MS:W-5
Indianapolis, IN 46206-0420

332. Richard L. Helferich
Duriron Company, Inc.
Post Office Box 1145
Dayton, OH 45401

333. H. E. Helms
General Motors Corporation
Allison Gas Turbine Division
2001 South Tibbs Avenue
Post Office Box 420
Indianapolis, IN 46206-0420

334. Robert W. Hendricks
Virginia Polytechnic Institute and State University
Materials Engineering Department
210 Holden Hall
Blacksburg, VA 24061-0237

335. Wayne Henley
Hertel Cutting Technologies Inc.
1000 Clearview Court
Oak Ridge, TN 37830

336. Thomas L. Henson
GTE Products Corporation
Chemical & Metallurgical Division
Hawes Street
Towanda, PA 18848

337. Thomas P. Herbell
NASA Lewis Research Center
21000 Brookpark Road
MS:49-3
Cleveland, OH 44135

338. Marlene Heroux
Rolls-Royce, Inc.
2849 Paces Ferry Road
Suite 450
Atlanta, GA 30339-3769

339. Robert L. Hershey
Science Management Corporation
1255 New Hampshire Ave., NW
Suite 1033
Washington DC 20036

340. Hendrik Heystek
Bureau of Mines
Tuscaloosa Research Center
Post Office Box L
University, AL 35486

341. Robert V. Hillery
GE Aircraft Engines
One Neumann Way, M.D. H85
Cincinnati, OH 45215

342. Arthur Hindman
Instron Corporation
100 Royall Street
Canton, MA 02021

343. Jon Hines
American Ceramic Society, Inc.
757 Brooksedge Plaza Drive
Westerville, OH 43081-6136

344. Hans Erich Hintermann
CSEM
Materials and Micromechanics Division
Rue Breguet 2
Neuchatel 2000
SWITZERLAND

345. Shinichi Hirano
Mazda R&D of North America, Inc.
1203 Woodridge Avenue
Ann Arbor, MI 48105

346. Tommy Hiraoka
NGK Locke, Inc.
1000 Town Center
Southfield, MI 48075

347. John M. Hobday
U.S. Department of Energy
Morgantown Energy Technology Center
Collins Ferry Road
P.O. Box 880
Morgantown, WV 26507

348. Greg Hoenes
Vista Chemical Company
900 Threadneedle
P.O. Box 19029
Houston, TX 77079-2990

349. Clarence Hoenig
Lawrence Livermore National Laboratory
P.O. Box 808, Mail Code L-369
Livermore, CA 94550

350. Thomas Hollstein
Fraunhofer-Institut fur Werkstoffmechanik IWM
Wohlerstrabe 11
D-7800 Freiburg
GERMANY

351. Richard Holt
National Research Council
of Canada
Structures and Materials
Laboratory
Ottawa Ontario K1A 0R6
CANADA

352. Joe Homeny
University of Illinois
Department of Materials Science
and Engineering
105 South Goodwin Avenue
Ceramics Building
Urbana, IL 61801

353. A. T. Hopper
Battelle Columbus
Laboratories
Metals and Ceramics Department
505 King Avenue
Columbus, OH 43201-2693

354. Woodie Howe
Coors Technical Ceramics
Company
1100 Commerce Park Drive
Oak Ridge, TN 37830

355. George Hsu
Jet Propulsion Laboratory
4800 Oak Grove Drive
MS:512-103
Pasadena, CA 91109

356. Shih Hsu
Digital Equipment Corporation
77 Reed Road
MS:HL02-1/L08
Hudson, MA 01749-2895

357. Stephen M. Hsu
National Institute of
Standards and Technology
Gaithersburg, MD 20899

358. Gene Huber
Precision Ferrites & Ceramics
5576 Corporate Drive
Cypress, CA 90630

359. M. L. Huckabee
GTE Laboratories, Inc.
40 Sylvan Road
Waltham, MA 02254

360. Harold A. Huckins
Princeton Advanced
Technology, Inc.
56 Finley Road
Princeton, NJ 08540

361. Fred Huettic
Advanced Magnetics Inc.
45 Corey Lane
Mendham, NJ 07945

362. Bill Huffman
Zircar
110 North Main Street
Florida, NY 10921

363. O. Richard Hughes
Celanese Research Company
86 Morris Avenue
Summit, NJ 07901

364. Brian K. Humphrey
Lubrizol Petroleum
Chemicals Co.
3000 Town Center, Suite 1340
Southfield, MI 48075-1201

365. Robert M. Humrick
Dylon Ceramic Technologies
3100 Edgehill Road
Cleveland Heights, OH 44118

366. Joseph E. Hunter, Jr.
General Motors Corporation
Research Labs Metallurgy
Department
30200 Mound Road
Warren, MI 48090-9055

367. Louis C. Ianniello
U.S. Department of Energy
Office of Material Sciences
ER-13 GTN
Germantown, MD 20545

368. M. S. Inoue
Kyocera International, Inc.
Corporate Technology and Planning
8611 Balboa Avenue
San Diego, CA 92123-1580

369. Osama Jadaan
University of Wisconsin-Platteville
General Engineering Division
1 University Plaza
Platteville, WI 53818

370. Curtis A. Johnson
General Electric Corporate R&D
Room MB-187
Post Office Box 8
Schenectady, NY 12301

371. Sylvia Johnson
SRI International
333 Ravenswood Avenue
Menlo Park, CA 94025

372. Thomas A. Johnson
Lanxide Corporation
1300 Marrows Road
P.O. Box 6077
Newark, DE 19714-6077

373. L. A. Joo
Great Lakes Research Corporation
Post Office Box 1031
Elizabethton, TN 37643

374. A. David Joseph
SPX Corporation
700 Terrace Point
Muskegon, MI 49443

375. Adam Jostsons
Australian Nuclear Science & Technology Organization
Lucas Heights Research Laboratories
New Illawarra Road
Lucas Heights, New South Wales
AUSTRALIA

376. Matthew K. Juneau
Ethyl Corporation
451 Florida Street
Baton Rouge, LA 70801

377. Hartmut Kainer
Didier-Werke AG
Anlagentechnik Wiesbaden
Abraham-Lincoln-Str. 16
D-62 Wiesbaden
GERMANY

378. Tom Kalamasz
Norton/TRW
7A-4 Raymond Avenue
Salem, NH 03079

379. Lyle R. Kallenbach
Phillips Petroleum Company
R&D
Mail Drop:123AL
Bartlesville, OK 74004

380. Nick Kamiya
Kyocera Industrial Ceramics Corporation
2700 River Road
Des Plaines, IL 60018

381. Roy Kamo
Adiabatics, Inc.
3385 Commerce Drive
Columbus, IN 47201

382. S. Kang
GTE Laboratories, Inc.
40 Sylvan Road
Waltham, MA 02254

383. Chih-Chun Kao
Industrial Technology Research Institute
Materials Research Laboratories
195 Chung-Hsing Road, Sec. 4
Chutung Hsinchu 31015 R.O.C.
TAIWAN

384. Keith R. Karasek
Allied-Signal, Inc.
Engineered Materials Research Center
50 East Algonquin Road
P.O. Box 5016
Des Plaines, IL 60017-5016

385. Robert E. Kassel
Ceradyne, Inc.
3169 Redhill Avenue
Costa Mesa, CA 92626

386. Allan Katz
Wright Laboratory
Metals and Ceramics Division
WL/MLLM
Wright-Patterson AFB, OH 45433

387. R. Nathan Katz
Worcester Polytechnic Institute
Dept. of Mechanical Engineering
100 Institute Road
Worcester, MA 01609

388. Ted Kawaguchi
Tokai Carbon
375 Park Avenue, Suite 3802
New York, NY 10152

389. Noritsugu Kawashima
TOSHIBA Corporation
Mechanical Engineering Laboratory
4-1 Ukishima-Cho
Kawasaki-Ku Kawasaki 210
JAPAN

390. Lisa Kempfer
Penton Publishing
Materials Engineering
1100 Superior Avenue
Cleveland, OH 44114-2543

391. Frederick L. Kennard, III
General Motors Corporation
AC Rochester
Department 32-24, EB
1300 North Dort Highway
Flint, MI 48556

392. David O. Kennedy
Lester B. Knight Cast Metals Inc.
549 West Randolph Street
Chicago, IL 60661

393. George Keros
Photon Physics
3175 Penobscot Building
Detroit, MI 48226

394. Pramod Khandelwal
Allison Gas Turbine Division - GMC
P.O. Box 420, MS:W-5
Indianapolis, IN 46206

395. J. R. Kidwell
Allied-Signal Aerospace Company
Garrett Auxiliary Power Division
2739 East Washington Street
Post Office Box 5227
Phoenix, AZ 85010

396. Han J. Kim
GTE Laboratories, Inc.
40 Sylvan Road
Waltham, MA 02254

397. W. C. King
Mack Truck, Z-41
1999 Pennsylvania Avenue
Hagerstown, MD 21740

398. Carol Kirkpatrick
MSE, Inc.
CDIF Technical Library
P.O. Box 3767
Butte, MT 59702

399. Tony Kirn
Caterpillar Inc.
Defense Products Department, JB7
Peoria, IL 61629

400. James D. Kiser
NASA Lewis Research Center
21000 Brookpark Road, MS:49-3
Cleveland, OH 44135

401. Max Klein
Gas Research Institute
Thermodynamics
8600 West Bryn Mawr Avenue
Chicago, IL 60631

402. Richard N. Kleiner
Coors Ceramics Company
4545 McIntyre Street
Golden, CO 80403

403. Stanley J. Klima
NASA Lewis Research Center
21000 Brookpark Road
MS:6-1
Cleveland, OH 44135

404. C. E. Knapp
Norton Research Corporation
8001 Daly Street
Niagara Falls, Ontario L2G 6S2
CANADA

405. Albert S. Kobayashi
University of Washington
Mechanical Engineering
Department
MS:FU10
Seattle, WA 98195

406. Shigeki Kobayashi
Toyota Central Research
Labs, Inc.
Nagakute Aichi 480-11
JAPAN

407. Richard A. Kole
Z-Tech Corporation
8 Dow Road
Bow, NH 03304

408. E. Kostiner
University of Connecticut
Chemistry Department, U-60
Storrs, CT 06269-3060

409. Joseph A. Kovach
Eaton Corporation
Manufacturing Technologies
Center
32500 Chardon Road
Willoughby Hills, OH 44094

410. Ralph G. Kraft
Spraying Systems Company
North Avenue at Schmale Road
Wheaton, IL 60189-7900

411. Bruce Kramer
George Washington University
Aerodynamic Center
Room T715
Washington, DC 20052

412. Saunders B. Kramer
U.S. Department of Energy
Office of Transportation
Technologies
1000 Independence Avenue, S.W.
Forrestal Building CE-322
Washington, DC 20585

413. Arthur Kranish
Trends Publishing Inc.
1079 National Press Building
Washington DC 20045

414. A. S. Krieger
Radiation Science, Inc.
Post Office Box 293
Belmont, MA 02178

415. Pieter Krijgsman
Ceramic Design International
Holding B.V.
Post Office Box 68
Hattem 8050-AB
THE NETHERLANDS

416. Waltraud M. Kriven
University of Illinois
Materials Science &
Engineering Department
105 South Goodwin Avenue
Urbana, IL 61801

417. Dave Kupperman
Argonne National Laboratory
9700 South Cass Avenue
Argonne, IL 60439

418. Oh-Hun Kwon
Norton Company
Advanced Ceramics
Goddard Road
Northboro, MA 01532-1545

419. W. J. Lackey
Georgia Tech Research Institute
Georgia Institute of Technology
Materials Science and Technology
Atlanta, GA 30332

420. Hari S. Lamba
General Motors Corporation
Electro-Motive Division
LaGrange, IL 60525

421. Richard L. Landingham
Lawrence Livermore National Laboratory
Ceramics, Corrosion, and Thermochemistry
P.O. Box 808, L-369
Livermore, CA 94550

422. Manfred Langer
Volkswagen AG
Material Technology
3180 Wolfsburg 1
GERMANY

423. James Lankford
Southwest Research Institute
Department of Materials Sciences
6220 Culebra Road
San Antonio, TX 78228-0510

424. David C. Larsen
Corning Glass Works
Materials Research Department
Sullivan Park, FR-51
Corning, NY 14831

425. Stanley B. Lasday
Business News Publishing Co.
Manor Oak One
1910 Cochran Road, Suite 630
Pittsburgh, PA 15220

426. Mark S. Laser
Solar Turbines Inc.
2211 Erie Street
San Diego, CA 92110

427. S. K. Lau
Carborundum Company
Technology Division
Post Office Box 832
Niagara Falls, NY 14302

428. Edward A. Lauder
Advanced Composite Materials Corporation
1525 South Buncombe Road
Greer, SC 29651-9208

429. J. Lawrence Lauderdale
Babcock & Wilcox
Contract Research Division
1850 "K" Street, Suite 950
Washington DC 20006

430. Harry A. Lawler
Carborundum Company
Technology Division
Post Office Box 832
Niagara Falls, NY 14302

431. Jean F. LeCostaouec
Textron Speciality Materials
2 Industrial Avenue
Lowell, MA 01851

432. Benson P. Lee
Interscience, Inc.
9718 Lake Shore Boulevard
Cleveland, OH 44108

433. Burtrand I. Lee
Clemson University
Department of Ceramic Engineering
Olin Hall
Clemson, SC 29634-0907

434. June-Gunn Lee
KIST
Structural Ceramic Lab
Post Office Box 131
Cheong-Ryang
130-650
KOREA

435. Ran-Rong Lee
Ceramics Process Systems
Corporation
155 Fortune Boulevard
Milford, MA 01757

436. Stanley R. Levine
NASA Lewis Research Center
21000 Brookpark Road
MS:49-3
Cleveland, OH 44135

437. Alan V. Levy
Lawrence Berkeley Laboratory
One Cyclotron Road, MS:62-203
Berkeley, CA 94720

438. David Lewis
Naval Research Laboratory
Materials Science and Technology
Division
4555 Overlook Avenue, S.W.
Code 6370
Washington, DC 20375

439. Ai-Kang Li
Materials Research
Laboratories, ITRI
195-5 Chung-Hsing Road, Sec. 4
Chutung Hsinchu 31015 R.O.C.
TAIWAN

440. Winston W. Liang
Hong Kong Industrial
Technology Centre Co. Ltd.
78 Tat Chee Avenue
4/F, HKPC Building
Howloon
HONG KONG

441. Robert Licht
Norton Company
Advanced Ceramics
Goddard Road
Northboro, MA 01532-1545

442. E. Lilley
Norton Company
Advanced Ceramics
Goddard Road
Northboro, MA 01532-1545

443. Laura J. Lindberg
Allied-Signal Aerospace
Company
Garrett Fluid Systems Division
1300 West Warner
MS: 93-901-1207-4TT
Post Office Box 22200
Tempe, AZ 85285-2200

444. Leonard C. Lindgren
General Motors Corporation
Allison Gas Turbine Division
2001 South Tibbs Avenue
P.O. Box 420, Speed Code:T-20A
Indianapolis, IN 46206-0420

445. Hans A. Lindner
Cremer Forschungsinstitut
GmbH&Co.KG
Oeslauer Strasse 35
D-8633 Rodental 8866
GERMANY

446. Ronald E. Loehman
Sandia National Laboratories
Division 1840
P.O. Box 5800
Albuquerque, NM 87185

447. Jeffrey C. Logas
Winona State University
Composite Materials Engineering
115 Pasteur Hall
Winona, MN 55987

448. Bill Long
Babcock and Wilcox
Post Office Box 11165
Lynchburg, VA 24506

449. William D. Long
Wacker Chemicals (USA), Inc.
ESK Engineered Ceramics
50 Locust Avenue
New Canaan, CT 06840

450. L. A. Lott
EG&G Idaho, Inc.
Idaho National Engineering Laboratory
Post Office Box 1625
Idaho Falls, ID 83415-2209

451. Raouf O. Loutfy
MER Corporation
7960 South Kolb Road
Tucson, AZ 85706

452. Gordon R. Love
Aluminum Company of America
Alcoa Technical Center
Alcoa Center, PA 15069

453. Lydia Luckevich
Ortech International
2395 Speakman Drive
Mississauga Ontario L5K 183
CANADA

454. Bryan K. Luftglass
Chem Systems, Inc.
303 South Broadway
Tarrytown, NY 10591

455. Michael J. Lynch
General Electric Company
Medical Systems Group
Post Office Box 414, 7B-36
Milwaukee, WI 53201

456. Jim MacBeth
Carborundum Company
Structural Ceramics Division
P.O. Box 1054
Niagara Falls, NY 14302

457. H. MacLaren
General Electric Company
Thomson Laboratory, Materials Engineering 36807
1000 Western Avenue
Lynn, MA 01910

458. David Maginnis
Tinker AFB
OC-ALC/LIIRE
Tinker AFB OK 73145-5989

459. Frank Maginnis
Aspen Research, Inc.
220 Industrial Boulevard
Moore, OK 73160

460. Vincent L. Magnotta
Air Products and Chemicals, Inc.
Technical Diversification R&D Department
Post Office Box 538
Allentown, PA 18105

461. Tai-il Mah
Universal Energy Systems, Inc.
Ceramics and Composites Research
4401 Dayton-Xenia Road
Dayton, OH 45432

462. S. G. Malghan
National Institute of Standards and Technology
I-270 & Clopper Road
Gaithersburg, MD 20899

463. Lars Malmrup
United Turbine AB
Box 13027
Malmo S-200 44
SWEDEN

464. L. Manes
Commission of the European Communities
Joint Research Centre
Ispra Establishment
1-21020 Ispra (Varese)
ITALY

465. John Mangels
Ceradyne, Inc.
3169 Redhill Avenue
Costa Mesa, CA 92626

466. Russell V. Mann
Matec Applied Sciences, Inc.
75 South Street
Hopkinton, MA 01748

467. William R. Manning
Champion Aviation Products
Old Norris Road
P.O. Box 686
Liberty, SC 29657

468. Giel Marijnissen
Interturbine Holding B.V.
Spiktweg 36
5943 AD Lomm (L.)
THE NETHERLANDS

469. Robert A. Marra
Aluminum Company of America
Alcoa Technical Center
Advanced Ceramics Center - E
Alcoa Center, PA 15069

470. Chauncey L. Martin
3M Company
3M - MMC Program
Building 60-1N-01
St. Paul, MN 55144

471. Gerald R. Martin
Fleetguard, Inc.
Cookeville, TN 38501

472. Steven C. Martin
Advanced Refractory
Technologies, Inc.
699 Hertel Avenue
Buffalo, NY 14207

473. Kelly J. Mather
Williams International
Corporation
2280 West Maple Road
P.O. Box 200
Walled Lake, MI 48088

474. James P. Mathers
3M Company
3M Center
Building 201-3N-06
St. Paul, MN 55144

475. Marshall Mayer
Instron Corporation
3815 Presidential Parkway,
Suite 100
Atlanta, GA 30340

476. Ron Mayville
Arthur D. Little, Inc.
15-163 Acorn Park
Cambridge, MA 02140

477. F. N. Mazadarany
General Electric Company
Research Laboratory
Building K-1, Room MB-159
P.O. Box 8
Schenectady, NY 12301

478. James W. McCauley
Alfred University
NYS College of Ceramics
Binns-Merrill Hall
Alfred, NY 14802

479. Louis R. McCreight
2763 San Ramon Drive
Rancho Palos Verdes, CA 90274

480. Colin F. McDonald
McDonald Thermal Engineering
1730 Castellana Road
La Jolla, CA 92037

481. Bryan J. McEntire
Norton Company, TRW Ceramics
Goddard Road
Northboro, MA 01532-1545

482. Thomas D. McGee
Iowa State University
Materials Science and Engineering
Department
110 Engineering Annex
Ames, IA 50011

483. Carol McGill
Corning Inc.
Sullivan Park, FR-02-08
Corning, NY 14831

484. H. Christopher McGowan
Advanced Ceramic Technologies, Inc.
72 Veronica Avenue, Unit 10
Somerset, NJ 08873

485. Malcolm G. McLaren
Rutgers University
Department of Ceramics
Post Office Box 909
Piscataway, NJ 08854

486. T. C. McLaren
Cameron Forged Products Company
P.O. Box 1212
Houston, TX 77251-1212

487. James McLaughlin
Sundstrand Power Systems
4400 Ruffin Road
P.O. Box 85757
San Diego, CA 92186-5757

488. Dennis McMurtry
EG&G Idaho, Inc.
Idaho National Engineering Laboratory
P.O. Box 1625
Idaho Falls, ID 83415

489. D. B. Meadowcroft
National Power
Technology and Environmental Centre
Kelvin Avenue
Leatherhead Surrey KT22 7SE
ENGLAND

490. Arthur F. McLean
6225 North Camino Almonte
Tucson, AZ 85718

491. Pankaj K. Mehrotra
Kennametal Inc.
P.O. Box 639
Greensburg, PA 15601

492. Joseph J. Meindl
Reynolds International, Inc.
6603 West Broad Street
Post Office Box 27002
Richmond, VA 23261-7003

493. Michael D. Meiser
Allied-Signal Aerospace Company
Garrett Ceramic Components Division
19800 South Van Ness Avenue
Torrance, CA 90509

494. George Messenger
National Research Council of Canada
Engine laboratory
Building M-7
Ottawa Ontario K1A OR6
CANADA

495. D. Messier
U.S. Army Materials Technology Laboratory
SLCMT-EMC
405 Arsenal Street
Watertown, MA 02172-0001

496. Gary L. Messing
Pennsylvania State University
Ceramic Science and Engineering Department
119 Steidle Building
University Park, PA 16802

497. Arthur G. Metcalfe
Arthur G. Metcalfe and Associates, Inc.
2108 East 24th Street
National City, CA 91950

498. R. Metselaar
Eindhoven University
Centre for Technical Ceramics
P.O. Box 513
Eindhoven 5600 MB
THE NETHERLANDS

499. David J. Michael
Harbison-Walker Refractories Company
P.O. Box 98037
Pittsburgh, PA 15227

500. Ken Michaels
Chrysler Motors Corporation
Ceramics Development
Metallurgical Processes
P.O. Box 1118, CIMS:418-17-09
Detroit, MI 48288

501. Bernd Michel
Institute of Mechanics
Fracture and Micromechanics
Department
P.O. Box 408
D-9010 Chemnitz
GERMANY

502. John V. Milewski
Superkinetics, Inc.
P.O. Box 8029
Santa Fe, NM 87504

503. Brad Miller
Norton Company
Advanced Ceramics
Goddard Road
Northboro, MA 01532-1545

504. Mike Miller
McGraw Hill Aviation Week
Performance Materials
1156 15th Street, N.W.
Washington DC 20005

505. Charles W. Miller, Jr.
Centorr Furnaces/Vacuum
Industries
542 Amherst Street
Nashua, NH 03063

506. R. Mininni
Enichem America
2000 Cornwall Road
Monmouth Junction, NJ 08852

507. Michele V. Mitchell
Allied-Signal Aerospace
Company
Garrett Ceramic Components
Division
19800 South Van Ness Avenue
Torrance, CA 90501-1149

508. Howard Mizuhara
GTE - WESGO
477 Harbor Boulevard
Belmont, CA 94002

509. Bill Moehle
Ethyl Corporation
R&D Laboratories
Post Office Box 341
Baton Rouge, LA 70821

510. Helen Moeller
Babcock and Wilcox
Post Office Box 11165
Lynchburg, VA 24506-1165

511. Francois R. Mollard
Metalworking Technology, Inc.
1450 Scalp Avenue
Johnstown, PA 15904

512. Phil Mooney
Panametrics
NDE Division
221 Crescent Street
Waltham, MA 02254

513. Thomas Morel
Ricardo North America
645 Blackhawk Drive
Westmont, IL 60559

514. Geoffrey P. Morris
3M Company
3M Traffic Control Materials
Division
Bldg. 209-BW-10, 3M Center
St. Paul, MN 55144-1000

515. Jay A. Morrison
Rolls-Royce, Inc.
Engineering and Information
Center, Overlook 1
2849 Paces Ferry Road,
Suite 450
Atlanta, GA 30339-3769

516. Joel P. Moskowitz
Ceradyne, Inc.
3169 Redhill Avenue
Costa Mesa, CA 92626

517. Brij Moudgil
University of Florida
Material Science &
Engineering
Gainesville, FL 32611

518. Thomas W. Mullan
Vapor Technologies Inc.
345 Route 17 South
Upper Saddle River, NJ 07458

519. Lawrence M. Murphy
Solar Energy Research Institute
Thermal Systems Research Branch
1617 Cole Boulevard
Golden, CO 80401

520. M. K. Murthy
MKM Consultants International
10 Avoca Avenue, Unit 1906
Toronto Ontario M4T 2B7
CANADA

521. Solomon Musikant
TransCon Technologies, Inc.
Materials Science & Engineering
1508 Waynesboro Road
Paoli, PA 19301

522. David L. Mustoe
Custom Technical Ceramics
8041 West I-70 Service Road,
Unit 6
Arvada, CO 80002

523. Curtis V. Nakaishi
U.S. Department of Energy
Morgantown Energy Technology
Center
Collins Ferry Road
P.O. Box 880
Morgantown, WV 26507-0880

524. Voshio Nakamura
Faicera Research Institute
2-5-8 Hiyakunin-cho Shinjuku-Ko
Tokyo
JAPAN

525. Pero Nannelli
Pennwalt Corporation
900 First Avenue
Post Office Box C
King of Prussia, PA 19406-0018

526. Samuel Natansohn
GTE Laboratories, Inc.
40 Sylvan Road
Waltham, MA 02254

527. Robert Naum
Applied Resources, Inc.
P.O. Box 241
Pittsford, NY 14534

528. Malcolm Naylor
Cummins Engine Company, Inc.
P.O. Box 3005, Mail Code 50183
Columbus, IN 47202-3005

529. Jeffrey Neil
GTE Laboratories, Inc.
40 Sylvan Road
Waltham, MA 02254

530. Joseph R. Nelli
FMC Corporation
Lithium Division
P.O. Box 3925
Gastonia, NC 28053

531. Fred A. Nichols
Argonne National Laboratory
9700 South Cass Avenue
MCT - Building 212
Argonne, IL 60439

532. H. Nickel
Furschungszentrum Jüelich GmbH
P.O. Box 1913
Jüelich 1-5170 BRD NRW
GERMANY

533. Dale E. Niesz
Rutgers University
Center for Ceramic Research
P.O. Box 909
Piscataway, NJ 08855-0909

534. William D. Nix
Stanford University
Department of Materials Science and Engineering
Stanford, CA 94305

535. Richard D. Nixdorf
ReMaxCo Technologies, Inc.
11317 Snyder Road
Knoxville, TN 37932

536. Bruce E. Novich
Ceramics Process Systems Corporation
155 Fortune Boulevard
Milford, MA 01757

537. Stephen D. Nunn
University of Michigan
Materials Science and Engineering
2300 Hayward Street
2126 H. H. Dow Building
Ann Arbor, MI 48109-2136

538. Brian M. O'Connor
Lubrizol Corporation
Tribology Section
29400 Lakeland Boulevard
Wickliffe, OH 44092

539. Daniel Oblas
GTE Laboratories, Inc.
40 Sylvan Road
Waltham, MA 02254

540. Don Ohanehi
Magnetic Bearings, Inc.
1908 Sussex Road
Blacksburg, VA 24060

541. N. R. Osborne
University of Dayton Research Institute
Metals & Ceramics
300 College Park
Dayton, OH 45469-0172

542. W. Richard Ott
Alfred University
Center for Advanced Ceramic Technology
Alfred, NY 14802

543. William C. Owen
Sundstrand Turbomach
Division of Sundstrand Corporation
4400 Ruffin Road
Post Office Box 85757
San Diego, CA 92138-5757

544. Russell J. Page
Kanthal-Artcor
3001 Redhill Avenue, II-109
Costa Mesa, CA 92705

545. Richard Palicka
Cercom, Inc.
1960 Watson Way
Vista, CA 92083

546. Muktesh Paliwal
GTE Products Corporation
Hawes Street
Towanda, PA 18848-0504

547. Joseph E. Palko
General Electric Company
Research Laboratory
TTD Building, 55-113
P. O. Box 8
Schenectady, NY 12345

548. Hayne Palmour, III
North Carolina State University
Materials Science and Engineering Dept.
Raleigh, NC 27605-7905

549. Joseph N. Panzarino
Norton Company
Advanced Ceramics
Goddard Road
Northboro, MA 01532-1545

550. Pellegrino Papa
Corning Inc.
MP-WX-02-1
Corning, NY 14831

551. E. Beth Pardue
Technology for Energy Corporation
One Energy Center
P.O. Box 22996
Knoxville, TN 37933-0996

552. Soon C. Park
3M Company
3M Center
Building 142-4N-02
P.O. Box 2963
St. Paul, MN 55144

553. Marina R. Pascucci
GTE Laboratories, Inc.
40 Sylvan Road
Waltham, MA 02254

554. Arvid E. Pasto
GTE Laboratories Inc.
40 Sylvan Road
Waltham, MA 02254

555. James W. Patten
Cummins Engine Company, Inc.
Materials Engineering
P.O. Box 3005, Mail Code 50183
Columbus, IN 47202-3005

556. Robert A. Penty
Eastman Kodak Company
KAD/D73 - 35612
901 Elmgrove Road
Rochester, NY 14653

557. Robert W. Pepper
Textron Specialty Materials
2 Industrial Avenue
Lowell, MA 01851

558. Peter Perdue
Detroit Diesel Corporation
Research Advanced Development Group
13400 West Outer Drive, Speed Code A-07
Detroit, MI 48239-4001

559. Bruce Peters
Dow Chemical Company
Building 52
Midland, MI 48667

560. Gary R. Peterson
U.S. Department of Energy
Idaho Operations Office
785 D.O.E. Place
Idaho Falls, ID 83402

561. John J. Petrovic
Los Alamos National Laboratory
Group MST-4, MS:6771
Los Alamos, NM 87545

562. Frederick S. Pettit
University of Pittsburgh
Pittsburgh, PA 15261

563. Ben A. Phillips
Phillips Engineering Company
721 Pleasant Street
St. Joseph, MI 49085

564. Richard C. Phoenix
Ohmtek, Inc.
2160 Liberty Drive
Niagara Falls, NY 14302

565. R. Byron Pipes
University of Delaware
Center for Composite Materials
2001 Spencer Laboratory
Newark, DE 19716

566. Bruce J. Pletka
Michigan Technological University
Metallurgical & Materials Engineering Department
Houghton, MI 49931

567. Robert C. Pohanka
Office of Naval Research
800 North Quincy Street
Code 431
Arlington, VA 22217

568. J. P. Pollinger
Allied-Signal Aerospace Company
Garrett Ceramic Components Division
19800 South Van Ness Avenue
Torrance, CA 90509

569. P. Popper
High Technology Ceramics International Journal
22 Pembroke Drive
Westlands Newcastle-under-Lyme Staffs ST5 2JN
ENGLAND

570. F. Porz
Universitat Karlsruhe
Institut fur Keramik Im Maschinendau
Postfach 6980
D-7500 Karlsruhe
GERMANY

571. Harry L. Potma
Royal Netherlands Embassy
Science and Technology
4200 Linnean Avenue, N.W.
Washington DC 20008

572. Bob Powell
General Motors Research Laboratories
Metallurgy Department
30500 Mound Road
Box 9055
Warren, MI 48090-9055

573. David B. Powell
Southern Research Institute
Experimental Mechanics Section
2000 Ninth Avenue South
P.O. Box 55305
Birmingham, AL 35255-5305

574. Stephen C. Pred
ICD Group, Inc.
1100 Valley Brook Avenue
Lyndhurst, NJ 07071

575. Karl M. Prewo
United Technologies Corporation
Research Center
Silver Lane, MS:24
East Hartford, CT 06108

576. Peter E. Price
Industrial Materials Technology, Inc.
P.O. Box 9565
Andover, MA 01810

577. Joseph M. Proud
GTE Laboratories Inc.
Materials Science Laboratory
40 Sylvan Road
Waltham, MA 02254

578. D. W. Prouse
Ceramatec, Inc.
2425 South 900 West
Salt Lake City, UT 84119

579. Vimal K. Pujari
Norton Company
Advanced Ceramics
Goddard Road
Northboro, MA 01532-1545

580. Carr Lane Quackenbush
Norton Company
Advanced Ceramics
Goddard Road
Northboro, MA 01532-1545

581. Brian Quigy
National Aeronautics and Space Administration
Energy Systems Office
Washington, DC 20546

582. George Quinn
National Institute of Standards and Technology
Inorganic Materials Division
Building 223
Gaithersburg, MD 20899

583. Dennis T. Quinto
Kennametal, Inc.
Phillip M. McKenna Laboratory
Post Office Box 639
Greensburg, PA 15601

584. Ramas V. Raman
Ceracon, Inc.
1101 North Market Boulevard, Suite 9
Sacramento, CA 95834

585. K. S. Ramesh
Battelle Columbus Laboratories
Metals and Ceramics Department
505 King Avenue
Columbus, OH 43201-2693

586. Charles F. Rapp
Owens Corning Fiberglass
2790 Columbus Road
Granville, OH 43023-1200

587. Dennis W. Readey
Colorado School of Mines
Department of Metallurgy and Materials Engineering
Golden, CO 80401

588. Michael J. Readey
Coors Ceramics Company
R&D
17750 West 32nd Street
Golden, CO 80401

589. Wilfred J. Rebello
PAR Enterprises, Inc.
12601 Clifton Hunt Lane
Clifton, VA 22024

590. H. E. Rebenne
GTE Laboratories, Inc.
40 Sylvan Road
Waltham, MA 02254

591. Harold Rechter
Chicago Fire Brick Company
R&D
7531 South Ashland Avenue
Chicago, IL 60620

592. Robert R. Reeber
U.S. Army Research Office
Post Office Box 12211
Research Triangle Park, NC 27709

593. K. L. Reifsnider
Virginia Polytechnic Institute and State University
Department of Engineering Science and Mechanics
Blacksburg, VA 24061

594. Paul E. Rempes
McDonnell Douglass Missle Systems Company
Department EPE-3
Building 107, Level 1
Post Office Box 516
Mail Code 106608
St. Louis, MO 63166-0516

595. Gopal S. Revankar
John Deere Company
Metals Research
3300 River Drive
Moline, IL 61265

596. K. T. Rhee
Rutgers University
Mechanical Engineering
Post Office Box 909
Piscataway, NJ 08854

597. James Rhodes
Advanced Composite Materials Corporation
1525 South Buncombe Road
Greer, SC 29651

598. Roy W. Rice
W. R. Grace and Company
7379 Route 32
Columbus, MD 21044

599. David W. Richerson
Ceramatec, Inc.
2425 South 900 West
Salt Lake City, UT 84119

600. Scott L. Richlen
U.S. Department of Energy
Office of Industrial Technologies
1000 Independence Avenue, S.W.
Forrestal Building CE-221
Washington, DC 20585

601. Michel Rigaud
Ecole Polytechnique
Campus Universite De Montreal
P.O. Box 6079, Station A
Montreal, P.Q Quebec H3C 3A7
CANADA

602. R. E. Riman
Rutgers University
Ceramics Engineering Department
P.O. Box 909
Piscataway, NJ 08855-0909

603. Barry Ringstrom
Superior Graphite Company
P.O. Box 2373
Smyrna, GA 30081

604. John E. Ritter
University of Massachusetts
Mechanical Engineering Department
Amherst, MA 01003

605. Frank L. Roberge
Allied-Signal Aerospace Company
Garrett Auxiliary Powder Division
2739 East Washington Street
P.O. Box 5227
Phoenix, AZ 85010

606. W. Eric Roberts
Advanced Ceramic Technology, Inc.
990 "F" Enterprise Street
Orange, CA 92667

607. Martha Rohr
U.S. Department of Energy
Oak Ridge Operations
Building 4500N
P.O. Box 2008, MS:6269
Oak Ridge, TN 37831-6269

608. Y. G. Roman
TNO TPD Keramick
P.O. Box 595
Einhoven 5600 AN
HOLLAND

609. Mark D. Roos
Carborundum Company
P.O. Box 156
Niagara Falls, NY 14302

610. Michael Rossetti
Arthur D. Little, Inc.
15 Acorn Park
Cambridge, MA 01240

611. Barry R. Rossing
Lanxide Corporation
1300 Marrows Road
Newark, DE 19714-6077

612. Steven L. Rotz
Lubrizol Corporation
29400 Lakeland Boulevard
Wickliffe, OH 44092

613. Bruce Rubinger
Global Competitiveness, Inc.
One Devonshire Place
Suite 1011
Boston, MA 02109

614. Robert Ruh
Wright Laboratory
WL/MLLM
Wright-Patterson AFB, OH 45433

615. Robert J. Russell
17 Highgate Road
Framingham, MA 01701

616. L. William Sahley
Supermaterials Company
24400 Highland Road
Richmond Heights, OK 44143

617. Jon A. Salem
NASA Lewis Research Center
21000 Brookpark Center
Cleveland, OH 44135

618. W. A. Sanders
NASA Lewis Research Center
21000 Brookpark Road
MS:49-3
Cleveland, OH 44135

619. J. Sankar
North Carolina A&T State University
Department of Mechanical Engineering
Greensboro, NC 27411

620. Vin K. Sarin
Boston University
Department of Manufacturing Engineering
44 Cummington Street
Boston, MA 02215

621. Yasushi Sato
NGK Spark Plugs (U.S.A.), Inc.
1200 Business Center Drive, Suite 300
Mt. Prospect, IL 60056

622. Maxine L. Savitz
Allied-Signal Aerospace Company
Garrett Ceramic Components Division
19800 South Van Ness Avenue
Torrance, CA 90501

623. Ashok Saxena
Georgia Institute of Technology
Materials Engineering
Atlanta, GA 30332-0245

624. David W. Scanlon
Instron Corporation
100 Royall Street
Canton, MA 02021

625. Charles A. Schacht
Schacht Consulting Services
12 Holland Road
Pittsburgh, PA 15235

626. Richard Schapery
Texas A&M University
Civil Engineering Department
College Station, TX 77843

627. Jim Schienle
Allied-Signal Aerospace Company
Garrett Auxiliary Power Division
2739 East Washington Street
Post Office Box 5227, MS:1302-2P
Phoenix, AZ 85010

628. Liselotte J. Schioler
Air Force Office of Scientific Research
Bolling AFB
Washington, DC 20332-6448

629. Richard A. Schmidt
Battelle Columbus Laboratories
Mechanics Section
505 King Avenue
Columbus, OH 43201-2693

630. Arnie Schneck
Deere & Company Technical Center
Post Office Box 128
Wood-Ridge, NJ 07075

631. John C. Schneider
San Juan Technologies
P.O. Box 49326
Colorado Springs, CO 80949-9326

632. Gary Schnittgrund
Rocketdyne, BA05
6633 Canoga Avenue
Canoga Park, CA 91303

633. Mark Schomp
Lonza, Inc.
Corporate Headquarters
17-17 Route 208
Fair Lann, NJ 07410

634. Joop Schoonman
Delft University of Technology
Laboratory for Inorganic Chemistry
P.O. Box 5045
2600 GA Delft
THE NETHERLANDS

635. John Schuldies
Industrial Ceramic Technology, Inc.
37 Enterprise Drive
Ann Arbor, MI 48103

636. R. B. Schulz
U.S. Department of Energy
Office of Transportation Technologies
Forrestal Building CE-34
Washington, DC 20585

637. Murray A. Schwartz
Materials Technology Consulting, Inc.
30 Orchard Way, North
Potomac, MD 20854

638. Peter Schwarzkopf
SRI International
333 Ravenswood Avenue
Menlo Park, CA 94025

639. Thomas C. Schweizer
Princeton Economic Research, Inc.
12300 Twinbrook Pkwy., Suite 650
Rockville, MD 20852

640. Nancy Scoville
Thermo Electron Technologies
74 West Street
P.O. Box 9046
Waltham, MA 02254-9046

641. Thomas M. Sebestyen
U.S. Army Tank Automotive Command
AMSTA-RGRT
Warren, MI 48397-5000

642. Brian Seegmiller
Coors Ceramics Company
17750 West 32nd Street
Golden, CO 80401

643. T. B. Selover
AICRE/DIPPR
3575 Traver Road
Shaker Heights, OH 44122

644. Charles E. Semler
Semler Materials Services
4160 Mumford Court
Columbus, OH 43220

645. Thomas Service
Service Engineering Laboratory
324 Wells Street
Greenfield, MA 01301

646. Kish Seth
Ethyl Corporation
R&D Laboratories
P.O. Box 341
Baton Rouge, LA 70821

647. Peter T. B. Shaffer
Technical Ceramics Laboratories, Inc.
4045 Nine/McFarland Drive
Alpharetta, GA 30201

648. Richard K. Shaltens
NASA Lewis Research Center
21000 Brookpark Road, MS:301-2
Cleveland, OH 44135

649. Robert S. Shane
238 Hemlock Road
Wynnewood, PA 19096

650. Daniel Shanefield
Rutgers University
Ceramics Engineering Department
P.O. Box 909
Piscataway, NJ 08855-0909

651. Laurel M. Sheppard
Advanced Materials and Processes
Route 87
Metals Park, OH 44073

652. Dinesh K. Shetty
University of Utah
Department of Materials Science and Engineering
Salt Lake City, UT 84112

653. Masahide Shimizu
Ceramic Society of Japan
2-2-503 Takiyama 6-chome
Higashikurume-Shi Tokyo 203
JAPAN

654. John Shipinski
Toyota Technical Center
Technical Research Department
2000 Town Center, Suite 500
Southfield, MI 48075

655. Thomas Shreves
American Ceramic Society, Inc.
Library
757 Brooksedge Plaza Drive
Westerville, OH 43081-2821

656. Jack D. Sibold
Coors Ceramics Company
17750 West 32nd Street
Golden, CO 80401

657. George H. Siegel
Point North Associates, Inc.
P.O. Box 907
Madison, NJ 07940

658. Neal Sigmon
U.S. House of Representatives
Subcommittee on Interior and Related Events
Rayburn Building, Room B308
Washington, DC 20515

659. Richard Silberglitt
Quest Research Corporation
7600 Leesburg Pike #A
Falls Church, VA 22043

660. Mary Silverberg
Norton Company
Advanced Ceramics Library
Goddard Road
Northboro, MA 01532-1545

661. Gurpreet Singh
Department of the Navy
Internal Combustion & Gas Turbine Engine Division
Code 56X31
Washington DC 20362-5101

662. A. Sinha
North Carolina A&T State University
Department of Mechanical Engineering
Greensboro, NC 27411

663. Maurice J. Sinnott
University of Michigan
Chemical and Metallurgical Engineering
5106 IST Building
Ann Arbor, MI 48109-2099

664. John Skildum
3M Company
3M Center
Building 224-2S-25
St. Paul, MN 55144

665. David P. Smith
Hoskins, Rees & Smith
1910 Cochran Road
Manor Oak II, Suite 658
Pittsburgh, PA 15220

666. Jay R. Smyth
Allied-Signal Aerospace Company
Garrett Auxillary Power Division
2739 East Washington Street
Post Office Box 5227
MS:93-173/1303-207
Phoenix, AX 85010

667. Rafal Sobotowski
British Petroleum Company
Technical Center, Broadway
3092 Broadway Avenue
Cleveland, OH 44115

668. E. Solidum
Allied-Signal Aerospace Company
Garrett Ceramic Components Division
19800 South Van Ness Avenue
Torrance, CA 90509

669. S. Somiya
Nishi Tokyo University
3-7-19 Seijo, Setagaya
Tokyo 157
JAPAN

670. Thomas M. Sopko
Lubrizol Enterprises, Inc.
29400 Lakeland Boulevard
Wickliffe, OH 44092

671. Boyd W. Sorenson
DuPont Lanxide Composites
1300 Marrows Road
P.O. Box 6077
Neward, DE 19707

672. Richard M. Spriggs
Alfred University
Center for Advanced Ceramic Technology
Alfred, NY 14802

673. Charles Spuckler
NASA Lewis Research Center
21000 Brookpark Road
MS: 5-11
Cleveland, OH 44135-3191

674. M. Srinivasan
Material Solutions
Post Office Box 663
Grand Island, NY 14702-0663

675. L. Brian Starling
ICI Advanced Ceramics
2055 East Technology Circle
Tempe, AZ 85284

676. Gordon L. Starr
Cummins Engine Company, Inc.
Design & Technology
Post Office Box 3005
Mail Code 50182
Columbus, IN 47202-3005

677. Jim Stevenson
Windrock, Inc.
103-B Fairbanks Road
Oak Ridge, TN 37830

678. Tom Stillwagon
Allied-Signal Aerospace Company
AiResearch Los Angeles Division, Dept. 93274
2525 West 190th Street, MS:T-42
Torrance, CA 90509

679. Harold L. Stocker
Allison Gas Turbines
Post Office Box 420
Indianapolis, IN 46206

680. Paul D. Stone
Dow Chemical Company
1801 Building
Midland, MI 48674

681. Roger Storm
Carborundum Company
Niagara Falls Technology Center
Post Office Box 832
Niagara Falls, NY 14302

682. Peter A. Stranges
4 Chittenden Lane
Owings Mills, MD 21117

683. F. W. Stringer
Aero & Industrial Technology Ltd.
P.O. Box 46 Woodtop
Burnley Lancs BB11 4BX
ENGLAND

684. Thomas N. Strom
NASA Lewis Research Center
21000 Brookpark Road
MS: 86-6
Cleveland, OH 44135

685. Jerry Strong
Albright & Wilson
Post Office Box 26229
Richmond, VA 23260

686. M. F. Stroosnijder
Institute for Advanced Materials
Joint Research Centre
21020 Ispra (VA)
ITALY

687. T. S. Sudarshan
Materials Modification, Inc.
2946-2H Sleepy Hollow Road
P.O. Box 4817
Falls Church, VA 22044

688. Karsten Styhr
30604 Ganado Drive
Rancho Palos Verdes, CA 90274

689. Richard Suddeth
Boeing Motor Airplane Company
Post Office Box 7730
MS:K-76-67
Wichita, KS 67277

690. M. J. Sundaresan
University of Miami
Mechanical Engineering
Department
P.O. Box 248294
Coral Gables, FL 33124

691. Paul Sutor
Midwest Research Institute
425 Volker Boulevard
Kansas City, MO 64116

692. P. L. Sutton
U.S. Department of Energy
Office of Transportation
Technologies
1000 Independence Avenue, S.W.
Forrestal Building CE-322
Washington, DC 20585

693. Willard H. Sutton
United Technologies
Corporation
Research Center, MS:24
Silver Lane
East Hartford, CT 06108

694. Ron Sviben
100 Indel Avenue
Rancocas, NJ 08073

695. J. J. Swab
U.S. Army Materials Technology
Laboratory
Ceramics Research Division
SLCMT-EMC
405 Arsenal Street
Watertown, MA 02172

696. John W. Swain, Jr.
Kollmorgen Corporation
PCK Technology Division
15424 Garrison Lane
Southgate, MI 48195

697. Robert E. Swanson
Metalworking Technology, Inc.
1450 Scalp Avenue
Johnstown, PA 15904

698. Steve Szaruga
Air Force Wright Aeronautical
Laboratory
Materials Directorate
WL/MLBC
Wright-Patterson
AFB, OH 45433-6533

699. Yo Tajima
NGK Spark Plug Company, Ltd.
NTK Technical Ceramic Division
2808 Iwasaki
Komaki-shi Aichi-ken 485
JAPAN

700. Anthony C. Taylor
U.S. House of Representatives
Committee on Science and
Technology
Rayburn Building, Room 2321
Washington, DC 20515

701. Fred Teeter
5 Tralee Terrace
East Amherst, NY 14051

702. Monika O. Ten Eyck
Carborundum Company
Technology Division
Post Office Box 832
Niagara Falls, NY 14302

703. David F. Thompson
Corning Glass Works
SP-DV-02-1
Corning, NY 14831

704. Eberhard Tiefenbacher
Daimler-Benz AG Abt. F1S
Mercedes-Strabe 136
Stuttgart 60
GERMANY

705. John K. Tien
Columbia University
Center for Strategic Materials
1137 S.W. Mudd Building
New York, NY 10027

706. T. Y. Tien
University of Michigan
Materials Science and
Engineering Department
Dow Building
Ann Arbor, MI 48103

707. Julian M. Tishkoff
Air Force Office of Scientific
Research
AFOSR/NA
Bolling AFB, DC 20332-6448

708. Louis E. Toth
National Science Foundation
Division of Materials Research
1800 "G" Street, N.W.
Washington, DC 20550

709. D. M. Tracey
Norton Company
Advanced Ceramics
Goddard Road
Northboro, MA 01532-1545

710. Richard E. Tressler
Pennsylvania State University
Ceramic Science and
Engineering Department
201 Steidle Building
University Park, PA 16802

711. Dick Trippett
Allison Gas Turbine
P.O. Box 420, MS:W-16
Indianapolis, IN 46206-0420

712. L. J. Trostel, Jr.
Box 199
Princeton, MA 01541

713. W. T. Tucker
General Electric Company/CRD
Building K1-4C35
P. O. Box 8
Schenectady, NY 12301

714. Masanori Ueki
Nippon Steel Corporation
Central R&D Bureau
1618 Ida
Nakahara-Ku Kawasaki 211
JAPAN

715. Filippo M. Ugolini
ATA Studio
Via Degli Scipioni, 268A
ROMA 00192
ITALY

716. Donald L. Vaccari
General Motors Corporation
Allison Gas Turbine Division
2001 South Tibbs Avenue
Post Office Box 420
Speed Code T10B
Indianapolis, IN 46206-0420

717. Carl F. Van Conant
Boride Products, Inc.
2879 Aero Park Drive
Traverse City, MI 49684

718. Marcel H. Van De Voorde
Commission of the European Communities
Institute for Advanced Materials
Joint Research Centre
P.O. Box 2
1755 ZG Petten
THE NETHERLANDS

719. O. Van Der Biest
Katholieke Universiteit Leuven
Departement Metaalkunde en Toegepaste
de Croylaan 2
B-3030 Leuven
BELGIUM

720. Edward C. Van Reuth
Technology Strategies, Inc.
10722 Shingle Oak Court
Burke, VA 22015

721. Mark Van Roode
Solar Turbines, Inc.
2200 Pacific Highway
Mail Zone R-1
San Diego, CA 92138

722. Michael Vannier
Washington University, St. Louis
Mallinckrodt Institute of Radiology
510 South Kings Highway
St. Louis, MO 63110

723. Stan Venkatesan
Southern Coke & Coal Corporation
P.O. Box 52383
Knoxville, TN 37950

724. V. Venkateswaran
Carborundum Company
Niagara Falls R&D Center
Post Office Box 832
Niagara Falls, NY 14302

725. Dennis Viechnicki
U.S. Army Materials Technology Laboratory
405 Arsenal Street
Watertown, MA 02172-0001

726. Ted Vojnovich
U.S. Department of Energy
Office of Transportation Technologies
1000 Independence Avenue, S.W.
Forrestal Building CE-34
Washington, DC 20585

727. John D. Volt
E. I. Dupont de Nemours & Company, Inc.
P.O. Box 80262
Wilmington, DE 19880

728. John B. Wachtman
Rutgers University
Ceramics Department
Post Office Box 909
Piscataway, NJ 08855

729. Shigetaka Wada
Toyota Central Research Labs, Inc.
Nagakute Aichi 480-11
JAPAN

730. Janet Wade
Allied-Signal Aerospace Company
Garrett Auxiliary Power Division, Department 93-772
2739 East Washington Street
P.O. Box 5227, MS:1303-2
Phoenix, AZ 85010

731. Richard L. Wagner
Ceramic Technologies, Inc.
537 Turtle Creek South Drive, Suite 24D
Indianapolis, IN 46227

732. Daniel J. Wahlen
Kohler, Co.
444 Highland Drive
Kohler, WI 53044

733. Ingrid Wahlgren
Royal Institute of Technology
Studsvik Library
S-611 82 Nykoping
SWEDEN

734. Ron H. Walecki
Garrett Ceramics
19800 Van Ness Avenue
Torrance, CA 90501

735. Michael S. Walsh
Vapor Technologies Inc.
2100 Central Avenue
Boulder, CO 80301

736. Chien-Min Wang
Industrial Technology Research Institute
Materials Research Laboratories
195 Chung-Hsing Road, Sec. 4
Chutung Hsinchu 31015 R.O.C.
TAIWAN

737. Robert M. Washburn
ASMT
11203 Colima Road
Whittier, CA 90604

738. Harlan L. Watson
U.S. House of Representatives
Committee on Science and Technology
Rayburn Building, Suite 2321
Washington, DC 20515

739. John D. Watson
Broken Hill Proprietary Company, Ltd.
Melbourne Research Laboratories
245 Wellington Road
Mulgrave 3170 Victoria
AUSTRALIA

740. Gerald Q. Weaver
Carborundum Specialty Products
42 Linus Allain Avenue
Gardner, MA 01440-2478

741. R. W. Weeks
Argonne National Laboratory
MCT-212
9700 South Cass Avenue
Argonne, IL 60439

742. Ludwig Weiler
ASEA Brown Boveri AG
Corporate Research
Eppelheimer Str. 82
D-6900 Heidelberg
GERMANY

743. James Wessel
Dow Corning Corporation
1800 "M" Street, N.W.,
Suite 325 South
Washington DC 20036

744. Albert R. C. Westwood
Martin Marietta Laboratories
R&D
1450 South Rolling Road
Baltimore, MD 21227

745. Thomas J. Whalen
Ford Motor Company
26362 Harriet
Dearborn Heights, MI 48127

746. Ian A. White
Hoeganaes
River Road and Taylors Lane
Riverton, NJ 08077

747. Alan Whitehead
General Electric Company
1 River Road, 55-111
Schenectady, NY 12345

748. Sheldon M. Wiederhorn
National Institute of Science and Technology
Building 223, Room A329
Gaithersburg, MD 20814

749. D. S. Wilkinson
McMaster University
Materials Science and
Engineering Department
1280 Main Street, West
Hamilton Ontario L8S 4L7
CANADA

750. James C. Williams
General Electric Company
Engineering Materials
Technology Labs
One Neumann Way
Mail Drop: H85
Cincinnati, OH 45215-6301

751. Janette R. Williams
Kollmorgen Corporation
PCK Technology Division
322 L.I.E. South Service Road
Melville, NY 11747

752. Steve Williams
RCG Hagler Bailly, Inc.
370 L'Enfant Promonade, S.W.,
Suite 700
Washington DC 20024

753. Craig A. Willkens
Norton Company
Advanced Ceramics
Goddard Road
Northboro, MA 01532-1545

754. Roger R. Wills
TRW, Inc.
Valve Division
1455 East 185th Street
Cleveland, OH 44110

755. David Gordon Wilson
Massachusetts Institute of
Technology
Mechanical Engineering Department
77 Massachusetts Avenue,
Room 3-455
Cambridge, MA 02139

756. Matthew F. Winkler
Seaworthy Systems, Inc.
P.O. Box 965
Essex, CT 06426

757. Gerhard Winter
Hermann C. Starck Berlin GmbH,
Werk Goslar
P.O. Box 25 40
D-3380 Goslar 3380
GERMANY

758. W. L. Winterbottom
Ford Motor Company
Material Systems Reliability
Department
20000 Rotunda Drive
SRL, Room E-3182
P.O. Box 2053
Dearborn, MI 48121

759. David Wirth
Coors Ceramics Company
600 9th Street
Golden, CO 80401

760. Thomas J. Wissing
Eaton Corporation
Engineering & Research Center
26201 Northwestern Highway
Post Office Box 766
Southfield, MI 48037

761. James C. Withers
MER Corporation
7960 South Kolb Road
Building F
Tucson, AZ 85706

762. Dale Wittmer
Southern Illinois University
Department of Mechanical
Engineering
Carbondale, IL 62901

763. Stanley M. Wolf
U.S. Department of Energy
Office of Industrial
Technologies
1000 Independence Avenue, S.W.
Forrestal Building CE-232
Washington, DC 20585

764. Warren W. Wolf
Owens Corning Fiberglass
2790 Columbus Road, Route 16
Granville, OH 43023

765. George W. Wolter
Howmet Turbine Components Corporation
Technical Center
699 Benston Road
Whitehall, MI 49461

766. James C. Wood
NASA Lewis Research Center
21000 Brookpark Road
MS:86-6
Cleveland, OH 44135

767. Marrill Wood
LECO Corporation
Augusta Division
P.O. Box 211688
Augusta, GA 30917-1688

768. John H. Woody, Jr.
D. M. Steward Mfg. Company
1200 East 36th Street
P.O. Box 510
Chattanooga, TN 37401

769. Wayne L. Worrell
University of Pennsylvania
Department of Materials Science and Engineering
3231 Walnut Street
Philadelphia, PA 19104

770. Roger P. Worthen
Eaton Corporation
Engineering and Research Center
26201 Northwestern Highway
Post Office Box 766
Southfield, MI 48076

771. John F. Wosinski
Corning Inc.
ME-2 E-5 H8
Corning, NY 14830

772. Ian G. Wright
Battelle Columbus Laboratories
505 King Avenue
Columbus, OH 43201

773. Ruth Wroe
ERDC
Metals & Materials Industries Division
Capenhurst Chester CH1 6ES
ENGLAND

774. Bernard J. Wrona
Advanced Composite Materials Corporation
1525 South Buncombe Road
Greer, SC 29651

775. Carl C. M. Wu
Naval Research Laboratory
Ceramic Branch, Code 6373
Washington DC 20375

776. J. G. Wurm
Commission of the European Communities
Advanced Materials Research Programme
Rue de la Loi 200
B-1049 Brussels
BELGIUM

777. John C. Wurst
University of Dayton Research Institute
300 College Park
Dayton, OH 45469-0101

778. Roy Yamamoto
Texaco Inc.
P.O. Box 509
Beacon, NY 12508-0509

779. John Yamanias
Allied-Signal, Inc.
Ceramics Program
Post Office Box 1021
Morristown, NJ 07962-1021

780. Harry C. Yeh
Allied-Signal Aerospace Company
Garrett Ceramic Components Division
19800 South Van Ness Avenue
Torrance, CA 90509

781. Hiroshi Yokoyama
Hitachi Research Lab
4026 Kuji-Cho
Hitachi-shi Ibaraki 319-12
JAPAN

782. Thomas M. Yonushonis
Cummins Engine Company, Inc.
Post Office Box 3005
Mail Code 50183
Columbus, IN 47202-3005

783. Thomas J. Yost
Corning Inc.
Technical Products Division,
Main Plant 21-1-2
Corning, NY 14831

784. Jong Yung
Sundstrand Aviation Operations
Department 789-6
4747 Harrison Avenue
Rockford, IL 61125

785. Don Zabierek
Air Force Wright
Aeronautical Laboratory
AFWAL/POTC
Wright-Patterson AFB, OH 45433

786. A. L. Zadoks
Caterpillar Inc.
Technical Center, Building L
P.O. Box 1875
Peoria, IL 61656-1875

787. Avi Zangvil
University of Illinois
Materials Research Laboratory
104 South Goodwin Avenue
Urbana, IL 61801

788. Anne Marie Zerega
U.S. Department of Energy
Office of Energy Research,
ER-42
Washington, DC 20585

789. Martin Zlotnick
Nichols Research Corporation
8618 Westwood Center Drive
Suite 200
Vienna, VA 22180-2222

790. Carl Zweben
General Electric Company
P.O. Box 8555, VFSC/V4019
Philadelphia, PA 19101

791. Klaus M. Zwilsky
National Research Council
National Materials
Advisory Board
2101 Constitution Avenue
Washington, DC 20418

792. Department of Energy
DOE Field Office, Oak Ridge
Assistant Manager for Energy
Research and Development
Post Office Box 2001
Oak Ridge, TN 37831-8600

793-802. Department of Energy
Office of Scientific and
Technical Information
Office of Information
Services
Post Office 62
Oak Ridge, TN 37831

For distribution by microfiche
as shown in DOE/OSTI-4500,
Distribution Category UC-332
(Ceramics/Advanced Materials).

*U.S. GOVERNMENT PRINTING OFFICE: 1991-548-134/40024